Częstochowa University of Technology

Faculty of Mechanical Engineering

Department of Thermal Machinery

Doctoral Thesis

# Numerical modeling of a turbulent boundary layer on wavy and irregular surfaces

by

**Piotr Kamiński**

Supervisor: Prof. dr hab. inż. Artur Tyliszczak
Co-supervisor: Dr hab. inż. Paweł Niegodajew, prof. PCz

January 2026

# Acknowledgements

In the first place, I would like to thank my supervisor, Prof. Artur Tyliszczak, for giving me the opportunity to undertake this PhD journey. It has been an invaluable period of academic development and growth. His guidance and support have been greatly appreciated throughout, and his mentorship has profoundly shaped my work and my academic development.

I would like to express my gratitude to Prof. Witold Elsner for supporting my scholarship within his NCN project, *Development of a new passive flow control method based on in-depth analysis of near-wall physical phenomena*. The tasks carried out within this project were a strong driving force in my development and enabled me to gain knowledge and experience that I would not have acquired otherwise. I am sincerely grateful for this opportunity.

I would also like to thank Dr. Paweł Niegodajew for his extensive support throughout my PhD. His involvement went far beyond what could be expected, and our many discussions were essential to my progress. I am honoured to have him as the co-supervisor of this work.

Finally, I gratefully acknowledge the Polish high-performance computing infrastructure PLGrid (ACK Cyfronet AGH) for providing computing resources under grants PLG/2022/015892, PLG/2023/016731, PLG/2024/017751, and PLG/2025/018864. Without these resources, this work would not have been possible.

# Preface

This thesis is based on a series of peer-reviewed publications, listed in the 'List of Publications', each contributing to the research goal of exploring passive control of turbulent boundary layer using surface waviness. The structure of the thesis is designed to guide the reader from a broad introduction to the research context through the literature review, specific methodologies of performing simulations and analyses, the obtained results, and conclusions arising from the publications.

The thesis opens with the 'Introduction and objectives', which provides a brief overview of the research motivation. This is followed by a description of the research problem, which directly leads to the formulation of the study's objectives.

Chapter 1 (Literature Review) presents a critical examination of the current state of the art in research devoted to passive flow control, with a particular focus on surface waviness and its relevance in both aerodynamic and hydrodynamic contexts. The review highlights existing knowledge gaps and positions the present study within the broader framework of ongoing research. Moreover, it explores an alternative application of surface waviness, namely its potential to enhance heat transfer in scenarios where appropriate thermal management, such as intensified cooling or heating, is required.

Chapter 2 (Methodology) outlines the investigative approaches employed in this thesis, with particular emphasis on numerical methods, namely Large Eddy Simulations (LES) and Reynolds-averaged Navier-Stokes (RANS) approaches. The chapter also details the computational domains used in the simulations, providing the necessary foundation for the subsequent analyses.

Additionally, since experimental data are used to validate the numerical results, a description of the experimental setup is included in this chapter.

The central part of the thesis is presented in Chapter 3 (Comments to the Articles), where each publication is summarized and placed in context. This chapter synthesizes the key findings and highlights the logical development of the research, illustrating how successive studies build upon one another to construct a cohesive and systematic exploration of the overall research objective.

The thesis concludes with Chapter 4 (Conclusions), which outlines the key findings and critical contributions of the research. This chapter also reflects on the extent to which the objective of the thesis has been achieved. Finally, the original peer-reviewed articles are included in their entirety (Chapter 5 - Papers), serving as a formal record of the scientific work conducted throughout the doctoral studies.

# List of publications

Paper 1 Kamiński, P., Niegodajew, P., Dróżdż, A., Sokolenko, V., Tyliszczak, A., & Elsner, W. (2024). Numerical analysis of novel wavy wall based control of turbulent boundary layer separation. Aerospace Science and Technology, 149, 109167.

Paper 2 Kamiński, P., Elsner, W., Tyliszczak, A., & Niegodajew, P. (2025). Sensitivity analysis of wavy wall performance in turbulent separation control: Effects of amplitude and period variations. Journal of Wind Engineering and Industrial Aerodynamics, 260, 106048.

Paper 3 Kamiński, P., Tyliszczak, A., Elsner, W., & Niegodajew, P. (2025). Turbulent separation control with a tilted wavy wall: A promising approach for energy savings in aerodynamic systems. Energy, 324, 135758.

Paper 4 Kamiński, P., Niegodajew, P., Tyliszczak, A., & Elsner, W. (2025). Turbulent separation control on an airfoil surface using a wavy wall. Physics of Fluids, 37(7).

Paper 5 Kamiński, P., Li, Y., Wawrzak, K., Tyliszczak, A., & Noack, B. R. (2024, November). Machine learning-supported CFD optimization of heat transfer in a pipe with a corrugated wall shape. Journal of Physics: Conference Series (Vol. 2899, No. 1, p. 012013). IOP Publishing.

Paper 6 Kamiński, P., Wawrzak, K., Li, Y., Noack, B. R., & Tyliszczak, A. (2025). Design of the wavy wall in a partially heated channel using CFD simulations and human-assisted Bayesian optimization. arXiv preprint arXiv:2509.04030.

# Contents

**Acknowledgements** i

**Preface** iii

**List of publications** v

**Abstract** xi

**Streszczenie** xiii

**Introduction and objectives** xvii

**1 Literature review** 1

1.1 Passive flow control in aerodynamics . . . . . 1

1.1.1 Surface waviness . . . . . 11

1.1.2 Surface waviness as a mean to delay the turbulent separation . . . . . 14

1.2 Passive flow control in heat transfer studies . . . . . 15

1.2.1 Surface waviness for improved heat transfer . . . . . 17

1.2.2 Machine learning aided optimization . . . . . 18

**2 Methodology** **21**

2.1 Turbulent separation control . . . . . 22

2.1.1 Objective outline . . . . . 22

2.1.2 Experimental data . . . . . 23

2.1.3 Large eddy simulations (LES) . . . . . 25

2.2 Heat transfer enhancement . . . . . 28

2.2.1 Objective outline . . . . . 28

2.2.2 Bayesian optimization . . . . . 29

2.2.3 Reynolds-averaged Navier-Stokes (RANS) . . . . . 31

**3 Comments to a series of articles** **35**

3.1 Paper 1 . . . . . 37

3.2 Paper 2 . . . . . 44

3.3 Paper 3 . . . . . 50

3.4 Paper 4 . . . . . 54

3.5 Paper 5 . . . . . 61

3.6 Paper 6 . . . . . 66

**4 Conclusions** **75**

**5 Papers** **79**

**Bibliography** **181**

# Abstract

This dissertation is devoted to the passive control of the turbulent boundary layer (TBL) through the design and optimization of surface waviness. It follows a structured approach based on five research papers (Papers 1–5) and one preprint (Paper 6). Two fields of surface waviness application are explored: aerodynamics and heat transfer. The primary focus is aerodynamics, specifically mitigating TBL separation, which is promoted by an adverse pressure gradient (APG) and occurs when the wall shear stress reaches $\tau_w = 0$. TBL separation is a fundamental problem in aerodynamic applications, leading to increased drag and reduced energy efficiency. Historically, numerous passive flow control methods, which influence TBL without external energy input, have been employed to mitigate separation. Among these, wavy wall (WW), being the research object of this dissertation, has emerged as a promising solution.

Four research papers (Papers 1–4) are devoted to the control of TBL separation, presenting a logical progression of the investigation. In the first stage (Paper 1), LES method is employed to examine APG and zero pressure gradient (ZPG) flows over flat and wavy surfaces, with a detailed focus on near-wall flow physics. The numerical domain is a cuboid and represents a simplification of the real-flow setup, with pressure gradients imposed via boundary conditions. In this configuration, due to the insufficient length of the domain, the detachment of TBL is not observed. Hence, the conclusions regarding TBL separation control are drawn based on changes in $\tau_w$, assuming that its increase indicates a delay in TBL separation. The LES results, validated against experimental data, show that a two-dimensional sinusoidal WW enhances $\tau_w$. Furthermore, it is found that the global pressure gradient strongly influences both the effectiveness of WW in modifying $\tau_w$ and the flow structures that form over WW. A subsequent parametric analysis (Paper 2) explores the influence of WW amplitude ($A$) and wavelength ($\lambda$) on $\tau_w$. The results indicate that both variables critically impact $\tau_w$, enabling either its increase or reduction relative

to the reference configuration. An optimal combination of $A$ and $\lambda$ is identified, which enhances $\tau_w$ significantly compared to the reference design. Building on these findings, a refinement is introduced by incorporating a streamwise or counter-streamwise tilt into the WW design (Paper 3). This modification, which addresses limitations observed in previous studies, ensures an increase in $\tau_w$ by 70% compared to the best-performing sinusoidal WW from Paper 2. Moreover, the new configuration eliminates flow separation in the troughs of WW, thereby reducing the total drag coefficient $C_d$ by 14%. The final stage of the part devoted to aerodynamics (Paper 4) extends this research by evaluating the performance of WW in a more realistic scenario, i.e. where it is embedded into an airfoil-type surface, enabling direct investigation of the separation region, which was not possible in Papers 1-3. It is shown that, in this configuration, WW retains its ability to enhance $\tau_w$. Moreover, a downstream shift of the separation point is observed, confirming the conclusions from previous studies (Papers 1–3). Furthermore, a Reynolds number ($Re$) sensitivity analysis reveals that the effectiveness of WW is strongly dependent on the inflow conditions, with its performance diminishing as $Re$ decreases.

Motivated by the promising achievements in controlling flow separation by WW, its application is extended to enhance heat transfer (Papers 5 and 6). Specifically, the shape of a heated WW section of a channel and of a pipe is optimized. This analysis is particularly relevant for practical applications, since these constitute fundamental components of compact heat exchangers, where wall geometry critically impacts the flow. The objective is to identify a WW configuration that ensures maximal temperature uniformity with minimal losses due to pressure drop. The optimization procedure employs an element of machine learning, the Bayesian optimization method, and combines it with flow simulations and researcher intuition (human-assisted optimization). Consequently, by strategically designing the surface of either the pipe or channel, the thermal-hydraulic efficiency can be significantly altered. For the pipe, the optimal WW shape features two outward-oriented cavities leading approximately threefold reduction in the temperature variance at insignificant rise in the pressure drop. For the channel, the optimal shape is characterized by a progressively increasing WW amplitude. Depending on the number of parameters defining the WW shape, e.g., number of waviness periods, the observed temperature variance can be reduced up to approximately 62 times, with a moderate pressure drop. The optimal and nearly optimal WW shapes promote recirculation within the cavities, which enhances fluid mixing and augments heat transfer from the wall to the core of the flow, while maintaining minimal pressure losses.

# Streszczenie

Niniejsza rozprawa poświęcona jest pasywnemu, t.j. niewymagającemu zewnętrznego źródła energii, sterowaniu turbulentną warstwą przyścienną (ang. *turbulent boundary layer*, TBL) poprzez odpowiednie kształtowanie pofalowanej powierzchni ściany (ang. *wavy wall*, WW). Rozprawa oparta jest na pięciu artykułach (Papers 1–5) oraz jednym preprincie (Paper 6). Praca koncentruje się na dwóch zagadnieniach związanych z aerodynamiką i wymianą ciepła. Główny nacisk położono na pierwsze z nich, gdzie jako cel przyjęto redukcję bądź eliminację oderwania TBL. Zjawisko to, wywołane dodatnim gradientem ciśnienia (ang. *adverse pressure gradient*, APG) i zachodzące, gdy naprężenie styczne na ścianie zanika ($\tau_w = 0$), stanowi fundamentalny problem w aerodynamice, prowadząc do wzrostu współczynnika oporu i znacznych strat energii. Historycznie, w literaturze badano liczne metody kontroli przepływu, oddziałujące w sposób pasywny na przepływ przyścienny i umożliwiające jego modyfikację w zależności od potrzeb. Spośród nich WW, będąca głównym obiektem badań w niniejszej pracy, wyłania się jako obiecujące rozwiązanie pozwalające sterować oderwaniem TBL.

Cztery artykuły (Papers 1–4), stanowiące cykl badań, poświęcono sterowaniu oderwaniem TBL. W pierwszym etapie (Paper 1) zastosowano symulacje wielkich wirów (ang. *Large Eddy Simulations*, LES) do analizy przepływu pod wpływem APG oraz zerowego gradientu ciśnienia (ang. *zero pressure gradient*, ZPG) nad powierzchniami płaskimi i pofalowanymi. Szczególną uwagę poświęcono badaniom fizyki przepływu w pobliżu ściany. Zastosowano prostopadłościenny obszar obliczeniowy, stanowiący uproszczenie rzeczywistej konfiguracji przepływowej, a gradient ciśnienia narzucano poprzez warunki brzegowe. Ze względu na ograniczoną długość domeny nie zaobserwowano oderwania; wnioski na jego temat wyciągano z analizy zmian $\tau_w$ – jego wzrost wskazuje na przesunięcie oderwania w dół przepływu. Wyniki LES, zweryfikowane danymi eksperymentalnymi, pokazują, że WW o sinusoidalnym kształcie prowadzi do

zwiększenia $\tau_w$. Ponadto zaobserwowano, że globalny gradient ciśnienia silnie wpływa zarówno na skuteczność WW w modyfikowaniu $\tau_w$, jak i na struktury przepływu rozwijające się nad ścianą. Następnie przeprowadzono analizę parametryczną (Paper 2), w której zbadano wpływ amplitudy WW ($A$) i długości fali ($\lambda$) na $\tau_w$. Wyniki wskazują, że oba parametry w sposób istotny determinują $\tau_w$, umożliwiając jego zwiększenie lub zmniejszenie względem konfiguracji referencyjnej. Zidentyfikowano optymalną kombinację $A$ i $\lambda$, która zapewnia istotny wzrost $\tau_w$ w porównaniu z przypadkiem referencyjnym, co powinno skutkować opóźnieniem separacji. W oparciu o te obserwacje, w następnym kroku badań, wprowadzono udoskonalenie kształtu WW poprzez jego pochylenie zgodnie lub przeciwnie do kierunku przepływu (Paper 3). Modyfikacja ta prowadzi do wzrostu $\tau_w$ o 70% względem najlepszego WW o sinusoidalnym kształcie z Paper 2. Co więcej, pochylenie WW eliminuje lokalne oderwanie w zagłębieniach WW, redukując całkowity współczynnik oporu ($C_d$) o 14%. W końcowym etapie badań (Paper 4), związanym z głównym celem rozprawy, zastosowano domenę obliczeniową odzwierciedlającą geometrię profilu lotniczego. Zastosowanie takiej konfiguracji umożliwiło odwzorowanie warunków przepływu zbliżonych do rzeczywistych i, w szczególności, pozwoliło na zbadanie wpływu WW na przepływ w obszarze oderwania. Wykazano, że zintegrowanie WW z krzywizną profilu lotniczego zapewnia przyrost $\tau_w$ oraz zaobserwowano przesunięcie punktu oderwania w dół przepływu, potwierdzając wnioski z wcześniejszych prac (Papers 1–3). Dodatkowo, przeprowadzona analiza czułości na liczbę Reynoldsa ($Re$) ujawniała, że skuteczność WW w zwiększaniu $\tau_w$ jest silnie zależna od warunków napływowych; działanie WW słabnie wraz ze spadkiem $Re$.

Zaobserwowana w Papers 1–4 możliwość znacznego przesunięcia punktu oderwania TBL za pomocą WW skłoniła do podjęcia dalszych badań (Papers 5–6), w których poszerzono jej zastosowanie i wykorzystano ją do intensyfikacji wymiany ciepła w przewodzie cylindrycznym (ang. *pipe*) oraz kanale (ang. *channel*). Analiza ta jest szczególnie ważna, ponieważ obie te konfiguracje geometryczne są elementami kompaktowych wymienników ciepła, a ich kształt w istotny sposób wpływa na pola przepływu. Odpowiednio zaprojektowana ich powierzchnia może zatem znacząco poprawić sprawność termiczną wymiennika. Celem tego etapu badań jest optymalizacja kształtu WW tak, aby maksymalnie zintensyfikować wymianę ciepła przy minimalnych stratach ciśnienia. Dla przewodu cylindrycznego optymalna ściana charakteryzuje się dwoma zagłębieniami WW skierowanymi na zewnątrz (względem osi przepływu), natomiast dla kanału – narastającą amplitudą WW. Taki kształt sprzyja powstawaniu obszarów recyrkulacji wewnątrz zagłębień, co intensy-

fikuje mieszanie płynu i zwiększa wymianę ciepła między grzaną ścianą a rdzeniem przepływu, przy jednoczesnym utrzymaniu niewielkich strat ciśnienia.

# Introduction and objectives

Passive flow control refers to techniques that influence fluid flow without the input of external energy. These approaches have long been of interest in the fluid mechanics community, not only due to their energy efficiency but also because of their simplicity and robustness compared to active methods. Numerous passive flow control strategies have been investigated to date. In wall-bounded flows, where the global dynamics are strongly influenced by the development of the turbulent boundary layer (TBL), common examples include dimples, vortex generators, flaps, spoilers, and others. Among these, two-dimensional (2D) streamwise waviness has emerged as a promising topology for modifying TBL evolution. Experimental investigations by Drozdz et al. (2021) have shown that such surface geometry can increase wall shear stress ($\tau_w$) and effectively delay turbulent separation under high $Re$ conditions. This is particularly relevant for practical applications, e.g., horizontal-axis wind turbines or planes, where the detachment of the flow from blades or wings contributes to energy losses. Despite the encouraging results presented by Drozdz et al. (2021), the fundamental physical mechanisms driving the observed WW-induced improvements remain insufficiently understood.

In particular, since the waviness is applied to control the separation, which is driven by the APG conditions, the relative influence of local APG (induced on the downhill slopes of the waves) versus the global APG remains unclear and requires further investigation. Furthermore, the evolution of flow structures developing over successive periods of WW, and their correlation with the progressively growing APG, is yet to be explored. A detailed investigation of the near-wall flow behavior, wall shear stress distribution, and their dependence on the geometric parameters defining the waviness is therefore essential. Importantly, the potential to enhance performance through further geometric refinement of WW remains largely unexplored. An additional consideration arises from a practical standpoint: the study by Drozdz et al. (2021) examined

a configuration in which the waviness was embedded in a flat surface, with the adverse pressure gradient imposed via the deflection of the upper wall and supplementary suction. In real-world applications, however, APG typically results from the intrinsic shape variations (e.g. curvature) of components such as airfoils, wings, or turbine blades. This raises an important question regarding whether the separation-delay effectiveness of surface waviness persists on curved surfaces. Moreover, given the variability of flow conditions, such as alterations in wind speed, it is crucial to assess the sensitivity of waviness performance to changes in $Re$.

The aim of this dissertation is to address the identified knowledge gaps by investigating the physical mechanisms governing turbulent flow over WWs. In particular, the study focuses on: (i) evaluating the respective roles of local and global APG in the development of the turbulent boundary layer; (ii) analyzing the evolution of flow structures developing over WW; (iii) exploring the relationship between near-wall flow characteristics, global flow statistics, and the defining geometric parameters of the waviness; (iv) assessing the potential for performance enhancement through geometric refinement of the surface; and (v) examining the effectiveness of the waviness in more realistic conditions, specifically when applied to airfoil-like curved surfaces and subjected to variations in $Re$, which represent the ever-changing nature of the flow encountered in real life.

The promising effectiveness of WW in controlling TBL separation, identified during this PhD research, motivated further exploration of its practical applicability in the context of heat-transfer enhancement. WW was found to substantially influence near-wall turbulence, thereby promoting mixing. This condition enhances heat transfer, which is highly beneficial for the energy efficiency of systems such as compact heat exchangers. In addition, the smooth geometry of WW generally induces lower pressure losses compared with more aggressive shapes such as rectangular or triangular grooves. Despite growing interest in surface-based thermal performance enhancement, relatively few studies have systematically examined how to tune waviness for optimal heat transfer with minimal pressure losses. Accordingly, a complementary component of this PhD thesis is devoted to demonstrating the broader potential of WW in TBL control, extending beyond separation mitigation. Specifically, the optimisation of WW is pursued with the aim of maximising mixing while minimising pressure losses. An additional aspect of practical relevance is also addressed: the design of shapes with manufacturing simplicity in mind.

# Chapter 1

# Literature review

Passive flow control encompasses a range of strategies designed to modify and manage the behavior of fluid flows, e.g. air or water, through purely mechanical means, without relying on any form of external energy input or real-time control systems. Unlike active flow control techniques, which involve actuators, sensors, or feedback mechanisms, passive methods operate by leveraging inherent structural features or material properties to influence the flow dynamics. These techniques are extensively employed across a wide spectrum of engineering disciplines. In aerospace engineering, for instance, they are often employed to reduce drag and control the TBL separation, which is a fundamental problem from the perspective of aircraft performance and fuel efficiency. In the automotive sector, they help improve vehicle aerodynamics, contributing to lower emissions and enhanced stability. Similarly, civil and environmental engineering applications might use passive flow features to manage wind loads on buildings or improve the efficiency of water distribution systems.

## 1.1 Passive flow control in aerodynamics

Over the years, numerous passive flow control techniques have been developed and successfully implemented within the field of aerodynamics. They have been employed in both laminar and turbulent flow regimes, as well as in a wide range of configurations, including airplanes, wind turbines (in both

horizontal and vertical arrangements), turbomachinery, and others. These methods have been extensively researched and documented in a wide range of review papers published over the decades (Hak and Bushnell, 1991; Hak, 1996; Pollard, 1998; Fish and Lauder, 2006; Gursul et al., 2007; Izawa et al., 2011; Joshi and Gujarathi, 2016; Ricco et al., 2021; Rashid et al., 2022; Gardner et al., 2023; Tayebi and Torabi, 2024; Ab Satar et al., 2024; Zhang and Wang, 2025). Given the comprehensive coverage already available in the literature, and considering the vast number of techniques explored, far exceeding the scope of the present dissertation, only the ones, which are most prominent, widely used, or particularly significant will be discussed here. The literature review begins with a description of the most conventional passive flow control methods, followed by an overview of more complex approaches. Subsequently, nature-inspired strategies will be addressed, along with relatively novel ones, which fall outside the realm of what may be considered standard or commonly applied. Finally, although the primary focus is on aerodynamics, attention will also be given to passive flow control techniques applied in the context of heat transfer enhancement, where similar principles are employed.

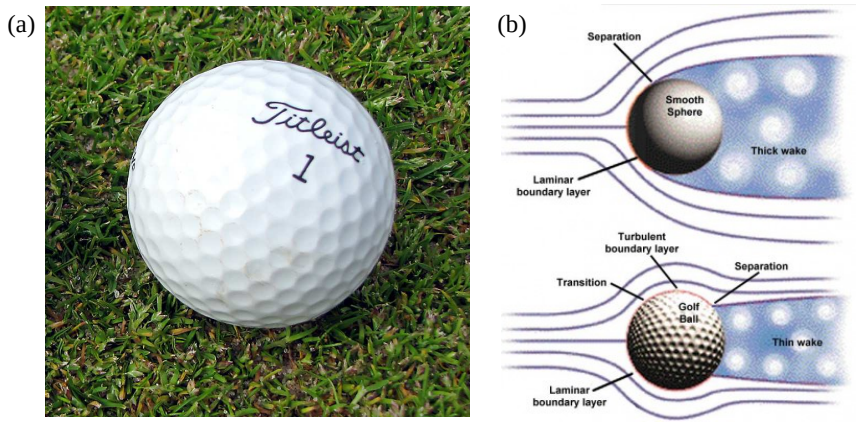



Figure 1.1: Dimpled golf ball (a); wakes of smooth and dimpled surfaces compared (b). Sources: Petey21, licensed under CC0 (left); Chear and Dol (2015) (right);

One of the most prominent conventional examples of passive TBL control is the use of dimples, shown in Figure 1.1a, which were initially popularised through their application in golf ball design (Bearman and Harvey, 1976; Lorenz, 2006), where they enhance flight stability by inducing turbulence in the boundary layer. This increase in turbulence is attributed to the fact that each dimple tends to generate a pair of streamwise vortices (Bearman and Harvey, 1993), which trail downstream. In doing so, dimples promote an earlier laminar-to-turbulent transition (see Fig. 1.1b), increasing boundary layer stability and delaying separation, which ultimately reduces total force ($F_d$) exerted on a sphere by up to 50% compared to a smooth surface. Moreover, the drag coefficient, defined

as $C_d = F_d/(0.5U_\infty^2 S)$, where $U_\infty$ is the freestream velocity and $S$ the cross-sectional area of the sphere, remains nearly constant over a range of $Re$ equal to $Re = 5 \cdot 10^5 - 3 \cdot 10^6$ (Bearman and Harvey, 1976). These beneficial effects have made dimples the subject of continued research aimed at further delaying flow separation and reducing drag (Veldhuis and Vervoort, 2009; Tay, 2011; Aoki et al., 2012; Tay et al., 2015; Tay and Lim, 2018; Tay et al., 2019; Gattere et al., 2022).

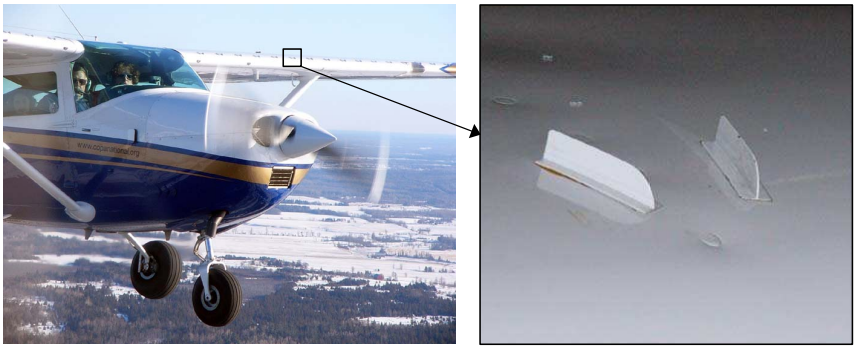


Figure 1.2: Vortex generators on a wing of the Cessna airplane. Source: Ahunt at English Wikipedia, public domain.

Another commonly used method are vortex generators (VGs, see Figure 1.2) in a form of small, fin-shaped devices mounted on airfoil surfaces, rotor blades, or vehicle bodies. VGs generate streamwise vortices that draw high-momentum fluid from the freestream into the near-wall region, thereby turbulising the flow and promoting an earlier laminar-to-turbulent transition, which in turn helps to delay flow separation. VGs are widely employed across various systems, including airfoil surfaces, helicopter rotors (Gibertini et al., 2015), wind turbine blades (Wang et al., 2017; Zhu et al., 2019), as well as civil (Islam et al., 2013) and agricultural (Lo and Kontis, 2016; Phan, 2024) vehicle bodies. It is worth noting that VGs have also been installed on the underside of plane wings. For instance, on the Airbus A320, which, according to the Lufthansa company, resulted in a 2 dB noise reduction (Lufthansa, 2014).

Beyond these standard tools, the field of passive flow control has seen growing interest in more advanced techniques. One such approach involves modifying the airfoil surface by introducing slots (Whitman et al., 2006; Belamadi et al., 2016; Coder and Somers, 2020), an example of which is shown in Figure 1.3. This concept dates back to the early 20$^{th}$ century (Parker, 1920), when slotted airfoils had already been shown to significantly reduce energy losses under specific conditions (Weick and Shortal, 1933). Whitman et al. (2006) demonstrated that, at low angles of attack, slotted airfoils exhibit lower $C_d$ compared to non-slotted configurations. At high angles of attack, exceeding 25°, slots

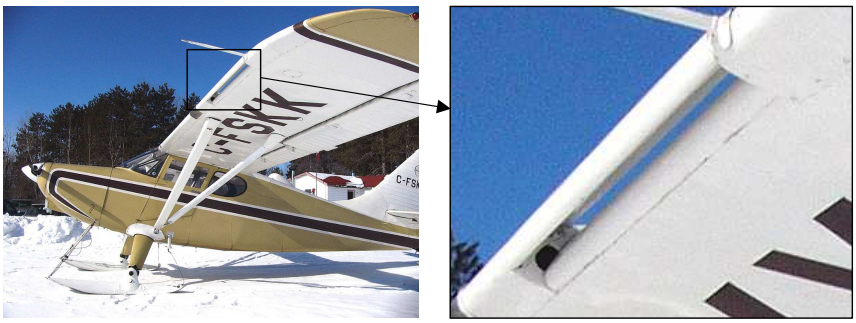


Figure 1.3: Partial-span leading-edge slot in the wing of a Stinson 108-3 airplane. Image modified from original by Ahunt at English Wikipedia, public domain.

ensure significant reduction of drag, likely due to their role in mitigating the effects of stall, i.e., a sudden loss of lift force caused by flow separation on the upper airfoil surface. Therefore, the benefits of slots are not limited to drag reduction but they are also effective in the lift force enhancement. Specifically, slotted airfoils achieve higher lift coefficients than their non-slotted counterparts at angles of attack greater than 15˚.

An interesting passive flow control technique is the use of a micro-cylinder mounted upstream of the airfoil (Wang et al., 2018; Mostafa et al., 2022). When properly implemented, this approach can ensure complete elimination of TBL separation under specific flow conditions. This beneficial effect is achieved by the micro-cylinder interacting passively with TBL and generating so-called secondary vortices in its wake, which extract momentum from the freestream and transfer it into the downstream boundary layer. As a result, the near-wall flow over the airfoil surface is accelerated, enhancing its ability to resist APG, and thereby fully suppressing flow separation over the otherwise unmodified airfoil. In the literature, this mechanism is referred to as the *momentum injection* (Wang et al., 2023).

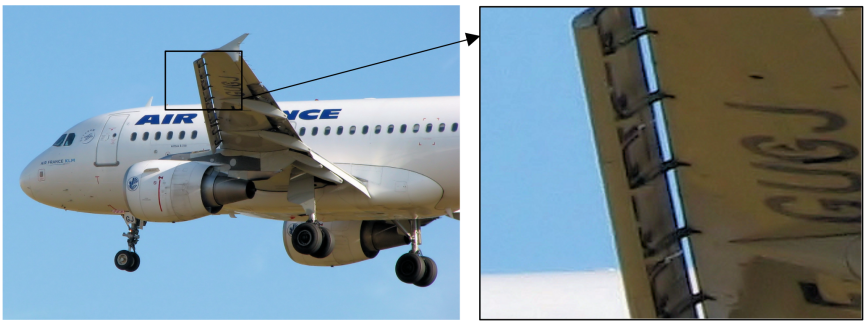


Figure 1.4: Slats on the leading edge of an Airbus A318. Image modified from original by Arpingstone, public domain.

An another control method, which operates via a mechanism similar to that of the micro-cylinder approach, is the use of a leading-edge slat (Wang et al., 2019; Zaki et al., 2022), example of which is shown in Figure 1.4. This involves adding an external airfoil with a smaller chord upstream of the main airfoil. Due to the gap formed between the two, a stream of higher-momentum air is injected onto the suction side. This, under certain conditions, can effectively suppress flow separation and lead to an increase in lift (Elhadidi et al., 2015; Halawa et al., 2018). Furthermore, experimental and numerical studies by Genç et al. (2009) demonstrated that, at transitional *Re* values, a leading-edge slat can increase maximum lift coefficient and the angle at which stall occurs.

Trip wires are a passive flow control method involving thin wires, typically with a diameter not exceeding 1% of the airfoil chord length, positioned at a specific distance from the leading edge. This technique operates by introducing small disturbances into the boundary layer, promoting an earlier transition from laminar to turbulent flow. In doing so, the trip wire alters the development of the boundary layer, which can influence separation behavior, reduce stall intensity and improve post-stall flow characteristics. Specifically, Choudhry et al. (2014) demonstrated that this approach reduces the amplitude of aerodynamic force fluctuations compared to an unmodified airfoil. However, one disadvantage is a slight reduction in maximum lift. A similar effect on lift was reported by Leknys et al. (2018), who found that in scenarios involving dynamic stall, the use of trip wires can further reduce lift and impose higher aerodynamic loads.

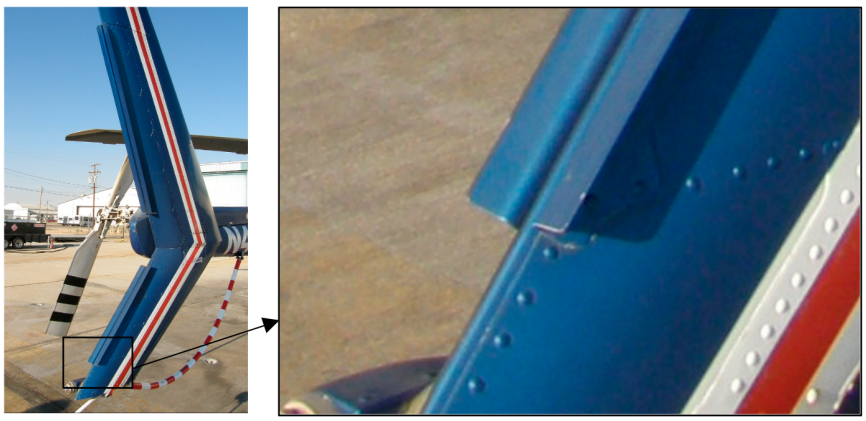


Figure 1.5: Double Gurney flaps on a Bell 222U helicopter. Image modified from original by Alan Radecki (Akradecki), licensed under CC BY-SA 3.0.

The Gurney flap (GF), presented in Figure 1.5 in a double configuration, is a device consisting of a small plate mounted perpendicularly on the lower surface at the trailing edge of an airfoil. It increases an effective camber of the airfoil, which delays flow separation. The main benefit of using GF is a significant lift coefficient enhancement (Liebeck, 1978; Maughmer and Brames-

feld, 2008; Traub, 2014). However, this improvement comes at the expense of increased drag and aerodynamic noise, largely due to intensified turbulence downstream of the flap. To mitigate these disadvantages, various geometric modifications have been proposed. For example, introducing serrations to the GF shape has been shown to reduce both drag and noise levels (Ye et al., 2023), providing a more balanced aerodynamic performance.

A particularly innovative approach involves aero-elastic membranes (Bottasso et al., 2016; Piquee et al., 2022), which adapt to changing flow conditions. During gusts, rise in the pressure induces instantaneous force exerted on the airfoil, causing the membrane to deform accordingly. The primary benefit of such deformation is a substantial reduction in the axial forces acting on the airfoil, thereby lowering the overall aerodynamic load. Additionally, at certain angles of attack, aeroelastic membranes have also been shown to delay flow separation. Another variant of this concept can be implemented in the form of a flap or a pitching airfoil that passively responds to vortex-shedding-induced vibrations by shifting position or changing its angle due to temporal variations in flow. By opposing these oscillations, such a mechanism contributes to load reduction.



Figure 1.6: The Taipei 101 building. Image modified from original by Sinsyuan, licensed under CC BY-SA 4.0.

In civil engineering, it is often necessary to design structures, such as buildings, to accommodate the surrounding flow conditions in a manner that reduces loads and mechanical stress. Consequently, a number of unconventional and creative passive approaches have been developed in this field. A prominent example is the use of vertical fin-like protrusions, which serve to disrupt vortex shedding patterns, thereby reducing vortex-induced vibrations. These are commonly found on tall chimneys, bridge pylons, or cables, such as those on the Akashi Kaikyō Bridge in Japan (Fujino et al., 2012). Another notable approach involves stepped corners, which are integrated into the structural design of the Taipei 101 building, shown in Figure 1.6. These features are

the result of an aerodynamic optimization process and have led to a significant reduction in drag, and thus a decrease in base moment due to wind loads by approximately 25 % (Kourakis, 2007). In some cases, the overall shape of the building, rather than individual components, is aerodynamically optimized. A clear example is the Burj Khalifa, the tallest building in the world, which not only tapers gradually toward the top through a setback structure, but also features a Y-shaped plan (Günel and Ilgin, 2014) that disrupts coherent vortex formation and reduces drag, thereby lessening loads.

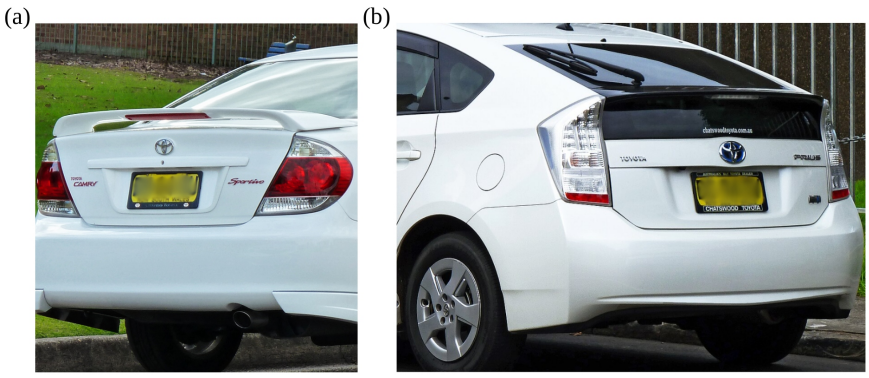



Figure 1.7: Spoiler on a Toyota Camry (a); Kammback type rear on a Toyota Prius (b). Images modified from original ones by: OSX, public domain.

The automotive industry offers a range of interesting passive approaches to controlling the flow around vehicles. For example, in the early days of automobile design, during the 1920s and 1930s, some custom luxury cars, such as the 1938 Ford Boat-Tail Roadster, were modified so that their rear end resembled the tail of a boat. This design enhanced streamlining, reduced wake size, and thereby lowered drag (Javed et al., 2017). A more widespread approach is the use of rear spoilers (shown in Figure 1.7a), commonly seen on both sports cars and family sedans (e.g., the Toyota Camry). These devices are typically mounted to manage lift, increase downforce for improved manoeuvrability and shorter braking distances, and, in some cases, to reduce drag (Kheirkhah et al., 2025). Another notable design is the Kammback-type rear (see Fig. 1.7b), which features an abrupt cutoff. This configuration has been shown to significantly reduce drag and improve fuel efficiency (Chow, 2022). Over the years, this design has been adopted by many manufacturers; prominent examples include the Toyota Prius, Honda Insight, and Audi A7. Side mirrors are a component that significantly affects aerodynamic performance and flow-induced noise. The separation of flow at the mirror's edge leads to pressure fluctuations on the side window (Chen et al., 2018). To address this problem, mirror shapes are optimized for aerodynamic performance. As a result, modern vehicles from Audi, Toyota, and Tesla incorporate refined mirror designs to minimize drag.

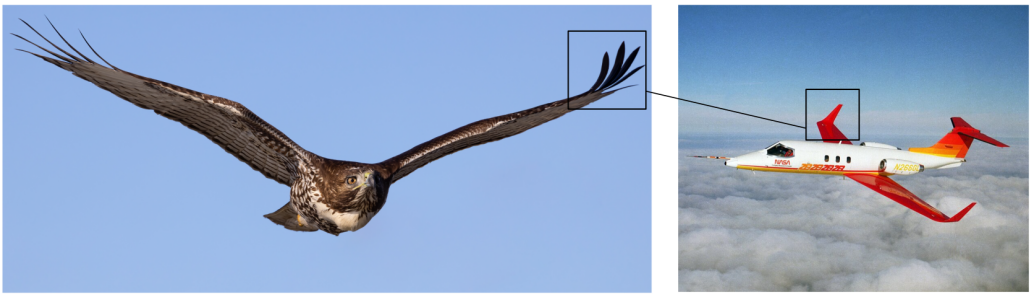


Figure 1.8: The wings of a bird as an inspiration for winglets. Sources: Frank Schulenburg, licensed under CC BY-SA 4.0 (left); NASA, public domain (right).

Quite often, nature itself provides solutions that are optimal for specific flow scenarios and serves as a source of inspiration for researchers and engineers to apply them in practice. Since the second half of the 20$^{th}$ century, researchers have begun studying the flight characteristics of soaring birds such as eagles, hawks, condors, vultures, and ospreys. These birds possess high-lift wings featuring distinct feather structures at the tips (Smith et al., 2001). Following these observations, a device known as a winglet (shown in Figure 1.8) was developed and subsequently investigated (Guerrero et al., 2012; Wu et al., 2018; Khaled et al., 2019; Guerrero et al., 2020; Jeong et al., 2022; Zhang et al., 2023b). Studies to date have demonstrated that winglets can significantly reduce lift-induced drag by suppressing the formation of vortices at the airfoil tips.

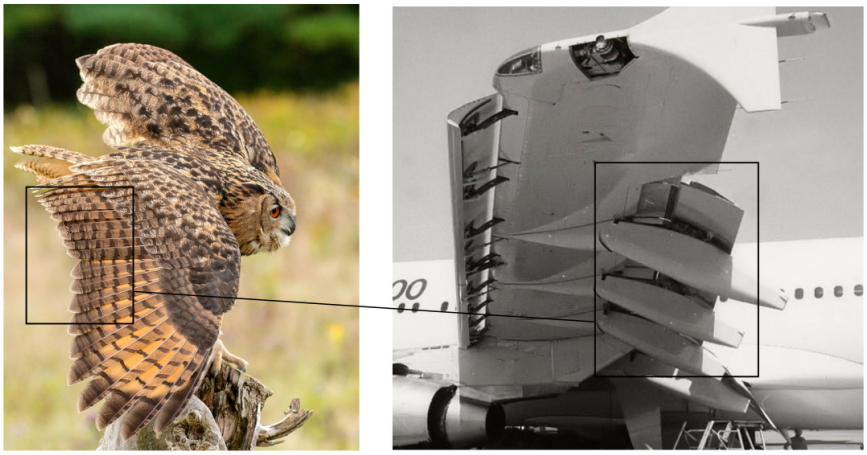


Figure 1.9: Adaptive flaps designed after feathers on the rears of the bird's wings. Sources: Peter K Burian, licensed under CC BY-SA 4.0, via Wikimedia Commons (left); Adrian Pingstone, public domain (right).

The adaptive flap, shown in Figure 1.9, is an another approach inspired by bird wing feathers. It mitigates the development of full flow separation by suppressing the backflow induced during the initial onset of separation (Hao and Li, 2020; Yossri et al., 2023). Several observations have shown that some birds possess feathers on the upper surface near the wing's trailing edge,

which are raised in response to gusts or during landing. Earlier investigation revealed that the onset of flow separation causes these feathers to lift into the boundary layer, where they interfere with the separating flow and help mitigate full flow separation (Bechert et al., 1997). The adaptive flap mimics this behavior and is typically implemented as a rigid flap rotating about a hinge. Its effectiveness largely depends on both the flap geometry and its angle relative to the airfoil surface.



Figure 1.10: Examples of skin textures of animals: owl feathers (left); fish scales (right). Sources: Peter K Burian, licensed under CC BY-SA 4.0, via Wikimedia Commons (left); H. Zell, licensed under CC BY-SA 3.0, via Wikimedia Commons (right).

Animal skin surfaces, often covered with feathers, scales (examples shown in Figure 1.10), or various protrusions, are *designed by nature* to provide camouflage, improve defensive capabilities or perform optimally under changing environmental (e.g. flow) conditions thereby reducing drag and enhancing maneuverability. These structures, shaped through evolution, serve not only as protection but also to interact efficiently with the surrounding fluid. Riblets, for example, represent a flow control strategy inspired by surface patterns observed on certain fast-swimming shark species (Bechert and Hage, 2006; Chen et al., 2013; Schlieter et al., 2016) and dolphins (Lang et al., 2017). In practical applications, these minute surface protrusions, typically aligned with the flow direction, impart anisotropic roughness to the surface. As such, riblets are employed to reduce drag in flows at lower $Re$ (García-Mayoral and Jiménez, 2011). Moreover, they have demonstrated a wall shear stress reduction in TBL, both in laboratory settings and full-scale aerodynamic configurations (Walsh, 1982; García-Mayoral and Jiménez, 2011). Raayai-Ardakani and McKinley (2017) investigated the influence of periodic sinusoidal riblet-type surfaces aligned with the flow on the development of a laminar boundary layer. Their results indicated that such topology reduces wall shear compared to unmodified surface, thereby lowering the overall viscous drag force. Another surface that has been shown to be effective in boundary layer control is the

fish scale-inspired microstructure (Wu et al., 2018). Under certain conditions, specifically at low *Re* typical of small fish motion, it increases wettability, which has been associated with a reduction in total drag. Research conducted by Ball (1999) demonstrated that coating an aircraft surface with a transparent plastic film featuring a microscopic texture mimicking shark scales could reduce drag by up to 8%, which led to approximately 1.5% fuel savings. The authors explained that the tooth-like micro-scales covering the skin of certain shark species generate vortices over the surface. These vortices suppress turbulent bursts near the groove walls, allowing water to move more easily over the surface and resulting in effective drag-reduction performance.

A particularly interesting flow control mechanism is the presence of ridged structures on the mouthparts of the honeybee (Li et al., 2015; Li et al., 2016). These bees feed using tongues that are solid and stiff, by employing a mechanism known as *viscous dipping*. The ridged surface of the mouthpiece reduces drag by offering less resistance to the upward movement of fluid, thereby facilitating more efficient feeding.

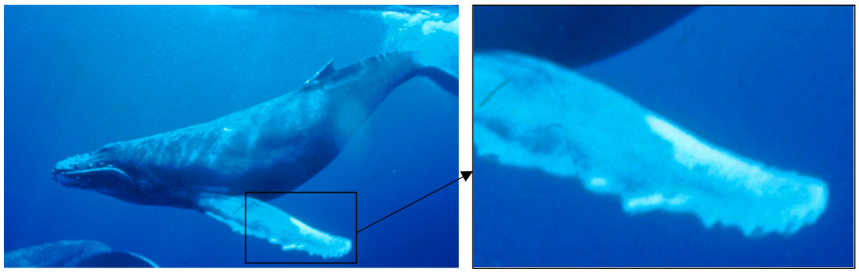


Figure 1.11: Tubercles on the flippers of a humpback whale. Source: public domain.

Tubercles represent another nature-inspired flow control technique mounted at the airfoil leading edge. They mimic the protuberances found on the flippers of humpback whales (Aftab et al., 2016; Schmidt and Redonnet, 2024), shown in Figure 1.11. These structures ensure high maneuverability during swimming, which is believed to result from the flipper's distinctive undulated leading edge. In a pioneering study on this subject (Fish and Battle, 1995), it was proposed that these leading-edge tubercles enhance lift retention beyond stall. Numerous subsequent investigations have examined this concept, further demonstrating its ability to modify the aerodynamic behavior of airfoils, specifically by facilitating a smoother transition between pre- and post-stall regimes (Johari et al., 2007; Hansen et al., 2011; Zhang et al., 2013; Biedermann, 2019; Chen et al., 2020). An interesting observation is that the vortices generated by the tubercles appear to assimilate with those produced by conventional vortex generators. These vortex pairs increase the energy of the

boundary layer within the near-wall area, thereby delaying flow separation and reducing stall (Bolzon et al., 2016).

### 1.1.1 Surface waviness

In the broader context of bioinspired flow control strategies, certain natural surface geometries have demonstrated high potential. Among these, and building on the encouraging findings related to leading-edge tubercles, wavy surfaces emerge as a particularly promising direction for further investigation. A review of the literature suggests that flows over wavy-type surfaces occur frequently in nature. Examples include flow over ocean or sea waves (Janssen, 1989; Belcher and Hunt, 1998), sand dunes (Willetts and Barndorff-Nielsen, 1991), and atmospheric flows over hilly terrain (Zeman and Jensen, 1987; Belcher and Hunt, 1998). Given the ubiquity of such phenomena in natural environment, and the fact that nature has evolved these surface geometries, it is worthwhile to examine this type of topology as a passive flow control strategy. In addition to their aerodynamic potential, such surfaces offer practical advantages from a manufacturing standpoint, as they can be produced through simple stamping processes. The existing literature has explored a wide variety of waviness configurations, with surface undulations aligned in the streamwise, spanwise, or oblique directions (examples shown in Fig. 1.12) relative to the flow. These configurations are discussed in greater detail in the following subsection.

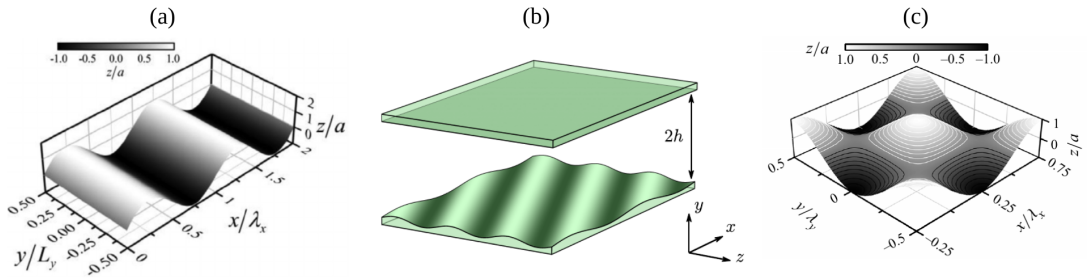



Figure 1.12: Examples of WW shapes. Transverse (a), oblique (b), egg carton type (c). Images borrowed from: Zhang et al. (2022), Zhang et al. (2023a), and Ghebali et al. (2017).

The so-far literature contains a broad range of studies focused on flow over streamwise WWs. Most of these investigations have been conducted under ZPG conditions (De Angelis et al., 1997; Cherukat et al., 1998; Kruse and Von Rohr, 2006; Koyama et al., 2007; Yoon et al., 2009; Kuhn et al., 2010; Fujii

et al., 2011; Tyson and Sandham, 2013; Hamed et al., 2015; Ghebali et al., 2017; Hamed et al., 2017; Sun et al., 2018; Segunda et al., 2018; Akselsen and Ellingsen, 2020; Fernex et al., 2020). Early experimental studies by Sigal (1971), Hsu and Kennedy (1971), Zilker et al. (1977), and Zilker and Hanratty (1979) revealed key characteristics of flow over WWs, showing that turbulence intensities and shear stresses vary periodically along the wave profile. In some cases, surface waviness was found to amplify them, indicating elevated turbulence levels. Building on these foundational efforts, later studies employed numerical simulations to gain further insight into the flow physics. For example, direct numerical simulations (DNS) performed by Maaß and Schumann (1996) and De Angelis et al. (1997) confirmed many of the experimental observations and provided new perspectives. Notably, these simulations identified the formation of recirculation zones within the wave cavities, contributing to increased pressure drag. De Angelis et al. (1997) also showed that shear layers form above the recirculation zones, promoting elevated turbulent kinetic energy (TKE) within the boundary layer. Further observations revealed that as the flow progresses on the uphill face of the waviness, the wall shear stress ($\tau_w$) rises sharply, enabling reattachment of the previously separated boundary layer. Additionally, increasing the amplitude-to-wavelength ratio ($A/\lambda$) was found to enlarge the separation region in troughs, potentially leading to greater aerodynamic losses. Higher $A/\lambda$ values were also shown to promote vortex shedding from the wave crests, with these vortices tending to change orientation and migrate away from the wall. A DNS-based study conducted by Koyama et al. (2007) demonstrated that turbulence intensities, pressure fluctuations, and Reynolds shear stress increase significantly within specific $A/\lambda$ ranges. This was further expanded upon by Yoon et al. (2009), who performed a similar investigation and showed that a surface corrugation characterized by $A/\lambda = 0.03$ resulted in a minor increase in $\tau_w$ in the area of the waviness compared to a smooth wall. This finding is promising, as such an increase in $\tau_w$ may propagate downstream and could be beneficial for delaying flow separation, which occurs when $\tau_w \to 0$. Other studies have also shown that wall waviness can increase velocity fluctuations and thereby elevate TKE (Cherukat et al., 1998; Tyson and Sandham, 2013; Sun et al., 2018). On the other hand, further increase in $A/\lambda$ has been associated with higher aerodynamic drag and a reduction in wall shear stress (Fujii et al., 2011; Ghebali et al., 2017; Hamed et al., 2017; Segunda et al., 2018). Casalino et al. (2019) reported that applying sinusoidal serrations, resembling tubercles, to the leading edge of stator vanes in a realistic fan stage of a turbine engine can reduce rotor–stator interaction noise and thus the overall aircraft noise, to a measurable margin.

In general, the key findings regarding flows over WWs can be summarized as follows:

- Sinusoidal waviness leads to a significant increase in TKE.
- The level of TKE amplification depends on the corrugation parameters, such as amplitude $A$, wavelength $\lambda$, and their ratio $A/\lambda$.
- Waviness typically induces higher pressure drag compared to a smooth surface; however, this effect can be mitigated for certain values of $A/\lambda$.
- For specific $A/\lambda$ values, waviness was shown to locally increase $\tau_w$ relative to the flat wall.
- In some cases, waviness has been shown to effectively reduce the aerodynamic noise.

A main drawback of the passive flow control approaches, including the surface waviness is that they are beneficial primarily under laminar, transitional, or weakly turbulent flow conditions characterized by low $Re$. However, with increasing $Re$, the effectiveness of these passive methods generally diminishes. This trend is consistent with the observations of Lissaman (1983) and Mueller and DeLaurier (2003), who noted that in nature, the surfaces of aquatic and airborne animals tend to be rough or structured only when operating within laminar or transitional regimes, under which surface texture can offer performance benefits. At higher $Re$, however, surfaces tend to be smooth. Moreover, as highlighted by McMasters and Henderson (1979), the use of passive techniques at high $Re$ may even be detrimental. For example, on airfoils or turbine blades, such modifications can lead to premature flow separation, thereby compromising aerodynamic performance. Given these findings, it has long been assumed that effective control of the turbulent boundary layer, particularly in preventing separation, may require active flow control strategies. A few major examples include the synthetic jets (You and Moin, 2008), blowing and suction (Atzori et al., 2020) or plasma actuators (Ebrahimi and Hajipour, 2018). These methods modify the flow field in a precisely controlled manner, enabling various beneficial effects such as friction drag reduction or separation delay. However, their primary disadvantage lies in their complexity and reliance on external energy sources, which underscores the preference for passive approaches.

### 1.1.2 Surface waviness as a mean to delay the turbulent separation

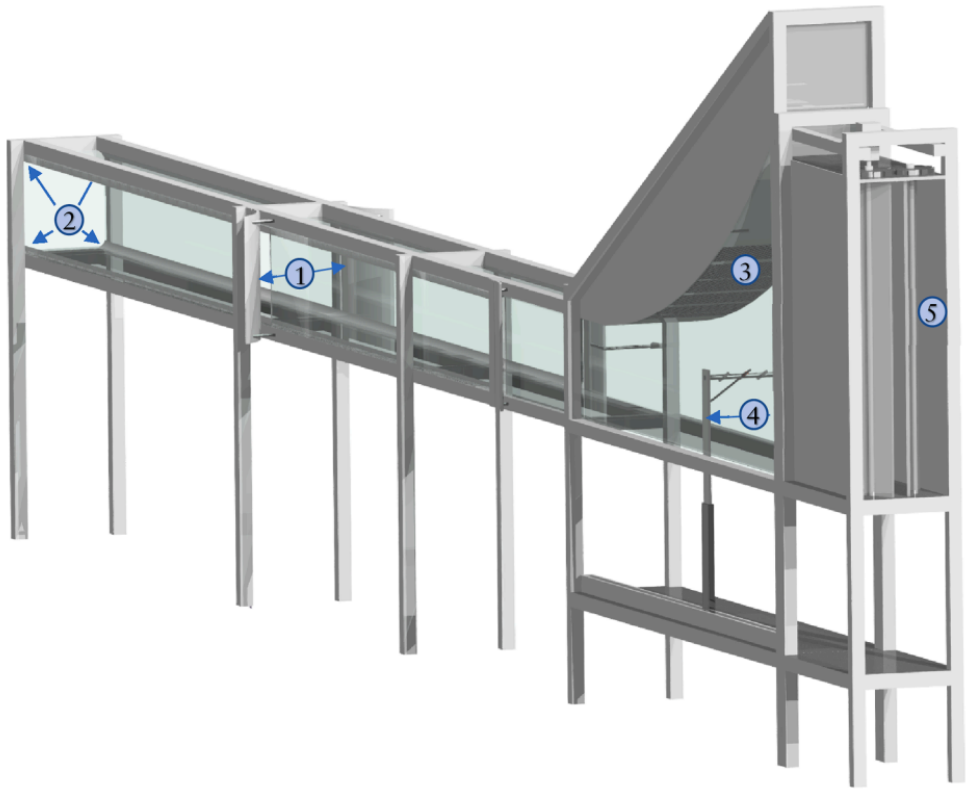



Figure 1.13: Wind tunnel at CUT. Inlet and test sections geometry: 1 - lateral suction gaps; 2 - triangular inserts; 3 - perforated upper wall; 4 - probe support; 5 - throttling chamber. Image borrowed from Dróżdż et al. (2021).

An important finding in the context of separation control at high $Re$, which so far was not achieved via passive approaches, was reported by Drozdz et al. (2021). They conducted an experimental study demonstrating the possibility of increasing local $\tau_w$, thereby enabling the separation delay. This was achieved in a wind tunnel at the Częstochowa University of Technology (CUT), presented schematically in Fig. 1.13, under adverse pressure gradient conditions through the application of a two-dimensional (2D) streamwise wall waviness. Specifically, the authors showed that separation delay could be attained by carefully tuning the waviness parameters, such as $A$ and $\lambda$. The experiment was conducted at $Re = 5.0 \times 10^5$, corresponding to $Re_\tau = u_\tau \delta / \nu = 4000$ (at the inlet to the APG section), where $u_\tau = \sqrt{\tau_w / \rho}$ is the friction velocity, $\delta$ is the boundary layer thickness and $\rho$ the fluid density. Such a value of $Re_\tau$ was an effect of TBL evolving within 5 m long inlet section and it ensures the presence of a well-developed logarithmic layer and a clear separation of turbulent scales (Hutchins and Marusic, 2007). Furthermore, such value of $Re_\tau$ is more representative of real-world aerodynamic applications, such as the conditions under which the horizontal air turbine airfoils operate. The study

of Drozdz Drozdz et al. (2021) was later complemented by the work of Elsner et al. (2022), who conducted a similar investigation, both experimentally and numerically, at approximately three times lower $Re$ ($Re = 1.5 \times 10^5$, $Re_\tau = 1350$). In such flow conditions, the application of WW did not lead to any increase in $\tau_w$ and, therefore, did not result in delayed separation.

Although the ability of WW to increase wall shear stress has been demonstrated, the physical mechanisms responsible for this effect remain insufficiently understood, highlighting the need for further investigation. Gaining a deeper understanding of the near-wall flow behavior directly above WW may provide critical insight into the mechanisms underlying wall shear stress enhancement and turbulent separation control. Within this context, several fundamental questions arise: (i) to what extent do local and global APGs contribute to the development of the turbulent boundary layer over a WW surface; (ii) how do flow structures evolve across successive wave cycles, and how does this evolution correlate with the progressively increasing APG along the streamwise direction; (iii) what is the connection between near-wall dynamics, global flow statistics, and the geometric parameters defining the waviness; (iv) can the performance be further enhanced by refining the surface geometry beyond configurations explored in prior studies; and (v) how effective is the waviness under more realistic conditions, such as when applied to airfoil-type curved surfaces. Moreover, in the real world the inflow conditions vary, it is crucial to examine the impact of waviness when subjected to varying Reynolds numbers, thereby bridging the gap between the $Re_\tau = 1350$ and 4000 regimes previously investigated by Elsner et al. (2022) and Drozdz et al. (2021), respectively. Addressing these questions forms the central objective of this dissertation.

## 1.2 Passive flow control in heat transfer studies

Despite continued progress in the development of renewable energy technologies (Khaleel et al., 2022; Maxmut O'g'li, 2023), minimizing energy consumption remains a critical research objective in both industrial and academic domains. Significant efforts are devoted to optimizing energy usage across a wide range of applications. In this context, heat exchangers play a vital role due to their extensive use in areas such as automotive engineering (Krásnỳ et

al., 2016), compact electronic cooling (Zhu et al., 2013; Ahammed et al., 2016), and domestic systems including air conditioning and heating (Abd El-Baky and Mohamed, 2007). These devices typically comprise channels or pipes in which thermal energy is transferred between a working fluid and the channel walls through thin boundary layers.

Passive control strategies are commonly employed to address the aforementioned challenges and to improve energy efficiency. Many of these techniques are identical to those used in the aerodynamic sector and operate in a similar fashion. They are designed to modify the flow behavior and regulate turbulence in a manner that enhances heat transfer. It is well established that improving thermal performance generally requires increased flow mixing. However, any surface modification intended to enhance heat transfer can also lead to additional pressure losses, particularly in systems such as pipes or channels, where deviations from a smooth surface act as obstructions to the flow, potentially offsetting the thermal gains.

Among passive approaches enhancing heat transfer, closely aligned with those used in the field of aerodynamics, the most prominent techniques are vortex generators (Awais and Bhuiyan, 2018); dimples (Turnow et al., 2012; Rao et al., 2015); twisted tapes (Garg et al., 2016); wire-type turbulators (Akyürek et al., 2018); and a broad range of fins, such as offset, sinusoidal, and louvred configurations (Jabardo et al., 2006; Cuevas et al., 2011; Searle et al., 2020). In some cases, these methods are combined to form compound surfaces that benefit from the synergistic effects of their individual features (Kays and London, 1984; Bhuiyan et al., 2012; Hesselgreaves et al., 2016). In addition to these conventional strategies, other, more elaborate approaches have gained attention. A notable example involves the use of porous wall structures, which serve the dual function of enlarging the heat transfer area and intensifying localized mixing (Mahmood et al., 2007; Bovand et al., 2016). Although many of these techniques deliver high performance, their often-intricate geometries can present substantial manufacturing challenges. As a result, simpler configurations, such as plate-fin heat exchangers (Xue et al., 2018) and heat sinks (Tan et al., 2019) are frequently favored for practical implementation. These can be commonly found in car radiators or computer processor cooling units.

### 1.2.1 Surface waviness for improved heat transfer

Recent progress in additive manufacturing (Searle et al., 2020; Rastan et al., 2020; Kaur and Singh, 2021) has broadened the design landscape , enabling more complex structures such as corrugated surfaces to be fabricated with increasing ease. These geometries promote convective heat transfer by disturbing the boundary layer and generating flow recirculation, thereby enhancing energy exchange between slower and faster fluid regions. A prominent example involves grooved walls, which have been the subject of numerous investigations (Saha and Acharya, 2014; Dewan and Srivastava, 2015; Zheng et al., 2017). Zontul et al. (2021) showed that rectangular grooves significantly improved thermal performance compared to smooth surfaces. Similarly, Li et al. (2008) demonstrated that periodically spaced rectangular grooves trigger oscillatory flow and unsteady dynamics, leading to enhanced mixing. Ramadhan and Al Anii (2013) further confirmed the heat transfer benefits of such grooves via elevated Nusselt number, while also highlighting the drawback of increased pressure losses. To address this limitation, alternative groove shapes such as triangular corrugations have been proposed. Hoang et al. (2021) identified a corrugation amplitude, which, for an investigated configuration, optimally balances heat transfer enhancement and frictional penalty, maximizing the thermal performance factor. Other efforts have focused on trapezoidal grooves (Ahmed and Ahmed, 2015; Zhu et al., 2021), as well as hybrid profiles that integrate multiple groove geometries (Rabby and Uddin, 2023). While these structured surfaces consistently outperform flat-wall configurations in terms of heat transfer, their effectiveness is strongly influenced by geometric design variables, such as groove depth and pitch, as well as their associated pressure drop characteristics. In this regard, rectangular or triangular grooves present a notable drawback. Due to their sharp edges, they can lead to increased pressure losses as well as elevated thermal stresses. Under such conditions, these surface geometries may not only be inefficient but may also experience accelerated material degradation.

Due to the limitations associated with sharp-edged geometries, sinusoidal surfaces, characterized by their smooth contours, have received increasing attention in the literature (Dellil et al., 2004; Harikrishnan and Tiwari, 2019; Al-Zurfi et al., 2020; Alsabery et al., 2020; Cheng et al., 2021; Dong et al., 2021; Kumari and Kumar, 2021; Mehta et al., 2022; Brodnianská and Kotšmíd, 2023; Kumar et al., 2023; Madlool et al., 2023). The aerodynamic implications of sinusoidal waviness were discussed in detail in Section 1.1, and the mechanisms

relevant to enhanced mixing for improved heat transfer are of a similar nature. Specifically, the key principle remains the promotion of turbulence to facilitate better thermal performance. The following list briefly summarizes key findings from the literature:

- Sinusoidal surfaces can substantially increase TKE.
- TKE enhancement, and consequently heat transfer performance, increases with $A/\lambda$.
- In some cases, performance improvements saturate beyond a critical $A/\lambda$ threshold.
- Elevated values of $A/\lambda$ may induce significant pressure losses.

The findings to date regarding the use of surface waviness as a means to enhance heat transfer suggest that this approach is a promising candidate for further investigation in thermal applications. However, most existing studies have examined limited amount of geometric variations. Therefore, it is reasonable to pursue the optimization of surface waviness to achieve a balanced trade-off between pressure losses and heat transfer enhancement.

### 1.2.2 Machine learning aided optimization

While previous optimization efforts do exist, as noted by Rostami et al. (2015), most studies investigate only a narrow range of parameters that define the corrugated surface geometry. The presence of numerous tunable parameters gives rise to a high-dimensional design space, which is challenging to explore using conventional optimization techniques. In this context, machine learning (ML) presents a promising alternative. One of the earliest documented applications of ML methods to shape optimization problems in fluid mechanics dates back to the 1960s, when Rechenberg (1964) attempted to optimize a physical surface composed of five segments in order to achieve minimal drag.

The increasing integration of ML methods into fluid dynamics research can be attributed to three main enablers: the availability of extensive datasets, the rise

in affordable computational resources, and significant progress in open-source algorithm development (Brunton et al., 2020). A range of ML techniques has been explored for flow control, with notable examples including genetic algorithms (GAs) (Benard et al., 2016), genetic programming (GPr) (Duriez et al., 2016; Noack, 2018), and reinforcement learning (RL) (Rabault et al., 2019; Guastoni et al., 2023; Nair and Goza, 2023).

Although ML methods have shown considerable promise in various areas of fluid mechanics, their application to the optimization of WW geometry remains comparatively limited. To date, most studies in this domain have relied predominantly on genetic algorithms (GAs). In an early example, Fabbri (2000) employed GA techniques to optimize corrugated wall profiles, identifying wave shape that is upstream-tilted with alternating wavelengths, which achieve up to a 30% improvement in heat transfer. Subsequent work by Joodaki and Ashrafizadeh (2014) produced optimal surface shapes featuring periodic cavities that resembled inverted bump profiles. A multi-objective variant of GA, NSGA-II, was utilized by Wang et al. (2016), who reported substantial gains in thermal performance, though these were accompanied by a 310% increase in pumping power due to elevated flow resistance. More recently, Kirkar et al. (2023) applied NSGA-II to the design of helically corrugated channels. However, their study was constrained to a two-dimensional design space defined by corrugation pitch and depth.

Although GAs are well-suited for optimizing predefined sets of control parameters, their computational demand scales rapidly with increasing problem dimensionality, often making them inefficient for high-dimensional tasks. More flexible alternatives, such as GPr and RL, are capable of exploring more complex design landscapes. However, these methods may still face challenges in reliably identifying globally optimal solutions within feasible computational times.

Bayesian Optimization (BO) has emerged as an efficient alternative for flow control applications, demonstrating notable success in jet and wake optimization problems (Blanchard et al., 2021; Pino et al., 2023; Li et al., 2024). This surrogate-assisted approach commonly utilizes Gaussian process (GP) regression to model the underlying objective function (Williams and Rasmussen, 2006). The BO framework proceeds iteratively through two key phases: (1) building a probabilistic surrogate model using available data, followed by (2) intelligent selection of subsequent sampling locations that ensure optimal trade

off between exploring uncertain regions and exploiting promising areas. Such methodology enables accelerated convergence with minimal function evaluations, a particularly advantageous feature for expensive computational fluid dynamics (CFD) simulations and ML parameter tuning tasks (Li et al., 2024).

The limited number of studies focused on adapting surface waviness to achieve maximum heat transfer enhancement with minimal pressure losses, combined with the demonstrated efficiency of the BO algorithm, forms the second, complementary objective of this PhD dissertation. Specifically, a BO-powered, multi-parameter optimization of a WW geometry is conducted. In addition to the core objective of the thesis, it aims to demonstrate the potential of surface waviness as a passive mechanism for enhancing heat transfer.

# Chapter 2

# Methodology

The research presented in this thesis was conducted using CFD, selected for its ability to provide high-resolution, time-dependent, and spatially detailed flow field data, particularly valuable in the near-wall region, where flow behavior is highly complex and difficult to capture experimentally. Moreover, CFD enables systematic variation of boundary conditions and geometric parameters, making it especially well-suited for parametric investigations that would be prohibitively time-consuming and resource-intensive in an experimental setting. Although experimental approaches remain essential for validation, CFD serves as an effective and versatile tool for exploring the fundamental physics of turbulent flows.

As outlined in the Introduction and Objectives section, this thesis is guided by the primary goal of achieving passive control of turbulent separation using surface waviness, with a particular focus on its influence on near-wall flow physics, wall shear stress, and separation behavior. In addition, a supplementary part of the thesis addresses the optimization of a heated WW to enhance heat transfer while minimizing losses, thereby demonstrating the broader practical applicability of surface waviness beyond separation control. The main objective, alongside the heat transfer part, require distinct methodological strategies and CFD modeling approaches, employing both LES and RANS methods. As a result, the methodology is divided into separate parts, each aligned with one of the two research aims.

## 2.1 Turbulent separation control

### 2.1.1 Objective outline

The scope of the investigation is broad and includes a parametric analysis of a wide range of waviness geometries, defined by multiple design variables. To achieve the research objectives, both time-averaged and instantaneous flow quantities are examined. In particular, analyzing the instantaneous flow field, essential for revealing the underlying flow structures, necessitates the selection of an appropriate computational approach. For this reason, LES method was chosen as the primary research tool. This choice raises a relevant question: *"Is LES the most suitable approach among the available alternatives, specifically RANS and DNS"* A previous study (Kaminski and Tyliszczak, 2022) compared RANS and LES models for the configuration with WW adopted from Elsner et al. (2022). Although RANS offered significantly lower computational cost, approximately $1/50^{\text{th}}$ of that required for LES, it was found inadequate for capturing the key flow phenomena central to this investigation. DNS, on the other hand, while offering the highest fidelity and being commonly regarded as the numerical analogue of a physical experiment, was excluded early on due to its prohibitively high computational cost, estimated to be roughly ten times greater than that of LES. As a result, LES was used exclusively in the part of the thesis devoted to TBL control.

The LES computations were first applied to the baseline waviness configuration proposed by Drozdz et al. (2021), followed by a parametric study to quantify the influence of individual waviness parameters on flow separation control. In the final stage, a modified geometry incorporating a tilting adjustment was analyzed to further enhance separation-delay performance. The following sections provide a detailed overview of the research methodologies employed throughout this part of the dissertation.

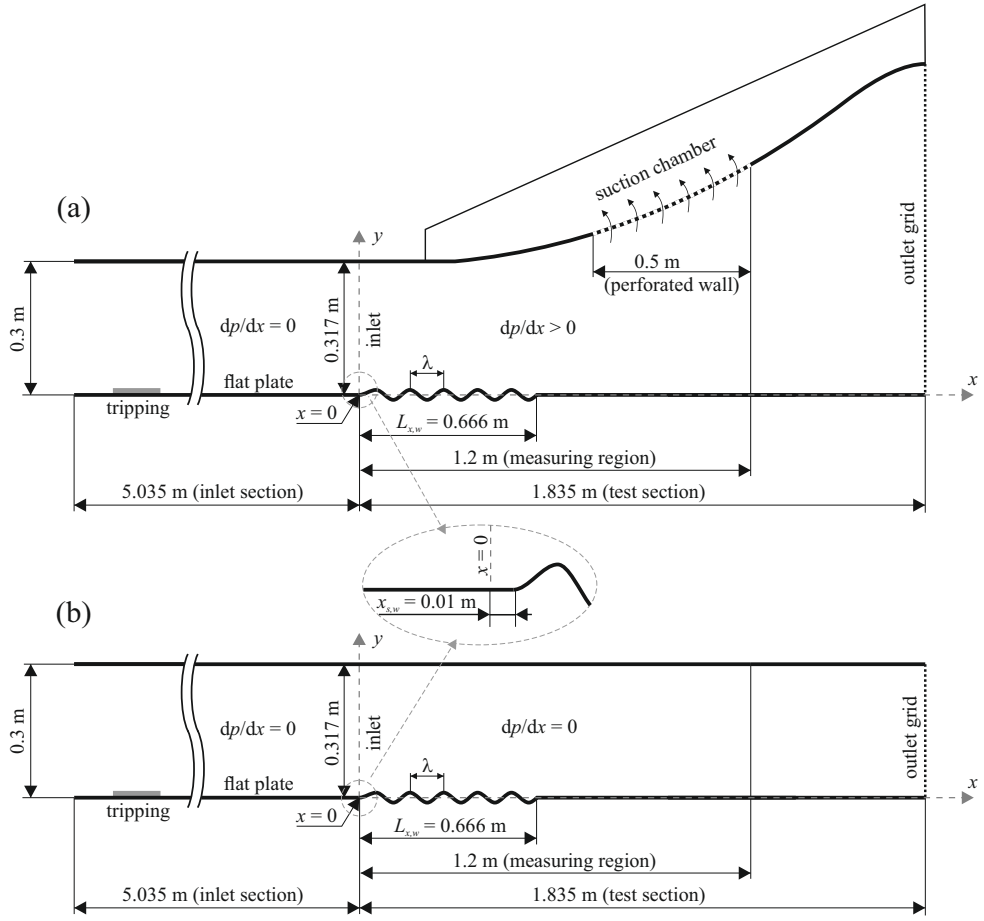



Figure 2.1: Experimental stand for flow configurations subjected to APG (a) and ZPG (b).

### 2.1.2 Experimental data

The experimental data, essential for the validation of numerical calculations, were obtained by Dr Vasyl Sokolenko and Dr habil. Artur Dróżdż. from the Czestochowa University of Technology. The measurements were conducted in an open-circuit wind tunnel, schematically illustrated in Fig. 2.1. Subfigure (a) presents the APG configuration, identical to that used by Drozdz et al., 2021, while subfigure (b) shows its modified version configured to ensure ZPG conditions throughout the entire channel. In the former case, the APG magnitude was controlled by deflection of the upper wall and a suction through a perforated section. In the ZPG configuration, a constant pressure along the channel was achieved by implementing a slight, gradual rise of the top wall in the streamwise direction. In both cases (cf. Figs. 2.1a,b), additional 5.035 m-long ZPG inlet section was installed upstream of the test section, which starts at $x = 0$. At the beginning of this channel, as shown in Fig. 2.1, tripping was applied in the form of coarse-grained sandpaper to bypass the

laminar-to-turbulent transition. To minimise the influence of sidewall boundary layers, their thickness within the long inlet section was controlled by two sets of suction gaps mounted on the sidewalls. This configuration ensured that a well-developed TBL entered the test section.

The WW section begins at $x_{s,w}$ = 0.01 m within the measurement region and extends over a total length of $L_{x,w}$ = 0.666 m. The waviness consists of 5 periods, each with a wavelength of $\lambda$ = 0.1332 m. The amplitude, $A(x)$, is defined as $A(x) = (0.00366x^2 + 0.000614x + 0.003351)$ m. Accordingly, the amplitude ranges from a minimum value of $A(x = 0.01\text{ m}) = 0.0034$ m to a maximum of $A(x = 0.676\text{ m}) = 0.0054$ m. This design choice is not arbitrary; it is motivated by the findings of Drozdz et al. (2021). Specifically, to be effective in delaying separation, the WW geometry is designed such that $A(x)$ increases proportionally with the boundary layer thickness $\delta$.

Velocity and velocity fluctuation profiles were acquired using a single hot-wire anemometry (HWA) probe at four streamwise positions above WW. The measurement locations, shown in Fig. 2.2, correspond to the first and last crests (labelled B-W1 and B-W5) and the first and last troughs (labelled D-W1 and D-W5). The streamwise coordinate $x$ is presented in a normalised form as $(x - x_{s,w})/\lambda$.

The freestream velocity was maintained at a constant level of $U_{in}$ = 14.42 m/s, which yielded to $Re_\tau(x = 0) = 2500$ with $T_i(x = 0) \approx 0.7$ % ($T_i$ - turbulence intensity). Additional details of the wind tunnel configuration and the experimental methodology are provided in Drozdz et al. (2021) and Elsner et al. (2022).

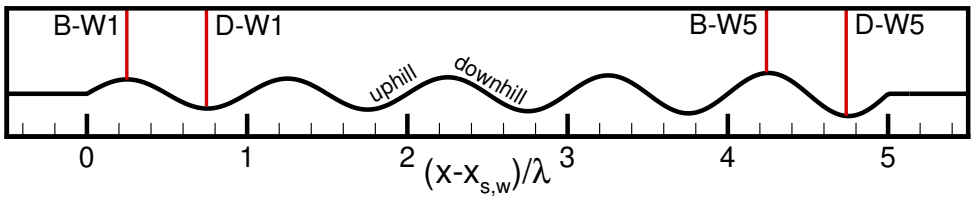



Figure 2.2: The streamwise locations of the HWA measurements.

### 2.1.3 Large eddy simulations (LES)

The flow is assumed to be incompressible and of constant density, governed by the continuity and Navier–Stokes equations. Within the LES framework, spatial filtering is applied to decompose the flow into resolved large-scale motions and unresolved subgrid-scale (SGS) components of which impact must be modeled (B.J. Geurts, 2004). Filtering the governing equations yields:

$$\frac{\partial \overline{u}_i}{\partial x_i} = 0 \tag{2.1}$$

$$\frac{\partial \overline{u}_i}{\partial t} + \frac{\partial \overline{u}_i \overline{u}_j}{\partial x_j} + \frac{1}{\rho}\frac{\partial \overline{p}}{\partial x_i} = \frac{\partial}{\partial x_j}\left[\nu\left(\frac{\partial \overline{u}_i}{\partial x_j} + \frac{\partial \overline{u}_j}{\partial x_i}\right)\right] + \frac{\partial \tau_{ij}}{\partial x_j} \tag{2.2}$$

where $t$ denotes the time, $x_i$ the spatial coordinates, the bar symbol denotes the filtered variable (B.J. Geurts, 2004), $\bar{f}(\mathbf{x}, t) = \int_\Omega f(\mathbf{x}', t) G(\mathbf{x} - \mathbf{x}', \Delta) d\mathbf{x}'$, where $f$ denotes an arbitrary variable, $\Omega$ is a flow domain, $G(\mathbf{x}, \Delta)$ is a box filter function fulfilling the condition $\int_\Omega G(\mathbf{x} - \mathbf{x}', \Delta) d\mathbf{x}' = 1$ and $\Delta$ is a filter width equal to a cube root of a local computational cell volume. The symbol $u_i$ represents the velocity component in the $i$–direction, $p$ the pressure, $\rho$ the density, $\nu$ the kinematic viscosity, and $\tau_{ij} = \overline{u}_i \overline{u}_j - \overline{u_i u_j}$ the subgrid stress tensor modeled with the subgrid viscosity ($\nu_t$) concept involving the Wall-Adapting Local Eddy-viscosity (WALE) model proposed by Nicoud and Ducros (1999). In this approach, the subgrid tensor is defined as $\tau_{ij} = 2\nu_t \overline{S}_{ij}$, where the symbol $\overline{S}_{ij}$ represents the strain rate tensor of the filtered velocity field

$$\overline{S}_{ij} = \frac{1}{2}\left(\frac{\partial \overline{u}_i}{\partial x_j} + \frac{\partial \overline{u}_j}{\partial x_i}\right) \tag{2.3}$$

and $\nu_t$ is given as

$$\nu_t = (C_w \Delta)^2 \frac{(S^d_{ij} S^d_{ij})^{3/2}}{(\overline{S}_{ij}\overline{S}_{ij})^{5/2} + (S^d_{ij} S^d_{ij})^{5/4}} \tag{2.4}$$

$$S^d_{ij} = \frac{1}{2}(\overline{g}^2_{ij} + \overline{g}^2_{ij}) - \frac{1}{3}\delta_{ij}\overline{g}^2_{kk} \tag{2.5}$$

where $\overline{g}_{ij} = \frac{\partial \overline{u}_i}{\partial x_j}$ represents the gradient components of the filtered velocity field, $C_w = 0.325$ the model constant (Nicoud and Ducros, 1999), and $\Delta = V^{1/3}$ the LES filter width, with $V$ being the local cell volume.

As discussed previously, LES enables accurate resolution of near-wall flow.

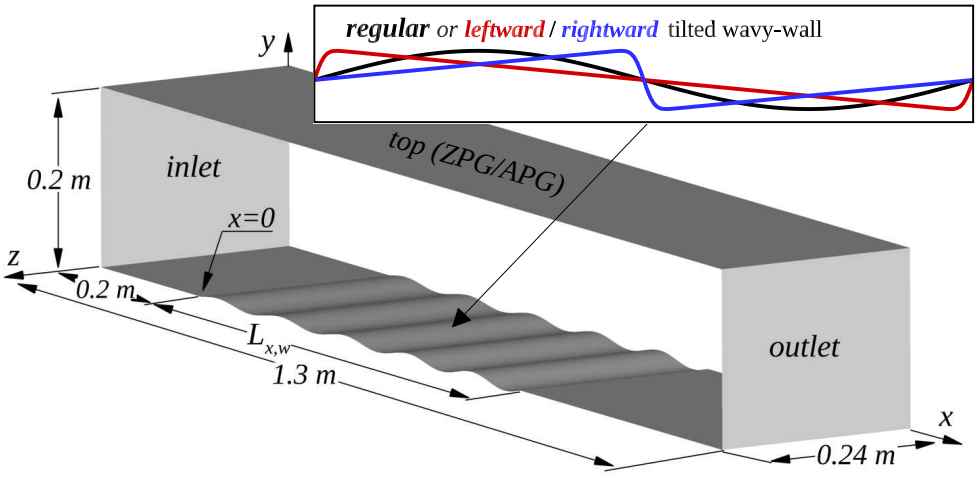



Figure 2.3: Simplified computational domain with the specification of the boundary conditions.

However, this comes at the cost of significant computational demands, resulting from the need to utilize highly refined computational meshes that comprise a large number of elements in the near-wall region. To address this, a common strategy is to reduce the size of the computational domain to include only the flow region essential for the analysis. This approach was adopted in the present research, where the full channel geometry (cf. Fig. 2.1) was simplified into a rectangular configuration, shown in Fig. 2.3. This domain corresponds to the measurement region of the experimental setup. As confirmed by preliminary simulations, this simplification enabled the computational time to be decreased twofold, from approximately 2 months of continuous CPU time to just 1 month for each analyzed test case. In the simplified computational domain, the air enters through the inlet located at $x$ = −0.2 m and exits at the outlet positioned at $x$ = 1.1 m. The lower boundary is configured either as a flat wall along the entire domain or as WW, with the corrugation beginning at $x$ = 0 m and extending over a length of $L_{x,w}$ = 0.666 m. The upper boundary, set at $y$ = 0.2 m, is used to impose a controlled pressure gradient within the channel. Periodic boundary conditions are applied in the spanwise direction, with a domain width of $z$ = 0.24 m. The total streamwise extent of the domain is $L_x$ = 1.3 m.

The simulations were carried out using the ANSYS Fluent code, a well-validated CFD solver widely employed for similar studies (Menter, 1994; Sharma and Kalamkar, 2016; Ravi et al., 2017; Kumar et al., 2017; Tu et al., 2022; Saleem et al., 2023). Spatial discretization of the Navier–Stokes equations employed a bounded second-order central difference scheme for the convective terms,

while a second-order central difference scheme was used for the continuity equation, pressure gradient, and viscous terms. Pressure–velocity coupling was handled using the SIMPLE algorithm (C.A.J. Fletcher, 1991), and time integration was performed with a second-order implicit scheme (C.A.J. Fletcher, 1991; J.H. Ferziger, M. Peric, 1996).

In all cases, the flow field was initialized with zero velocity in all directions. A transient phase, during which the flow evolved and reached a fully turbulent state, lasted approximately three flow-through time units, defined as $t_{FT} = L_x/U_{in}$. The time-averaging procedure was then performed over a duration of 40 $t_{FT}$. Additionally, spatial averaging was applied by sampling data from 10 uniformly distributed cross-sections along the spanwise direction. Convergence of the time-averaged results was verified by comparing statistical quantities obtained at $20t_{FT}$ and $40t_{FT}$. The simulations employed a constant time step of $\Delta t = 1 \times 10^{-4}$ s, resulting in a Courant–Friedrichs–Lewy (CFL) number not exceeding $CFL \approx 0.82$.

The inlet boundary, located at $x = -0.2$ m (see Fig. 2.3), was prescribed with a streamwise velocity profile, $U_x$, reconstructed using high-order polynomials to closely match the experimental measurements. Turbulent fluctuations at the inlet were introduced via the Fourier-based synthetic turbulence generation (STG) technique (Adamian et al., 2011; Shur et al., 2014). In this method, the fluctuating velocity field $\mathbf{u_i'}(\mathbf{r}, t)$ is synthesized as a weighted sum of spatio-temporal Fourier modes, scaled to ensure that the turbulent kinetic energy $K_t$ at the inlet corresponds to the target mean kinetic energy specified at the inflow.

$$\mathbf{u_i'}(\mathbf{r}, t) = 2K_t \sum_{n=1}^{N} \sqrt{q_n} \left[ \sigma^n \cos\left( k^n \mathbf{D}^n \cdot \mathbf{r} + \phi + s^n \frac{t}{\tau} \right) \right] \tag{2.6}$$

Here, $N$ represents the total number of Fourier modes; $q^n$ the normalized amplitude of the $n$-th mode; $k^n$ the magnitude of the wave number vector for mode $n$; $\mathbf{d}^n$ the randomly oriented unit direction vector; $\sigma^n$ the unit vector perpendicular to $\mathbf{d}^n$; $\phi^n$ the phase angle; $\tau$ the global time scale, and $s^n$ corresponds to the non-dimensional frequency of the $n$-th mode. The turbulent kinetic energy at the inlet was defined as $K_t = \frac{3}{2}\langle u_x u_x \rangle$, where brackets $\langle$ and $\rangle$ denote time averaging operators. The $K_t$ profile was prescribed based on experimental measurements of $\langle u_x u_x \rangle$, assuming isotropic turbulence.

The computational mesh, which was employed in papers 1-3, is shown in

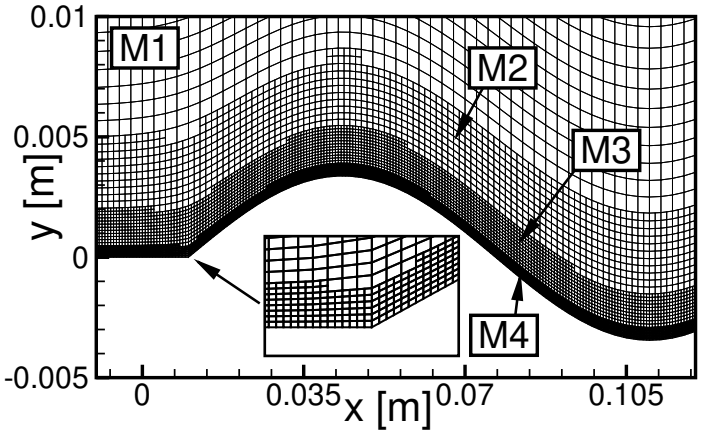



Figure 2.4: Computational mesh in the near-wall region. Note that the figure is stretched in the $y$–direction to better expose the view of the near-wall mesh adaptation.

Fig. 2.4. It was composed of a base part, labeled M1, and three successive refinement layers, M2 through M4. Each refinement level was generated by subdividing the cells of the preceding layer into eight smaller elements. This hierarchical refinement strategy enabled a high near-wall mesh resolution sufficient to resolve small-scale flow structures by placing the first node in the wall normal direction at $y^+ < 1$ ($y^+ = (y\sqrt{\tau_w/\rho})/\nu$), which is a commonly accepted requirement for wall-resolved LES (Pope, 2001). After such refinement, the mesh consisted of approximately $41.1 \times 10^6$ cells. The mesh was uniform in both the streamwise and spanwise directions, with grid spacings equal to: $0.3125 < \Delta x^+ < 2.5$, $0.3 < \Delta y^+ < 0.92$, and $0.3125 < \Delta z^+ < 2.5$.

## 2.2 Heat transfer enhancement

### 2.2.1 Objective outline

This part of the thesis examines the potential of WW for modifying heat transfer and temperature distribution in pipes and channels. Two test cases are considered: (i) an axisymmetric circular pipe, and (ii) a three-dimensional channel (see Fig. 2.5). In both cases, the objective is to minimize losses associated with the pressure drop, $\Delta p = p_2 - p_1$ (where $p_1$ and $p_2$ denote the static pressures measured upstream and downstream of WW, respectively), while simultaneously maximizing the uniformity of the downstream temperature

distribution, quantified by its standard deviation $\sigma_T$. To combine these metrics, a cost function $J$ is defined as

$$J = \left(\frac{\sigma_T}{\sigma_{T,\text{ref.}}}\right) \times \left(\frac{\Delta p}{\Delta p_{\text{ref.}}}\right), \tag{2.7}$$

where $\sigma_{T,\text{ref.}}$ and $\Delta p_{\text{ref.}}$ represent the reference values for a non-wavy heated surface. From the optimization perspective, wall shapes yielding $J \approx 1$ are equivalent to the flat channel, whereas $J > 1$ and $J < 1$ correspond to degraded and improved performance, respectively.

This objective, particularly the focus on temperature uniformity, is motivated by practical applications such as fuel injection systems, where uniform preheating the fuel prior to combustion can substantially enhance efficiency. Channels also play a central role in cooling applications, for example, in radiators commonly used for CPU thermal management. To address this objective, an optimization procedure is employed that couples Bayesian optimization (BO) with RANS computations in an active learning loop. The details of this procedure and description of the applied RANS model are provided in the next subsections, while the geometric parameters of both pipe (Fig. 2.5a) and channel (Fig. 2.5b) configurations, along with the specification of flow characteristics, are described in Sections 3.5 and 3.6.

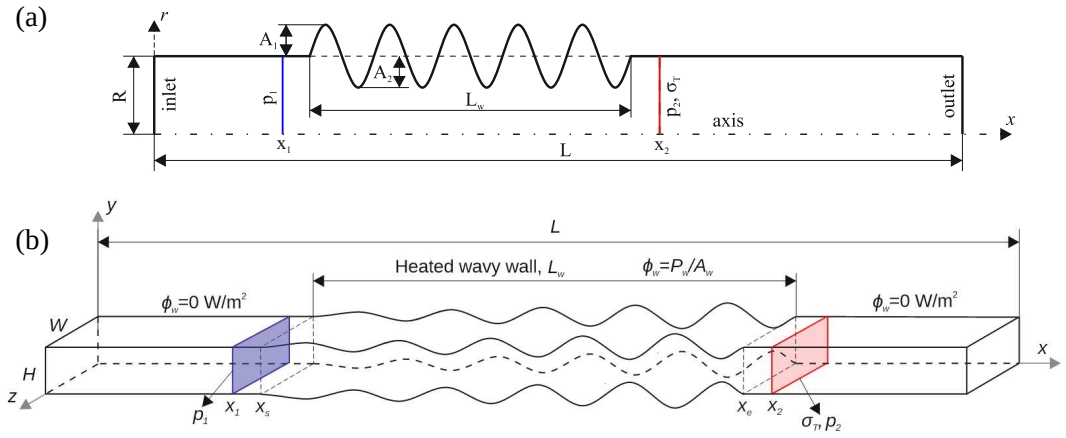



Figure 2.5: Test cases: (a) pipe configuration, (b) channel configuration.

### 2.2.2 Bayesian optimization

The goal of the optimization is to determine the optimal corrugation configuration $\mathbf{b}^*$, where the design vector $\mathbf{b}$ contains the parameters describing the wall

waviness, such that the cost function $J$ is minimized:

$$\mathbf{b}^* = \arg\min_{\mathbf{b}\in B} J(\mathbf{b}). \tag{2.8}$$

The optimization process is carried out using the BO method (Blanchard and Sapsis, 2021a), combined with the RANS simulations described in Section 2.2.3. BO is particularly well-suited for scenarios in which evaluations of the objective function are computationally expensive or time-consuming. The method treats the objective as a black-box function and builds a surrogate model in the form of a Gaussian process (GP), which provides a probabilistic approximation of the function's behavior (Blanchard and Sapsis, 2021b; Blanchard and Sapsis, 2022). The BO algorithm strategically balances exploration, that is, sampling in regions with high model uncertainty, and exploitation, which is sampling where predicted performance is promising. It enables rapid convergence to an optimal solution with far fewer evaluations than traditional optimization techniques. This efficiency makes BO especially valuable in tasks such as hyperparameter tuning or the optimization of complex simulation-based systems (Li et al., 2024).

**Algorithm 1:** Bayesian optimization

**Data:** $f$, $B$, $M_D$, $M$
**Result:** $\mathbf{b}^* = \arg\min_{\mathbf{b}\in B} f(\mathbf{b})$
Initialize: $D_{m-1} = \{\mathbf{b}_i, J_i\}|_{i=0}^{M_D}, \bar{f}, m = 1$
**while** $m \leq M$ **do**
  $\mathbf{b}_m = \arg\min_{\mathbf{b}\in B} \alpha(\bar{f}, D_{m-1})$ /* Derive the next sample */
  $J_m = f(\mathbf{b}_m)$ /* Test the sample, RANS */
  $D_m \leftarrow D_{m-1} \cup \{\mathbf{b}_m, J_m\}$ /* Enrich the dataset */
  Update $\bar{f}$
**end**
$\mathbf{b}^* = \arg\min_{\mathbf{b}_m\in D_m} J_m$

The complete procedure, outlined in Algorithm 1, has been implemented in a Python script. Starting from the initially generated data (sets of $\mathbf{b}$ parameters), the subsequent $M$ iterations involve performing the RANS computations, carrying out the optimization, and enriching the data set. In particular, at each iteration $m = 1, \ldots, M$, the current best cost function value $J_m$ and corresponding design vector $\mathbf{b}_m$ are used to update the GP model, which then proposes the next candidate design $\mathbf{b}_{m+1}$. Based on this updated parameter set, the wall

geometry is modified as shown in Fig. 2.6, and a corresponding RANS simulation is conducted. Once the simulation is completed, a new value of the cost function $J_{m+1}$ is extracted, incorporated into the dataset, and used to further refine the GP surrogate. The optimization loop continues until a maximum of $M = 1200$ iterations is reached.

### 2.2.3 Reynolds-averaged Navier-Stokes (RANS)

The flow is modeled as an incompressible ideal gas, with density treated as a temperature dependent variable determined via the equation of state. To reduce computational expense while enabling a broad parametric study, the flow is assumed to be steady and simulations are conducted using the RANS framework. Under these assumptions, the governing equations for continuity, momentum, and energy take the following form:

$$\frac{\partial(\rho\overline{u}_i)}{\partial x_i} = 0 \tag{2.9}$$

$$\rho\overline{u}_j\frac{\partial\overline{u}_i}{\partial x_j} = -\frac{\partial\overline{p}}{\partial x_i} + \frac{\partial}{\partial x_j}\left[(\mu+\mu_t)\left(\frac{\partial\overline{u}_i}{\partial x_j}+\frac{\partial\overline{u}_j}{\partial x_i}\right)\right] + \rho g_i \tag{2.10}$$

$$\rho c_p\overline{u}_j\frac{\partial\overline{T}}{\partial x_j} = \frac{\partial}{\partial x_j}\left[(\kappa+\kappa_t)\frac{\partial\overline{T}}{\partial x_j}\right] \tag{2.11}$$

where the bar symbol stands for the time-averaged variables, $T$ denotes the temperature, $g_i$ the gravitational acceleration, $\mu$ the dynamic viscosity is calculated using Sutherland's law, $\kappa = c_p\mu/Pr$, $\kappa_t = c_p\mu_t/Pr_T$ the molecular and turbulent thermal conductivities, $Pr$ and $Pr_T$ are the molecular and turbulent Prandtl numbers, $c_p$ the specific heat. The turbulent viscosity $\mu_t$ is modelled in two ways, depending on the RANS formulation employed. For the research presented in Paper 5 (Section 3.5), the transitional SST variant is used. In Paper 6 (Section 3.6), by contrast, the realizable $k$-$\epsilon$ model is adopted. Comparisons with experimental data for a rectangular-shaped wall (Zontul et al., 2021) showed that it provided the best agreement with the measurements

among various models tested. Details of the transitional SST model are given in Menter (1994) and Menter et al. (2006), while the realizable $k$-$\epsilon$ model is described in Shih et al. (1995).

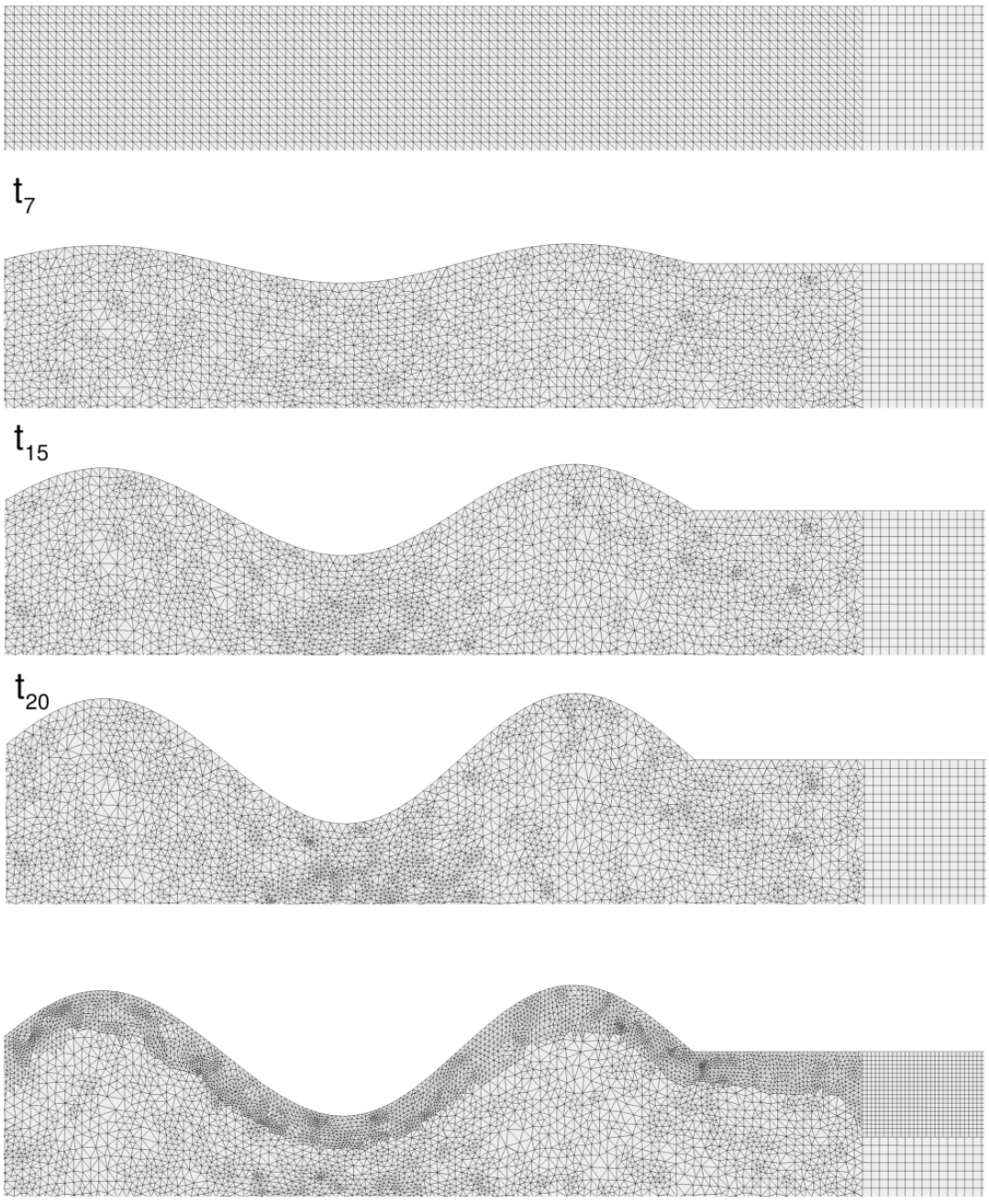



Figure 2.6: Stages of mesh generation for the sample waviness shape.

All simulations are carried out using ANSYS Fluent. A second-order spatial discretization scheme was applied to the governing equations for momentum, turbulent kinetic energy, specific dissipation rate, intermittency, and energy. Convective terms were treated using a second-order upwind scheme. For pressure–velocity coupling, the coupled algorithm was employed to improve con-

vergence stability. Near-wall flow behavior was modeled using the enhanced wall treatment approach (*Ansys Fluent Theory Guide* 2021), ensuring accurate resolution of the boundary layer under the applied meshing strategy. The strategy of generating the computational mesh is the same in Papers 5 and 6. The mesh is divided into two regions, as illustrated in Fig. 2.6, which presents an example mesh corresponding to a representative WW configuration. In the vicinity of the wavy section, the mesh is unstructured and composed of triangular elements, while the remainder of the domain is meshed using a block-structured grid consisting of quadrilateral cells. During each iteration of the optimization loop, when the BO algorithm (described in Section 2.2.2) proposes a new set of parameters defining the wall shape, the mesh is updated to conform to the modified geometry. The initial configuration for each case is based on a straight pipe, with its mesh shown at the top of Fig. 2.4. Following the modification of the wall shape, mesh adaptation is handled using ANSYS Fluent's Dynamic Meshing (DM) capability, which combines mesh smoothing and re-meshing techniques to generate a valid mesh for the new geometry. This process yields the mesh configurations shown at selected optimization stages ($t_7$, $t_{15}$, and $t_{20}$) in Fig. 2.4. To ensure accurate resolution of the near-wall region, an additional refinement is applied by subdividing the first ten layers of cells adjacent to the wall, as depicted in the bottom panel of Fig. 2.4. This procedure ensures adequate resolution of the viscous sublayer and maintains $y^+ \approx 1$, which is essential for the enhanced wall treatment.

# Chapter 3

# Comments to a series of articles

This dissertation is based on five original research articles and one preprint (so, 6 papers in total) developed over the course of four years of the author's PhD studies. The first four Papers focus on the control of turbulent flow separation and follow a logical progression. Paper 1 undertakes a validation of the LES approach against experimental data, specifically HWA measurements of velocity and fluctuations taken along the reference waviness. It then offers a detailed investigation of the near-wall flow both directly above WW and in its wake. The analysis focuses on time-averaged and instantaneous flow fields and examines how they are influenced by varying pressure gradient conditions. Building on this foundation, Paper 2 conducts a parametric analysis across a broad range of WW geometries. The goal of this analysis is to determine the sensitivity of separation-delay performance to the geometric parameters of WW. Paper 3 concludes this sequence by proposing an improved wall topology that demonstrates twice the performance of the reference shape considered in the preceding Papers. It is worth noting that in Papers 1–3, separation does not occur owing to the limited domain length. Consequently, the conclusions regarding its control are drawn based on $\tau_w$. Real separation is examined in Paper 4, which employs domain of sufficient length and investigates whether the separation-delay characteristics of WW persist under more realistic conditions, specifically, when embedded in a curved airfoil-type surface, in contrast to the flat-wall configurations examined in Papers 1–3. Furthermore, it evaluates the performance of waviness across a $Re_\tau$ range of 1200 – 2500, representing the variability in inflow conditions typically encountered in real-world scenarios. Papers 5 and 6 aim to present an additional application of surface

waviness, extending its use beyond separation control. It expands the scope of the research by applying BO in combination with RANS to design such WW configuration that maximizes heat transfer performance while minimizing pressure losses. This chapter presents the key findings from each of these studies, structured such that each section corresponds to one of the five publications.

## 3.1 Paper 1

**Kamiński, P., Niegodajew, P., Dróżdż, A., Sokolenko, V., Tyliszczak, A., & Elsner, W. (2024). Numerical analysis of novel wavy wall based control of turbulent boundary layer separation. Aerospace Science and Technology, 149, 109167.**

| Case name | Description |
|---|---|
| F-ZPG | Flat channel under ZPG |
| F-APG | Flat channel under APG |
| W-ZPG | Wavy channel under ZPG |
| W-APG | Wavy channel under APG |

Table 3.1: Description of test cases.

Paper 1 employs LES to investigate the effect of transversely oriented sinusoidal waviness (described in Section 2.1.2) on an incompressible, isothermal TBL developing both in the vicinity of WW and the downstream region. To analyse the contributions of the global APG to the flow field, alongside the modifications induced by WW, the results are compared with those obtained under ZPG conditions. The computational domain used for these simulations is described in detail in Section 2.1.3. The flow upstream of the wavy section is characterized by $Re_\tau = 2500$, which bridges the gap between $Re_\tau = 1350$ and 4000 considered and in the works of Drozdz et al. (2021) and Elsner et al. (2022). This Paper focuses on the flow dynamics near the crests and along the uphill and downhill sections of the waviness, where local variations in surface geometry are expected to induce flow separation, leading to significant flow complexity. These local detachment regions affect not only the boundary layer directly above the corrugation but also its downstream development. Consequently, the analysis includes both instantaneous flow quantities and mean flow statistics. The test cases considered in Paper 1 are summarized in Table 3.1.

A partial objective of the investigation presented in Paper 1 is to validate the employed LES approach. As previously discussed, the results are compared against HWA measurements obtained from the experiment described in Section 2.1.2. A direct comparison is shown in Fig. 3.1, which presents velocity and velocity fluctuation profiles obtained from LES alongside measurements reported by Kamiński et al. (2024). All profiles are normalized using the boundary layer thickness and the waviness wavelength. The validation is performed for the WW geometry investigated in Drozdz et al. (2021), at four characteristic

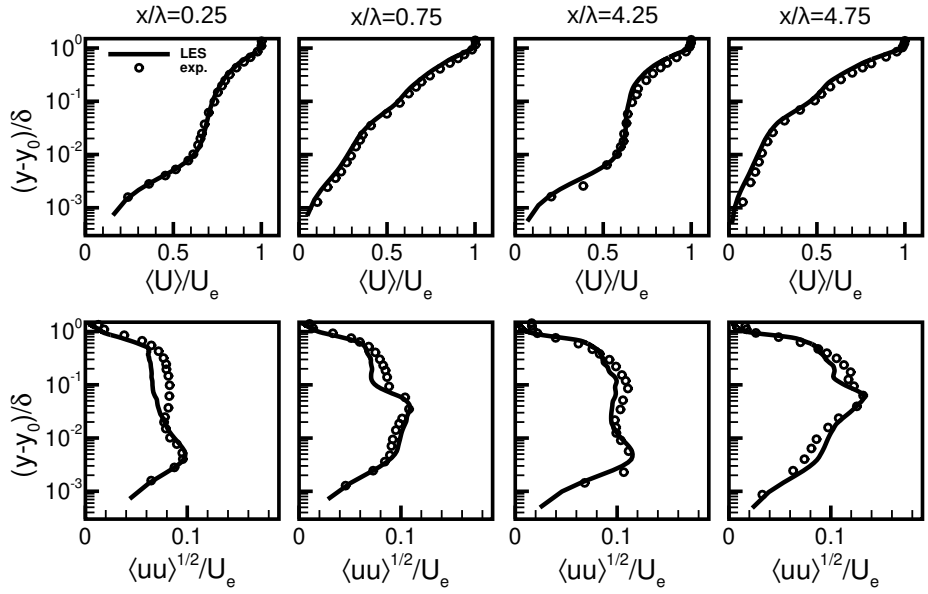



Figure 3.1: Comparison of simulation results with the experimental data.

streamwise locations: the crest and trough of the first wave ($x/\lambda$ = 0.25 and 0.75) and of the fifth wave ($x/\lambda$ = 4.25 and 4.75), respectively. As illustrated in Fig. 3.1, the numerical predictions show very good agreement with the experimental data. The mean velocity profiles (upper row) closely match the experimental results in both shape and magnitude. Although minor deviations are observed in the fluctuation profiles, the overall agreement remains strong. This level of consistency confirms the reliability of the numerical methodology and supports the credibility of the simulation results.

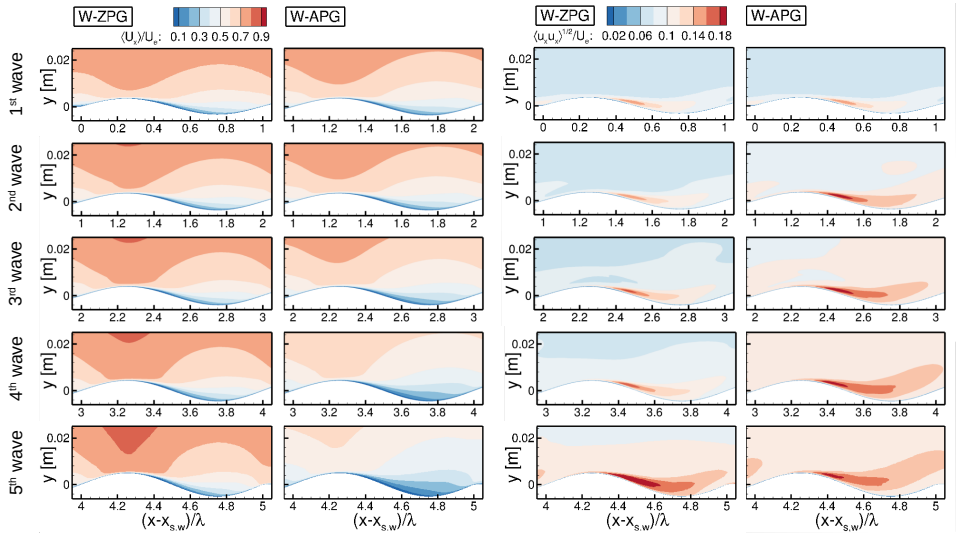



Figure 3.2: Contour maps of streamwise velocity (1st and 2nd columns) and its fluctuation (3rd and 4th columns) for cases W-ZPG and W-APG.

Paper 1 demonstrates that the waviness has a significant impact on the flow

field, influencing not only the mean velocity but also causing substantial modifications in the velocity fluctuations. These changes can be qualitatively identified by examining the flow field from a global perspective using contour maps of the streamwise velocity ($\langle U_x \rangle / U_e$) and its fluctuation ($\langle u_x u_x \rangle^{0.5} / U_e$), with both quantities normalized by the edge velocity $U_e = 0.99 U_\infty$, where $U_\infty$ denotes the freestream velocity. These results are presented in Fig. 3.2. Examination of the streamwise mean velocity reveals that the introduced waviness generates regions of local favorable pressure gradient (FPG, $dP/dx < 0$) on the uphill side and local APG on the downhill side of the waviness. This leads to an increase in streamwise velocity over the crest and a reduction within the trough. While this effect is present in both the W-ZPG and W-APG cases, the presence of a global APG in W-APG results in an overall reduction in streamwise velocity further downstream. Analysis of the streamwise velocity fluctuations shows that WW induces a local maximum on the downhill side. These peaks increase in magnitude and extend in the streamwise direction with increasing waviness amplitude, with the effect being slightly more pronounced in the W-ZPG case than in W-APG. However, further away from the wall, significantly higher levels of $\langle u_x u_x \rangle^{0.5} / U_e$ are observed with increasing waviness amplitude for W-APG compared to W-ZPG.

The analysis shown in Fig. 3.2 is further extended through a detailed examination of velocity and fluctuation profiles within successive waviness crests and troughs. It is shown that the waviness significantly influences the flow field, as evidenced by a pronounced reduction in velocity along the downhill slopes, i.e., where local APG develops, while the opposite trend is observed on the uphill sides due to local FPG. These modifications in the mean velocity are generally confined to the region $(y - y_0)/(h - y_0) \approx 10^{-1}$, which approximately marks the upper limit of the near-wall region for the present configuration. Moreover, on the uphill slopes, a noticeable upward shift of the logarithmic layer is observed relative to the uncorrucated case. In contrast, on the downhill slopes, particularly within the troughs, the log layer becomes indistinct. The influence of surface waviness is not limited to the mean velocity profile but also extends to the velocity fluctuations. These are found to increase on the downhill slopes and decrease on the uphill slopes within the near-wall region. The most pronounced changes occur within the troughs, where flow separation leads to the formation of a shear layer and a substantial amplification of $\langle u_x u_x \rangle^{0.5} / U_e$ near the wall. This overall effect of the waviness on TBL is further modulated when a global APG is present. The resulting changes, strongly dependent on the pressure gradient, are illustrated in Fig. 3.3, which presents profiles of streamwise velocity (rows 1 and 2) and fluctuations (rows 3 and 4) for both

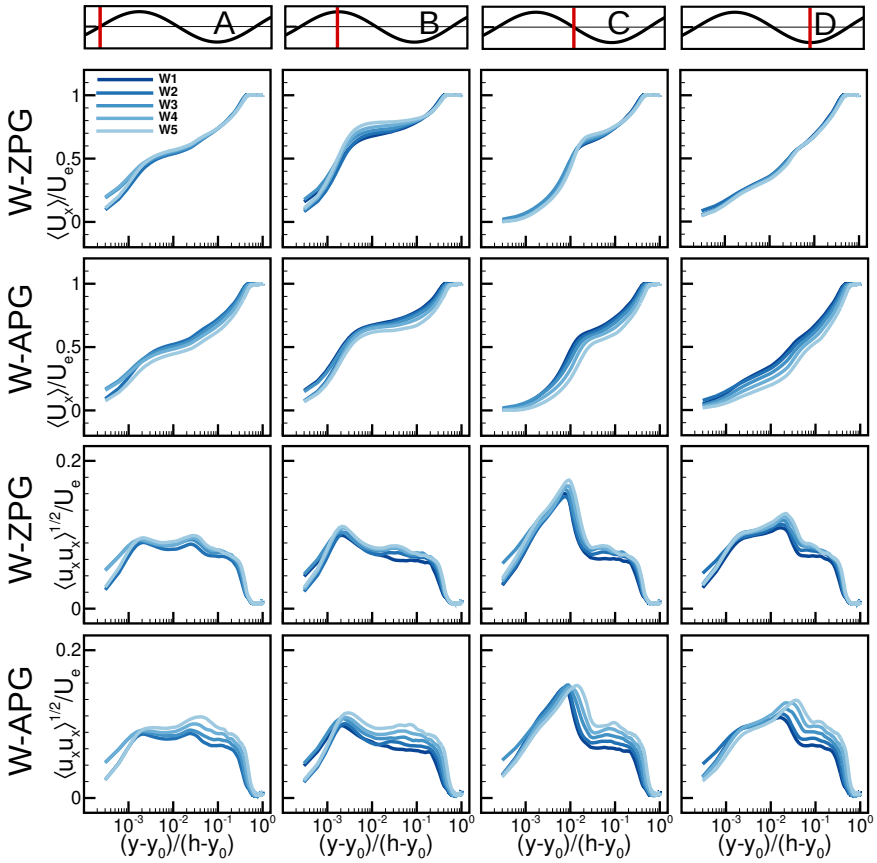



Figure 3.3: Streamwise velocity (rows 1 and 2) and fluctuation (rows 3 and 4) profiles for cases W-ZPG and W-APG presented as a function of $(y-y_0)/(h-y_0)$. Different characteristic location points of WW (A-D) on consecutive waves (W1-W5 indicated by shades of blue) are presented.

W-ZPG and W-APG cases, plotted as a function of $(y - y_0)/(h - y_0)$. The figure includes data at various characteristic wall locations (A–D) and at multiple streamwise positions (W1–W5), indicated by shades of blue. For the W-APG case, a consistent reduction in streamwise velocity is observed along WW (W1–W5), reflecting the effect of a progressively intensifying APG. In contrast, the velocity fluctuations are amplified by APG, with $\langle u_x u_x \rangle^{0.5}/U_e$ increasing downstream. Additionally, the outer peak of the fluctuation profile shifts farther from the wall as the streamwise distance increases.

In the subsequent part of Paper 1, the focus of the analysis shifts to the wall shear stress, specifically its time-averaged streamwise component, denoted as $\langle \tau_{w,x} \rangle$. Figure 3.4 presents $\langle \tau_{w,x} \rangle$ along both the flat and wavy wall ($0 < (x - x_{s,w})/\lambda < 5$), as well as in the downstream region ($5 < (x - x_{s,w})/\lambda < 8$), for all test cases. The grey line indicates $\langle \tau_{w,x} \rangle = 0$, corresponding to the onset of flow separation. A key observation is that the waviness results in an increase in wall shear stress in the downstream region only when the boundary layer is subjected to APG (Fig. 3.4c). Under ZPG conditions (Fig. 3.4b),

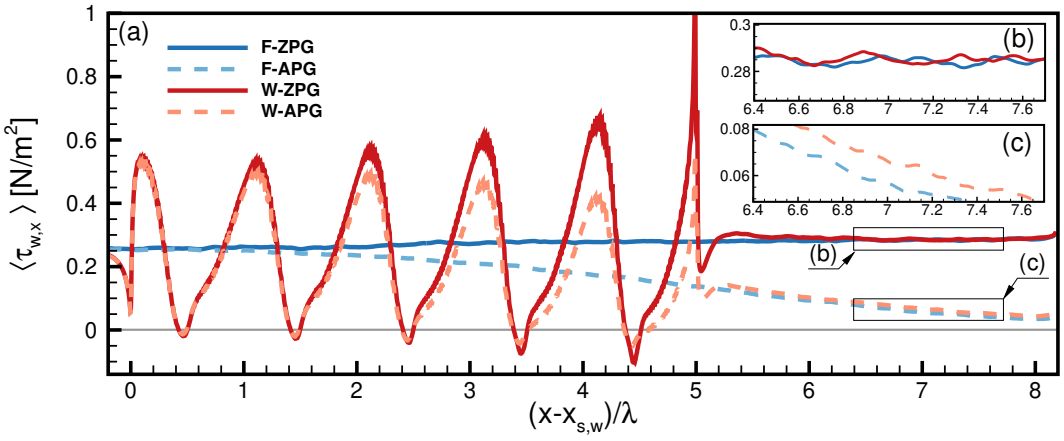



Figure 3.4: Time-averaged streamwise component of the wall-shear stresses at WW ($0 < x/\lambda < 5$) and downstream ($5 < x/\lambda < 8$) regions for all test cases. Grey line indicates separation manifested by $\langle\tau_{w,x}\rangle \leq 0$.

a local amplification of $\langle\tau_{w,x}\rangle$ is observed just downstream of the waviness ($(x - x_{s,w})/\lambda \approx 5.2$–$5.4$), after which it diminishes. Additionally, examination of regions where the profiles fall below the grey line (i.e., $\langle\tau_{w,x}\rangle \leq 0$) reveals that, in the W-APG case, the separation region increases in length with increasing streamwise distance considerably more than in the case of W-ZPG. This behavior is attributed to the progressively rising APG. This trend is further confirmed by identifying the locations where the $\langle\tau_{w,x}\rangle$ profiles intersect the grey line. These intersection points indicate the positions of boundary layer separation and reattachment, and are shown in Fig. 3.5, along with the distribution of the Clauser pressure gradient parameter $\beta = (\delta^*/\tau_w) \cdot (dP/dx)$, where $\delta^*$ denotes the displacement thickness. It should be noted that the Clauser parameter is commonly used to quantify the influence of the pressure gradient on a TBL. For $\beta > 5$, TBL is treated as largely influenced by APG (Vinuesa et al., 2017).

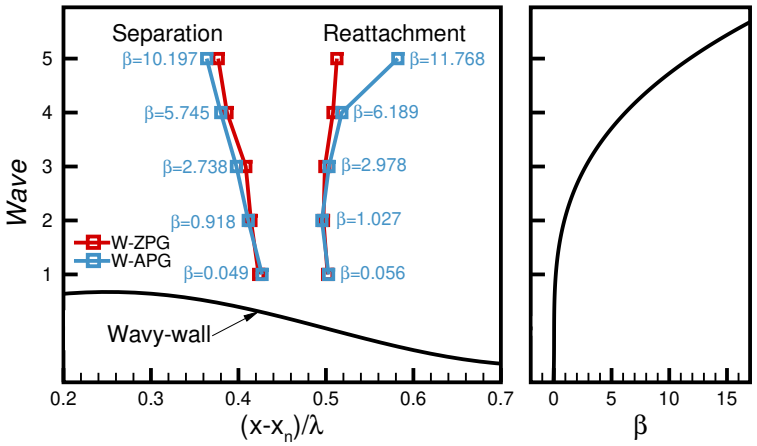



Figure 3.5: Locations of separation and reattachment points $(x - x_n)/\lambda$ and also $\beta$ distribution on each consecutive wave ($y$–axis).

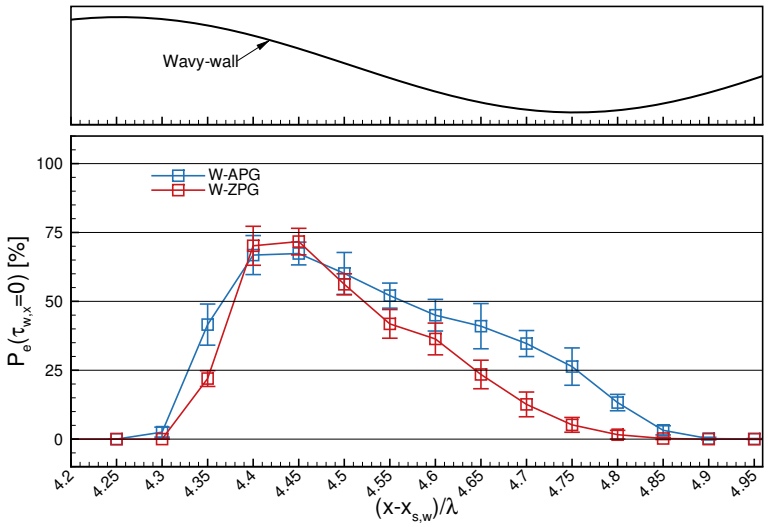



Figure 3.6: Exceedance probability ($P_e(\tau_{w,x} = 0)$) at selected locations of the downhill slope of the 5$^{th}$ wave for W-ZPG and W-APG cases.

Another important observation contributing to a more complete understanding of the flow within waviness cavities arises from the analysis of the instantaneous streamwise wall shear stress component, denoted as $\tau_{w,x}$. Specifically, it is found that the flow separation along the downhill slopes is a transient phenomenon. For example, in regions where $\langle\tau_{w,x}\rangle \leq 0$, such as at $(x - x_n)/\lambda \approx 0.45$ in Fig. 3.5, where TBL is detached (on average), instantaneous values of $\tau_{w,x}$ reveal that the flow is attached for some time periods, as indicated by the occurrences of positive $\tau_{w,x}$. This observation motivated the analysis involving the extraction of spanwise distributions of $\tau_{w,x}$ along the downhill slope of the fifth wave for both W-ZPG and W-APG cases. From these, the exceedance probability $P_e$ is computed using $\tau_{w,x} = 0$ as the threshold (to extract the share of locations with $\tau_{w,x} < 0$). The resulting distributions are presented in Fig. 3.6. It is observed that $P_e(\tau_{w,x} = 0)$ maintains higher values throughout most of the downhill slope in the W-APG case compared to W-ZPG, indicating a greater proportion of time during which $\tau_{w,x} < 0$. Notably, the locations where $P_e(\tau_{w,x} = 0) \approx 50$ % align well with the statistically determined separation and reattachment points shown in Fig. 3.5. This suggests that TBL may be considered separated (on average) when $P_e(\tau_{w,x} = 0) \approx 50$ %, a condition that also corresponds to $\langle\tau_{w,x}\rangle = 0$. For values where $P_e(\tau_{w,x} = 0) > 50$ %, the mean wall shear stress becomes negative, i.e., $\langle\tau_{w,x}\rangle < 0$.

To briefly summarize Paper 1, it has demonstrated that WW significantly alters the flow field. In many respects, its influence is consistent regardless of whether the TBL is subjected to APG or ZPG. However, for certain parameters, such as $\tau_{w,x}$, the waviness contributes positively only under APG conditions,

enhancing $\tau_w$ in the downstream region and promoting a delay in flow separation. Moreover, a detailed analysis of the instantaneous $\tau_{w,x}$ revealed the transient nature of TBL detachment within the wave cavities and enabled its quantification.

## 3.2 Paper 2

**Kamiński, P., Elsner, W., Tyliszczak, A., & Niegodajew, P. (2025). Sensitivity analysis of wavy wall performance in turbulent separation control: Effects of amplitude and period variations. Journal of Wind Engineering and Industrial Aerodynamics, 260, 106048.**

Paper 2 builds upon the findings from Paper 1 by employing an identical numerical configuration and conducting a parametric analysis to examine the impact of variations in waviness shape. Based on the conclusion from Paper 1 that WW enhances $\tau_w$ only under APG conditions, the focus is directed to this flow regime. The W-APG configuration (Tab. 3.1) is used as the reference case, and attention is put on the influence of waviness parameters, specifically the amplitude ($A$) and the number of waviness periods ($N_\lambda$), on TBL separation. To quantify the changes in amplitude, a scaling factor $A_0$ is introduced and used as a control variable. A new parameter is employed to characterize the waviness geometry: the effective slope (Napoli et al., 2008), given by:

$$ES = \frac{1}{L_{x,w}} \int_{L_{x,w}} \left| \frac{\partial A}{\partial x} \right| dx \tag{3.1}$$

This parameter is defined as the mean streamwise gradient of the corrugation and inherently accounts for both $A$ and $N_\lambda$. The primary objective is to identify combinations of $A$ and $N_\lambda$, corresponding to specific values of $ES$, that result in the greatest increase in $\tau_w$ relative to the flat wall case, to achieve maximum delay of the separation point. The analyzed cases span a range of effective slopes, from $ES = 0$ (flat wall) to $ES = 0.2455$ ($A/\lambda = 0.051$), and are summarized in Tables 3.2 and 3.3.

The main objective of Paper 2 is to determine the impact of the waviness parameters $A_0 = 0, 0.25, \ldots, 2.0$ and $N_\lambda = 1, 2, \ldots, 7$ on $\tau_w$ in the region downstream of the corrugation. In this area, an increase or decrease in $\tau_w$, denoted here as $\Delta\tau_w$ and expressed as a percentage, directly translates into a delay or advancement of the separation onset. The influence of the control parameters $A_0$ at fixed $N_\lambda$ on $\tau_w$ is presented in Fig. 3.7. It shows its variations as a function of $A_0$ at fixed $N_\lambda = 5$ (left) and as a function of $N_\lambda$ at fixed $A_0 = 1.0$ (right). With respect to amplitude, it is observed that increasing $A_0$ leads to a rise in $\Delta\tau_w$, reaching a maximum at $A_0 = 1.2$. Beyond this point, $\Delta\tau_w$ begins to decline. A

| $A_0$ | $A$ [m] | $A/\lambda$ | $ES$ | $A^+$ | $A/\delta$ |
|---|---|---|---|---|---|
| 0 | 0 | 0 | 0 | 0 | 0 |
| 0.2 | 0.00068 | 0.0051 | 0.0245 | 23 | 0.0083 |
| 0.4 | 0.00136 | 0.0102 | 0.0491 | 46 | 0.0166 |
| 0.6 | 0.00204 | 0.0153 | 0.0736 | 69 | 0.0249 |
| 0.8 | 0.00272 | 0.0204 | 0.0982 | 92 | 0.0332 |
| 0.9 | 0.00306 | 0.0230 | 0.1105 | 104 | 0.0373 |
| 1.0 | 0.00340 | 0.0255 | 0.1227 | 115 | 0.0414 |
| 1.1 | 0.00374 | 0.0280 | 0.1350 | 127 | 0.0456 |
| 1.2 | 0.00408 | 0.0306 | 0.1473 | 139 | 0.0497 |
| 1.3 | 0.00442 | 0.0331 | 0.1595 | 150 | 0.0539 |
| 1.4 | 0.00476 | 0.0357 | 0.1719 | 162 | 0.0580 |
| 1.5 | 0.00510 | 0.0382 | 0.1841 | 157 | 0.0622 |
| 1.6 | 0.00544 | 0.0408 | 0.1964 | 183 | 0.0663 |
| 1.8 | 0.00612 | 0.0459 | 0.2209 | 207 | 0.0746 |
| 2.0 | 0.00680 | 0.0510 | 0.2455 | 231 | 0.0829 |

Table 3.2: Test cases with the constant $\lambda = 0.133\ m$ ($\lambda/\delta_{avg} \approx 1.25$) and varying amplitude. The amplitude $A$ [m] and $\delta$ (used for calculating $A/\delta$) are measured at the tip of the first wave.

| $N_\lambda$ | $\lambda$ [m] | $\lambda/\delta_{avg}$ | $A/\lambda$ | $ES$ |
|---|---|---|---|---|
| 1 | 0.666 | 6.25 | 0.0051 | 0.0244 |
| 2 | 0.333 | 3.12 | 0.0102 | 0.0491 |
| 3 | 0.222 | 2.08 | 0.0153 | 0.0736 |
| 4 | 0.166 | 1.56 | 0.0204 | 0.0982 |
| 5 | 0.133 | 1.25 | 0.0255 | 0.1227 |
| 6 | 0.111 | 1.04 | 0.0306 | 0.1473 |
| 7 | 0.095 | 0.89 | 0.0357 | 0.1719 |

Table 3.3: Test cases with the constant $A_0 = 1.0$ and varying number of periods. The TBL thickness $\delta$ in $3^{rd}$ column is taken as the average value over the streamwise corrugation length $\delta_{avg}$.

similar trend is observed for variations in $N_\lambda$: $\Delta\tau_w$ increases with $N_\lambda$, peaking at $N_\lambda = 5$, after which a rapid decline follows. Notably, for $N_\lambda = 7$, a significant reduction in $\Delta\tau_w$ is observed compared to the reference case. In contrast to the behavior seen at lower values of $N_\lambda$, this leads to an earlier onset in separation.

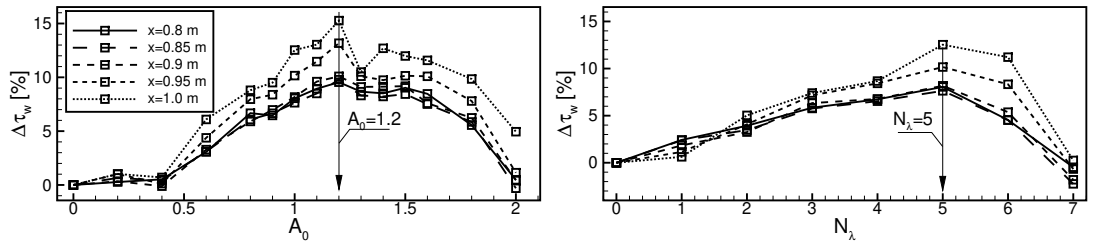



Figure 3.7: Wall-shear stress increase for variable $A_0$ (left) and $N_\lambda$ (right) at different distances from $x_0$.

The results presented in Fig. 3.7 allow for the identification of the most effective configurations among all those tested. It is found that, to achieve maximal wall shear stress enhancement at $Re_\tau = 2500$, the amplitude must be approximately 20 % greater ($A_0 = 1.2$) than that used by Drozdz et al. (2021) at $Re_\tau = 4000$ ($A_0 = 1.0$). To verify whether the enhancement in $\tau_w$ is sustained along the surface downstream of the waviness, the spatial distribution of $\tau_w$ in this region is shown in Fig. 3.8. The results confirm that the increase in $\tau_w$ persists throughout the entire downstream area, which satisfies the necessary condition for delaying the onset of flow separation.

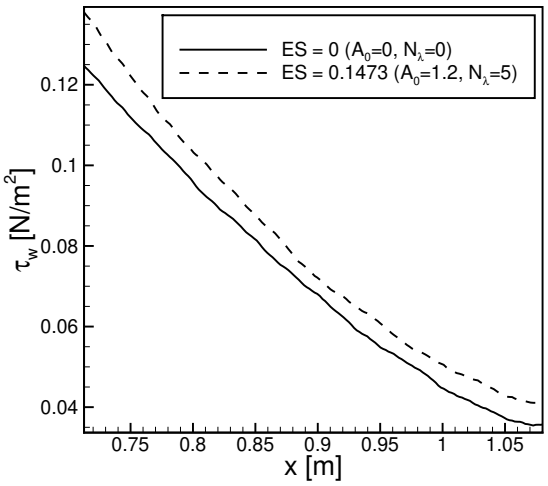



Figure 3.8: Wall-shear stress distribution for the optimal $ES = 0.1473$ ($N_\lambda = 5$, $A_0 = 1.2$) with respect to the flat wall configuration ($A_0 = 0$).

The decreasing trend in $\Delta\tau_w$ observed for $A_0 > 1.2$ or $N_\lambda > 5$, shown in Fig. 3.7, is suspected to result from increasingly large separation regions forming within the waviness troughs at higher values of $A_0$ or $N_\lambda$. To investigate this, Fig. 3.10 presents contour maps of the streamwise velocity component ($\langle U_x \rangle$), with regions where $\langle U_x \rangle < 0$, indicative of flow separation, highlighted in red. It can be observed that at $A_0 = 1.2$, flow separation is minimal and barely detectable. However, beyond this amplitude, the separation region grows rapidly, reaching a substantial extent at $A_0 = 2.0$. This behavior is believed to promote the shedding of large-scale vortices by the waviness geometry. Their presence is well seen in Fig. 3.9 showing the Q-parameter for the cases with $A_0 = 0.0, 1.0, 2.0$. The Q-parameter is defined as $Q = 0.5(\Omega_{ij}\Omega_{ij} - S_{ij}S_{ij})$, where $\Omega_{ij}$ and $S_{ij}$ are anti-symmetric and symmetric velocity gradient tensors. It shows the occurrence of coherent vortices (Hunt et al., 1988), which for $A_0 = 2.0$ are undoubtedly of the largest size. As these vortices convect downstream, they disrupt the boundary layer by extracting momentum from the near-wall region and transporting it away from the wall, via ejection events (Corino and Brodkey, 1969). This process effectively reduces the near-wall flow velocity, thereby diminishing $\tau_w$.

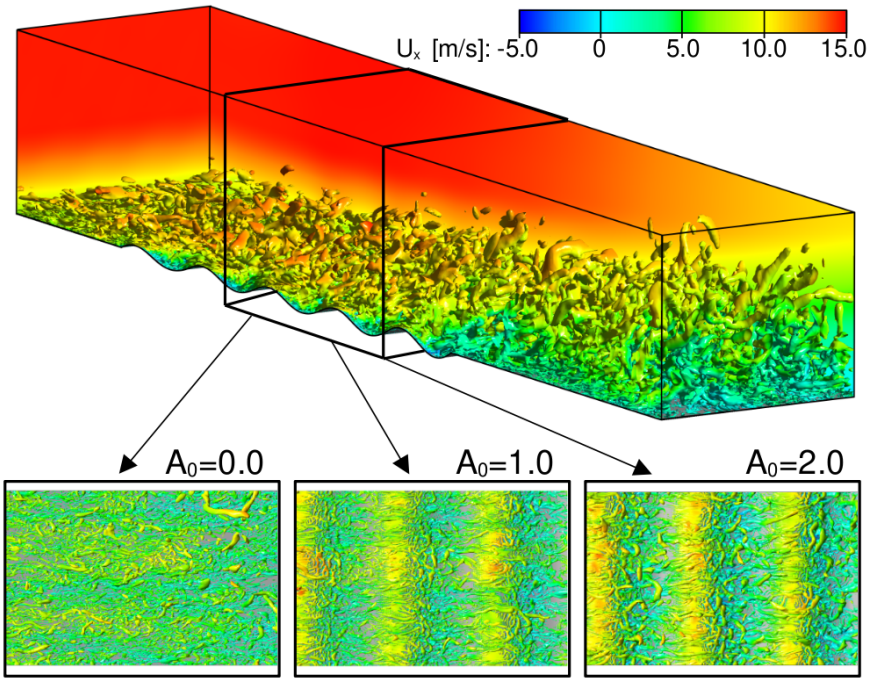



Figure 3.9: Q-parameter isosurface coloured by the streamwise velocity shown on the back side of the computational geometry.

To investigate the suspected momentum redistribution caused by variations in waviness shape, profiles of the mean streamwise velocity and its fluctuation, extracted at two downstream locations ($x$ = 0.8, 0.9 m), are presented in Fig. 3.11. Starting with the profiles of $\langle U_x \rangle$ (two subfigures on the left-hand side), it is observed that increasing $A_0$ leads to a reduction in velocity within the outer region of TBL ($y/\delta > 10^{-1}$). More pronounced differences emerge upon closer inspection of the near-wall region. Specifically, configurations that exhibit a higher or lower $\tau_w$ relative to that on the straight wall (Fig. 3.7) also show correspondingly higher or lower velocities in this near-wall zone. Regarding the streamwise velocity fluctuations $\langle u_x u_x \rangle^{1/2}$, it can be seen that their values are also significantly affected by changes in $A_0$. They increase throughout the entire boundary layer along with the increase in $A_0$. The most substantial changes occur at the so-called outer peak ($y/\delta \approx 0.3$), where the $\langle u_x u_x \rangle^{1/2}$ enhancement is most pronounced, especially for the case with $A_0 = 2.0$.

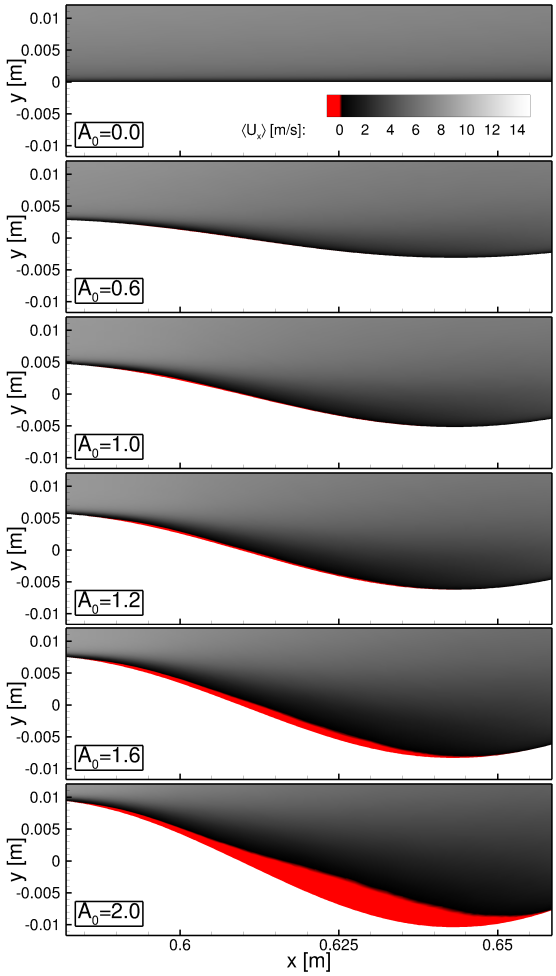



Figure 3.10: Contour maps of $\langle U_x \rangle$ at the last trough of the corrugation for the chosen $A_0$ cases at a constant $N_\lambda = 5$. The values of $\langle U_x \rangle < 0$ m/s, indicating the separation area, are marked with red.

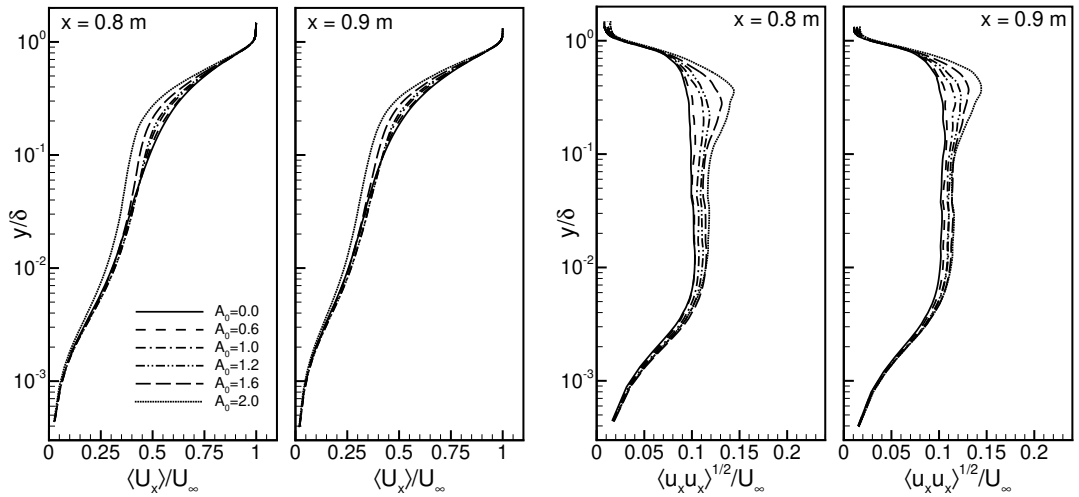



Figure 3.11: Comparison of the mean streamwise velocity (left) and its fluctuations (right) for variable $A_0$ and a constant $N_\lambda = 5$ at $x = 0.8\ m$ and $x = 0.9\ m$.

To briefly summarize Paper 2, the performed research enabled a detailed analysis of the influence of waviness geometry on wall shear stress enhancement, which directly translated into changes in flow separation behavior. The most

effective configuration, yielding the highest values of $\tau_w$, is identified for the considered flow conditions. In addition, the examination of both time-averaged and instantaneous flow quantities provided deeper insight into the underlying flow mechanisms, thereby extending the understanding established in Paper 1.

## 3.3 Paper 3

**Kamiński, P., Tyliszczak, A., Elsner, W., and Niegodajew, P. (2025). Turbulent separation control with a tilted wavy wall: A promising approach for energy savings in aerodynamic systems. Energy, 324, 135758.**

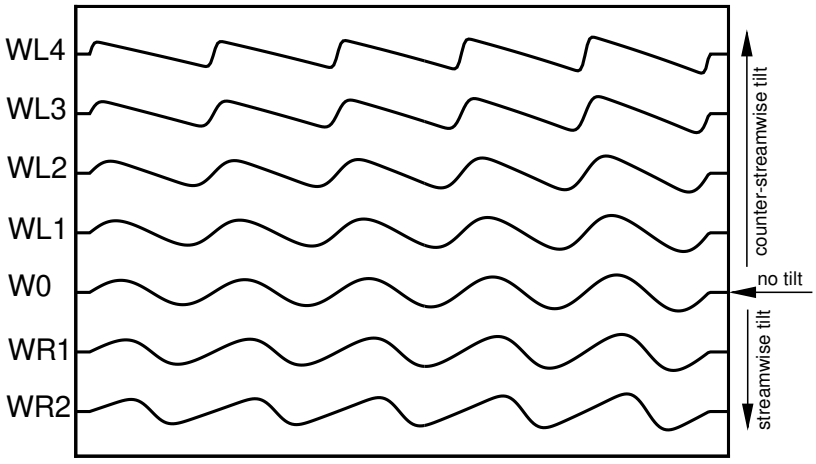



Figure 3.12: Waviness shapes.

Paper 3 concludes the efforts described in Papers 1 and 2 by demonstrating that the approach of controlling turbulent separation via the surface waviness can be substantially improved by introducing a novel type of WW characterized by tilting the subsequent waves. The research employs the same numerical setup and approach as in Papers 1 and 2 (also described in detail in Section 2.1.3). The waviness shape is a modified version of the regular sinusoidal shape considered previously. It is defined as:

$$y_0 = \sin\left(x\frac{2\pi N_\lambda}{L_{x,w}}\right); \quad \text{initial sinusoidal waviness} \tag{3.2}$$

$$y_i = \sin\left(x\frac{2\pi N_\lambda}{L_{x,w}} + \frac{y_{i-1}}{s}\right) + y_{i-1} \quad i = 1, 2, ..., I \tag{3.3}$$

$$y_{final} = A \times \left(\frac{y_I}{\max(|y_I|)}\right); \quad \text{normalization, scaling} \tag{3.4}$$

Here, $s$ is a parameter that defines the degree of tilt, and $I$ denotes the number of iterations ($i = 1, 2, ..., I$). Increasing $I$ results in a waviness profile that becomes progressively less smooth. This iterative approach allows for the gener-

ation of a wide range of waviness shapes. The specific geometries considered in Paper 3 are illustrated in Fig. 3.12, and the corresponding parameters used in the iterative procedure (3.2–3.4) are summarized in Table 3.4.

| Case | F | WL4 | WL3 | WL2 | WL1 | W0 | WR1 | WR2 |
|---|---|---|---|---|---|---|---|---|
| *s* | - | 1 | 1 | 1 | 2 | - | -2 | -1 |
| *l* | - | 4 | 3 | 2 | 2 | 0 | 2 | 2 |

Table 3.4: Parameters of the iterative procedure (3.2) for WW configurations.

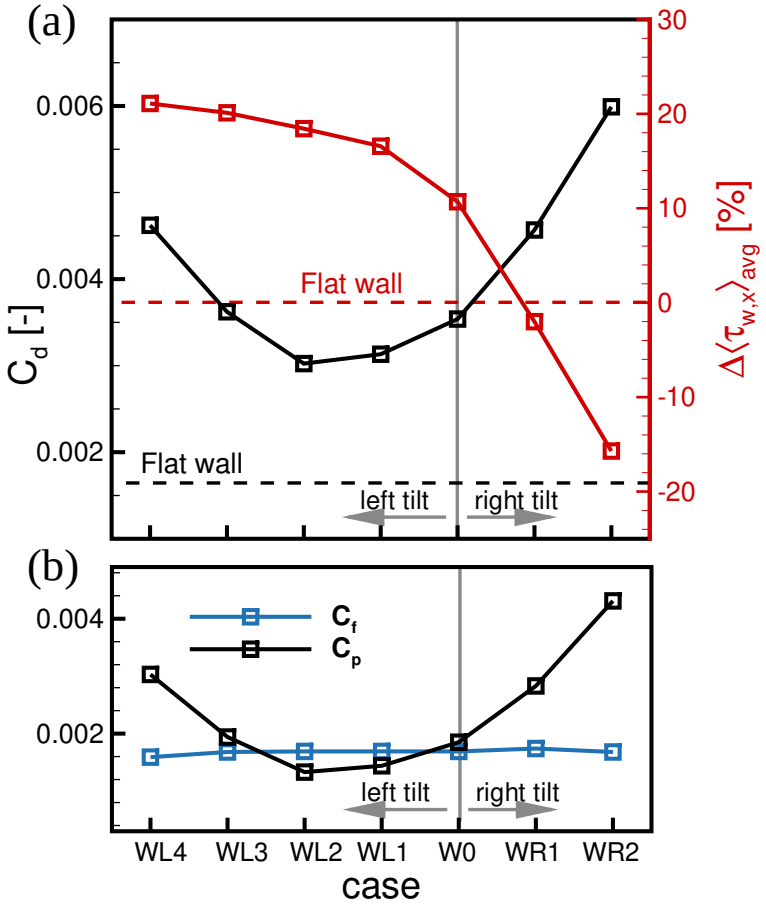



Figure 3.13: Profiles of: $C_d$, $\Delta\langle\tau_{w,x}\rangle_{avg}$ (a) and $C_p$ with $C_f$ (b) for all considered WW configurations.

Figure 3.13a presents the dependence of the spatially averaged streamwise wall shear stress $\langle\tau_{w,x}\rangle_{\text{avg}}$, relative to its counterpart on the flat wall, for all configurations considered (red line with symbols). It is expressed in percentage as $\Delta\langle\tau_{w,x}\rangle_{\text{avg}} = \langle\tau_{w,x}\rangle_{\text{avg}}/\langle\tau_{w,x,flat}\rangle_{\text{avg}} \times 100\%$. The spatial averaging, denoted $\langle\cdot\rangle_{\text{avg}}$, is carried out over all nodes spanning the full domain width of 0.24 m in the spanwise direction. The presented results are supplemented by the corresponding total drag coefficient values, $C_d = 2F_d/(\rho U_{\text{in}}^2 S_{\text{ref}})$, where $S_{\text{ref}}$ is the reference area, and $F_d$ is the drag force, computed as the surface integral of pressure and wall shear stress over the waviness section. Additionally, in Fig. 3.13b, the coefficients of viscous drag $C_f = \frac{2}{\rho U_{\text{in}}^2 S_{\text{ref}}} \int \tau_w \cdot \mathbf{i}\, dS$ and pressure drag $C_p = \frac{2}{\rho U_{\text{in}}^2 S_{\text{ref}}} \int (-p\mathbf{n})\hat{\mathbf{i}}\, dS$ (where $\tau_w$ denotes the wall shear stress vector, $\mathbf{i}$

and **n** the unit vectors in the free stream and wall normal directions respectively and $p$ the pressure at surface $dS$) are presented, which allows assessing their contribution to the total drag and mutual relation. A general observed trend is that leftward tilting increases $\Delta\langle\tau_{w,x}\rangle_{\text{avg}}$, whereas rightward tilting results in its reduction. These changes are accompanied by variations in $C_d$, whose value either increases or decreases depending on the tilt direction and magnitude. Notably, the configuration WL2 achieves a minimum in $C_d$ while yielding $\Delta\langle\tau_{w,x}\rangle_{\text{avg}}$ = 18.4 %, representing a 72.4 % improvement in wall shear stress relative to the baseline case W0, constituting a significant enhancement. Furthermore, configuration WL3 yields an even higher $\Delta\langle\tau_{w,x}\rangle_{\text{avg}}$ = 20.1 %, nearly doubling the improvement over W0 while maintaining the same $C_d$. If increased drag is not a limiting factor, further tilting, as in the configuration WL4, can be employed to achieve even greater gains in $\Delta\langle\tau_{w,x}\rangle_{\text{avg}}$. A notable finding is that WL2, followed closely by WL1, exhibits a dominance of viscous over pressure drag (i.e., $C_f > C_p$; see Fig. 3.13b), suggesting that these waviness configurations begin to resemble streamlined body shapes. For the remaining wall shapes, $C_p$ evidently dominates, which is the effect of local separation bubbles within WW, as will be discussed shortly.

The reduction in $C_d$ observed for the WL2 configuration, relative to the other cases, can most likely be attributed to the specific surface shape it adopts. As previously noted, this shape resembles that of a streamlined body, such as a teardrop, and is therefore expected to minimize flow separation along its surface. To investigate this, Fig. 3.14 presents contour maps of the mean streamwise velocity $\langle U_x\rangle$ at the final waviness trough for configurations W0, WL2, and WR2. As shown, the WL2 configuration fully eliminates separation on the downhill slope, thereby preserving near-wall momentum in the downstream region. In contrast, in the WR2 configuration, the opposite effect is found. It leads to a substantial increase in $C_d$ accompanied by a significant reduction in $\Delta\langle\tau_{w,x}\rangle_{\text{avg}}$.

The results presented thus far show that carefully adjusted waviness tilting can yield substantial benefits for TBL control. In the context of Paper 3, which addresses separation and drag reduction, the optimal choice is a leftward tilt, as it increases wall shear stress and decreases $C_d$ relative to a non-tilted surface. These effects suggest that the flow field, and in particular the turbulence, is strongly influenced by WW tilt. To inspect this, Figure 3.15 displays TKE fields for configurations F, W0, WL2, and WR2. An increase in TKE is observed for all wavy configurations compared to the flat reference case, with

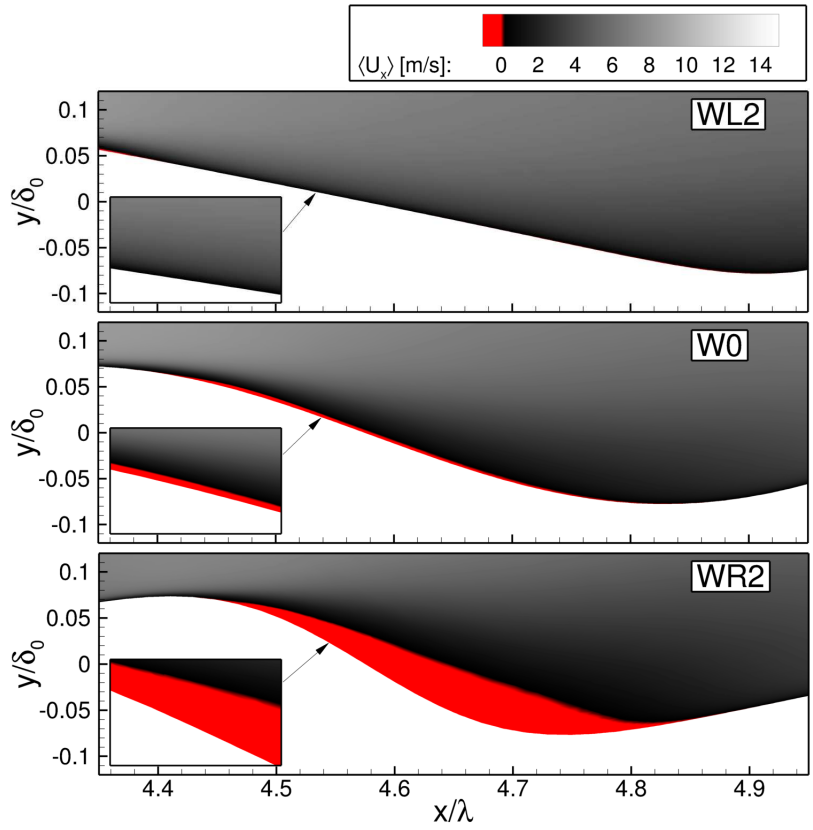



Figure 3.14: Contour maps of $\langle U_x \rangle$ at the last waviness trough.

the WR2 configuration exhibiting the highest levels, as indicated by the dark blue regions. As shown in the zoomed-in inset, the most elevated TKE values occur within the shear layer formed by the large recirculation zone downstream of the separation point, visualized by streamlines. These flow conditions are expected to promote significantly enhanced mixing, which can improve heat transfer efficiency at the wall, potentially facilitating more effective cooling in applications where thermal management is critical.

Summing up the findings presented in Paper 3, one may conclude that the control of turbulent separation via surface waviness can be significantly improved via tilting of WW. By applying an iterative sinusoidal transformation, a new class of waviness shapes is introduced, characterized by directional tilting of the wave peaks. Among the tested configurations, leftward tilting (WL1-WL4) substantially improves wall shear stress, with WL4 achieving the highest increase. Furthermore, WL2 combines enhanced shear stress with reduced drag, owing to its streamlined, separation-free geometry. The analysis of pressure and friction drag contributions confirms this aerodynamic benefit. Finally, investigation of turbulent kinetic energy fields reveals that tilted waviness shapes, particularly those with larger recirculation zones, promote increased mixing.

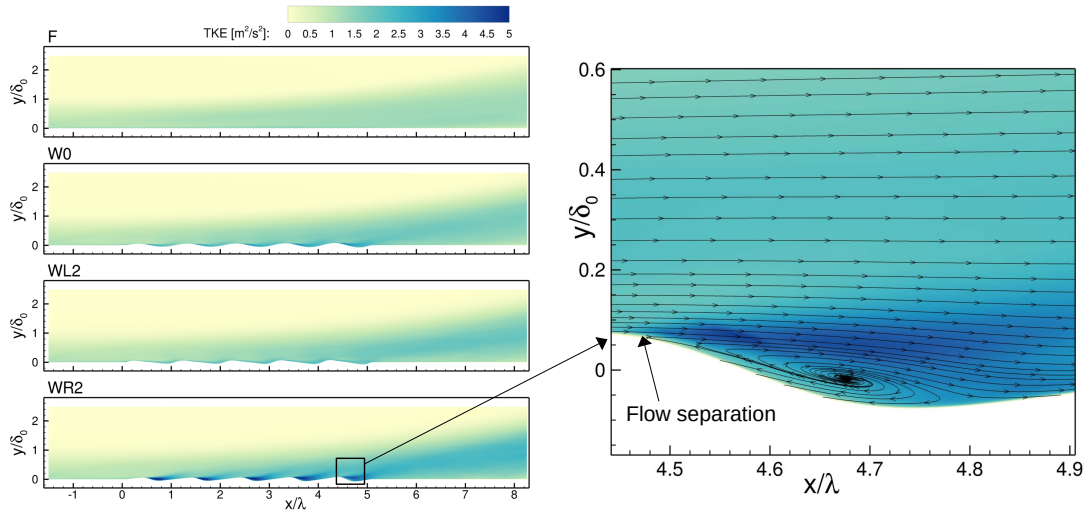



Figure 3.15: Contour maps of TKE for cases F, W0, WL2, and WR2.

## 3.4 Paper 4

**Kamiński, Piotr, et al. "Turbulent separation control on an airfoil surface using a wavy wall." Physics of Fluids 37.7 (2025).**

In previous works (Papers 1-3), waviness is shown to be particularly effective in enhancing $\tau_w$ and thereby contributing to the delay of turbulent separation. However, in those studies, the waviness is embedded in a flat surface, while the APG is imposed through the curvature of the top wall and additional suction. In contrast, real-world applications, such as wind turbine blades, involve surfaces where curvature, combined with a variable angle of attack, generates an APG that leads to TBL separation. Therefore, it is reasonable to examine the effectiveness of WW when embedded in a realistic surface, such as that of an airfoil. Paper 4 addresses this issue by embedding WWs into the suction side of a NACA 4412 airfoil. Furthermore, recognizing that flow conditions in real-world applications vary continuously, Paper 4 includes a $Re_\tau$ sensitivity analysis, in which the impact of WW is evaluated over a range of $Re_\tau = 1200 - 2500$.

The numerical approach is the same as in Papers 1-3, described in Section 2, with the primary modification being the use of a different computational domain, presented in Fig. 3.16. It shows a two-dimensional cross-section of a channel, with the horizontal and vertical directions denoted by $x$ and $y$, respectively. The spanwise depth extends to $z = 0.12$ m. Unlike in the previously discussed

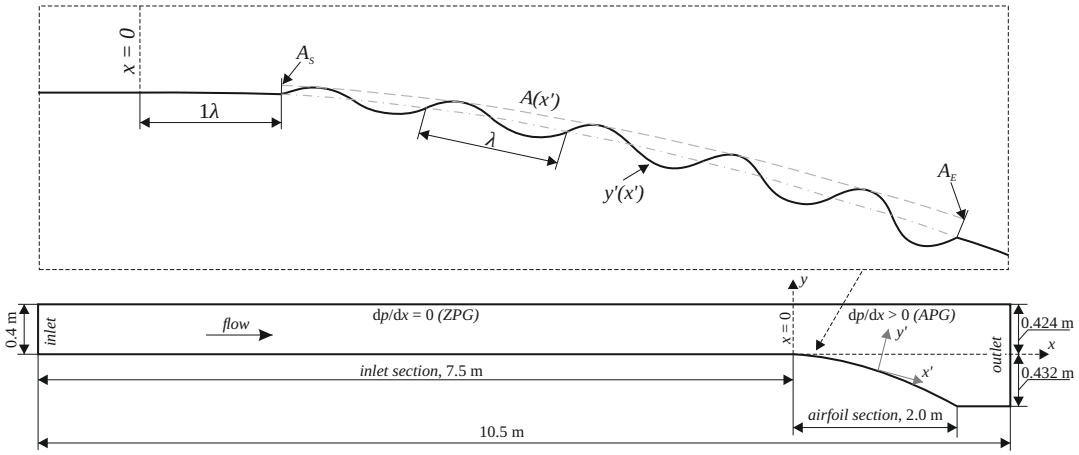



Figure 3.16: Schematic of the computational domain.

Papers, to establish a well-developed TBL and minimize the influence of synthetically generated turbulence at the inlet, a ZPG inlet section 7.5 m in length is placed upstream of the airfoil section. The latter begins at $x = 0$, has a length of 2.0 m and transitions into the outlet through a flat wall segment. The curvature responsible for inducing the APG reflects the suction side of a NACA 4412 airfoil, inclined at an angle of attack of 5°. The waviness begins at a distance of $1.0\lambda$ from $x = 0$ and its shape is defined as:

$$y'(x') = A(x') \cdot sin\left(\frac{2\pi}{\lambda} \cdot x'\right) \tag{3.5}$$

where $\lambda$ is the wavelength and $A(x')$ is the amplitude, and $x' - y'$ is the local coordinate system. Similarly to Papers 1-3, $A(x')$ increases in the streamwise direction proportionally to the growth of $\delta$ as:

$$A(x') = \frac{A_e - A_s}{(x_e - x_s)^2} \cdot (x')^2 + A_s \tag{3.6}$$

where $A_e$ and $x_e$ are the amplitude and streamwise position at the ending point of WW, while $A_s$ and $x_s$ are the amplitude and streamwise position at the starting point of WW, respectively. Test cases, as well as the variability of $\lambda$, $A_s$, $A_e$, and $N$ are outlined in Table 3.5. To provide information regarding the slope of the waviness, the parameter $ES$ is provided (Napoli et al., 2008). Its original definition given by (3.1) adopted for the present configurations read as $ES = 1/L_w \int_{x_s}^{x_e}(|\frac{\partial A(x')}{\partial x'}|)dx'$, where $L_w = N\lambda$ is the total WW length. The cases labeled W1 to W6 are arranged in ascending order of ES. The smooth airfoil surface is denoted as S.

Previous Papers have focused on the influence of WWs on $\tau_w$, which is expected to affect the location of flow separation. However, due to the limited

| Case | $\lambda$ [m] | $A_s$ [m] | $A_e$ [m] | $N$ | $ES$ |
|---|---|---|---|---|---|
| S | - | - | - | - | - |
| W1 | 0.110 | 0.00282 | 0.00464 | 6 | 0.125 |
| W2 | 0.135 | 0.00366 | 0.00641 | 5 | 0.136 |
| W3 | 0.150 | 0.00457 | 0.00802 | 5 | 0.153 |
| W4 | 0.135 | 0.00457 | 0.00802 | 5 | 0.170 |
| W5 | 0.120 | 0.00457 | 0.00802 | 6 | 0.183 |
| W6 | 0.110 | 0.00457 | 0.00802 | 6 | 0.208 |

Table 3.5: Test cases for the present work.

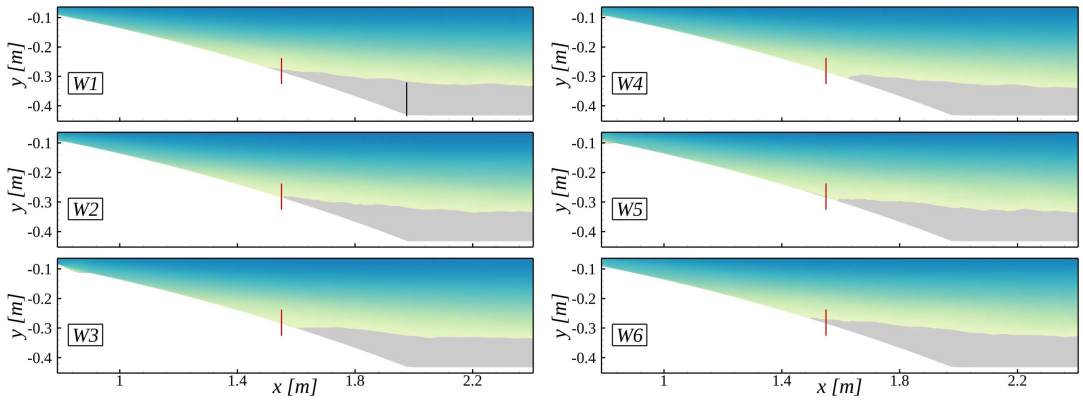



Figure 3.17: Contour maps of $\langle U_x \rangle$ for all tested configurations. The area with negative values of $\langle U_x \rangle$ is greyed–out to highlight the separation bubble. Red line marks the location of the separation point for the smooth airfoil (S).

length of the computational domain in Papers 1-3, separation did not occur. The domain considered in Paper 4 is significantly longer and therefore partially contains the separation region. This is illustrated in Fig. 3.17, which shows contour maps of $\langle U_x \rangle$ for all tested WW configurations. Regions with negative $\langle U_x \rangle$ values are shaded in grey to highlight the extent of the separation zone. A red line indicates the separation point for the smooth airfoil (S), while a black line (shown only for case W1) marks the boundary at $x$ = 2.0 m used to compute the cross-sectional area of the separation, $A_{sep.}$, which is discussed in detail later. Both the separation location and $A_{sep.}$ are significantly influenced by the presence of WW. In some cases, the waviness delays the onset of separation and reduces its extent, while in others, the opposite effect takes place. In the configuration W6, where the separation occurs even earlier than on the smooth airfoil, $A_{sep.}$ is the largest. In contrast, the most pronounced reduction in $A_{sep.}$ occurs in configuration W4, where the waviness postpones separation to the largest extent. The results obtained for this configuration will be compared against those for the S case. The analysis begins with a new element of the research, concerning what has been presented in Papers 1-3. As shown in Drozdz et al. (2021), the increments in $\tau_w$ are related to how the specific WW geometry impacts the energy distribution across turbulent scales. Figure 3.18

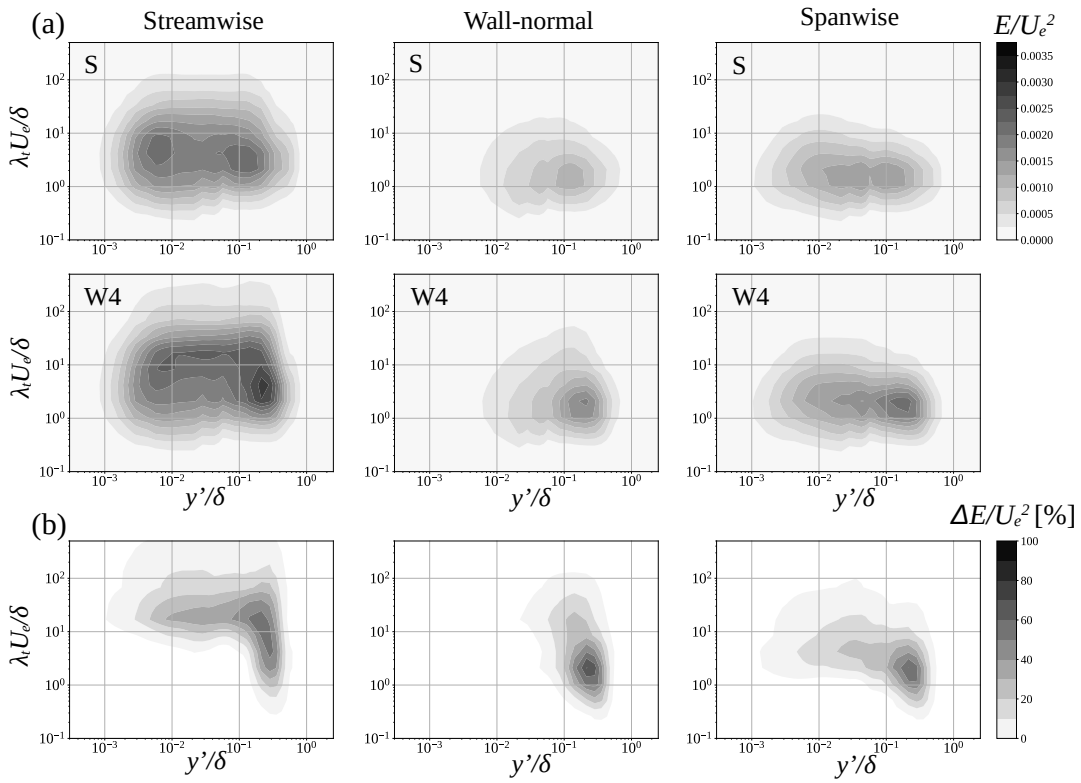



Figure 3.18: Energy spectra ($E$) computed based on the streamwise, wall-normal and spanwise components of velocity (consecutive columns) scaled by $U_e$ for S and W4 configurations (a). The difference in $E/U_e^2$ between S and W4 computed relative to the maximum value of $E/U_e^2$ reported for S (b).

shows the spectrograms computed based on the streamwise, wall-normal and spanwise velocity components scaled by $U_e^2$, for the S and W4 configurations. For the sake of simplicity, when referring to spectra computed based on specific velocity components, the terms such as streamwise, wall-normal or spanwise spectra are used. The results are presented in a normalized coordinate system, where both the time scale $\lambda_t$ and the wall-normal distance are scaled by $U_e$ and $\delta$. Such scaling is employed by Ganapathisubramani et al. (2012), who noted that, to distinguish between large and small scales, the threshold value of $\lambda_t U_e/\delta$ should be selected such that it barely touches the edge of the outer peak of the fluctuation profile. Here, $\lambda_t U_e/\delta = 2$ is adopted as the cutoff between large and small scales, consistent with findings from the work of Ganapathisubramani et al. (2012).

Streamwise spectra calculated for the S case exhibit two distinct peaks in $E/U_e^2$, a characteristic feature of APG boundary layers (Mathis et al., 2009), whereas for W4, a broad region of elevated $E/U_e^2$ is observed. Notably, in W4 the energy increases across a wide range of wavelengths ($1 < \lambda_t U_e/\delta < 80$), with a peak enhancement of approximately 70 % at $\lambda_t U_e/\delta \approx 10$. Furthermore,

the outer energy peak shifts significantly in the wall-normal direction, from $y'/\delta \approx 0.15$ (S) to 0.25 (W4), accompanied by intensified large-scale activity throughout the TBL thickness. Wall-normal spectra exhibit a single outer peak that shifts closer to the wall, from $y'/\delta \approx 0.25$ (S) to 0.15 (W4), and show a substantial energy enhancement (up to 80 %) at intermediate wavelengths ($\lambda_t U_e/\delta \approx 2$), primarily in the outer region. Interestingly, the same region shows a marked increase in the energy of small scales, likely because of the relatively high wall-normal velocity gradient in this area, as will be discussed shortly. Spanwise spectra, similarly to the wall-normal spectra, exhibit a single peak that shifts outward due to the presence of waviness. However, the enhancement in $E/U_e^2$ extends closer to the wall compared to the wall-normal spectra. The near-wall large-scale energy amplification observed in the streamwise and spanwise directions for W4 suggests increased activity of quasi-streamwise vortices, indicating enhanced momentum transfer toward the wall and contributing to higher $\tau_w$.

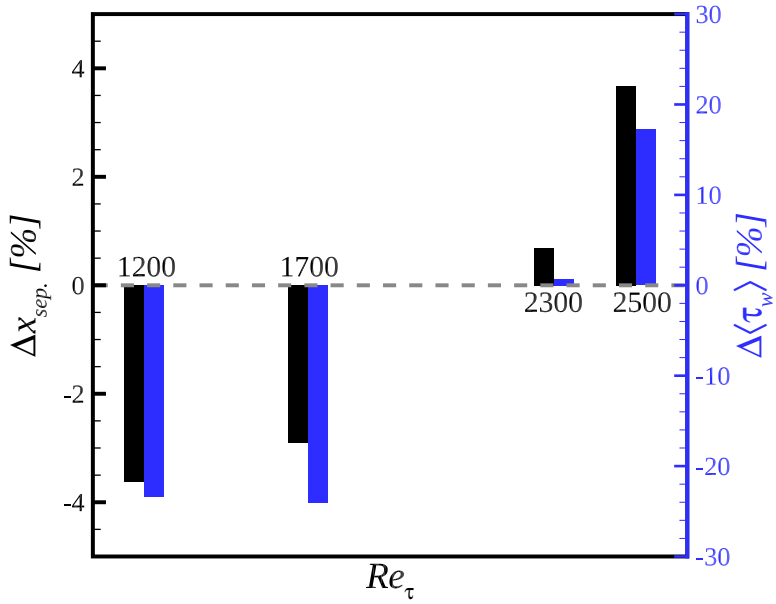



Figure 3.19: The effect of $Re_\tau$ on the change in the position of separation point for wave W4 with respect to smooth airfoil.

In practical applications, flow conditions frequently fluctuate, making it essential to evaluate the robustness of the proposed flow control strategy across a range of $Re$. Figure 3.19 presents the displacement of the flow separation point ($\Delta x_{sep.}$, shown in black) and the corresponding increase in mean wall shear stress ($\Delta\langle\tau_w\rangle$, shown in blue) for the W4 configuration relative to the S case. To assess the influence of $Re$ on the performance of WW, these metrics are reported for four values of $Re_\tau$: 1200, 1700, 2300, and 2500. The results indicate that W4 achieves the most pronounced separation delay (maximum

$\Delta x_{sep.}$) at $Re_\tau$ = 2500, accompanied by the largest $\Delta\langle\tau_w\rangle$. As $Re_\tau$ decreases, both $\Delta x_{sep.}$ and $\Delta\langle\tau_w\rangle$ diminish. The configuration remains effective down to $Re_\tau$ = 2300, and below this value, the trend reverses, i.e., both metrics become negative. This behavior is likely linked to the increase in TBL thickness at lower $Re_\tau$ compared to higher values. In effect, the waviness amplitude is not sufficiently large to penetrate the lower bound of the TBL, which is regarded to be the necessary condition for achieving separation delay (Drozdz et al., 2021). However, in the performed research, the same waviness profile is used across all $Re_\tau$ values. Consequently, at lower $Re_\tau$, $A(x')$ becomes too small relative to the growing $\delta$ to reach the region critical for effective modulation. This geometric limitation likely explains the observed decline in flow control performance at lower $Re_\tau$. On the other hand, it underscores the importance of designing the waviness profile in accordance with the expected flow conditions.

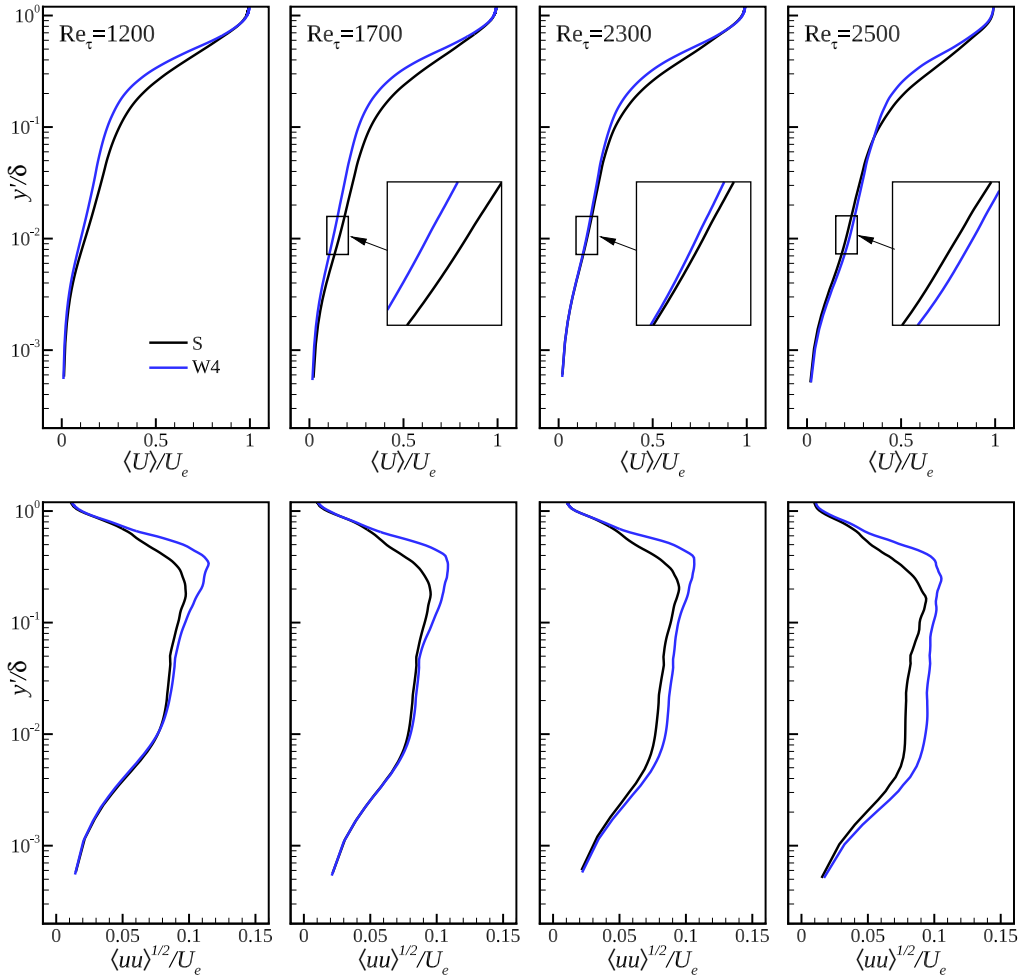



Figure 3.20: Profiles of velocity and fluctuations for various $Re_\tau$ taken for constant value of $\beta$ equal to 45.

To further explore the effect of the $Re_\tau$ variability, the profiles of $\langle U\rangle$ (upper row) and $\langle uu\rangle^{1/2}$ (bottom row) are presented in Fig. 3.20 for all the considered values of $Re_\tau$ (subsequent columns). The results are shown for cases S (black lines) and W4 (blue lines) at the locations corresponding to $\beta$ equal to 45. As

stated in Tanarro et al. (2020), such an approach ensures identical APG conditions regardless of $Re_\tau$. At $Re_\tau$ = 1200 and 1700, W4 shows reduced near-wall velocity at $y'/\delta < 7 \cdot 10^{-2}$, contributing to lower $\tau_w$. This difference fades at $Re_\tau$ = 2300 and at 2500 the trend reverses, where W4 exhibits increased near-wall velocity and thereby $\tau_w$. However, beyond $y'/\delta \approx 0.1$, in W4 the velocity consistently decreases regardless of $Re_\tau$. Such behaviour of TBL indicates an elevated rate of momentum transfer towards the wall (Hutchins and Marusic, 2007; Drozdz et al., 2021). The fluctuation profiles ($\langle uu \rangle^{1/2}$) show minimal differences near the wall for lower $Re_\tau$, but start to diverge once $Re_\tau$ exceeds 2300, with W4 exhibiting markedly higher fluctuations at 2500. Elevated fluctuation levels persist farther from the wall across all $Re_\tau$, indicating enhanced large-scale motion, which has also been observed in the spectrograms.

To briefly summarize Paper 4, the performed investigations aimed at the analysis of the impact of WWs on TBL developing along the airfoil-type surface. It represents a more realistic aerodynamic scenario compared to the previously studied flat-channel configuration (Papers 1-3). Building on earlier findings that demonstrated WW-induced enhancement of the wall shear stress, the present work examined the effect of WWs on the spectra of the energy distribution across a range of $Re$ representative of flow variability occurring in real-world flows. Among the tested configurations, case W4 is identified as the most effective in delaying separation and reducing its extent. This performance is associated with a broad amplification of turbulent energy across scales and enhanced momentum transport. The analysis shows that W4 increases large-scale energy both near the wall and in the outer region, which may contribute to improved momentum transfer toward the wall via large-scale structures. $Re_\tau$ sensitivity analysis reveals that the effectiveness of separation control improves with increasing $Re_\tau$, peaking at 2500, but degrades below 2300 due to the waviness amplitude being insufficient to reach the critical region of the boundary layer. These findings highlight the importance of properly tailoring the WW geometry to the expected inflow conditions in order to ensure desired separation control performance.

## 3.5 Paper 5

**Kamiński, P., Li, Y., Wawrzak, K., Tyliszczak, A., & Noack, B. R. (2024, November). Machine learning-supported CFD optimization of heat transfer in a pipe with a corrugated wall shape. Journal of Physics: Conference Series (Vol. 2899, No. 1, p. 012013). IOP Publishing.**

Previous papers, particularly No. 3, have demonstrated the considerable potential of surface waviness not only for controlling turbulent separation but also for enhancing turbulent kinetic energy, thereby facilitating mixing. These findings motivate a further extension of the WW application scope to control the heat exchange process, whose efficiency largely depends on the mixing intensity. In this context, the present work investigates the use of machine learning to optimize the WW shape in two cases: (i) an axisymmetric circular pipe and (ii) a three-dimensional channel. In both cases, the aim is to improve temperature uniformity while minimizing pressure losses. The content of Paper 5 is devoted to the first configuration.

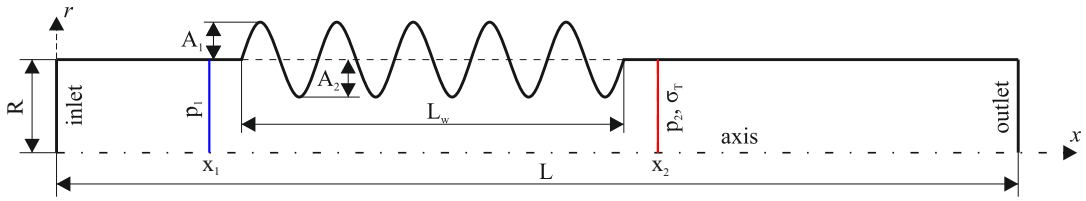



Figure 3.21: Axisymmetric circular pipe geometry.

The pipe (shown in Fig. 3.21) has a radius of $R = 0.005$ m and a total length of $L = 0.25$ m. The heated WW, which is subject to optimization, begins at $x = 0.05$ m from the inlet and extends over a length of $L_w = 0.1$ m. The inlet velocity is set to $U_{in} = 6.0$ m/s, yielding $Re = U_{in}D/\nu = 4000$ (where $D = 2R$), which falls within the range commonly studied in prior research (Liu and Sakr, 2013; Kurtulmuş et al., 2020; Zontul et al., 2021). The incoming flow is assumed to be turbulent, with a turbulence intensity of $T_i = u'/U_{in} = 2\%$, where $u'$ denotes the RMS of velocity fluctuations, and the inlet temperature is set to $T_{in} = 300$ K. A no-slip condition is applied at the wall, with thermal conditions varying along its length. Upstream of the WW, the wall temperature is held constant at $T_w = 300$ K. Within the heated segment, independent of the wall geometry, a constant heat flux is applied, defined as $\phi_w = P_w/A_w$, where $P_w = 10$ W is the supplied heating power and $A_w$ the surface area of WW. Beyond this section, the wall is treated as adiabatic with zero heat flux,

$\phi_w = 0$ W/m$^2$. It is important to note that imposing a constant heat flux implies that the local wall temperature adapts to the flow and geometric conditions at each point. In the reference case of a smooth-walled pipe, the wall temperature in the heated section reaches an average value of $T_{w,ave} = 395$ K, while the average fluid temperature at the outlet of the heated region is $T_{f,ave} = 317.5$ K.

The beneficial effect of the waviness, namely enhanced mixing, comes typically with a consequence of greater pressure drop along the pipe with respect to the uncorrugated configuration. The optimization goal is to find the wall shape ensuring the maximum temperature uniformity without a significant increase of $\Delta p$. Temperature uniformity is quantified using the standard deviation

$$\sigma_T = \frac{1}{S} \int \sqrt{(T(r,x) - T_{\text{ave}}(x))^2}\, \mathrm{d}r \tag{3.7}$$

where $S = \pi R^2$ is the surface area of the pipe cross-section, and $T(r,x)$ and $T_{\text{ave}}(x)$ denote the local and cross-section-averaged temperatures, respectively, at the location $x_2$ indicated by the red line in Fig. 3.21. The pressure loss is defined as $\Delta p = |p_2 - p_1|$, where $p_2$ and $p_1$ are the average static pressures at locations $x_2$ and $x_1$, respectively (also shown in Fig. 3.21). Combining together the parameters $\sigma_T$ and $\Delta p$ form the cost function $J$ - see Eq. 2.7.

The optimization process employs BO, which operates iteratively in conjunction with ANSYS Fluent to carry out RANS-based flow and heat transfer simulations. The details regarding this combined approach are given in Section 2.2.3. The optimization procedure involves shaping of the heated wall waviness in the central part of the pipe (see Fig. 3.21). Starting from a sinusoidal wall, its shape is modified through an iterative formula defined as:

$$r_1 = \sin\left(x \frac{2\pi N}{L_w}\right) \tag{3.8}$$

$$r_{i+1} = \sin\left(x \frac{2\pi N}{L_w} + \frac{r_i}{s}\right) + r_i; \quad i = 1, \ldots, I \tag{3.9}$$

where $r_i$ denotes the local pipe radius, $N$ stands for the number of periods along $L_w$, $s$ is a parameter defining the tilt, and $I$ denotes the number of iterations ($i = 1, \ldots, I$). The waviness becomes less smooth when $I$ increases. The amplitude of the waviness at $I$ is normalized to one and then multiplied by desired amplitudes $A_1$ and $A_2$ for radii $r > R$ and $r < R$ as follows

$$r_{I,1} = A_1 \times \left(\frac{r_I}{\max(r_I)}\right); \quad r_{I,2} = A_2 \times \left(\frac{r_I}{|\min(r_I)|}\right) \tag{3.10}$$

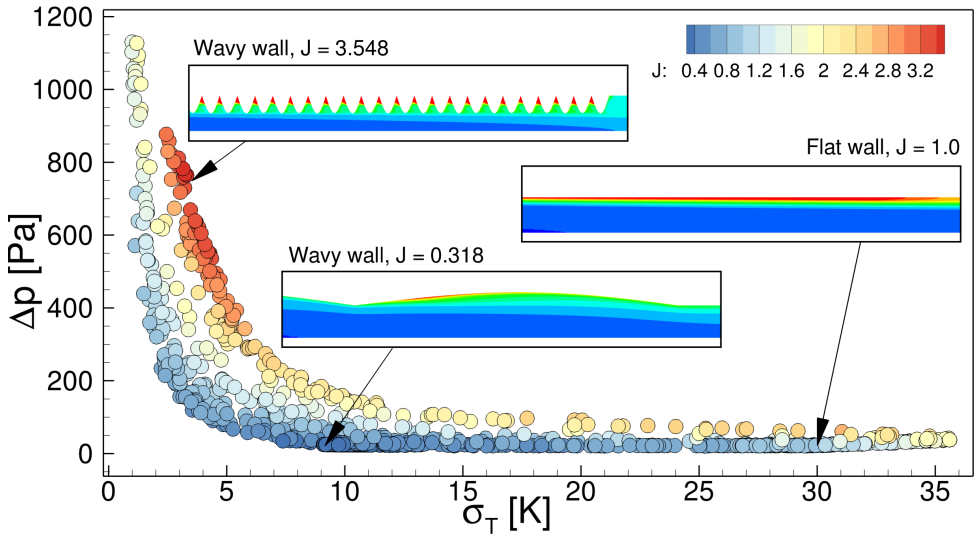



Figure 3.22: Scatter plot of $\Delta p = f(\sigma_T)$ coloured with $J$.

Paper 5 considers five control parameters ($A_1$, $A_2$, $s$, $I$, and $N$), which belong to the design vector **b** (see Algorithm (1) in Section 2.2.2), which undergo successive modifications in the BO-RANS optimization procedure (see Section 2.2.2) within 1200 iterations $m$. The results are presented in Fig. 3.22, which shows a scatter plot of all evaluated solutions, with $\Delta p$ plotted against the corresponding $\sigma_T$. The color of each marker represents the value of the objective function $J$. Note that when $J \approx 1$, the impact of waviness is minimal compared to the flat wall. On the other hand, its large values indicate a significant increase in $\sigma_T$ or $\Delta p$, or in both these parameters. Hence, the 'better cases' are only those with $J < 1$. The solutions depicted in Fig. 3.22 form a Pareto front, along which any change in **b** leads to a trade-off: a decrease in $\sigma_T$ is accompanied by an increase in $\Delta p$, and vice versa. It is clearly visible that configurations yielding small $\sigma_T$ values ($\sigma_T \to 0$ means the temperature uniformity) are associated with very high pressure drops. As a result, despite low $\sigma_T$, such configurations lead to unfavorable values of $J$. The combined BO–RANS process successfully identified an optimal configuration (see inset labeled "Wavy wall, $J = 0.318$"), characterized by two outward-facing waviness cavities. This shape enhances TKE production while minimizing obstruction in the pipe, thereby avoiding the large pressure losses seen in less favorable designs. By contrast, the worst-performing configuration, with all of the waviness peaks oriented inward, (see inset labeled "Wavy wall, $J = 3.548$") exhibits a pressure drop that heavily penalizes its performance. Notably, the optimal configuration yields an objective function value $J$ that is an order of magnitude lower than that of the worst case.

The inward orientation of the worst-performing waviness configuration is undoubtedly a major contributor to the high pressure drop $\Delta p$, and consequently the large value of $J$. However, another critical factor that indirectly contributes

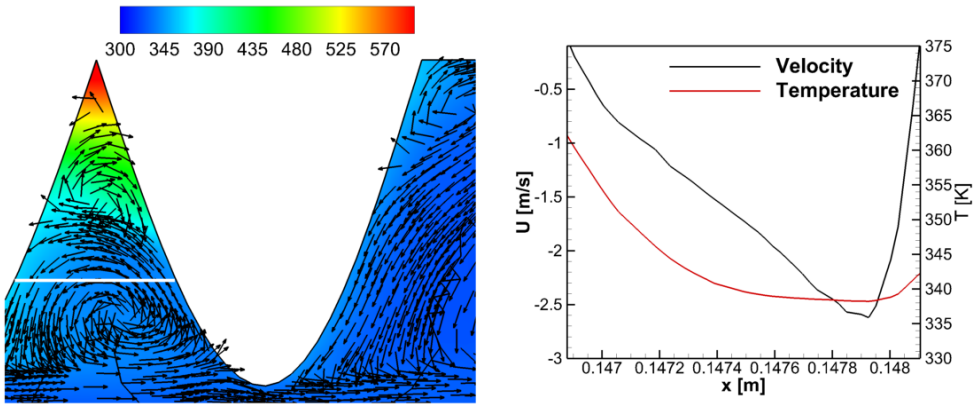



Figure 3.23: Temperature contours with the velocity vectors (left) and the velocity and temperature profiles (right) extracted along the white line inside the waviness for the worst wall shape.

to the detrimental character of this configuration is the presence of extensive recirculation zones between the waviness peaks. An example of such a zone is shown in Fig. 3.23, which presents temperature contours overlaid with velocity vectors (left), as well as velocity and temperature profiles (right) extracted along the white line inside the last waviness cavity. As shown, throughout its entire span, the flow undergoes strong recirculation. Two distinct recirculation regions are observed: a primary (large) driven by the core flow, and a secondary (small) where the recirculation is induced by the primary recirculation zone. Local flow velocities within the primary recirculation reach high negative values, nearly half the inlet value ($U_{in}$ = 6 m/s), as evident from the velocity profiles (right), leading to intense mixing and heat exchange closer to the flow core. However, the secondary recirculation region restricts heat transfer from the sharp corners of the cavity, where temperatures can reach nearly 600 K. As a result, even though the temperature closer to the pipe axis drops to a range of 340 – 360 K, this configuration would likely be unsuitable for practical applications due to the severe thermal gradients and resulting thermal stresses. Such conditions pose a high risk of material degradation and surface failure over a relatively short operational period.

In summary, Paper 5 extends prior research on surface waviness by applying a combined BO-RANS approach to optimize the corrugation of a heated pipe wall for enhanced thermal performance. The objective is to minimize temperature non-uniformity while limiting pressure losses. The performed optimization successfully identifies an outward-facing waviness configuration that achieves significant mixing and thermal uniformity with only moderate pressure drop, yielding over a tenfold improvement in the objective function $J$ over the worst-performing case. In contrast, inward-oriented shapes with deep cavities

generate extensive recirculation zones and severe pressure losses, ultimately resulting in high thermal gradients and increased risk of material failure.

## 3.6 Paper 6

**Kamiński, P., Wawrzak, K., Li, Y., Noack, B. R., & Tyliszczak, A. (2025). Design of the wavy wall in a partially heated channel using CFD simulations and human-assisted Bayesian optimization. arXiv preprint arXiv:2509.04030.**

Paper 5 demonstrated that an appropriately designed WW shape can substantially enhance heat transfer while inducing only a minimal pressure drop in pipes. Paper 6 extends this work to a different configuration, namely a thin channel, which represents a critical component of compact heat exchangers. The computational domain and numerical procedure are described in Section 2.2.3. As in the pipe (Paper 5), the objective is to minimize the pressure drop $\Delta p$ and maximize the temperature uniformity ($\sigma_T \to 0$), combined through the same cost function (Eq. 2.7). However, to preclude the detrimental thermal stress effects on sharp wall edges, identified in Paper 5, the wall-deforming function is modified.

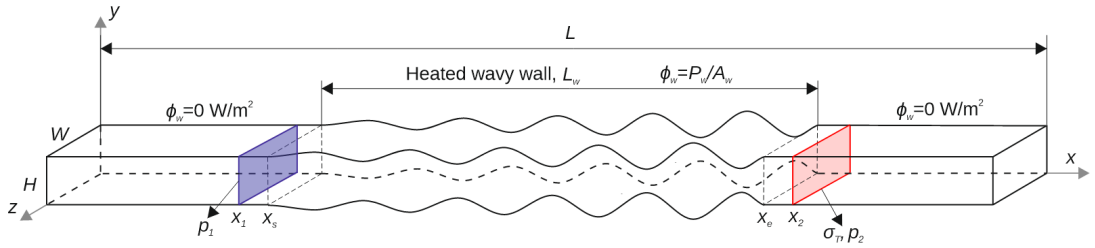



Figure 3.24: Geometry of the 3D channel.

The channel geometry and flow parameters are adapted from Zontul et al. (2021). The original configuration comprised a straight inlet section, followed by a heated wall with a series of rectangular cavities, and terminated with a flat wall. In the present work, the central section of the domain is modified into a WW shape, as illustrated in Fig. 3.24. The channel dimensions are $H = 0.018$ m in height, $W = 0.15$ m in width, and $L = 1.22$ m in length. The heated WW section has a length of $L_w = 0.5$ m and extends from $x_S = 0.36$ m to $x_E = 0.86$ m.

At the inlet, water enters with a velocity of $U_{in} = 0.112$ m/s, corresponding to a Reynolds number $Re = \rho U_{in} H/\mu = 2000$ ($\rho$ is the mass density and $\mu$ the molecular viscosity). This value lies well within the range of Reynolds numbers

considered in previous studies (Liu and Sakr, 2013; Kurtulmuş et al., 2020; Zontul et al., 2021). The inflow is assumed to be in a low-turbulence regime with an intensity $T_i$ = 1%, The inlet temperature is set to $T_{in}$ = 300 K.

To eliminate the influence of side boundaries on the flow in the central region, periodic boundary conditions are applied. This treatment removes the need to resolve near-corner flows, which would otherwise require specially tailored computational meshes. All sections of the upper and lower channel walls are treated as no-slip. In the sections upstream and downstream of WW, the walls are adiabatic, with zero heat flux ($\phi_w$ = 0 W/m$^2$). In the WW section, regardless of shape, a constant heating power of $P_w$ = 10000 W is imposed, yielding a wall heat flux $\phi_w = P_w/A_w$, where $A_w$ is the surface area of WW. Specifying the thermal boundary condition in terms of heat flux implies that the local wall temperature varies with the WW geometry and the flow state near the wall. For a non-wavy channel, the heated wall reaches an average temperature of $T_{w,\text{mean}}$ = 379.2 K, while the mean fluid temperature downstream of the heated section is independent of wall shape and equals $T_{f,\text{mean}}$ = 307.9 K.

Two approaches are employed to alter the wall shape, differing in the number of control parameters and hence in the flexibility of the waviness. The first approach modifies a sinusoidal wave by adjusting the number of periods, amplitudes, and tilt. Examples of wall shapes generated by this method are shown in Fig. 3.25.

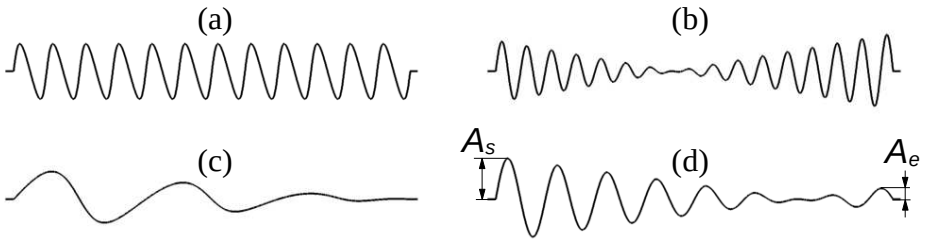



Figure 3.25: Schematic drawings of sample wall shapes generated by the waviness function.

In this approach, the wall shape is generated through an iterative procedure, starting from a sinusoidal profile and deforming it according to 4 control parameters. The procedure is defined as:

$$y_1(x) = \sin\left(x\frac{2\pi N}{L_w}\right) \tag{3.11}$$

$$y_{i+1}(x) = \sin\left(x\frac{2\pi N}{L_w} + s y_i(x)\right) + y_i(x); \quad i = 1, \ldots, I \tag{3.12}$$

Here, $y_i(x)$ denotes the local amplitude of the waviness relative to $y = \pm H/2$, $N$ is the number of periods along $L_w$, $s$ defines the tilt, and $I$ is the number of iterations ($i = 1, \ldots, I$). As $I$ increases, the waviness becomes progressively tilted. For simplicity, the number of iterations is fixed at $I = 5$.

During the successive iterations, the waviness height is unconstrained and may become arbitrarily large or small. In extreme cases, this could lead to complete channel blockage if $y_i \geq H/2$. To avoid this and to maintain the external dimensions of the channel, the maximum waviness amplitude at iteration step $I$ is normalised to unity and then scaled by the prescribed amplitude, as follows:

$$y_I(x) = A(x) \times \left( \frac{y_I(x)}{\max(y_I(x))} \right) \tag{3.13}$$

with $A(x)$ varying along the streamwise direction. In the range $x \in [x_S, x_E]$, it defined as

$$A(x) = A_s + \frac{A_e - A_s}{L_w}(x - x_S) \tag{3.14}$$

where $A_s$ and $A_e$ denote the amplitudes at the beginning and end of the waviness, respectively (see Fig. 3.25). The four-parameter design space defining the wall shape thus consists of $A_s$, $A_e$, $N$, and $s$.

The second approach employs a spline-type interpolation function (PCHIP, Kahaner et al. (1989)), enabling free-form modifications of the waviness without the periodic restriction of the sinusoidal pattern. Sample wall shapes obtained by applying this method are shown in Fig. 3.26.

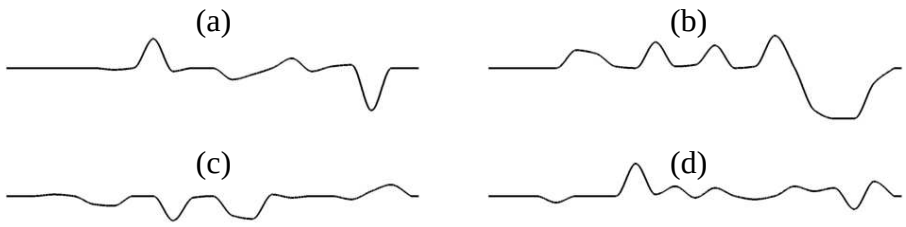



Figure 3.26: Schematic drawings of sample wall shapes generated by PCHIP.

PCHIP is defined by 21 control points uniformly distributed between $x_S$ and $x_E$. With the exception of the first and last points, their amplitudes are treated as control parameters subject to optimization. At the first and last points, the amplitudes ($y_0$ and $y_{20}$) are fixed at zero. This constraint ensures continuity of both the polynomial and the channel walls, while also enforcing the condition $dy/dx = 0$ at $x = x_S$ and $x = x_E$. Consequently, the design space comprises

19 parameters corresponding to the amplitudes $y_{1-19}$. PCHIP between two successive control points $x_j$ and $x_{j+1}$ is defined as:

$$y(x) = h_{00}y_j + h_{10}\left(\frac{\partial y}{\partial x}\right)_j (x_{j+1} - x_j) + h_{01}y_{j+1} + h_{11}\left(\frac{\partial y}{\partial x}\right)_{j+1} (x_{j+1} - x_j) \tag{3.15}$$

where $h_{00}$, $h_{10}$, $h_{01}$, $h_{11}$ are the basis functions, defined as

$$\begin{aligned} h_{00} &= (1+2t)(1-t)^2,\ h_{10} = t(1-t)^2 \\ h_{01} &= t^2(3-2t),\ h_{11} = t^2(t-1) \end{aligned}$$

with $t = (x - x_j)/h_j$, where $h_j = x_{j+1} - x_j$. To preserve monotonicity, the derivatives of the polynomial are defined in a manner that prevents spurious oscillations between data points. As a result, PCHIP closely follows the control-point profile, ensuring that the polynomial extrema do not exceed those of the data. The derivatives are given by:

$$\left(\frac{\partial y}{\partial x}\right)_j = \begin{cases} 0 & \text{if } \Delta y_j \Delta y_{j-1} \le 0 \\ \dfrac{(w_1+w_2)}{(w_1/\Delta y_{j-1} + w_2/\Delta y_j)} & \text{otherwise} \end{cases} \tag{3.16}$$

with $w_1 = 2h_j + h_{j-1}$, $w_2 = h_j + 2h_{j-1}$, $\Delta y_j = (y_{j+1} - y_j)/h_j$.

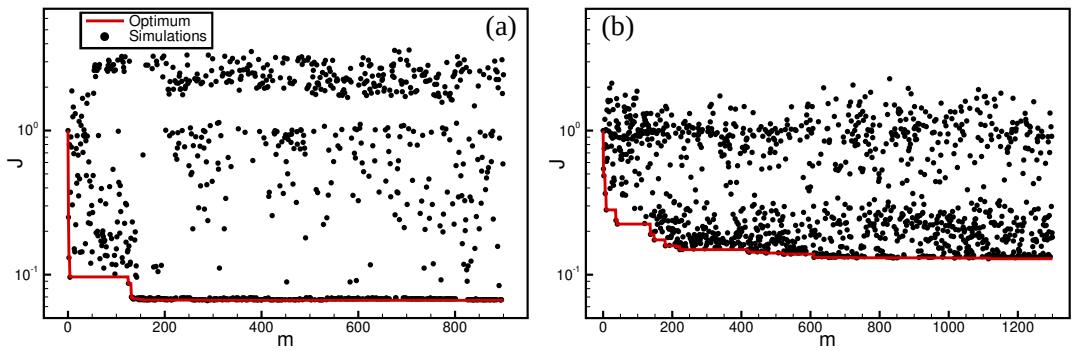



Figure 3.27: Learning curves of $J$ obtained from optimizations for sinusoidal WW (a) and PCHIP (b).

The completion time of the optimization procedure varied with the method of the wall-deformation and, consequently, with the number of control vari-

ables. For the sinusoidal WW, convergence is achieved within 150 iterations, whereas for PCHIP it requires about 600 iterations. The so-called learning curves, showing values of $J$ for all samples (black dots) and mimimum of $J$ (red line), are presented in Fig. 3.27. The results of the optimization are shown in Fig. 3.28, which displays scatter plots of pairs $\Delta p$ – $\sigma_T$ coloured by $J$. The contour maps presented aside show the temperature distribution for four selected wall shapes. These shapes, labelled A–D, correspond to: non-wavy (A), optimal (lowest $J$, B), worst (highest $J$, C), and a suboptimal case with the largest $\Delta p$ (D). The top row shows results for the sinusoidal WW, while the bottom row corresponds to PCHIP.

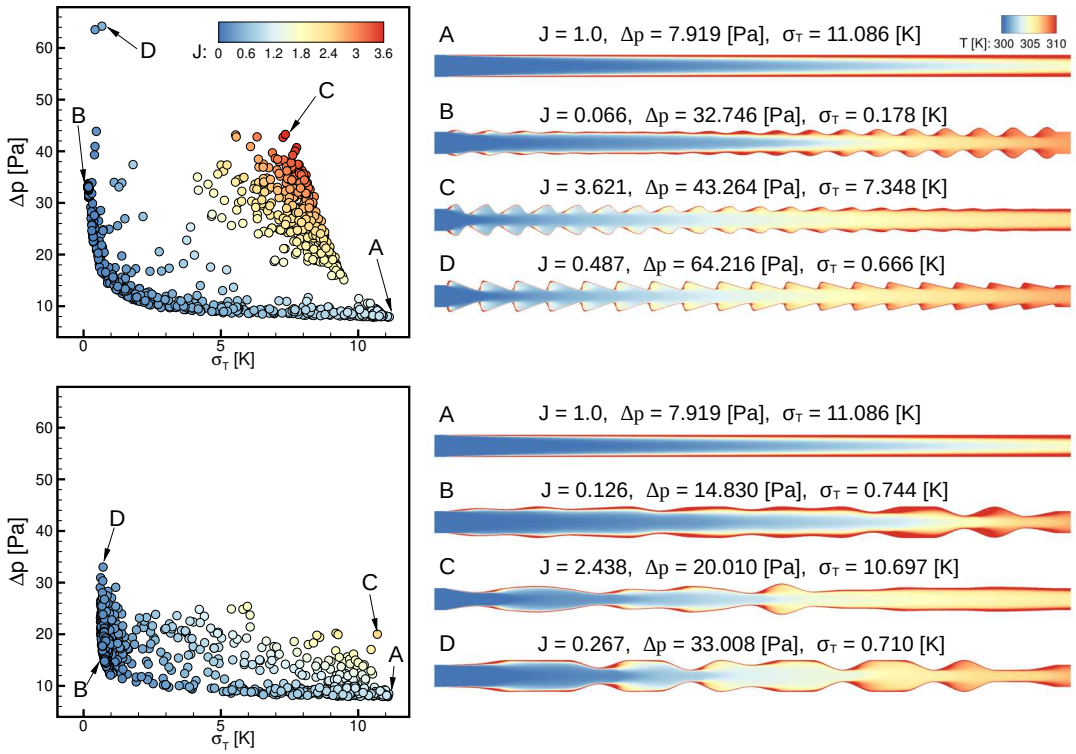



Figure 3.28: Scatter plot of $\Delta p$ – $\sigma_T$ colored by $J$ for the sinusoidal wall type (top row) and spline-shaped wall (bottom row).

For the sinusoidal wall type, a well-defined Pareto front is obtained, along which the Pareto-optimal configurations are located. These are characterised by the fact that no further improvement in $\sigma_T$ can be achieved without a corresponding deterioration in $\Delta p$. Conversely, moving along the Pareto front toward lower $\Delta p$ necessarily leads to higher $\sigma_T$. For the spline-shaped wall, a Pareto front is also observed, although in this case it is less sharp and well defined owing to the sparsity of data in the high-dimensional design space.

For both wall-deforming methods, the configuration B shows a relatively low and smooth amplitude at the start of the heated section, which gradually increases downstream and reaches its maximum near the end of the heated

section. This is expected to enhance mixing in the region where temperature gradients naturally weaken, as the fluid temperature has risen in the upstream part of the channel. The configuration C exhibits the opposite behaviour, with a progressively decreasing amplitude. The configuration D, by contrast, maintains a large and nearly uniform amplitude along the entire wall, which promotes strong mixing but at the cost of a very large $\Delta p$.

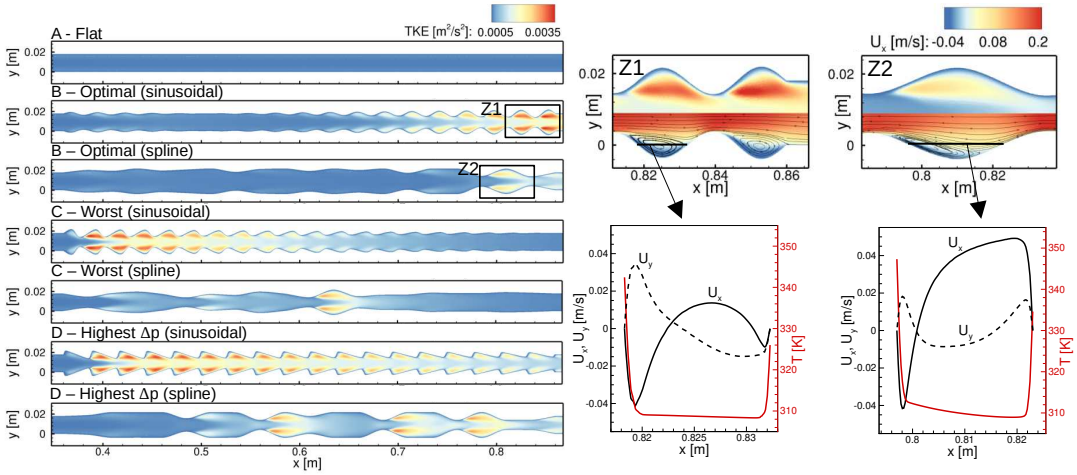



Figure 3.29: Contour maps of TKE for the cases with the optimal, worst, and exhibiting highest $\Delta p$ wall shapes created with sinusoidal and spline functions. Close-up views of the recirculation areas and profiles of velocity and temperature.

To interpret the variations in $J$ values, the analysis of TKE is performed, as it is a key parameter related to the mixing process, and thus, affecting the heat exchange. Figure 3.29 presents contour maps of TKE for the optimal, worst, and highest-$\Delta p$ wall shapes generated with both sinusoidal and spline functions, together with close-up views of the recirculation regions and profiles of velocity and temperature. Examination of the TKE fields reveals that both optimal configurations (sinusoidal WW and PCHIP) exhibit significantly enhanced TKE within the last cavities. As shown in Z1 and Z2, this increase arises from recirculation zones forming in this region. In both cases, the minimum values of $U_x$ remain relatively large, approximately -0.04 m/s, corresponding to about 36% of the inlet velocity ($U_{in}$ = 0.112 m/s). This behaviour sustains strong mixing in the downstream part of the heated section, where temperature gradients diminish due to prior heat exchange between the wall and the fluid. In contrast, the highest-$\Delta p$ configurations display such recirculation areas along the entire WW length. This enhances mixing and benefits in $\sigma_T$ (see Fig. 3.28), since recirculations are more abundant. However, the large protrusions of the cavities reduce the effective channel height and obstruct the flow. As a result, $\Delta p$ becomes excessive, rendering this wall arrangement suboptimal. The worst-performing cases, by comparison, are almost the mirror opposites of the optimal shapes. They promote strong TKE production in the initial part

of the WW section, where temperature gradients are high and wall–fluid heat exchange is intense. Excessive TKE in this region accelerates fluid heating, which lowers the temperature gradients downstream, where the wall becomes smoother, thereby reducing the effectiveness of heat transfer.

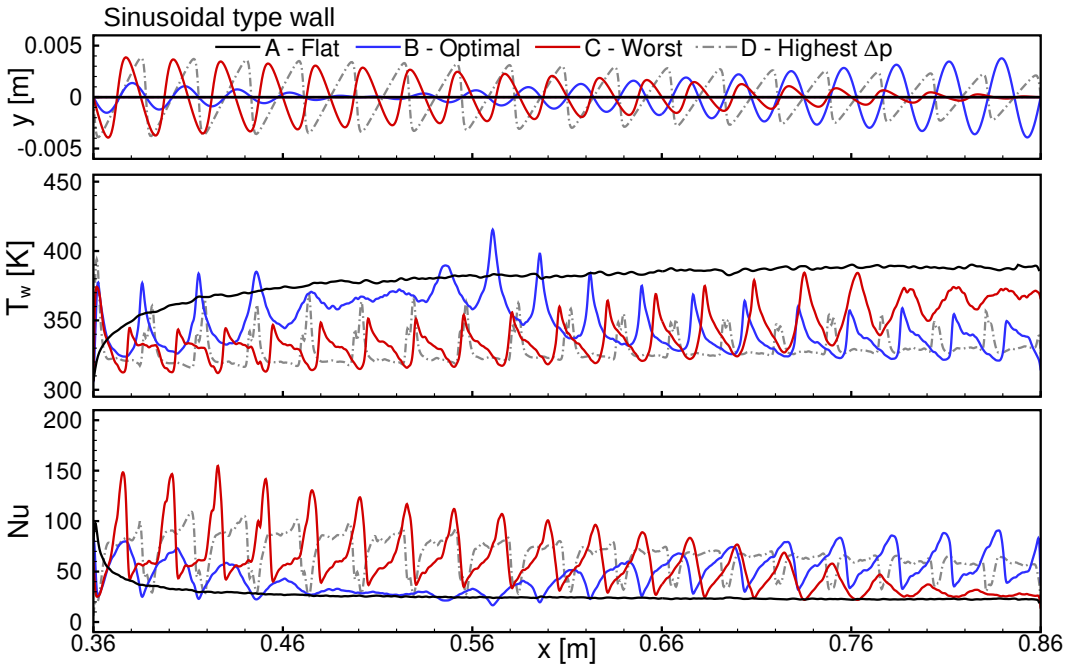



Figure 3.30: Profiles of temperature at the wall for optimal, worst and exhibiting highest $\Delta p$ cases of the sinusoidal type wall. The upper row indicates the shape of the particular waviness.

From the values of $J$ and $\sigma_T$ in Fig. 3.28, together with the TKE contour maps in Fig. 3.29, it is evident that the better-performing configurations are obtained with the sinusoidal WW. Although PCHIP offers greater geometric freedom, its performance is constrained by the number of control variables. In this case, 19 parameters do not permit walls with an amplitude-to-period ratio comparable to that of the sinusoidal WW, while increasing the number of control points would exceed the commonly accepted limit of 20 variables for the applicability of the BO approach (Frazier, 2018). For this reason, the following discussion focuses on the sinusoidal walls. Figure 3.30 presents profiles of the wall temperature ($T_w$) for the optimal, worst, and highest-$\Delta p$ configurations, along with the corresponding Nusselt number profile, $Nu = (\partial T/\partial n|_w)H/(T_w - T_{in})$, where $\partial T/\partial n|_w$ is the wall-normal temperature gradient. The upper row illustrates the respective waviness geometries.

For the A configuration, $T_w$ increases asymptotically along the heated section, approaching a nearly constant level of $T \approx 388$ K. Simultaneously, $Nu$ is highest near the inlet ($x = 0.36$ m) and reaches $Nu = 100$, then, it decreases to $Nu \approx 30$ within the first 1/3 length of the heated section and remains nearly

constant. The wavy configurations, by contrast, display oscillatory behaviour in both $T$ and $Nu$, reflecting the underlying waviness geometry. Notably, local minima in $T$ coincide with local peaks in $Nu$. The configuration B exhibits a distinctive pattern: $Nu$ remains low near the inlet, comparable to the case A, but increases rapidly from $x$ = 0.56 m onward, where the waviness amplitude begins to grow. Toward the outlet, $Nu$ increases and attains the highest values of all cases. Correspondingly, $T$ remains lowest, indicating efficient wall-fluid heat transfer. In the configuration C, on the other hand, $Nu$ converges toward the behaviour observed for the configuration A, with low values at the end of the heated section. The configuration associated with the highest $\Delta p$ maintains elevated $Nu$ values relative to A, though gradually decreasing downstream, while $T$ shows the opposite trend.

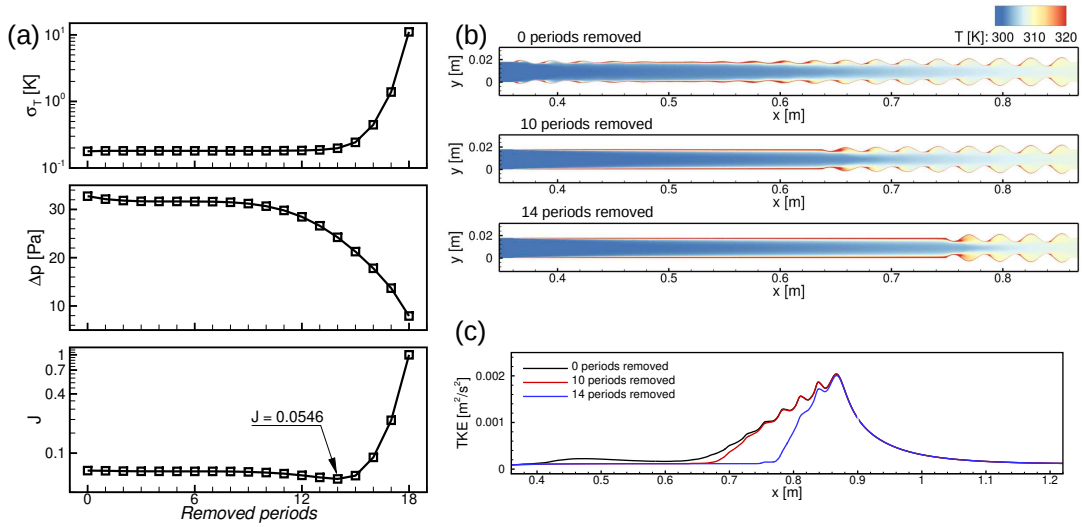



Figure 3.31: Profiles of $\sigma_T$, $\Delta p$, and $J$ as a function of the removed periods (a) ; sample contour maps of $T$ illustrating three shapes of walls (b); streamwise profiles of TKE for three considered cases taken at $y$ = 0.009 m, i.e. the middle section of the channel.

From the observations so far, it can be concluded that for the analyzed configurations, the wall waviness that enhances heat transfer most efficiently should begin smoothly with a gradually increasing amplitude toward the outlet. It is also important to recognize that in practical applications, efficiency is not the sole criterion. The applicability must also be considered, including the ease of manufacturing a given wall surface. To address this aspect, the BO-optimal result (configuration B, sinusoidal WW) is complemented with human intuition, forming a Human-Aided Optimization (HAO) approach. Since the initial waves of the BO-optimal configuration contribute little to the reduction of $\sigma_T$, it is natural to examine whether replacing them with a flat surface is beneficial. The analysis proceeds by progressively substituting the initial periods of waviness in the BO-optimal configuration with a flat wall segments. This strategy is expected to reduce the pressure drop while simplifying manufacturing process by

decreasing overall channel complexity.

Figure 3.31 presents: $\sigma_T$, $\Delta p$, and $J$ as the functions of the number of removed waviness periods (panel a), sample wall shapes and corresponding temperature fields (panel b), and streamwise profiles of TKE at $y = 0.009$ m, i.e., the channel mid-plane (panel C). Removing the first 10 periods has only a marginal effect on both $\sigma_T$ and $\Delta p$, with no noticeable change in $J$. Differences appear when more periods are removed, and notably $J$ attains a new minimum when 14 periods are flattened. In this case, $J$ decreases from 0.0664 (BO-optimal case) to 0.0546 (HAO-optimal case), a reduction of 17.7%. The remaining four waves constitute 22.2% of the original 18 and account for the majority of the WW role is supposed to play. This result, though not exact, resonates strongly with the Pareto 80/20 principle. The temperature fields near the ending part of WW (Fig. 3.31b, $x > 0.8$ m) are nearly indistinguishable between cases, indicating similar or close to identical flow conditions in this region. Similar behaviour is found for TKE, as evidenced by the TKE profiles in Fig. 3.31c, which converge beyond $x > 0.8$ m. This suggests that the highest levels of turbulence occur in the last few cavities. In fact, retaining only the last four ensures that the downstream WW effect is preserved, with identical TKE distributions for $x > 0.9$ m.

In summary, Paper 6 shows that the optimization procedure formulated for the simple circular pipe can be applied to channels, a configuration of central importance in compact heat exchangers. Two wall shaping methods were investigated: a sinusoidal formulation with four variables and a PCHIP approach with 19 control points. Both revealed Pareto fronts balancing temperature uniformity and pressure drop, although the sinusoidal WWs achieved superior performance. Optimal shapes featured smooth upstream sections with amplitudes growing downstream, thereby sustaining turbulence and mixing where temperature gradients weaken owing to better wall-fluid heat transfer. By contrast, excessive or misplaced waviness generated strong upstream recirculation with large pressure losses or produced inefficient heat transfer further downstream. The proposed HAO strategy simplified the BO-optimal wall by replacing the initial waviness periods with the flat segments, leading to a 17.7% reduction in the cost function $J$, while preserving nearly identical temperature uniformity. Thus, it has been demonstrated that effective channel designs can be achieved by combining ML-based optimization with human intuition, simplifying the wall manufacturing process.

# Chapter 4

# Conclusions

This thesis addresses passive control of turbulent flow by means of surface waviness. It is based on five research papers and one preprint, and is organized into two parts, each devoted to a distinct objective. This section provides a brief summary of the most critical findings, while extended discussions are presented at the end of each subsection in 'Comments to a series of articles'.

The first part of this thesis is devoted to a systematic investigation of turbulent flow separation control through surface-geometry modifications, specifically by employing and optimizing WWs. The research, comprising four original studies (Papers 1-4), progresses from validation of the LES approach to simulations of flow over various waviness shapes embedded either in a flat channel or in an airfoil surface. The main focus is on enhancing $\tau_w$ to delay separation using different wavy geometries, with emphasis on both physical mechanisms and practical applicability. Initially, simulations were conducted in a rectangular domain representing a simplified configuration compared with practical applications such as wings or wind-turbine blades. In this setup, separation did not occur due to insufficient domain length, and conclusions were therefore drawn from $\tau_w$. These results were subsequently verified by performing LES of flow over WW embedded in a realistic airfoil surface, which enabled direct investigation of the separation region. The most critical findings are as follows:

- LES results demonstrate that WWs substantially modify the flow field, particularly the velocity profiles and $\tau_w$ distribution. The effectiveness

of the waviness in enhancing $\tau_w$ is strongly dependent on the pressure gradient conditions. Specifically, the increase in $\tau_w$ is observed only in the presence of APG.

- A parametric analysis revealed that the enhancement of $\tau_w$ by sinusoidal waviness is maximized for a specific combination of amplitude and wavelength. On the other hand, excessively large amplitudes or short wavelengths induce flow separation.

- Introducing tilt into the waviness geometry is shown to be substantially beneficial in delaying the flow separation. The configuration with a moderate leftward tilt achieved an approximately 70% increase in $\tau_w$ while simultaneously reducing total drag compared to the standard sinusoidal shape. Moreover, an even higher enhancement in $\tau_w$ can be obtained ( 100%), at a minor tradeoff in drag, if steeper tilting is introduced.

- It is found that waviness is equally effective in enhancing $\tau_w$ when embedded in an airfoil-type surface as it is in flat channel configurations. Moreover, simulations involving the airfoil surface provided insight into separation behavior, confirming that alterations in $\tau_w$ directly contribute to a shift in the separation point.

- The spectral analysis shows that the waviness enhances large-scale contributions in the near-wall region. These structures are suspected to induce large-scale sweeps that transport momentum toward the wall, thereby increasing near-wall flow velocity, enhancing $\tau_w$, and delaying separation.

- Simulations performed at Reynolds numbers ranging from $Re_\tau$ = 1200 to 2500 show that the beneficial effect of a sinusoidal corrugation is present only at $Re_\tau$ = 2500 and diminishes with decreasing $Re_\tau$. At $Re_\tau$ = 1700 and 1200, the effect reverses, and the waviness causes an upstream shift of the separation point.

The second part of the thesis comprises of one research paper and one preprint (Papers 5 and 6). It addresses the use of waviness for heat-transfer enhancement in either a pipe (Paper 5) or a channel (Paper 6), with a particular focus on optimizing its shape to balance temperature uniformity (minimize $\sigma_T$) against losses due to pressure drop (minimize $\Delta p$). The combination of these two goals forms the cost function $J$, which is minimized through a combined RANS and BO framework.

- The optimization procedure identifies configurations that minimize pressure drop while maximizing temperature uniformity, with the BO-optimal design depending on the flow setup.
- For the pipe arrangement, the optimal solution is an outward-oriented waviness, achieving a tenfold improvement in $J$ relative to the worst-case design and a threefold improvement over a smooth-wall case.
- The optimal wall shape promotes the formation of recirculation zones that enhance mixing while simultaneously avoiding obstruction of the pipe flow, thereby not increasing $\Delta p$ significantly.
- For the channel configuration, the optimal wall shape exhibits a progressively increasing waviness amplitude. This shape yields an improvement in $J$ by a factor of 55 compared to the worst-case design and a factor of 15 relative to the reference smooth-wall case.
- The BO-optimal channel configuration is further refined by combining BO with human intuition, resulting in the human-assisted optimization (HAO) method. In this approach, selected waviness periods are replaced with smooth wall sections to reduce $\Delta p$ and thus $J$, with the added benefit of improved manufacturability. HAO identifies a configuration retaining only the final four periods of the BO-optimal case, achieving a 17.7% reduction in $J$.

In summary, this dissertation demonstrates that appropriately designed surface waviness is a powerful tool for manipulating turbulent boundary layer behavior. Through successive refinement and optimization, substantial improvements in both aerodynamic and thermal performance can be achieved.

# Chapter 5

# Papers

Aerospace Science and Technology 149 (2024) 109167

Contents lists available at ScienceDirect

Aerospace Science and Technology

journal homepage: www.elsevier.com/locate/aescte

# Numerical analysis of novel wavy wall based control of turbulent boundary layer separation

Piotr Kamiński, Paweł Niegodajew *, Artur Dróżdż, Vasyl Sokolenko, Artur Tyliszczak, Witold Elsner

*Department of Thermal Machinery, Czestochowa University of Technology, Al. Armii Krajowej 21, 42-200 Czestochowa, Poland*

ARTICLE INFO

Communicated by Mehdi Ghoreyshi

*Keywords:*
Turbulent separation
Computational fluid dynamics
Large eddy simulation
Wall-shear stresses
Corrugation
Wavy wall

ABSTRACT

In this work, a comprehensive insight into the new passive flow control method, i.e. a two-dimensional streamwise waviness (recently proposed by Dróżdż et al. [1]) is provided using Large Eddy Simulations. This approach was demonstrated to be effective in postponing turbulent boundary layer separation at high $Re$, which is out of reach for other commonly known passive flow control strategies. Although the effectiveness of the wavy wall in delaying flow separation has been confirmed, the physical mechanisms standing behind the skin friction enhancement are not fully understood which opens a space for future work. Of particular interest is an insight into the fluid flow in the near-wall region just above the waviness and this paper is aimed at doing so. To separate the effect of the global adverse pressure gradient, the results were confronted with the ones obtained under zero pressure gradient conditions for the identical wavy wall geometry and the same $Re_\tau = 2500$. Also additional simulations of the turbulent boundary layer building up on the flat wall were conducted to have an additional reference for the flow fields obtained above the wavy wall under zero and adverse pressure gradients respectively. A detailed inspection of the streamwise velocity and its fluctuation profiles indicated that the contribution of the global adverse pressure gradient to the flow statistics begins when the Rotta-Clauser pressure gradient parameter $\beta \geq 3$. The paper confirms an enhancement of the wall shear stress $\tau_w$ downstream the corrugation, which is the necessary condition to postpone the separation. Interestingly, the effect of increased $\tau_w$ was not observed for the case with the same waviness and without pressure gradient.

## 1. Introduction

Turbulent flows exposed to pressure gradients are commonly seen in a number of industrial applications. An excellent example is the evolution of a turbulent boundary layer (TBL) over an airfoil [2–4] since it experiences favourable pressure gradient (FPG) and adverse pressure gradient (APG) conditions. Other examples can be the flow inside a diffuser [5–7] or around a turbine blade [8–10]. Of particular interest is APG since it can cause the flow to separate from the surface [11–13] which enhances the total drag and leads to a significant loss of energy and increased fuel consumption. As suggested by Abbas et al. [14], even up to 15% of total drag reduction can be achieved by introducing separation control technologies [15]. This scenario has triggered research activities worldwide aimed at searching for new or improving the available flow control techniques.

In general, flow control approaches can be classified as active or passive [16]. The former ones involve complex systems, which although very effective, require an external power supply. Examples of these methods are: blowing and suction [17], heating and cooling [18,19] and plasma actuators [20–22]. Passive methods usually involve some degree of modification of surface geometry and do not require an external energy source, which makes them advantageous over active approaches. Among available passive flow control methods, the following techniques are most commonly employed in practice: dimples [23–31]; vortex generators [32,33], which are used not only on airfoil surfaces but also on helicopter's rotor [34], car bodies [35] or bridges [36]. A considerable attention has already been paid to investigate some unconventional control methods, e.g., slotted airfoils [37,38], streamwise waviness for reducing the leading edge interaction noise [39,40] or by placing microcylinder near a blade leading edge [41–43]. Some passive solutions are inspired by nature. Prominent examples include wingtip

* Corresponding author.
*E-mail address:* pawel.niegodajew@pcz.pl (P. Niegodajew).

https://doi.org/10.1016/j.ast.2024.109167
Received 8 February 2024; Received in revised form 12 April 2024; Accepted 23 April 2024
Available online 29 April 2024
1270-9638/© 2024 The Author(s). Published by Elsevier Masson SAS. This is an open access article under the CC BY license (http://creativecommons.org/licenses/by/4.0/).

devices known as winglets which shape has been inspired by bird's wings [44–48]; herringbone riblets reflecting shapes of a bird's feathers [49]; skin-type microstructure and microscale riblets borrowed from shark or dolphin skin [47,50,51].

It is important to note that all known passive approaches thus far are effective when the flow experiences laminar or transitional conditions [52,53]. At higher Reynolds numbers ($Re$), when the flow becomes fully turbulent, the effectiveness of passive methods diminishes. Moreover, as pointed out by McMasters and Henderson [54] the employment of passive methods at high $Re$ may even have a detrimental effect on the flow. For instance, on airfoils or turbine blades it may lead to earlier separation, which negatively impacts their aerodynamic performance. Given these facts, for a long time it seemed that the only effective solution to control TBL, especially the separation, was the use of the active methods mentioned above.

In the experimental work of Dróżdż et al. [1], the authors demonstrated the possibility of increasing local wall-shear stress $\tau_w = \mu(dU/dy)$ (where $\mu$ is the dynamic viscosity and $dU/dy$ is the near-wall velocity gradient) and consequently the postponement of the flow separation. It has been achieved in a wind tunnel in APG conditions by applying a corrugation in the form of a two-dimensional (2D) streamwise wall waviness. It was also found that the flow separation can be controlled by the amplitude $A(x)$ and period length $\lambda$ of the wavy wall (WW). The experiment was conducted for the friction-based Reynolds number equal to $Re_\tau = u_\tau \delta/\nu = 4000$ (where $\delta$ is the boundary layer thickness, $u_\tau$ is the friction velocity and $\nu$ is the kinematic viscosity). Such a value of $Re_\tau$ guarantees that the logarithmic region is well developed and ensures a clear separation of scales [55]. Worth to mention is that the effect of $\tau_w$ enhancement had not been observed before since all the previous works exploring the flow downstream different WW configurations were conducted for low $Re$ and under zero-pressure-gradient conditions [56–69].

Although the effectiveness of WW in delaying the flow separation at high $Re_\tau$ has been confirmed, the physical mechanisms standing behind the $\tau_w$ enhancement are not fully understood and this opens space for future work. An insight into the fluid flow in the near-wall region just above the waviness can allow a better understanding of the mechanisms responsible for delaying turbulent separation. In particular, the following issues are worth studying: (i) verification of whether the local or global APG contributes more to the TBL developing over WW; (ii) inspection of changes in flow dynamics within consecutive waves and correlation of these changes with the escalating APG along the streamwise direction; and (iii) evaluation of the relation between the global mean flow statistics and both, the near-wall TBL and alterations in the wall-shear stresses within WW.

To address these objectives, this paper comes with large eddy simulations (LES) of isothermal and incompressible flow over an identical WW surface as in the experimental research of Dróżdż et al. [1] at the friction Reynolds number $Re_\tau = 2500$ for which performing the comparative LES study is feasible at reasonable computational costs. To separate the effects of local APG (downhill subsequent waviness slopes) and global APG, additional simulations are conducted under ZPG conditions. Moreover, to have a reference point, the simulations for the configuration with a flat wall are also performed both for APG and ZPG conditions.

## 2. Methods

### 2.1. Research object

The focus of this research is to examine an incompressible and isothermal TBL developing over a 2D streamwise WW subjected to ZPG and APG conditions at $Re_\tau = 2500$. Table 1 outlines the test cases considered in the current investigation. The purpose of the simulations conducted under ZPG conditions, denoted as F-ZPG and W-ZPG, is to extract the effect of APG regime and wall waviness by comparing the results with the ones obtained for F-APG, W-APG. To validate the accuracy of the LES results the experimental measurements were performed for configurations W-ZPG and W-APG, which are characterised by a larger complexity than the cases with the flat wall.

### 2.2. Experiment

The experiment, which was designed to provide data for validation of numerical calculation, was conducted in an open circuit wind tunnel schematically illustrated in Fig. 1. A subfigure (a) presents the APG configuration, identical as in Ref. [1], while (b) shows its modified version ensuring ZPG conditions within the entire channel. To achieve a well-developed TBL, a 5.035 m-long ZPG inlet section was mounted before the test section. To speed-up the turbulisation of TBL, the tripping method was applied via the coarse-grained sandpaper glued to the bottom wall of the inlet ZPG section, as shown in Fig. 1. The thickness of side boundary layers in this long inlet section was controlled by two sets of suction gaps mounted at the side walls. To have additional control of APG conditions, the flow was sucked off through a perforated part of the upper wall (see Fig. 1a).

The 2D wavy wall section begins at $x_{s,w} = 0.01$ m (in the measuring region) and its total length equals $L_{x,w} = 0.666$ m. The waviness consists of 5 periods of length $\lambda = 0.1332$ m each. As indicated in [1], WW should be designed in a way to ensure the amplitude of waviness $A(x)$ to increase proportionally to $\delta$ and should barely touch the outer region of TBL. This growth of $A(x)$ was expressed using the following formula $A(x) = (0.00366x^2 + 0.000614x + 0.003351)$ m. So, the minimum and maximum values of the given WW amplitude are $A(x = 0.01\ \text{m}) = 0.0034$ m and $A(x = 0.676\ \text{m}) = 0.0054$ m respectively.

The measurements of the velocity and its fluctuation profiles were performed using a single hot-wire anemometry (HWA) probe at four streamwise locations above the waviness, identical for both W-ZPG and W-APG (see Table 1). Fig. 2 demonstrates the locations where the measurements were made and these are the first and the last crest (marked as B-W1 and B-W5, respectively), and the first and the last troughs (marked as D-W1 and D-W5, respectively). The $x$-axis representing the streamwise $x$-coordinate is presented in normalised form $(x - x_{s,w})/\lambda$.

The inlet velocity was kept at a constant level of $U_{e,in} = 14.42$ m/s which corresponds to $Re_\tau = 2500$, whereas the turbulence intensity at the inlet to APG/ZPG measuring region was kept at the level of approximately $I_{in} = 0.7\%$. More details regarding the construction of the wind tunnel and experimental setup can be found in our previous works [1,70].

### 2.3. Numerical model

Large eddy simulations were conducted using the ANSYS Fluent software, employing the subgrid Wall-Adapting Local Eddy-viscosity (WALE) model [71]. The spatial discretization of the Navier-Stokes equations was accomplished with a 2nd order bounded central differencing scheme (BCD). Preliminary tests revealed no discrepancies in the results obtained using the classical central differencing scheme and BCD scheme. The 2nd order method was used for discretization of the pressure gradient. Pressure-velocity coupling was enforced through the SIMPLE algorithm and 2nd order implicit time integration method was applied. The time-averaging process lasted for 40 flow-through time units ($t_{FT} = L_x/U_{e,in} = 0.09$ s) and started when the flow became fully developed, i.e. after 3 $t_{FT}$. Furthermore, the solutions were spatially averaged by collecting and averaging data from 10 uniformly spaced cross-sections in the spanwise direction. The convergence of the time-averaged solutions was confirmed by comparing the results at two distinct time moments $38t_{FT}$ and $40t_{FT}$. The computations were carried out with a constant time-step ($\Delta t = 1 \times 10^{-4}$ s), which resulted in the CFL number $CFL \approx 0.82$.

**Table 1**
Test cases for the present study.

| Case name | Description |
|---|---|
| F-ZPG | Flat channel under ZPG |
| F-APG | Flat channel under APG |
| W-ZPG | Wavy channel under ZPG |
| W-APG | Wavy channel under APG |

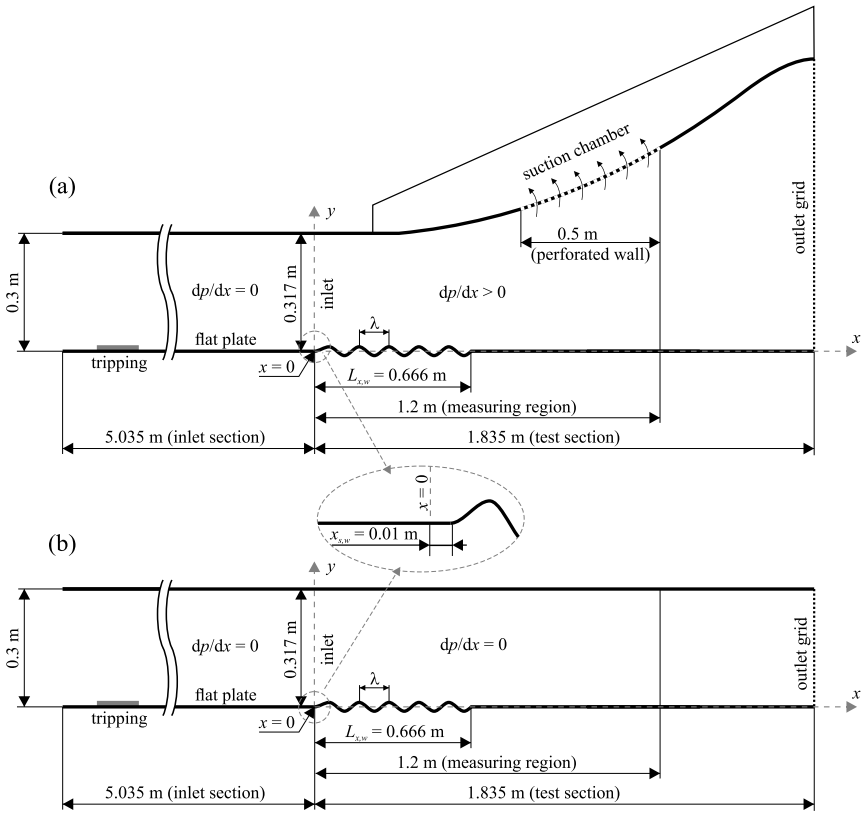



**Fig. 1.** Experimental stand for flow configurations subjected to APG (a) and ZPG (b).

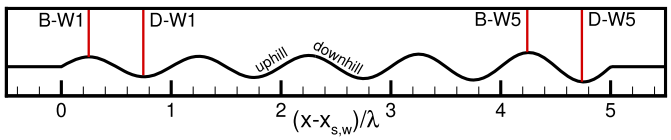



**Fig. 2.** The locations of the HWA measurements.

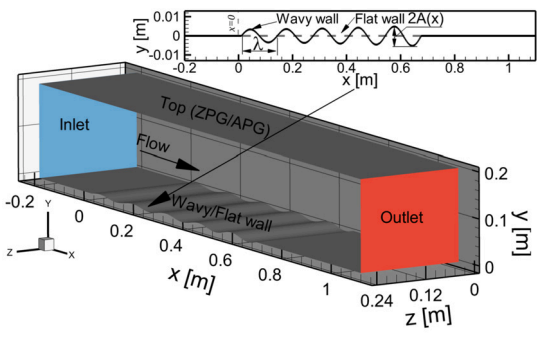



**Fig. 3.** Computational domain with the assumed boundary conditions.

### 2.4. Computational domain and boundary conditions

The computational domain illustrated in Fig. 3 reflects the measurement section of the experimental setup employed by Drózdż et al. [1]. The reduction of the domain from the full channel (see Fig. 1) to the rectangular geometry significantly decreased computational costs. In this simplified configuration, the air enters through the inlet (located at $x = -0.2$ m) and leaves through the outlet (located at $x = 1.1$ m). The bottom wall is either flat throughout a whole domain or corrugated. The upper boundary (top), situated at $y = 0.2$ m, provides control over the pressure gradient within the channel. The left and right boundaries are spaced by $z = 0.24$ m and the total length of the domain is equal to $L_x = 1.3$ m. This channel configuration was previously examined in experimental and numerical research [70,72].

To correctly reproduce the physical conditions within the flow domain, a precise formulation of the boundary conditions is crucial. Fig. 4 shows the inlet conditions (velocity profiles, $\beta$ parameter) applied for all test cases. The velocity profiles used at the inlet boundary (Fig. 4a) were measured with a single hot-wire probe. They were combined with turbulent fluctuations generated by applying the Synthetic Turbulence Generator approach. This method allows specifying the turbulent kinetic energy and dissipation rate, which are then used to determine the turbulent length and time scales needed to generate the time-varying velocity fluctuations. The turbulent kinetic energy and dissipation rate are defined via the User Defined Functions in such a way as to reproduce

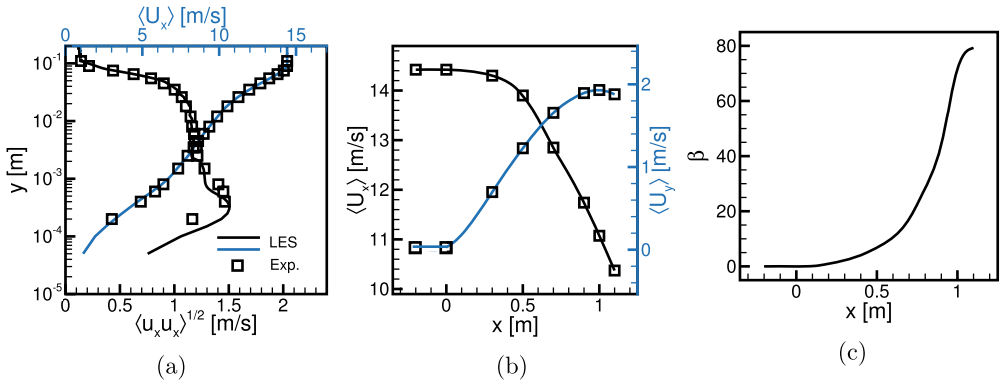



**Fig. 4.** The approximated profiles for the inlet boundary (a) and for the top boundary (b) responsive for the APG condition; axial development of $\beta$ parameter (c) for APG configuration.

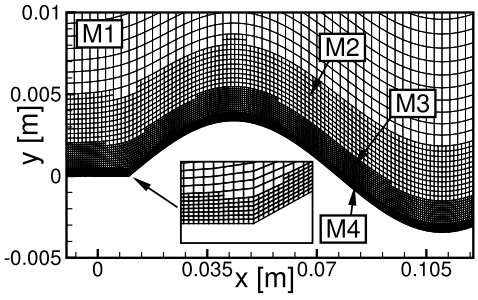



**Fig. 5.** Computational mesh in the near-wall region. Note that the figure is stretched in the $y$-direction to better expose the view of the near-wall mesh adaptation.

the experimental data. On the top boundary (Fig. 4b), due to negligibly small fluctuations, only the streamwise $\langle U_x \rangle$ and wall-normal $\langle U_y \rangle$ velocity components were assumed based on the experimental profiles measured with an X-wire probe. This procedure simplifies the computational geometry and reduces the simulation costs. Among others, it has been used in [73,74]. They induced the APG conditions precisely reflecting the regimes in the full channel. To obtain ZPG conditions, the values of $\langle U_x \rangle = U_{e,in} = const.$ and $\langle U_y \rangle = 0$ m/s were prescribed at the top boundary. Fig. 4c depicts the axial development of the Clauser-Rotta pressure gradient parameter $\beta = (\delta^*/\tau_w) \cdot (dP/dx)$ (where $\delta^*$ is the displacement thickness and $dP/dx$ the streamwise pressure gradient) [75] for the APG configuration. The bottom wall was treated as a non-slip wall. The side boundary conditions in the spanwise direction were treated as periodic. A constant pressure (101325 Pa) was assumed at the outlet.

### 2.5. Computational mesh

The computational mesh, presented in Fig. 5, consisted of a base part, denoted as M1, and three refined meshes M2, M3 and M4, which differed by the refinement levels. Subsequent mesh layers were constructed by dividing computational cells of the upper layer into eight smaller cells. Such an approach allowed obtaining near-wall mesh density correctly capturing small flow scales with the fulfilment of $y^+ < 1$ criterion [76] along the entire computational domain. The refined mesh consists of $41.1 \times 10^6$ cells which are characterised by the following dimensions expressed in viscous units: $0.3125 < \Delta x^+ < 2.5$; $0.3 < \Delta y^+ < 0.92$ and $0.3125 < \Delta z^+ < 2.5$. The superscript $+$ is used to denote the viscous scaling of lengths (e.g., $\Delta x^+ = \Delta x \cdot u_\tau(x)/\nu$). The near-wall element aspect ratio is equal to $AR_w = \Delta x/\Delta y = \Delta z/\Delta y = 5.2$. The mesh is uniform in $x$ and $z$ directions, hence, $\Delta x = \Delta z$.

To assess whether the mesh is sufficiently dense for the LES, the ratio of the subgrid turbulent kinetic energy (TKE) to the total TKE was calculated as $k_{sgs}/k_{tot}$, where $k_{sgs}$ is the subgrid TKE and the total TKE $k_{tot} = k_{sgs} + k_{res}$ with $k_{res}$ - the resolved TKE. According to [76] this ratio should be kept below 20% for LES. As illustrated in Fig. 6, thanks to the applied mesh refinement strategy, in the present simulations $k_{sgs}/k_{tot}$ is even below 1%.

### 2.6. Model validation

To validate the numerical model, HWA measurements using a single hot-wire probe were conducted for the W-ZPG and W-APG cases at four specific locations. These locations corresponded to the crest and trough of the first and last waves. The selection of these particular locations was deliberate, as at the 1st wave TBL is still under ZPG for W-APG case, while at 5th wave, the strength of the global APG is the highest.

Fig. 7 shows the velocity and its fluctuation profiles obtained from both, LES and experiment for W-ZPG. The results are presented for four locations, i.e. B-W1, D-W1, B-W5 and D-W5 in subsequent columns (the exact locations are indicated in the first row of Fig. 7, i.e. above the results). The profiles are normalised by the free-stream velocity $U_e$ (taken as 99% of the undisturbed velocity at the given location). The normal distance $(y - y_0)/(h - y_0)$ was normalised in a similar way as in previous related works [56,58,67,77–80]), where $h = 0.2$ m whereas $y_0$ is the location of the first node at the wall. As can be seen from Fig. 7, the velocity profiles obtained with LES agree very well with the ones from measurements, only for location B-W5, a small overprediction of the near-wall velocity by LES can be noted, i.e. at $(y - y_0)/(h - y_0) < 0.03$. The fluctuations are also well reproduced by LES. In particular the locations of local maxima were accurately captured. Some discrepancies can be mostly seen in the near-wall region for the locations D-W1 and D-W5.

Fig. 8 presents an identical set of the data as in Fig. 7, however, this time for the W-APG case. Note that Fig. 8 includes additional information about the effect of the mesh density and time step on the flow statistics. Blue dashed line represents the results obtained on the mesh refined only to the layer M3 (see Fig.5) which consisted of 18.3 mln cells and for $\Delta t = 1.0 \times 10^{-4}$ s. Green dash-dotted line represents the data obtained using a larger time-step, i.e. $\Delta t = 2.0 \times 10^{-4}$ s on the mesh M4. It can be seen that the numerical solutions obtained for the considered combinations of the mesh density and time-step are very close to each other. The only noteworthy contribution of these parameters is seen close to the wall, i.e. at $(y - y_0)/(h - y_0) < 0.05$ where small-scale activity plays an important role. Therefore, conduction of LES on the mesh M4 and under $\Delta t = 1.0 \times 10^{-4}$ s seems to be justified. In general, the accuracy of LES (for the W-APG case) in reproduction of velocity and its fluctuation is at a comparable level as in the case of W-ZPG.

Summing up, the validation presented in this subsection indicates that the LES results agree well with the experimental measurements and the numerical model can be successfully used for an in-depth analysis

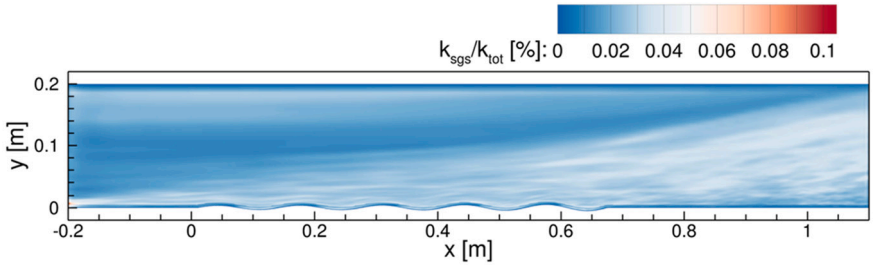



**Fig. 6.** Contours of the time averaged $k_{sgs}/k_{tot}$ for W-APG configuration.

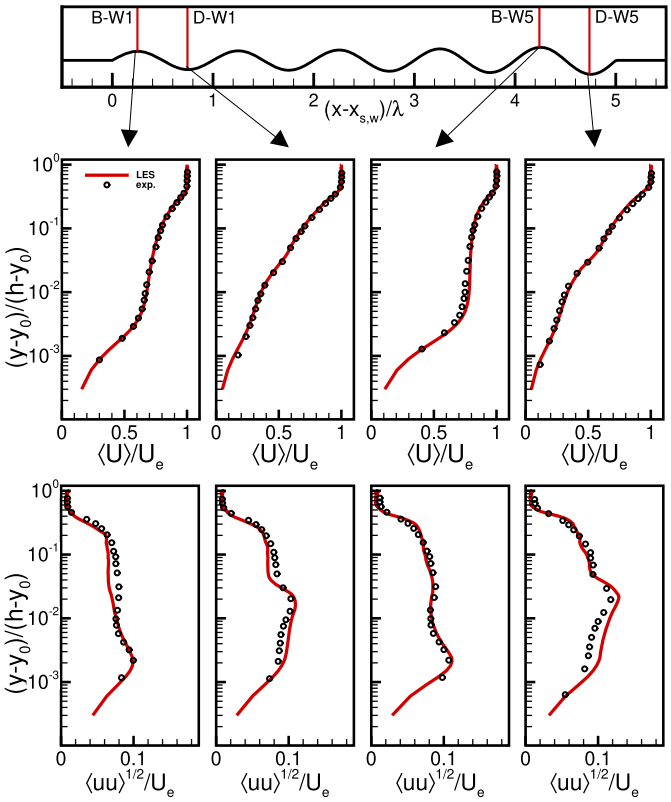



**Fig. 7.** Comparison of streamwise velocity (upper row) and its fluctuations (lower row) with experimental data for ZPG at crests (B-) and troughs (D-) of 1st (W1) and last, i.e. 5th wave (W5).

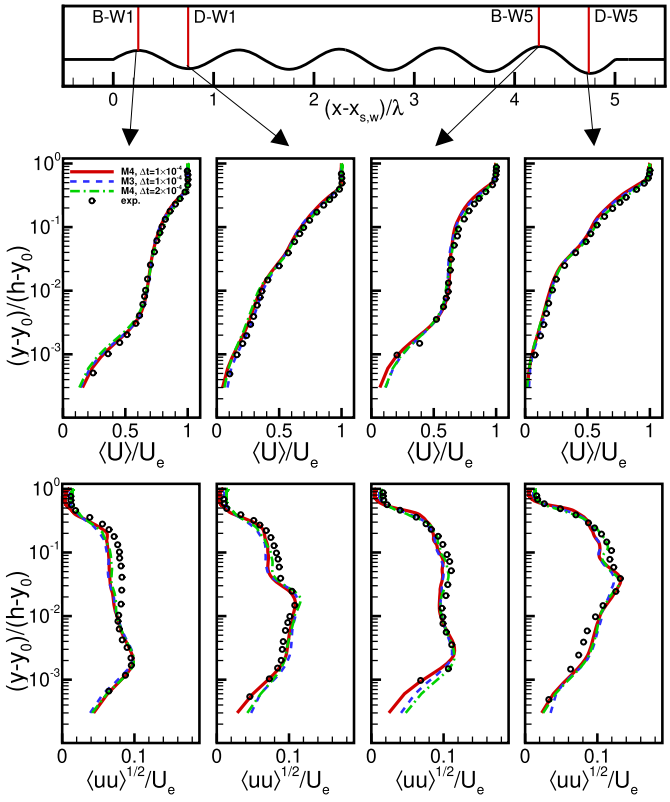



**Fig. 8.** Comparison of streamwise velocity (upper row) and its fluctuations (lower row) with experimental data for APG at crests (B-) and troughs (D-) of 1st (W1) and last, i.e. 5th wave (W5).

of the TBL development over the WW with and without global pressure gradient conditions.

## 3. Results

Since the key goal of the paper is to distinguish the effects of local (caused by WW) and global pressure gradients on TBL, this section provides a detailed analysis of the flow statistics across successive waves of the considered surface undulation. The effect of WW on the local wall-shear stress is also examined in this section. Moreover, the results acquired are confronted with those obtained on the flat plate under ZPG and APG conditions (F-ZPG and F-APG).

### 3.1. General flow picture

The presentation of the results begins with a visualisation of the instantaneous velocity field in the form of the $Q$-parameter isosurfaces obtained for W-ZPG and W-APG (Fig. 9). Such a form of visualisation ensures identifying different types of coherent structures [81,82]. Colours correspond to the local instantaneous streamwise velocity above the corrugated surface.

When looking at the W-ZPG case, two distinct types of structures can be clearly identified. First, the longitudinal vortices emerge on the uphill side of each WW period. Second, the spanwise structures which appear always on the downhill side of the waviness. The formation of the latter ones is an effect of the breakdown of the longitudinal vortices just behind the crests. A similar scenario has already been observed in some previous works [63,66,83,84] examining the effect of WW on the flow under ZPG conditions. When taking a closer look on the flow in troughs, small separation bubbles (indicated by a dark blue colour) can be identified closer to the downhill side of each waviness. This phenomenon can be attributed to the local APG conditions that cause the flow to decelerate in that particular region.

Regarding the W-APG case, a very similar arrangement of vortices can be observed especially within the streamwise distance barely affected by the global APG, i.e. for $0 < (x - x_{s,w})/\lambda < 2$. Further downstream, towards stronger APG, the arrangement of vortices starts to deviate from the one that is seen for the W-ZPG case. It is mostly manifested by an increasing size of the structures being present in the

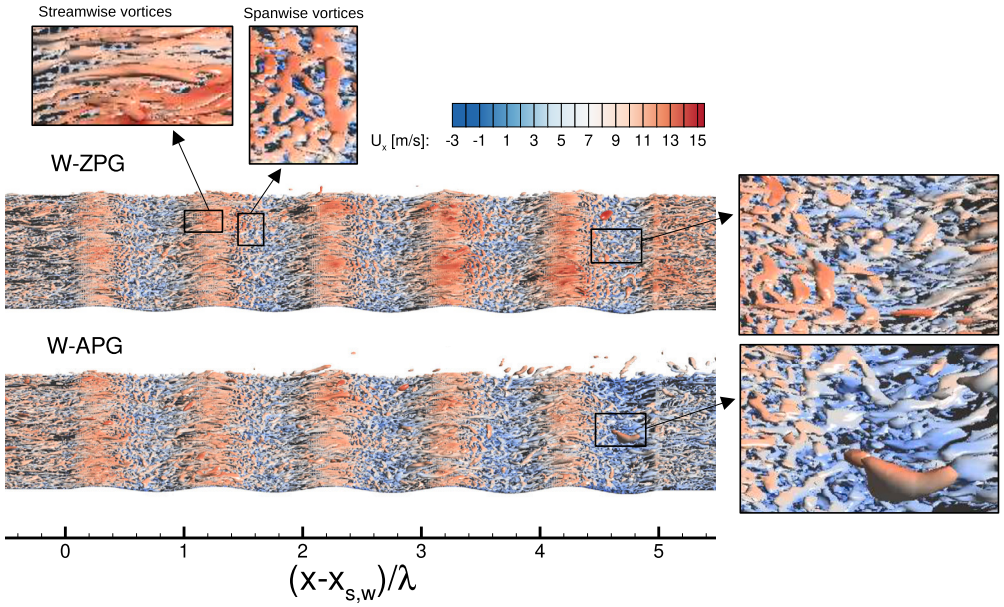



**Fig. 9.** $Q$–parameter isosurface ($Q = 0.05\ s^{-2}$) coloured by the instantaneous streamwise velocity for cases W-ZPG and W-APG.

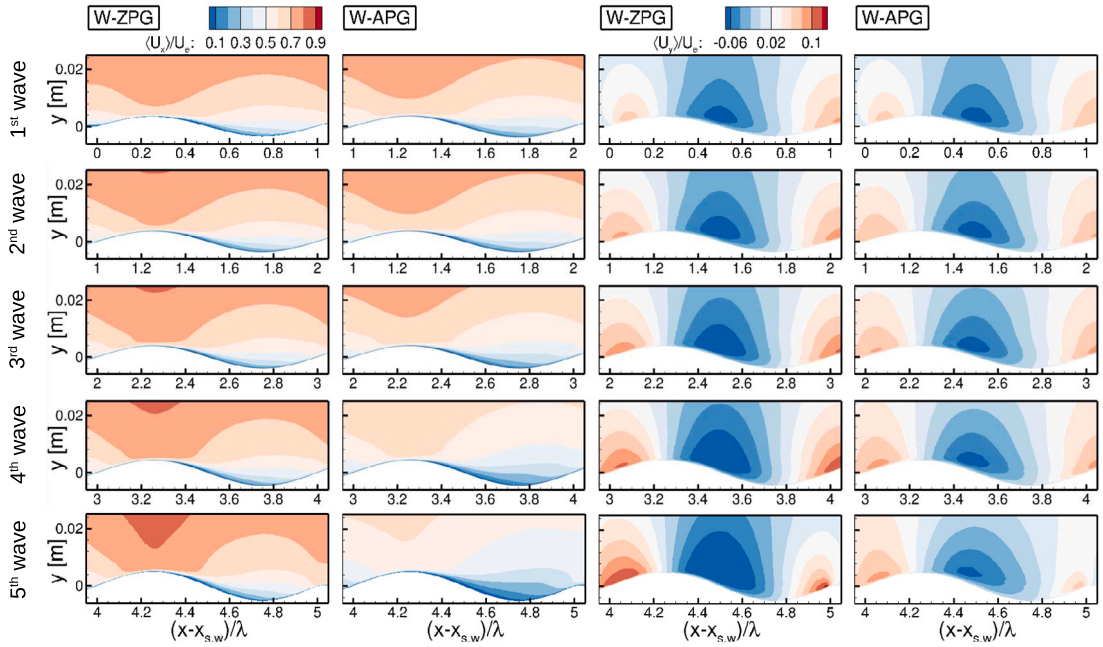



**Fig. 10.** Contour maps of streamwise (1st and 2nd column) and wall-normal (3rd and 4th column) velocity components. Each row denotes consecutive waves of the corrugation.

flow. Such a scenario is commonly seen when TBL is exposed to APG conditions, namely, a growing pressure gradient is accompanied with emergence of highly-energetic large-scale structures [85–87]. It can also be observed that the separation bubble size in waviness troughs is larger for W-APG when compared to W-ZPG which is particularly well seen for the last wave ($4 < (x - x_{s,w})/\lambda < 5$). Also the behaviour of vortices among considered cases seems to be different at this location. For W-APG, the uphill-travelling structures are notably thicker, and the small-scale activity appears to diminish, which is consistent with observations from the Ref. [88], whereas for the W-ZPG case, the vortices are visibly thinner in that region.

A more detailed examination of the near-wall flow in the form of the time-averaged flow fields for the cases W-ZPG and W-APG is presented in Fig. 10. The depicted streamwise range is almost the same as the one in Fig. 9 as it captures the entire waviness, however, for clarity the view is split into five parts (periods), each shown in a separate row. The contour maps shown here illustrate the mean streamwise $\langle U_x \rangle$ (1st and 2nd column) and wall-normal $\langle U_y \rangle$ (3rd and 4th column) velocity components, both normalised by the free-stream velocity $U_{e,in}$ (at the inlet to the APG section).

There are few observations that can be gleaned from the presented data. For W-ZPG, the streamwise component of velocity becomes increased locally above crests of WW for subsequent waves. It is because the flow accelerates just before crests as it experiences favourable pressure gradient (FPG). Moreover, even higher values of $\langle U_x \rangle / U_{e,in}$ can be observed above each subsequent crest downstream which can be attributed to the increasing amplitude of the waviness in the streamwise direction. A local increase in $\langle U_x \rangle / U_{e,in}$ above crests is also visible in

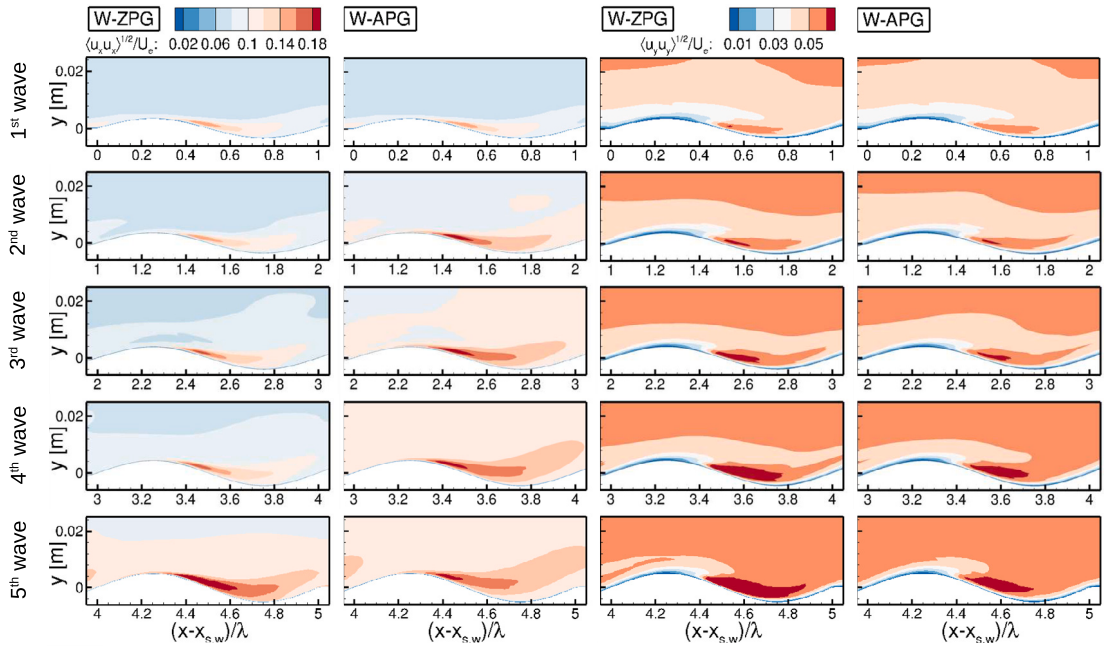



**Fig. 11.** Contour maps of streamwise (1st and 2nd column) and wall-normal (3rd and 4th column) velocity fluctuation components. Each row denotes consecutive waves of the corrugation.

the W-APG case, however, an overall decrease in $\langle U_x \rangle / U_{e,in}$ is generally seen downstream the flow. The latter effect is certainly associated with the presence of the global APG. The other effect that is clearly seen, this time for the W-APG case only, is a considerable decrease in $\langle U_x \rangle / U_{e,in}$ in troughs along the corrugation which is manifested by expanding blue region, indicating low (or even negative) values of velocity. This effect can be attributed to the global deceleration of the flow caused by APG.

Some distinctive differences in the flow response to WW can be also distinguished from the contour maps of the wall-normal component of velocity. In particular, the presence of corrugation contributes to an increase (downstream the flow) in local positive and negative maxima of $\langle U_y \rangle / U_e$ that are present on the uphill and downhill slopes, respectively, for the W-ZPG configuration. This particular effect seems to be dumped for W-APG case since the contour maps look more or less the same for each consecutive wave. It is because the effect of growing $A(x)$ is compensated by the global APG.

Fig. 11 presents contour maps of the streamwise (1st and 2nd column) and wall-normal (3rd and 4th column) components of the velocity fluctuations normalised by $U_{e,in}$. Arrangement of the results is identical as in Fig. 10. Let us first focus on $\langle u_x u_x \rangle^{0.5} / U_e$. In general, the further downstream, the higher $\langle u_x u_x \rangle^{0.5} / U_e$ with a clear local maximum in the vicinity of the downhill side of each crest and this tendency is similar for W-ZPG and W-APG cases. A similar observation has already been made in available literature [62,66,67,70,79,84]. Nonetheless, the growth in fluctuations is stronger for the W-ZPG case. It is noteworthy that an increase in $\langle u_x u_x \rangle^{0.5} / U_e$ along the streamwise coordinate is also present in the external flow, i.e., above the corrugation. This time, an enhancement of the streamwise fluctuations is much more pronounced for the W-APG case which can be attributed to the fact that the global APG stimulates the generation of more energetic, large-scale vortices [85], which are also seen in the waves W4 and W5 in Fig. 9 ($3 < (x - x_{s,w})/\lambda < 5$).

Regarding the wall-normal fluctuations, they become definitely enhanced along WW to a comparable level in both cases W-ZPG and W-APG. Also the values of the local maxima located near the troughs are similar for both considered configurations. Therefore, $\langle u_y u_y \rangle^{0.5} / U_e$ seems to be barely sensitive to global APG conditions.

### 3.2. Mean flow statistics

To explore in more detail how the near-wall flow is modified by WW under different pressure gradient conditions, this section provides a detailed insight into flow statistics such as the velocity and its fluctuation profiles. The focus is first put on analysing how the statistics change at selected locations within each wave among investigated configurations outlined in Table 1. Fig. 12 illustrates the mean velocity profiles (normalised with the local free-stream velocity) obtained at four different streamwise locations within a single period (presented in subsequent columns) and for each consecutive wave (presented in subsequent rows). The selected locations (shown schematically in the first row of Fig. 12) correspond to the beginning of a wave (location A), crest (location B), middle of the wave (location C) and through (location D). Note that the profiles obtained for F-ZPG case are almost identical regardless the location that they were collected from (the blue, bold line in Fig. 12). It is justified as for this configuration the flow was developing over the flat plate under ZPG conditions and over a relatively short distance. This is not the case for F-APG as one can observe that from the 3rd wave the profiles start to depart more and more from the ones obtained for F-ZPG. This effect is typical for APG flows and it is associated with the flow deceleration in that region. Note that the F-ZPG case presented here serves as a reference for the remaining cases from Table 1.

Within the first two waves, the global pressure gradient for both F-ZPG and F-APG cases is almost identical and so the changes in average profiles caused by the wavy surface are clearly visible. In the 2nd row at the location A, where each period begins, the slight enhancement of the velocity near the wall emerges with respect to the flat plate configurations (i.e. F-ZPG and F-APG). This suggests that the enhanced near-wall velocity at the location A should, most probably, be attributed to the presence of the trough upstream and consequently, local APG. This effect is not seen at the 1st wave location since therein WW is preceded by the flat wall upstream. Further away from the wall, where the logarithmic region begins the profiles almost perfectly overlap.

At the location B, i.e. at the waviness crest (see the 2nd column in Fig. 12), the enhancement of $\langle U_x \rangle / U_e$ is seen within almost whole TBL for both W-ZPG and W-APG with respect to the flat plate cases. Only near the outer border of TBL the profiles converge. This time this effect

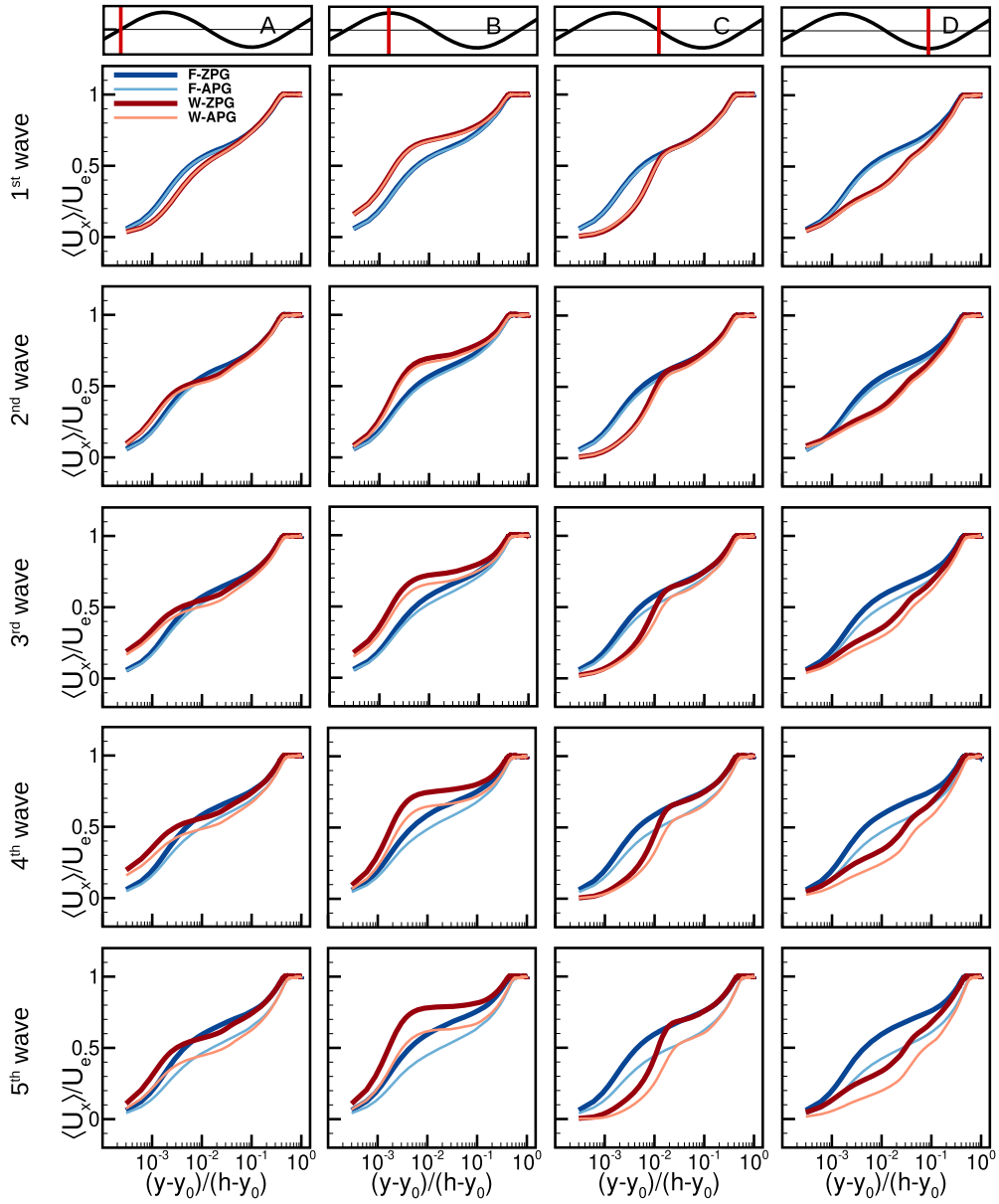



**Fig. 12.** Streamwise velocity profiles as a function of the normalised normal distance $(y - y_0)/(h - y_0)$ for cases: F-ZPG, F-APG, W-ZPG, W-APG (see Table 1). Different characteristic location points of the wavy wall (from left to right) on consecutive waves (top to bottom) are presented.

can be attributed to the local FPG induced by the uphill slopes prior to each crest.

In the middle of waviness (where $(y - y_0)/(h - y_0) = 0$) at the location C a large velocity deficit emerges near the wall for W-ZPG and W-APG cases. This effect occurs up to $(y - y_0)/(h - y_0) \approx 2 \cdot 10^{-2}$ away from the wall (which is approximately equal to the height of the crest) and it is maintained within the whole corrugation. Its presence is due to the local APG formed on the downhill side of each waviness. In the outer region of TBL, the waviness has no impact on $\langle U_x \rangle / U_e$. The deficit of $\langle U_x \rangle / U_e$ for W-ZPG and W-APG is also visible at the location D, in the WW troughs, however, this time it is shifted further away from the wall. As it is explained later in the paper, this shift as well as the deficit of $\langle U_x \rangle / U_e$ are associated with the flow reattachment taking place a little bit upstream of this location. In this case, all the profiles overlap not only at the outer region of the boundary layer, but also right at the wall, indicating similar wall-shear stresses at this location.

For successive waves from 3rd to the 5th one, i.e. when $3 < \beta < 13$, an increasing influence of the global APG is observed, which is manifested by a shift of the thin lines (representing APG) away from the bold ones (representing ZPG). Interestingly, the differences between F-APG and W-APG remain very similar within subsequent waves. In the outer region, a clear overlapping (F-APG vs. W-APG) of the profiles is seen for pretty much every location from A to D.

The above observations indicate that the waviness, by generating a local pressure gradient, affects the inner part of the boundary layer, while its outer region is essentially modified by the global APG.

Fig. 13 shows the mean velocity fluctuations profiles for cases: F-ZPG, F-APG, W-ZPG, W-APG. The results are arranged in the same manner as in Fig. 12. The profiles obtained for F-ZPG (reference ones) are almost identical for all the considered locations and exhibit a local maximum close to the wall, and elevated $\langle u_x u_x \rangle^{1/2} / U_e$ in the logarithmic region [55,89]. Regarding the F-APG case, a reduction of the near-wall maximum and enhancement of $\langle u_x u_x \rangle^{1/2} / U_e$ further away from the flat surface is seen with development of the global APG downstream.

The effect of WW on $\langle u_x u_x \rangle^{1/2} / U_e$ is seen at each location. At the location A (from the 2nd wave), the near-wall maximum in $\langle u_x u_x \rangle^{1/2} / U_e$ is shifted to the overlapping region (the effect of TKE production on pre-

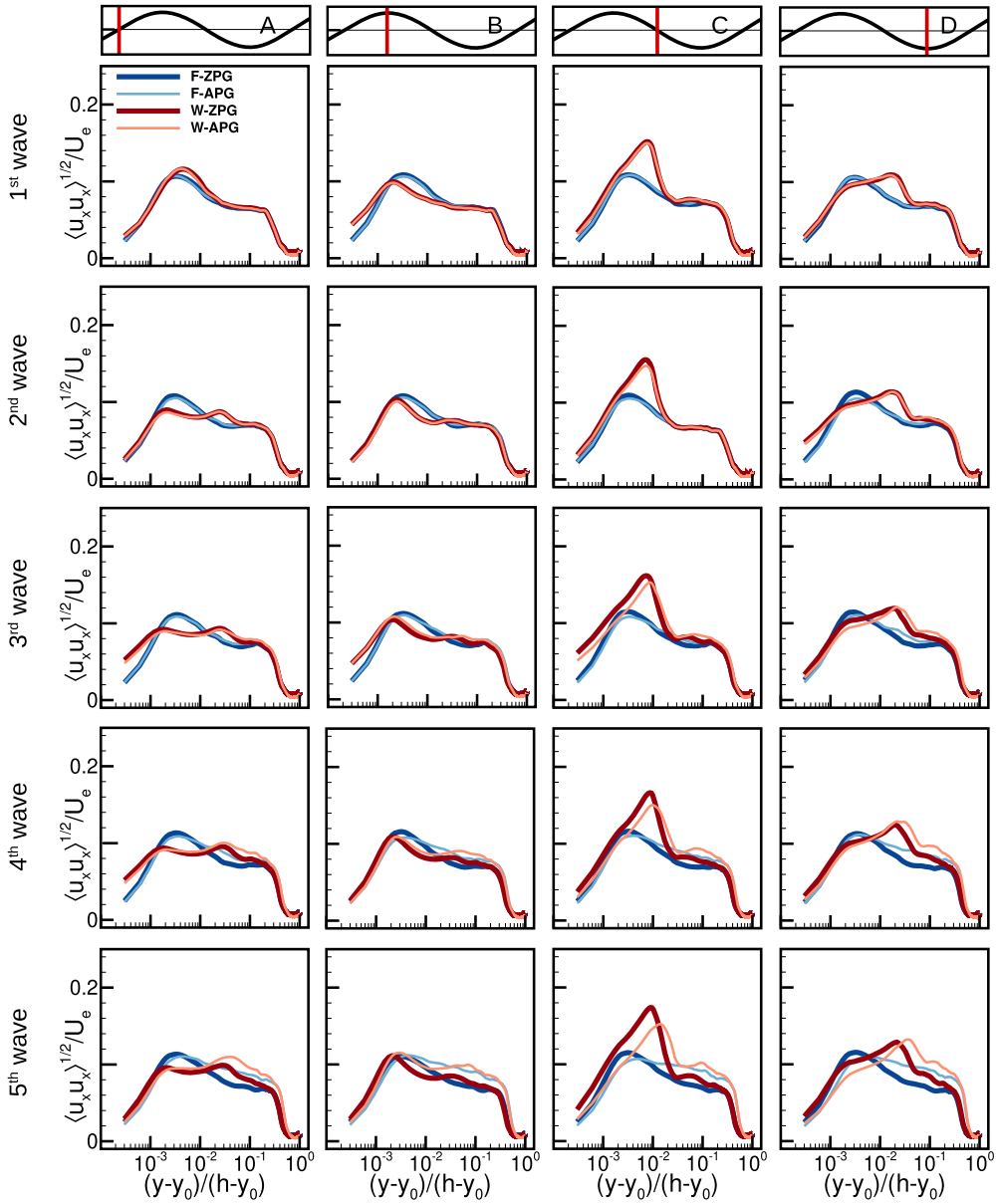



**Fig. 13.** Streamwise velocity fluctuation profiles a function of the normalised normal distance $(y-y_0)/(h-y_0)$ for cases: F-ZPG, F-APG, W-ZPG and W-APG. Different characteristic location points of the wavy wall (from left to right) on consecutive waves (top to bottom) are presented.

vious crest). At the location B, a contribution of WW to $\langle u_x u_x\rangle^{1/2}/U_e$ is small and mainly limited to narrowing of the characteristic local maximum. The most remarkable change in $\langle u_x u_x\rangle^{1/2}/U_e$ profile takes place at the location C, which is a substantial growth of the local maximum (up to 67% with respect to the value obtained for the flat-plate configuration) and its shift further away from the wall (the effect is maintained within the whole waviness). This modification of the profile can be certainly attributed to a considerable growth in the velocity gradient in that region due to WW that is visible in Fig. 12. Moreover, it is also to some extent related to increased convection velocity close to the wall in APG TBL and so, an increased sweeping motion [90]. At the location D, the enhancement of local maximum is still visible to some extent, however, much more pronounced is its shift further away from the wall.

From the 3rd to the 5th wave, i.e. when $\beta > 3$, a growing influence of the global APG is observed, which is manifested by a shift of the thin lines (representing APG) away from the bold ones (representing ZPG). For locations A and B right next to the wall below $2\times10^{-2}$, a change in pressure has virtually no effect on the level of fluctuation. The global APG also forces a slight shift of the inner maximum of $\langle u_x u_x\rangle^{1/2}/U_e$ further away from the wall, in a similar way for W-ZPG and W-APG. These results and increased level of fluctuations in the region $(y-y_0)/(h-y_0) > 5\times10^{-2}$, are consistent with those demonstrated in Fig. 12, which might suggest that there is an increased activity of large-scale motion.

To better expose the effect of both, each waviness period and APG, the already discussed profiles of $\langle U_x\rangle/U_e$, and $\langle u_x u_x\rangle^{1/2}/U_e$ for W-ZPG, and W-APG are presented in a different manner in Fig. 12. Namely, profiles of $\langle U_x\rangle/U_e$ are presented separately for W-ZPG and W-APG in the 1st and 2nd row, whereas the profiles of $\langle u_x u_x\rangle^{1/2}/U_e$ in 3rd and 4th row and for all the so far considered locations (A, B, C and D) in subsequent columns. Moreover, each subfigure shows the evolution of either $\langle U_x\rangle/U_e$ or $\langle u_x u_x\rangle^{1/2}/U_e$ profiles within consecutive waves (W1 - W5). Note that the results obtained for the first wave (W1) are not presented for the location A (first column of Fig. 14). It is because this is the location where the waviness begins in the domain and $\langle U_x\rangle/U_e$, and $\langle u_x u_x\rangle^{1/2}/U_e$ profiles taken from this region depart from the general trends (see the 1st columns in Fig. 12 and Fig. 13) and therefore this would impede interpretation of the data from Fig. 14.

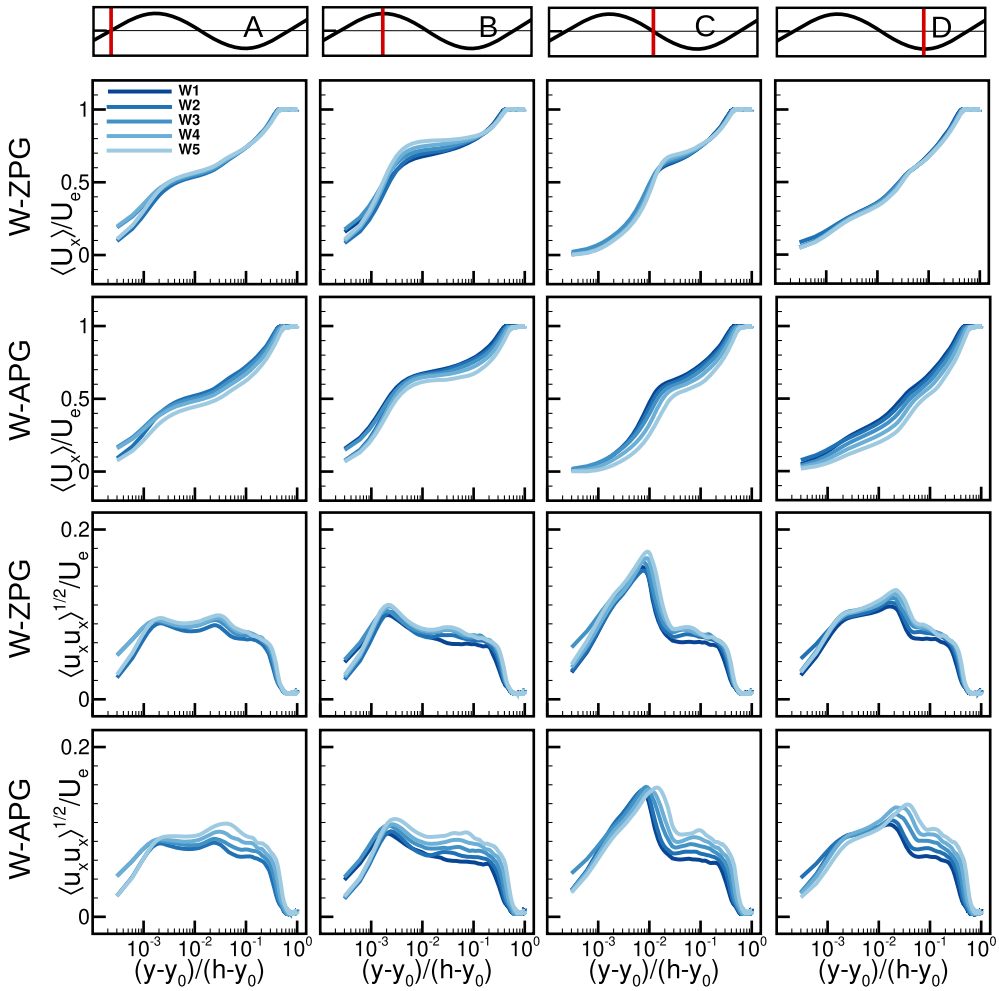



**Fig. 14.** Streamwise velocity (rows 1 and 2) and fluctuation (rows 3 and 4) profiles for cases W-ZPG and W-APG presented as a function of $(y-y_0)/(h-y_0)$. Different characteristic location points of the wavy wall (A-D) on consecutive waves (W1-W5 indicated by shades of blue) are presented.

Although the amplitude of WW grows up in the streamwise direction, its effect on $\langle U_x\rangle/U_e$ for W-ZPG is marginal in locations A, C and D and only more pronounced contribution of $A(x)$ can be observed at the location B (at the waviness crest). Also the effect of $A(x)$ on $\langle u_x u_x\rangle^{1/2}/U_e$ can be considered as very small at all the studied locations. This scenario changes for the W-APG configuration as moderate changes in $\langle U_x\rangle/U_e$ profiles are seen within consecutive waves. In particular, a reduction of $\langle U_x\rangle/U_e$ takes place with growing $A(x)$, i.e. downstream the corrugation (from W1 to W5) for all the considered locations. Even more substantial changes can be observed in $\langle u_x u_x\rangle^{1/2}/U_e$ for the W-APG case, which is manifested by a large growth in the energy in particular in the overlapping region with increasing $A(x)$ at all the locations. These results indicate that the influence of $A(x)$, and hence the local pressure change induced by the curvature of the wall, can be regarded as small whereas the most pronounced changes that are seen in the flow statistics should be ascribed to the global APG.

### 3.3. Wall-shear stresses

To go further into the details, one needs to explore the effect of WW on the wall-shear stresses. As first, the instantaneous streamwise component of the wall-shear stresses obtained on WW surface for W-ZPG (1st column) and W-APG (2nd column) configurations is illustrated in Fig. 15. The results obtained for consecutive waves of the corrugation are presented in subsequent rows. In order to simplify an identification of the local position within WW, a schematic depiction of the shape of the waveform is provided above the contour maps.

The obtained results indicate that the flow experiences the detachment from the surface and this effect is visible in every WW period for both W-ZPG and W-APG. It is manifested by negative values of the wall-shear stress ($\tau_{w,x} \leq 0$) that can be seen locally (see the regions coloured in shades of blue). For the W-ZPG case, as $A(x)$ grows (i.e. within subsequent waves), the regions with negative values of $\tau_{w,x}$ occupy wider and wider streamwise distance range. This effect is even more pronounced for the W-APG case which is particularly well seen on the surfaces of the 4th and 5th waves. It is because APG is responsible for an enhancement of the velocity deficit in the near-wall region on the downhill side of the waviness (see the velocity profiles for W-APG for 4th and 5th waves at the location C in Fig. 12). Worth noting is also that W-ZPG case exhibits greater local minima and maxima than W-APG which again can be attributed to the velocity deficit caused by the global APG.

Fig. 16 illustrates the time-averaged streamwise component of $\langle\tau_{w,x}\rangle$ along the measuring region for all test cases considered in this study. The grey line representing $\langle\tau_{w,x}\rangle = 0$ is shown here just to indicate the locations where the flow is detached from the surface, i.e. when $\langle\tau_{w,x}\rangle \leq 0$. Obviously, for the F-ZPG case $\langle\tau_{w,x}\rangle$ takes the near-constant value within the whole section. This is not the case for F-APG, since the pressure gradient causes a gradual decrease in $\langle\tau_{w,x}\rangle$ downstream the flow.

Regarding W-ZPG and W-APG, one can observe a large oscillation in $\langle\tau_{w,x}\rangle$ within the entire waviness. For W-ZPG, the amplitude of this oscillation becomes enhanced within consecutive waves which is due to increasing $A(x)$ of WW downstream the flow. Interestingly, for W-APG this oscillation, although exhibiting the decaying trend, its amplitude

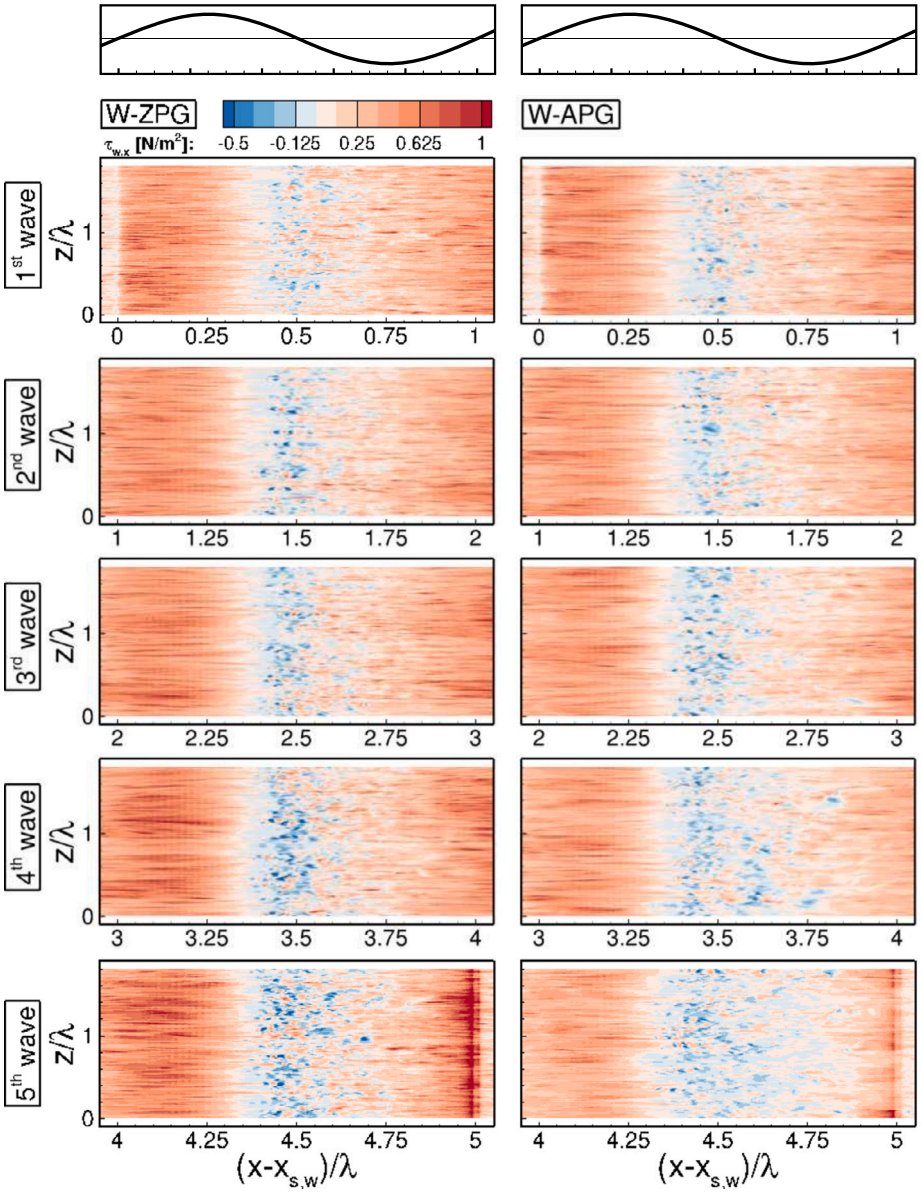



**Fig. 15.** Contour maps of instantaneous streamwise component of the wall-shear stresses for W-ZPG (1st column) and W-APG (2nd column). Rows indicate consecutive waves of the corrugation.

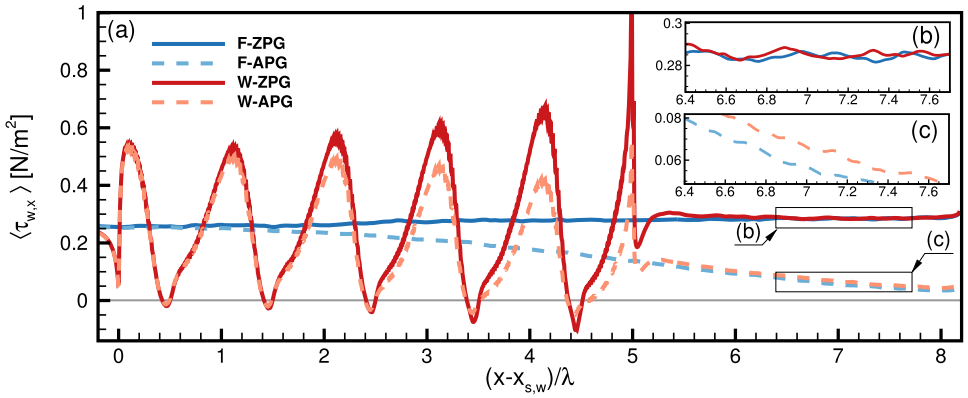



**Fig. 16.** Time-averaged streamwise component of the wall-shear stresses at the wavy wall ($0 < x/\lambda < 5$) and downstream ($5 < x/\lambda < 8$) regions for all test cases. Grey line indicates separation manifested by $\langle \tau_{w,x} \rangle \leq 0$.

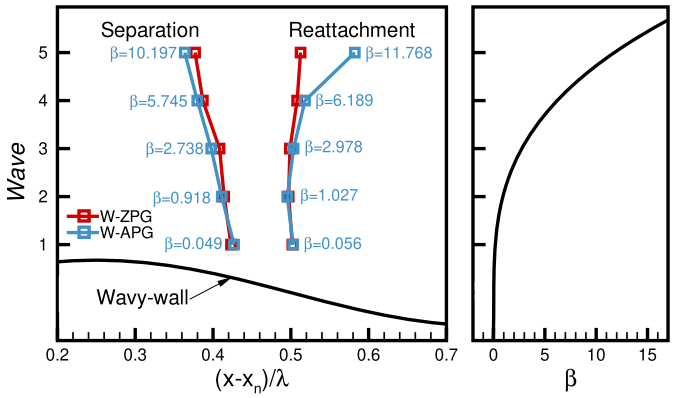



**Fig. 17.** Locations of separation and reattachment points $(x - x_n)/\lambda$ and also $\beta$ distribution on each consecutive wave ($y-$ axis).

remains relatively constant. It suggests that the global APG compensates the growth in $\langle \tau_{w,x} \rangle$ oscillation induced by the amplitude of WW (being present for the W-ZPG case). The results also indicate that the flow detachment takes place locally within each period of the WW for both W-ZPG and W-APG. Moreover, it looks that a higher and higher share of negative values of $\langle \tau_{w,x} \rangle$ occur within each wave (for both cases) which means that a wider and wider streamwise distance is occupied by the flow detachment downstream. A large peak in $\langle \tau_{w,x} \rangle$ is present near the end of WW, i.e. at $(x - x_{s,w})/\lambda \approx 5$ for both W-ZPG and W-APG cases. A similar peak was also reported when studying the flow over a half-corrugated channel in Ref. [91]. It is worth to note that the maximal value of $\langle \tau_{w,x} \rangle$ occurs prior to the tip of each wave. On the other hand, the minimal values of $\langle \tau_{w,x} \rangle$ appear just downstream the downhill slopes (not, as intuitively one could expect, directly in the trough centre). Similar observation was also reported in the work [92].

The zoomed parts of Fig. 16, i.e. (b) and (c) highlight the region downstream WW for W-ZPG and W-APG, respectively. Interestingly, for W-ZPG configuration, the value of $\langle \tau_{w,x} \rangle$ obtained in that region converges quickly to the one reported for the F-ZPG case. On the other hand, for W-APG higher values of $\langle \tau_{w,x} \rangle$ are observed and maintained at an approximately constant level (4.5% with respect to the inlet value, i.e. at $x = 0$) all the way downstream. It may suggest that a necessary condition to sustain an enhancement of $\langle \tau_{w,x} \rangle$ downstream the corrugation is to have the flow exposed to the global APG. However, this finding should be treated with some caution due to the following reasons: (i) as indicated in [1], WW was designed in a way to ensure $A(x)$ to grow up proportionally to $\delta$ and should barely touch the outer region of the TBL; (ii) in W-ZPG case, TBL builds up much slower and so the crests of WW are more and more immersed into the outer region stimulating TBL in a more extensive way. As also indicated in [1], the WW geometry should be adjusted to the size of the inner region of TBL which is the necessary condition for the enhancement of both the amplitude modulation effect [93–95] and the convection velocity of small scales which consequently leads to increased contribution of the sweep event [90]. This issue requires, however, further research to formulate some constructive conclusions.

Nevertheless, the results presented in Fig. 16 constitute a numerical confirmation of the finding of Dróżdż et al. [1] that the specific wavy wall geometry can be used to postpone the turbulent flow separation in an effective and long-lasting way. Moreover, the effectiveness of the considered WW geometry is still at a high level even though $Re_\tau = 2500$ considered in this work is lower than the one considered in [1], i.e. $Re_\tau = 4000$.

Fig. 17 illustrates how the points of separation and reattachment ($(x - x_n)/\lambda$, where $x_n$ is the local beginning of $n$-th waviness period) changes within consecutive waves for W-ZPG and W-APG. These predictions were evaluated based on the data from Fig. 16, in particular, subsequent values of $(x - x_n)/\lambda$ were taken from the locations where the profiles of $\tau_w$ cross the grey line indicating $\tau_w = 0$. The black line represents the shape of a part of a waviness period to indicate for which location the subsequent results correspond to. Also the values of $\beta$ (global) for the W-APG configuration are included to support the discussion.

In general, one can observe that the points of separation and reattachment move upstream and downstream, respectively within consecutive waves, i.e. with growing $A(x)$, so the separation bubble becomes larger. The points of separation and reattachment are identical for the 1st and 2nd wave for both cases. From the 3rd wave, this scenario changes as W-APG case starts exhibiting separation over an even wider streamwise distance compared to W-ZPG. The most substantial change is seen for the reattachment point at the 5th wave where $\beta > 10$. This is an effect of the global APG which causes an increase in $\langle U_y \rangle$ and so a deflection of the mean velocity vector away from the wall.

Fig. 18 presents spanwise distributions of the instantaneous streamwise component of $\tau_{w,x}$ for five streamwise locations along WW from $(x - x_{s,w})/\lambda = 4.25$ to $(x - x_{s,w})/\lambda = 4.65$, i.e. within the downhill part of the 5th wave where the local separation emerges. The results obtained for W-ZPG and W-APG are presented on the left and on the right column, respectively. The exact streamwise locations can be directly identified from the figure showing the geometry of WW within the considered period range in the first row. The grey line that can be seen in each subfigure represents $\tau_{w,x} = 0$ and it is shown here for an easy identification of local separation regions, i.e. where $\tau_{w,x} < 0$.

At the first location $(x - x_{s,w})/\lambda = 4.25$, which is exactly at the crest of the 5th wave, much greater values of $\tau_{w,x}$ are seen for the W-ZPG case. It is because W-APG case experiences a relatively strong pressure gradient since $\beta > 10$ at this location. Not so far downstream, at the second location ($(x - x_{s,w})/\lambda = 4.35$) values of $\tau_{w,x}$ become comparable for both cases and also some negative values of $\tau_{w,x} < 0$ begin to emerge indicating local separation. At the next location ($(x - x_{s,w})/\lambda = 4.45$), even greater share of negative values of $\tau_{w,x}$ is seen for both cases, however, with substantially enhanced fluctuation of $\tau_{w,x}$ for W-ZPG. This scenario is similar at the fourth location, whereas at the last location ($(x - x_{s,w})/\lambda = 4.65$) the flow seems to less likely detach from the surface for W-ZPG. However, the higher fluctuation of $\tau_{w,x}$ for this case is still maintained.

Fig. 19 presents a statistical evaluation of the extended range of the data from Fig. 18 in the form of the exceedance probability $P_e$ with $\tau_{w,x} = 0$ used as a threshold (to extract the share of locations with $\tau_{w,x} < 0$) for W-ZPG and W-APG. To have statistically independent results, $P_e$ values computed from 10 spanwise $\tau_{w,x}$ distributions were averaged to obtain each point. It allowed also obtaining the error bars indicating a potential deviation of the probability.

As can be seen from Fig. 19, just a little bit downstream the crest (at $(x - x_{s,w})/\lambda = 4.3$) $P_e$ becomes rapidly growing until it reaching the maximum ($P_e \approx 70\%$) at $(x - x_{s,w})/\lambda = 4.4$ for both cases. Further downstream, when exceeding $(x - x_{s,w})/\lambda = 4.45$, $P_e$ starts gradually decreasing, more for W-ZPG compared to W-APG. Worth noting is also that the variation in $P_e$, manifested by bars, is generally larger for W-APG configuration. This indicates a considerable contribution of the global APG to the local separation especially closer to the reattachment point.

Of interest is also to quantify the contribution of WW to the total drag. For this purpose, information about the drag coefficient $C_d = 2F_d/\rho U_{e,in} A_{ref}$ (where $F_d$ is the drag force and $A_{ref}$ is the reference area) calculated for the streamwise distance occupied by WW (i.e. at 0.01 m$< x <$ 0.676 m) for all four considered test cases are collected in Table 2. In general one can observe that $C_d$ takes smaller values for configurations exposed to the global APG. It is due to gradual decrease in $\tau_w$ downstream the flow caused by APG (see Fig. 16). The overall growth in $C_d$ due to the presence of WW with respect to the flat case is almost identical for both pressure gradient configurations (i.e. with and without APG). Note that the verification to what extent the increase in

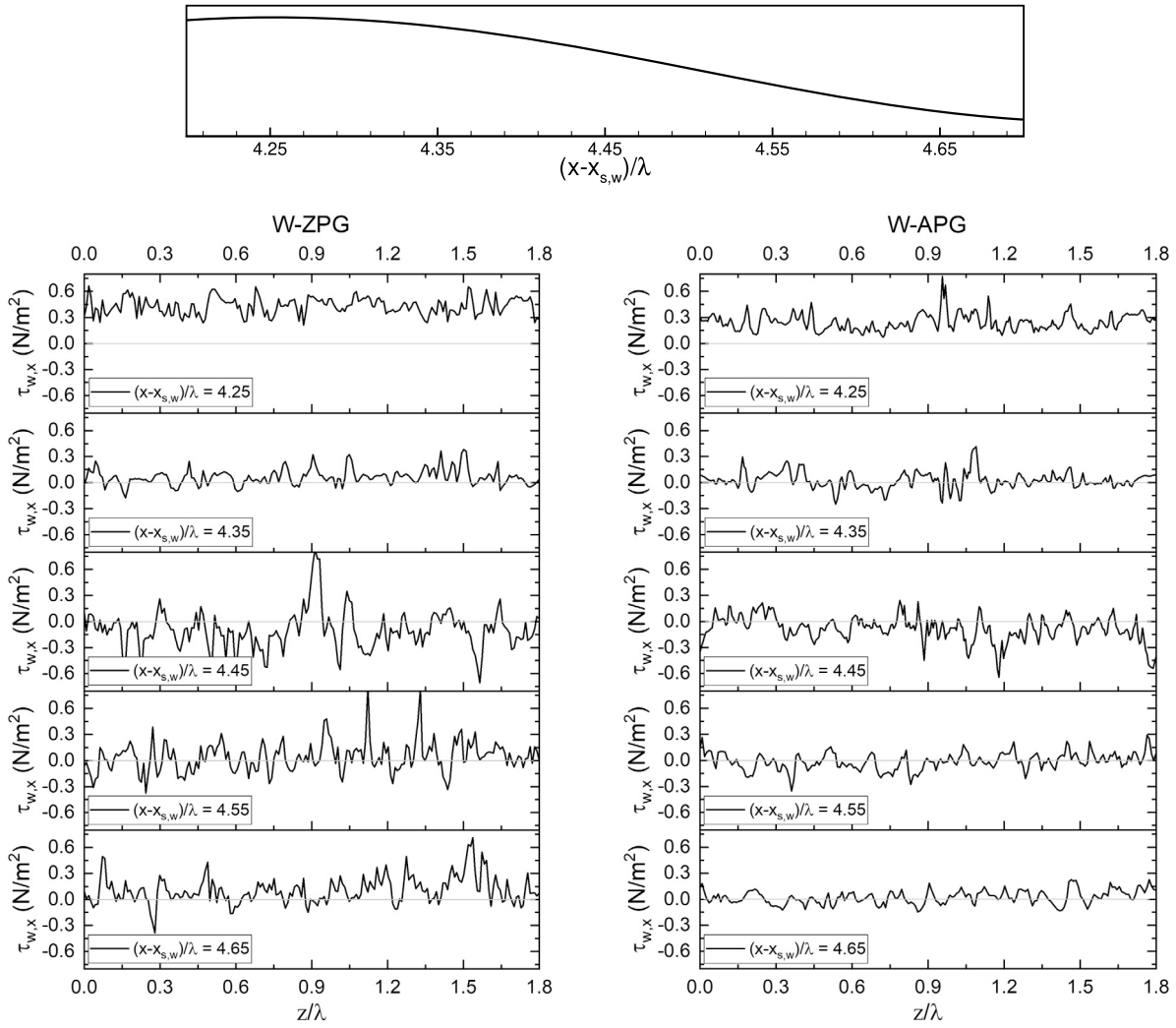



**Fig. 18.** Spanwise distributions of instantaneous streamwise component of wall-shear stresses for three streamwise positions on 5th wave for the W-APG case.

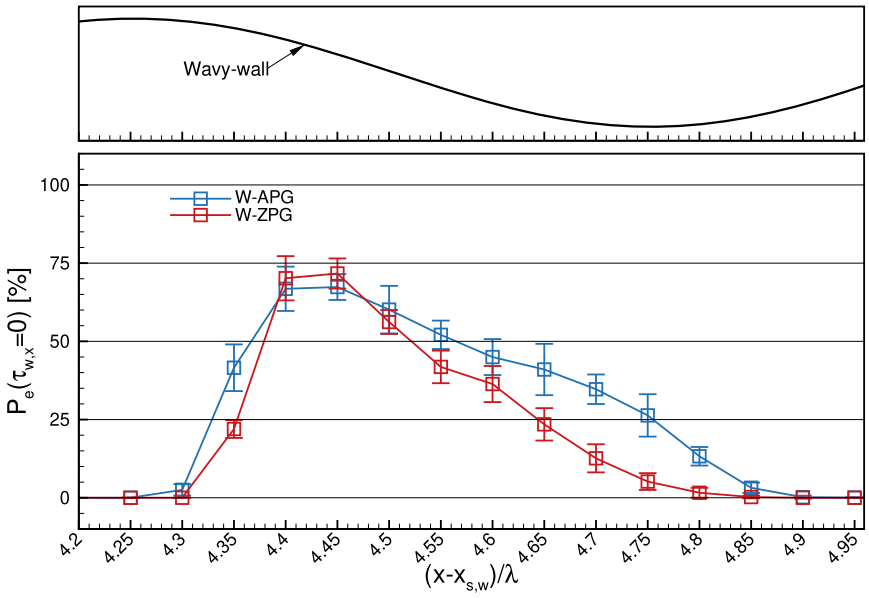



**Fig. 19.** Exceedance probability ($P_e(\tau_{w,x} = 0)$) at selected locations of the downhill slope of the 5th wave for W-ZPG and W-APG cases (Fig. 15).

**Table 2**
Values of $C_d$ obtained for all the considered configurations and the drag coefficient increase $\Delta C_d$ due to the presence of WW under ZPG and APG conditions.

| | F-ZPG | W-ZPG | F-APG | W-APG |
|---|---|---|---|---|
| $C_d$ | 0.070 | 0.125 | 0.056 | 0.110 |
| $\Delta C_d$ | | 0.055 | | 0.054 |

$\tau_w$ in the case of the separation occurrence contributes to the total drag reduction is planned for future studies.

## 4. Summary

This study provides a comprehensive insight into the new passive flow separation control method which employs 2D streamwise waviness to control the turbulent separation. This method, recently proposed by Dróżdż et al. [1], was proved to be effective at high $Re$ TBL where other commonly known passive flow control methods fail. In particular, this work explores, using LES, the fluid flow in the near-wall region just above waviness geometry at $Re_\tau = 2500$ under APG conditions (W-APG case). Characteristic feature of this WW geometry is that it exhibits an increasing amplitude in the streamwise direction. To separate the effect of global APG and local pressure gradient, the results were confronted with the ones obtained under ZPG conditions for the same WW geometry and $Re$ (W-ZPG case). Also additional simulations of TBL building up on the flat wall were conducted to have an additional reference for the flow fields obtained above WW under ZPG and APG (F-ZPG and F-APG cases).

A clear difference between W-ZPG and W-APG cases emerges when exploring just the general picture of the coherent structure arrangement above the waviness. Namely, an increasing size of the structures becomes present in the flow due to the presence of the global APG and it becomes particularly pronounced when $\beta \gtrsim 10$. This scenario, however, is typical for APG flows, i.e. a growing pressure gradient is accompanied with emergence of highly-energetic large-scale structures. The other thing that is seen in the flow for W-APG is that the small-scale activity becomes dumped.

The considered waviness produces areas with local FPG (on the uphill side of WW) and APG (on the downhil side of WW). In turn, an enhancement and reduction of the streamwise flow velocity is seen over the crest and within trough, respectively. This effect is generally seen for both W-ZPG and W-APG cases, however, due to the presence of the global APG, W-APG experiences an overall decrease in the streamwise velocity downstream the flow. Regarding the wall-normal component of the velocity, the regions with enhanced and reduced $\langle U_y \rangle / U_e$ emerge on the uphill and downhill sides of the waviness and both effects become more pronounced with increasing WW amplitude for W-ZPG. The global pressure gradient compensates the effect of growing amplitude of WW which ensures keeping the values of $\langle U_y \rangle / U_e$ at a comparable level within consecutive waves for the considered configuration.

Wavy wall causes an emergence of a local maximum in $\langle u_x u_x \rangle^{0.5} / U_e$ and $\langle u_y u_y \rangle^{0.5} / U_e$ on the downhill side which grows up and becomes wider (in the streamwise direction) with increasing $A(x)$. This effect is slightly more pronounced for the W-ZPG case. On the other hand, in the overlapping region a considerably higher levels of $\langle u_x u_x \rangle^{0.5} / U_e$ are seen with growing $A(x)$ for W-APG comparing to W-ZPG. Global APG seems to have a minor impact on $\langle u_y u_y \rangle^{0.5} / U_e$ as its levels are very similar for both W-ZPG and W-APG cases.

A closer inspection of the streamwise velocity and its fluctuation profiles indicated that the contribution of the global APG to the flow statistics begins when $\beta \gtrsim 3$, i.e. from the third wave for the given WW geometry. Apart from some notable changes of $\langle U_x \rangle / U_e$ at the location of the waviness crest, in general contribution of $A(x)$ either on $\langle U_x \rangle / U_e$ in the remaining locations or on $\langle u_x u_x \rangle^{1/2} / U_e$ within the entire waviness seem to be negligible for the W-ZPG case. This is not the case for W-APG, since the reduction of $\langle U_x \rangle / U_e$ and a substantial enhancement of $\langle u_x u_x \rangle^{1/2} / U_e$ in the overlapping region is seen with growing $A(x)$ or to be more precise with growing pressure gradient for all the considered locations.

A large oscillation in $\langle \tau_{w,x} \rangle$ within the entire waviness is reported for both W-ZPG and W-APG. This oscillation becomes enhanced downstream the flow for W-ZPG case, due to increasing $A(x)$ and it is maintained at relatively constant level for W-APG since the global APG compensates the effect of $A(x)$ for the given both WW geometry and the global pressure gradient. This oscillation makes $\langle \tau_{w,x} \rangle$ to take negative values on the downhill slope of each waviness period for both W-ZPG and W-APG. It causes the flow separation to occur in that region which, due to increasing $A(x)$ occupies wider and wider streamwise distance within subsequent waves. For W-APG, when $\beta > 3$, this effect is even more pronounced due to the contribution of the global APG.

It was also found that in contrast to W-APG, for W-ZPG WW has no permanent effect on $\langle \tau_{w,x} \rangle$ downstream the corrugation, for the given WW geometry, as its value reaches quickly the one obtained for F-ZPG. This, however, can be an effect of different streamwise evolution of $A(x)/\delta$ for each case since for W-ZPG case, TBL builds up much slower and so the crests of WW are more and more immersed into the outer region stimulating TBL in a more extensive way comparing to W-APG.

The presence of the wavy wall induces additional drag and its overall growth was found to be comparable for W-ZPG and W-APG with respect to the flat plate configurations, i.e. F-ZPG and F-APG, respectively.

In future work, one needs to examine the performance of the given wavy wall geometry under a wide range of $Re$ as well as different pressure gradient histories. Even more importantly, the effectiveness of WW in postponement of TBL separation should be examined on the real geometry of the wing.

## CRediT authorship contribution statement

**Piotr Kamiński:** Writing – review & editing, Writing – original draft, Visualization, Software, Methodology, Investigation, Formal analysis, Data curation, Conceptualization. **Paweł Niegodajew:** Writing – review & editing, Writing – original draft, Visualization, Supervision, Methodology, Investigation, Formal analysis, Data curation, Conceptualization. **Artur Dróżdż:** Writing – review & editing, Supervision, Methodology, Conceptualization. **Vasyl Sokolenko:** Validation. **Artur Tyliszczak:** Writing – review & editing, Supervision. **Witold Elsner:** Writing – review & editing, Supervision, Resources, Project administration, Funding acquisition, Conceptualization.

## Declaration of competing interest

The authors declare that they have no known competing financial interests or personal relationships that could have appeared to influence the work reported in this paper.

## Data availability

Data will be made available on request.

## Acknowledgements

The investigation was supported by the National Science Centre under Grant No. DEC-2020/39/B/ST8/01449. The simulations were carried out using the PL-Grid computer infrastructure.

## References


[1] A. Dróżdż, P. Niegodajew, M. Romańczyk, V. Sokolenko, W. Elsner, Effective use of the streamwise waviness in the control of turbulent separation, Exp. Therm. Fluid Sci. 121 (2021) 110291.

[2] T. Lee, P. Gerontakos, Investigation of flow over an oscillating airfoil, J. Fluid Mech. 512 (2004) 313.

[3] Á. Tanarro, R. Vinuesa, P. Schlatter, Effect of adverse pressure gradients on turbulent wing boundary layers, J. Fluid Mech. 883 (2020) A8.

[4] C.S. Vila, R. Vinuesa, S. Discetti, A. Ianiro, P. Schlatter, R. Örlü, Separating adverse-pressure-gradient and reynolds-number effects in turbulent boundary layers, Phys. Rev. Fluids 5 (2020) 064609.

[5] R.S. Azad, Turbulent flow in a conical diffuser: a review, Exp. Therm. Fluid Sci. 13 (1996) 318.

[6] S. Salehi, M. Raisee, M. Cervantes, Computation of developing turbulent flow through a straight asymmetric diffuser with moderate adverse pressure gradient, J. Appl. Fluid Mech. 10 (2017) 1029.

[7] M. Yadegari, A.B. Khoshnevis, Numerical study of the effects of adverse pressure gradient parameter, turning angle and curvature ratio on turbulent flow in 3d turning curved rectangular diffusers using entropy generation analysis, Eur. Phys. J. Plus 135 (2020) 548.

[8] J. Bons, A critical assessment of reynolds analogy for turbine flows, J. Heat Transf. 127 (2005) 472.

[9] J.P. Bons, S.T. McClain, The effect of real turbine roughness with pressure gradient on heat transfer, in: Turbo Expo: Power for Land, Sea, and Air, vol. 36886, 2003, pp. 611–622.

[10] R. Goyal, B.K. Gandhi, M.J. Cervantes, Experimental study of mitigation of a spiral vortex breakdown at high reynolds number under an adverse pressure gradient, Phys. Fluids 29 (2017).

[11] Y. Nagano, M. Tagawa, T. Tsuji, Effects of adverse pressure gradients on mean flows and turbulence statistics in a boundary layer, in: Turbulent Shear Flows 8: Selected Papers from the Eighth International Symposium on Turbulent Shear Flows, Munich, Germany, September 9–11, 1991, Springer, 1993, pp. 7–21.

[12] V. Kitsios, A. Sekimoto, C. Atkinson, J.A. Sillero, G. Borrell, A.G. Gungor, J. Jiménez, J. Soria, Direct numerical simulation of a self-similar adverse pressure gradient turbulent boundary layer at the verge of separation, J. Fluid Mech. 829 (2017) 392.

[13] C.J. Peterson, B. Vukasinovic, A. Glezer, Control of a closed separation domain in adverse pressure gradient over a curved surface, in: AIAA Scitech 2019 Forum, 2019, p. 1900.

[14] A. Abbas, G. Bugeda, E. Ferrer, S. Fu, J. Periaux, J. Pons-Prats, E. Valero, Y. Zheng, Drag reduction via turbulent boundary layer flow control, Sci. China, Technol. Sci. 60 (2017) 1281.

[15] M. Quadrio, P. Ricco, Critical assessment of turbulent drag reduction through spanwise wall oscillations, J. Fluid Mech. 521 (2004) 251.

[16] P. Ashill, J. Fulker, K. Hackett, A review of recent developments in flow control, Aeronaut. J. 109 (2005) 205.

[17] T. Moghaddam, N.B. Neishabouri, On the Active and Passive Flow Separation Control Techniques over Airfoils, IOP Conference Series: Materials Science and Engineering, vol. 248, IOP Publishing, 2017, p. 012009.

[18] I. Harwigsson, M. Hellsten, Environmentally acceptable drag-reducing surfactants for district heating and cooling, J. Am. Oil Chem. Soc. 73 (1996) 921.

[19] H.S. Yoon, O.A. El-Samni, H.H. Chun, Drag reduction in turbulent channel flow with periodically arrayed heating and cooling strips, Phys. Fluids 18 (2006) 025104.

[20] J.A. Vernet, R. Örlü, P.H. Alfredsson, Flow separation control behind a cylindrical bump using dielectric-barrier-discharge vortex generator plasma actuators, J. Fluid Mech. 835 (2018) 852.

[21] J.A. Vernet, R. Örlü, D. Söderblom, P. Elofsson, P.H. Alfredsson, Plasma streamwise vortex generators for flow separation control on trucks: a proof-of-concept experiment, Flow Turbul. Combust. 100 (2018) 1101.

[22] J.A. Vernet, R. Örlü, P.H. Alfredsson, Separation control by means of plasma actuation on a half cylinder approached by a turbulent boundary layer, J. Wind Eng. Ind. Aerodyn. 145 (2015) 318.

[23] J. Choi, W.-P. Jeon, H. Choi, Mechanism of drag reduction by dimples on a sphere, Phys. Fluids 18 (2006).

[24] J. Tay, T.T. Lim, Drag reduction with teardrop-shaped dimples, in: 2018 Flow Control Conference, 2018, p. 3528.

[25] C. Tay, B. Khoo, Y. Chew, Mechanics of drag reduction by shallow dimples in channel flow, Phys. Fluids 27 (2015).

[26] F. Gattere, A. Chiarini, M. Quadrio, Dimples for skin-friction drag reduction: status and perspectives, Fluids 7 (2022) 240.

[27] K. Aoki, K. Muto, H. Okanaga, Mechanism of drag reduction by dimple structures on a sphere, J. Fluid Sci. Technol. 7 (2012) 1.

[28] P.W. Bearman, J.K. Harvey, Golf ball aerodynamics, Aeronaut. Q. 27 (1976) 112.

[29] L. Veldhuis, E. Vervoort, Drag effect of a dented surface in a turbulent flow, in: 27th AIAA Applied Aerodynamics Conference, 2009, p. 3950.

[30] C. Tay, Determining the effect of dimples on drag in a turbulent channel flow, in: 49th AIAA Aerospace Sciences Meeting Including the New Horizons Forum and Aerospace Exposition, 2011, p. 682.

[31] J. Tay, T.T. Lim, B.C. Khoo, Drag reduction with diamond-shaped dimples, in: AIAA Aviation 2019 Forum, 2019, p. 3296.

[32] M. Koike, T. Nagayoshi, N. Hamamoto, Research on Aerodynamic Drag Reduction by Vortex Generators, Mitsubishi Motors Technical Review, vol. 16, 2004, p. 11.

[33] J.-L. Aider, J.-F. Beaudoin, J.E. Wesfreid, Drag and lift reduction of a 3d bluff-body using active vortex generators, Exp. Fluids 48 (2010) 771.

[34] G. Gibertini, J. Boniface, A. Zanotti, G. Droandi, F. Auteri, R. Gaveriaux, A. Le Pape, Helicopter drag reduction by vortex generators, Aerosp. Sci. Technol. 47 (2015) 324.

[35] M.R. Islam, M.A. Hossain, M. Mashud, M.T.I. Gias, Drag reduction of a car by using vortex generator, Int. J. Sci. Eng. Res. 4 (2013) 1298.

[36] D. Xin, H. Zhang, J. Ou, Experimental study on mitigating vortex-induced vibration of a bridge by using passive vortex generators, J. Wind Eng. Ind. Aerodyn. 175 (2018) 100.

[37] R. Belamadi, A. Djemili, A. Ilinca, R. Mdouki, Aerodynamic performance analysis of slotted airfoils for application to wind turbine blades, J. Wind Eng. Ind. Aerodyn. 151 (2016) 79.

[38] J.G. Coder, D.M. Somers, Design of a slotted, natural-laminar-flow airfoil for commercial transport applications, Aerosp. Sci. Technol. 106 (2020) 106217.

[39] D. Casalino, F. Avallone, I. Gonzalez-Martino, D. Ragni, Aeroacoustic study of a wavy stator leading edge in a realistic fan/ogv stage, J. Sound Vib. 442 (2019) 138.

[40] C. Teruna, L. Rego, D. Casalino, D. Ragni, F. Avallone, A numerical study on aircraft noise mitigation using porous stator concepts, Aerosp. 9 (2022) 70.

[41] Y. Wang, G. Li, S. Shen, D. Huang, Z. Zheng, Influence of an off-surface small structure on the flow control effect on horizontal axis wind turbine at different relative inflow angles, Energy 160 (2018) 101.

[42] W. Mostafa, A. Abdelsamie, M. Sedrak, D. Thévenin, M.H. Mohamed, Quantitative impact of a micro-cylinder as a passive flow control on a horizontal axis wind turbine performance, Energy 244 (2022) 122654.

[43] J.-S. Wang, J. Wu, J.-J. Wang, Wake-triggered secondary vortices over a cylinder/airfoil configuration, Exp. Fluids 64 (2023) 6.

[44] M. Smith, N. Komerath, R. Ames, O. Wong, J. Pearson, Performance analysis of a wing with multiple winglets, in: 19th AIAA Applied Aerodynamics Conference, 2001, p. 2407.

[45] U. La Roche, H.L. La Roche, Induced drag reduction using multiple winglets, looking beyond the prandtl-munk linear model, in: 2nd AIAA Flow Control Conference, 2004, p. 2120.

[46] J.E. Guerrero, D. Maestro, A. Bottaro, Biomimetic spiroid winglets for lift and drag control, C. R. Mecanique 340 (2012) 67.

[47] L. Wu, Z. Jiao, Y. Song, C. Liu, H. Wang, Y. Yan, Experimental investigations on drag-reduction characteristics of bionic surface with water-trapping microstructures of fish scales, Sci. Rep. 8 (2018) 12186.

[48] J.E. Guerrero, M. Sanguineti, K. Wittkowski, Variable cant angle winglets for improvement of aircraft flight performance, Meccanica 55 (2020) 1917.

[49] H. Chen, F. Rao, X. Shang, D. Zhang, I. Hagiwara, Biomimetic drag reduction study on herringbone riblets of bird feather, J. Bionics Eng. 10 (2013) 341.

[50] A. Schlieter, R. Pflumm, I. Shakhverdova, R. Naraparaju, U. Schulz, C. Leyens, M. Schütze, W. Reimers, Mechanical properties of shark-skin like structured surfaces for high-temperature applications, Adv. Eng. Mater. 18 (2016) 688.

[51] A.W. Lang, E.M. Jones, F. Afroz, Separation control over a grooved surface inspired by dolphin skin, Bioinspir. Biomim. 12 (2017) 026005.

[52] P. Lissaman, Low-reynolds-number airfoils, Annu. Rev. Fluid Mech. 15 (1983) 223.

[53] T.J. Mueller, J.D. DeLaurier, Aerodynamics of small vehicles, Annu. Rev. Fluid Mech. 35 (2003) 89.

[54] J.H. McMasters, M.L. Henderson, Low-Speed Single-Element Airfoil Synthesis, NASA. Langley Res. Center the Sci. and Technol. of Low Speed and Motorless Flight, Pt. 1, 1979.

[55] N. Hutchins, I. Marusic, Large-scale influences in near-wall turbulence, Philos. Trans. R. Soc. A, Math. Phys. Eng. Sci. 365 (2007) 647.

[56] C. Maass, U. Schumann, Numerical simulation of turbulent flow over a wavy boundary, in: Direct and Large-Eddy Simulation I: Selected Papers from the First ERCOFTAC Workshop on Direct and Large-Eddy Simulation, Springer, 1994, pp. 287–297.

[57] W. Gong, P.A. Taylor, A. Dörnbrack, Turbulent boundary-layer flow over fixed aerodynamically rough two-dimensional sinusoidal waves, J. Fluid Mech. 312 (1996) 1.

[58] D.S. Henn, R.I. Sykes, Large-eddy simulation of flow over wavy surfaces, J. Fluid Mech. 383 (1999) 75.

[59] L. Ding, W. Shi, H. Luo, Numerical simulation of viscous flow over non-smooth surfaces, Comput. Math. Appl. 61 (2011) 3703.

[60] P. Cherukat, Y. Na, T. Hanratty, J. McLaughlin, Direct numerical simulation of a fully developed turbulent flow over a wavy wall, Theor. Comput. Fluid Dyn. 11 (1998) 109.

[61] V.M. Segunda, S.J. Ormiston, M.F. Tachie, Experimental and numerical investigation of developing turbulent flow over a wavy wall in a horizontal channel, Eur. J. Mech. B, Fluids 68 (2018) 128.

[62] W.-Y. Zhang, W.-X. Huang, C.-X. Xu, Very large-scale motions in turbulent flows over streamwise traveling wavy boundaries, Phys. Rev. Fluids 4 (2019) 054601.

[63] C. Wagner, S. Kenjereš, P.R. von Rohr, Dynamic large eddy simulations of momentum and wall heat transfer in forced convection over wavy surfaces, J. Turbul. N7 (2011).

[64] Z. Sun, Y. Zhu, Y. Hu, S. Zhang, Direct numerical simulation of a fully developed compressible wall turbulence over a wavy wall, J. Turbul. 19 (2018) 72.

[65] E. Zhang, X. Wang, Q. Liu, Effects of the spanwise heterogeneity of a three-dimensional wavy wall on momentum and scalar transport, Phys. Fluids 33 (2021) 055116.
[66] E. Zhang, X. Wang, Q. Liu, Large-Eddy Simulation of Turbulent Flow over Wavy Wall with Different Wave Steepness, E3S Web of Conferences, vol. 299, EDP Sciences, 2021, p. 03012.
[67] E. Zhang, X. Wang, Q. Liu, Numerical investigation on the temporal and spatial statistical characteristics of turbulent mass transfer above a two-dimensional wavy wall, Int. J. Heat Mass Transf. 184 (2022) 122260.
[68] S. Harikrishnan, S. Tiwari, Heat transfer characteristics of sinusoidal wavy channel with secondary corrugations, Int. J. Therm. Sci. 145 (2019) 105973.
[69] L.-H. Wang, C.-X. Xu, H.J. Sung, W.-X. Huang, Wall-attached structures over a traveling wavy boundary: turbulent velocity fluctuations, Phys. Rev. Fluids 6 (2021) 034611.
[70] W. Elsner, A. Dróżdż, E. Szymanek, A. Tyliszczak, P. Niegodajew, Experimental and numerical studies of turbulent flows over two-dimensional and three-dimensional rough surfaces under an adverse pressure gradient, Appl. Math. Model. 106 (2022) 549.
[71] F. Nicoud, F. Ducros, Subgrid-scale stress modelling based on the square of the velocity gradient tensor, Flow Turbul. Combust. 62 (1999) 183.
[72] P. Kaminski, A. Tyliszczak, Numerical Analysis of the Influence of Wall Roughness on the Turbulent Boundary Layer Separation, Journal of Physics: Conference Series, vol. 2367, IOP Publishing, 2022, p. 012011.
[73] V. Kitsios, C. Atkinson, J.A. Sillero, G. Borrell, A. Gungor, J. Jiménez, J. Soria, Direct numerical simulation of a self-similar adverse pressure gradient turbulent boundary layer, Int. J. Heat Fluid Flow 61 (2016) 129.
[74] J.-H. Lee, H.J. Sung, Effects of an adverse pressure gradient on a turbulent boundary layer, Int. J. Heat Fluid Flow 29 (2008) 568.
[75] F.H. Clauser, The turbulent boundary layer, Adv. Appl. Mech. 4 (1956) 1.
[76] S.B. Pope, Turbulent flows, Meas. Sci. Technol. 12 (2001) 2020.
[77] A. Dörnbrack, U. Schumann, Numerical simulation of turbulent convective flow over wavy terrain, Bound.-Layer Meteorol. 65 (1993) 323.
[78] J. Finnigan, K. Ayotte, I. Harman, G. Katul, H. Oldroyd, E. Patton, D. Poggi, A. Ross, P. Taylor, Boundary-layer flow over complex topography, Bound.-Layer Meteorol. 177 (2020) 247.
[79] J. Nam, F. Lien, Assessment of ghost-cell based cut-cell method for large-eddy simulations of compressible flows at high reynolds number, Int. J. Heat Fluid Flow 53 (2015) 1.
[80] T. Pu, C. Zhou, J. Ai, Extension of the local domain-free discretization method to large eddy simulation of turbulent flows, Int. J. Numer. Methods Fluids 90 (2019) 456.
[81] J.C. Hunt, A.A. Wray, P. Moin, Eddies, Streams, and Convergence Zones in Turbulent Flows, Studying Turbulence Using Numerical Simulation Databases, vol. 2, Proceedings of the 1988 Summer Program, 1988.
[82] S.J. Lee, S. Lee, Y.A. Hassan, Numerical investigation of turbulent flow in an annular sector channel with staggered semi-circular ribs using large eddy simulation, Int. J. Heat Mass Transf. 123 (2018) 705.
[83] V. De Angelis, P. Lombardi, S. Banerjee, Direct numerical simulation of turbulent flow over a wavy wall, Phys. Fluids 9 (1997) 2429.
[84] H. Yoon, O. El-Samni, A. Huynh, H. Chun, H. Kim, A. Pham, I. Park, Effect of wave amplitude on turbulent flow in a wavy channel by direct numerical simulation, Ocean Eng. 36 (2009) 697.
[85] Z. Harun, J.P. Monty, R. Mathis, I. Marusic, Pressure gradient effects on the large-scale structure of turbulent boundary layers, J. Fluid Mech. 715 (2013) 477.
[86] R. Vinuesa, S.M. Hosseini, A. Hanifi, D.S. Henningson, P. Schlatter, Pressure-gradient turbulent boundary layers developing around a wing section, Flow Turbul. Combust. 99 (2017) 613.
[87] R. Vinuesa, P.S. Negi, M. Atzori, A. Hanifi, D.S. Henningson, P. Schlatter, Turbulent boundary layers around wing sections up to rec = 1,000,000, Int. J. Heat Fluid Flow 72 (2018) 86.
[88] Y. Maciel, M.P. Simens, A.G. Gungor, Coherent structures in a non-equilibrium large-velocity-defect turbulent boundary layer, Flow Turbul. Combust. 98 (2017) 1.
[89] J. Monty, N. Hutchins, H. Ng, I. Marusic, M. Chong, A comparison of turbulent pipe, channel and boundary layer flows, J. Fluid Mech. 632 (2009) 431.
[90] A. Dróżdż, P. Niegodajew, M. Romańczyk, W. Elsner, Convection velocity in turbulent boundary layers under adverse pressure gradient, Exp. Therm. Fluid Sci. 110900 (2023).
[91] M. Mirzaei, A. Sohankar, L. Davidson, F. Innings, Large eddy simulation of the flow and heat transfer in a half-corrugated channel with various wave amplitudes, Int. J. Heat Mass Transf. 76 (2014) 432.
[92] S. Ghebali, S.I. Chernyshenko, M.A. Leschziner, Can large-scale oblique undulations on a solid wall reduce the turbulent drag?, Phys. Fluids 29 (2017).
[93] R. Mathis, J.P. Monty, N. Hutchins, I. Marusic, Comparison of large-scale amplitude modulation in turbulent boundary layers, pipes, and channel flows, Phys. Fluids 21 (2009) 111703.
[94] B. Ganapathisubramani, N. Hutchins, J.P. Monty, D. Chung, I. Marusic, Amplitude and frequency modulation in wall turbulence, J. Fluid Mech. 712 (2012) 61–91.
[95] K. Talluru, R. Baidya, N. Hutchins, I. Marusic, Amplitude modulation of all three velocity components in turbulent boundary layers, J. Fluid Mech. 746 (2014) R1.

Journal of Wind Engineering & Industrial Aerodynamics 260 (2025) 106048

Contents lists available at ScienceDirect

Journal of Wind Engineering & Industrial Aerodynamics

journal homepage: www.elsevier.com/locate/jweia

# Sensitivity analysis of wavy wall performance in turbulent separation control: Effects of amplitude and period variations

Piotr Kamiński, Witold Elsner, Artur Tyliszczak, Paweł Niegodajew *

*Department of Thermal Machinery, Czestochowa University of Technology, Al. Armii Krajowej 21, 42-200 Czestochowa, Poland*

ARTICLE INFO

*Keywords:*
Large Eddy Simulation
Turbulent separation
Wall-shear stress
Wavy wall
Effective slope
Flow control

ABSTRACT

The influence of transversely oriented sinusoidal wall corrugation on an incompressible isothermal flow in the near-wall region, subjected to adverse pressure gradient conditions at a friction Reynolds number of $Re_\tau = 2500$, is investigated using Large Eddy Simulation. This study is a continuation of the work (Kamiński et al., 2024) devoted to dynamics of the flow in the regions of crests and downhill/uphill waviness parts, and where the impact of the local and global pressure gradient were analysed. It focuses on the influence of the waviness parameters, such as amplitude ($A$) and number of waviness periods ($N_\lambda$) on the turbulent boundary layer separation. In terms of the effective slope, $ES \propto |dA/dx|$, where $x$ is the streamwise direction, the analysed cases included the configurations with $ES$ ranging from $ES = 0$ (flat wall) to $ES = 0.2455$ ($A/\lambda = 0.051$, where $\lambda$ is the length of a single waviness). Specifically, the primary objective was to identify a combination of $A$ and $N_\lambda$ that would result in the greatest increase in the wall-shear stress $\tau_w$, relative to the flat plate configuration, aiming to achieve the maximum postponement of turbulent separation. It is shown that the waviness significantly affects the flow field by enhancing the turbulent kinetic energy that leads to increased $\tau_w$. In particular, it is shown that the enhancement in TKE depends mainly on $ES$ and not on particular values of $A$ and $N_\lambda$. Namely, the cases which are significantly diversified by $A$ and $N_\lambda$ but are characterised by the same $ES$ exhibit almost identical TKE profiles. The highest increase in the wall-shear stress compared to the reference flat plate configuration was observed for the combination of $A$ and $N_\lambda$ corresponding to $ES = 0.1473$.

## 1. Introduction

The phenomenon of a turbulent flow being exposed to the adverse pressure gradient (APG) is a very common scenario that is seen in practice — the flow over the suction side of an airfoil (Lee and Gerontakos, 2004; Tanarro et al., 2020; Vila et al., 2020), diffuser flows (Azad, 1996; Apsley and Leschziner, 2000; Salehi et al., 2017; Yadegari and Khoshnevis, 2020) or flow around a turbine blade (Bons, 2005; Bons and McClain, 2003; Goyal et al., 2017) are all well-known application examples. At strong APG conditions the turbulent boundary layer (TBL) separation (Nagano et al., 1993; Kitsios et al., 2017; Peterson et al., 2019; Oehme et al., 2022) may occur which leads to increased aerodynamic drag (Gad-el Hak and Bushnell, 1991). As such, a major decrease in the energy efficiency of a system takes place. The flow separation occurs when the wall-shear stress reaches zero ($\tau_w = \mu(dU/dy_w) = 0$, where: $\mu$ is the dynamic viscosity and $dU/dy_w$ is the near-wall velocity gradient along the wall-normal direction $y_w$). Various techniques are available to control this phenomenon which are generally classified as active or passive (Joshi and Gujarathi, 2016; Ashill et al., 2005; Tayebi and Torabi, 2024). The first group involves systems, often quite complex, requiring an external energy source. Some examples include: synthetic jets (You and Moin, 2008), blowing and suction (Moghaddam and Neishabouri, 2017), heating and cooling (Jahanmiri, 2010; Yoon et al., 2006; Harwigsson and Hellsten, 1996), moving wall systems (Quadrio, 2011; Leschziner, 2020), electromagnetic Lorentz force actuators (Jahanmiri, 2010), plasma actuators (Vernet et al., 2018a,b, 2015), dielectric actuators (Karimi et al., 2021; Awada et al., 2022) and so on. Due to high costs, complexity and energy consumption of the active methods, the passive flow control is favoured as it does not require any external source of energy. The passive techniques involve some degree of surface modification or roughness and among these, the most common are for example: dimples on a golf ball (Lorenz, 2006; Choi et al., 2006; Tay and Lim, 2018; Tay et al., 2015; Gattere et al., 2022; Aoki et al., 2012; Bearman and Harvey, 1976; Veldhuis and Vervoort, 2009; Tay, 2011; Tay et al., 2019) as well as vortex generators on an airfoil (Koike et al., 2004; Aider et al., 2010; Seshagiri et al., 2009; Manolesos and Voutsinas, 2015) or the agricultural vehicle body (Lo and Kontis, 2016). Both of them are tools for flow turbulisation, postponement of separation and drag force re-

* Corresponding author.
*E-mail address:* pawel.niegodajew@pcz.pl (P. Niegodajew).

https://doi.org/10.1016/j.jweia.2025.106048
Received 20 August 2024; Received in revised form 10 February 2025; Accepted 10 February 2025
Available online 21 February 2025
0167-6105/© 2025 Elsevier Ltd. All rights are reserved, including those for text and data mining, AI training, and similar technologies.

duction. Among unconventional flow control methods few of them are worth mentioning, i.e.: slotted airfoils (Belamadi et al., 2016; Coder and Somers, 2020; Whitman et al., 2006), streamwise waviness for reducing the leading edge interaction noise (Casalino et al., 2019; Teruna et al., 2022), blade splits (Moshfeghi et al., 2017) or placing microcylinder near a blade leading edge (Wang et al., 2018; Mostafa et al., 2022; Wang et al., 2023). Furthermore, the aeroelastic membranes, which passively adapt to the flow conditions, were investigated (Piquee et al., 2022; Bottasso et al., 2016). There are also other solutions that are quite often nature-inspired. Some examples of these include: winglets (Smith et al., 2001; La Roche and La Roche, 2004; Guerrero et al., 2012; Wu et al., 2018; Guerrero et al., 2020), which are the wingtip devices often seen at the end of an airfoil and these are inspired by the ends of bird's wing; fish scale microstructure, which are able to reduce drag at lower Reynolds numbers (Wu et al., 2018; Dou et al., 2012); herringbone riblets inspired by the bird's feather (Chen et al., 2013); micro-scale riblets inspired by the skins of sharks (Schlieter et al., 2016) or dolphins (Lang et al., 2017); leading edge trips (Leknys et al., 2018), slots (Beyhaghi and Amano, 2018) or tubercles (Schmidt and Redonnet, 2024) which mimic the protuberances of a humpback whale flipper, and so forth.

The passive flow control methods, which were discussed so far, can employ either relatively simple or very complex surface modifications. These techniques are mostly applicable for laminar or transitional flows (Lissaman, 1983; Mueller and DeLaurier, 2003) since their effectiveness diminishes with increasing $Re$ (McMasters and Henderson, 1979) and when applied to fully turbulent flows the separation occurs earlier. This might be attributed to the momentum deficit caused by the wall irregularities (Aubertine et al., 2004; Mejia-Alvarez and Christensen, 2013).

In the literature, one can find several works devoted to the flow over the wavy wall surfaces conducted under ZPG conditions (Cherukat et al., 1998; Sun et al., 2018; Kuhn et al., 2010; Tyson and Sandham, 2013; Kruse and Von Rohr, 2006; Hamed et al., 2015; Elsner et al., 2022; Akselsen and Ellingsen, 2020; Fernex et al., 2020; De Angelis et al., 1997; Koyama et al., 2007; Yoon et al., 2009; Fujii et al., 2011; Ghebali et al., 2017; Segunda et al., 2018; Hamed et al., 2017). A direct numerical simulation (DNS) of De Angelis et al. (1997) has shown that for a certain amplitude range of a sinusoidal corrugation, the areas with increased wall-shear stress emerge. A flow field study over walls modified by waviness examined by Koyama et al. (2007) indicated enhancement of $\tau_w$ for one of the tested configurations. Yoon et al. (2009) showed that a corrugation with amplitude ($A$) to the period ($\lambda$) ratio $A/\lambda = 0.03$ allows for a maximal enhancement of $\tau_w$ for Reynolds number based on the free-stream velocity $Re = (U_\infty H/\nu) = 6760$ (where $U_\infty$ is the free-stream velocity, $H$ is the mean height of the channel and $\nu$ is the kinematic viscosity). The presence of wall waviness generally leads to the increase in velocity fluctuations and consequently to the increase in the turbulent kinetic energy (TKE) (Cherukat et al., 1998; Sun et al., 2018; Tyson and Sandham, 2013). On the other hand, when increasing $A/\lambda$, an enhancement of the aerodynamic drag as well as the decrease in wall-shear stress is observed (Fujii et al., 2011; Ghebali et al., 2017; Segunda et al., 2018; Hamed et al., 2017).

Enhancement of $\tau_w$ due to the wavy wall in some of the mentioned studies, although obtained for ZPG flows, triggered the research group of Dróżdż et al. (2021a) to verify whether the effect can be obtained under APG conditions. In particular, the authors examined experimentally the usefulness of the surface undulation in the enhancement of the wall-shear and postponement of the turbulent separation at high $Re$. It was shown that for a certain amplitude and period of a transverse wall waviness, a 13% increase in skin-friction can be obtained at Reynolds number defined based on the boundary layer thickness $\delta$ and the friction velocity $u_\tau = \sqrt{\tau_w/\rho}$ (where $\rho$ is the mass density) equal to $Re_\tau = u_\tau\delta/\nu = 4000$. This allows to move significantly the point of turbulent separation downstream. They also showed that the mechanisms governing the increase in $\tau_w$ caused by the wavy wall are similar to the amplitude modulation of small scales by the large scales (Mathis et al., 2009; Dogan et al., 2019; Andreolli et al., 2023).

In our previous work (Elsner et al., 2022) we examined, experimentally and numerically, the effects of different surface topology (two-dimensional and three-dimensional) on the turbulent flow development over a smooth wall downstream the corrugation at $Re_\tau = 1350$ under APG conditions. It was found that for this particular $Re_\tau$ value, none of the investigated surface topologies ensured an enhancement in the wall-shear stress in the region of interest (i.e. downstream the corrugation) with respect to the flat plate case. The lack of enhancement in $\tau_w$ should be attributed to the insufficiently high value of $Re_\tau$ examined. It is because, in the most recent work of Kamiński et al. (2024) exploring the flow over a wavy wall under zero and adverse pressure gradient conditions indicated that enhancement in $\tau_w$ and so, a postponement of TBL separation, is possible at higher $Re_\tau$ of 2500.

This work further extends the research of Kamiński et al. (2024) by a systematic search for the values of corrugated wall parameters, i.e., the amplitude ($A$) and a number of periods ($N_\lambda$), allowing for a maximum increase in $\tau_w$ and also further examination of the impact of these parameters on the flow picture under APG conditions. The analysis is conducted with the use of the Large Eddy Simulations (LES) in ANSYS Fluent software for the same Reynolds number as in Kamiński et al. (2024) equal to $Re_\tau = 2500$ corresponding to Reynolds number defined based on the momentum thickness $\theta = (\int_0^\delta \langle U(y)\rangle/U_\infty)(1 - \langle U(y)\rangle/U_\infty)dy$ equal to $Re_\theta = U_\infty\theta/\nu = 9800$. The model's performance was verified in our previous work (Kamiński et al., 2024) where an identical numerical setup was employed. Now, the focus is put on the near-wall turbulence within the waviness as well as downstream within the flat plate region. In particular, it is investigated with LES whether the transverse corrugation has a long-lasting effect on the near-wall flow downstream. The key goal is to find an optimal combination of $A$ and $N_\lambda$, allowing for the maximum increase in skin-friction that should ensure the maximum postponement of TBL detachment. An important outcome of the research is a better understanding of the physics of the flow modified by the corrugation that may be beneficial for further wall topology optimisation under different flow conditions.

The present manuscript is organised as follows: the description of the research object and numerical methods, together with details of the wavy wall configurations, as well as mesh characteristics, are described in Section 2; the results obtained using LES are presented in Section 3; and the conclusions and suggestions for future work are provided in Section 4.

## 2. Methods

### 2.1. Research object

This research examines an incompressible and isothermal TBL developing over a 2D streamwise wavy wall subjected to APG conditions at $Re_\tau = 2500$ using LES. In particular, the present work extends the previous one (Kamiński et al., 2024) by providing a detailed systematic study aimed at distinguishing the most effective combination of amplitude and period of the waviness in postponement of turbulent separation.

The waviness is defined using the sine function parametrised by $A$ and $\lambda$ according to the relation:

$$y_w(x) = A \cdot \sin(\omega x) \tag{1}$$

The reference shape reflects the one analysed in Kamiński et al. (2024) and is characterised by the amplitude defined as:

$$A = A_0(0.00366x^2 + 0.000614x + 0.003351) \tag{2}$$

The parameter $A_0$ is the dimensionless amplitude scale that allows for increasing or decreasing the amplitude with respect to the basic one $A_0 = 1.0$ that was examined in Kamiński et al. (2024) for identical $Re_\tau = 2500$. The variation of the amplitude in the streamwise direction

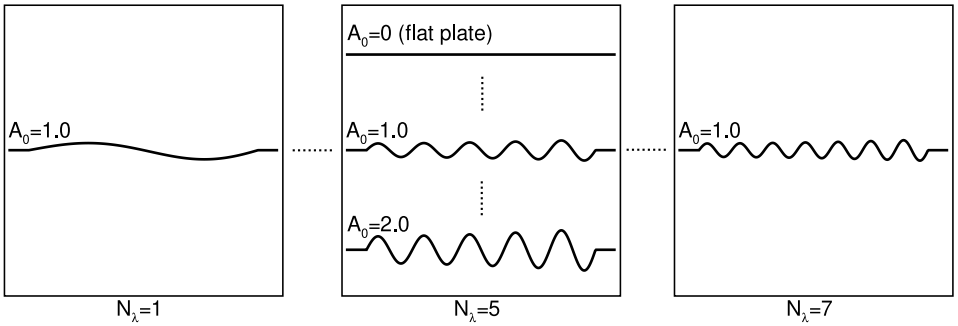



**Fig. 1.** Schematic drawing illustrating corrugation geometries described in Tables 1 and 2.

ensured that $A$ increases proportionally to $\delta$ and barely touched the outer region of TBL as suggested in Dróżdż et al. (2021a). The frequency of the waviness is defined as $\omega = 2\pi/\lambda$ with $\lambda = L_{x,w}/N_\lambda$, which for the reference case with $N_\lambda = 5$ equals $\lambda = 0.1332$ m. Cases with (i) the constant period number $N_\lambda = 5$ and varying amplitude in the range $A_0 = 0 - 2.0$; (ii) the cases with the constant amplitude $A_0 = 1.0$ and varying periods number $N_\lambda = 1-7$ were considered. Note, that the case with $A_0 = 0$ corresponds to the configuration with the flat wall.

Fig. 1 presents the schematic drawing of selected surfaces considered in the study, involving changing $A_0$ and $N_\lambda$, whereas Tables 1 and 2 report the main parameters of all test cases investigated, such as the amplitude $A$ at the localisation of the tip of the first period ($x = 0.043$ m), the amplitude expressed in viscous units, i.e. $A^+ = A \cdot u_\tau(x)/\nu$ (where $u_\tau(x)$ is measured on the flat wall) and averaged across the wavy wall, the ratio $A(x = 0.043\text{ m})/\lambda$ and the effective slope defined as the mean absolute streamwise gradient of the corrugation ($ES = \frac{1}{L_{x,w}} \int_{L_{x,w}} |\frac{dA}{dx}| dx$) (Napoli et al., 2008) for particular combinations of $A_0$ and $N_\lambda$. The wavelength to period ratio for $N_\lambda = 5$ (Table 2) is $\lambda/\delta_{avg} \approx 1.25$. The boundary layer thickness used for calculating $\lambda/\delta_{avg}$ is taken as an average $\delta$ measured at 0.01 m$< x <$ 0.676 m for the flat wall case ($A_0 = 0$), i.e. at the exact location of the corrugation (see Fig. 2 illustrating a schematic view of the experimental setup from Kamiński et al. (2024)). Since $A$ grows along the $x$ direction, the averaged value of $ES$ along the whole wavy wall is given instead of the one for a single period. According to the literature (Napoli et al., 2008; Schultz and Flack, 2009; Nugroho et al., 2021), based on the value of $ES$, the surface roughness can be classified as: waviness region for $ES < 0.15$; transition region for $0.15 < ES < 0.35$; roughness regime for $ES > 0.35$. In the waviness regime, the viscous drag is dominant while in the rough regime the dependence of $U^+ = U/u_\tau$ on $ES$ weakens. As shown by De Marchis (2016) and Forooghi et al. (2017), for corrugated walls, $ES$ is regarded as the key factor controlling the near-wall flow, while for rough surfaces, the flow depends on the height of the roughness rather than on $ES$. Since the values of $ES$ in the present study are within the range $0 \leq ES \leq 0.2455$ for all cases considered, the investigated surfaces can fit into the waviness or transition regime.

**Table 1**
Test cases with the constant $\lambda = 0.133\ m$ ($\lambda/\delta_{avg} \approx 1.25$) and varying amplitude. The amplitude $A$ [m] and $\delta$ (used for calculating $A/\delta$) are measured at the tip of the first wave, i.e. at $x = 0.043$ m.

| $A_0$ | $A$ [m] | $A/\lambda$ | $ES$ | $A^+$ | $A/\delta$ |
|---|---|---|---|---|---|
| 0 | 0 | 0 | 0 | 0 | 0 |
| 0.2 | 0.00068 | 0.0051 | 0.0245 | 23 | 0.0083 |
| 0.4 | 0.00136 | 0.0102 | 0.0491 | 46 | 0.0166 |
| 0.6 | 0.00204 | 0.0153 | 0.0736 | 69 | 0.0249 |
| 0.8 | 0.00272 | 0.0204 | 0.0982 | 92 | 0.0332 |
| 0.9 | 0.00306 | 0.0230 | 0.1105 | 104 | 0.0373 |
| 1.0 | 0.00340 | 0.0255 | 0.1227 | 115 | 0.0414 |
| 1.1 | 0.00374 | 0.0280 | 0.1350 | 127 | 0.0456 |
| 1.2 | 0.00408 | 0.0306 | 0.1473 | 139 | 0.0497 |
| 1.3 | 0.00442 | 0.0331 | 0.1595 | 150 | 0.0539 |
| 1.4 | 0.00476 | 0.0357 | 0.1719 | 162 | 0.0580 |
| 1.5 | 0.00510 | 0.0382 | 0.1841 | 157 | 0.0622 |
| 1.6 | 0.00544 | 0.0408 | 0.1964 | 183 | 0.0663 |
| 1.8 | 0.00612 | 0.0459 | 0.2209 | 207 | 0.0746 |
| 2.0 | 0.00680 | 0.0510 | 0.2455 | 231 | 0.0829 |

**Table 2**
Test cases with the constant $A_0 = 1.0$ and varying number of periods. The TBL thickness $\delta$ in 3rd column was taken as the average value over the streamwise corrugation length $\delta_{avg}$.

| $N_\lambda$ | $\lambda$ [m] | $\lambda/\delta_{avg}$ | $A/\lambda$ | $ES$ |
|---|---|---|---|---|
| 1 | 0.666 | 6.25 | 0.0051 | 0.0244 |
| 2 | 0.333 | 3.12 | 0.0102 | 0.0491 |
| 3 | 0.222 | 2.08 | 0.0153 | 0.0736 |
| 4 | 0.166 | 1.56 | 0.0204 | 0.0982 |
| 5 | 0.133 | 1.25 | 0.0255 | 0.1227 |
| 6 | 0.111 | 1.04 | 0.0306 | 0.1473 |
| 7 | 0.095 | 0.89 | 0.0357 | 0.1719 |

### 2.2. Numerical model

The LES method has been developed for over 60 years, leading to its current maturity and perception as a reliable CFD tool (Georgiadis et al., 2010; Zhiyin, 2015; Geurts et al., 2019). In this research, the computations were performed with the help of well-known and widely used ANSYS Fluent software applying the 2nd order bounded central differencing scheme for the spatial discretisation of the convective terms of the Navier–Stokes equations and 2nd order central scheme for the viscous terms. The SIMPLE algorithm with the 2nd order discretisation of the pressure gradient was used for the pressure–velocity coupling. The time integration method was performed by applying the 2nd order implicit method. The sub-grid scale tensor was modelled using the WALE model (Nicoud and Ducros, 1999), which is dedicated especially for wall-bounded flows. In all analysed cases the initial velocity in the computational domain was set to zero. A transient phase, until a fully turbulent flow was developed, lasted for approximately 0.27 s, which corresponds to 3 flow-through time units defined as $t_{FT} = L_x/U_\infty = 0.09$ s. The time-averaging procedure lasted for the next 40 $t_{FT}$. Additionally, the solutions were spatially averaged in the $z$-direction by collecting and averaging data extracted from 10 uniformly spaced cross-sections. This led to a good convergence of the time-averaged solutions, which was checked by comparing the results at the time instants $38t_{FT}$ and $40t_{FT}$.

### 2.3. Numerical domain and boundary conditions

LES allows for deep and detailed insights into flow dynamics, but its computational expense can make its application in parametric or optimisation-oriented studies prohibitive. Therefore, for the present investigations only the central part of the experimental stand (Kamiński et al., 2024; Dróżdż et al., 2021a), indicated by the red, grey and

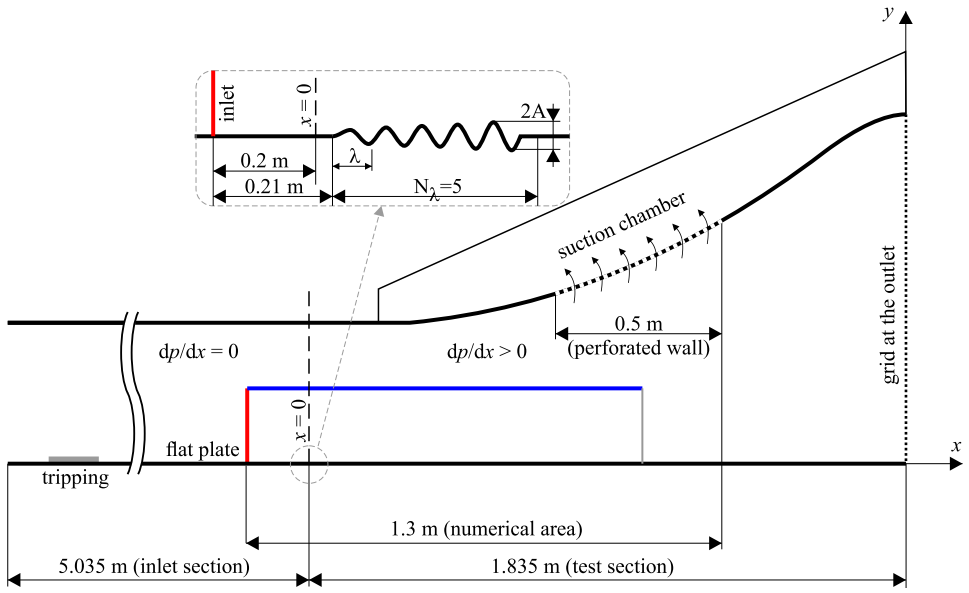



**Fig. 2.** The geometry of the experimental stand used in the present work as the basis for CFD simulations and also employed in Kamiński et al. (2024).

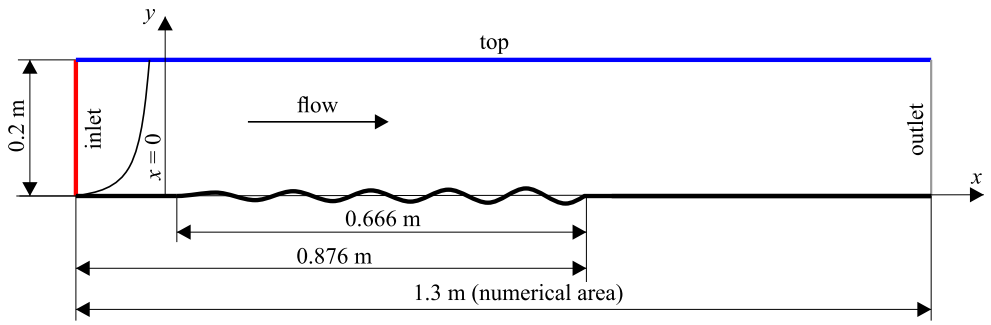



**Fig. 3.** Computational domain for LES study.

blue lines in Fig. 2, was considered in the simulations. Fig. 3 shows the localisation of the wavy wall and the boundary conditions in the computational domain. Its dimensions were $L_x = 1.3$ m ($L_x/\delta_{in} = 16.17$, where $\delta_{in}$ is the inlet boundary layer thickness) in the streamwise direction, $L_y = 0.2$ m in the wall-normal direction, and $L_z = 0.24$ m in the spanwise $z$-direction. Despite this simplification, the simulations remained relatively time-consuming. A single run, which included both the initial transient phase and the time required to obtain convergent statistics, lasted for 20 days of continuous computations on a computer cluster equipped with 96 CPUs.

The assumed rectangular computational geometry required a prescription of the boundary conditions on its inlet and the top side reflecting precisely the experimental data. To do that, the measured velocity values in these localisations were approximated by high-order polynomials. On the inlet side, the streamwise velocity $\langle U_x \rangle$ and TKE profiles were defined. The former corresponded to the measured time-averaged data while the TKE profile served as a mask imposed on instantaneous turbulent velocity components generated by applying the Fourier-based synthetic turbulence generator method (Adamian et al., 2011; Shur et al., 2014). This method turns out more stable and ensures faster solution procedure, compared to other methods available in ANSYS code (Vortex Method or Spectral Synthesiser (Anon, 2021)). The TKE profile was defined such that $\langle u_x u_x \rangle^{1/2}$ obtained in the simulations agreed almost exactly with the measurements.

Fig. 4 shows the profiles of the mean streamwise velocity and its fluctuation which were imposed on the inlet (Fig. 4a). On the top boundary (Fig. 4b), the velocity fluctuations were negligibly small, as will be shown later, and therefore only the mean streamwise $\langle U_x \rangle$ and wall-normal $\langle U_y \rangle$ velocity components were assumed in this localisation. On the side boundaries, spaced by $z = 0.24$ m, the periodic boundary conditions were applied. This allowed eliminating the need to refine the computational mesh near these boundaries that would be necessary if they were treated as non-slip walls. The test computations showed that the assumed periodicity has no impact on the solution obtained in the central part of the domain. The bottom wall of the domain was treated as the non-slip wall. At the outlet, the constant atmospheric pressure (101325 Pa) was assumed. The computational configuration described above closely corresponds to the one used in Kamiński et al. (2024). In that study, the correctness of the applied simplifications of the computational geometry and prescribed boundary conditions was thoroughly verified. A high accuracy of the LES method was confirmed by comparing the computed and measured velocity and fluctuation profiles at selected locations above the waviness. We will not repeat these comparisons here and refer the interested reader to Kamiński et al. (2024).

Fig. 5 presents the profiles of characteristic TBL quantities along the domain for the case with the flat bottom wall, including the Clauser–Rotta pressure-gradient parameter $\beta = \delta^*/\tau_w \cdot dP_\infty/dx$ (Clauser, 1956) (where $\delta^* = \int_0^\delta (1 - \langle U(y) \rangle / U_\infty) dy$ is the displacement thickness), $u_\tau$ and the shape factor $H = \delta/\theta$, skin-friction coefficient ($C_f = 2(u_\tau/U_\infty)^2$), and the Reynolds numbers calculated based on $\theta$ and $\delta$. The $x$-axis, representing the streamwise coordinate, was also provided in the non-dimensional form, i.e., normalised by $\delta_{in}$. The $\beta$ distribution shows that up to $x = 0.3$ m, the flow can be regarded as ZPG and the APG section

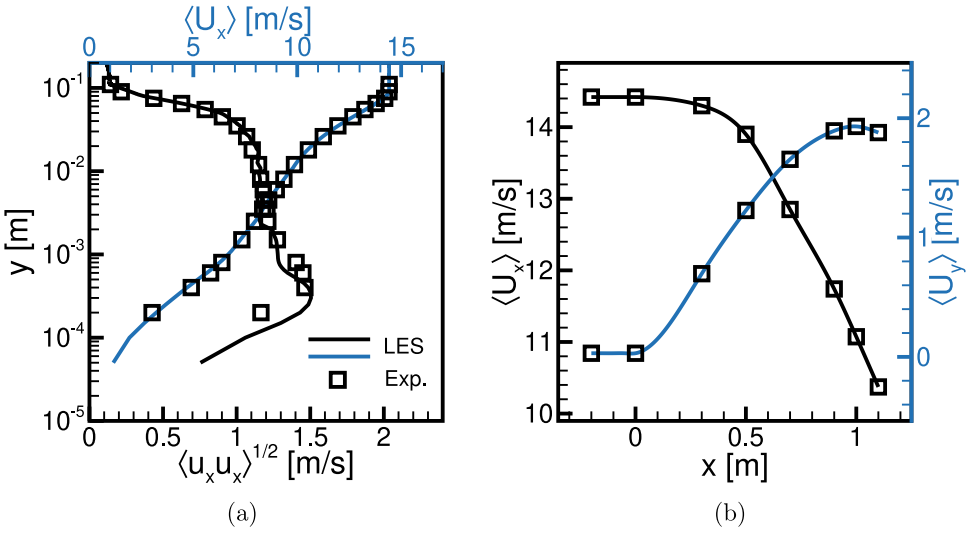



**Fig. 4.** The approximated profiles at the inlet boundary (a) and the top boundary (b) generating the APG condition used in the present study and also applied in Kamiński et al. (2024).

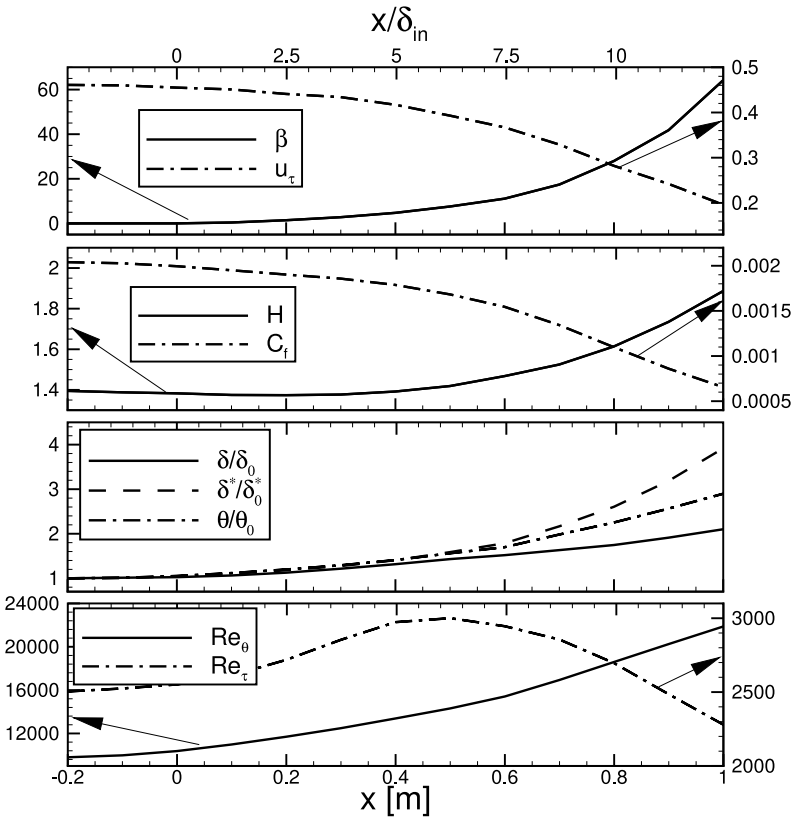



**Fig. 5.** Main parameters of the turbulent boundary layer. The values of $\delta$, $\delta^*$, $\theta$ are normalised by their initial values at $x_0$.

starts downstream. This causes $\delta$, $\delta^*$ and $\theta$ to grow proportionally with $\beta$. Thus, enhancement of $H$ is also observed. As a result, $u_\tau$, $C_f$ and $Re_\tau$ decrease respectively, which indicates that the flow approaches separation.

### 2.4. Computational mesh

The impact of mesh density on solution accuracy was analysed in Kamiński et al. (2024), where solutions obtained on four block-structured meshes (M1-M4, see Table 3) were compared. These meshes differed in near-wall refinement, as illustrated in Fig. 6. Specifically, Fig. 6 depicts mesh M4 for configurations with both the flat wall ($A_0 = 0$) and the wavy wall with $A_0 = 1.0$ and $N_\lambda = 5$. Mesh M4 is composed of a one-block structural mesh M1, which was then refined near the wall. The first level of refinement, denoted as Ref. 1, resulted in mesh M2. Subsequent refinements, Ref. 2 and Ref. 3, led to meshes M3 and M4. Each refinement involved dividing a single cell into eight smaller cells. This strategy is useful for increasing mesh resolution near the wall while maintaining coarser mesh in regions with smaller velocity gradients in the upper part of the boundary layer and the free-stream

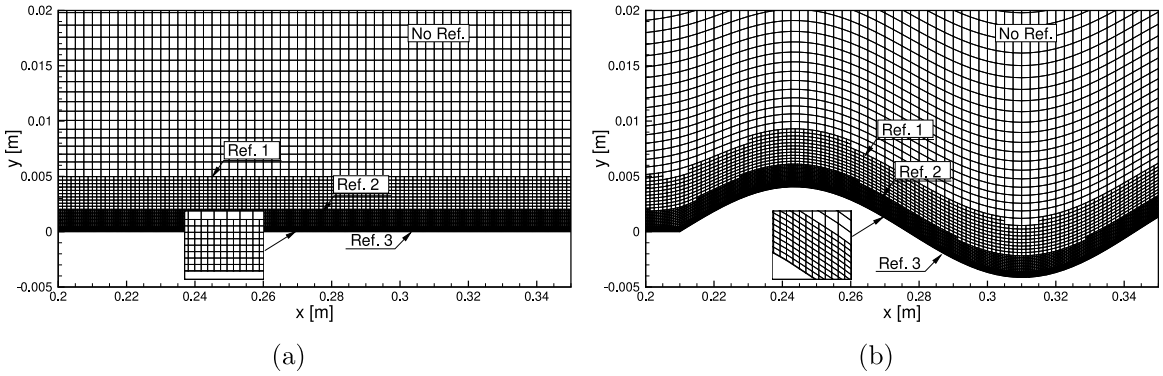



**Fig. 6.** Computational mesh M4 for cases $A_0 = 0$ (a) and $A_0 = 1.0$, $N_\lambda = 5$ (b) used in the simulations.

**Table 3**
Parameters of the computational meshes. The cell sizes at the wall are given in viscous units.

| Mesh | No. of cells | $y^+_{MIN,MAX}$ | $x^+_{MIN,MAX}$ | $z^+_{MIN,MAX}$ | $AR_w$ |
|---|---|---|---|---|---|
| M1 | $4.0 \times 10^6$ | 1.98/6.61 | 20.68/68.85 | 20.68/68.85 | 5.2 |
| M2 | $7.2 \times 10^6$ | 1.05/3.54 | 10.89/36.88 | 10.89/36.88 | 5.2 |
| M3 | $18.3 \times 10^6$ | 0.52/1.88 | 5.47/19.56 | 5.47/19.56 | 5.2 |
| M4 | $41.1 \times 10^6$ | 0.29/0.92 | 3.07/9.43 | 3.07/9.43 | 5.2 |

**Table 4**
Number of elements along the $x$, $y$ and $z$ directions for all the considered meshes. Please note that the number of elements along the $x$ and $z$ directions on the top boundary is equal for all meshes, due to the refinement approach.

| Mesh | $n_{x,wall}$ | $n_{x,top}$ | $n_y$ | $n_{z,wall}$ | $n_{z,top}$ |
|---|---|---|---|---|---|
| M1 | 523 | 523 | 82 | 96 | 96 |
| M2 | 1046 | 523 | 96 | 192 | 96 |
| M3 | 2092 | 523 | 104 | 384 | 96 |
| M4 | 4184 | 523 | 110 | 768 | 96 |

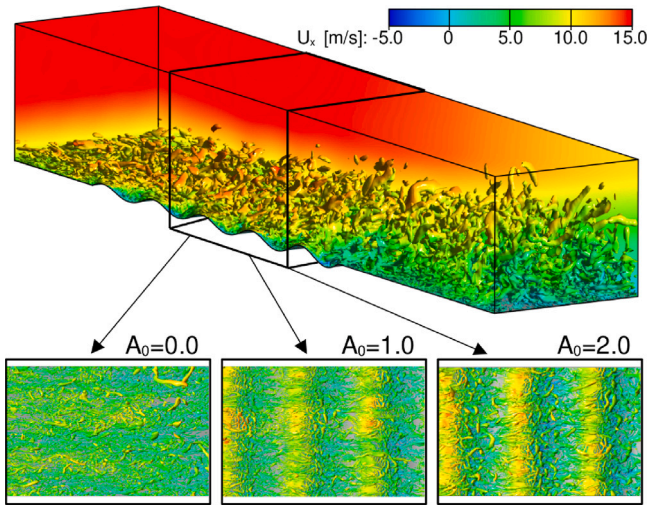



**Fig. 7.** Q-parameter isosurface ($Q = 0.05$ s$^{-2}$) coloured by the streamwise velocity shown on the back side of the computational geometry.

flow. A similar mesh generation procedure was applied in the LES of the NACA4412 airfoil (Vinuesa, 2021).

Table 3 presents the main parameters of all four meshes, including the minimum and maximum cell sizes neighbouring the wall expressed in viscous units ($y^+$, $x^+$, $z^+$). These values were calculated after performing computations on the respective meshes. It is worth noting that the spanwise and streamwise cell sizes ($\Delta z$, $\Delta x$) were the same, ensuring that the aspect ratios of the near-wall cells ($AR_w = \Delta x/\Delta y = \Delta z/\Delta y$) remained the same across all meshes. Table 4 presents the number of elements along the $x$, $y$, and $z$ directions for all considered meshes. Please note that the number of elements along the $x$ and $z$ directions at the top boundary ($n_{x,top}$ and $n_{z,top}$) is identical for all meshes, due to the refinement approach discussed earlier in the paper. In Kamiński et al. (2024), it was shown that the solutions obtained on meshes M3 and M4 were almost identical. However, for the present studies, similarly as in Kamiński et al. (2024), the mesh M4 was selected. On this mesh, the condition $y^+ < 1$, which is regarded as necessary for LES of wall-bounded flows (Pope, 2001), was fulfilled for all near-wall cells. Additionally, according to Pope (2001), to consider LES well resolved, the computational mesh should ensure that the ratio of sub-grid to total TKE, expressed as $k_{sgs}/k_{tot}$ must be below 20%. In the case of mesh M4 this ratio was below 1%. The computations were performed with the time-step $\Delta t = 1.0 \times 10^{-4}$ s that on the mesh M4 led to $CFL \approx 0.8$. Comparisons of the solutions obtained with the $\Delta t = 2.0 \times 10^{-4}$ s did not reveal any significant differences, see also Kamiński et al. (2024).

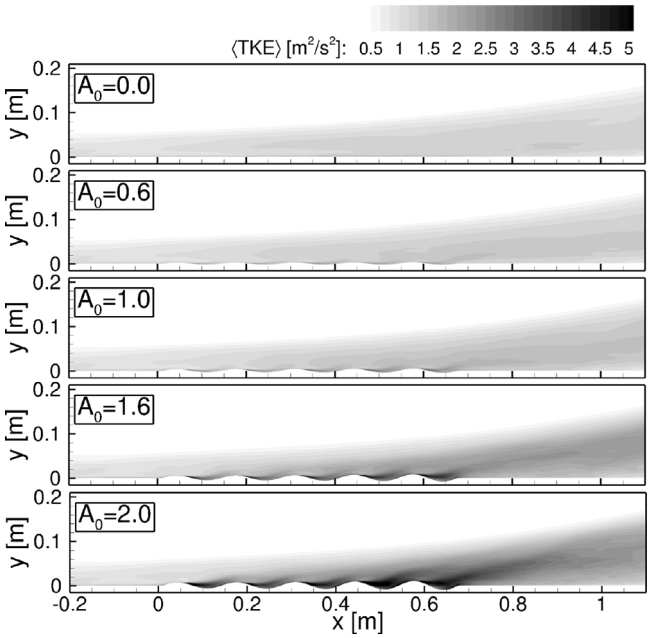



**Fig. 8.** Turbulent kinetic energy maps for $A_0 = var.$ and $N_\lambda = 5$.

## 3. Results

In the following sections, we discuss the results obtained on the densest mesh M4 with $\Delta t = 1.0 \times 10^{-4}$ s. As the complexity of the analysed cases does not differ from those for which the accuracy

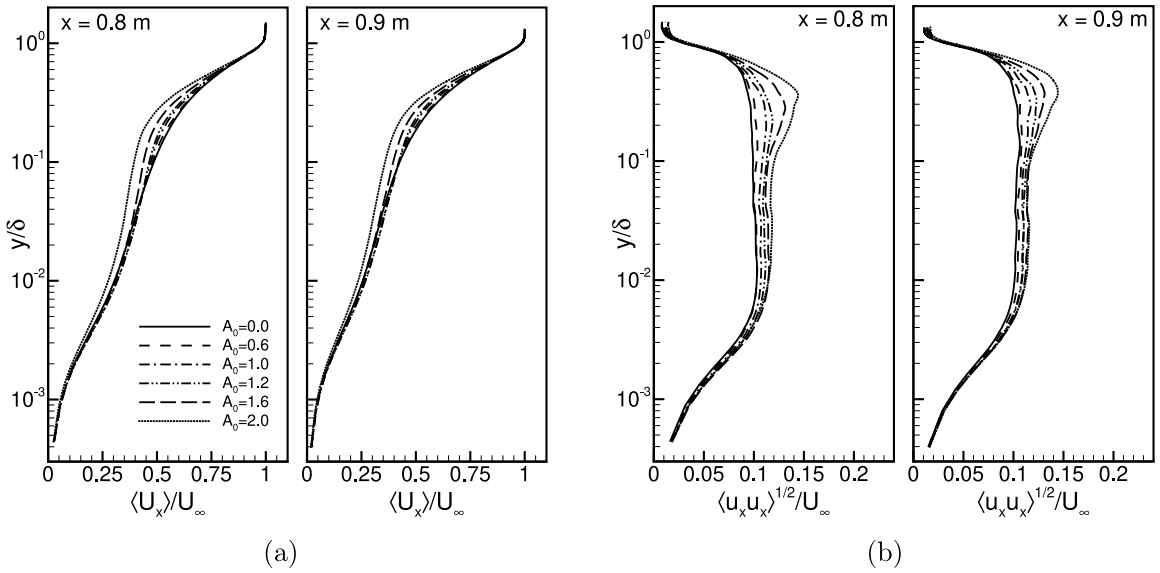



**Fig. 9.** Comparison of the mean streamwise velocity (a) and its fluctuations (b) for variable $A_0$ and a constant $N_\lambda = 5$ at $x = 0.8$ m and $x = 0.9$ m.

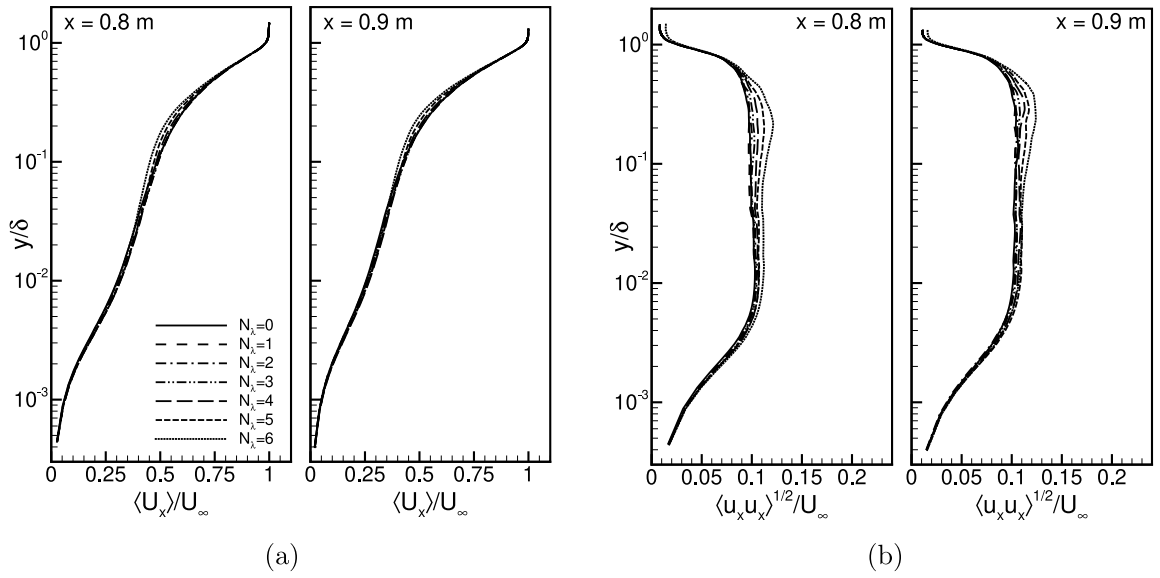



**Fig. 10.** Comparison of the mean streamwise velocity (a) and its fluctuations (b) for variable $N_\lambda$ and a constant $A_0 = 1.0$ at $x = 0.8$ m and $x = 0.9$ m.

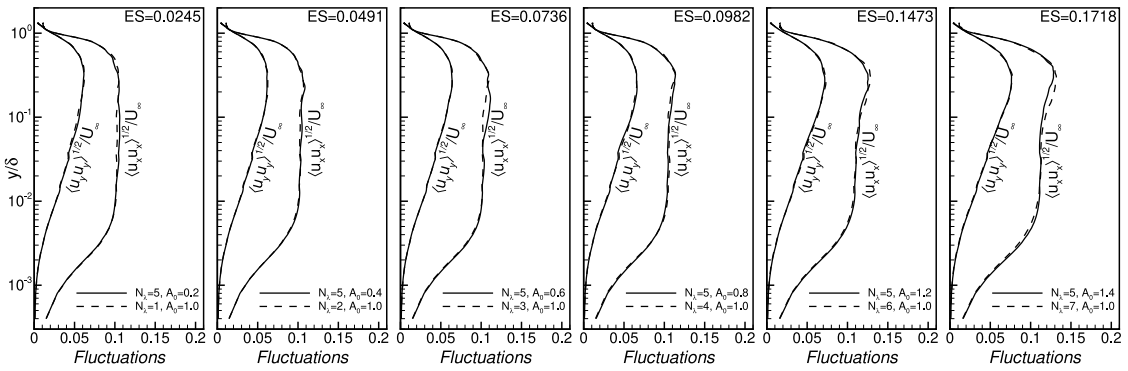



**Fig. 11.** Evolution of $\langle u_x u_x \rangle^{1/2}/U_\infty$ and $\langle u_y u_y \rangle^{1/2}/U_\infty$ profiles for variable $A_0$ and $N_\lambda$ for six different $ES$ values obtained at $x = 0.9$ m.

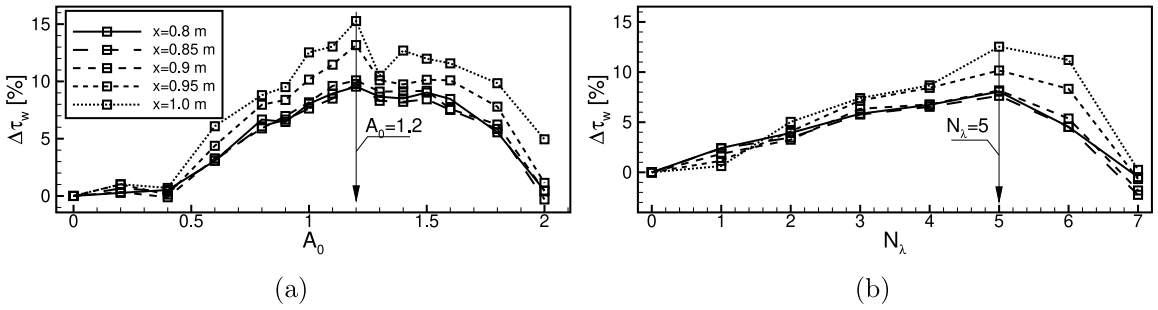



**Fig. 12.** Wall-shear stress increase for variable $A_0$ (a) and $N_\lambda$ (b) at different distances from $x_0$.

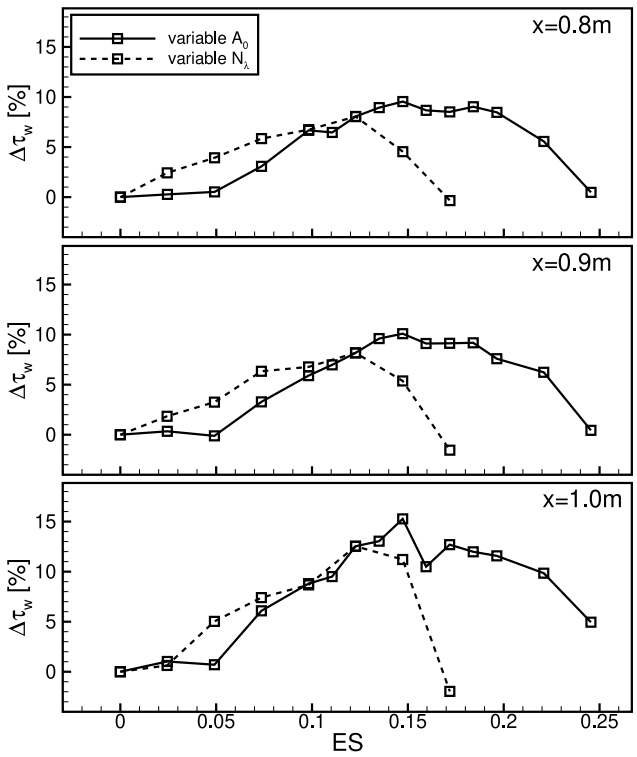



**Fig. 13.** Wall-shear stress increase for variable $A_0$ (a) and $N_\lambda$ (b) at different distances from $x_0$.

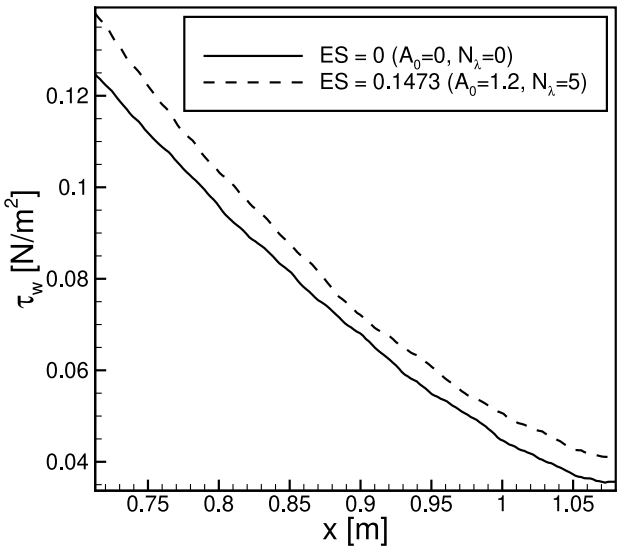



**Fig. 14.** Wall-shear stress distribution for the optimal $ES = 0.1473$ ($N_\lambda = 5$, $A_0 = 1.2$) with respect to the flat wall configuration ($A_0 = 0$).

assessment was carried out the previous work (Kamiński et al., 2024), one can assume that the obtained results are accurate and reliable to a comparable extent.

Fig. 7 shows a sample view of instantaneous values of the $Q$–parameter coloured by the streamwise velocity component for the cases with $A_0 = 0$, $A_0 = 1.0$ and $A_0 = 2.0$. The $Q$–parameter is defined as $Q = 0.5(\Omega_{ij}\Omega_{ij} - S_{ij}S_{ij})$, where $\Omega_{ij}$ and $S_{ij}$ are antisymmetric and symmetric velocity gradient tensors. Positive values of the $Q$–parameter are often used as indicators of coherent vortical structures (Hunt et al., 1988). Here, the $Q$–parameter ($Q = 0.05$ s$^{-2}$) nicely visualises the complexity of the flow and the presence of near-wall structures. In the case with $A_0 = 0$, structures are evidently smaller and more irregular than for $A_0 = 1.0$ and $A_0 = 2.0$. In these configurations, two types of elongated small-scale vortices prevail, namely, parallel to the waviness (spanwise vortices) and longitudinally oriented according to the flow direction (streamwise vortices). The former are stemming just behind the tops of the waviness due to a roll-up process induced by the shear force. The size of the structures clearly increases as a function of $A_0$. The fluid, which accelerates on the waviness tops (see the vortices' colour), interacts with a low-speed flow in the valleys. A close inspection of this region reveals the occurrence of small separation bubbles on the downhill sides of the tops in which the streamwise velocity is negative.

### 3.1. Effect of the corrugated wall on the flow in the vicinity of separation

The introduced surface modification affects the flow just above the corrugation as well as after a transition to the smooth surface. The analysis of the flow characteristics will be then carried out in these two regions. First, the area behind the corrugation will be examined and then attention will be paid to changes in the statistical parameters of the boundary layer above the modified surface.

Fig. 8 presents the contour maps of TKE at the streamwise cross-section in the middle of the domain for five values of $A_0$ and under a constant value of $N_\lambda = 5$. It can be observed that the growth in $A_0$ causes TKE enhancement which is especially visible for cases with $A_0 > 1.0$. For these configurations, a considerable increase in TKE originates from waviness crests. This phenomenon agrees with the observations from the DNS of Yoon et al. (2009). The LES research conducted by Zhang et al. (2022a, 2021a) also showed that increasing the corrugation amplitude leads to the TKE increase in the flow in a similar manner as it is observed in Fig. 8.

Fig. 9 presents the evolution of the mean streamwise velocity and its fluctuations with the changing $A_0$ taken for two traverses $x = 0.8$ m and $x = 0.9$ m. It can be observed that the velocity, normalised by the free-stream velocity, decreases with the amplitude growth for $0.001 < y/\delta < 0.6$. Fig. 9b shows that the velocity fluctuations increase with growing $A_0$ and the location of clearly seen outer maximum moves

further away from the wall which is associated with the large flow scale activity (see for instance Bobke et al. (2017), Niegodajew et al. (2019) for more details).

Fig. 10 presents the comparison of the mean streamwise velocity and its fluctuations for different values of $N_\lambda$ and $A_0 = 1.0$. As $N_\lambda$ increases, the velocity at $0.001 < y/\delta < 0.6$ decreases slightly. When it comes to fluctuations, also an increase is seen with growing $N_\lambda$ which is the most pronounced at the location of the outer maximum. The effect of the corrugation on $\langle U_x \rangle$ and $\langle u_x u_x \rangle^{1/2}$ profiles seems to be the same regardless of whether changing $A_0$ or $N_\lambda$. This may suggest that there is another representative factor involving both already mentioned parameters. An interesting candidate for further exploration seems to be $ES$, frequently used in other works to describe surface irregularities (De Marchis, 2016; Forooghi et al., 2017). Such an analysis is illustrated in Fig. 11 where it is clearly seen that for cases with different $A_0$ and $N_\lambda$ but with the same $ES$, the fluctuation profiles are virtually identical.

One of the main goals of the investigation was to find such a combination of $A_0$ and $N_\lambda$ allowing for the highest increase in $\tau_w$ downstream. In the experiment (Dróżdż et al., 2021a), the waviness which ensured the highest wall-shear increase was found to be characterised by $A_0 = 1.0$ and $N_\lambda = 5$ for $Re_\tau = 4000$. Although in the present study a lower value of $Re_\tau = 2500$ is studied, the above-mentioned values of $A_0$ and $N_\lambda$ were used as reference parameters.

Fig. 12a presents the effect of $A_0$ under constant $N_\lambda = 5$ on the wall-shear stress for several selected streamwise distances, i.e. $x = 0.8$ m, 0.85 m, 0.9 m, 0.95 m, 1.0 m. It can be observed that with the increase in $A_0$, $\Delta\tau_w$ also increases until $A_0 = 1.2$. However, with further growth in $A_0$, $\Delta\tau_w$ starts decreasing. A local minimum is observed at $A_0 = 1.3$ for all of the traverses which, however, becomes less and less visible with decreasing distance from the waviness. It indicates that compared to the case with $A = 0$, the surface waviness with $A_0 = 1.2$ corresponding to $A^+ = 139$ (Table 1), yields the highest enhancement of $\Delta\tau_w$ ranging from 9% up to 15.5%, depending on the traverse ($x$ location). Fig. 12b presents, on the other hand, the effect of $N_\lambda$ when keeping constant $A_0 = 1.0$ on $\tau_w$ for various $x$−distances. It can be observed that the most beneficial effect appears for $N_\lambda = 5$. For $N_\lambda > 5$, the decrease in $\Delta\tau_w$ can be noted.

The results presented so far suggest that $ES$, rather than $A_0$ or $N_\lambda$, is a more effective parameter in determining changes in the near-wall flow. This is supported by the collapse of velocity fluctuation profiles observed for fixed $ES$ and different combinations of $A_0$ or $N_\lambda$ shown in Fig. 11. It is therefore worth checking whether there is a correlation between $ES$ and $\Delta\tau_w$. To verify it, Fig. 13 shows the already presented data (Fig. 12) but this time as a function of $ES$, for three selected traverses, i.e. $x = 0.8$ m, 0.9 m and 1.0 m. The results indicate an increase in $\Delta\tau_w$ up to $ES \approx 0.12$ regardless of whether changing either $A_0$ or $N_\lambda$, despite the fact that the curves representing the two waviness parameters do not perfectly coincide. However, for $ES > 0.12$ $\Delta\tau_w$ starts decreasing when changing $N_\lambda$. This might indicate that as long as the near-wall flow is dominated by viscous drag (waviness regime (Napoli et al., 2008; Schultz and Flack, 2009; Nugroho et al., 2021)), the enhancement of $\tau_w$ may be expected.

As indicated by Dróżdż et al. (2021a), the optimal corrugation for $Re_\tau = 4000$ was $A_0 = 1.0$ and $N_\lambda = 5$ ($ES = 0.1227$). For higher $ES$ values, the beneficial effect quickly disappears. In the present numerical investigation, for $Re_\tau = 2500$, the corrugation which provides the highest increase in wall-shear stress is $A_0 = 1.2$ and $N_\lambda = 5$ ($ES = 0.1473$). The distribution of $\tau_w$ for this case is presented in Fig. 14. An increment in $\tau_w$ caused by the corrugation is kept relatively constant throughout the flat part of the domain downstream of the waviness.

The obtained results reported in De Marchis (2016), Forooghi et al. (2017), indicate that a two-dimensional corrugated surface is effective in preventing turbulent separation although its effectiveness depends on $Re$ and $ES$. In Table 5, it can be observed that $ES$ which provides the highest increase in $\tau_w$ compared to the flat wall configuration

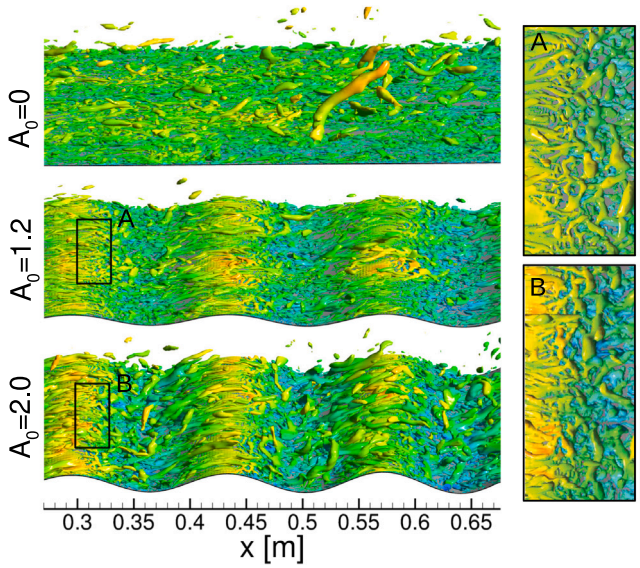



**Fig. 15.** Q–parameter isosurface ($Q = 0.05$ s$^{-2}$) coloured by the instantaneous streamwise velocity for cases $A_0 = 0$, $A_0 = 1.2$, $A_0 = 2.0$ at a constant $N_\lambda = 5$.

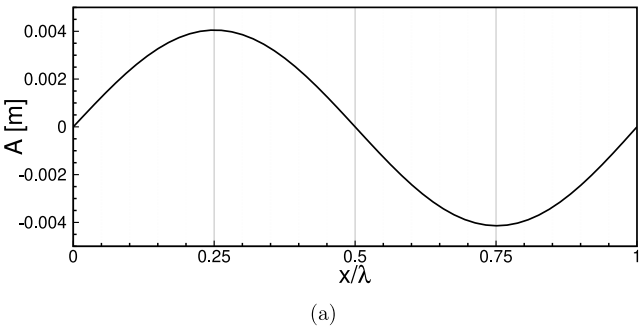



**Fig. 16.** Position of the waveform as a function of $x_{sep}/\lambda$.

decreases with growing $Re_\tau$. The opposite trend is observed with $A^+$, which increases with $Re$. Interestingly, it seems that the corrugations ensuring the highest growth in the wall-shear stress are characterised by amplitudes as high as the size of the near-wall region, namely, the part of TBL up to the logarithmic region, i.e. up to $y^+ = 150$ (Buschmann and Gad-el Hak, 2006). So, $ES$ that maximises the wall-shear stress decreases with $Re$, which is consistent with the observations of Nugroho et al. (2021). Moreover, in the work (Elsner et al., 2022), neither of the corrugations studied for a wide range of $A_0$ ensured an increase in $\tau_w$ for $Re_\tau = 1350$. The above discussion suggests that below a certain value of $Re_\tau$ the wavy wall becomes ineffective in enhancing the wall-shear stress in the presence of a strong APG. This can be explained by referring to the work of Dróżdż et al. (2021a) who showed a diminishing effect of the so-called amplitude modulation on APG TBL (see Mathis et al. (2009) for more details), in particular on the near-wall flow, with decreasing $Re$.

### 3.2. Insight into the flow above the corrugation

The previous Section 3.1 was focused on the effect of the corrugation parameters ($A_0$, $N_\lambda$ and $ES$) on the flow downstream the modified surface, i.e. in the streamwise region from the end of the waviness towards the outlet of the computational domain (from $x = 0.676$ m to $x = 1.1$ m). This section summarises how these parameters affect the flow and most importantly the wall-shear stress on the waviness location (from $x = 0.01$ m to $x = 0.676$ m). The analysis is focused on

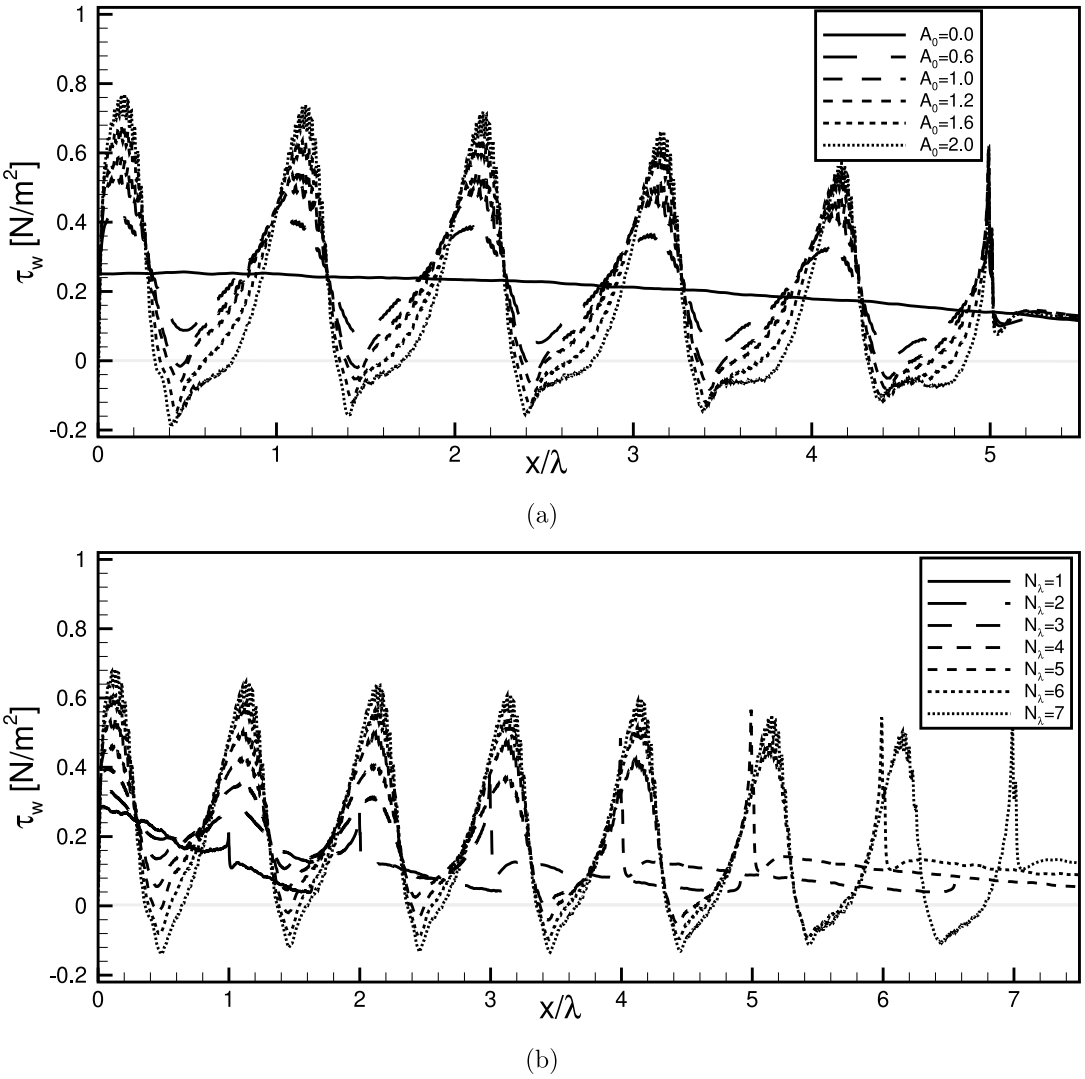



**Fig. 17.** Distribution of the $x$−component of wall-shear stress on the wavy wall for variable $A_0$ at constant $\lambda = 0.133$ m (a) and variable $N_\lambda$ at constant $A_0 = 1.0$ (b). The $x$-axis is the streamwise coordinate normalised by the length of the corrugation period $\lambda$ (Tables 1, 2.). Grey line indicates $\tau_w = 0$.

**Table 5**
Parameters of wavy wall ensuring the highest growth in $\tau_w$ for previous databases and the present study.

| *Source* | *Type* | $U_\infty$ [m/s] | $Re_\tau$ | $ES$ | $A^+$ |
|---|---|---|---|---|---|
| Elsner et al. (2022) | Experiment/LES | 6 | 1350 | —— | —— |
| Present study (2023) | LES | 15 | 2500 | 0.1473 | 139 |
| Dróżdż et al. (2018) | Experiment | 20 | 3300 | 0.1242 | 151 |
| Dróżdż et al. (2021a) | Experiment | 24 | 4000 | 0.1227 | 170 |

the point of the separation within subsequent corrugation periods. No less interesting is also the separation bubble length inside each trough as well as how $A_0$ and $N_\lambda$ contribute to detachment point locations.

Fig. 15 shows the zoom of the $Q$−parameter isosurface for three selected cases, ranging from $x = 0.27$ m to $x = 0.676$ m. For the flat plate ($A_0 = 0$), small ordered vortices with fragments of hairpin-type structures can be identified at $x \approx 0.3$ m. Further downstream, as APG becomes stronger, the near-wall turbulent activity decreases and larger structures appear in the outer region of the boundary layer. For cases with $A_0 > 0$, a lot of longitudinal structures appear on the uphill side of the crest, which is consistent with observation from De Angelis et al. (1997). While on the downhill side of the crest, spanwise vortices are generated (see insets A and B) through the Kelvin–Helmholtz instability mechanism. This process begins at the point of local flow separation (discussed later in the paper) and is accompanied by the formation of a separated shear layer (SSL). As suggested by Zhang et al. (2022b), SSL is believed to enhance the spanwise vorticity, thereby contributing to the generation of spanwise vortices. Further downstream, for $A_0 = 1.2$ and $A_0 = 2.0$, an increase in the size of structures in the outer region of the boundary layer can also be seen. A close inspection of this region reveals the occurrence of small separation bubbles on the downhill sides of the waviness in which the streamwise velocity is negative. The activity of the spanwise vortices is strong downhill (local APG effect) which is consistent with previous observations (Yoon et al., 2009; Zhang et al., 2021b, 2022a). The stronger activity of the spanwise vortices in APG prevents the flow separation (for moderate $ES$) as the sweep events generated by these spanwise vortices are stronger which is the result of a stronger convection velocity (Dróżdż et al., 2023). The second type of vortices exists on the uphill side, where the local favourable pressure gradient (FPG) occurs. These are the quasi-streamwise type structures, similar to ones that can be observed for

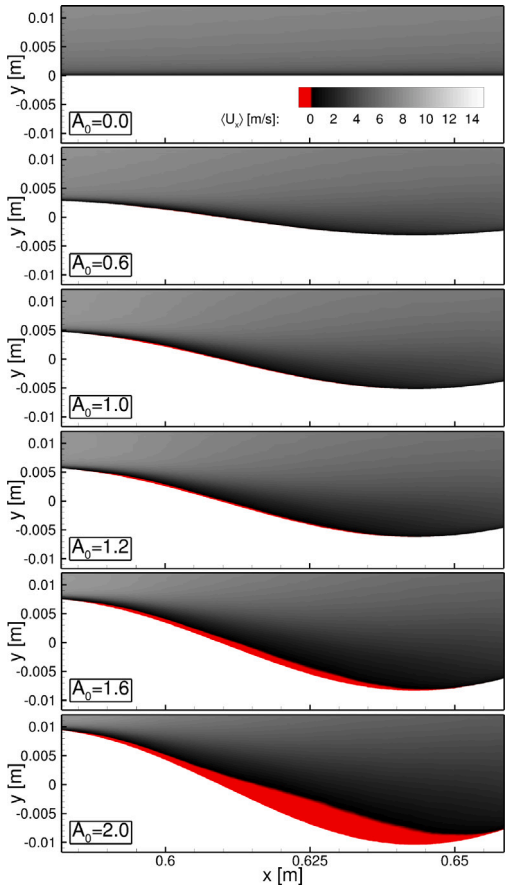



**Fig. 18.** Contour maps of $\langle U_x \rangle$ at the last trough of the corrugation for the chosen $A_0$ cases at a constant $N_\lambda = 5$. The values of $\langle U_x \rangle < 0$ m/s, indicating the separation bubble, are marked with red colour.

canonical TBLs (Schlatter et al., 2014; Schoppa and Hussain, 2002) at high Reynolds number, which are generated downstream the reattachment point (documented later) in the local FPG region generated by waviness. Furthermore, as observed by De Angelis et al. (1997), when $A/\lambda$ increases, the reattachment point moves towards the crest ahead and so, the region occupied by the quasi-streamwise vortices becomes reduced.

For convenience, let us introduce the non-dimensional parameter $x/\lambda$ that is used further to explore the results above the waviness. The graphical interpretation of this parameter is presented in Fig. 16.

Fig. 17 presents the distribution of the $x-$component of the wall-shear stress along the corrugated surface for different amplitudes (a) and different numbers of periods (b). The streamwise distance $x$ is normalised by the length of the waviness period $x/\lambda$. The bold line indicates the distribution of $\tau_w$ for the reference case $A_0 = 0$ (flat plate) while the grey horizontal line indicates $\tau_w = 0$. The streamwise decrease in $\tau_w$ for the flat plate case is due to the presence of APG. When corrugation emerges, even for small values of $A_0$ and $N_\lambda$ and thus for low $ES$, a streamwise oscillation of the wall-shear stress is seen. The maximal values of $\tau_w$ are just before the waviness crests, while the minimal shear is noted just before troughs. An increase either in $A_0$ or $N_\lambda$ leads to a strong reaction of the flow manifested by enhanced variability of $\tau_w$. In Fig. 17a, for $A_0 > 1.0$, the separation is seen in all troughs (manifested by $\tau_w < 0$). The separation is less likely to occur when changing $N_\lambda$ (Fig. 17b), which may be attributed to the fact that the analysed $ES$ range is smaller than in Fig. 17a (see Tables 1 and 2). In general, an increase in the amplitude of the wall-shear stress oscillation with increasing $A_0$ might indicate that the higher the amplitude of the waviness the stronger the local FPG and local APG.

The presence of the local APG causes the flow detachment to occur within the corrugation when $A_0$ and $N_\lambda$ are large enough. It can be assumed that the presence of local separation in waviness troughs has a significant effect on the change in $\tau_w$ downstream of the corrugation. To study this effect, the contour maps of the $x-$component of velocity for selected $A_0$ within the last (fifth) trough are presented in Fig. 18. For convenience of analysis, the area of separation has been highlighted in red.

Fig. 19 presents the location of the point of separation $x_{sep}/\lambda$ (a) and the separation bubble length $L_{sep}/\lambda$ (b) within each subsequent wave. To have a better view of the localisation where the separation occurs within a waviness, please refer to Fig. 16. It can be observed (in Fig. 19) that, apart from $A_0 = 2.0$ case, the point of separation within each consecutive corrugation period moves upstream (towards the crest) with each subsequent wave. This is manifested by decreasing values of $x_{sep}/\lambda$ approaching $x/\lambda = 0.25$ (Fig. 16) i.e., the corrugation peak. The same effect occurs with growth of $A_0$ and $N_\lambda$. This generally means that the separation within subsequent waves occurs earlier because the amplitude of the wavy wall increases downstream. As the detachment occurs earlier, the point of reattachment moves downstream causing the growth of the size of the separation bubble. This is even better illustrated in Fig. 19b, where one can note that when $A_0$ and $N_\lambda$ increase, the separation bubble increases as well. This effect is evidently seen for the higher values of $A_0$. The separation did not occur for amplitudes lower than $A_0 = 0.8$, so the results for $A_0 < 0.8$ are not shown here.

Fig. 20 presents the location of the point of separation (a) and the separation bubble length (b) within subsequent waves. It can be observed that the point of flow detachment moves downstream within subsequent periods (decreasing values of $x_{sep}/\lambda$, similarly as with increasing $A_0$ in Fig. 19) and the separation bubble grows up. It is worth noting, that the flow separation appears when $N_\lambda \geq 5$, while for $N_\lambda < 5$ the flow field is free of that effect. Interestingly, although the case $N_\lambda = 4$ and $A_0 = 1.0$ (Table 2) has the same effective slope $ES = 0.0982$ and amplitude to period ratio $A/\lambda = 0.0204$ as the case $A_0 = 0.8$ and $N_\lambda = 5$ (Table 1) the former one does not lead to separation in any trough. In the latter case, the separation is seen in 4th and 5th trough (see Fig. 19). This may suggest that neither $ES$ nor $A/\lambda$ can serve as a representative indicator on whether the separation will or will not occur in corrugation troughs.

Fig. 21 presents $L_{sep}/\lambda = f(ES)$ (a) and $\Delta\tau_w = f(L_{sep}/\lambda)$ (b) for cases with variable $A_0$ at constant $N_\lambda = 5$ (solid line) and cases with variable $N_\lambda$ at constant $A_0 = 1.0$ (dashed line and grey symbols). It can be observed that for cases with identical $ES$ (outlined with red colour), the separation bubble length is comparable but the wall-shear stress enhancement at $x = 1.0$ m (downstream of corrugation at the flat plate) differs significantly (see Fig. 13), especially for $ES \geq 0.1719$. On the other hand, cases with identical or comparable $L_{sep}/\lambda$ exhibit very similar levels of $\Delta\tau_w$ (see Fig. 21b). This is especially true for $L_{sep}/\lambda \leq 0.35$. The results characterised by $L_{sep}/\lambda = 0.2$ and $L_{sep}/\lambda \approx 0.35$ exhibit a very similar $\Delta\tau_w = 12.7\%$ and $\Delta\tau_w \approx 11\%$ respectively. On the other hand, there are two cases with $L_{sep}/\lambda \approx 0.44$ (and identical $ES = 0.1719$) giving either marginal ($\Delta\tau_w = 0.25\%$) or huge ($\Delta\tau_w = 12\%$) growth in wall-shear stress. This might suggest that the separation bubble length $L_{sep}/\lambda$ is not a representative parameter that would potentially provide the information about $\Delta\tau_w$ change downstream the wavy wall.

To sum up, it seems that $ES$ is not the only parameter determining an enhancement of the wall-shear stress due to the wavy wall. Bearing in mind that the amplitude modulation effect becomes enhanced with growing $Re$ (Dróżdż et al., 2021b), one may expect that also more high-speed zones will emerge, and the separation point will move downstream. The results already discussed indicate that the wavy wall crests act in a similar manner as growing $Re$ in APG, namely, high-speed zones are generated above crests causing an enhanced production of small-scale spanwise vortices and the convection velocity of such

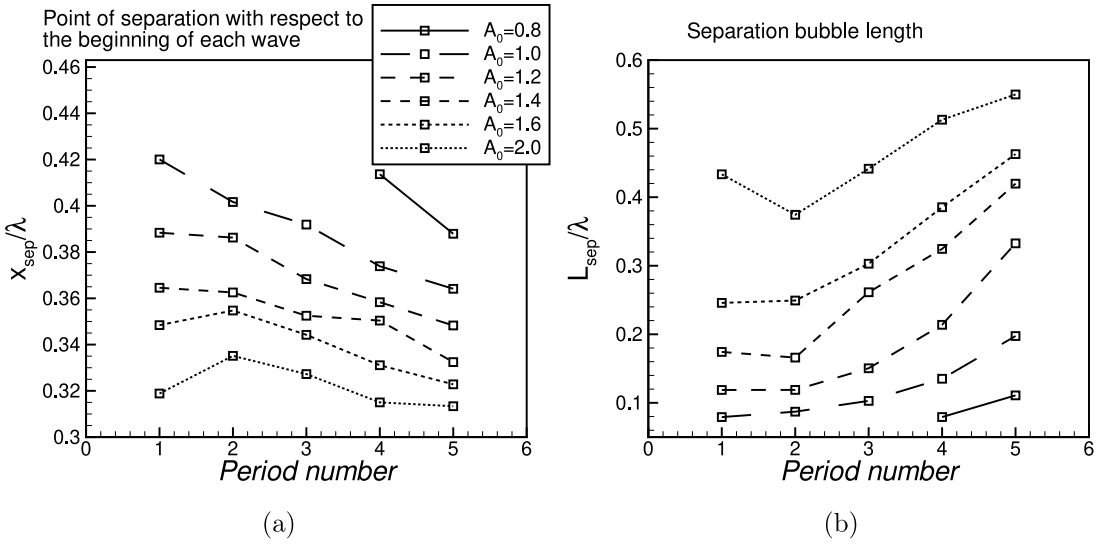



**Fig. 19.** The location of the point of separation (a) and the separation bubble length (b) within each wave for variable $A_0$ cases at constant $N_\lambda = 5$.

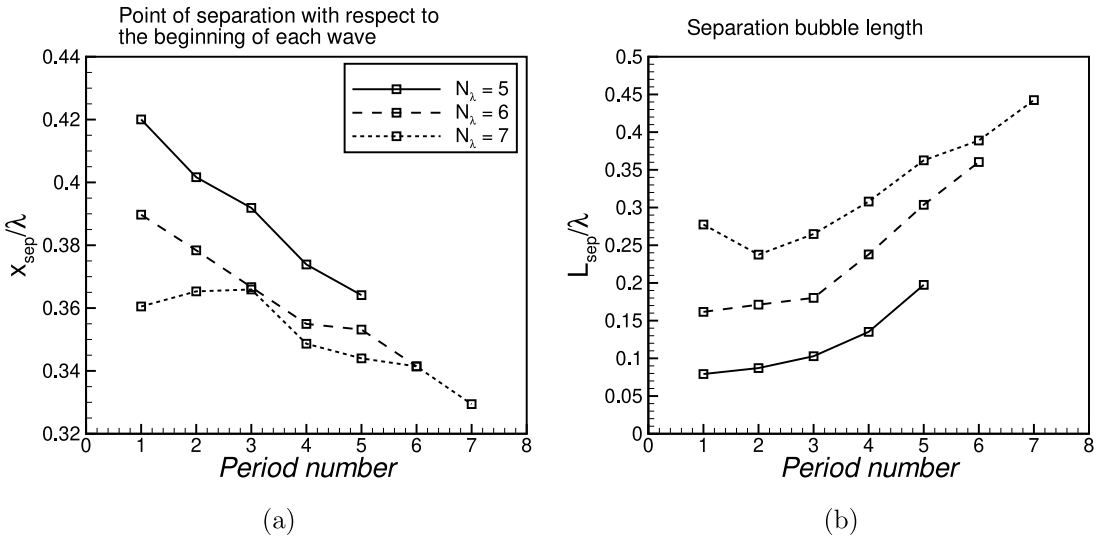



**Fig. 20.** The location of the point of separation (a) and the separation bubble length (b) within each wave for variable $N_\lambda$ cases at constant $A_0 = 1.0$.

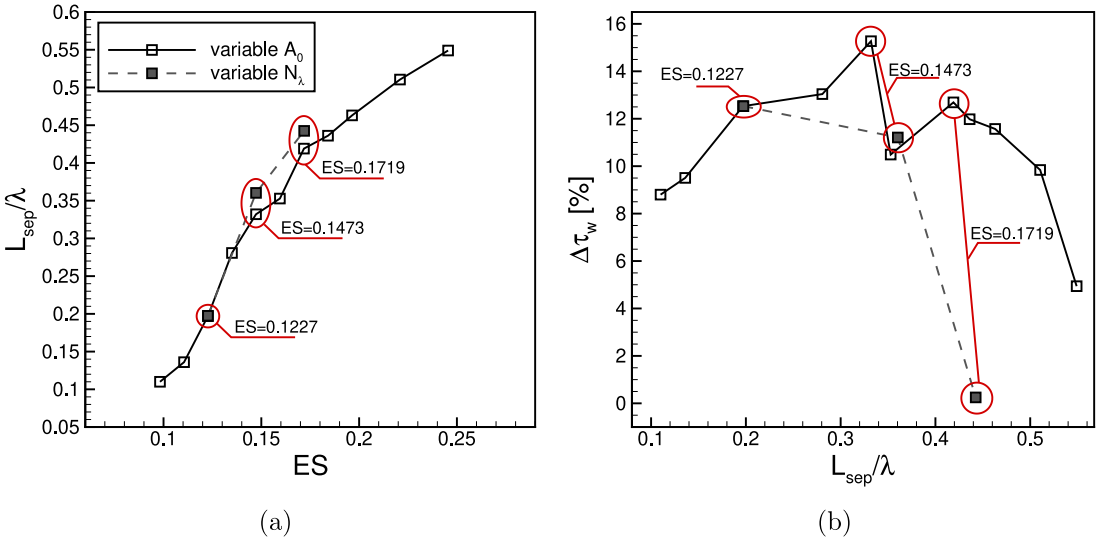



**Fig. 21.** Separation bubble length as a function of effective slope (a) wall-shear growth at $x = 1.0$ m as a function of separation bubble length (b).

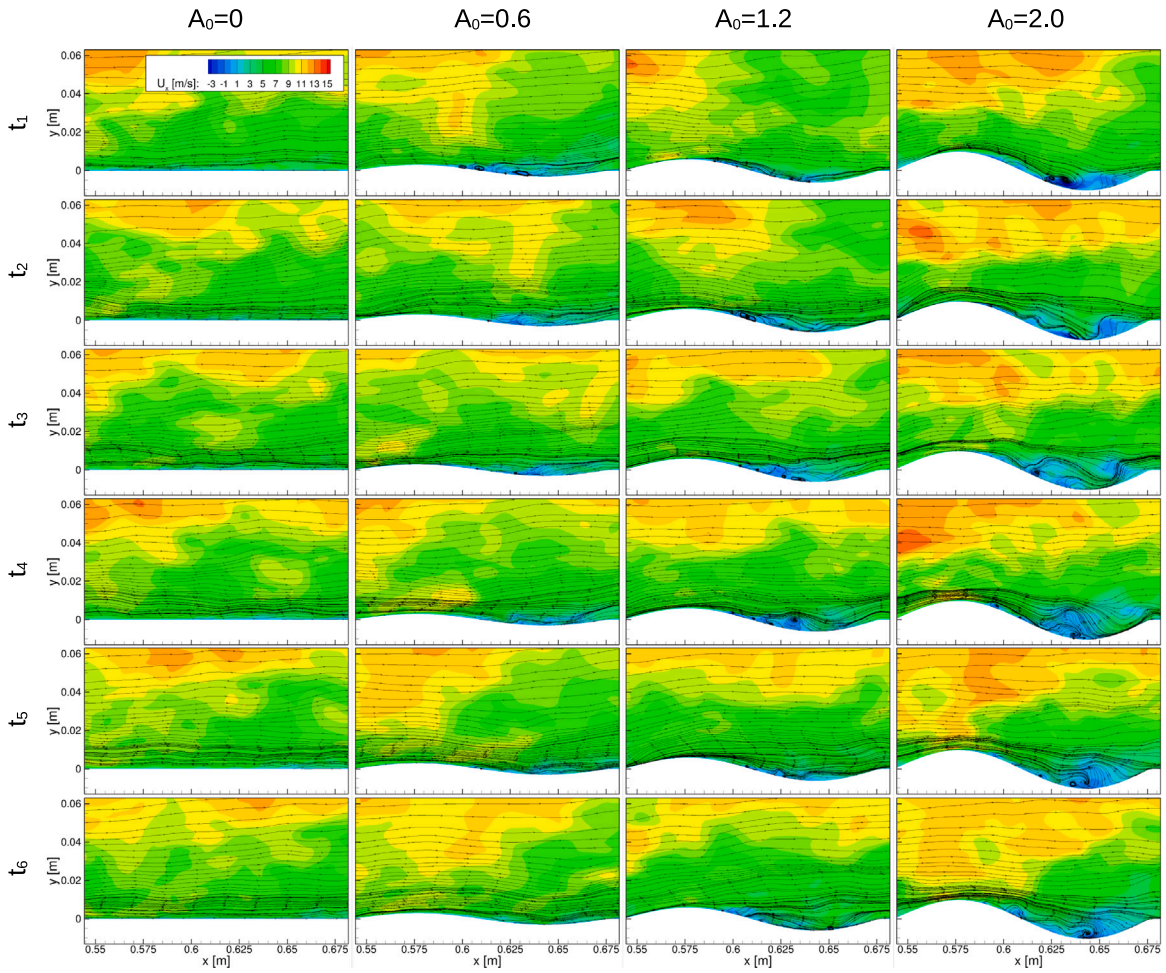



**Fig. 22.** Instantaneous $U_x$ maps with streamlines for four $A_0$ at constant $N_\lambda = 5$ and six time-instants $t_1 - t_6$. Interval between each time-instant is equal to $\Delta t = 0.004$ s.

structures decelerates slower than the mean flow on the downhill side of each crest. Since the convection of the spanwise small-scale vortices is higher, it generates strong sweeping motion in the troughs which, in result, enhances $\tau_w$ on the uphill side of the next crests. To obtain a greater production of the small-scale turbulence in high-speed zones and so, the higher wall-shear stress, one needs a large enough period of the corrugation. As suggested in Dróżdż et al. (2021a), the length of such a period should be of the order of the boundary layer thickness. From the so-far analysis of the separation bubble length change in troughs, one can conclude that the optimal geometry of the wavy wall (that ensures the highest growth in $\tau_w$) is that for which the flow is maintained in such a way that the detachment in the troughs does not exceed $L_{sep}/\lambda \approx 0.3$. This observation is consistent with the work of Nugroho et al. (2021), who stated that for condition where $\lambda \approx \delta$, $ES$ is sufficiently low such that flow separations were minimised. This may suggest that the condition is desirable to obtain also the highest increase in the convection velocity of spanwise small-scale vortices with respect to the mean flow. On the other hand, this condition may be specific for a given $Re$ and APG. As shown in Table 5, $ES$ that ensures the highest growth in $\tau_w$ decreases with the Reynolds number.

In Fig. 22, the solutions at four different instants are plotted to provide an even more detailed insight into the effect of the corrugations on the near-wall region. A zoom of the domain showing a single period (fifth/last period) is presented. Although there are some clear changes over time in the external flow, the analysis is focused on the near wall region. The dark blue colour and streamlines, superimposed to the contour plot, indicate regions with negative velocities that are in particular seen for larger amplitudes ($A_0 > 1.2$) within the waviness troughs and so, identifying in turn separation and reattachment zones. The recirculation region becomes larger with growing $A_0$ and for the largest amplitude ($A_0 = 2.0$) it occupies the streamwise distance wider than $\lambda/2$. This effect is not seen for the lower amplitudes. Worth noting is that the size of the separation bubble changes in time, which can be observed for instance for $A_0 = 1.2$, as it is relatively small at $t_1$ and becomes larger in time. Also, for $A_0 = 1.2$ at $t_2 - t_4$ a strong sweeping motion, which prevents the downstream separation, can be seen just before the trough minimum. This is generated by the spanwise structures visible in Fig. 15. Not less interesting is that if statistically-converged flow field of the case $A_0 = 0.6$ is analysed, no TBL detachment is observed (see Figs. 18 and 19). However, when looking at the instantaneous flow field (Fig. 22), zones with negative velocities emerge ($A_0 = 0.6$). For large enough $A_0$, regions with a substantially enhanced velocity (for $y > 0.03$ m) are seen, especially at $x = 0.575$ m, which are generated by the strong local FPG caused by the presence of waviness. This effect is especially visible for $A_0 = 2.0$ so for the largest amplitude of corrugation.

## 4. Conclusions

This study investigates (using LES) the effect of different geometries of transverse wall corrugation, in particular, the effect of such parameters as $A_0$ and $N_\lambda$ on the change in the wall-shear stress and the flow field under APG conditions. The key objective was to determine such a combination of $A_0$ and $N_\lambda$ leading to the highest possible enhancement of $\tau_w$ with respect to the configuration with the flat plate that should ensure the maximum postponement of TBL separation. LES simulations

have been conducted for $U_\infty = 15$ m/s which corresponds to relatively high $Re_\tau = 2500$.

The highest growth in the wall-shear with respect to the flow at the flat plate was found for $A_0 = 1.2$ and $N_\lambda = 5$ which corresponds to $ES = 0.1473$. For that case, the length of a waviness period is nearly of the order of the boundary layer thickness. An increase in $\Delta\tau_w$ is generally seen when $ES$ grows up to 0.15 (so, within the so-called waviness regime of the surface corrugation). When $ES$ exceeds 0.15 (so, when transitional waviness/roughness regime begins), $\Delta\tau_w$ starts decreasing.

The present and previous studies showed that $ES$ ensuring the highest growth in $\Delta\tau_w$ seems to decrease asymptotically to a certain value with increasing Reynolds number while $A^+$ increases with Reynolds number. This may suggest that the corrugation amplitude should be of the order of the size of the near-wall region ($y^+ \approx 150$) that would be observed for the same flow case without corrugation, i.e. on the flat plate.

A detailed insight into the flow field over the transverse surface waviness region has led to the following conclusions. The transverse surface waviness has a significant impact on the near-wall velocity gradient and consequently on the wall-shear stress, both, along the wavy wall and, what is more important, in the region further downstream. This is accompanied by the enhancement in TKE with the growth in either $A$ or $N_\lambda$. This change in TKE can be better described using $ES$ rather than $A$ or $N_\lambda$. Namely, the cases which are significantly diversified by $A$ and $N_\lambda$ but with identical $ES$ exhibit almost identical TKE profiles.

Local FPG and APG regions along the corrugation generate oscillations of $\tau_w$. Consequently, for large enough $A_0$ or $N_\lambda$, the separation inside the waviness trough is likely to occur. This effect is particularly evident for $A_0 > 0.8$ and $N_\lambda > 5$, and it seems not to be correlated with $ES$. Moreover, as $A_0$ and $N_\lambda$ increase, the point of separation within each period of a waviness moves upstream and thus, the separation bubble length grows.

The presence of the waviness crests affects the flow similarly as large-scale motions at high-$Re$ TBL through the amplitude modulation mechanism (Mathis et al., 2009). Generation of high-speed zones by the crests causes the enhanced production of small-scale spanwise vortices with convection velocity decreasing slower than the mean flow on the downhill side of the crest. As a result, a stronger sweeping motion in the troughs is expected, which is responsible for the enhancement of $\tau_w$.

The presence of the waviness triggers the production of the longitudinal structures. It happens when the flow approaches each crest of the corrugation. Just downstream each crest, the detachment starts to occur and the longitudinal vortices break down and become transformed into spanwise structures, reminiscent of a hairpin. This effect is more pronounced for greater values of $A$ and it may be attributed to the postponement of the separation downstream of the waviness.

Although the results obtained in the present and previous works provide a general picture of the $\tau_w$ enhancement process through the wavy wall for a wide range of $Re_\tau$ (Table 5), more results for even higher values of $Re_\tau$ as well as for different pressure gradient histories are of interest and so are recommended for future work.

## CRediT authorship contribution statement

**Piotr Kamiński:** Writing – review & editing, Writing – original draft, Visualization, Validation, Software, Methodology, Investigation, Formal analysis, Data curation, Conceptualization. **Witold Elsner:** Writing – review & editing, Supervision, Resources, Project administration, Funding acquisition, Conceptualization. **Artur Tyliszczak:** Writing – review & editing, Supervision, Methodology. **Paweł Niegodajew:** Writing – review & editing, Writing – original draft, Visualization, Validation, Supervision, Methodology, Investigation, Formal analysis, Conceptualization.

## Declaration of competing interest

The authors declare that they have no known competing financial interests or personal relationships that could have appeared to influence the work reported in this paper.

## Acknowledgements

The investigation was supported by the National Science Centre under grant UMO-2020/39/B/ST8/01449 and statutory funds of the Czestochowa University of Technology BS/PB 1-100-3011/2024/P. We gratefully acknowledge Poland's high-performance infrastructure PLGrid ACK Cyfronet AGH and PCSS for providing computer facilities and support within computational grants no PLG/2023/016731 and PL0356-01.

## Data availability

Data will be made available on request.

## References

Adamian, D.Y., Strelets, M.K., Travin, A.K., 2011. An efficient method of synthetic turbulence generation at LES inflow in zonal RANS–LES approaches to computation of turbulent flows. Mat. Model. 23 (7), 3–19.
Aider, J.-L., Beaudoin, J.-F., Wesfreid, J.E., 2010. Drag and lift reduction of a 3D bluff-body using active vortex generators. Exp. Fluids 48, 771–789.
Akselsen, A.H., Ellingsen, S.Å., 2020. Langmuir-type vortices in wall-bounded flows driven by a criss-cross wavy wall topography. J. Fluid Mech. 900, A19.
Andreolli, A., Gatti, D., Vinuesa, R., Örlü, R., Schlatter, P., 2023. Separating large-scale superposition and modulation in turbulent channels. J. Fluid Mech. 958, A37.
Anon, 2021. Ansys Fluent Theory Guide. ANSYS Inc.
Aoki, K., Muto, K., Okanaga, H., 2012. Mechanism of drag reduction by dimple structures on a sphere. J. Fluid Sci. Technol. 7 (1), 1–10.
Apsley, D., Leschziner, M., 2000. Advanced turbulence modelling of separated flow in a diffuser. Flow, Turbul. Combust. 63, 81–112.
Ashill, P., Fulker, J., Hackett, K., 2005. A review of recent developments in flow control. Aeronaut. J. 109 (1095), 205–232.
Aubertine, C.D., Eaton, J.K., Song, S., 2004. Parameters controlling roughness effects in a separating boundary layer. Int. J. Heat Fluid Flow 25 (3), 444–450.
Awada, A., Younes, R., Ilinca, A., 2022. Optimization of wind turbine performance by vibration control and deicing. J. Wind Eng. Ind. Aerodyn. 229, 105143.
Azad, R.S., 1996. Turbulent flow in a conical diffuser: A review. Exp. Therm. Fluid Sci. 13 (4), 318–337.
Bearman, P.W., Harvey, J.K., 1976. Golf ball aerodynamics. Aeronaut. Q. 27 (2), 112–122.
Belamadi, R., Djemili, A., Ilinca, A., Mdouki, R., 2016. Aerodynamic performance analysis of slotted airfoils for application to wind turbine blades. J. Wind Eng. Ind. Aerodyn. 151, 79–99.
Beyhaghi, S., Amano, R.S., 2018. A parametric study on leading-edge slots used on wind turbine airfoils at various angles of attack. J. Wind Eng. Ind. Aerodyn. 175, 43–52.
Bobke, A., Vinuesa, R., Örlü, R., Schlatter, P., 2017. History effects and near equilibrium in adverse-pressure-gradient turbulent boundary layers. J. Fluid Mech. 820, 667–692.
Bons, J., 2005. A critical assessment of Reynolds analogy for turbine flows. ASME J. Heat Mass Transf. 127 (5), 472–485.
Bons, J.P., McClain, S.T., 2003. The effect of real turbine roughness with pressure gradient on heat transfer. In: Turbo Expo: Power for Land, Sea, and Air, vol. 36886, pp. 611–622.
Bottasso, C.L., Croce, A., Gualdoni, F., Montinari, P., 2016. Load mitigation for wind turbines by a passive aeroelastic device. J. Wind Eng. Ind. Aerodyn. 148, 57–69.
Buschmann, M.H., Gad-el Hak, M., 2006. Recent developments in scaling of wall-bounded flows. Prog. Aerosp. Sci. 42 (5–6), 419–467.
Casalino, D., Avallone, F., Gonzalez-Martino, I., Ragni, D., 2019. Aeroacoustic study of a wavy stator leading edge in a realistic fan/OGV stage. J. Sound Vib. 442, 138–154.
Chen, H., Rao, F., Shang, X., Zhang, D., Hagiwara, I., 2013. Biomimetic drag reduction study on herringbone riblets of bird feather. J. Bionic Eng. 10 (3), 341–349.
Cherukat, P., Na, Y., Hanratty, T., McLaughlin, J., 1998. Direct numerical simulation of a fully developed turbulent flow over a wavy wall. Theor. Comput. Fluid Dyn. 11 (2), 109–134.
Choi, J., Jeon, W.-P., Choi, H., 2006. Mechanism of drag reduction by dimples on a sphere. Phys. Fluids 18 (4).
Clauser, F.H., 1956. The turbulent boundary layer. Adv. Appl. Mech. 4, 1–51.

Coder, J.G., Somers, D.M., 2020. Design of a slotted, natural-laminar-flow airfoil for commercial transport applications. Aerosp. Sci. Technol. 106, 106217.
De Angelis, V., Lombardi, P., Banerjee, S., 1997. Direct numerical simulation of turbulent flow over a wavy wall. Phys. Fluids 9 (8), 2429–2442.
De Marchis, M., 2016. Large eddy simulations of roughened channel flows: Estimation of the energy losses using the slope of the roughness. Comput. & Fluids 140, 148–157.
Dogan, E., Örlü, R., Gatti, D., Vinuesa, R., Schlatter, P., 2019. Quantification of amplitude modulation in wall-bounded turbulence. Fluid Dyn. Res. 51 (1), 011408.
Dou, Z., Wang, J., Chen, D., 2012. Bionic research on fish scales for drag reduction. J. Bionic Eng. 9 (4), 457–464.
Dróżdż, A., Elsner, W., Sikorski, D., 2018. Passive skin friction control near turbulent separation–preliminary results. J. Phys.: Conf. Ser. 1101 (1), 012004.
Dróżdż, A., Niegodajew, P., Romańczyk, M., Elsner, W., 2021b. Effect of Reynolds number on turbulent boundary layer approaching separation. Exp. Therm. Fluid Sci. 125, 110377.
Dróżdż, A., Niegodajew, P., Romańczyk, M., Elsner, W., 2023. Convection velocity in turbulent boundary layers under adverse pressure gradient. Exp. Therm. Fluid Sci. 110900.
Dróżdż, A., Niegodajew, P., Romańczyk, M., Sokolenko, V., Elsner, W., 2021a. Effective use of the streamwise waviness in the control of turbulent separation. Exp. Therm. Fluid Sci. 121, 110291.
Elsner, W., Dróżdż, A., Szymanek, E., Tyliszczak, A., Niegodajew, P., 2022. Experimental and numerical studies of turbulent flows over two-dimensional and three-dimensional rough surfaces under an adverse pressure gradient. Appl. Math. Model. 106, 549–566.
Fernex, D., Semaan, R., Albers, M., Meysonnat, P.S., Schröder, W., Noack, B.R., 2020. Actuation response model from sparse data for wall turbulence drag reduction. Phys. Rev. Fluids 5 (7), 073901.
Forooghi, P., Stroh, A., Magagnato, F., Jakirlić, S., Frohnapfel, B., 2017. Toward a universal roughness correlation. J. Fluids Eng. 139 (12).
Fujii, H., Sakurai, K., Nakano, T., Hagiwara, Y., 2011. Turbulence structure, friction drag and pressure drag due to turbulent flow over angled wavy surfaces. In: Seventh International Symposium on Turbulence and Shear Flow Phenomena. Begel House Inc.
Gattere, F., Chiarini, A., Quadrio, M., 2022. Dimples for skin-friction drag reduction: status and perspectives. Fluids 7 (7), 240.
Georgiadis, N.J., Rizzetta, D.P., Fureby, C., 2010. Large-eddy simulation: current capabilities, recommended practices, and future research. AIAA J. 48 (8), 1772–1784.
Geurts, B.J., Rouhi, A., Piomelli, U., 2019. Recent progress on reliability assessment of large-eddy simulation. J. Fluids Struct. 91, 102615.
Ghebali, S., Chernyshenko, S.I., Leschziner, M.A., 2017. Can large-scale oblique undulations on a solid wall reduce the turbulent drag? Phys. Fluids 29 (10).
Goyal, R., Gandhi, B.K., Cervantes, M.J., 2017. Experimental study of mitigation of a spiral vortex breakdown at high Reynolds number under an adverse pressure gradient. Phys. Fluids 29 (10).
Guerrero, J.E., Maestro, D., Bottaro, A., 2012. Biomimetic spiroid winglets for lift and drag control. C. R. Mec. 340 (1–2), 67–80.
Guerrero, J.E., Sanguineti, M., Wittkowski, K., 2020. Variable cant angle winglets for improvement of aircraft flight performance. Meccanica 55, 1917–1947.
Gad-el Hak, M., Bushnell, D.M., 1991. Separation control.
Hamed, A.M., Castillo, L., Chamorro, L.P., 2017. Turbulent boundary layer response to large-scale wavy topographies. Phys. Fluids 29 (6), 065113.
Hamed, A.M., Kamdar, A., Castillo, L., Chamorro, L.P., 2015. Turbulent boundary layer over 2D and 3D large-scale wavy walls. Phys. Fluids 27 (10), 106601.
Harwigsson, I., Hellsten, M., 1996. Environmentally acceptable drag-reducing surfactants for district heating and cooling. J. Am. Oil Chem.' Soc. 73 (7), 921–928.
Hunt, J.C., Wray, A.A., Moin, P., 1988. Eddies, streams, and convergence zones in turbulent flows. In: Studying Turbulence Using Numerical Simulation Databases, 2. Proceedings of the 1988 Summer Program.
Jahanmiri, M., 2010. Active Flow Control: A Review. Citeseer.
Joshi, S.N., Gujarathi, Y.S., 2016. A review on active and passive flow control techniques. Int. J. Recent. Technol. Mech. Electr. Eng. 3 (4), 1–6.
Kamiński, P., Niegodajew, P., Dróżdż, A., Sokolenko, V., Tyliszczak, A., Elsner, W., 2024. Numerical analysis of novel wavy wall based control of turbulent boundary layer separation. Aerosp. Sci. Technol. 109167.
Karimi, S., Mohammadikalakoo, B., Schito, P., 2021. Performance enhancement of single dielectric barrier discharge flow control actuators by means of rear linking tunnels on a reference bluff body using CFD. J. Wind Eng. Ind. Aerodyn. 209, 104488.
Kitsios, V., Sekimoto, A., Atkinson, C., Sillero, J.A., Borrell, G., Gungor, A.G., Jiménez, J., Soria, J., 2017. Direct numerical simulation of a self-similar adverse pressure gradient turbulent boundary layer at the verge of separation. J. Fluid Mech. 829, 392–419.
Koike, M., Nagayoshi, T., Hamamoto, N., 2004. Research on aerodynamic drag reduction by vortex generators. Mitsubishi Mot. Tech. Rev. 16, 11–16.
Koyama, S., Takashima, K., Hagiwara, Y., 2007. Turbulence modification in flow around a periodically deforming film. J. Turbul. (8), N19.
Kruse, N., Von Rohr, P.R., 2006. Structure of turbulent heat flux in a flow over a heated wavy wall. Int. J. Heat Mass Transf. 49 (19–20), 3514–3529.
Kuhn, S., Kenjereš, S., von Rohr, P.R., 2010. Large eddy simulations of wall heat transfer and coherent structures in mixed convection over a wavy wall. Int. J. Therm. Sci. 49 (7), 1209–1226.
La Roche, U., La Roche, H.L., 2004. Induced drag reduction using multiple winglets, looking beyond the Prandtl-Munk linear model. In: 2nd AIAA Flow Control Conference. p. 2120.
Lang, A.W., Jones, E.M., Afroz, F., 2017. Separation control over a grooved surface inspired by dolphin skin. Bioinspiration Biomimetics 12 (2), 026005.
Lee, T., Gerontakos, P., 2004. Investigation of flow over an oscillating airfoil. J. Fluid Mech. 512, 313–341.
Leknys, R., Arjomandi, M., Kelso, R., Birzer, C., 2018. Thin airfoil load control during post-stall and large pitch angles using leading-edge trips. J. Wind Eng. Ind. Aerodyn. 179, 80–91.
Leschziner, M.A., 2020. Friction-drag reduction by transverse wall motion–a review. J. Mech. 36 (5), 649–663.
Lissaman, P., 1983. Low-Reynolds-number airfoils. Annu. Rev. Fluid Mech. 15 (1), 223–239.
Lo, K.H., Kontis, K., 2016. Flow characteristics over a tractor-trailer model with and without vane-type vortex generator installed. J. Wind Eng. Ind. Aerodyn. 159, 110–122.
Lorenz, R.D., 2006. Spinning Flight: Dynamics of Frisbees, Boomerangs, Samaras, and Skipping Stones. Springer.
Manolesos, M., Voutsinas, S.G., 2015. Experimental investigation of the flow past passive vortex generators on an airfoil experiencing three-dimensional separation. J. Wind Eng. Ind. Aerodyn. 142, 130–148.
Mathis, R., Monty, J.P., Hutchins, N., Marusic, I., 2009. Comparison of large-scale amplitude modulation in turbulent boundary layers, pipes, and channel flows. Phys. Fluids 21 (11), 111703.
McMasters, J.H., Henderson, M.L., 1979. Low-speed single-element airfoil synthesis. NASA. Langley Res. Center The Sci. and Technol. of Low Speed and Motorless Flight, Pt. 1.
Mejia-Alvarez, R., Christensen, K.T., 2013. Wall-parallel stereo particle-image velocimetry measurements in the roughness sublayer of turbulent flow overlying highly irregular roughness. Phys. Fluids 25 (11).
Moghaddam, T., Neishabouri, N.B., 2017. On the active and passive flow separation control techniques over airfoils. In: IOP Conference Series: Materials Science and Engineering, vol. 248, IOP Publishing, 012009.
Moshfeghi, M., Shams, S., Hur, N., 2017. Aerodynamic performance enhancement analysis of horizontal axis wind turbines using a passive flow control method via split blade. J. Wind Eng. Ind. Aerodyn. 167, 148–159.
Mostafa, W., Abdelsamie, A., Sedrak, M., Thévenin, D., Mohamed, M.H., 2022. Quantitative impact of a micro-cylinder as a passive flow control on a horizontal axis wind turbine performance. Energy 244, 122654.
Mueller, T.J., DeLaurier, J.D., 2003. Aerodynamics of small vehicles. Annu. Rev. Fluid Mech. 35 (1), 89–111.
Nagano, Y., Tagawa, M., Tsuji, T., 1993. Effects of adverse pressure gradients on mean flows and turbulence statistics in a boundary layer. In: Turbulent Shear Flows 8: Selected Papers from the Eighth International Symposium on Turbulent Shear Flows, Munich, Germany, September 9–11, 1991. Springer, pp. 7–21.
Napoli, E., Armenio, V., De Marchis, M., 2008. The effect of the slope of irregularly distributed roughness elements on turbulent wall-bounded flows. J. Fluid Mech. 613, 385–394.
Nicoud, F., Ducros, F., 1999. Subgrid-scale stress modelling based on the square of the velocity gradient tensor. Flow, Turbul. Combust. 62 (3), 183–200.
Niegodajew, P., Dróżdż, A., Elsner, W., 2019. A new approach for estimation of the skin friction in turbulent boundary layer under the adverse pressure gradient conditions. Int. J. Heat Fluid Flow 79, 108456.
Nugroho, B., Monty, J.P., Utama, I.K.A.P., Ganapathisubramani, B., Hutchins, N., 2021. Non-$k$-type behaviour of roughness when in-plane wavelength approaches the boundary layer thickness. J. Fluid Mech. 911, A1.
Oehme, F., Gleichauf, D., Suhr, J., Balaresque, N., Sorg, M., Fischer, A., 2022. Thermographic detection of turbulent flow separation on rotor blades of wind turbines in operation. J. Wind Eng. Ind. Aerodyn. 226, 105025.
Peterson, C.J., Vukasinovic, B., Glezer, A., 2019. Control of a closed separation domain in adverse pressure gradient over a curved surface. In: AIAA Scitech 2019 Forum. p. 1900.
Piquee, J., García-Risco, A., López, I., Breitsamter, C., Wüchner, R., Bletzinger, K.-U., 2022. Numerical investigations of a membrane morphing wind turbine blade under gust conditions. J. Wind Eng. Ind. Aerodyn. 224, 104921.
Pope, S.B., 2001. Turbulent flows. Meas. Sci. Technol. 12 (11), 2020–2021.
Quadrio, M., 2011. Drag reduction in turbulent boundary layers by in-plane wall motion. Philos. Trans. R. Soc. A: Math. Phys. Eng. Sci. 369 (1940), 1428–1442.
Salehi, S., Raisee, M., Cervantes, M., 2017. Computation of developing turbulent flow through a straight asymmetric diffuser with moderate adverse pressure gradient. J. Appl. Fluid Mech. 10 (4), 1029–1043.
Schlatter, P., Li, Q., Örlü, R., Hussain, F., Henningson, D., 2014. On the near-wall vortical structures at moderate Reynolds numbers. Eur. J. Mech. B Fluids 48, 75–93.

Schlieter, A., Pflumm, R., Shakhverdova, I., Naraparaju, R., Schulz, U., Leyens, C., Schütze, M., Reimers, W., 2016. Mechanical properties of shark-skin like structured surfaces for high-temperature applications. Adv. Eng. Mater. 18 (5), 688–702.
Schmidt, T.G., Redonnet, S., 2024. Exploring a bio-inspired passive flow control strategy for wind turbines: Experimental characterization of the aerodynamics of a wind turbine blade section possibly equipped with leading-edge tubercles. J. Wind Eng. Ind. Aerodyn. 250, 105768.
Schoppa, W., Hussain, F., 2002. Coherent structure generation in near-wall turbulence. J. Fluid Mech. 453, 57–108.
Schultz, M.P., Flack, K.A., 2009. Turbulent boundary layers on a systematically varied rough wall. Phys. Fluids 21 (1).
Segunda, V.M., Ormiston, S.J., Tachie, M.F., 2018. Experimental and numerical investigation of developing turbulent flow over a wavy wall in a horizontal channel. Eur. J. Mech. B Fluids 68, 128–143.
Seshagiri, A., Cooper, E., Traub, L.W., 2009. Effects of vortex generators on an airfoil at low Reynolds numbers. J. Aircr. 46 (1), 116–122.
Shur, M.L., Spalart, P.R., Strelets, M.K., Travin, A.K., 2014. Synthetic turbulence generators for RANS-LES interfaces in zonal simulations of aerodynamic and aeroacoustic problems. Flow, Turbul. Combust. 93, 63–92.
Smith, M., Komerath, N., Ames, R., Wong, O., Pearson, J., 2001. Performance analysis of a wing with multiple winglets. In: 19th AIAA Applied Aerodynamics Conference. p. 2407.
Sun, Z., Zhu, Y., Hu, Y., Zhang, S., 2018. Direct numerical simulation of a fully developed compressible wall turbulence over a wavy wall. J. Turbul. 19 (1), 72–105.
Tanarro, Á., Vinuesa, R., Schlatter, P., 2020. Effect of adverse pressure gradients on turbulent wing boundary layers. J. Fluid Mech. 883, A8.
Tay, C., 2011. Determining the effect of dimples on drag in a turbulent channel flow. In: 49th AIAA Aerospace Sciences Meeting Including the New Horizons Forum and Aerospace Exposition. p. 682.
Tay, C., Khoo, B., Chew, Y., 2015. Mechanics of drag reduction by shallow dimples in channel flow. Phys. Fluids 27 (3).
Tay, J., Lim, T.T., 2018. Drag reduction with teardrop-shaped dimples. In: 2018 Flow Control Conference. p. 3528.
Tay, J., Lim, T.T., Khoo, B.C., 2019. Drag reduction with diamond-shaped dimples. In: AIAA Aviation 2019 Forum. p. 3296.
Tayebi, A., Torabi, F., 2024. Flow control techniques to improve the aerodynamic performance of darrieus vertical axis wind turbines: A critical review. J. Wind Eng. Ind. Aerodyn. 252, 105820.
Teruna, C., Rego, L., Casalino, D., Ragni, D., Avallone, F., 2022. A numerical study on aircraft noise mitigation using porous stator concepts. Aerospace 9 (2), 70.
Tyson, C., Sandham, N., 2013. Numerical simulation of fully-developed compressible flows over wavy surfaces. Int. J. Heat Fluid Flow 41, 2–15.
Veldhuis, L., Vervoort, E., 2009. Drag effect of a dented surface in a turbulent flow. In: 27th AIAA Applied Aerodynamics Conference. p. 3950.
Vernet, J.A., Örlü, R., Alfredsson, P.H., 2015. Separation control by means of plasma actuation on a half cylinder approached by a turbulent boundary layer. J. Wind Eng. Ind. Aerodyn. 145, 318–326.
Vernet, J.A., Örlü, R., Alfredsson, P.H., 2018a. Flow separation control behind a cylindrical bump using dielectric-barrier-discharge vortex generator plasma actuators. J. Fluid Mech. 835, 852–879.
Vernet, J.A., Örlü, R., Söderblom, D., Elofsson, P., Alfredsson, P.H., 2018b. Plasma streamwise vortex generators for flow separation control on trucks: a proof-of-concept experiment. Flow, Turbul. Combust. 100, 1101–1109.
Vila, C.S., Vinuesa, R., Discetti, S., Ianiro, A., Schlatter, P., Örlü, R., 2020. Separating adverse-pressure-gradient and Reynolds-number effects in turbulent boundary layers. Phys. Rev. Fluids 5 (6), 064609.
Vinuesa, R., 2021. High-fidelity simulations in complex geometries: Towards better flow understanding and development of turbulence models. Results Eng. 11, 100254.
Wang, Y., Li, G., Shen, S., Huang, D., Zheng, Z., 2018. Influence of an off-surface small structure on the flow control effect on horizontal axis wind turbine at different relative inflow angles. Energy 160, 101–121.
Wang, J.-S., Wu, J., Wang, J.-J., 2023. Wake-triggered secondary vortices over a cylinder/airfoil configuration. Exp. Fluids 64 (1), 6.
Whitman, N., Sparks, R., Ali, S., Ashworth, J., 2006. Experimental investigation of slotted airfoil performance with modified slot configurations. In: 24th AIAA Applied Aerodynamics Conference. p. 3481.
Wu, L., Jiao, Z., Song, Y., Liu, C., Wang, H., Yan, Y., 2018. Experimental investigations on drag-reduction characteristics of bionic surface with water-trapping microstructures of fish scales. Sci. Rep. 8 (1), 12186.
Yadegari, M., Khoshnevis, A.B., 2020. Numerical study of the effects of adverse pressure gradient parameter, turning angle and curvature ratio on turbulent flow in 3D turning curved rectangular diffusers using entropy generation analysis. Eur. Phys. J. Plus 135 (7), 548.
Yoon, H.S., El-Samni, O.A., Chun, H.H., 2006. Drag reduction in turbulent channel flow with periodically arrayed heating and cooling strips. Phys. Fluids 18 (2), 025104.
Yoon, H., El-Samni, O., Huynh, A., Chun, H., Kim, H., Pham, A., Park, I., 2009. Effect of wave amplitude on turbulent flow in a wavy channel by direct numerical simulation. Ocean Eng. 36 (9–10), 697–707.
You, D., Moin, P., 2008. Active control of flow separation over an airfoil using synthetic jets. J. Fluids Struct. 24 (8), 1349–1357.
Zhang, E., Wang, X., Liu, Q., 2021a. Large-eddy simulation of turbulent flow over wavy wall with different wave steepness. In: E3S Web of Conferences, vol. 299, EDP Sciences, p. 03012.
Zhang, E., Wang, X., Liu, Q., 2021b. Effects of the spanwise heterogeneity of a three-dimensional wavy wall on momentum and scalar transport. Phys. Fluids 33 (5), 055116.
Zhang, E., Wang, X., Liu, Q., 2022a. Numerical investigation on the temporal and spatial statistical characteristics of turbulent mass transfer above a two-dimensional wavy wall. Int. J. Heat Mass Transf. 184, 122260.
Zhang, E., Wu, W., Liu, Q., Wang, X., 2022b. Effects of vortex formation and interaction on turbulent mass transfer over a two-dimensional wavy wall. Phys. Rev. Fluids 7 (11), 114607.
Zhiyin, Y., 2015. Large-eddy simulation: Past, present and the future. Chin. J. Aeronaut. 28 (1), 11–24.

Energy 324 (2025) 135758

Contents lists available at ScienceDirect

Energy

journal homepage: www.elsevier.com/locate/energy

# Turbulent separation control with a tilted wavy wall: A promising approach for energy savings in aerodynamic systems

Piotr Kamiński, Artur Tyliszczak, Witold Elsner, Paweł Niegodajew *

*Department of Thermal Machinery, Czestochowa University of Technology, Al. Armii Krajowej 21, 42-200 Czestochowa, Poland*

ARTICLE INFO

*Keywords:*
Turbulent boundary layer
Adverse pressure gradient
Passive flow control
Flow separation
Wall-shear stress

ABSTRACT

Recently, Kamiński et al. (2024) demonstrated that a two-dimensional streamwise waviness with carefully selected amplitude and period can be effectively used in postponement of a flow separation at high Reynolds number which is out of reach for other commonly known passive flow control strategies. This paper demonstrates that this approach can be substantially improved by introducing a novel type of surface waviness characterized by tilting the subsequent waves. The research is performed by applying the Large Eddy Simulation (LES) method allowing for a detailed analysis of both instantaneous and time-averaged flow characteristics. It is shown that the tilting eliminates the occurrence of separation zones in waviness troughs, which minimizes the shape drag and maximizes the wall shear stress. In particular, compared to an optimal classical sinusoidal waviness shape the drag coefficient drops 14%. Simultaneously, 70% better performance in separation control is achieved. Moreover, it is also shown that when this issue is a priority, even further improvement can be achieved, though at the expense of greater drag.

## 1. Introduction

The energy efficiency of aerodynamic systems, such as an airplane wing, strongly depends on its near-wall flow dynamics. When a flow experiences an adverse pressure gradient (APG), which is present on the suction side of an airfoil, the separation of the turbulent boundary layer (TBL) is likely to occur when the streamwise component of the wall-shear stress $\tau_w = \mu(dU/dy)$ (where $\mu$ is the dynamic viscosity and $dU/dy$ is the near-wall velocity gradient) reaches zero locally. Detachment of TBL from a surface is accompanied with a significant increase in total drag, resulting in a substantial energy loss and consequently, increased fuel consumption [1,2]. Other examples where separation can significantly affect energy efficiency include the flow inside a diffuser [3–5], around a wind turbine blade [6–10] or within axial or centrifugal pumps used as turbines [11,12]. Ricco et al. [13], in their review paper, suggested that considerable energy savings, particularly in aerodynamic systems, may be obtained by introducing appropriate flow control methods, which can contribute up to 15% of total drag reduction. Bearing this in mind, the control of separation is critical to minimize energy losses and thus reduce fuel consumption. This scenario has motivated scientists to search for new or to improve already known flow control techniques.

In general, there are two types of flow control approaches: active and passive [14–16]. Active control involves systems, often quite complicated in construction, that require an external energy source [17]. Their complexity ranges from relatively low, as seen with jets [18] and blowing and/or suction [16,19], to high, as with plasma actuators, which have been utilized across a wide range of flow regimes. For instance, they have been employed to control separation in subsonic turbulent flows [20–22] as well as to manage the performance of supersonic inlets [23–25]. In certain instances, the complexity of active methods can become extreme, as with morphing surfaces [26], which require elaborate systems comprising a multitude of components. This, combined with the necessity for external input and high cost, often makes the active methods less appealing from the perspective of energy savings. On the other hand, passive control strategies, which typically involve surface geometry modifications or introducing roughness, do not require external energy input and are generally more cost-effective, which makes them significantly more attractive for practical applications. A number of passive approaches have so far been developed and the following ones are the most commonly employed in practice: dimples [27–32]; vortex generators [33,34], which are employed in various types of systems, i.e., airfoil surfaces, helicopter rotors [35], wind turbine blades [36,37], and car bodies [38]. Also a considerable attention is paid to investigating some more complex control methods, such as modifying the airfoil surface shape by introducing slots [39,40], slats [41,42], Gurney flaps [43,44], or placing microcylinders near a blade leading edge [45–48]. Quite often, nature itself suggests solutions

* Corresponding author.
*E-mail address:* pawel.niegodajew@pcz.pl (P. Niegodajew).

https://doi.org/10.1016/j.energy.2025.135758
Received 9 July 2024; Received in revised form 29 November 2024; Accepted 21 March 2025
Available online 31 March 2025
0360-5442/© 2025 Elsevier Ltd. All rights are reserved, including those for text and data mining, AI training, and similar technologies.

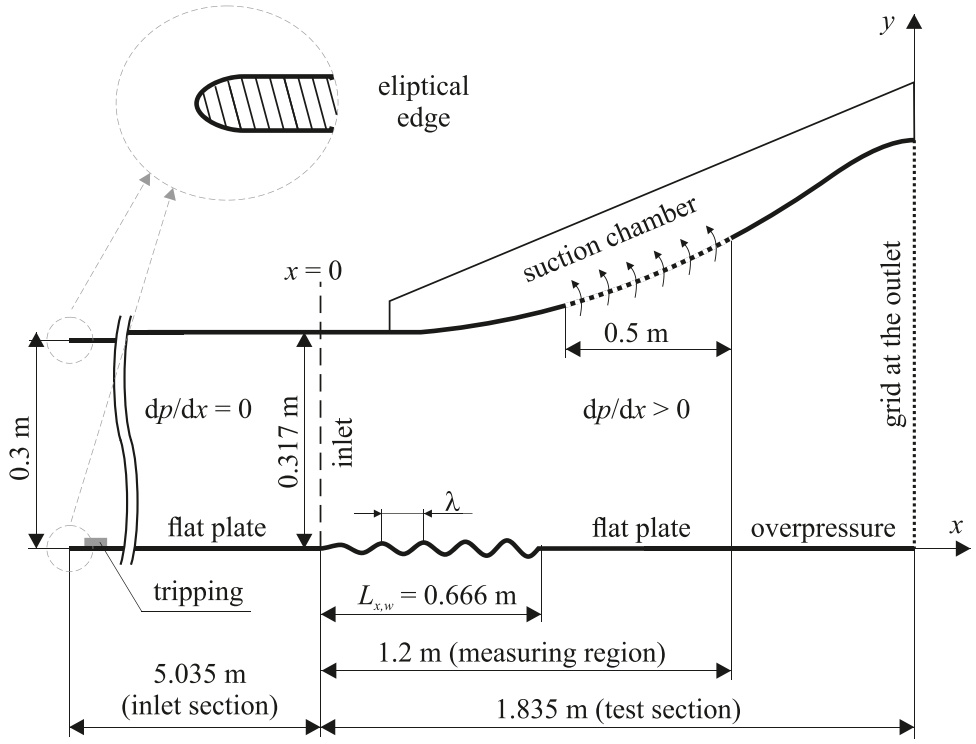



**Fig. 1.** Schematic of the experimental stand from [61].

that are optimal for the given flow scenario and inspires researchers and engineers to employ them in practice. Good examples of such solutions are wingtip devices known as winglets, which are inspired by bird wings [49–54]; riblets [55] or adaptive flaps [56] reflecting the shapes of bird feathers [57,58]; and various types of microstructures borrowed from the skin of aquatic animals [50,59,60].

Furthermore, considerable effort has recently been placed into researching novel flow control techniques or applying these in unconventional scenarios. For instance, employing circular arcs around a cylinder has been shown to significantly reduce aerodynamic drag [62]. In a combined numerical and experimental study, Xia et al. [63] investigated an improved tri-section vortex-induced vibration harvesting device, which was proven to be more efficient than conventional single-section ones. The employment of symmetrical dual outlet energy concentration pipes (ECP), as demonstrated by Wang et al. [64], led to a 12.6% improvement in efficiency compared to conventional ECPs. Aksoy [65] showed that by utilizing an arrangement of triangular vortex generators, reductions in drag of up to 30% can be achieved. Convex domes have been proposed by Zhao et al. [66] as a method to effectively reduce sediment erosion in Francis turbines by at least 50%. The use of unconventional approaches is also extending into heavy agricultural machinery. Specifically, novel rear-flap designs have been used to control separation at the rear edges of tractors, thereby achieving drag reduction [67].

Unfortunately, as suggested in Refs. [68,69], the effectiveness of the outlined passive approaches is limited to flows experiencing laminar or transitional conditions. For high Reynolds numbers, when the flow becomes fully turbulent, employment of, in particular, an artificial roughness is not recommended as it may lead to increased total drag and even to earlier separation [70,71]. In light of these facts, it appears that the use of active methods is the most reasonable choice to prevent TBL separation at high $Re$.

In the experimental study by Dróżdż et al. [72], the authors investigated air flow exposed to APG conditions at a friction Reynolds number of $Re_\tau = u_\tau \delta/\nu = 4000$ (where $u_\tau$ is the friction velocity, $\delta$ is the boundary layer thickness, and $\nu$ is the kinematic viscosity). They demonstrated that precisely adjusting the amplitude $A$ and the period length $\lambda$ of a two-dimensional (2D) streamwise waviness on a wall surface can energize large-scale motions (LSMs), which, in turn, stimulate the small scales dominating the near-wall area. This mechanism, known as amplitude modulation (AM) [73–75], directly contributes to a significant increase in $\tau_w$ downstream of the corrugation, thereby delaying TBL separation. Dróżdż et al. [72] suggested that the amplitude of the waviness should be scaled to the size of the inner layer, meaning $A$ should increase proportionally to the TBL thickness $\delta$ found in the same area for a configuration with a flat wall. Moreover, the corrugation crests should not penetrate the outer region of TBL. In their subsequent work [76], Dróżdż et al. showed that the beneficial effect of waviness is strongly dependent on the Reynolds number. Furthermore, the increase in $\tau_w$, which ensures a delay of turbulent separation, could be achieved in a fully turbulent flow regime (high $Re_\tau$), i.e. in scenarios where passive flow control typically fails. Subsequently, the experimental research of Dróżdż et al. [72,76] were further supplemented with LES. Specifically, Elsner et al. [77] evaluated the performance of waviness at a relatively low $Re_\tau$ of 1300. It was observed that at such a low Reynolds number, no beneficial effect of WW could be achievable, which aligns well with previous observations. Recently, Kamiński et al. [61] performed Large Eddy Simulation (LES) studies of a flow over 2D streamwise wavy wall (WW) under APG and ZPG conditions at the friction Reynolds number equal to $Re_\tau = 2500$. In agreement with the experimental research of Dróżdż et al. [72] it has been proven that by using a WW shape one can increase $\tau_w$ locally, thereby postponing the point of TBL separation. Interestingly, enhancement of $\tau_w$ was reported only under APG conditions. The authors also demonstrated that the benefit of augmented $\tau_w$ comes at the cost of increased total drag in the area occupied by the waviness. Worth noting is that the streamwise waviness has found so far some other applications such as reducing the leading-edge interaction noise of an airfoil [78,79] or enhancing flow mixing, which directly facilitates improved heat transfer process as highlighted in [80,81].

The studies of Kamiński et al. [61] and Dróżdż et al. [72], though demonstrated a large potential of WW in the control of $\tau_w$, were limited

only to a sinusoidal type of the waviness in which the adjustable parameter was the amplitude $A$ of the sine wave. In the present study, we maintain a constant $A/\delta$ ratio as in [61,72] and additionally modify the waviness by introducing streamwise and counter-streamwise tilting to its sinusoidal shape.

The research is performed by applying the LES method. It is shown that by employing a particular type of tilted waviness, one can achieve not only a significant $\tau_w$ enhancement compared to sinusoidal waviness, but also a considerable reduction in the local drag coefficient $C_d = 2F_d/(\rho U_{e,in}^2 S_{ref})$ (where $S_{ref}$ is the reference area, $\rho$, $U_{e,in}$ denote the density and edge velocity taken as 99% of the free-stream velocity, and $F_d$ stands for the drag force computed as the surface integral of pressure and the wall-shear stress). Both of these findings are highly attractive from the perspective of energy efficiency in aerodynamic systems and serve as valuable clues indicating areas for further development of efficient passive separation control.

The manuscript is organized as follows. The description of the experimental configuration constituting the research object adopted for LES is presented in Section 2. Details of the boundary conditions and numerical methods are given in Section 3. The results obtained are presented in Section 5 and include a qualitative description of the flow field followed by comprehensive analysis of the time-averaged solutions aimed at finding the sources of reported performance improvement of the new wall shape. The conclusions and suggestions for future work are provided in Section 6.

## 2. Research object

Fig. 1 shows a schematic of the experimental setup employed by Dróżdż et al. [72] and later investigated by Kamiński et al. [61] using LES. In this setup, the flow develops along a 5035 mm long flat plate, which ensures that before the APG section, i.e. at $x = 0$ (see Fig. 1), TBL is well-formed. The section with the 2D waviness ($y = A\sin(x2\pi N_\lambda/L_{x,w})$, $N_\lambda = 5$ - number of periods) has the total length $L_{x,w}$ of 0.666 m ($\lambda = 0.1332$ m - the waviness period length). The amplitude $A$ changes along the waviness and grows according to the formula $A(x) = 0.00366x^2 + 0.000614x + 0.003351$ m. For $Re_\tau = 4000$ considered in [72], this wall shape ensured a constant $A(x)/\delta(x)$ and led to the maximum increase in $\tau_w$ ($\Delta\tau_w = 32$ % compared to a flat wall). However, as shown in [82] it turned out to be not optimal for $Re_\tau = 2500$ with a larger $\delta(x)$. Parametric studies performed with a scaling factor $A_0$ ($A(x) = A_0 \cdot (0.00366x^2 + 0.000614x + 0.003351)$ m) showed that with $A_0 = 1.2$, a 20% higher $\tau_w$ is obtained compared to the basic wall waviness ($A_0 = 1.0$). In this research, we maintain $A_0 = 1.2$ and demonstrate that significantly higher $\tau_w$ values can be achieved by tilting the waviness. The results suggest that future research for different $Re_\tau$ should treat the wavy wall shape and its amplitude equally important. To obtain a tilted waviness shape, an iterative procedure is proposed according to the following formulas:

$$y_0 = \sin\left(x\frac{2\pi N_\lambda}{L_{x,w}}\right); \quad \text{initial sinusoidal waviness} \tag{1}$$

$$y_i = \sin\left(x\frac{2\pi N_\lambda}{L_{x,w}} + \frac{y_{i-1}}{s}\right) + y_{i-1} \quad i = 1,2,\ldots,I \tag{2}$$

$$y_{final} = A \times \left(\frac{y_I}{\max(|y_I|)}\right); \quad \text{normalization, scaling} \tag{3}$$

where $s$ is the parameter defining the level of tilt and $I$ denotes the number of iterations ($i = 1,2,\ldots,I$). An increase in $I$ causes the waviness to become less smooth. Shapes of the wavy walls considered in this study are shown in Fig. 2 while Table 1 outlines the parameters used in the iterative procedure (1)–(3).

The basic configuration is denoted as W0. The cases WL1-4 and WR1-2 represent tilted WW configurations with counter-streamwise and streamwise tilting of waviness crests, respectively. Please note that the flat channel configuration, marked in Table 1 as case F, is not included in Fig. 2.

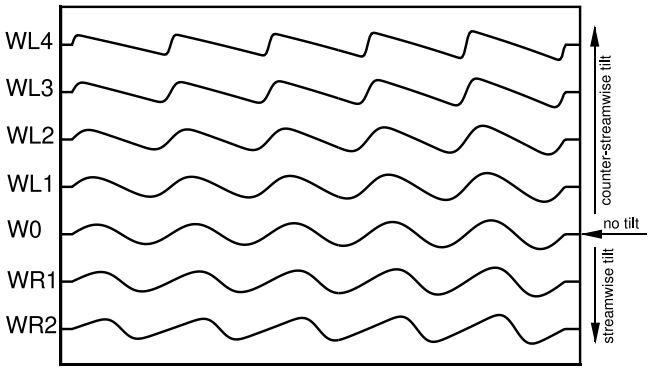



**Fig. 2.** Waviness shapes.

**Table 1**
Parameters of the iterative procedure (1) for WW configurations.

| Case | F | WL4 | WL3 | WL2 | WL1 | W0 | WR1 | WR2 |
|---|---|---|---|---|---|---|---|---|
| $s$ | – | 1 | 1 | 1 | 2 | – | −2 | −1 |
| $I$ | – | 4 | 3 | 2 | 2 | 0 | 2 | 2 |

## 3. Mathematical model and computational domain

### 3.1. LES method

In the present study, we consider an incompressible constant density flow governed by the continuity and Navier–Stokes equations. In the LES method, the flow scales are separated through spatial filtering, dividing them into large scales, which are directly resolved on the numerical mesh, and small subgrid scales, whose influence on the flow field must be modeled [83]. Applying the filtering operation to the continuity and Navier–Stokes equations results in

$$\frac{\partial \overline{u}_i}{\partial x_i} = 0 \tag{4}$$

$$\frac{\partial \overline{u}_i}{\partial t} + \frac{\partial \overline{u}_i\overline{u}_j}{\partial x_j} + \frac{\partial \overline{p}}{\partial x_i} = \frac{\partial}{\partial x_j}\left[\nu\left(\frac{\partial \overline{u}_i}{\partial x_j} + \frac{\partial \overline{u}_j}{\partial x_i}\right)\right] + \frac{\partial \tau_{ij}}{\partial x_j}, \quad i = 1,2,3 \tag{5}$$

where $t$ stands for time, $x_i$ are the spatial coordinates, the bar symbol denotes the LES filter [83], $u_i$ is the velocity component in the $i-$direction, $p$ denotes the pressure, $\nu$ is the kinematic viscosity, and $\tau_{ij} = \overline{u_i}\overline{u_j} - \overline{u_iu_j}$ represents the subgrid stress tensor resulting from the filtering of the non-linear advection term. The subgrid stress involves the product of unknown unfiltered velocity components and must be modeled. In this work, the Wall-Adapting Local Eddy-viscosity (WALE) [84] model is employed for this purpose. It reads as $\tau_{ij} = 2\nu_t\overline{S}_{ij}$, where the symbol $\overline{S}_{ij}$ represents the strain rate tensor of the filtered velocity field and $\nu_t$ is the subgrid viscosity defined as

$$\nu_t = (C_w\Delta)^2\frac{(S_{ij}^dS_{ij}^d)^{3/2}}{(\overline{S}_{ij}\overline{S}_{ij})^{5/2} + (S_{ij}^dS_{ij}^d)^{5/4}} \tag{6}$$

$$S_{ij}^d = \frac{1}{2}(\overline{g}_{ij}^2 + \overline{g}_{ij}^2) - \frac{1}{3}\delta_{ij}\overline{g}_{kk}^2 \tag{7}$$

where $\overline{g}_{ij} = \frac{\partial \overline{u}_i}{\partial x_j}$ are the gradient components of the filtered velocity field, $C_w = 0.325$ is the model constant [84] and $\Delta = V^{1/3}$ is the LES filter width ($V$ - the local cell volume). The WALE model was specifically designed for modeling wall-bounded flows. Using it ensures a proper $\nu_t$ scaling near the near wall vicinity and vanishing of $\nu_t$ in laminar or pure shear regions.

The simulations are performed applying a widely used ANSYS Fluent code [85–90]. The spatial discretization of the Navier–Stokes equations was accomplished with a bounded 2nd order central differencing scheme for the convection terms and the central differencing 2nd

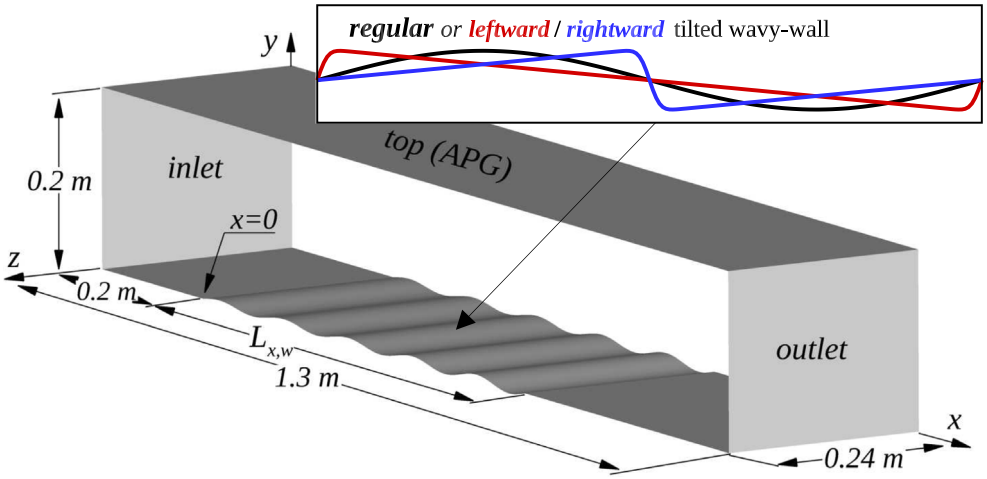



**Fig. 3.** Computational domain.

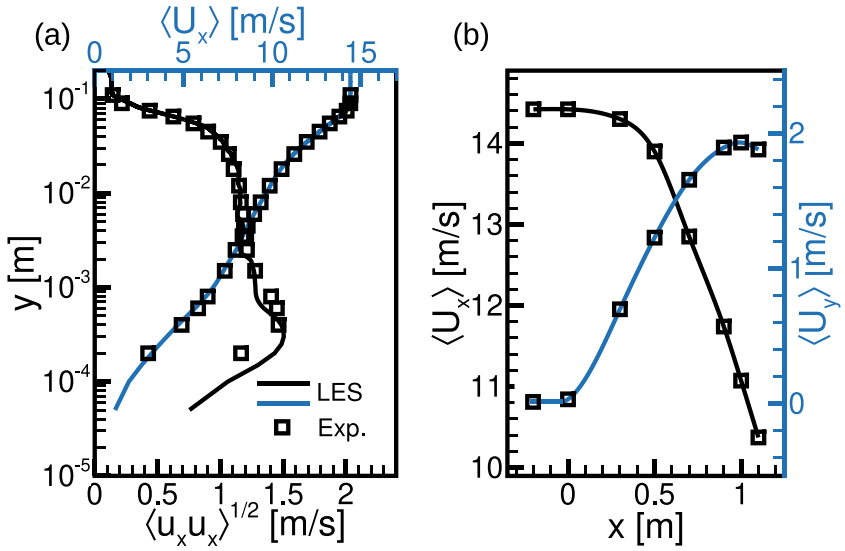



**Fig. 4.** The approximated profiles: for the inlet boundary (a) and for the top boundary (b) generating the APG condition.

order scheme for the discretization of the continuity equation and the pressure gradient and viscous terms in the Navier–Stokes equations. Pressure-velocity coupling is enforced through the SIMPLE algorithm [91] and the time integration is performed by applying the 2nd order implicit method [91,92].

### 3.2. Computational domain and boundary conditions

The computational domain, shown in Fig. 3, is smaller than the geometry of the experimental stand and it represents the measuring region (see Fig. 1) of the length $L = 1.3$ m. Such a simplification is necessary to reduce the computational cost of the simulations. With the present setting, the time required for modeling a single test case on a 96CPUs cluster equals 20 days. It covers an initial transient phase when the flow develops and the time-averaging period lasting over 3.6 s that corresponds to 40 flow-through times defined as $L/U_{x,\infty}$, where $U_{x,\infty} = 14.42$ m/s is the free-stream velocity. In all cases, the computations were carried out with a constant time step of $\Delta t = 1 \times 10^{-4}$ s, resulting in a Courant–Friedrichs–Lewy [93] (CFL) number defined based on the local flow velocity and the computational cell volume in the range $0.78-0.82$ depending on the configuration.

The air flows from the inlet at $x = -0.2$ and leaves through the outlet located at $x = 1.1$ m. Fig. 4a shows the profiles of the mean streamwise velocity and fluctuations obtained through HWA measurements performed on a test stand described in Section 2 and imposed on the inlet. To model the velocity disturbances at the inflow, the Synthetic Turbulence Generator approach was applied. It determines the turbulent length and time scales to generate the time-varying velocity fluctuations based on the turbulent kinetic energy and dissipation rate defined via the User Defined Function. As seen in Fig. 4a, the approach led to inlet conditions prescribed in great agreement with HWA measurements. On the top boundary, the velocity fluctuations were negligibly small and therefore only the mean streamwise $\langle U_x \rangle$ and wall-normal $\langle U_y \rangle$ velocity components were assumed as the boundary conditions (Fig. 4b). The side boundaries, spaced by $z = 0.24$ m, were assumed periodic and the bottom wall was treated as non-slip. At the outlet, the atmospheric pressure (101325 Pa) was assumed.

## 4. Numerical model validation

The validation of the aforementioned solution procedure and the correctness of using simplified geometry are demonstrated in Fig. 5, which presents profiles of velocity and fluctuations obtained from the simulations compared with the hot-wire anemometry (HWA) measurements from [61]. The data are normalized by the boundary layer thickness ($\delta$) and the wavelength of the waviness ($\lambda = 0.1332$ m).

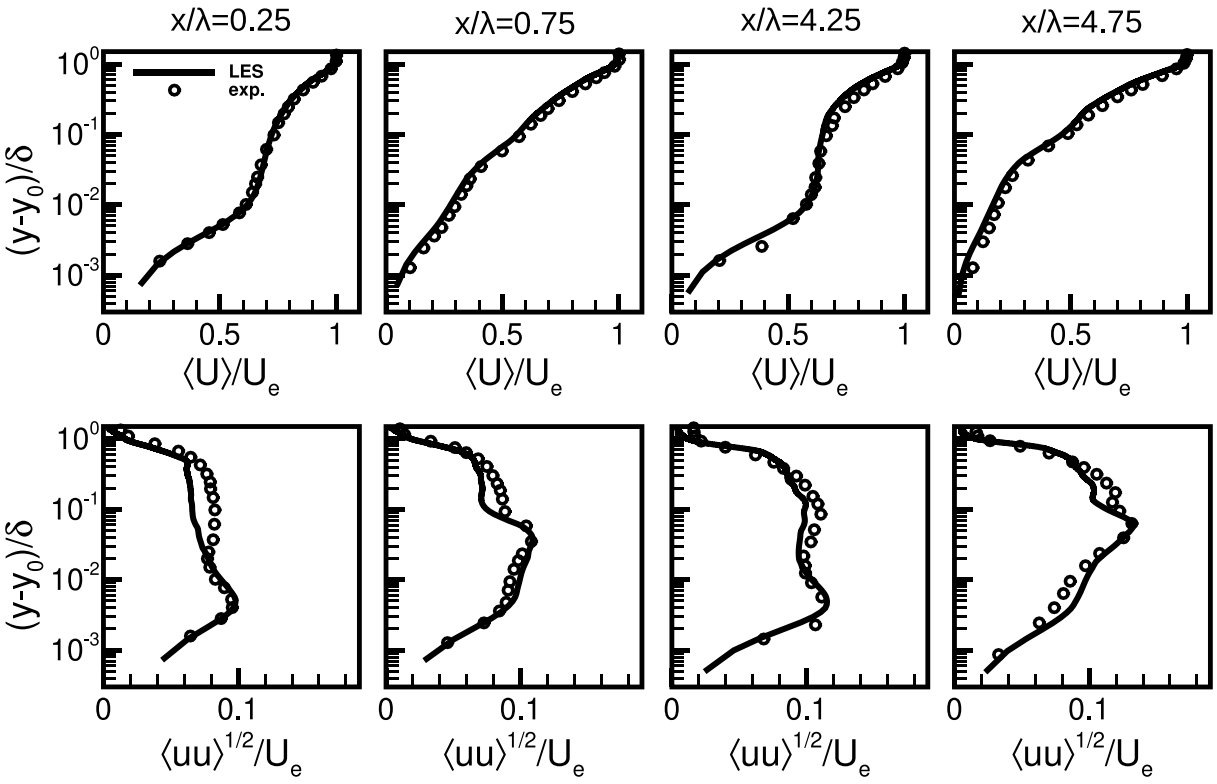



**Fig. 5.** Comparison of simulation results with the experimental data.

The validation is performed for a waviness shape identical to that in [61,72] at four specific locations corresponding to the tip and trough of the first wave ($x/\lambda = 0.25$ and 0.75, respectively) as well as the last (fifth) wave ($x/\lambda = 4.25$ and 4.75, respectively). As shown in Fig. 5, the computational results agree very well with the HWA measurements. Specifically, the velocity profiles (upper row) exhibit shapes nearly identical to those obtained from the experiment. Regarding fluctuations, some minor discrepancies are noted; however, the accuracy remains at a very good level. In the present study, we employ an identical numerical configuration to that in [61], where extensive tests of the influence of mesh density and time step on the obtained solutions were conducted. In [61], it was demonstrated that a multi-layer block-structured mesh consisting of $41.1 \times 10^6$ cells ensures virtually grid-independent results. In the present analyzed cases, the meshes differ slightly depending on the waviness shape, but all consist of $41.1 \times 10^6$ cells. The complexity of these configurations is similar to that of the problems studied previously, and it is expected that the simulations presented in this paper are as accurate as those reported earlier.

## 5. Results

As discussed in the introduction, the main goal of the research is to increase $\tau_w$, which will ensure the delay or complete elimination of TBL separation under the influence of a strong positive pressure gradient. On the other hand, it is known that any interference with the shape of the streamlined surface can contribute to the total drag. The purpose of this paper is to examine the effect of WW tilt on $\tau_w$ and the drag coefficient $C_d$ while maintaining the previously defined amplitude.

The analysis of the results is organized as follows: it begins with a description of the general flow dynamics and the identification of differences between the solutions in selected cases based on instantaneous results. Then we focus on the differences in $\tau_w$ and $C_d$, and try to explain them based on velocity and pressure distributions. We begin the discussion with a description of the basic TBL properties.

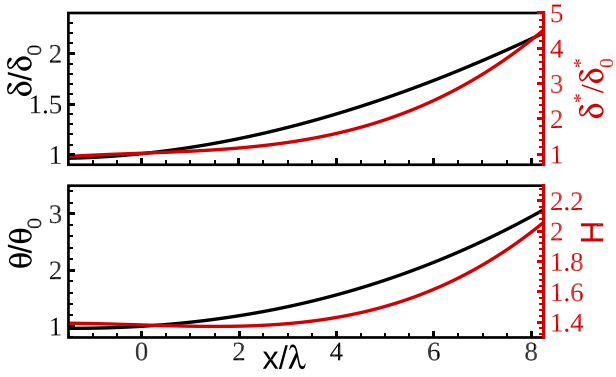



**Fig. 6.** Properties of TBL.

Fig. 6 illustrates the evolution of $\delta$, displacement thickness $\delta^* = \int_0^\delta (1 - \langle U(y)\rangle/U_\infty)\,dy$, momentum thickness $\theta = \int_0^\delta (\langle U(y)\rangle/U_\infty)(1 - \langle U(y)\rangle/U_\infty)\,dy$, and shape factor $H = \delta^*/\theta$. All these quantities are normalized by their values at $x = 0$, while the $x$-axis, representing the streamwise distance, is normalized with respect to the waviness wavelength $\lambda$. In general, when TBL is exposed to APG, $\delta$ builds up much faster, as observed in the second part of the domain, i.e. at approx. $x/\lambda > 5$. A similar trend is evident for the shape factor. The fact that the $H$ value does not reach a level close to 2.2 indicates that the boundary layer is not separating.

Fig. 7 shows a near-wall flow region with isosurfaces of the Q-parameter colored by the vorticity modulus obtained for the cases W0, WL2 and WR2. The Q-parameter is defined as $Q = 0.5(\Omega_{ij}\Omega_{ij} - S_{ij}S_{ij})$, where $\Omega_{ij}$ and $S_{ij}$ are antisymmetric and symmetric parts of the velocity gradient tensor. The subfigures present an enlarged view of the flow near the tops of the last waviness period and the beginning of the flat wall section. It can be seen that large values of the vorticity occur mainly on the tops of the waviness. This is due

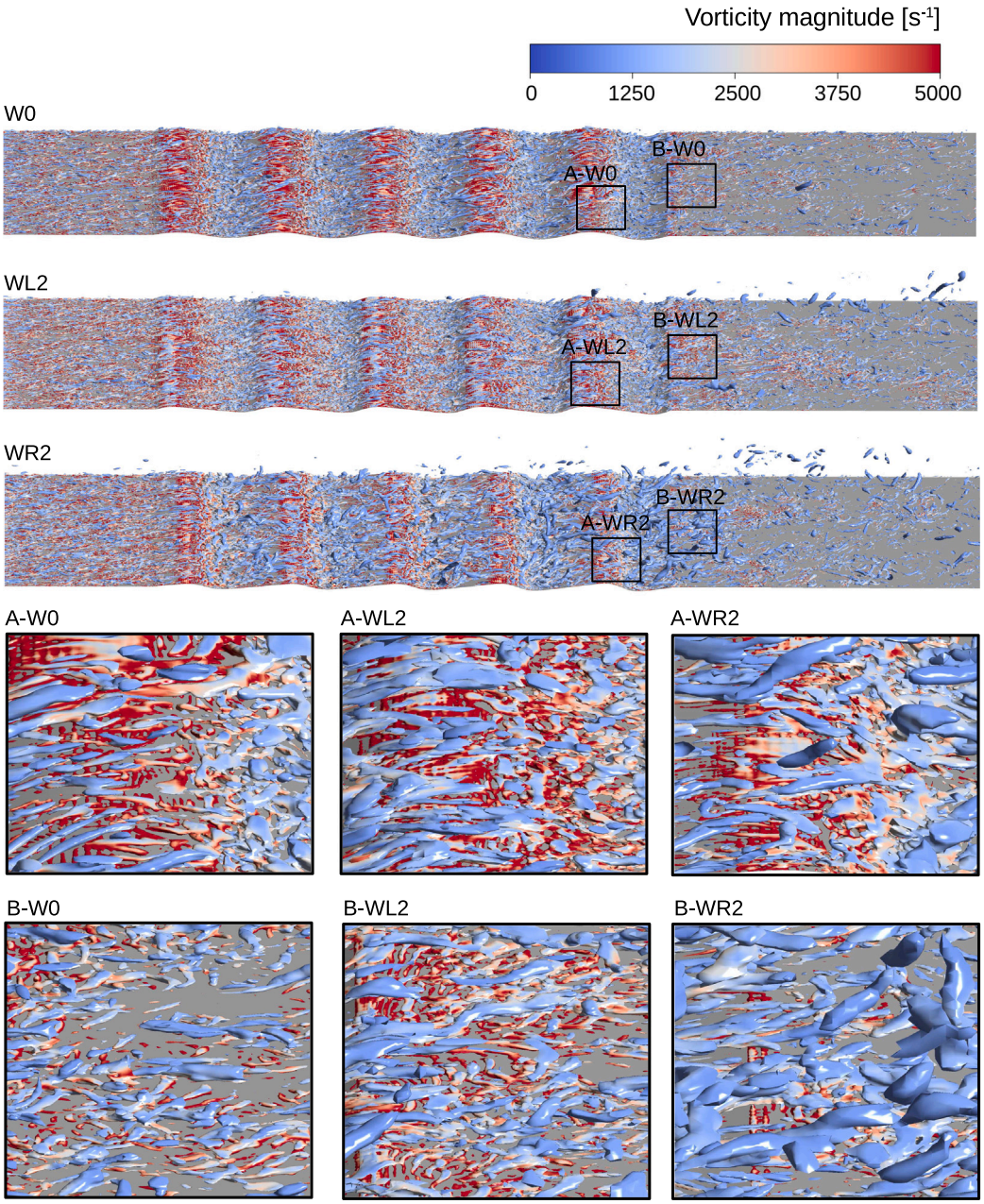



**Fig. 7.** Isosurface of the Q-parameter, colored by the vorticity magnitude, in the near wall region in the cases W0, WL2 and WR2. (For interpretation of the references to color in this figure legend, the reader is referred to the web version of this article.)

to a strong velocity gradient close to the wall being the effect of a flow acceleration in this region. The Q-parameter is often used as an indicator of coherent vortical structures [94], and here it reveals the simultaneous occurrence of tiny vortices and larger longitudinal structures on the uphill slopes of the waviness. These streamwise-oriented structures break up into spanwise vortices in the downhill areas of the corrugation. Such a vortical arrangement is typical of shear dominated flow regions [95], which often occur in separation zones. Upon closer examination, differences between the particular cases emerge. The mechanism of vortices generation and their break up process appear to be strongest for case WR2 (right tilt), where the largest structures are found over the waviness cavities. In these areas, as will be discussed later in the paper, a local deceleration of the flow is observed, leading to strong recirculation zones that contribute to an enhanced shear forces [96,97]. A similar pattern of vortices has been noted in the literature [98,99]. Conversely, for case WL2 (left tilt), where, as shown later, separation is nearly non-existent, the vortices sizes are the least enlarged by the waviness. In this case, also the proportion of existing small to large vortices seem to be larger than in case WR2. Furthermore, at the beginning of the flat wall sections, the differences are also pronounced. Although the flow exhibits strongly turbulent behavior in all cases, the sizes of vortices significantly vary in particular configurations. The largest vortical structures occur in case WR2, while for WL2, a much higher proportion of smaller turbulent scales and elevated levels of vorticity are noted.

Fig. 8 shows how the observed differences in the Q–parameter translate to the instantaneous streamwise component of the wall shear stress $\tau_{w,x}$ distribution in subsequent waviness periods. Comparing the cases W0 and WR2, although the latter exhibits larger negative $\tau_{w,x}$ values ($|\tau_{w,x,W0}| < |\tau_{w,x,WR2}|$), these solutions are qualitatively similar. The regions with $\tau_{w,x} < 0$ occur on the inclined wall parts and starting from the $2^{nd}$ waviness period their streamwise extents grow in the subsequent waves. Note, that when $\tau_{w,x} < 0$ the instantaneous flow separation occurs. In the case of WL2, unlike in the cases W0 and WR2, on

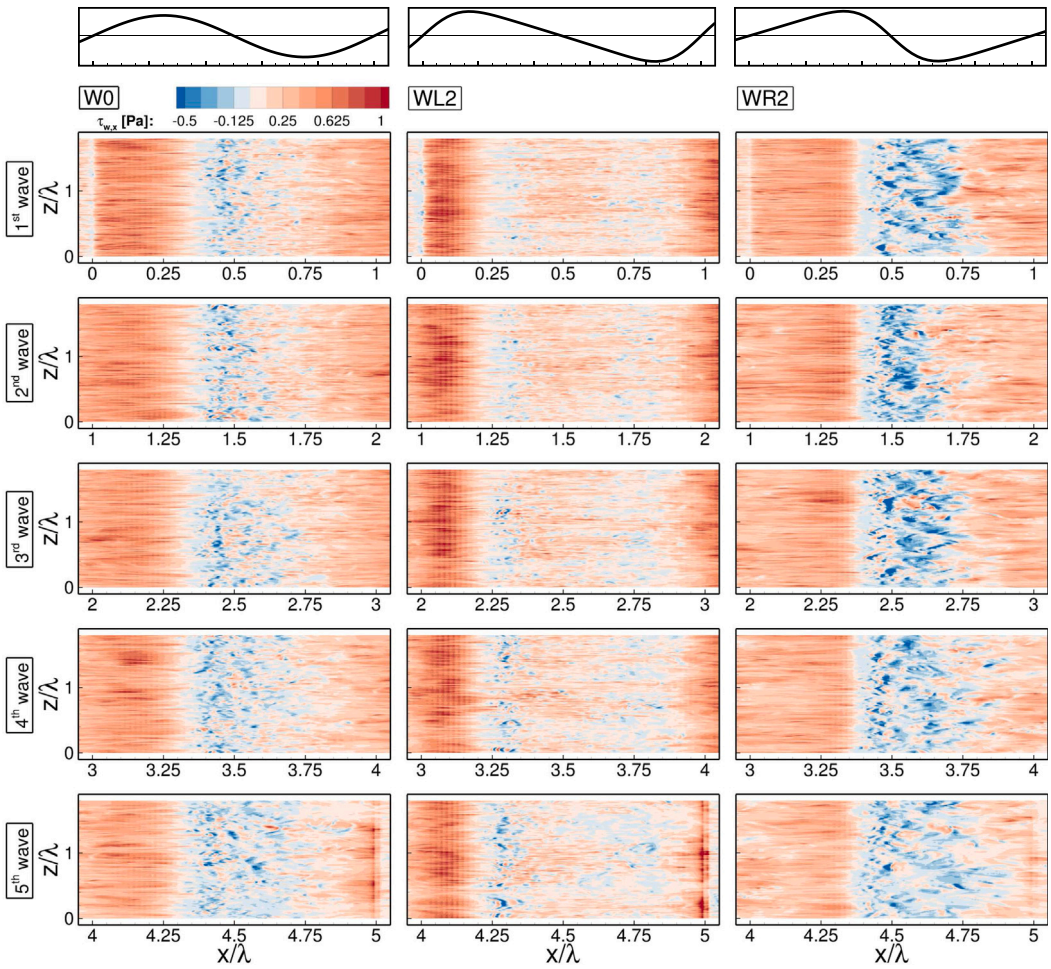



**Fig. 8.** Contours of $\tau_{w,x}$ on the wall in the cases W0, WL2 and WR2. The 'x-z' coordinates are normalized by the waviness length $\lambda$. The upper schematics plots show the wall shapes.

the uphill slope, $\tau_{w,x}$ takes exceptionally large values. Downstream, the negative $\tau_{w,x}$ values are significantly smaller ($(|\tau_{w,x,WL2}| < |\tau_{w,x,W0}| < |\tau_{w,x,WR2}|)$), and although they occur almost over the entire downhill length, it should be noted that the localizations of regions with $\tau_{w,x} < 0$ are less frequent. This is reflected in its time-averaged profiles ($\langle\tau_{w,x}\rangle$) shown in Fig. 9, where additionally the pressure distribution on the wall is presented. For the ease of interpreting the graphs, the top panel shows the shape and location of each wavy geometry. Please note that the $y$-axis is normalized by $\delta_0 = 0.0804$ m, the boundary layer thickness measured at $x = 0$. In the case with the flat wall (case F) $\langle\tau_{w,x}\rangle$ changes only slightly and decreases along the streamwise direction as the overall pressure increases. On the contrary, when the wall is wavy, both $\langle\tau_{w,x}\rangle$ and pressure exhibit strong variations along the waviness. In the WL2 configuration, the maxima of $\langle\tau_{w,x}\rangle$ are significantly higher than in the other cases as evidenced by the $\tau_w$ maps presented in Fig. 8. This is related to a change in the local pressure, which strongly decreases on the uphill waviness sides, where the flow accelerates. Also note the variation of the wall shear stress on the downhill slope, where two local minima, for WL2, can be observed within each period (for example, at $x/\lambda = 1.29$ and $x/\lambda = 1.78$). As a result of the acceleration on the uphill slope and the strong change in wall curvature, the boundary layer moves away from the surface, generating first local minimum in $\langle\tau_{w,x}\rangle$ and forming a small (temporary, as seen in Fig. 8) separation bubbles. The second local minimum in $\langle\tau_{w,x}\rangle$ is formed just before reaching the lowest part of the wave cavity, slightly preceding the local pressure maximum that is seen for the same case (WL2). This phenomenon is well visualized in Fig. 10 depicting the mean velocity field over the $2^{nd}$ wave of WL2.

Fig. 11 shows the profiles of the streamwise velocity component $\langle U_x\rangle/U_e$ along the wall-normal direction on the tops of the waviness. The presented results are normalized by the boundary layer thickness ($\delta$), taken as the distance from the wall to the point where the velocity $U_e$ equals 99% of $U_{x,\infty}$ at a particular streamwise $x-$location. It can be seen that in the case WL2 the velocity near the wall takes the largest values among the presented solutions and the differences increase in the subsequent waviness. In addition, these differences are also seen further away from the wall for successive periods, which is especially evident between WR2 and the other two cases. Note here the unfavorably strong deceleration of the flow in the inner zone of TBL for the case WR2 which had a direct attenuating effect on the wall shear stress. The acceleration of the flow on the tops causes the rise of the wall-normal velocity gradient resulting in the observed maxima of $\langle\tau_{w,x}\rangle$. Their values are sufficient to prevent the local flow separation ($\langle\tau_{w,x}\rangle < 0$) on smoothly inclined walls of the downhill slopes. The velocity fluctuation distributions shown in the bottom row of Fig. 11 indicate an increased rate of momentum transfer normal to the wall (see arrows in Fig. 11), explaining the increase in velocity in the near-wall region and the rise of $\langle\tau_{w,x}\rangle$ for the WL2 case. In this regard, the worst solution is found for the configuration WR2, where the regions with $\langle\tau_{w,x}\rangle < 0$ are wide. The reason for that seems to be a too small pressure drop on the uphill waviness part, which compared to the cases W0 and WL2 is the least inclined. Simultaneously, the flow accelerates less than in the W0 and WL2 cases (see Fig. 11) and near the tops, the maxima of $\langle\tau_{w,x}\rangle$ do not exceed even those obtained in the case W0. In effect, the flow separates on the abrupt downhill waviness parts.

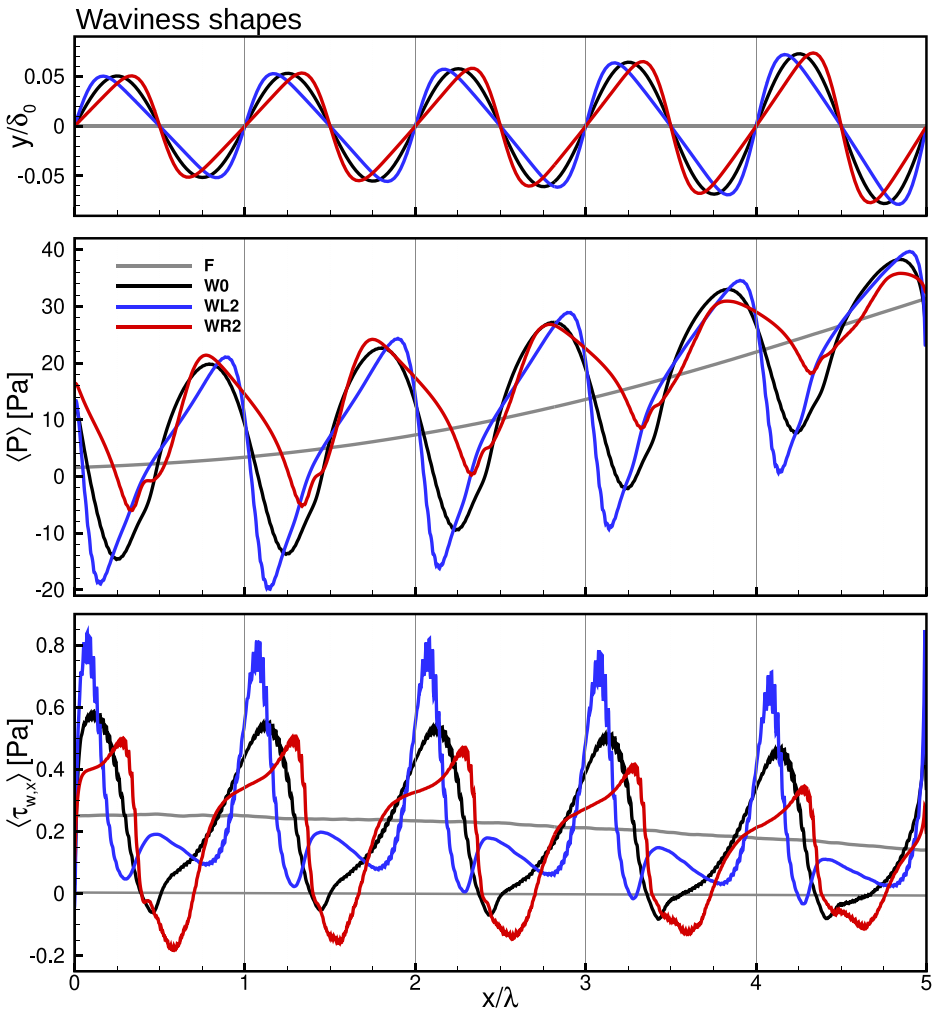



**Fig. 9.** Profiles of $\langle \tau_{w,x} \rangle$ and $\langle P \rangle$ along the wavy wall section in the cases W0, WL2 and WR2. The lower figure shows the wall shapes in the waviness section.

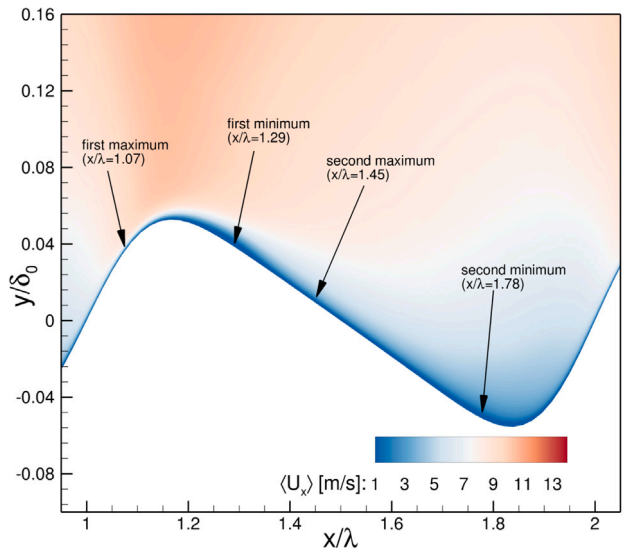



**Fig. 10.** Contour maps of $\langle U_x \rangle$ for the case WL2, depicting near-wall area of the $2^{nd}$ waviness period.

The separation areas, determined based on $\langle \tau_{w,x} \rangle < 0$, and previously discussed (see Figs. 8 and 9), are illustrated in Fig. 12 as red zones (where $\langle U_x \rangle < 0$) on the streamwise velocity contour maps. These are depicted specifically for the downhill slope of the $5^{th}$ wave (i.e. at $4.35 \leq x/\lambda \leq 4.95$) to emphasize the magnitude of detachment. Consistent with the observations from Figs. 8 and 9, the largest separation zone appears for WR2, followed by W0. Additionally, although $\langle \tau_{w,x} \rangle < 0$ is observed for WL2 around $x/\lambda = 4.27$ (see Fig. 9), it is too minor to be visible on the $\langle U_x \rangle$ contours. This lack of detachment for WL2 is believed to lead to its lowest $C_d$ and possibly contributes to a significant improvement of $\tau_{w,x}$ enhancement over the sinusoidal waviness W0. This aspect is discussed in more detail later.

Fig. 13 presents contour maps of vorticity, denoted as $\langle \omega \rangle$, for cases WL2, W0, and WR2 at the last trough of the waviness, i.e., at $3.95 \leq x \leq 5.05$. It highlights areas where the fluid exhibits strong rotational behavior. It can be observed that, in all three cases, elevated levels of $\langle \omega \rangle$ are found in regions just downstream of the waviness tip. This location marks the point where streamwise, longitudinal vortices break down and transform into spanwise ones due to roll-up process (strong rotational behavior). The observed phenomenon is particularly evident in zooms A-W0, A-WL2, and A-WR2 of Fig. 7, which highlight this area. Furthermore, this observation is consistent with findings from our previous work [61] and from the DNS study of DeAngelis et al. [98].

The above-discussed differences between the instantaneous results and between the profiles of the time-averaged pressure, streamwise velocity and $\tau_w$ along the waviness affect the flow behavior downstream in the APG region. To minimize the risk of the TBL separation or postpone its occurrence, the $\tau_w$ values should be possibly large. In this respect, as an indicator of the performance of the WW geometries,

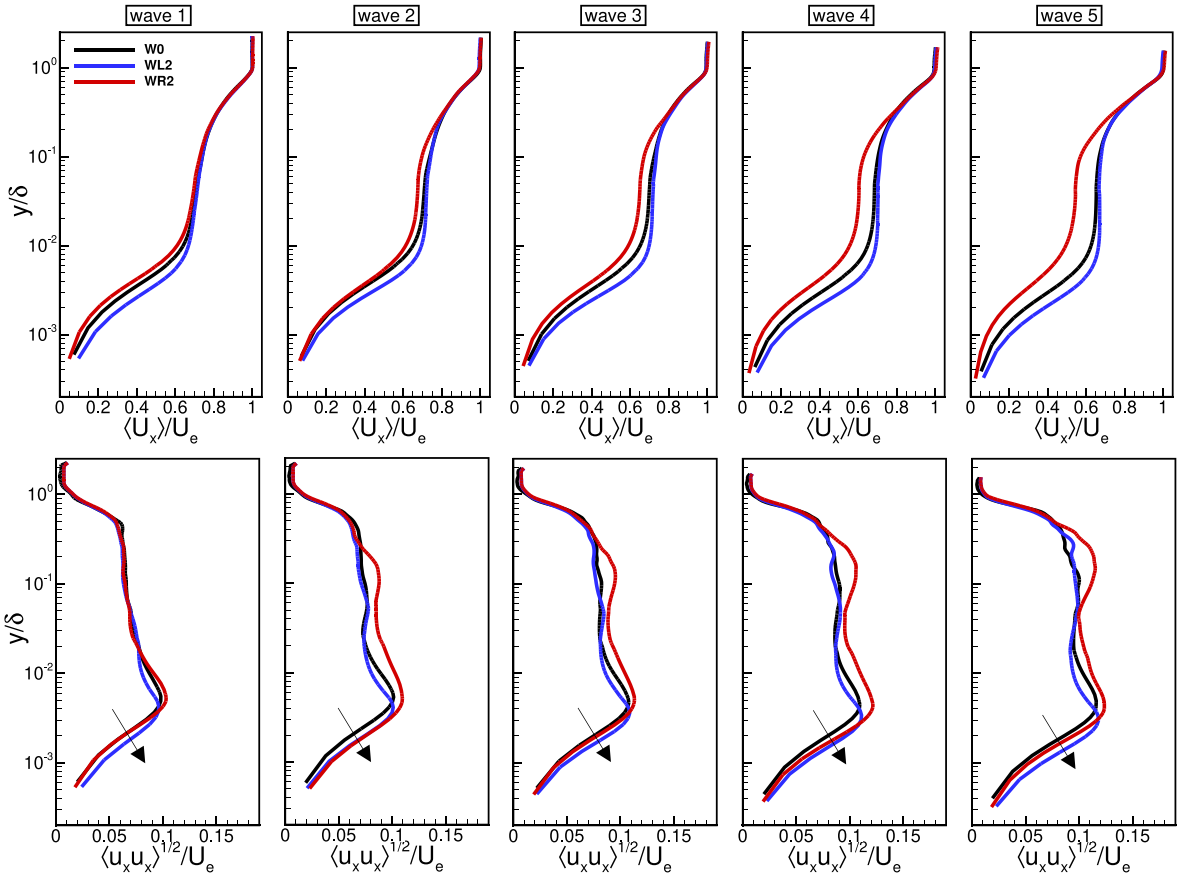



**Fig. 11.** Profiles of $\langle U_x \rangle / U_e$ and $\langle u_x u_x \rangle^{1/2} / U_e$ along the vertical direction on the tops of the waviness in the cases W0, WL2, and WR2.

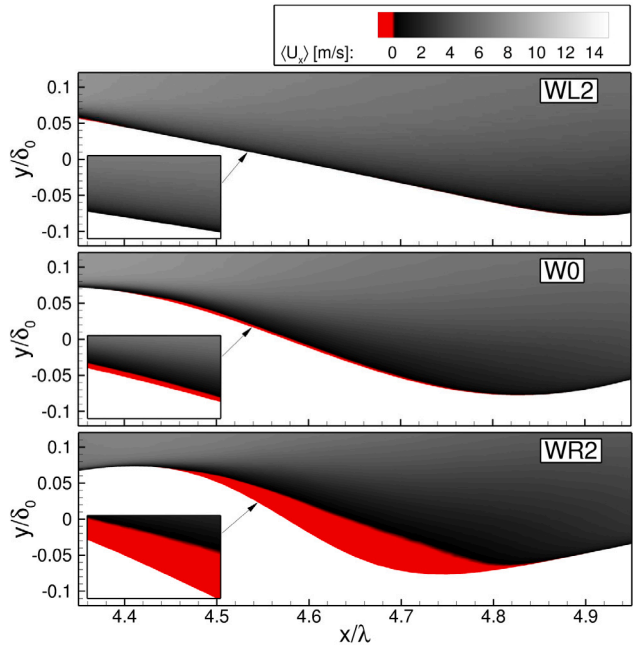



**Fig. 12.** Contour maps of $\langle U_x \rangle$ at the last waviness trough.

we use $\Delta\langle \tau_{w,x} \rangle$ or $\Delta\langle \tau_{w,x} \rangle_{avg} = \overline{(\langle \tau_{w,x} \rangle_{WW} - \langle \tau_{w,x} \rangle_F)/\langle \tau_{w,x} \rangle_F}$. Here, the triangular brackets represent the time averaging operator, the overline is the operator of the spatial averaging over the streamwise distance

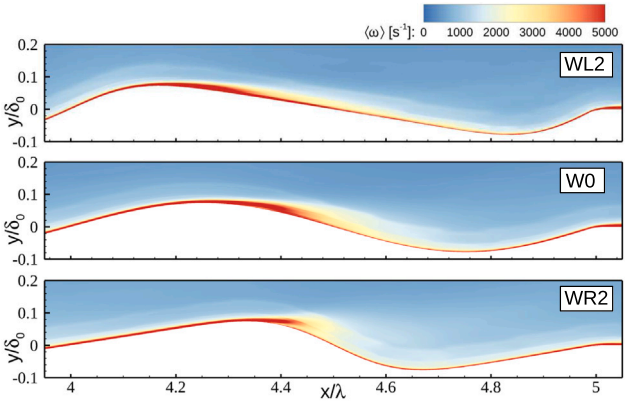



**Fig. 13.** Contour maps of $\langle \omega \rangle$ at the last waviness trough for cases WL2, W0 and WR2.

0.7 m $< x <$ 1.1 m, while $\langle \tau_{w,x} \rangle_{WW}$ and $\langle \tau_{w,x} \rangle_F$ indicate the wall shear stress computed for wavy and flat walls, respectively.

Fig. 14 shows local values of $\Delta\tau_w$ for cases WL2, W0 and WR2 measured in the region downstream the waviness, i.e. at $5 \leq x/\lambda \leq 7.5$. It can be seen that $\Delta\langle \tau_{w,x} \rangle$ levels for each configuration stay relatively constant but their values significantly differ from each other not only in the absolute levels but also in the sign. For WR2, $\Delta\tau_w$ is negative, which means that the overall value of $\tau_w$ is reduced and so the effect is detrimental compared to the case F. The benefits of using WW are seen for W0 and WL2 for which a growth in $\tau_w$ is exceptionally high.

Fig. 15a shows $\Delta\langle \tau_{w,x} \rangle_{avg}$ for all considered configurations (red line with symbols). Moreover, the presented results are supplemented with the corresponding values of $C_d$, computed for the waviness section,

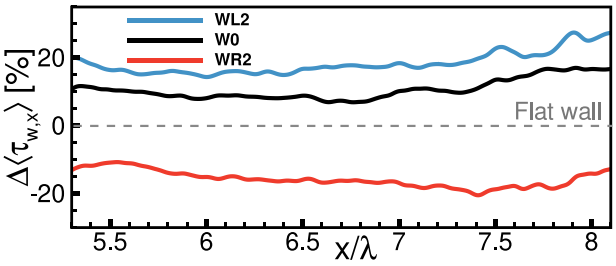



**Fig. 14.** Profiles of: $\Delta\langle\tau_{w,x}\rangle$ for W0, WL2 and WR2 (a); $C_d$, $\Delta\langle\tau_{w,x}\rangle_{avg}$ (b) and $C_p$ with $C_f$ for all considered WW configurations.

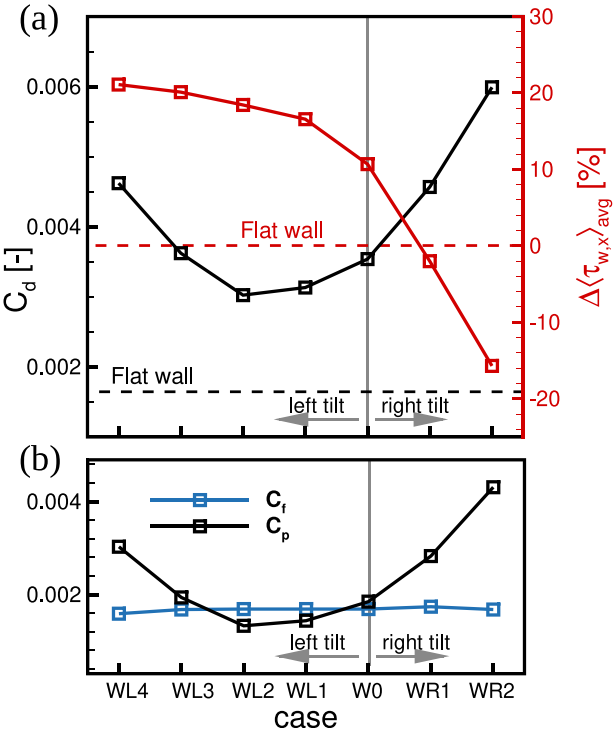



**Fig. 15.** Profiles of: $C_d$, $\Delta\langle\tau_{w,x}\rangle_{avg}$ (a) and $C_p$ with $C_f$ (b) for all considered WW configurations.

i.e., 0 m < $x$ < 0.666 m. Note, that $C_d$ is the crucial parameter from the point of view of energy savings, and the smaller it is the better. In Fig. 15b, the total drag coefficient is divided into its viscous and pressure contributions ($C_f$, $C_p$). The latter, usually called the shape drag coefficient, allows assessing how the shape of the body (here, the waviness) affects the total drag force.

For convenience, red and black dash lines representing $\Delta\langle\tau_{w,x}\rangle_{avg}$ = 0 and $C_d$ obtained for the case F are also included in Fig. 15a to serve as a reference. As can be seen from Fig. 15a, the basic sinusoidal waviness geometry W0 ensures $\Delta\langle\tau_{w,x}\rangle_{avg}$ = 10.7%, which is already a significant achievement. However, this can be substantially improved by tilting the waviness. When looking at the results obtained for the tilted WWs, it can be seen that the configurations with leftward tilt (WL1–WL4) cause an increase in $\Delta\langle\tau_{w,x}\rangle_{avg}$, while the cases with rightward tilt (WR1, WR2) lead to a drop in $\Delta\langle\tau_{w,x}\rangle_{avg}$. Worth noticing is also a considerable gradual growth in $\Delta\langle\tau_{w,x}\rangle_{avg}$ with increasing counter-streamwise tilting of the waviness WL1 → WL4. The changes in $\langle\tau_{w,x}\rangle_{avg}$ are accompanied by the alteration in $C_d$. It is commonly known that, compared to the flat wall, the waviness causes an increase in $C_d$ [77,96,98,100–111], however, this behavior can be controlled to some extent, as demonstrated in the present work. The distribution of $C_d$ exhibits a local minimum for the case WL2 which is approximately 14% lower than in the case W0. Moreover, WL2, directly followed by WL1, display the dominance of viscous over pressure drag component (i.e. $C_f > C_p$, see Fig. 15b), which is particularly interesting as it indicates that both of these WWs approach the shape of a streamlined body. For WL2 $\Delta\langle\tau_{w,x}\rangle_{avg}$ = 18.4%, which translates to 72.4% higher $\tau_w$ than obtained for case W0. Assuming $\Delta\langle\tau_{w,x}\rangle_{avg}$ as the main indicator of the wavy wall performance, one can also see that it can be increased even further than in configuration WL2. In cases WL3 and WL4 $\Delta\langle\tau_{w,x}\rangle_{avg}$ = 20.11% and $\Delta\langle\tau_{w,x}\rangle_{avg}$ = 21.57%, which compared the case W0 correspond to 88.1% and 101.7% rise in $\Delta\langle\tau_{w,x}\rangle_{avg}$. This, however, is connected with an unfavorable increase in $C_d$ in which the shape drag dominates (see Fig. 15b). The reason for the increase in $C_d$ and, in fact, its component $C_p$ for rightward tilt configurations is the presence of a large area of separation, as demonstrated in Fig. 12. Nevertheless, the WL3 configuration is still better than W0, as $C_d$ in these two cases are almost identical. In the configuration WL4, $C_d$ rises significantly, and assessing the superiority of WL4 over the W0 case depends on the actual needs. If the increase in $\Delta\langle\tau_{w,x}\rangle_{avg}$ is the priority, the configuration WL4 proves to be the best among all the cases analyzed.

In order to better explain the differences in $\tau_w$ levels, we analyze the mean velocity and its fluctuation distributions on the flat plate region in the measuring section as shown in Fig. 1. Fig. 16 presents profiles of the streamwise velocity component $\langle U_x\rangle/U_e$ (upper row) and its fluctuation $\langle u_x u_x\rangle^{1/2}/U_e$ (bottom row) along the wall-normal direction for three different streamwise locations ($x$ = 0.8 m, $x$ = 0.9 m, $x$ = 1.0 m, which correspond to 0.124 m, 0.224 m, and 0.324 m downstream the WW section, respectively). As can be seen, except for the WR2 configuration, the mean velocity profiles are roughly very similar. The pronounced velocity deficit for WR2 and thus the low velocity gradient at the wall translate into a low $\tau_{w,x}$. It should be noted that among the other three cases, WL2 exhibits the highest velocity gradient at the wall, which implies enhanced wall shear stress. These results are consistent with changes in velocity fluctuation profiles. It is apparent that fluctuations in the near-wall region ($y/\delta \leq 0.01$) are the highest for WL2 which is accompanied by an increase in vorticity near the wall, as shown in Fig. 7. This fluctuation increment, according to [13,73], is the result of the downwash of a high momentum fluid toward the wall by large vortical structures active in the outer layer. In contrast, $\langle u_x u_x\rangle^{1/2}$ for the F and WR2 cases is low in this region despite the fact that the level of $\langle u_x u_x\rangle^{1/2}$, i.e., the so-called outer peak, is highest in the outer layer. It is clear, however, that this does not translate into momentum transfer to the wall. All already described effects can be consistently noted at all considered downstream locations, i.e., $x$-distances.

The results presented thus far demonstrate that employing a waviness with a suitably adjusted tilt, a considerable enhancement in the wall shear stress, leading to the postponement of TBL separation, can be obtained with regard to a waviness without tilt. Moreover, this improvement is accompanied by a reduction of total drag. However, the benefits coming from tilting of the corrugation are not limited only to separation control, they can also be extended over, for instance, the heat transfer process. Namely, the considerable increase in fluctuations found in the outer region of TBL, provided by tilted waviness, could be beneficial for potential applications where heat transfer augmentation (by improving mixing) is sought after. For such applications, enhanced total drag is usually of lesser interest and so the corrugation with streamwise tilt (such as WR2) would be an excellent solution. Furthermore, if the goal is to enhance mixing while minimizing $C_d$, a wall with counter-streamwise tilt (like WL2) seems more attractive. To further support the beneficial effects of the waviness in possible heat transfer enhancement, Fig. 17 presents the turbulent kinetic energy (TKE) for cases F, W0, WL2, and WR2. It is observed that the WR2 configuration exhibits the highest level of TKE. Additionally, as highlighted in the zoomed-in inset, the most elevated levels of TKE occur within the shear layer resulting from the large recirculation region (visualized by streamlines) forming downstream of the separation location. Consequently, as highlighted in [112,113], such conditions are likely to significantly enhance heat transfer efficiency.

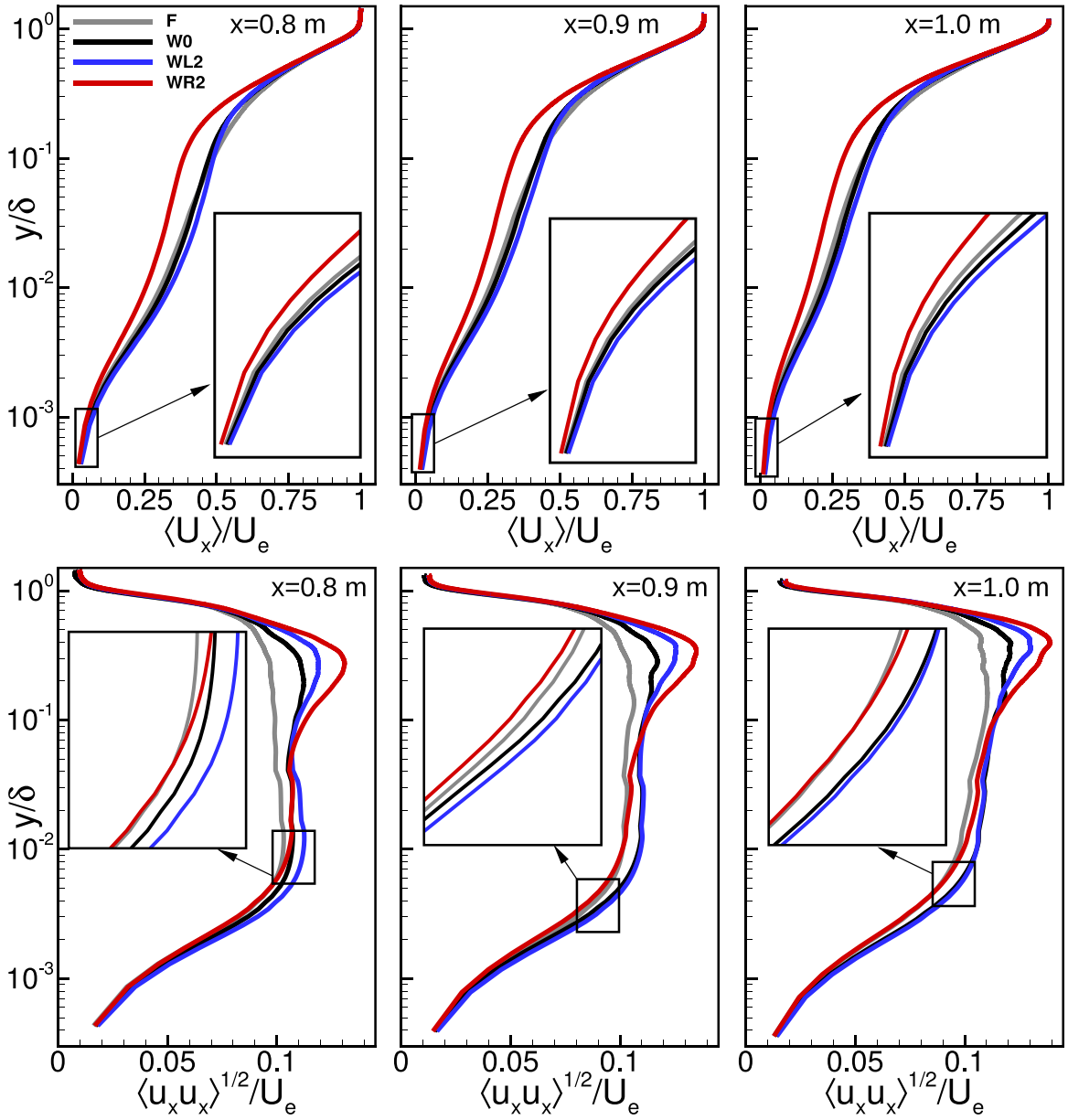



**Fig. 16.** Profiles of $\langle U_x \rangle / U_e$ and $\langle u_x u_x \rangle^{1/2} / U_e$ at $x = 0.8$ m, $x = 0.9$ m, $x = 1.0$ m.

## 6. Summary

This paper demonstrates that counter-streamwise tilting of the wall waviness leads to a significant increase in wall shear stress compared to that observed with the classical sinusoidal wall shape. Moreover, this increase is accompanied by a local reduction in the drag force coefficient. At its minimum value, $C_d$, computed for the area occupied by the wavy wall, is 14% smaller compared to the sinusoidal waviness, while the wall shear stress attains a level approximately 70% higher. It turns out, this is not the limiting case. When a further enhancement of the wall shear stress is a priority to postpone separation, it can be achieved by steeper waviness tilting. This, however, comes at the cost of an increased drag coefficient.

With the performed analysis of the flow in the wavy wall proximity, we can formulate the following advice. To increase the wall shear stress with a simultaneous decrease in the drag coefficient, one should shape the waviness in a way that prevents the occurrence of separation bubbles in the troughs. The waviness causes growth in the streamwise velocity fluctuations in the upper boundary layer region, making the flow more turbulent. This manifests in a larger near-wall streamwise velocity gradient, and thus, an increased wall shear stress.

On the other hand, configurations with streamwise waviness tilt, although disadvantageous from the viewpoint of flow separation postponement, provide a considerable increase in fluctuations in the outer region and thus an increase in turbulent kinetic energy. This makes them attractive for applications where enhanced mixing is beneficial, such as in heat transfer processes.

In real-life applications, such as wind turbine blades, where the wing does not operate in stable, constant conditions, i.e., the wind velocity may change rapidly, causing deviations in $Re$. Since passive flow control methods are susceptible to operating conditions, all aspects engaging their performance should be considered meticulously. This opens a space for future work aimed at further optimization of the corrugation to achieve the highest $\tau_w$ enhancement at minimal $C_d$. The

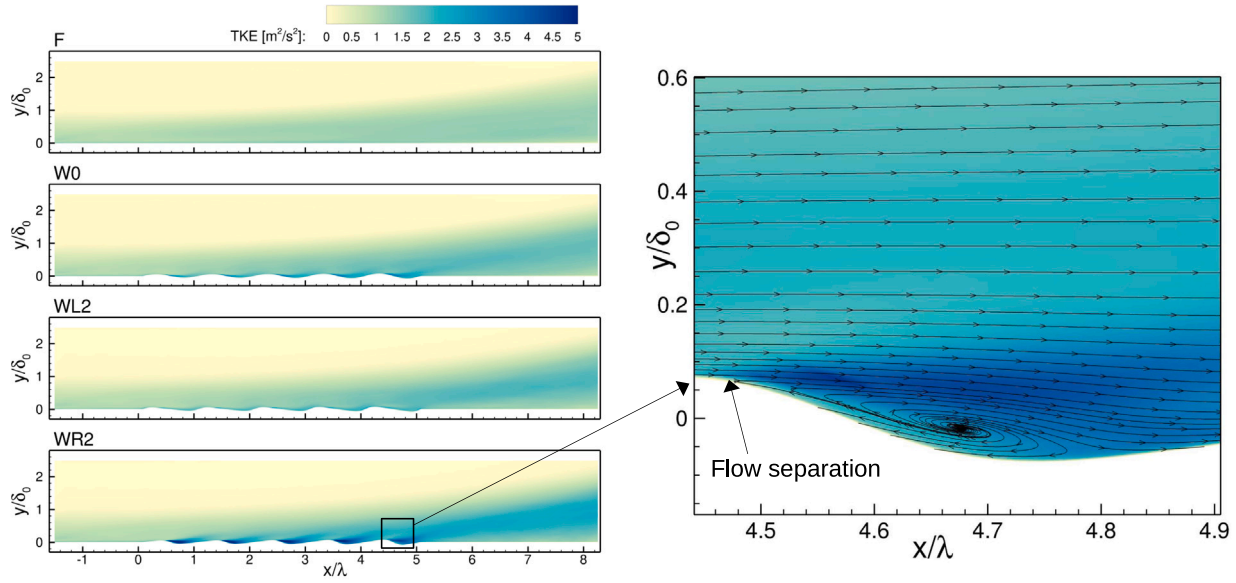



**Fig. 17.** Contour maps of TKE for cases F, W0, WL2, and WR2.

results obtained in the present research are crucial for this task, as they highlight areas where the waviness can be further improved.

## CRediT authorship contribution statement

**Piotr Kamiński:** Writing – review & editing, Writing – original draft, Visualization, Software, Methodology, Investigation, Formal analysis, Data curation, Conceptualization. **Artur Tyliszczak:** Writing – review & editing, Visualization, Supervision, Software, Resources, Investigation, Formal analysis, Conceptualization. **Witold Elsner:** Writing – review & editing, Supervision, Resources, Project administration, Funding acquisition, Conceptualization. **Paweł Niegodajew:** Writing – review & editing, Writing – original draft, Visualization, Supervision, Methodology, Investigation, Formal analysis, Conceptualization.

## Declaration of competing interest

The authors declare that they have no known competing financial interests or personal relationships that could have appeared to influence the work reported in this paper.

## Acknowledgments

The investigation was supported by the National Science Centre under grant UMO-2020/39/B/ST8/01449 and statutory funds of the Czestochowa University of Technology BS/PB 1-100-3011/2024/P. We gratefully acknowledge Poland's high-performance Infrastructure PLGrid ACK Cyfronet AGH and PCSS for providing computer facilities and support within computational grants no PLG/2023/016731 and PL0356-01.

## Data availability

Data will be made available on request.

## References

[1] Lin JM, Pauley LL. Low-Reynolds-number separation on an airfoil. AIAA J 1996;34(8):1570–7.
[2] Tanarro Á, Vinuesa R, Schlatter P. Effect of adverse pressure gradients on turbulent wing boundary layers. J Fluid Mech 2020;883:A8.
[3] Azad RS. Turbulent flow in a conical diffuser: A review. Exp Therm Fluid Sci 1996;13(4):318–37.
[4] Salehi S, Raisee M, Cervantes M. Computation of developing turbulent flow through a straight asymmetric diffuser with moderate adverse pressure gradient. J Appl Fluid Mech 2017;10(4):1029–43.
[5] Yadegari M, Khoshnevis AB. Numerical study of the effects of adverse pressure gradient parameter, turning angle and curvature ratio on turbulent flow in 3D turning curved rectangular diffusers using entropy generation analysis. Eur Phys J Plus 2020;135(7):548.
[6] Devinant P, Laverne T, Hureau J. Experimental study of wind-turbine airfoil aerodynamics in high turbulence. J Wind Eng Ind Aerodyn 2002;90(6):689–707.
[7] Cui W, Xiao Z, Yuan X. Simulations of transition and separation past a wind-turbine airfoil near stall. Energy 2020;205:118003.
[8] Abdolahifar A, Karimian S. A comprehensive three-dimensional study on darrieus vertical axis wind turbine with slotted blade to reduce flow separation. Energy 2022;248:123632.
[9] Xu H-Y, Qiao C-L, Yang H-Q, Ye Z-Y. Delayed detached eddy simulation of the wind turbine airfoil S809 for angles of attack up to 90 degrees. Energy 2017;118:1090–109.
[10] Wang Y, Li G, Shen S, Huang D, Zheng Z. Influence of an off-surface small structure on the flow control effect on horizontal axis wind turbine at different relative inflow angles. Energy 2018;160:101–21.
[11] Shojaeefard MH, Saremian S. Analyzing the impact of blade geometrical parameters on energy recovery and efficiency of centrifugal pump as turbine installed in the pressure-reducing station. Energy 2024;289:130004.
[12] Nguyen D-A, Kim J-H. Co-adjustable guide vane and diffuser vane to improve the energy generation potential of an axial-flow pump as turbine. Energy 2024;291:130325.
[13] Ricco P, Skote M, Leschziner MA. A review of turbulent skin-friction drag reduction by near-wall transverse forcing. Prog Aerosp Sci 2021;123:100713. http://dx.doi.org/10.1016/j.paerosci.2021.100713.
[14] Ashill P, Fulker J, Hackett K. A review of recent developments in flow control. Aeronaut J 2005;109(1095):205–32.
[15] Ghaemi S. Passive and active control of turbulent flows. Phys Fluids 2020;32(8).
[16] Moghaddam T, Neishabouri NB. On the active and passive flow separation control techniques over airfoils. In: IOP conference series: materials science and engineering, vol. 248, IOP Publishing; 2017, 012009.
[17] Collis SS, Joslin RD, Seifert A, Theofilis V. Issues in active flow control: theory, control, simulation, and experiment. Prog Aerosp Sci 2004;40(4–5):237–89.
[18] You D, Moin P. Active control of flow separation over an airfoil using synthetic jets. J Fluids Struct 2008;24(8):1349–57.
[19] Fahland G, Stroh A, Frohnapfel B, Atzori M, Vinuesa R, Schlatter P, et al. Investigation of blowing and suction for turbulent flow control on airfoils. AIAA J 2021;59(11):4422–36.

[20] Vernet JA, Örlü R, Alfredsson PH. Separation control by means of plasma actuation on a half cylinder approached by a turbulent boundary layer. J Wind Eng Ind Aerodyn 2015;145:318–26.
[21] Vernet JA, Örlü R, Alfredsson PH. Flow separation control behind a cylindrical bump using dielectric-barrier-discharge vortex generator plasma actuators. J Fluid Mech 2018;835:852–79.
[22] Vernet JA, Örlü R, Söderblom D, Elofsson P, Alfredsson PH. Plasma streamwise vortex generators for flow separation control on trucks: a proof-of-concept experiment. Flow, Turbul Combust 2018;100:1101–9.
[23] Sun H, Zhang J, Ma X, Xue R. Shock wave control for supersonic inlet with high-frequency pulsed arc discharge plasma. AIAA J 2024;1–5.
[24] Zhang W, Shi Z, Zhang C, Geng X, Li K, Chen Z. A study on flow control in a hypersonic inlet using a plasma synthetic jet actuator. Phys Fluids 2022;34(10).
[25] Prasad ALN, Unnikrishnan S. Effect of plasma actuator-based control on flow-field and acoustics of supersonic rectangular jets. J Fluid Mech 2023;964:A11.
[26] Parancheerivilakkathil MS, Pilakkadan JS, Amoozgar M, Asadi D, Zweiri Y, Friswell MI, et al. A review of control strategies used for morphing aircraft applications. Chin J Aeronaut 2024.
[27] Tay J, Lim TT. Drag reduction with teardrop-shaped dimples. In: 2018 flow control conference. 2018, p. 3528.
[28] Tay C, Khoo B, Chew Y. Mechanics of drag reduction by shallow dimples in channel flow. Phys Fluids 2015;27(3).
[29] Gattere F, Chiarini A, Quadrio M. Dimples for skin-friction drag reduction: status and perspectives. Fluids 2022;7(7):240.
[30] Aoki K, Muto K, Okanaga H. Mechanism of drag reduction by dimple structures on a sphere. J Fluid Sci Technol 2012;7(1):1–10.
[31] Tay J, Lim TT, Khoo BC. Drag reduction with diamond-shaped dimples. In: AIAA aviation 2019 forum. 2019, p. 3296.
[32] Azlan F, Tan MK, Tan BT, Ismadi M-Z. Passive flow-field control using dimples for performance enhancement of horizontal axis wind turbine. Energy 2023;271:127090.
[33] Koike M, Nagayoshi T, Hamamoto N. Research on aerodynamic drag reduction by vortex generators. Mitsubishi Mot Tech Rev 2004;16:11–6.
[34] Aider J-L, Beaudoin J-F, Wesfreid JE. Drag and lift reduction of a 3D bluff-body using active vortex generators. Exp Fluids 2010;48:771–89.
[35] Gibertini G, Boniface J, Zanotti A, Droandi G, Auteri F, Gaveriaux R, et al. Helicopter drag reduction by vortex generators. Aerosp Sci Technol 2015;47:324–39.
[36] Zhu C, Chen J, Wu J, Wang T. Dynamic stall control of the wind turbine airfoil via single-row and double-row passive vortex generators. Energy 2019;189:116272.
[37] Wang H, Zhang B, Qiu Q, Xu X. Flow control on the NREL S809 wind turbine airfoil using vortex generators. Energy 2017;118:1210–21.
[38] Islam MR, Hossain MA, Mashud M, Gias MTI. Drag reduction of a car by using vortex generator. Int J Sci Eng Res 2013;4(7):1298–302.
[39] Belamadi R, Djemili A, Ilinca A, Mdouki R. Aerodynamic performance analysis of slotted airfoils for application to wind turbine blades. J Wind Eng Ind Aerodyn 2016;151:79–99.
[40] Coder JG, Somers DM. Design of a slotted, natural-laminar-flow airfoil for commercial transport applications. Aerosp Sci Technol 2020;106:106217.
[41] Zaki A, Abdelrahman M, Ayad SS, Abdellatif O. Effects of leading edge slat on the aerodynamic performance of low Reynolds number horizontal axis wind turbine. Energy 2022;239:122338.
[42] Wang H, Jiang X, Chao Y, Li Q, Li M, Zheng W, et al. Effects of leading edge slat on flow separation and aerodynamic performance of wind turbine. Energy 2019;182:988–98.
[43] Ye X, Hu J, Zheng N, Li C. Numerical study on aerodynamic performance and noise of wind turbine airfoils with serrated gurney flap. Energy 2023;262:125574.
[44] Ni L, Miao W, Li C, Liu Q. Impacts of gurney flap and solidity on the aerodynamic performance of vertical axis wind turbines in array configurations. Energy 2021;215:118915.
[45] Wang Y, Li G, Shen S, Huang D, Zheng Z. Influence of an off-surface small structure on the flow control effect on horizontal axis wind turbine at different relative inflow angles. Energy 2018;160:101–21. http://dx.doi.org/10.1016/j.energy.2018.06.070.
[46] Mostafa W, Abdelsamie A, Sedrak M, Thévenin D, Mohamed MH. Quantitative impact of a micro-cylinder as a passive flow control on a horizontal axis wind turbine performance. Energy 2022;244:122654.
[47] Wang J-S, Wu J, Wang J-J. Wake-triggered secondary vortices over a cylinder/airfoil configuration. Exp Fluids 2023;64(1):6.
[48] Zhong J, Li J, Liu H. Dynamic mode decomposition analysis of flow separation control on wind turbine airfoil using leading- edge rod. Energy 2023;268:126656.
[49] Guerrero JE, Maestro D, Bottaro A. Biomimetic spiroid winglets for lift and drag control. Comptes Rendus Mec 2012;340(1–2):67–80.
[50] Wu L, Jiao Z, Song Y, Liu C, Wang H, Yan Y. Experimental investigations on drag-reduction characteristics of bionic surface with water-trapping microstructures of fish scales. Sci Rep 2018;8(1):12186.
[51] Guerrero JE, Sanguineti M, Wittkowski K. Variable cant angle winglets for improvement of aircraft flight performance. Meccanica 2020;55:1917–47.
[52] Zhang Z, Kuang L, Han Z, Zhou D, Zhao Y, Bao Y, et al. Comparative analysis of bent and basic winglets on performance improvement of horizontal axis wind turbines. Energy 2023;281:128252.
[53] Jeong JS, Bong SW, Lee SW. An efficient winglet coverage for aeroengine turbine blade flat tip and its loss map. Energy 2022;260:125153.
[54] Khaled M, Ibrahim MM, Hamed HEA, AbdelGwad AF. Investigation of a small Horizontal–Axis wind turbine performance with and without winglet. Energy 2019;187:115921.
[55] Lowrey P, Harasha J. A preliminary assessment of the feasibility of using riblets in internal flows to conserve energy. Energy 1991;16(3):631–42.
[56] Hao W, Li C. Performance improvement of adaptive flap on flow separation control and its effect on VAWT. Energy 2020;213:118809.
[57] Chen H, Rao F, Shang X, Zhang D, Hagiwara I. Biomimetic drag reduction study on herringbone riblets of bird feather. J Bionic Eng 2013;10(3):341–9.
[58] Yossri W, Ayed SB, Abdelkefi A. Evaluation of the efficiency of bioinspired blade designs for low-speed small-scale wind turbines with the presence of inflow turbulence effects. Energy 2023;273:127210.
[59] Schlieter A, Pflumm R, Shakhverdova I, Naraparaju R, Schulz U, Leyens C, et al. Mechanical properties of shark-skin like structured surfaces for high-temperature applications. Adv Eng Mater 2016;18(5):688–702.
[60] Lang AW, Jones EM, Afroz F. Separation control over a grooved surface inspired by dolphin skin. Bioinspiration & Biomimetics 2017;12(2):026005.
[61] Kamiński P, Niegodajew P, Dróżdż A, Sokolenko V, Tyliszczak A, Elsner W. Numerical analysis of novel wavy wall based control of turbulent boundary layer separation. Aerosp Sci Technol 2024;149:109167.
[62] Eydi F, Mojra A, Kamel H. A novel passive flow control technique using circular arcs coupled with downstream splitters. Ocean Eng 2024;313:119393.
[63] Xia C, Tang L, Yin P, Aw KC. Multi-directional and multi-modal vortex-induced vibrations for wind energy harvesting. Appl Phys Lett 2024;125(20).
[64] Wang J, Han C, Yurchenko D, Zhou Y, Meng X, Zhang W. Energy concentration pipe based on passive jet control for enhancing flow induced vibration energy harvesting. Energy Convers Manage 2024;319:118948.
[65] Aksoy MH. Flow characteristics and passive flow control of circular cylinders with triangular vortex generators: An experimental investigation. Appl Ocean Res 2024;142:103836.
[66] Zhao Z, Guo Z, Qian Z. Passive flow control of a francis turbine operating in sand-laden rivers for mitigating sediment erosion. Phys Fluids 2024;36(9).
[67] Phan T-L. Optimal configuration of passive flow control devices to reduce the aerodynamics drag of a tractor-trailer model. Results Eng 2024;23:102425.
[68] Lissaman P. Low-Reynolds-number airfoils. Annu Rev Fluid Mech 1983;15(1):223–39.
[69] Xie Y, Rao Y, Cheng Y, Tian W. Investigation into the laminar separation control of airfoils at low Reynolds numbers by dimple vortex generators. Aerosp Sci Technol 2022;129:107841.
[70] McMasters JH, Henderson ML. Low-speed single-element airfoil synthesis. In: NASA. Langley res. center the sci. and technol. of low speed and motorless flight, Pt. 1. 1979.
[71] Wu W, Piomelli U. Effects of surface roughness on a separating turbulent boundary layer. J Fluid Mech 2018;841:552–80. http://dx.doi.org/10.1017/jfm.2018.101.
[72] Dróżdż A, Niegodajew P, Romańczyk M, Sokolenko V, Elsner W. Effective use of the streamwise waviness in the control of turbulent separation. Exp Therm Fluid Sci 2021;121:110291.
[73] Hutchins N, Marusic I. Large-scale influences in near-wall turbulence. Philos Trans R Soc A: Math Phys Eng Sci 2007;365(1852):647–64.
[74] Mathis R, Monty JP, Hutchins N, Marusic I. Comparison of large-scale amplitude modulation in turbulent boundary layers, pipes, and channel flows. Phys Fluids 2009;21(11):111703.
[75] Vila CS, Vinuesa R, Discetti S, Ianiro A, Schlatter P, Örlü R. Separating adverse-pressure-gradient and Reynolds-number effects in turbulent boundary layers. Phys Rev Fluids 2020;5(6):064609.
[76] Dróżdż A, Niegodajew P, Romańczyk M, Elsner W. Effect of Reynolds number on turbulent boundary layer approaching separation. Exp Therm Fluid Sci 2021;125:110377.
[77] Elsner W, Dróżdż A, Szymanek E, Tyliszczak A, Niegodajew P. Experimental and numerical studies of turbulent flows over two-dimensional and three-dimensional rough surfaces under an adverse pressure gradient. Appl Math Model 2022;106:549–66.
[78] Casalino D, Avallone F, Gonzalez-Martino I, Ragni D. Aeroacoustic study of a wavy stator leading edge in a realistic fan/OGV stage. J Sound Vib 2019;442:138–54.
[79] Teruna C, Rego L, Casalino D, Ragni D, Avallone F. A numerical study on aircraft noise mitigation using porous stator concepts. Aerospace 2022;9(2):70.
[80] Bhardwaj S, Dalal A, Pati S. Influence of wavy wall and non-uniform heating on natural convection heat transfer and entropy generation inside porous complex enclosure. Energy 2015;79:467–81.
[81] Abbaspour P, Alipoor A. Numerical study of wavy-wall effects on premixed H2/air flammability limits, propagation modes, and thermal performance of micro combustion chambers. Appl Energy 2024;359:122727.

[82] Kamiński P, Elsner W, Tyliszczak A, Niegodajew P. Estimation of the optimal amplitude and period of a wavy wall for controlling turbulent separation at $Re_\tau = 2500$. Submitt J Wind Eng Ind Aerodyn 2024.
[83] Geurts B. Elements of direct and large-eddy simulation. Philadelphia, USA: Edwards Publishing; 2004.
[84] Nicoud F, Ducros F. Subgrid-scale stress modelling based on the square of the velocity gradient tensor. Flow, Turbul Combust 1999;62(3):183–200.
[85] Menter FR. Two-equation eddy-viscosity turbulence models for engineering applications. AIAA J 1994;32(8):1598–605.
[86] Saleem BKM, Mustafa A, Kareem DA, Yuce MI, Szydłowski M, Al-Ansari N. Numerical analysis of turbulent flow over a backward-facing step in an open channel. Arch Hydro- Eng Environ Mech 2023;70(1):49–69.
[87] Ravi BV, Singh P, Ekkad SV. Numerical investigation of turbulent flow and heat transfer in two-pass ribbed channels. Int J Therm Sci 2017;112:31–43.
[88] Tu J, Qi C, Li K, Tang Z. Numerical analysis of flow and heat characteristic around micro-ribbed tube in heat exchanger system. Powder Technol 2022;395:562–83.
[89] Kumar A, Maithani R, Suri ARS. Numerical and experimental investigation of enhancement of heat transfer in dimpled rib heat exchanger tube. Heat Mass Transf 2017;53:3501–16.
[90] Sharma SK, Kalamkar VR. Computational fluid dynamics approach in thermo-hydraulic analysis of flow in ducts with rib roughened walls–A review. Renew Sustain Energy Rev 2016;55:756–88.
[91] Fletcher C. Computational techniques for fluid dynamics. Berlin Heidelberg: Springer-Verlag; 1991.
[92] Ferziger J, Peric M. Computational methods for fluid dynamics. Berlin Heidelberg: Springer-Verlag; 1996.
[93] Courant R, Friedrichs K, Lewy H. On the partial difference equations of mathematical physics. IBM J Res Dev 1967;11(2):215–34.
[94] Hunt JC, Wray AA, Moin P. Eddies, streams, and convergence zones in turbulent flows. In: Studying turbulence using numerical simulation databases, 2. Proceedings of the 1988 summer program. 1988.
[95] Omidyeganeh M, Piomelli U. Large-eddy simulation of two-dimensional dunes in a steady, unidirectional flow. J Turbul 2011;(12):N42.
[96] Kruse N, Von Rohr PR. Structure of turbulent heat flux in a flow over a heated wavy wall. Int J Heat Mass Transfer 2006;49(19–20):3514–29.
[97] Kuhn S, Wagner C, von Rohr PR. The influence of wavy walls on the transport of a passive scalar in turbulent flows. J Turbul 2008;(9):N10.
[98] De Angelis V, Lombardi P, Banerjee S. Direct numerical simulation of turbulent flow over a wavy wall. Phys Fluids 1997;9(8):2429–42.
[99] Chang K, Hughes TJR, Calo V. Isogeometric variational multiscale large-eddy simulation of fully-developed turbulent flow over a wavy wall. Comput & Fluids 2012;68:94–104.
[100] Cherukat P, Na Y, Hanratty T, McLaughlin J. Direct numerical simulation of a fully developed turbulent flow over a wavy wall. Theor Comput Fluid Dyn 1998;11(2):109–34.
[101] Sun Z, Zhu Y, Hu Y, Zhang S. Direct numerical simulation of a fully developed compressible wall turbulence over a wavy wall. J Turbul 2018;19(1):72–105.
[102] Kuhn S, Kenjereš S, von Rohr PR. Large eddy simulations of wall heat transfer and coherent structures in mixed convection over a wavy wall. Int J Therm Sci 2010;49(7):1209–26.
[103] Tyson C, Sandham N. Numerical simulation of fully-developed compressible flows over wavy surfaces. Int J Heat Fluid Flow 2013;41:2–15.
[104] Hamed AM, Kamdar A, Castillo L, Chamorro LP. Turbulent boundary layer over 2D and 3D large-scale wavy walls. Phys Fluids 2015;27(10):106601.
[105] Akselsen AH, Ellingsen SÅ. Langmuir-type vortices in wall-bounded flows driven by a criss-cross wavy wall topography. J Fluid Mech 2020;900:A19.
[106] Koyama S, Takashima K, Hagiwara Y. Turbulence modification in flow around a periodically deforming film. J Turbul 2007;(8):N19.
[107] Yoon H, El-Samni O, Huynh A, Chun H, Kim H, Pham A, et al. Effect of wave amplitude on turbulent flow in a wavy channel by direct numerical simulation. Ocean Eng 2009;36(9–10):697–707.
[108] Fujii H, Sakurai K, Nakano T, Hagiwara Y. Turbulence structure, friction drag and pressure drag due to turbulent flow over angled wavy surfaces. In: Seventh international symposium on turbulence and shear flow phenomena. Begel House Inc.; 2011.
[109] Ghebali S, Chernyshenko SI, Leschziner MA. Can large-scale oblique undulations on a solid wall reduce the turbulent drag? Phys Fluids 2017;29(10).
[110] Segunda VM, Ormiston SJ, Tachie MF. Experimental and numerical investigation of developing turbulent flow over a wavy wall in a horizontal channel. Eur J Mech B Fluids 2018;68:128–43.
[111] Hamed AM, Castillo L, Chamorro LP. Turbulent boundary layer response to large-scale wavy topographies. Phys Fluids 2017;29(6):065113.
[112] Brodnianská Z, Kotšmíd S. Heat transfer enhancement in the novel wavy shaped heat exchanger channel with cylindrical vortex generators. Appl Therm Eng 2023;220:119720.
[113] Kurtulmuş N, Sahin B. A review of hydrodynamics and heat transfer through corrugated channels. Int Commun Heat Mass Transfer 2019;108:104307.

Physics of Fluids

RESEARCH ARTICLE | JULY 18 2025

# Turbulent separation control on an airfoil surface using a wavy wall

Piotr Kamiński ; Paweł Niegodajew ; Artur Tyliszczak ; Witold Elsner

Check for updates

*Physics of Fluids* 37, 075157 (2025)
https://doi.org/10.1063/5.0268407

View Online
Export Citation

## Articles You May Be Interested In

Aerodynamic performance of a fan with porous-wavy leading edge

*Physics of Fluids* (April 2025)

Effects of the spanwise heterogeneity of a three-dimensional wavy wall on momentum and scalar transport

*Physics of Fluids* (May 2021)

On the airfoil leading-edge noise reduction using poro-wavy leading edges

*Physics of Fluids* (March 2024)

20 July 2025 21:28:44

AIP Publishing

Physics of Fluids

Special Topics Open for Submissions

Learn More

AIP Publishing

Physics of Fluids ARTICLE pubs.aip.org/aip/pof

# Turbulent separation control on an airfoil surface using a wavy wall

Cite as: Phys. Fluids **37**, 075157 (2025); doi: 10.1063/5.0268407
Submitted: 1 March 2025 · Accepted: 26 May 2025 ·
Published Online: 18 July 2025

View Online Export Citation CrossMark

Piotr Kamiński, Paweł Niegodajew,[a] Artur Tyliszczak, and Witold Elsner

## AFFILIATIONS

Department of Thermal Machinery, Czestochowa University of Technology, Al. Armii Krajowej 21, 42-200 Czestochowa, Poland

[a]Author to whom correspondence should be addressed: pawel.niegodajew@pcz.pl

## ABSTRACT

This study investigates the effects of two-dimensional streamwise wall waviness (WW) on turbulent boundary layer separation over an airfoil surface (National Advisory Committee for Aeronautics, NACA 4412) under adverse pressure gradient (APG) conditions. Various WW configurations are analyzed at a friction Reynolds number $Re_\tau = 2500$ to identify the most effective design for delaying flow separation. The most beneficial configuration (W4) is further examined under $Re_\tau = 1200 - 2500$ to assess the sensitivity of its performance to changes in $Re_\tau$. Results show that the effective slope ($ES$) parameter significantly influences separation delay and wall shear stress ($\tau_w$) enhancement. Separation is maximally delayed at $ES \approx 0.17$, beyond which the trend reverses. A strong correlation between the wavelength ($\lambda$) of WW and the downstream shift of the separation point is observed with increased $\lambda$ leading to higher $\tau_w$, while amplitude ($A$) shows no clear correlation. The enhancement of $\tau_w$ is highly dependent on the Reynolds number; the beneficial effects of W4 are prominent at $Re_\tau = 2500$ but diminish at lower values. It is demonstrated that the effectiveness of WW remains consistent whether it is integrated into a flat wall subjected to an external APG source or into a curved surface of an airfoil.

*Published under an exclusive license by AIP Publishing.* https://doi.org/10.1063/5.0268407

20 July 2025 21:28:44

## I. INTRODUCTION

Passive flow control refers to techniques used to influence the behavior of fluid flows without the need for external energy or active input. These methods typically involve modifying the geometry or surface characteristics of a structure to manipulate the flow in a desired way, such as reducing drag, delaying separation, or enhancing mixing. By altering the natural flow patterns, passive flow control aims to improve the efficiency or performance of systems while maintaining simplicity and reliability. These techniques are widely used in engineering applications, including aerospace, automotive, and civil engineering.

Numerous passive flow control strategies have been developed over the years, many of which are now routinely implemented in various aerodynamic and hydrodynamic systems. Among these, dimples have been widely explored for their ability to reduce drag and improve flow dynamics with significant contributions made to understanding their mechanics and application across different domains.[1–6] Vortex generators are another extensively used solution and applied to surfaces such as airfoils, helicopter rotors,[7] wind turbine blades,[8,9] and car bodies,[10] due to their effectiveness in manipulating boundary layers and reducing drag.

In addition to these conventional methods, researchers have increasingly focused on unconventional control techniques, such as modifying the airfoil geometry by adding slots,[11–14] slats,[15,16] guided vanes,[17] and Gurney flaps,[18,19] or integrating protrusions[20] and microcylinders near blade leading edges,[21–24] all of which have shown potential in enhancing aerodynamic performance. Among these, microcylinders have been consistently demonstrated in the literature to offer superior performance compared to some other conventional methods.[22,25,26] Furthermore, leading-edge modifications such as tubercles[27] have been shown to improve post-stall aerodynamics by mitigating flow separation over the airfoil surface.

In parallel to these advancements, novel and creative solutions have recently emerged. One such innovation involves the use of energy concentration pipes, designed to harvest energy from fluid-induced vibrations.[28] Similarly, a passive system based on circular arc geometries and piezoelectric materials has proven effective in capturing vibrational energy,[29] offering a promising approach to energy harvesting in aerodynamic applications. Finally, various rear-flap designs have been successfully applied in the agricultural machinery sector, where they are used to reduce aerodynamic drag on tractors by controlling flow separation at the rear edges.[30]

Furthermore, bio-inspired designs have garnered significant attention with nature offering optimal solutions for various flow scenarios. For example, winglets, inspired by bird wings, have proven


Published under an exclusive license by AIP Publishing

effective in reducing drag and improving lift.[31–36] Similarly, riblets and adaptive flaps, modeled after bird feathers, have demonstrated impressive performance in controlling flow separation and enhancing lift.[37–40] Additionally, microstructures derived from the skin of aquatic animals have been successfully implemented to manage flow separation and reduce drag, providing further evidence of nature's role in advancing passive flow control technologies.[32,41,42]

Recently, Dróżdż *et al.*[43] conducted an experimental study investigating the potential of delaying flow separation using streamwise waviness on wall surfaces. The research demonstrated that adjusting the amplitude ($A$) and wavelength ($\lambda$) of two-dimensional surface waviness could significantly enhance the wall shear stress $\tau_w$, effectively delaying the separation of the turbulent boundary layer (TBL). The authors observed that the amplitude of the waviness should be scaled proportionally to the thickness of TBL ($\delta$) measured for a flat surface under the same conditions. This can be achieved by adjusting $A$ so that $A^+ = u_\tau(x)A/\nu$ (where $u_\tau(x)$ denotes the friction velocity measured for a flat surface under the same conditions and $\nu$ is the kinematic viscosity) remains constant and equal approximately 150. This ensures that the waviness primarily influences the inner layer of TBL without penetrating the outer region. Notably, this method proved effective in fully turbulent flow, where many other passive flow control techniques appear to fail.

While the study by Dróżdż *et al.*[43] demonstrated significant potential for using wavy walls (WW) in controlling TBL separation, the research was limited to wind tunnel experiment, which represents a simplified geometry compared to real-world scenarios. In Ref. 43, the adverse pressure gradient was imposed by suction applied to the upper wall, and separation control was achieved using WW installed on the flat bottom wall of the tunnel. Therefore, the experimental setup did not account for the aerodynamic complexities inherent in real-world applications, where airfoils exhibit curvature and flow characteristics differ from those observed in simplified, flat-plate geometry. Therefore, it is essential to investigate the performance of WW in more realistic conditions, in particular over curved surfaces, such as those found on actual airfoil geometries.

This study addresses the existing gap by evaluating the effectiveness of WW in controlling flow separation on a wing-type surface using large-eddy simulations (LES). Extending the research performed in Ref. 43, the impact of WW on TBL separation is examined. Additionally, while embedding WWs on flat plates preserves symmetric waveforms, with equal crest and trough dimensions, the curvature of the airfoil introduces stretching and asymmetric distortion of their topology with respect to the mean flow. These geometric alterations affect the WW–TBL interaction mechanism compared to flat-plate cases, primarily through: (i) WW-induced modifications to local pressure gradients and (ii) chordwise variations in shear stress distribution specific to the WW configuration. In light of these effects, a dedicated assessment is necessary to determine whether the flow control mechanism observed in the present study differs from that identified in previous flat wall investigations. Furthermore, a broader range of Reynolds number is considered, enabling a more detailed investigation of how the effectiveness of WW varies under different inflow conditions, a scenario that is likely to occur in real-world applications. This, in turn, contributes to a more comprehensive understanding of the practical aerodynamic implications of wall waviness.

This paper is organized such that various WW configurations were initially analyzed on the suction side of a NACA (National Advisory Committee for Aeronautics) 4412 airfoil under APG conditions for a Reynolds number $Re_\tau = u_\tau\delta/\nu = 2500$ with the aim of identifying the most effective design for delaying flow separation. The results obtained for the most effective configuration were then compared with data from a previous study,[44] where the effects of waviness were examined using simplified geometry. Furthermore, this optimal configuration was subsequently evaluated under varying Reynolds numbers to assess the sensitivity of its performance to changes in $Re_\tau$.

## II. RESEARCH OBJECT

This research investigates incompressible, isothermal flow within a computational domain illustrated in Fig. 1. It shows a two-dimensional cross section of a channel, where the horizontal and vertical directions are represented by $x$ and $y$, respectively. The depth of the domain extends to $z = 0.12$ m in the spanwise direction. To establish a well-developed TBL, a ZPG inlet section of 7.5 m in length is positioned upstream of the airfoil section (responsible for the APG), which begins at $x = 0$. To ensure a stable ZPG condition throughout the inlet section, the channel height gradually increases in the streamwise

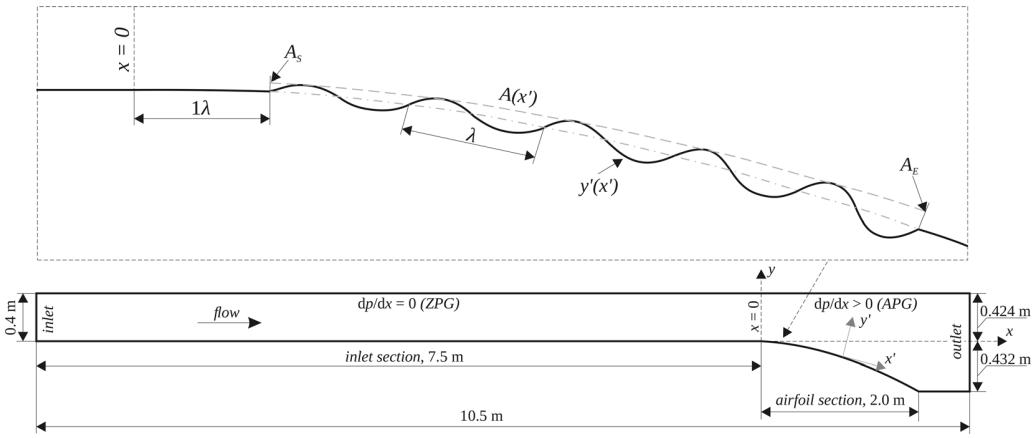



**FIG. 1.** Schematic of the computational domain.

20 July 2025 21:28:44


Published under an exclusive license by AIP Publishing

direction. The length of the airfoil section is 2.0 m. Beyond this, a smooth wall (at a constant $y = -0.432$ m) connects it to the outlet. The curvature responsible for inducing the APG is modeled after the suction side of a NACA 4412 airfoil, inclined at a 5° angle of attack. A local frame of reference, expressed in tangential and normal directions relative to the wing surface (i.e., given by the coordinates $x'$ and $y'$), is also shown in Fig. 1. This frame of reference is used for the spatial averaging of data employed in extracting velocity and fluctuation profiles along the airfoil surface, as well as for computing the characteristic parameters of TBL, such as $\delta$. The waviness begins at a distance of $1.0\lambda$ from $x = 0$ and follows the equation:

$$y'(x') = A(x') \cdot \sin\left(\frac{2\pi}{\lambda} \cdot x'\right), \tag{1}$$

where $\lambda$ is the wavelength and $A(x')$ is the amplitude, which increases in the streamwise direction proportionally to the growth of $\delta$ (as suggested in Ref. 43) and is expressed as

$$A(x') = \frac{A_e - A_s}{(x_e - x_s)^2} \cdot (x')^2 + A_s, \tag{2}$$

where $A_e$ and $x_e$ are the amplitude and streamwise position at the ending point of the wavy wall, while $A_s$ and $x_s$ are the amplitude and streamwise position at the starting point of the wavy wall respectively. Test cases, as well as the variability of $\lambda$, $A_s$, $A_e$, and $N$ are outlined in Table I. To provide more information regarding the slope of the waviness, the parameter $ES$ is provided which is defined as the mean absolute streamwise gradient of the corrugation,[45] according to the relation: $ES = 1/L_w \int_{x_s}^{x_e} (|\partial y'(x')/\partial x'|) dx'$. In this formula, the length of the waviness is denoted by $L_w = N\lambda$. The cases, ranging from W1 to W6, are sorted in ascending order based on $ES$, starting from the smallest value in W1 to the highest in W6. The smooth airfoil surface, i.e., the one without a waviness, is denoted as S.

It is important to note that, although the number of periods $N$ varied across the cases (as detailed in Table I), the waviness terminates approximately at the point where the Clauser–Rotta pressure gradient parameter[46] reaches $\beta = (\delta^*/\tau_w) \cdot (dP/dx) \approx 10$ (where $\delta^*$ is the displacement thickness defined as $\delta^* = \int_0^\delta (1 - \langle U(y') \rangle / U_\infty)\, dy'$, $dP/dx$ the streamwise pressure gradient, $\tau_w$ the wall-shear stress, and $U_\infty$ the freestream velocity). As hinted by Dróżdż *et al.*,[43] ending the wavy wall near $\beta \approx 10$ plays a vital role in increasing $\tau_w$ further downstream. The specific WW geometries examined in this study are illustrated in Fig. 2.

**TABLE I.** Test cases for the present study.

| Case | $\lambda$ (m) | $A_s$ (m) | $A_e$ (m) | $N$ | $ES$ |
|---|---|---|---|---|---|
| S | ... | ... | ... | ... | ... |
| W1 | 0.110 | 0.002 82 | 0.004 64 | 6 | 0.125 |
| W2 | 0.135 | 0.003 66 | 0.006 41 | 5 | 0.136 |
| W3 | 0.150 | 0.004 57 | 0.008 02 | 5 | 0.153 |
| W4 | 0.135 | 0.004 57 | 0.008 02 | 5 | 0.170 |
| W5 | 0.120 | 0.004 57 | 0.008 02 | 6 | 0.183 |
| W6 | 0.110 | 0.004 57 | 0.008 02 | 6 | 0.208 |

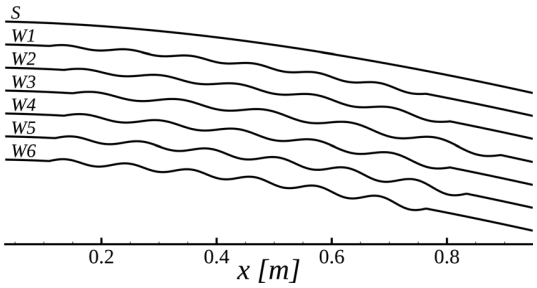



**FIG. 2.** Waviness shapes.

This research is divided into three key phases, each addressing specific aspects of the flow dynamics over a 2D streamwise WW under APG conditions. In the first phase, the study focuses on exploring how different WW configurations affect the flow parameters at a high Reynolds number ($Re_\tau = 2500$), corresponding to an inlet velocity of $U_{in} = 14.42$ m/s. The first goal is to examine the impact of the modified topology of the wavy wall on near-wall flow dynamics, turbulent separation point, and the cross-sectional area of the separation. Moreover, as a second objective, this impact will be compared to the results obtained for a simplified domain (i.e., the one without curvature) examined in Ref. 44. The last phase shifts attention to the effect of Reynolds number variation on flow behavior, using the best-performing WW configuration identified in the first phase. This involves analyzing how different inlet velocities, 5 m/s ($Re_\tau = 1200$), 8 m/s ($Re_\tau = 1700$), and 12 m/s ($Re_\tau = 2300$), in addition to the reference velocity of 14.42 m/s ($Re_\tau = 2500$) explored in the first phase influence flow characteristics, such as the shift in the location of turbulent separation and the behavior of TBL, to determine how the performance of the wavy wall varies with $Re_\tau$.

## III. METHODOLOGY

### A. Numerical model and boundary conditions

The numerical solutions presented in this study are obtained by solving the Navier–Stokes equations for incompressible, constant-density flow within the framework of LES. After applying spatial filtering, these equations take the following form:

$$\frac{\partial \overline{u}_i}{\partial x_i} = 0, \tag{3}$$

$$\frac{\partial \overline{u}_i}{\partial t} + \frac{\partial \overline{u}_i \overline{u}_j}{\partial x_j} + \frac{1}{\rho}\frac{\partial \overline{p}}{\partial x_i} = \frac{\partial}{\partial x_j}\left[\nu\left(\frac{\partial \overline{u}_i}{\partial x_j} + \frac{\partial \overline{u}_j}{\partial x_i}\right)\right] + \frac{\partial \tau_{ij}}{\partial x_j}, \tag{4}$$

where $t$ represents time, $x_i (i = 1, 2, 3) = x, y, z$ denote the spatial coordinates, and the bar symbol signifies the LES filtering operation.[47] The velocity component in the $i$-direction is given by $u_i$, while $p$, $\rho$ correspond to the pressure and density, and $\nu$ denotes the kinematic viscosity. The subgrid stress tensor, expressed as $\tau_{ij} = \overline{u_i u_j} - \overline{u_i}\,\overline{u_j}$ is modeled with the wall-adapting local eddy-viscosity (WALE) model,[48] which is dedicated especially for wall-bounded flows. It is given by $\tau_{ij} = 2\nu_t \overline{S}_{ij}$, where $\overline{S}_{ij}$ denotes the strain rate tensor of the filtered velocity field, and $\nu_t$ the subgrid viscosity, defined as

$$S_{ij}^d = \frac{1}{2}(\overline{g}_{ij}^2 + \overline{g}_{ij}^2) - \frac{1}{3}\delta_{ij}\overline{g}_{kk}^2, \tag{5}$$

20 July 2025 21:28:44


Published under an exclusive license by AIP Publishing

$$\nu_t = (C_w\Delta)^2 \frac{(S_{ij}^d S_{ij}^d)^{3/2}}{(\overline{S}_{ij}\overline{S}_{ij})^{5/2} + (S_{ij}^d S_{ij}^d)^{5/4}}, \quad (6)$$

where $\overline{g}_{ij} = \frac{\partial \overline{u}_i}{\partial x_j}$ represents the gradient components of the filtered velocity field, $C_w = 0.325$ is the model constant,[48] and $\Delta = V^{1/3}$ denotes the LES filter width, with $V$ being the local cell volume.

The computations were performed with the help of ANSYS Fluent software which, in our previous work,[44] was shown to correctly predict the relation between the modified wall topology and the near–wall flow. The spatial discretization of the convective terms of the Navier–Stokes equations was performed by applying the second order bounded central differencing scheme and second order central scheme for the viscous terms. The SIMPLE algorithm with the second order discretization of the pressure gradient was used for the pressure–velocity coupling. The time integration was performed using the second order implicit method. In all analyzed cases, the initial velocity in the computational domain was set to zero. A transient phase, until a fully turbulent flow was developed, lasted for approximately 4.37 s for $Re_\tau = 2500$ (the highest), which corresponds to 6 flow-through time units defined as $t_{FT} = L_x/U_{in} = 0.728$ s. For $Re_\tau = 1200$ (the lowest), the transient phase took three flow-through time units, while $t_{FT} = 2.1$ s. In each considered case, the time-averaging procedure lasted for the next 10 $t_{FT}$. Additionally, the solutions were spatially averaged in the $z$-direction by collecting and averaging data extracted from 11 uniformly spaced cross sections. This led to a good convergence of the time-averaged solutions, which was checked by comparing the results at the time instants $8t_{FT}$ and $10t_{FT}$. For the highest $Re_\tau$, a single run typically required approximately 30 days of continuous computations on a computer cluster with 144 CPUs for the densest mesh (see Sec. III B).

In this study, the inlet boundary condition, positioned at $x = -7.5$ m (see Fig. 1), was defined assuming a uniform rectangular velocity profile for each of the four examined $Re_\tau$ values. Turbulent fluctuations were generated using the Fourier-based synthetic turbulence generation (STG) method.[49,50] In this approach, the velocity fluctuation field $\boldsymbol{u}_i'(\boldsymbol{r}, t)$ is constructed as a superposition of weighted spatiotemporal Fourier modes, scaled such that the resulting turbulent kinetic energy $K_t$ at the inflow matches the prescribed mean kinetic energy at the inlet boundary

$$\boldsymbol{u}_i'(\boldsymbol{r}, t) = 2K_t \sum_{n=1}^{N} \sqrt{q_n}\left[\boldsymbol{\sigma}^n \cos\left(k^n \boldsymbol{D}^n \cdot \boldsymbol{r} + \phi + s^n \frac{t}{\tau}\right)\right], \quad (7)$$

where: $N$ denotes the number of Fourier modes; $q^n$ the normalized amplitude of mode $n$; $k^n$ the magnitude of the wave number vector associated with mode $n$; $\boldsymbol{d}^n$ the randomly oriented unit direction vector; $\boldsymbol{\sigma}^n$ the unit vector normal to $\boldsymbol{d}^n$; $\phi^n$ the phase of mode $n$; and $s^n$ the non-dimensional frequency of mode $n$. The global time scale $\tau$ depends on the hydraulic diameter, which, in this case, is equal to the domain height $H = 0.4$ m. The turbulence intensity at the inlet, needed to calculate the turbulent kinetic energy $K_t = \frac{3}{2}(T_i U_{in})^2$ with the assumption of fluctuations isotropy, was specified as $T_i = 0.7\%$. The 7.5 m long inlet section led to a well–developed TBL. The left and right boundaries, spaced by $z = 0.12$ m, were treated as periodic. The bottom and upper walls were treated as a non-slip wall and a constant pressure (101 325 Pa) was assumed at the outlet.

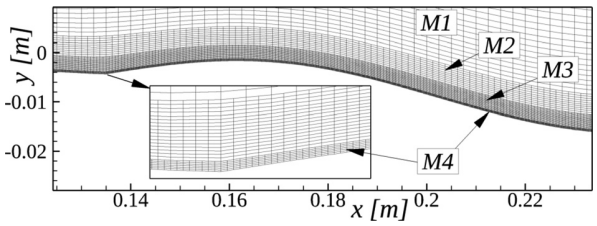



FIG. 3. Computational mesh shown at the first wave of wavy wall denoted as W3.

## B. Computational mesh

The computational mesh employed in the present study is presented in Fig. 3. It comprises a base mesh, labeled M1, along with three progressively refined regions. Although it is not shown in the presented figure, we note that the subsequent refinements start at some distance from the wall and extend up to the wall surface. Each refinement involves subdividing the cells of the previous layer into eight smaller elements. The meshes resulting from these refinements are denoted as M2, M3, and M4.

The numbers of cells that computational meshes consist of are provided in Table II. The study primarily focuses on the case with the highest $Re_\tau$ value of 2500, which is expected to be the most computationally demanding and to require the densest mesh in the near-wall region. To show the dependence of the mesh resolution close to the wall on the number of cells, Table II also provides the near-wall cell sizes expressed in viscous units, e.g., $\Delta y^+ = \Delta y_w \cdot u_\tau/\nu$ ($\Delta y_w$—the near-wall cell height), as usually reported in LES studies. The meshes are uniform in both the $x$ and $z$ directions with the number of cells selected such that $\Delta x^+ = \Delta z^+$. Note, that along the wall, the flow conditions change and thus $\Delta x^+$, $\Delta y^+$, and $z^+$ vary. The numbers in Table II refer to the maxima of $\Delta x^+$, $\Delta y^+$, and $\Delta z^+$ found along the entire wall. It can be seen, that their values on meshes M3 and M4 fall well in the range accepted for LES of wall-bounded flows.[51]

As mentioned in Sec. II, a part of the study focuses on evaluating the relationship between $Re_\tau$ and the impact exerted by the wavy wall on the near-wall flow. Accordingly, the details of the meshes selected for cases with considered $Re_\tau$ values are given in Table III.

## C. Computational model validation

The numerical procedure applied in this study has already been rigorously validated in a previous investigation,[44] where the LES results were compared with experimental data obtained for an APG channel configuration with a flat wall with a section of two-dimensional streamwise waviness. This analysis was performed for $Re_\tau = 2500$ and

TABLE II. Parameters of the computational meshes for $Re_\tau = 2500$. The cell sizes at the wall are given in viscous units.

| Mesh | No. of cells | $\Delta y^+_{MAX}$ | $\Delta x^+_{MAX}$ | $\Delta z^+_{MAX}$ |
|---|---|---|---|---|
| M1 | $32.2 \times 10^6$ | 9.87 | 76.44 | 76.44 |
| M2 | $46.3 \times 10^6$ | 5.01 | 40.95 | 40.95 |
| M3 | $102.8 \times 10^6$ | 2.48 | 21.71 | 21.71 |
| M4 | $170.5 \times 10^6$ | 1.27 | 10.47 | 10.47 |

20 July 2025 21:28:44


Published under an exclusive license by AIP Publishing

**TABLE III.** The cell sizes at the wall expressed in viscous units for all of $Re_\tau$ considered in this study.

| $Re_\tau$ | Mesh used | $\Delta y^+_{MAX}$ | $\Delta x^+_{MAX}$ | $\Delta z^+_{MAX}$ |
|---|---|---|---|---|
| 2500 | M4 | 1.27 | 10.47 | 10.47 |
| 2300 | M4 | 1.15 | 8.77 | 8.77 |
| 1700 | M3 | 1.57 | 12.61 | 12.61 |
| 1200 | M3 | 1.09 | 8.73 | 8.73 |

involved comprehensive tests on the effects of mesh density and time step size, demonstrating excellent agreement between the mean velocity and fluctuation profiles obtained in the simulations and those measured experimentally. Given the similarity in complexity between the present configurations and those from Ref. 44, it is reasonable to expect comparable accuracy in the simulations reported here. However, to further validate the robustness of the applied solution method across different Reynolds numbers, the results obtained presently for $Re_\tau = 2500$, 2300, 1700, 1200 are compared against the DNS (direct numerical simulation) data provided by Sillero *et al.*[52] for ZPG conditions. This comparison is depicted in Fig. 4, where the profiles of the streamwise velocity (upper row) and the fluctuation components (lower row) are presented. Additionally, for $Re_\tau = 2500$, a grid independence analysis is performed based on the solutions obtained on the meshes M1 to M4. In general, the present LES results exhibit good agreement with the DNS data, although certain discrepancies are evident, especially for $Re_\tau \geq 1700$. In particular, the streamwise velocity values within the range $10^{-2} < y/\delta < 10^{0}$ are larger compared to DNS solutions. Moreover, the agreement of the streamwise fluctuation component changes depending on the $y/\delta$ location. In the range $y/\delta > 10^{-1}$ the DNS profiles are underpredicted, whereas the peak of the fluctuations near $y/\delta = 6 \times 10^{-3}$ is overestimated and occurs slightly upper from the wall. In contrast to the under- and overprediction observed in the streamwise velocity fluctuations, the wall-normal and spanwise components are systematically underpredicted. The observed discrepancies are, however, typical for the LES results and have been often reported in the literature.[53–55] In particular, in the

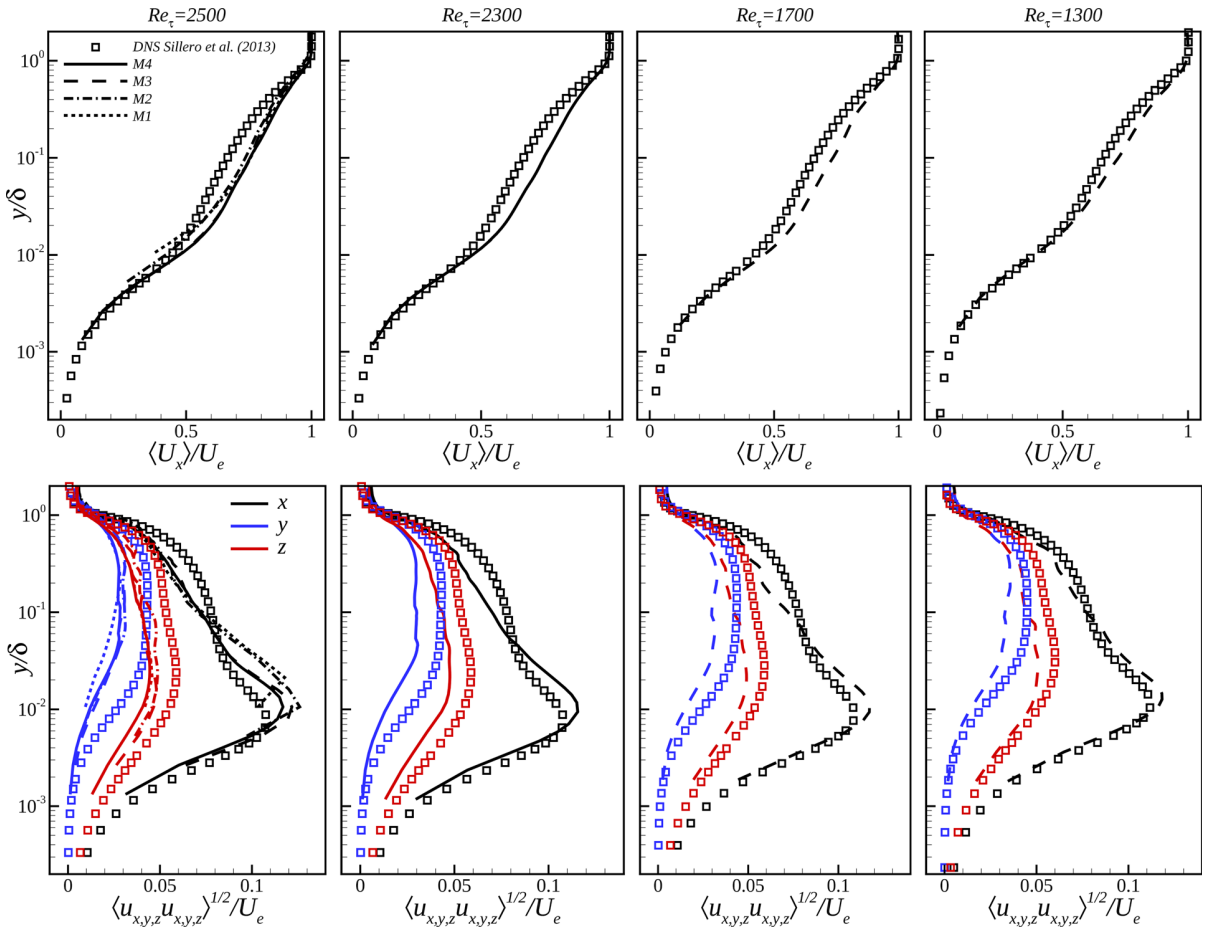



**FIG. 4.** Profiles of streamwise velocity and fluctuation components (streamwise, wall–normal and spanwise) compared to DNS.[52] Columns from left to right denote $Re_\tau$ considered in present study.

20 July 2025 21:28:44


Published under an exclusive license by AIP Publishing

LES study by Vinuesa *et al.*[56] performed using the Nek5000 code (https://nek5000.mcs.anl.gov/) for flow around an airfoil, the observed discrepancies were very similar to those reported here. In summary, insights from previous studies and the present comparisons suggest that the degree of discrepancy remains within an acceptable range, allowing for a reliable parametric analysis of the impact of waviness on flow dynamics.

Regarding the influence of mesh density on the results obtained for $Re_\tau = 2500$, it can be seen that increasing the number of cells does not significantly improve solution accuracy. The solutions obtained for meshes M3 and M4 are nearly identical, indicating that further refinement would not yield noticeable improvement, especially for lower $Re_\tau$, where the impact of mesh density is generally expected to be smaller. Hence, in the simulations performed for the cases at $Re_\tau = 2300$ and $Re_\tau = 2500$, the mesh M4 was used, as it ensures better near-wall resolution (see $\Delta y^+$ values in Tables II and III), while for the cases at $Re_\tau = 1700$ and $Re_\tau = 1200$, the mesh M3 was employed. This was motivated by the fact that $\Delta y^+$ values on this mesh for $Re_\tau = 1700$ and $Re_\tau = 1200$ are comparable to those obtained on the mesh M4 for $Re_\tau = 2300$ and $Re_\tau = 2500$.

## IV. RESULTS

The analysis of the results begins with the evolution of the TBL parameters presented in Fig. 5, which illustrates $\beta$ (a); the growth of $\delta$ relative to $\delta_0$ (measured at $x = 0$), expressed as $\delta/\delta_0$ (b); $Re_\tau$ (c); and the Reynolds number based on the momentum thickness, $Re_\theta = U_\infty \theta/\nu$ (where $\theta = \int_0^\delta (\langle U(y')\rangle/U_\infty)(1 - \langle U(y')\rangle/U_\infty), dy')$ (d), all evaluated along the airfoil section for the smooth wall (case S). In general, it is observed that for all cases, the pressure gradient parameter $\beta$ remains relatively constant up to $x \approx 0.8$ m, beyond which its noticeable increase is observed. This behavior is attributed to the increasing streamwise pressure gradient ($dP/dx$), induced by the progressively expanding channel height in the airfoil section. As $x$ grows, the resulting deceleration of the flow leads to a reduction in wall shear stress, eventually reaching $\langle \tau_{w,x} \rangle \approx 0$, indicating the onset of TBL separation. Furthermore, beyond $x \approx 0.8$ m, differences between the analyzed cases become apparent. Specifically, the influence of APG on TBL development, as reflected by the rise in $\beta$, becomes more pronounced with decreasing $Re_\tau(x = 0)$. This suggests that at lower Reynolds numbers, the boundary layer possesses less momentum when entering the airfoil section, leading to its higher susceptibility to APG and thus separation occurring further upstream. The growth of $\delta$ [Fig. 5(b)] remains relatively consistent across all $Re_\tau$ values up to $x \approx 0.6$ m. Beyond this point, it accelerates more rapidly with decreasing $Re_\tau$, with the highest growth rate observed for $Re_\tau = 1200$ and the lowest for $Re_\tau = 2500$. This indicates that, as $Re_\tau$ increases, TBL develops more steadily. Furthermore, the evolution of $Re_\tau$ along the airfoil surface shows an increasing trend up to approximately $x \approx 0.6$ m, beyond which the opposite occurs. This trend is consistent across all four flow cases and may be attributed to the more rapid growth of $\delta$ compared to the decrease in $u_\tau$ in the early part of the airfoil section, particularly for the case with $Re_\tau = 2500$. Simultaneously, $Re_\theta$ displays a continuous increase along the streamwise direction. However, despite a similar rate of growth across the four cases, a notable reduction in $Re_\theta$ is observed with decreasing $Re_\tau$.

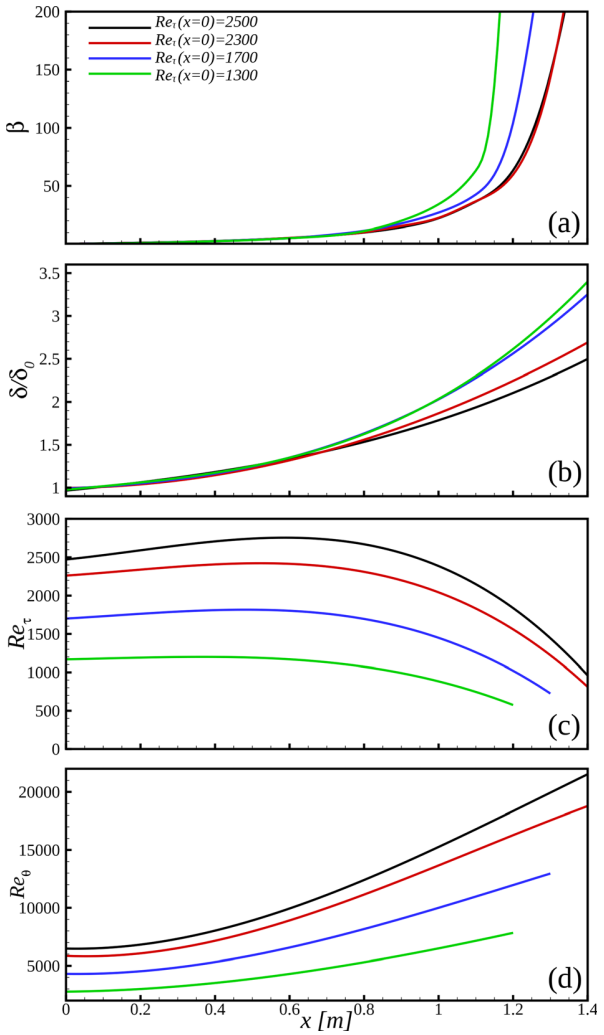



**FIG. 5.** The evolution of $\beta$ (a), $\delta/\delta_0$ (b), $Re_\tau$ (c), and $Re_\theta$ (d) over the smooth airfoil section (case S) for various Reynolds numbers.

### A. Effect of the waviness shape

In this section, we examine the effects of all WW topologies listed in Table I on the flow at the highest Reynolds number considered, i.e., $Re_\tau = 2500$. The presentation of results begins with general observations, particularly emphasizing the impact of each WW configuration on turbulent kinetic energy (TKE). Figure 6 provides contour maps of TKE for cases S and W1–W6. Two key observations arise. First, a large recirculation area forms downstream of $x \approx 1.5$ m, schematically marked with streamlines on a single figure for the smooth airfoil configuration (S). Just before the onset of this recirculation zone, a notable increase in TKE emerges near the region approaching the point of TBL separation, specifically at $1.2\,\text{m} \leq x \leq 1.5$ m. This rise in TKE is characteristic for separating TBLs and recirculating flows. Furthermore, for the wavy configurations, an additional increase in the area occupied by elevated levels of TKE is observed, originating from

20 July 2025 21:28:44


Published under an exclusive license by AIP Publishing

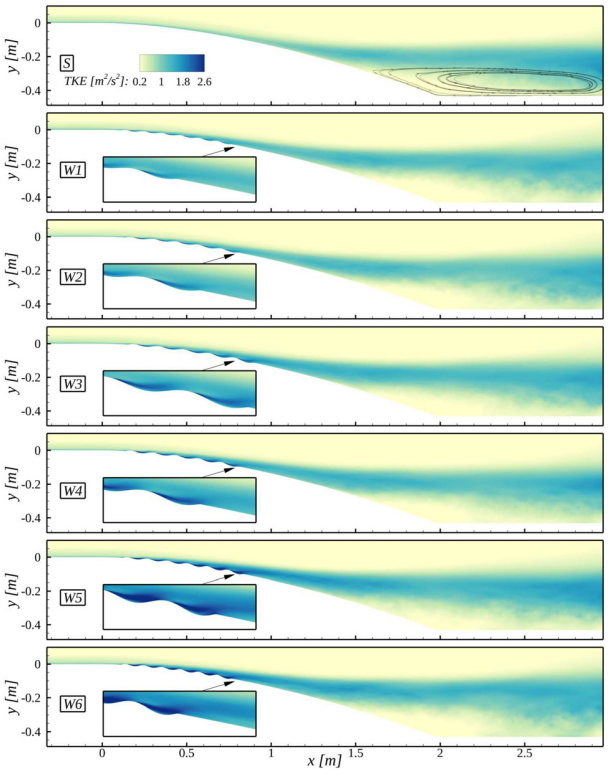



**FIG. 6.** Contour maps of TKE for all of the tested configurations.

the region of waviness. This can be seen in more detail in the close-up subfigures. This phenomenon appears to be dependent on ES, since the most pronounced increase in TKE can be observed in cases with the highest value of this parameter, namely W5 and W6.

To provide deeper insight into the dynamics observed previously, Fig. 7 illustrates the TKE profiles measured at $x = 2.0$ m, highlighting the complex behavior in the wake region downstream of the airfoil section. The comparison is drawn between the smooth surface (S) and the configurations that, as shown later in the paper, result in the most significant enhancement and reduction of $\langle \tau_w \rangle$, namely, W4 and W6, respectively. In the near-wall region, for $y/\delta < 0.05$, both W4 and W6 display reduced TKE compared to S, indicating a suppression of turbulence close to the surface. However, at $0.05 < y/\delta < 0.2$ TKE for W6 is growing with $y/\delta$ and at $y/\delta \approx 0.15$ is the highest. Farther away from the wall, particularly at $y/\delta \approx 0.5$, a sharp peak in TKE emerges across all configurations, indicating a region of intensified turbulence within the separated shear layer. This peak likely arises from shear layer instabilities that develop near the separated flow region, contributing to increased turbulence at its edge. Interestingly, for case W4, the level of TKE within the peak is only slightly elevated compared to that of S. However, configuration W6 stands out considerably above both S and W4, indicating stronger turbulent structures. Despite the reduced TKE within the core of the separation, the heightened turbulence at the shear layer suggests that local instabilities could dominate the flow behavior, potentially impacting the aerodynamic efficiency.

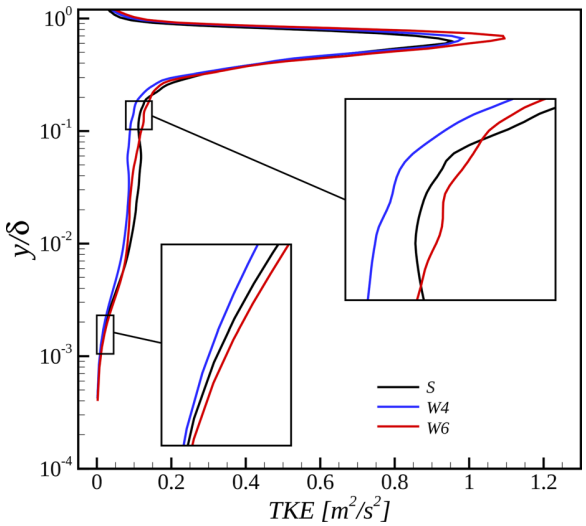



**FIG. 7.** Profiles of TKE extracted at $x = 2.0$ m, i.e., just at the ending of the airfoil section. Configurations S, W4 and W6.

In our previous works,[43,44] it was demonstrated that a wavy wall can be employed to postpone the onset of turbulent separation. However, a particularly intriguing issue is whether and to what extent the area of separation can be controlled by the introduction of waviness. This is illustrated in Fig. 8, which presents contour maps of $\langle U_x \rangle$ for all tested WW configurations. The regions with negative values of $\langle U_x \rangle$ are shaded gray to highlight the extent of the separation area. A red line marks the location of the separation point found for the smooth airfoil (S), while a black line (shown only for case S) indicates the boundary at $x = 2.0$ m, used for computing the cross-sectional area of the separation $A_{sep.}$, which is further discussed in detail. Both the detachment location and $A_{sep.}$ are notably influenced by the wavy wall. In certain cases, the waviness leads to a delayed onset of separation and a reduction in its area, while in others, the opposite effect is observed. The most significant reduction in the separation area $A_{sep.}$ occurs in configuration W4, where the waviness effectively postpones separation. In contrast, configuration W6 exhibits the largest increase in $A_{sep.}$, with an earlier onset of separation compared to the smooth airfoil case.

The analysis discussed in the previous paragraph addressed time–averaged quantities and the global effects exerted by the WW on the flow. To gain more detailed insight, Fig. 9 presents the instantaneous distributions of the streamwise component of wall shear stress ($\tau_{w,x}$) along the entire wavy surface, in the form of contour maps, for three selected cases: S, W4, and W6. Regions where $\tau_{w,x} \leq 0$, indicating temporarily separated flow, are shaded in blue. For reference, the locations of time–averaged detachment ($\langle \tau_{w,x} \rangle = 0$) are marked by a gray line for each configuration. Beginning with the waviness region, one major observation stands out. Namely, in the case of W4 (between $0.25\ \text{m} \leq x \leq 0.55$ m), large areas of very high and low $\tau_{w,x}$ (dark red and blue, respectively) appear on the wave crests and troughs. This can be seen in detail in zoom A, which includes a schematic illustration of the wavy wall shape. These variations result from flow acceleration on the uphill surface (where $\tau_{w,x}$ increases sharply) and deceleration on

20 July 2025 21:28:44


Published under an exclusive license by AIP Publishing

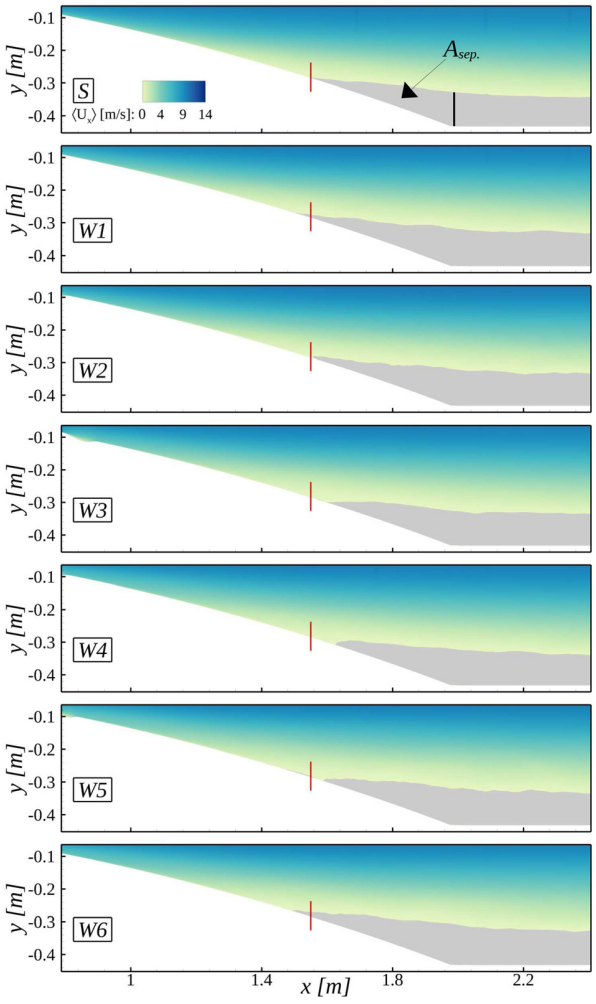



**FIG. 8.** Contour maps of $\langle U_x \rangle$ for all tested configurations. The area with negative values of $\langle U_x \rangle$ is greyed–out to highlight the separation bubble. Red line marks the location of the separation point for the smooth airfoil (S).

the downhill surface (where $\tau_{w,x}$ falls below zero, indicating flow separation). This effect is more pronounced for configuration W6, which exhibits a higher *ES* than W4 (see Table I). This observation aligns with our previous study,[44] where it was examined in further detail, hence the reader is referred to that work for additional discussion. In the region downstream of the waviness another important observation is that small, instantaneous separation zones (blue color) begin to form at $x \approx 1.0$ m in all three cases (for example, see zoom B for the S configuration). These separations occur approximately 0.5 m upstream of the time–averaged detachment locations, which are indicated by gray lines and correspond to the data shown in Fig. 8. This is a well-known phenomenon in the literature, first described by Simpson.[57] These initially appearing spots of negative wall shear stress are associated with backflow events induced by coherent structures descending from the outer region of the boundary layer toward the wall. As the flow progresses further downstream, the extent of negative $\tau_{w,x}$ increases, leading to fully separated flow in the region at $x > 1.5$ m. This is consistent with previous findings,[44] which analyzed the separation region on the downhill side of the wavy surface. It was found that, despite the presence of temporary separation bubbles, time-averaged separation does not occur unless the probability of exceedance, $P_e$, based on spanwise distributions of $\tau_{w,x} \leq 0$, reaches 50%. In the W6 configuration, where separation occurs furthest upstream, a greater number of local bubbles with $\tau_{w,x} \leq 0$ are observed earlier compared to the smooth airfoil configuration (S). The opposite trend is observed for W4.

To provide an in-depth quantitative analysis of how the various wavy wall configurations influence separation, Fig. 10 illustrates the effect of *ES* on the displacement of the separation point (a) and the cross-sectional area of the separation bubble (b). Additionally, the relationship between $\Delta A_{sep.}$ and $\Delta x_{sep.}$ is presented in Fig. 10(c). By examining $\Delta x_{sep.}(ES)$, a clear trend emerges. Separation is progressively delayed (i.e., increasing $\Delta x_{sep.}$) up to an *ES* value of approximately 0.17. However, as *ES* increases beyond this point, the opposite trend is observed, with the separation point shifting upstream, as seen in cases W5 and W6. The most advantageous configuration is W4, characterized by $ES = 0.17$. The shift in $\Delta x_{sep.}$ naturally affects the cross-sectional area of the separation bubble, as illustrated in Fig. 10(b), where $\Delta A_{sep.}$, the change in area relative to the smooth airfoil configuration, is depicted. The cross-sectional area of separation $A_{sep.}$ was

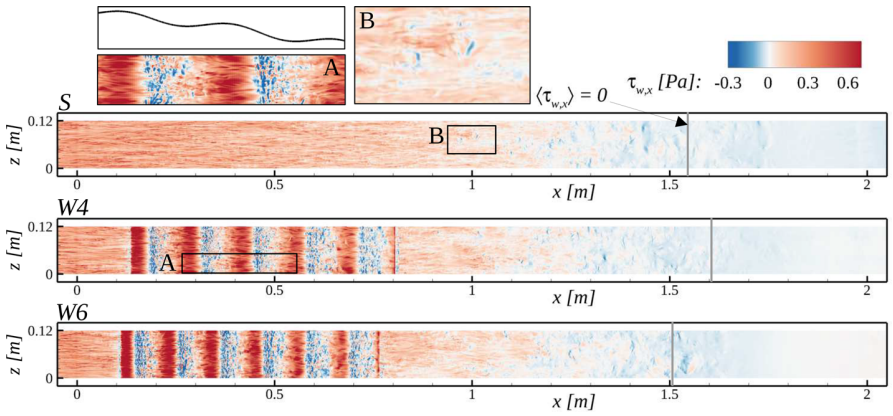



**FIG. 9.** Contour maps of $\tau_{w,x}$ for F, W4 (best), W6 (worst) configurations. Top view of the airfoil section, i.e., 0 m $\leq x \leq$ 2 m.

20 July 2025 21:28:44


Published under an exclusive license by AIP Publishing

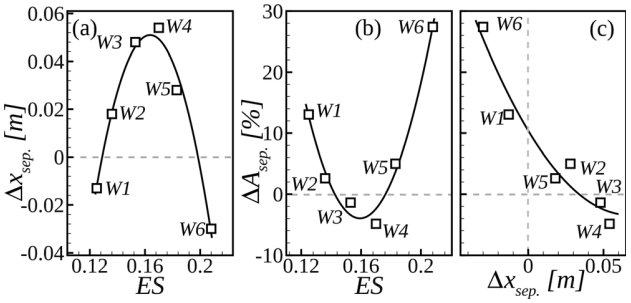



**FIG. 10.** Effect of *ES* on the change in location of separation point (a) and on the cross–sectional area of the separation bubble (b). The relationship between $\Delta A_{sep.}$ and $\Delta x_{sep.}$ (c).

computed based on the gray regions indicating $\langle U_x \rangle \leq 0$ in Fig. 8, and measured up to $x = 2.0$ m, corresponding to the end of the airfoil section. The plot of $\Delta A_{sep.}(ES)$ reflects a related effect to that seen in Fig. 8, where the shift in the flow separation point corresponds to a reduction in the separation bubble area. In both cases, $\Delta A_{sep.}$ and $\Delta x_{sep.}(ES)$ can be approximated by second-order polynomials. Figure 10(c) demonstrates that $\Delta A_{sep.} \sim (\Delta x_{sep.})^2$, indicating that any upstream displacement of the separation point results in a quadratic increase in the bubble area.

To complement the results presented in Fig. 10, Fig. 11 illustrates the effect of key wavy wall parameters such as amplitude (a), wavelength (b), and *ES* (c) on the wall shear enhancement, $\Delta\langle\tau_w\rangle$. This quantity is computed as a surface integral of $\tau_w$ over the region downstream of the waviness, i.e., $0.95\,\text{m} \leq x \leq 1.4$ m. First, upon evaluating the impact of amplitude [Fig. 11(a)], it is observed that there is no clear correlation between the amplitude $A$ and the wall shear stress. In contrast, when considering $\Delta\langle\tau_w\rangle = f(\lambda)$, a correlation is observed between $\lambda$ and $\Delta\langle\tau_w\rangle$. Based on the present data, it can be observed that the wall shear stress increases with $\lambda$. Furthermore, the plot of $\Delta\langle\tau_w\rangle = f(ES)$ follows a similar pattern to that observed in Fig. 10, and the relationship can again be approximated by a second-order polynomial. Notably, $\Delta\langle\tau_w\rangle$ grows with ES, reaching a maximum at $ES = 0.17$, beyond which it begins to decline.

Figure 12 presents the wall-normal profiles of velocity and its fluctuation measured at $x = 1.1$ m. To highlight the best-performing (W4) and worst-performing (W6) configurations, they are marked

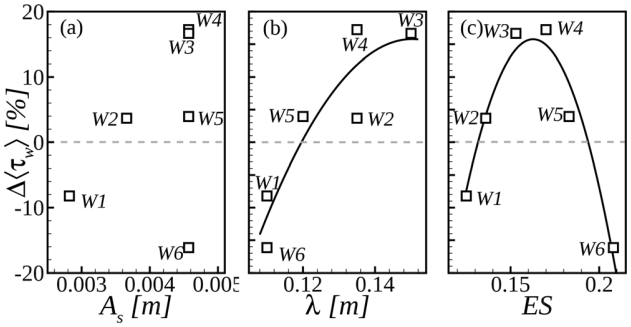



**FIG. 11.** Effect of wave amplitude (a), wavelength (b) and *ES* (c) on the wall shear enhancement.

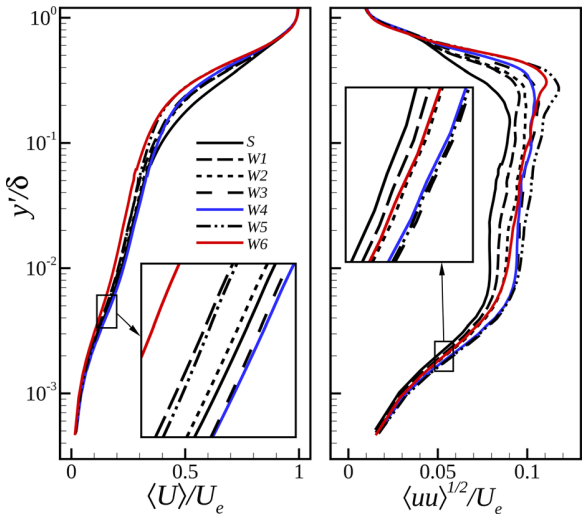



**FIG. 12.** Wall-normal profiles of velocity and fluctuations for all considered cases taken at $x = 1.1$ m. Best (W4) and worst (W6) configurations highlighted with blue and red color, respectively.

with blue and red, respectively. The profiles are normalized by the boundary layer thickness, $\delta$, defined as the distance from the wall to the point where the velocity $U_e$, equals 99% of $U_{x,\infty}$ at a given streamwise position. It is evident that the most favorable case in terms of $\Delta\langle\tau_w\rangle$ enhancement, i.e., W4 (blue solid line), produces the highest near-wall velocity, whereas the worst configuration W6 (red solid line) exhibits the opposite behavior. Notably, W3 shows near-wall values of $\langle U \rangle / U_e$ comparable to W4, which is consistent with the observations in Fig. 11. In the outer region, i.e., $0.1 < y'/\delta < 0.8$, all WW configurations tend to reduce the flow velocity, thereby generating a steeper velocity gradient. Examination of the fluctuation profiles ($\langle uu \rangle^{1/2} / U_e$) reveals several noteworthy observations. For the S configuration, two distinct peaks are identified at $y'/\delta \approx 8 \times 10^{-3}$ and $y'/\delta \approx 1.5 \times 10^{-1}$, corresponding to the inner and outer maxima, respectively.[58] These peaks also appear in the spectrograms presented later in Fig. 13. However, when waviness is introduced, the inner peak tends to be overshadowed due to enhanced fluctuations in the outer region, which is an effect observed across all WW configurations. The increase in $\langle uu \rangle^{1/2} / U_e$ in this location is most likely associated with the steeper velocity gradient at $y'/\delta > 10^{-1}$, which becomes more pronounced with increasing *ES*. In general, steeper velocity gradients intensify shear, which is a primary mechanism for turbulence production.[59] Furthermore, the observed enhancement of the outer peak of $\langle uu \rangle^{1/2} / U_e$ appears to exhibit characteristics similar to those found in TBLs subjected to progressively stronger APG.[60] Interestingly, while the configuration W4 shows mid-range fluctuation levels overall, it exhibits nearly the largest values of $\langle uu \rangle^{1/2} / U_e$ near the wall. In contrast, W6 displays an inverse trend, with large fluctuations in the outer region and relatively low values near the wall. An increase in near-wall fluctuations observed for the W4 case can be attributed to an elevated rate of momentum transfer normal to the surface, caused by the downwash of high-momentum fluid toward the wall by large-scale vortical structures from the outer layer. This phenomenon is also known as the

20 July 2025 21:28:44


Published under an exclusive license by AIP Publishing

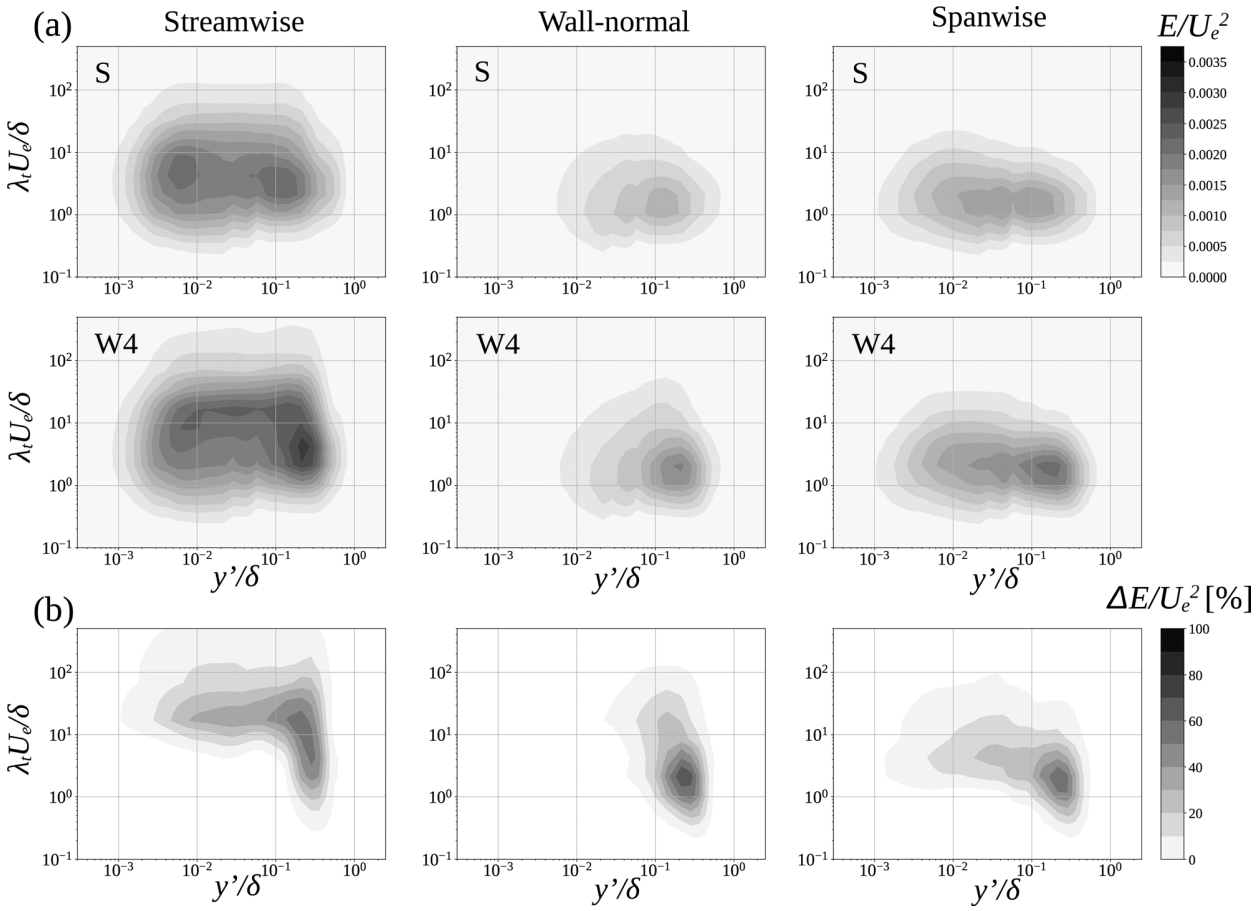



**FIG. 13.** Energy spectra ($E$) computed based on the streamwise, wall-normal and spanwise components of velocity (consecutive columns) scaled by $U_e$ for S and W4 configurations (a). The difference in $E/U_e^2$ between S and W4 computed relative to the maximum value of $E/U_e^2$ reported for S (b).

amplitude modulation process.[58,61–63] In Ref. 44, it has been shown that the wavy wall generates regions of high-speed flow within TBL. These regions, particularly in the downstream vicinity of WW, lead to an intensified near-wall turbulence which in turn, as suggested by Elnahhas and Johnson,[64] may contribute to the $\tau_w$ increments.

While the fluctuation profiles in Fig. 12 provide valuable insight into energy content in TBL, more details can be obtained by examining energy spectra ($E$), presented in Fig. 13(a). They are computed based on the streamwise, wall-normal and spanwise velocity components and scaled by $U_e^2$, for the S and W4 configurations. For the sake of simplicity, when referring to spectra computed based on specific velocity components, we will use terms such as streamwise, wall-normal or spanwise spectra. The results are presented in a normalized coordinate system, where both the timescale $\lambda_t$ and the wall-normal distance are scaled by $U_e$ and $\delta$. Such scaling was employed by Ganapathisubramani *et al.*,[65] who noted that, to distinguish between large and small scales, the threshold value of $\lambda_t U_e/\delta$ should be selected such that it barely touches the edge of the outer peak. In the present study, we adopt $\lambda_t U_e/\delta = 2$ as the cutoff between large and small scales, consistent with Ref. 65, which satisfies the required criterion.

The analysis commences with the streamwise spectra. A characteristic of the smooth wall is the occurrence of two distinct peaks of $E/U_e^2$, a characteristic feature of APG boundary layers,[66] also seen in Fig. 12, at $y'/\delta \approx 6 \times 10^{-3}$ and $y'/\delta \approx 0.15$. In the case W4, such a distinction does not occur, and the region of high $E/U_e^2$ is relatively continuous. It can be seen that in both cases, non-zero $E/U_e^2$ spans over a similar $\lambda_t U_e/\delta - y'/\delta$ region, though the local $E/U_e^2$ values differ significantly. To highlight the variation in the spectra computed for the S and W4 cases, Fig. 13(b) presents the difference in $E/U_e^2$ calculated for these configurations, normalized by the maximum $E/U_e^2$ value found for the S case. A notable enhancement of the outer maximum energy is observed for W4 relative to S. It spans over a broad range of wavelengths ($1 \times 10^0 < \lambda_t U_e/\delta < 8 \times 10^1$) and reaches its maximum value of $\sim 70\%$ at $\lambda_t U_e/\delta \approx 10^1$ [see Fig. 13(b)]. Additionally, a distinct shift of the outer maximum occurs, moving from $y'/\delta \approx 1.5 \times 10^{-1}$ for S to $y'/\delta \approx 2.5 \times 10^{-1}$ for W4. A notable $\Delta E/U_e^2$ rise is observed for $\lambda_t U_e/\delta \approx 2 \times 10^1$ indicating elevated large-scale activity throughout the TBL thickness. Small-scale activity associated with $\lambda_t U_e/\delta < 2$, around $4 \times 10^{-1} < \lambda_t U_e/\delta < 2 \times 10^0$ also increases. This effect, however, is limited mainly to the upper part

20 July 2025 21:28:44


Published under an exclusive license by AIP Publishing

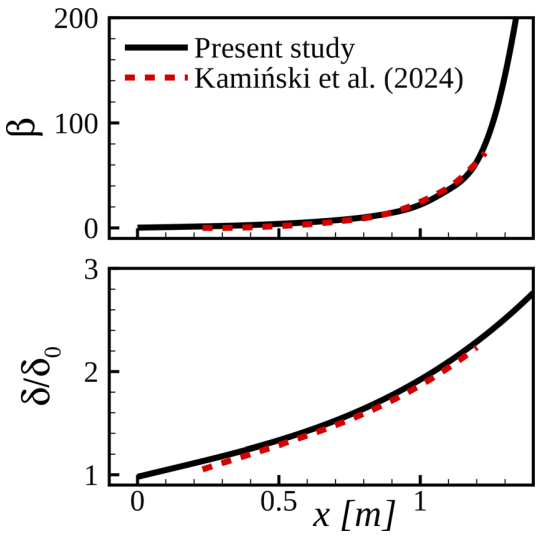



**FIG. 14.** Profiles of $\beta$ and $\delta/\delta_0$ for cases S and W4 compared to data from Kamiński *et al.*[44]

of TBL ($1 \times 10^{-1} < y'/\delta < 6 \times 10^{-1}$), without the amplification of smaller wavelengths near the wall as noted by Dróżdż *et al.*[43] Hence, it can be concluded that the waviness W4 tends to increase $E/U_e^2$ along the entire TBL with the large-scale motion enhanced more uniformly.

In the case of the wall-normal spectra, only a single peak can be identified. Such behavior is expected, as the wall-normal component of velocity is typically negligible in the near-wall region for TBLs under APG.[56] A slight shift in the location of the outer peak is also observed—from $y'/\delta \approx 2.5 \times 10^{-1}$ for S to $y'/\delta \approx 1.5 \times 10^{-1}$ for W4, similar to the trend seen in the streamwise spectra. Moreover, at the same location, an increase in $E/U_e^2$ is noted, as highlighted by the difference spectra [Fig. 13(b)], where the enhancement at $y'/\delta \approx 2.5$ reaches up to 80% locally. This increase is most pronounced at $\lambda_t U_e/\delta \approx 2 \times 10^0$, corresponding to the boundary between large- and small-scale motions, and extends up to $\lambda_t U_e/\delta \approx 10^2$, indicating elevated large-scale activity. The effect of the waviness on the wall-normal spectra appears to be confined to the outer region of TBL, specifically for $y'/\delta > 5 \times 10^{-1}$.

The spanwise spectra exhibit a trend very similar to that of their wall-normal counterpart. Specifically, only one distinct peak is observed, with an identical wall-distance shift induced by W4. The main difference is that non-zero values of $E/U_e^2$ extend much closer to the wall in spanwise spectra, reaching down to $y'/\delta = 10^{-3}$, as also seen in the streamwise energy maps. This is expected, since spanwise fluctuations are typically more pronounced near the wall compared to wall-normal ones. The second difference is that, near the wall, only the large-scale energy ($\lambda_t U_e/\delta > 2 \times 10^0$) is enhanced for W4, relative to S, showing similar behavior as the one seen in streamwise energy spectra. The amplification of $E/U_e^2$ visible in spanwise and streamwise spectra in the near-wall region may indicate increased activity of quasi-streamwise vortices. These structures are known to generate enhanced sweep events,[67] facilitating the transfer of momentum from the outer region of the boundary layer toward the wall and contributing to the increase in wall shear.[68] This momentum transfer is partially evident in Fig. 12, where, for the W4 configuration, the increase in near-wall velocity (momentum gain) is accompanied by a velocity deficit (momentum loss) in the outer region of TBL.

### B. Effect of the wall curvature

This section aims to compare the effect of a wavy wall embedded into the curvature of an airfoil with the effect observed in a configuration without curvature, as examined in Ref. 44. In both the present study and in Ref. 44, the turbulent boundary layer developing over WW is subjected to an APG. In such cases, as noted by Bobke *et al.*,[69] the local state of TBL is significantly influenced by the upstream flow history. Consequently, unlike in ZPG TBLs, the streamwise pressure gradient must be considered when comparing data. A critical parameter that incorporates information about the pressure gradient is the Clauser–Rotta parameter, denoted as $\beta$.[46] According to Refs. 70–73, $\beta$ provides a basis for comparing data from studies of APG TBLs. Therefore, in the present study, $\beta$ is employed as a common metric for comparison.

Figure 14 shows the development of $\beta$ and the growth of TBL thickness, expressed as $\delta/\delta_0$, for the present study in comparison with data from Ref. 44. Both parameters show good agreement across the two studies. In particular, the development of $\beta$ exhibits an almost identical evolution in both configurations. Similarly, $\delta/\delta_0$ follows a very comparable trend, with only a small discrepancy observed at $x < 0.5$ m. These results indicate that TBL develops in a similar manner in both cases, suggesting a comparable APG history. This condition of matched pressure gradient development is essential for meaningful comparison of TBL statistics between different configurations.[69,74]

To evaluate whether the impact of waviness is comparable across different surface types, the data from the present study, where waviness is embedded in the curvature of an airfoil, are compared to our previous work,[44] which investigated flow over waviness combined with a flat surface subjected to an external APG source. Figure 15 presents the evolution of the velocity and fluctuation profiles at various locations, corresponding to $\beta$ values of 25, 35, 45, 55, and 65 in subsequent columns. The comparison includes cases S and W4 (black and blue solid lines) from the present study and, from Ref. 44, cases F-APG and W-APG (black and blue dashed lines), which represent the flat and wavy wall configurations under APG, respectively. Examining the velocity profiles reveals that the wavy configurations (blue lines) exhibit enhanced velocity in the near-wall region compared to the smooth surfaces (black lines). Specifically, at approximately $y'/\delta < 0.1$, the levels of $\langle U \rangle$ are elevated (see the zoomed–in figures), indicating a higher velocity gradient, which translates into increased $\tau_w$. In the outer region of TBL ($y'/\delta > 0.1$), the opposite effect is observed in both the present and previous studies: the wavy configurations reduce the velocity. This behavior remains consistent throughout the considered $\beta$ range and is observed for both the present and previous studies.[44] However, some discrepancies between the two datasets are present. Specifically, in the current study, the velocity is generally lower at $y'/\delta < 0.2$ compared to the data from Ref. 44. An interesting pattern emerges upon examining the fluctuation profiles. Namely, the wavy configurations (blue lines) in both the present and previous studies show a notable increase in $\langle uu \rangle^{1/2}$ compared to smooth surfaces (black lines) across

20 July 2025 21:28:44


Published under an exclusive license by AIP Publishing

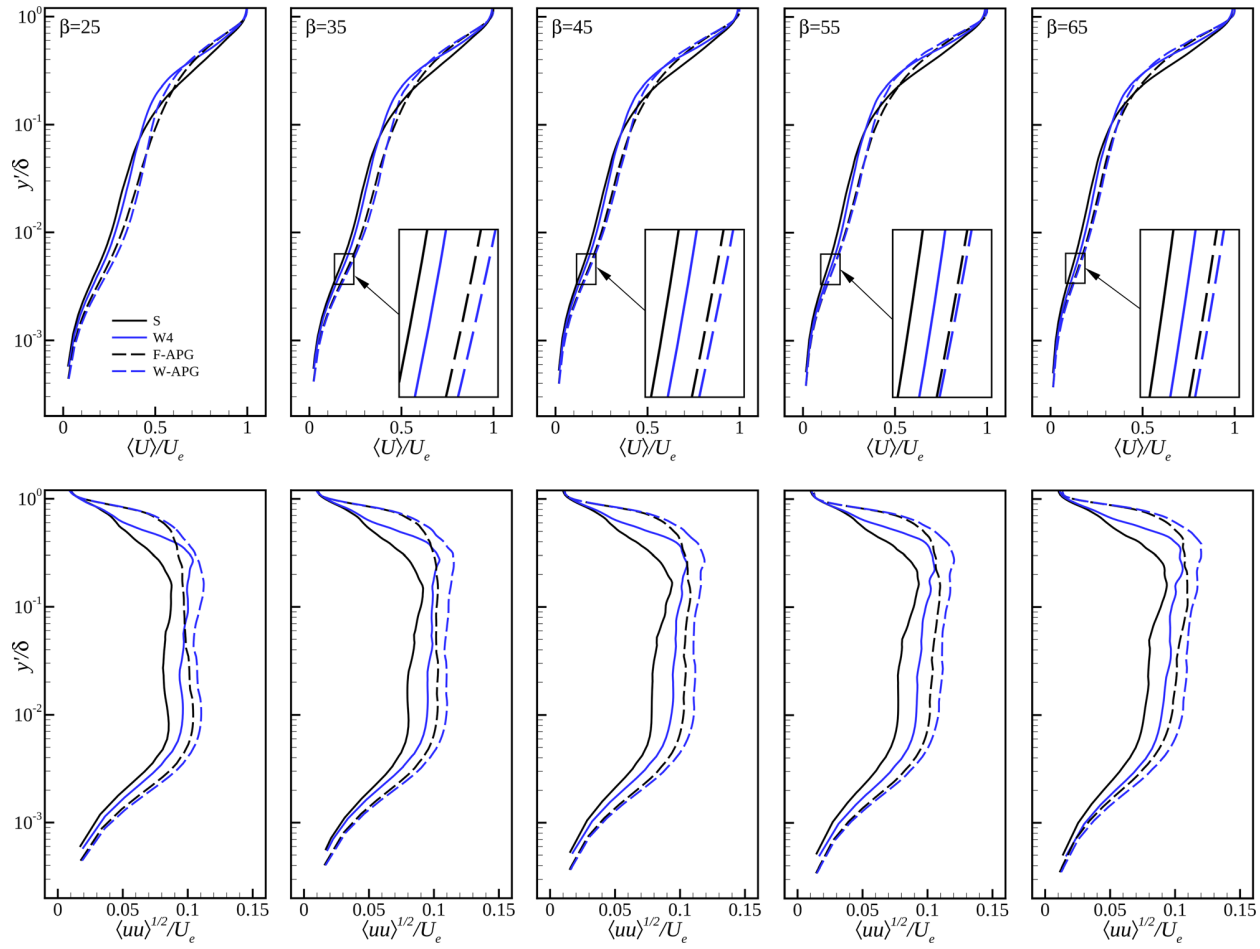



**FIG. 15.** Profiles of velocity and fluctuations for cases S and W4 compared to data from Ref. 44.

the entire considered $\beta$ range. Elevated fluctuations in the near-wall region are likely due to the greater $dU/dy$ induced by the wavy configurations. On the other hand, the enhancement of $\langle uu \rangle^{1/2}$ in the outer region, particularly at the outer peak ($y'/\delta \approx 0.3$), may be attributed to the increased energy of large–scale motions (LSMs) due to TBL interaction with the waviness,[75] which contribute to amplified fluctuations in this region. Similar to the $\langle U \rangle$ profiles, a discrepancy is observed in that the fluctuations are generally lower for configurations studied in the present work compared to those explored in Ref. 44.

In summary, the effects of the wavy wall on the flow are consistent whether it is integrated into a flat surface subjected to an APG or into a curved surface, such as that on the suction side of an airfoil. In both scenarios, employing WW results in a notable increase in near–wall velocity, which directly translates into an enhanced $\tau_w$. In the present study, as shown in Fig. 11(c), the most beneficial configuration (W4) enhances $\tau_w$ by approximately 15%. This improvement, compared to the approximately 10% enhancement reported in Ref. 44, indicates that a significantly stronger effect of WW can be achieved on the curvature of an airfoil. This is further illustrated by the velocity and fluctuation profiles presented in Fig. 15, where it is observed that, in the present study, WW enhances both $\langle U \rangle$ and $\langle uu \rangle^{1/2}$ to a greater extent (with respect to smooth surface) than the changes noted in Ref. 44.

### C. Reynolds number dependency

In real flow systems, conditions often vary; therefore, it is reasonable to evaluate the applicability of the proposed flow control method across a range of Reynolds numbers. Figure 16 illustrates the shift in the separation point ($\Delta x_{sep.}$, black bars) and the enhancement in wall shear stress ($\Delta\langle\tau_w\rangle$, blue bars) for the W4 configuration relative to the smooth airfoil (S). To assess the influence of the Reynolds number on the performance of the wavy wall, these parameters are presented for four values of $Re_\tau$: 1200, 1700, 2300, and 2500. It is evident that the W4 configuration delays separation the most (yielding the highest $\Delta x_{sep.}$) at $Re_\tau = 2500$, leading to the largest increase in $\Delta\langle\tau_w\rangle$. However, as the Reynolds number decreases, both $\Delta\langle\tau_w\rangle$

20 July 2025 21:28:44


Published under an exclusive license by AIP Publishing

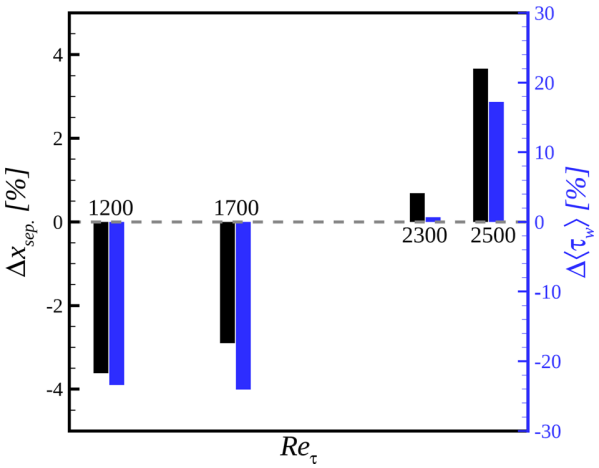



**FIG. 16.** The effect of $Re_\tau$ on the change in the position of separation point for wave W4 with respect to smooth airfoil.

and $\Delta x_{sep.}$ decline. It can be seen that the corrugation is effective down to $Re_\tau = 2300$. Below this Reynolds number, the favorable effect observed at $Re_\tau = 2500$ reverses, with both $\Delta\langle\tau_w\rangle$ and $\Delta x_{sep.}$ becoming negative. This behavior of WW is suspected to be connected with the amplitude modulation effect, which weakens proportionally with decreasing $Re_\tau$.[66,76] Furthermore, as suggested by Dróżdż *et al.*,[43] to enhance the amplitude modulation effect, the amplitude of a waviness must be sufficiently large to reach the lower bound of TBL. As $\delta$ increases with decreasing $Re_\tau$, the ratio $A/\delta$ decreases, given that the identical waviness (W4) is applied across all tested $Re_\tau$ values in this study. Consequently, at lower $Re_\tau$, the amplitude is likely insufficient to reach the critical region of TBL, thus reducing the effectiveness of WW.

To further explore the effect of changing $Re_\tau$, the profiles of $\langle U\rangle$ (upper row) and $\langle uu\rangle^{1/2}$ (bottom row) are presented in Fig. 17 for all the considered values of $Re_\tau$ (subsequent columns). The results are shown for cases S (black lines) and W4 (blue lines) at the locations corresponding to $\beta$ equal to 45. As stated in Ref. 71, such an approach ensures identical APG conditions regardless of $Re_\tau$. Upon examining the velocity profiles, it is observed that at $Re_\tau = 1200$ and 1700, where $\langle\Delta\tau_w\rangle$ takes negative values (see Fig. 16), the near-wall velocity for case W4 is lower than that of S. This indicates reduced values of $dU/dy$ and, consequently, lower $\tau_w$. The differences between S and W4 in the near-wall region become indistinguishable at $Re_\tau = 2300$, marking the pivot point where the trend begins to reverse. Furthermore, at $Re_\tau = 2500$, an increase in near-wall velocity is observed, contributing to an enhanced wall shear stress. It is worth noting that the variability in $Re_\tau$ results in velocity increments limited to $y'/\delta \approx 0.1$. Beyond this value, in the range $0.1 < y'/\delta < 1$, a consistent effect across all $Re_\tau$ is noted, i.e., the waviness tends to reduce the flow velocity. Noteworthy observations can also be drawn from the $\langle uu\rangle^{1/2}$ profiles. At $Re_\tau = 1200$ and 1700, the values of $\langle uu\rangle^{1/2}$ are nearly identical for $y'/\delta < 0.05$ between cases S and W4. Similar to the changes observed in the velocity profiles, a shift in trend becomes apparent at $Re_\tau = 2300$, where the fluctuation levels for case W4 exceed those of S. At $Re_\tau = 2500$, the greatest differences in near-wall fluctuation values are observed. Specifically, for W4, a significant enhancement in $\langle uu\rangle^{1/2}$ is found in contrast to case S. This effect, discussed earlier in the paper, can be linked to enhanced activity of the large-scale motion (see Fig. 13). Additionally, elevated levels of fluctuations are noted across all $Re_\tau$ further from the wall, i.e., at $0.05 < y'/\delta < 1$. This can most likely be attributed to the increased energy of the large-scale motions induced by WW, as already discussed.

## V. CONCLUSIONS

This study investigates the flow over a two-dimensional streamwise WW embedded in the curvature of the NACA 4412 airfoil under APG conditions, using LES. The focus is on evaluating how different WW configurations influence near-wall turbulence and separation characteristics at $Re_\tau = 1200 - 2500$, to identify the most effective geometry. Particular attention is paid to the case with $Re_\tau = 2500$, for which the obtained results are compared to those from a simplified flat-wall domain,[44] and a sensitivity analysis is conducted to assess the performance of the optimal configuration, W4, under varying Reynolds numbers. Furthermore, an attempt is made to identify the mechanism responsible for the observed changes in separation behavior.

At $Re_\tau = 2500$, configuration W4 yields the largest downstream shift in the separation point. This shift is governed by the *ES* parameter, which quantifies the waviness strength. As *ES* increases, separation is initially delayed, peaking at $ES \approx 0.17$. Beyond this point, the trend reverses, leading to earlier separation and growth of the separation bubble. A similar trend is observed for wall shear stress: $\Delta\langle\tau_w\rangle$ increases with *ES* up to 0.17, then declines.

Investigating the relationship between waviness parameters and flow response reveals that $\lambda$ has a strong correlation with both $\Delta\langle\tau_w\rangle$ and the separation point shift $\Delta x_{sep}$, whereas no clear trend is found with *A*.

W4 exhibits intensified fluctuations in both the near-wall and outer regions. Spectral analysis shows increased energy across all scales in the outer region, while near the wall, only large-scale activity is enhanced. This redistribution of turbulent energy appears to drive the observed increase in $\tau_w$ and highlights a potential mechanism through which surface waviness influences aerodynamic performance.

The impact of WW was found to be comparable between the curved and flat surfaces under APG. However, the increase in wall shear stress was about 5% greater on the airfoil, suggesting enhanced effectiveness in realistic geometries. This change in behavior may be attributed to the waviness enhancing large-scale energy near the wall, as shown by the streamwise and spanwise energy spectra, without the small-scale contributions observed in Ref. 43.

Importantly, the effectiveness of WW is sensitive to the Reynolds number. A significant $\Delta\langle\tau_w\rangle$ increase was observed only at $Re_\tau = 2500$. At $Re_\tau = 2300$, the effect was negligible, and at even lower values, WW became detrimental, accelerating separation. This decline is likely linked to increased TBL thickness at lower $Re_\tau$, which prevents the waviness from reaching the critical near-wall region.[43]

20 July 2025 21:28:44


Published under an exclusive license by AIP Publishing

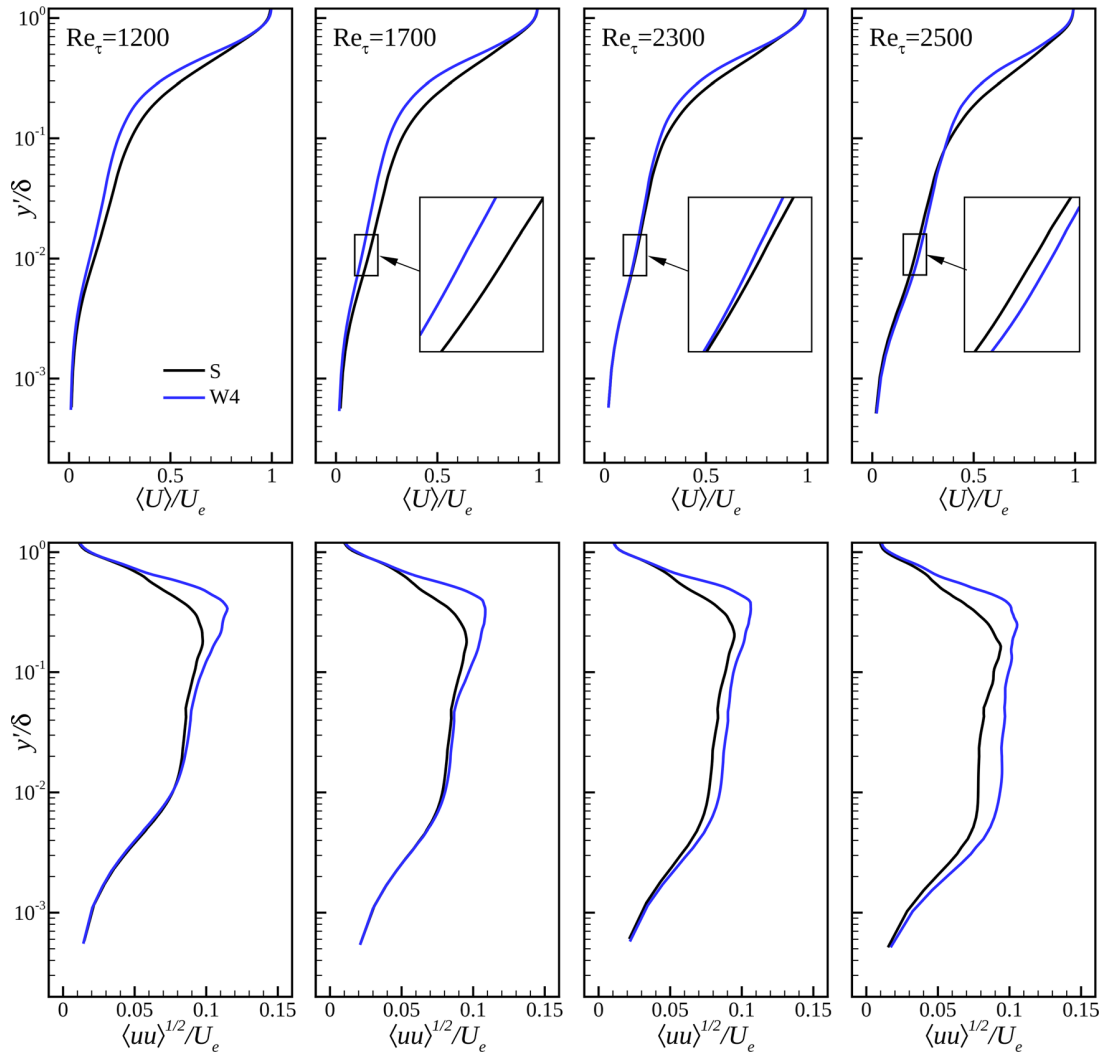



**FIG. 17.** Profiles of velocity and fluctuations for various $Re_\tau$ taken for constant value of $\beta$ equal to 45.

These findings highlight the potential of WW for flow control but also point to limitations under varying inflow conditions. Future work should investigate higher Reynolds numbers, where WW performance may also degrade, to better define the applicability range of this passive control strategy.

## ACKNOWLEDGMENTS

The investigation was supported by the Polish National Science Center in Poland for Grant No. UMO-2020/39/B/ST8/01449 and statutory funds of the Częstochowa University of Technology for Grant No. BS/BP 1-100-3011/2024/P. We gratefully acknowledge Poland's high-performance Infrastructure PLGrid ACK Cyfronet AGH for Grant No. PLG/2023/016731 and PCSS for providing computer facilities and support within computational and Poznan Supercomputing and Networking Center for Grant No. PL0356-01.

## AUTHOR DECLARATIONS

### Conflict of Interest

The authors have no conflicts to disclose.

### Author Contributions

**Piotr Kamiński:** Conceptualization (equal); Data curation (lead); Formal analysis (lead); Investigation (lead); Methodology (equal); Validation (lead); Visualization (lead); Writing – original draft (lead); Writing – review & editing (equal). **Paweł Niegodajew:** Conceptualization (equal); Formal analysis (equal); Methodology (equal); Supervision (equal); Writing – original draft (equal); Writing – review & editing (equal). **Artur Tyliszczak:** Conceptualization (equal); Methodology (equal); Resources (lead); Software (lead); Supervision (equal); Writing – original draft (equal); Writing – review & editing (equal). **Witold Elsner:** Conceptualization (equal); Funding

20 July 2025 21:28:44


Published under an exclusive license by AIP Publishing

acquisition (lead); Methodology (equal); Project administration (equal); Resources (equal); Supervision (equal); Writing – review & editing (equal).

## DATA AVAILABILITY

The data that support the findings of this study are available from the corresponding author upon reasonable request.

## REFERENCES


[1]J. Tay and T. T. Lim, "Drag reduction with teardrop-shaped dimples," in Flow Control Conference, AIAA Paper No. AIAA 2018-3528, 2018.
[2]C. M. J. Tay, B. C. Khoo, and Y. T. Chew, "Mechanics of drag reduction by shallow dimples in channel flow," Phys. Fluids **27**, 035109 (2015).
[3]F. Gattere, A. Chiarini, and M. Quadrio, "Dimples for skin-friction drag reduction: Status and perspectives," Fluids **7**, 240 (2022).
[4]K. Aoki, K. Muto, and H. Okanaga, "Mechanism of drag reduction by dimple structures on a sphere," J. Fluid Sci. Technol. **7**, 1–10 (2012).
[5]J. Tay, T. T. Lim, and B. C. Khoo, "Drag reduction with diamond-shaped dimples," in AIAA Aviation 2019 Forum, AIAA Paper No. AIAA 2019-3296, 2019.
[6]F. Azlan, M. K. Tan, B. T. Tan, and M.-Z. Ismadi, "Passive flow-field control using dimples for performance enhancement of horizontal axis wind turbine," Energy **271**, 127090 (2023).
[7]G. Gibertini, J. C. Boniface, A. Zanotti, G. Droandi, F. Auteri, R. Gaveriaux, and A. Le Pape, "Helicopter drag reduction by vortex generators," Aerosp. Sci. Technol. **47**, 324–339 (2015).
[8]C. Zhu, J. Chen, J. Wu, and T. Wang, "Dynamic stall control of the wind turbine airfoil via single-row and double-row passive vortex generators," Energy **189**, 116272 (2019).
[9]H. Wang, B. Zhang, Q. Qiu, and X. Xu, "Flow control on the NREL S809 wind turbine airfoil using vortex generators," Energy **118**, 1210–1221 (2017).
[10]M. R. Islam, M. A. Hossain, M. Mashud, and M. T. I. Gias, "Drag reduction of a car by using vortex generator," Int. J. Sci. Eng. Res. **4**, 1298–1302 (2013).
[11]R. Belamadi, A. Djemili, A. Ilinca, and R. Mdouki, "Aerodynamic performance analysis of slotted airfoils for application to wind turbine blades," J. Wind Eng. Ind. Aerodyn. **151**, 79–99 (2016).
[12]J. G. Coder and D. M. Somers, "Design of a slotted, natural-laminar-flow airfoil for commercial transport applications," Aerosp. Sci. Technol. **106**, 106217 (2020).
[13]B. B. Nia, M. Ja'fari, A. R. Ranjbar, and A. J. Jaworski, "Passive control of boundary layer flow separation on a wind turbine airfoil using vortex generators and slot," Ocean Eng. **283**, 115170 (2023).
[14]S. Huang, J. Wang, L. Hou, and Y. Wang, "Numerical study on a novel flapping-foil energy harvester with 2D vortex generator," Ocean Eng. **266**, 112415 (2022).
[15]A. Zaki, M. Abdelrahman, S. S. Ayad, and O. Abdellatif, "Effects of leading edge slat on the aerodynamic performance of low Reynolds number horizontal axis wind turbine," Energy **239**, 122338 (2022).
[16]H. Wang, X. Jiang, Y. Chao, Q. Li, M. Li, W. Zheng, and T. Chen, "Effects of leading edge slat on flow separation and aerodynamic performance of wind turbine," Energy **182**, 988–998 (2019).
[17]A. Aboelezz, H. Ghali, G. Elbayomi, and M. Madboli, "A novel VAWT passive flow control numerical and experimental investigations: Guided vane airfoil wind turbine," Ocean Eng. **257**, 111704 (2022).
[18]X. Ye, J. Hu, N. Zheng, and C. Li, "Numerical study on aerodynamic performance and noise of wind turbine airfoils with serrated gurney flap," Energy **262**, 125574 (2023).
[19]L. Ni, W. Miao, C. Li, and Q. Liu, "Impacts of gurney flap and solidity on the aerodynamic performance of vertical axis wind turbines in array configurations," Energy **215**, 118915 (2021).
[20]S. Roy, B. Das, and A. Biswas, "Effect of leading-edge protrusion shapes for passive flow control measure on wind turbine blades," Ocean Eng. **269**, 113688 (2023).
[21]Y. Wang, G. Li, S. Shen, D. Huang, and Z. Zheng, "Influence of an off-surface small structure on the flow control effect on horizontal axis wind turbine at different relative inflow angles," Energy **160**, 101–121 (2018).
[22]W. Mostafa, A. Abdelsamie, M. Sedrak, D. Thévenin, and M. H. Mohamed, "Quantitative impact of a micro-cylinder as a passive flow control on a horizontal axis wind turbine performance," Energy **244**, 122654 (2022).
[23]J.-S. Wang, J. Wu, and J.-J. Wang, "Wake-triggered secondary vortices over a cylinder/airfoil configuration," Exp. Fluids **64**, 6 (2023).
[24]J. Zhong, J. Li, and H. Liu, "Dynamic mode decomposition analysis of flow separation control on wind turbine airfoil using leading-edge rod," Energy **268**, 126656 (2023).
[25]M. H. A. Satar, N. Razak, M. S. Abdullah, and F. Ismal, "A comprehensive comparison of passive flow controls on the wind turbine blade lift and drag performances: A CFD approach," Eur. J. Mech., B: Fluids **108**, 119–133 (2024).
[26]D. Luo, D. Huang, and X. Sun, "Passive flow control of a stalled airfoil using a microcylinder," J. Wind Eng. Ind. Aerodyn. **170**, 256–273 (2017).
[27]T. G. Schmidt and S. Redonnet, "Exploring a bio-inspired passive flow control strategy for wind turbines: Experimental characterization of the aerodynamics of a wind turbine blade section possibly equipped with leading-edge tubercles," J. Wind Eng. Ind. Aerodyn. **250**, 105768 (2024).
[28]J. Wang, C. Han, D. Yurchenko, Y. Zhou, X. Meng, and W. Zhang, "Energy concentration pipe based on passive jet control for enhancing flow induced vibration energy harvesting," Energy Convers. Manage. **319**, 118948 (2024).
[29]F. Eydi, A. Mojra, and H. Kamel, "A novel passive flow control technique using circular arcs coupled with downstream splitters," Ocean Eng. **313**, 119393 (2024).
[30]T.-L. Phan, "Optimal configuration of passive flow control devices to reduce the aerodynamics drag of a tractor-trailer model," Results Eng. **23**, 102425 (2024).
[31]J. E. Guerrero, D. Maestro, and A. Bottaro, "Biomimetic spiroid winglets for lift and drag control," C. R. Mec. **340**, 67–80 (2011).
[32]L. Wu, Z. Jiao, Y. Song, C. Liu, H. Wang, and Y. Yan, "Experimental investigations on drag-reduction characteristics of bionic surface with water-trapping microstructures of fish scales," Sci. Rep. **8**, 12186 (2018).
[33]J. E. Guerrero, M. Sanguineti, and K. Wittkowski, "Variable cant angle winglets for improvement of aircraft flight performance," Meccanica **55**, 1917–1947 (2020).
[34]Z. Zhang, L. Kuang, Z. Han, D. Zhou, Y. Zhao, Y. Bao, L. Duan, J. Tu, Y. Chen, and M. Chen, "Comparative analysis of bent and basic winglets on performance improvement of horizontal axis wind turbines," Energy **281**, 128252 (2023).
[35]J. S. Jeong, S. W. Bong, and S. W. Lee, "An efficient winglet coverage for aero-engine turbine blade flat tip and its loss map," Energy **260**, 125153 (2022).
[36]M. Khaled, M. M. Ibrahim, H. E. A. Hamed, and A. F. AbdelGwad, "Investigation of a small horizontal–axis wind turbine performance with and without winglet," Energy **187**, 115921 (2019).
[37]P. Lowrey and J. Harasha, "A preliminary assessment of the feasibility of using riblets in internal flows to conserve energy," Energy **16**, 631–642 (1991).
[38]W. Hao and C. Li, "Performance improvement of adaptive flap on flow separation control and its effect on VAWT," Energy **213**, 118809 (2020).
[39]H. Chen, F. Rao, X. Shang, D. Zhang, and I. Hagiwara, "Biomimetic drag reduction study on herringbone riblets of bird feather," J. Bionic Eng. **10**, 341–349 (2013).
[40]W. Yossri, S. B. Ayed, and A. Abdelkefi, "Evaluation of the efficiency of bioinspired blade designs for low-speed small-scale wind turbines with the presence of inflow turbulence effects," Energy **273**, 127210 (2023).
[41]A. Schlieter, R. Pflumm, I. Shakhverdova, R. Naraparaju, U. Schulz, C. Leyens, M. Schütze, and W. Reimers, "Mechanical properties of sharkskin like structured surfaces for high-temperature applications," Adv. Eng. Mater. **18**, 688–702 (2016).
[42]A. W. Lang, E. M. Jones, and F. Afroz, "Separation control over a grooved surface inspired by dolphin skin," Bioinspiration Biomimetics **12**, 026005 (2017).
[43]A. Dróżdż, P. Niegodajew, M. Romańczyk, V. Sokolenko, and W. Elsner, "Effective use of the streamwise waviness in the control of turbulent separation," Exp. Therm. Fluid Sci. **121**, 110291 (2021).
[44]P. Kamiński, P. Niegodajew, A. Dróżdż, V. Sokolenko, A. Tyliszczak, and W. Elsner, "Numerical analysis of novel wavy wall based control of turbulent boundary layer separation," Aerosp. Sci. Technol. **149**, 109167 (2024).


20 July 2025 21:28:44


Published under an exclusive license by AIP Publishing

[45]E. Napoli, V. Armenio, and M. De Marchis, "The effect of the slope of irregularly distributed roughness elements on turbulent wall-bounded flows," J. Fluid Mech. **613**, 385–394 (2008).
[46]F. H. Clauser, "The turbulent boundary layer," Adv. Appl. Mech. **4**, 1–51 (1956).
[47]B. J. Geurts, *Elements of Direct and Large-Eddy Simulation* (Edwards Publishing, Philadelphia, 2004).
[48]F. Nicoud and F. Ducros, "Subgrid-scale stress modelling based on the square of the velocity gradient tensor," Flow, Turbul. Combust. **62**, 183–200 (1999).
[49]D. Y. Adamian, M. K. Strelets, and A. K. Travin, "An efficient method of synthetic turbulence generation at LES inflow in zonal RANS–LES approaches to computation of turbulent flows," Mat. Mod. **23**, 3–19 (2011).
[50]M. L. Shur, P. R. Spalart, M. K. Strelets, and A. K. Travin, "Synthetic turbulence generators for RANS-LES interfaces in zonal simulations of aerodynamic and aeroacoustic problems," Flow, Turbul. Combust. **93**, 63–92 (2014).
[51]L. Davidson, "Large eddy simulations: How to evaluate resolution," Int. J. Heat Fluid Flow **30**, 1016–1025 (2009).
[52]J. A. Sillero, J. Jiménez, and R. D. Moser, "One-point statistics for turbulent wall-bounded flows at Reynolds numbers up to $\delta^+ \approx 2000$," Phys. Fluids **25**, 105102 (2013).
[53]C. Hinterberger, J. Fröhlich, and W. Rodi, "2D and 3D turbulent fluctuations in open channel flow with $Re_\tau = 590$ studied by large eddy simulation," Flow, Turbul. Combust. **80**, 225–253 (2008).
[54]D. You and P. Moin, "A dynamic global-coefficient subgrid-scale eddy-viscosity model for large-eddy simulation in complex geometries," Phys. Fluids **19**, 065110 (2007).
[55]F. Nicoud, H. B. Toda, O. Cabrit, S. Bose, and J. Lee, "Using singular values to build a subgrid-scale model for large eddy simulations," Phys. Fluids **23**, 085106 (2011).
[56]R. Vinuesa, P. S. Negi, M. Atzori, A. Hanifi, D. S. Henningson, and P. Schlatter, "Turbulent boundary layers around wing sections up to $Re_c = 1{,}000{,}000$," Int. J. Heat Fluid Flow **72**, 86–99 (2018).
[57]R. L. Simpson, "Aspects of turbulent boundary-layer separation," Prog. Aerosp. Sci. **32**, 457–521 (1996).
[58]R. Mathis, J. P. Monty, N. Hutchins, and I. Marusic, "Comparison of largescale amplitude modulation in turbulent boundary layers, pipes, and channel flows," Phys. Fluids **21**, 111703 (2009).
[59]J. Jiménez, S. Hoyas, M. P. Simens, and Y. Mizuno, "Turbulent boundary layers and channels at moderate Reynolds numbers," J. Fluid Mech. **657**, 335–360 (2010).
[60]R. Vinuesa, R. Örlü, and P. Schlatter, "Characterisation of backflow events over a wing section," J. Turbul. **18**, 170–185 (2017).
[61]A. Andreolli, D. Gatti, R. Vinuesa, R. Örlü, and P. Schlatter, "Effects of sweeps and ejections on amplitude modulation in a turbulent channel flow," arXiv:2109.09486 (2021).
[62]N. Hutchins and I. Marusic, "Large-scale influences in near-wall turbulence," Philos. Trans. R. Soc. A **365**, 647–664 (2007).
[63]P. Ricco, M. Skote, and M. A. Leschziner, "A review of turbulent skin-friction drag reduction by near-wall transverse forcing," Prog. Aerosp. Sci. **123**, 100713 (2021).
[64]A. Elnahhas and P. L. Johnson, "On the enhancement of boundary layer skin friction by turbulence: An angular momentum approach," J. Fluid Mech. **940**, A36 (2022).
[65]B. Ganapathisubramani, N. Hutchins, J. P. Monty, D. Chung, and I. Marusic, "Amplitude and frequency modulation in wall turbulence," J. Fluid Mech. **712**, 61–91 (2012).
[66]R. Mathis, N. Hutchins, and I. Marusic, "Large-scale amplitude modulation of the small-scale structures in turbulent boundary layers," J. Fluid Mech. **628**, 311–337 (2009).
[67]R. D. Whalley and K.-S. Choi, "Turbulent boundary-layer control with plasma spanwise travelling waves," Exp. Fluids **55**, 1–16 (2014).
[68]L. Agostini and M. Leschziner, "The connection between the spectrum of turbulent scales and the skin-friction statistics in channel flow at $Re_\tau \approx 1000$," J. Fluid Mech. **871**, 22–51 (2019).
[69]A. Bobke, R. Vinuesa, R. Örlü, and P. Schlatter, "History effects and near equilibrium in adverse-pressure-gradient turbulent boundary layers," J. Fluid Mech. **820**, 667–692 (2017).
[70]J. P. Monty, Z. Harun, and I. Marusic, "A parametric study of adverse pressure gradient turbulent boundary layers," Int. J. Heat Fluid Flow **32**, 575–585 (2011).
[71]Á. Tanarro, R. Vinuesa, and P. Schlatter, "Effect of adverse pressure gradients on turbulent wing boundary layers," J. Fluid Mech. **883**, A8 (2020).
[72]R. Örlü, C. S. Vila, R. Vinuesa, A. Ianiro, S. Discetti, and P. Schlatter, "Scaling of adverse-pressure-gradient turbulent boundary layers," in 5th International Conference on Experimental Fluid Mechanics (ICEFM), 2018.
[73]C. S. Vila, R. Vinuesa, S. Discetti, A. Ianiro, P. Schlatter, and R. Örlü, "Experimental realisation of near-equilibrium adverse-pressure-gradient turbulent boundary layers," Exp. Therm. Fluid Sci. **112**, 109975 (2020).
[74]S. Pargal, H. Wu, J. Yuan, and S. Moreau, "Adverse-pressure-gradient turbulent boundary layer on convex wall," Phys. Fluids **34**, 035107 (2022).
[75]S. Ghebali, S. I. Chernyshenko, and M. A. Leschziner, "Can large-scale oblique undulations on a solid wall reduce the turbulent drag?," Phys. Fluids **29**, 105102 (2017).
[76]Y. C. Yao, W. X. Huang, and C. X. Xu, "Amplitude modulation and extreme events in turbulent channel flow," Acta Mech. Sin. **34**, 1–9 (2018).

20 July 2025 21:28:44


Published under an exclusive license by AIP Publishing

Journal of Physics:
Conference Series

PURPOSE-LED PUBLISHING™

PAPER • OPEN ACCESS

# Machine learning-supported CFD optimization of heat transfer in a pipe with a corrugated wall shape

To cite this article: P Kamiński *et al* 2024 *J. Phys.: Conf. Ser.* **2899** 012013

View the article online for updates and enhancements.

You may also like

- Thermal Plasma-Induced Modifications of ZnO Crystalline Facets
J Pila, A Mašláni, T Hostinský et al.
- Research on the application of automatic drilling system for aircraft flap composite titanium stacked structures
Chuanyi Cui, Pin Zhang, Xianglin Gao et al.
- Round-Robin test II – wake measurements of porous discs under clearly defined boundary conditions
M. Hölling, M. Wagner, E. Bocarov et al.

This content was downloaded from IP address 89.234.247.60 on 19/01/2026 at 15:47

Journal of Physics: Conference Series **2899** (2024) 012013 doi:10.1088/1742-6596/2899/1/012013

# Machine learning-supported CFD optimization of heat transfer in a pipe with a corrugated wall shape

**P Kamiński[1], Y Li[2], K Wawrzak[1], A Tyliszczak[1] and BR Noack[2,3]**

[1] Department of Thermal Machinery, Częstochowa University of Technology, al. Armii Krajowej 21, 42-201 Częstochowa, Poland
[2] Chair of Artificial Intelligence and Aerodynamics, School of Mechanical Engineering and Automation, Harbin Institute of Technology, 518055 Shenzhen, P.R. China
[3] Guangdong Provincial Key Laboratory of Intelligent Morphing Mechanisms and Adaptive Robotics, Harbin Institute of Technology, 518055 Shenzhen, P.R. China

E-mail: piotr.kaminski@pcz.pl

**Abstract.** The paper focuses on using machine learning to optimize the corrugation of a heated pipe wall to improve the uniformity of temperature distribution while minimizing pressure losses. The corrugation is characterized by a five-parameter function, allowing for extensive variations in wall shape. The machine learning process employs the Bayesian optimization method, iteratively working alongside the ANSYS Fluent code to perform RANS computations. A two-parameter cost function, which includes temperature variation and pressure drop, is used to define the optimization goal. The study demonstrates that substantial variations in flow patterns occur depending on the type of corrugation. An optimal set of corrugation parameters, ensuring the most uniform temperature distribution with minimal pressure losses, is determined within an optimization loop consisting of 1200 RANS simulations. The optimal configuration is characterized by a smooth waviness oriented outside the original wall location in a straight pipe. It ensures more than three times smaller temperature variation at only minor increase in the pressure drop.

## 1 Introduction

Studying the flow and heat transfer within a pipe is essential for optimizing heating or cooling processes in injection devices, heat exchangers, heat pipes [1] as well as in the food industry [2]. Various techniques can be employed to augment heat transfer, with wall surface alteration through corrugation (waviness) being a common method [3]. Such surfaces have been widely used in recent years for enhancing heat transfer [4, 5]. The geometric complexity of these walls significantly impacts flow patterns, frequently resulting in the formation of recirculation zones within the troughs [6]. The mixing and heat transfer intensification often comes at the expense of additional energy input to maintain the assumed mass flow rate at a higher pressure drop. Both the enhancement in heat transfer and the pressure drop are highly sensitive to changes in the parameters characterizing the waviness, making this subject attractive for an in-depth parametric study.

In literature, the prevalent and extensively investigated type of wavy walls is the regular sinusoidal shape, primarily due to its ease of production. However, recent advancements in 3D printing and manufacturing processes allow for the consideration of significantly more complex configurations. In this study, we perform an optimization of a wavy-type pipe wall by assuming the corrugation shape as a five-parameter function, allowing for its sharpening and tilting in the streamwise or counter-streamwise direction.

Content from this work may be used under the terms of the Creative Commons Attribution 4.0 licence. Any further distribution of this work must maintain attribution to the author(s) and the title of the work, journal citation and DOI.
Published under licence by IOP Publishing Ltd

## 2 Methodology

### *2.1 Research object*

Figure 1 shows the geometry of the analyzed pipe. The radius and length of the pipe are equal to $R = 0.005$ m and $L = 0.25$ m. The heated wavy section, which undergoes the optimization procedure starts at $x = 0.05$ m from the inlet and its length is $L_w = 0.1$ m. The inlet velocity equals $U_{in} = 6.0$ m/s, which corresponds to the Reynolds number equal to $Re = U_{in}D/\nu = 4000$ (where $\nu$ is the kinematic viscosity and $D = 2R$), which places well in the range of the Reynolds numbers investigated in literature [7, 8, 9]. The inlet Prandtl number was equal to $Pr = (c_p\mu)/k = 0.7$ (where $c_p$ is the specific heat of air, $\mu$ is the dynamic viscosity and $k$ denotes the thermal conductivity). We assume the incoming flow is turbulent and characterized by the turbulence intensity $T_i = 2\%$. The temperature at the inlet is equal to $T_{in} = 300$ K. The wall is treated as no-slip and its temperature varies depending on the section. In part preceding the waviness $T_w = 300$ K. Then, irrespective of the wall shape we assume that the amount of heat transferred to the flowing medium is constant and defined by the heat flux $\phi_w = P_w/A_w$, where $P_w = 10$ W is the heating power and $A_w$ denotes the surface area of the wavy wall. Downstream the wavy section, the wall is insulated ($\phi_w = 0$ W/m$^2$). Note, that specifying the thermal boundary conditions by the heat flux means that the local wall temperature changes depending on the wall shape and flow conditions in the direct vicinity of the wall surface. In the case of the straight pipe, the wavy wall section attains the average temperature $T_{w,ave} = 395$ K and the fluid leaving the wavy section is heated up to $T_{f,ave} = 317.5$ K. The research objective is to find the waviness shape that

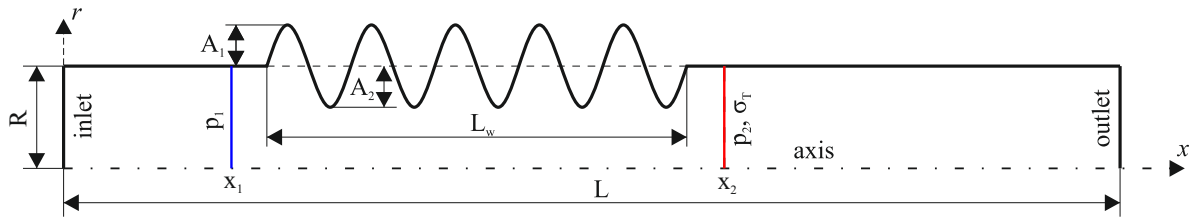



Figure 1: Computational domain.

ensures the most uniform radial temperature distribution downstream of the wavy section. Such flow conditions are often required in fuel injection systems, where preheating the fuel before it is injected into the combustion chamber results in more efficient combustion. The uniformity of the temperature is measured by a standard deviation $\sigma_T = 1/S \int \sqrt{(T(r,x) - T_{ave}(x))^2}\mathrm{dr}$ where $S = \pi R^2$ is the surface area of the pipe cross-section and $T(r,x)$ and $T_{ave}(x)$ are the local and average temperatures at the $x_2$ distance marked in Fig. 1 by the red line. A consequence of shaping the wall is an increase in the drag force, which manifests in the pressure drop along the pipe. The optimization goal is to find $\min(\sigma_T)$ without a significant increase of $\Delta p = |p_2 - p_1|$ where $p_2$ and $p_1$ are average static pressures in the localisations $x_2$ and $x_1$ (see Fig. 1). Combining together the parameters $\sigma_T$ and $\Delta p$ we define the cost function $J$ as

$$J = \left(\frac{\sigma_T}{\sigma_{T,flat}}\right) \times \left(\frac{\Delta p}{\Delta p_{flat}}\right) \tag{1}$$

where the variables $\sigma_{T,flat}$ and $\Delta p_{flat}$ stand for the reference values obtained for the straight pipe. The waviness is shaped starting from a sinusoidal function, which is then modified through an iterative formula defined as:

$$r_1 = \sin\left(x\frac{2\pi N}{L_w}\right) \tag{2}$$

$$r_{i+1} = \sin\left(x\frac{2\pi N}{L_w} + \frac{r_i}{s}\right) + r_i; \quad i = 1, ..., I \tag{3}$$

where $r_i$ denotes the local pipe radius, $N$ stands for the number of periods along $L_w$, $s$ is a parameter defining the tilt, and $I$ denotes the number of iterations ($i = 1, ..., I$). The waviness becomes less smooth when $I$ increases. Note, that in step 2 of the above procedure, the pipe radius is not limited which means that it may become arbitrarily large or small. In the latter case, the pipe could be completely blocked when $r_i \leq 0$. To avoid such a situation and to control the external size of the pipe, the amplitude of the

waviness at the iteration step $I$ is normalized to one and then multiplied by desired amplitudes $A_1$ and $A_2$ for radii $r > R$ and $r < R$ as follows

$$r_{I,1} = A_1 \times \left( \frac{r_I}{\max(r_I)} \right); \quad r_{I,2} = A_2 \times \left( \frac{r_I}{|\min(r_I)|} \right) \tag{4}$$

We note that such a normalization ensures continuity of function at $r = R$. However, with a significantly different $A_1$ and $A_2$ the slopes of the wall for $r > R$ and $r < R$ may be also substantially different.

### *2.2 The optimization procedure*

The optimization problem is to find the optimal corrugation design $\mathbf{b}^*$ to minimize the cost function $J$:

$$\mathbf{b}^* = \arg\min_{\mathbf{b}\in\mathcal{B}} J(\mathbf{b}). \tag{5}$$

The design vector $\mathbf{b}$ includes five parameters $A_1$, $A_2$, $s$, $N$ and $I$, limited in the search space $\mathcal{B} = [-0.0025, 0.0025] \times [-0.0025, 0.0025] \times [0.5, 100] \times [1, 20] \times [1, 10]$. The optimization procedure is performed by applying Bayesian Optimization (BO) method [10] combined with the Reynolds-Averaged Navier-Stokes (RANS) simulations discussed in § 2.3. BO is a technique used in machine learning and optimization tasks where evaluating the objective function is computationally expensive or time-consuming. It optimizes the black-box functions by modeling the objective function as a Gaussian process, which provides a probabilistic representation of the function behavior [11, 12]. The applied BO algorithm is based on a trade-off between exploration (sampling from areas with high uncertainty) and exploitation (sampling from areas with high predicted performance). This approach allows for fast convergence to the optimal solution with fewer evaluations compared to traditional methods, making it particularly useful for tasks such as hyperparameter tuning in machine learning models or optimizing complex simulations [13]. The BO procedure is given by algorithm 1. Here, we assume the maximum number of iterations $M = 1200$.

**Algorithm 1:** Bayesian optimization

**Data:** $f$, $\mathcal{B}$, $M_D$, $M$
**Result:** $\mathbf{b}^* = \arg\min_{\mathbf{b}\in\mathcal{B}} f(\mathbf{b})$
Initialize: $\mathcal{D}_{m-1} = \{\mathbf{b}_i, J_i\}|_{i=0}^{M_D}$, $\bar{f}$, $m = 1$
**while** $m \leq M$ **do**
  $\mathbf{b}_m = \arg\min_{\mathbf{b}\in\mathcal{B}} \alpha(\bar{f}, \mathcal{D}_{m-1})$ /* Derive the next sample */
  $J_m = f(\mathbf{b}_m)$ /* Test the sample, RANS */
  $\mathcal{D}_m \leftarrow \mathcal{D}_{m-1} \cup \{\mathbf{b}_m, J_m\}$ /* Enrich the dataset */
  Update $\bar{f}$
**end**
$\mathbf{b}^* = \arg\min_{\mathbf{b}_m\in D_m} J_m$

### *2.3 Numerical model*

For each set of parameters $b_m^*$ the simulations are performed with the help of the ANSYS Fluent software applying a RANS transitional SST model [14]. The Mach number for the present case is $Ma = 0.00176$. Hence we assume an incompressible ideal fluid (gas phase) with the temperature-dependent density computed from the equation of state. The viscosity is calculated according to the Sutherland law. The flow is treated as axisymmetric and steady, which allows for performing a large number of simulations at a relatively low computational cost and in a reasonable time. The 2nd-order spatial discretization method is used for the momentum, turbulent kinetic energy, specific dissipation rate, intermittency, and energy equations, with an upwind scheme used for the convective terms. The so-called coupled algorithm was employed for the pressure-velocity coupling. The enhanced wall-treatment method is used to model the flow in the wall vicinity [15].

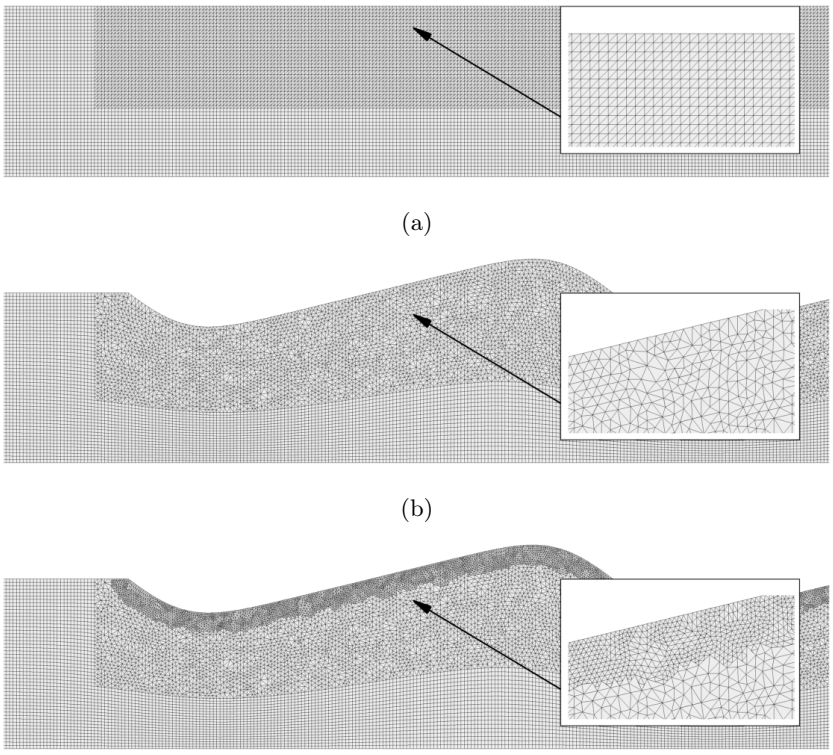


Figure 2: Three stages of mesh generation. The case with $A_{1,2} = 0.001$ m, $s = 1$, $N = 7$, $I = 2$.

*2.4 Computational mesh*

The computational mesh is divided into two parts, as depicted in Fig. 2 showing the mesh for the case with $A_1 = A_2 = 0.001$ m, $s = 1$, $N = 7$, and $I = 2$. In the region close to the waviness the mesh is unstructured and built of triangular elements. In the rest of the domain, the mesh is block-structured and composed of quadrilateral cells. Each time in the optimization loop when the BO returns the parameters $b_m^*$ the wall is deformed accordingly to Eqs. (2-4) and the mesh addapts to the new shape. The starting point for each wall configuration is the straight pipe with the mesh shown in Fig. 2a. After wall shaping, the mesh adaptation step is handled by the ANSYS Fluent software employing the Dynamic Meshing (DM) approach [15], which through the smoothing and re-meshing algorithms results in the mesh presented in Fig. 2b. At this stage, 10 layers of the cells in the nearest proximity of the wall are additionally refined by dividing the existing cells into smaller ones, as shown in Fig. 2c. Such an approach ensures a well-resolved near-wall viscous layer, which was verified by checking the $y+ = u_\tau h_w/\nu$ parameter, where $u_\tau$ is the friction velocity and $h_w$ is the height of the computational cell adjacent to the wall. In each case, $y^+ \approx 1$, which is considered a necessary condition for the enhanced wall treatment approach. Depending on the waviness shape, the number of the computational cells varied in the range $1.6 \times 10^5 - 1.8 \times 10^5$. The convergence level for all equations was set equal to $10^{-6}$ and depending on the mesh density this threshold was attained between 400-700 iterations.

## 3 Results

The optimization loop starts by performing simulations for fifty randomly chosen sets of parameters $\mathbf{b}$. Next, the BO method is turned on and the simulations are continued for $M = 1200$ iterations. Each time, the RANS solution is stored in external files, and the corresponding $J_m$ and $\mathbf{b}_m$ parameters are used in the learning and optimization process. The learning curve of $J$ obtained through the BO method is shown in Fig. 3 presenting the values of $J_m$ (black dots) and the actual minimum of $J$ (red line). It can be seen that already after $m = 50$ iterations the $J$ value is significantly reduced to $J = 0.361$. Then,

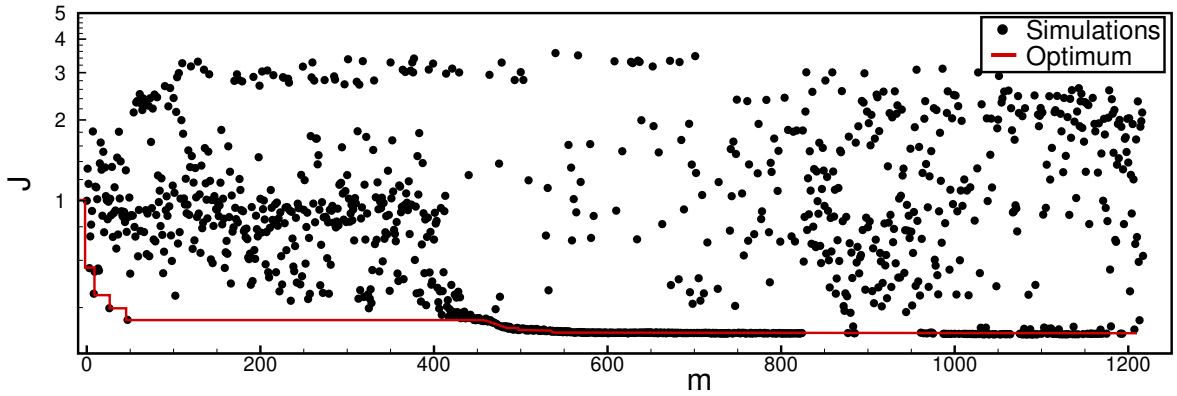



Figure 3: Learning curve of $J$ obtained in the BO procedure.

over approximately $m = 400$ iterations the optimization does not bring any improvement. This happens only between $m = 450 - 600$ after which $J$ drops to 0.318 and remains at this level until the end of the optimization loop. It is worth noting that for $m > 600$ there are several solutions close to the optimal one. In all these cases the waviness has a similar shape with minor differences found in the amplitudes $A_1$ and $A_2$. The wall-clock time needed to execute the entire optimization loop on a cluster of 16 CPUs equals approximately 168 hours.

Figure 4 shows the scatter plot of all obtained solutions showing $\Delta p$ at corresponding $\sigma_T$. The color of the symbols represents the values of $J$. The solutions presented in this plot form the Pareto front on which any change in $\mathbf{b}$ causes an increase/decrease of $\sigma_T$ with simultaneous decrease/increase of $\Delta p$. It can be readily noted that the configurations with a nearly uniform temperature distribution (small $\sigma_T$ close to one) characterise a very high high pressure drop, i.e., approximately two orders of magnitude larger than for the straight pipe. In effect, even if $\sigma_T$ is small, the cost function has large values. However, the most unfavorable waviness shape, shown in the inset figure with the caption "wavy wall, $J = 3.548$" occurs for $\sigma_T = 3.31$ K. This configuration is characterized by the waviness pushed towards the pipe axis. This shape enhances the mixing process but due to a local reduction in pipe diameter, generates a very large pressure drop. The optimal configuration, denoted as "wavy wall, $J = 0.318$", generates relatively low $\Delta p$, comparable to the one for the straight pipe, and also low $\sigma_T$. Analysis of the intermediate solutions shows that configurations close to the optimal one favor outward-oriented waviness in the pipe. This design enhances mixing without generating a large pressure drop. It is worth noting that for the same value of $\Delta p$, both low and high values of $\sigma_T$ and $J$ are observed. This indicates that some waviness shapes, despite resulting in a similar pressure drop, lead to substantially different heat transfer processes. For reference, a subfigure showing the straight pipe with $J = 1.0$ is also presented in Fig. 4. It should be noted that this configuration is not the worst one taking into account $\sigma_T$. There are cases for which $\sigma_T$ is 20 % larger and for which $\Delta p$ also slightly increases.

| Case | $J$ | $\Delta p$ [Pa] | $\sigma_T$ [K] | $A_1$ [m] | $A_2$ [m] | $s$ | $N$ | $I$ |
|---|---|---|---|---|---|---|---|---|
| Flat | 1.0 | 23.36 | 30.511 | 0.0 | 0.0 | - | - | - |
| Optimal | 0.318 | 24.91 | 9.09 | -0.002335 | 0.002049 | 50.4 | 1 | 5 |
| Worst | 3.548 | 764.86 | 3.31 | 0.002448 | -0.002500 | 58.2 | 20 | 6 |

Table 1: Wavy wall parameters of the optimal and the most non-optimal configurations.

The sets of parameters $\mathbf{b}$ for the optimal configuration with $J = 0.318$ and corresponding $\Delta p$, $\sigma_T$, as well as those for the worst case with $J = 3.548$ and those for the straight pipe ($J = 1$) are given in Table 1. The temperature fields and the wall shapes corresponding to these cases are shown in the inset figures in Fig. 4. In the worst case, the wall has a sawtooth shape resulting from the fact that the amplitude $A_1$ is negative and equals almost $A_2$, and additionally, $N = 20$ which is the maximum allowable value. In this configuration, the BO method leads to the solution with small $\sigma_T$ resulting from intensive mixing in the zones between the subsequent waves. Figure 5 shows the enlarged view of the very last part of the wavy section. This figure presents the temperature contours with the velocity vectors, and also, the

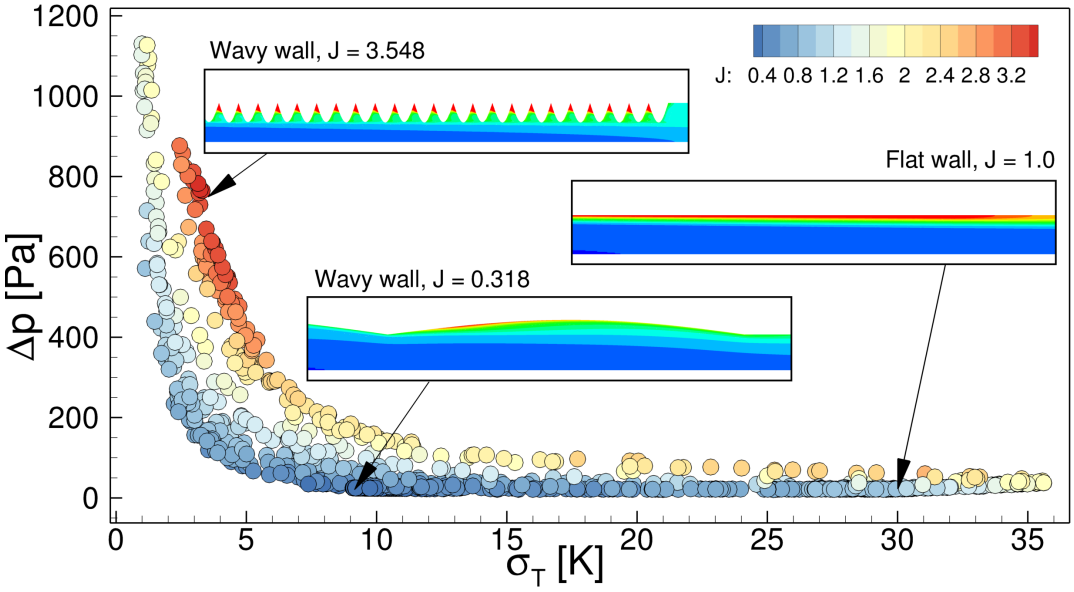



Figure 4: Scatter plot of $\Delta p = f(\sigma_T)$ coloured with $J$.

axial velocity and temperature profiles extracted along the white line indicated on the contour plot. As can be seen, the flow strongly recirculates, and the velocity inside the waviness reaches high negative values. i.e., almost half of the inlet velocity. This causes an intensive heat exchange but simultaneously also results in a very large temperature rise on the wall. In the sharp corners, the temperature reaches almost 600 K. Hence, even if the temperature drops towards the pipe axis to the range of 340 K to 360 K, this configuration would likely never be accepted for practical use due to the high thermal stress, which would destroy the wall surface in a relatively short time. Also, a very high pressure drop resulting from the blockage of the orifice pipe and near-wall drag force would preclude this configuration from practical use even if it yields small $\sigma_T$. In the case of the straight pipe, the fluid is aligned with the wall as in an isothermal flow in a cylindrical pipe. In this configuration, the near-wall thermal layer becomes thicker along the pipe and the wall temperature increases. In regards to the optimal waviness shape, the recirculation bubble appears at the beginning of the first wave (not shown), which causes an enhanced mixing and local temperature rise. Moreover, in the second wave, the flow recirculates only in the top part of the waviness in a thin layer near the wall. As can be seen in Table 1, this causes only a minor increase in the pressure drop compared to the one calculated for the straight pipe with $\sigma_T$ being reduced more than three times.

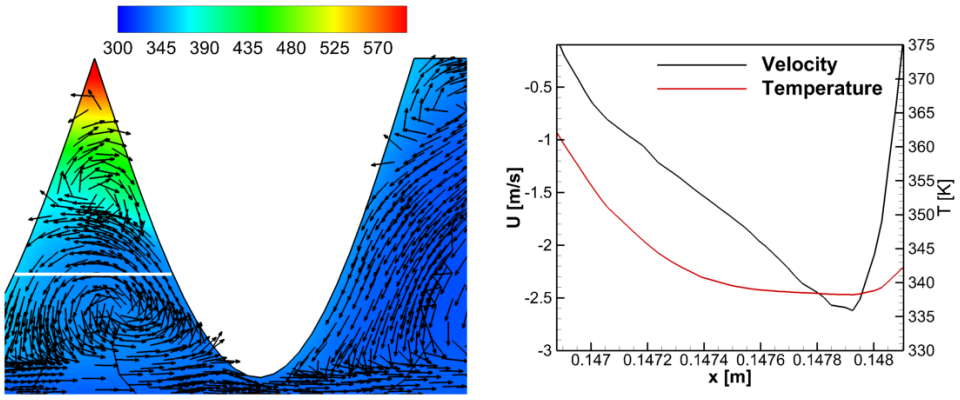
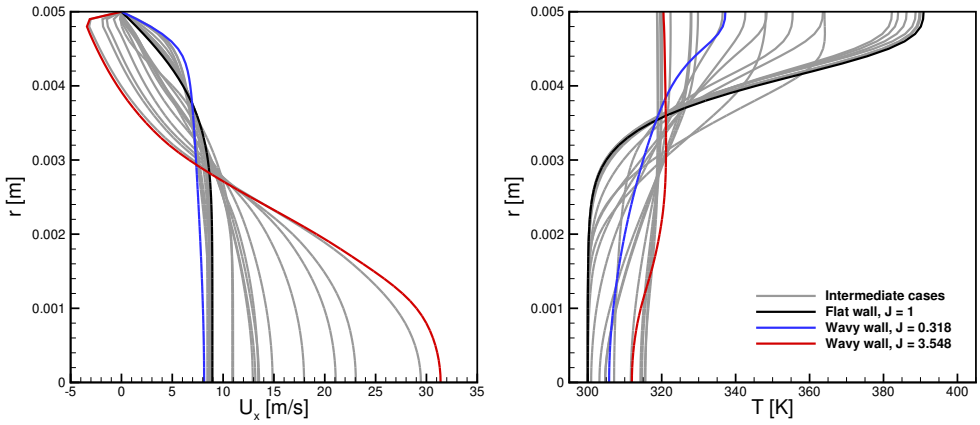



Figure 5: Temperature contours with the velocity vectors (left) and the velocity and temperature profiles (b) extracted along the white line inside the waviness for the worst wall shape.




(a) (b)

Figure 6: Profiles of temperature (a) and axial velocity (b) taken at $x = 0.16$ m, i.e. 0.01 m behind the waviness.

The differences discussed above between specific configurations undoubtedly affect the velocity field. Figure 6 shows the radial profiles of the axial velocity (a) and accompanied temperature distributions (b) at the location $x_2$ for the worst (red line), optimal (blue line), and straight pipe (black line) configurations. The grey lines correspond to the solutions for randomly selected intermediate configurations. The velocity profile for the straight pipe exhibits a typical shape for a developed turbulent flow. In this case, the near-wall boundary layer is relatively thick due to the strong viscous forces resulting from higher values of the molecular viscosity at a larger temperature. Its profile shows that the differences between the near wall and axis regions reach approximately 90 K. The velocity profile for the worst case shows the occurrence of the recirculation zone extending from the wall up to $r = 0.004$ m, which constitutes 20% of the pipe radius. The presence of a large recirculation bubble is one of the reasons for the significant pressure drop. The second factor that contributes to the pressure drop is a very large velocity increase in the central flow part. Compared to the inlet conditions the velocity increases more than five times. This is partially due to the density decrease at a higher temperature, which enforces the flow acceleration by the mass conservation law, but the main reason is the blockage of the pipe orifice by the wall waviness. Again, through the mass conservation law, the flow must accelerate. In effect, neglecting the the drag force on the wall and related local energy losses, and assuming preservation of the total pressure (dynamic+static), the static pressure must drop proportionally to the increase in the dynamic pressure ($\rho U^2/2$). In effect, the high value of $\Delta p$ diminishes the benefits resulting from small $\sigma_T$, which manifests by an almost flat temperature profile along the pipe radius. In the case of the optimal waviness configuration, the velocity profile is similar to that in the straight pipe, yet the differences in the temperature distributions are significant. This indicates that the flow domain geometry influences to a greater extent the velocity field than the temperature field. The main differences between the velocity profiles for the optimal configuration and the straight pipe occur near the wall and are related to two factors. First, and most importantly, the waviness induces a higher turbulence level near the wall, causing the boundary layer to become more turbulent and thus thinner. The increased turbulence enhances the mixing process, facilitating heat transfer from the near-wall region toward the pipe axis. As a result, the temperature in the central flow region is higher than in the straight pipe. On the other hand, lowering the temperature near the wall decreases the molecular viscosity, reducing the viscous forces compared to those in the straight pipe. This is the second factor contributing to the boundary layer's thickening.

## 4 Conclusions

In this study, the wavy wall shape was optimised, aiming to achieve the most uniform temperature distribution inside the pipe while minimizing losses resulting from pressure drop for the flow at a moderate Reynolds number equal to 4000. The optimal shape defined through the five parameters function was found with the help of the Bayesian optimization method working in a loop with the RANS simulations. In total, 1200 test cases were compared, yet, it has been demonstrated that the Bayesian optimization yields to a nearly optimal solution already in 50 iterations. The optimal wall shape is characterised by the waviness oriented outwards, locally increasing the diameter of the pipe. In this configuration, the

recirculation bubble occurs only in the initial waviness section near its upper part where it enhances the mixing process and heat transfer. This proves sufficient to decrease temperature variations more than threefold compared to the straight pipe configuration without causing a significant pressure drop. Conversely, the worst configuration, while resulting in very small temperature changes, led to a large pressure drop due to the narrowing of the pipe cross-section. Future work will focus on verifying to what extent the present findings translate to cases characterized by significantly different Reynolds numbers and whether the formulated Bayesian-RANS optimization strategy can be combined with more advanced machine learning algorithms employing deep learning methods.

**Acknowledgements**
The investigation was supported by the National Science Centre (Grant No. 2020/39/B/ST8/01449). On the Chinese side, this work is supported by the National Science Foundation of China (NSFC) (Grant No. 12172109), by the Guangdong Basic and Applied Basic Research Foundation (Grant No. 2022A1515011492), and by the Shenzhen Science and Technology Program (Grant No. JCYJ202205310 95605012).

**References**

[1] Mameli M, Marengo M, Khandekar S. Local heat transfer measurement and thermo-fluid characterization of a pulsating heat pipe. International journal of thermal sciences. 2014;75:140-52.

[2] Rainieri S, Pagliarini G, et al. Convective heat transfer to orange juice in smooth and corrugated tubes. International Journal of Heat and Technology. 1997;15:69-75.

[3] Bazdar H, Toghraie D, Pourfattah F, Akbari OA, Nguyen HM, Asadi A. Numerical investigation of turbulent flow and heat transfer of nanofluid inside a wavy microchannel with different wavelengths. Journal of Thermal Analysis and calorimetry. 2020;139:2365-80.

[4] Qi C, Wan YL, Li CY, Han DT, Rao ZH. Experimental and numerical research on the flow and heat transfer characteristics of TiO2-water nanofluids in a corrugated tube. International Journal of Heat and Mass Transfer. 2017;115:1072-84.

[5] Navickaitė K, Cattani L, Bahl CR, Engelbrecht K. Elliptical double corrugated tubes for enhanced heat transfer. International Journal of Heat and Mass Transfer. 2019;128:363-77.

[6] Mahmud S, Sadrul Islam A, Feroz C. Flow and heat transfer characteristics inside a wavy tube. Heat and mass transfer. 2003;39(5):387-93.

[7] Kurtulmuş N, Zontul H, Sahin B. Heat transfer and flow characteristics in a sinusoidally curved converging-diverging channel. International Journal of Thermal Sciences. 2020;148:106163.

[8] Zontul H, Hamzah H, Kurtulmuş N, Şahin B. Investigation of convective heat transfer and flow hydrodynamics in rectangular grooved channels. International Communications in Heat and Mass Transfer. 2021;126:105366.

[9] Liu S, Sakr M. A comprehensive review on passive heat transfer enhancements in pipe exchangers. Renewable and sustainable energy reviews. 2013;19:64-81.

[10] Blanchard A, Sapsis T. Bayesian optimization with output-weighted optimal sampling. Journal of Computational Physics. 2021;425:109901.

[11] Blanchard A, Sapsis T. Output-weighted optimal sampling for Bayesian experimental design and uncertainty quantification. SIAM/ASA Journal on Uncertainty Quantification. 2021;9(2):564-92.

[12] Blanchard A, Sapsis T. Informative path planning for anomaly detection in environment exploration and monitoring. Ocean Engineering. 2022;243:110242.

[13] Li Y, Noack BR, Wang T, Cornejo Maceda G, Pickering E, Shaqarin T, et al. Jet mixing enhancement with Bayesian optimization, deep learning, and persistent data topology. J Fluid Mech, in revision. 2024.

[14] Menter FR, Langtry R, Völker S. Transition modelling for general purpose CFD codes. Flow, turbulence and combustion. 2006;77:277-303.

[15] Ansys Fluent Theory Guide. ANSYS Inc.; 2021.

# Design of the wavy wall in a partially heated channel using CFD simulations and human-assisted Bayesian optimization

Piotr Kamiński[a], Karol Wawrzak[a], Yiqing Li[b,c], Bernd R. Noack[b,d], Artur Tyliszczak[a]

[a]*Department of Thermal Machinery, Czestochowa University of Technology, Al. Armii Krajowej 21, 42-200 Czestochowa, Poland*
[b]*Chair of Artificial Intelligence and Aerodynamics, School of Mechanical Engineering and Automation, Harbin Institute of Technology, 518055 Shenzhen, P.R. China*
[c]*Department of Mechanical Engineering, University College London, London, UK*
[d]*Guangdong Provincial Key Laboratory of Intelligent Morphing Mechanisms and Adaptive Robotics, Harbin Institute of Technology, 518055 Shenzhen, P.R. China*

arXiv:submit/6763884 [physics.flu-dyn] 4 Sep 2025

**Abstract**

This study explores heated wavy wall shape design in channel flow using machine learning, aiming to minimize temperature variation ($\sigma_T$) while limiting pressure loss ($\Delta p$). A cost function $J$ defined as a product of $\sigma_T$ and $\Delta p$ balances these competing objectives. Optimization is performed via Bayesian optimization (BO) coupled with Reynolds-Averaged Navier-Stokes (RANS) computations in an active learning loop involving up to 1000 subsequent iterations. Two shaping strategies are considered: a sinusoidal-type function defined by four parameters (two waviness amplitudes, wave count, and tilt), and a higher-dimensional approach employing a Piecewise Cubic Hermite Interpolation Polynomial (PCHIP) with 19 control points. Results show the sinusoidal design reduces $\sigma_T$ over 60-fold but increases $\Delta p$ fourfold, while the PCHIP shape offers only a 15-fold $\sigma_T$ reduction but with a twofold $\Delta p$ increase. Flow characteristics such as turbulent kinetic energy, pressure, temperature, and Nusselt number are examined for both optimal and suboptimal shapes along the Pareto front. The insights gained motivated a human-aided refinement of the BO result, leading to a further 17.7% reduction in $J$. This was achieved by replacing small-amplitude waviness periods with flat segments, which additionally significantly facilitates manufacturability.

*Keywords:* wall corrugation, flow control, Bayesian optimization, CFD-RANS.

## 1. Introduction

Despite the continuous advancement of renewable energy sources [1, 2, 3, 4], reducing energy consumption remains a critical area of research within both academia and industry. Studies primarily focus on enhancing the efficiency of energy production, which still largely depends on fossil fuel combustion [5, 6], and its application across various end-user systems. Among these, heat exchangers represent a key category of devices with applications spanning the automotive [7, 8] and food industries [9], as well as miniaturized cooling systems for computers [10, 11] and common household systems, including air-conditioning and heating [12, 13]. The primary components of heat exchangers are channels and pipes in which the heat transfer between a flowing medium and walls occurs in thin boundary layers. In general, two types of flow control methods can be employed to enhance heat exchange across them, active and passive. Active methods involve complex systems that, while highly effective, require an external energy source. Examples include the application of electrohydrodynamic methods in which an electric field of high voltage and low current act on electrorheological fluids [14, 15, 16]; synthetic jets [17, 18, 19]; sprays [20, 21]; forcing flow unsteadiness using vibrating surfaces [22, 23]; introducing pulsating flow [24, 25, 26]; or stirring the fluid [27, 28, 29]. Although the active approach is reported to be adaptable to varying flow conditions, it receives less attention due to its high cost. In contrast, passive flow con-

*Email address:* piotr.kaminski@pcz.pl (Piotr Kamiński)

trol is much more attractive because it does not require any external input, which effectively improves the ecological aspect of the system. The passive approach involves introducing unsteadiness into the flow via surface shape deformation [30], which strongly enhances mixing and, in turn, improves heat transfer. Various techniques have been employed to achieve this goal. Major examples include vortex generators [31, 32], widely used in the aerospace field; dimples [33, 34], commonly seen on golf balls, which can be utilized to promote mixing; various types of fins (offset, sinusoidal, louvred, and others) [35, 36, 37, 38, 39]; wire turbulizators [40, 41]; and twisted tapes [42, 43]. These techniques have also been combined to create compound approaches, often exhibiting the primary benefits of their components [44, 45, 46]. These methods considerably increase turbulence intensity and in some cases may also reduce losses [47]. Unconventional passive flow control approaches have also been examined in the literature. A prominent example is the use of porous walls, which from one side increase a heat exchange surface, and from the other, intensify a small-scale mixing process [48, 49].

The passive control approaches discussed thus far are highly effective in many applications. However, their intricate shapes can sometimes make them challenging to manufacture, often requiring advanced fabrication methods [50]. Consequently, simpler and more streamlined surfaces are often preferred, such as plate-fin exchangers [51] or heat sinks [52]. With advancements in additive manufacturing [38, 53, 50], corrugated surfaces have garnered significant attention. These geometries disrupt boundary layers and create flow circulations, enhancing heat exchange between core and low-velocity fluid regions. An important yet well-researched example of such methods is the use of walls with grooves [54, 55, 56]. In the experimental work by Zontul et al. [57], rectangular grooves on a wall were examined, revealing that this shape significantly improved thermal performance compared to a smooth reference configuration. Moreover, the authors reported that the wall deformation promotes a more uniform distribution of vortical structures, particularly as the Reynolds number increases. Li et al. [58] investigated heat transfer in a channel with periodically grooved rectangular walls. Their findings showed that this configuration induces flow oscillations, resulting in unsteadiness and substantial mixing enhancement. A study by Ramadhan et al. [59] reported that channels with rectangular grooves generally enhance the Nusselt number ($Nu$), but this comes with the drawback of an increased pressure drop. It has been shown that employing triangular grooves instead of rectangular ones can somewhat reduce these losses. Similar observations were made by Hoang et al. [60], where triangular corrugation was examined. Moreover, it was found that an optimal amplitude of the corrugation exists, which maximizes both $Nu$ and the so-called thermal performance factor, denoting a ratio of heat transfer rate to friction factor. Research efforts to improve heat transfer through the use of corrugations are not limited to rectangular or triangular surfaces. Other wall types, such as trapezoidal [61, 62], as well as combinations of rectangular, triangular, and trapezoidal shapes [63], have been employed with varying levels of success. These configurations generally enhance heat transfer compared to smooth walls, but their performance varies significantly depending on corrugation parameters, e.g., the depth and length of the grooves. Additionally, the shape of the grooves strongly influences pressure losses, which must be accounted for in design considerations.

A drawback of rectangular and triangular corrugation types is their sharp corners, which can lead to significant pressure losses. Additionally, sharp edges and corners cause an increase in local thermal stress, leading to premature damage to the wall in real-life scenarios. Additionally, in some extreme cases, such walls with sharp-type grooves may be difficult to manufacture with sufficient precision, particularly in small-scale devices. Due to these concerns, the use of sinusoidal walls for heat transfer enhancement is of greater interest, and thus, it has gathered widespread attention in the literature [64, 65, 66, 67, 68, 69, 70, 71, 72, 73, 74]. These works allow the formulation of the following conclusions. Sinusoidal waviness enables a considerable increase in the turbulent kinetic energy (TKE) (i); the level of the TKE increase depends on cor-

rugation parameters, $A$ - the amplitude, $\lambda$ - the waviness period length and when $A/\lambda$ ratio grows, the heat transfer efficiency rises (ii); in some cases, however, there is a certain threshold of $A/\lambda$ beyond which any further improvements do not occur (iii); pressure drop, considerably increasing with the growth of $A/\lambda$, is a major concern (iv). Worth noticing is that the use of wavy walls extends beyond heat transfer enhancement to the aerospace field. For instance, in aerospace science, they find applications in controlling laminar-turbulent transition [75] and separation [76, 77].

The summary above indicates that enhancing mixing and heat transfer in heat exchangers remains an active area of research, with wavy wall designs playing a prominent role. Optimizing these shapes for suitability in specific applications is a key focus. While some attempts have been made in this direction [78], the extent of investigated wall shape modifications has been limited. The large number of potential design parameters makes the design space multidimensional and challenging to explore using traditional optimization approaches. In this context, machine learning (ML) emerges as a highly suitable approach. Its application for optimizing surface shapes in fluid mechanics dates back to the 1960s [79]. Our generation is witnessing a convergence of large data volumes, affordable computation, advanced algorithms, open-source resources, and industry investment in data-driven solutions. This synergy is propelling rapid advancements in machine learning, with growing applications in fluid mechanics [80]. Machine learning frameworks such as genetic algorithms (GAs) [81], genetic programming (GP) [82, 83] and reinforcement learning (RL) [84, 85, 86] are becoming increasingly popular in flow control applications.

In the context of wavy wall shape optimization, the potential of ML remains largely untapped, with GAs being the most commonly used approach. Fabbri [87] employed GA to optimise the corrugated wall shape for maximising heat transfer. The resulting geometry featured waviness tilted in the upstream direction with alternating wavelengths, providing a 30% increase in transferred heat compared to a non-optimized surface. Joodaki and Ashrafizadeh [88] combined GA and particle swarm optimization (PSO) and starting from a waviness tilted downstream, they obtained an optimal configuration resembling periodic cavities similar to a reverse of bump function. Non-dominated Sorting Genetic Algorithms (NSGA-II) is widely recognized as a classic solver for multi-objective optimization. Wang et al. [89] employed NSGA-II for heat transfer enhancement. While the resultant shape improved it significantly, it was accompanied by up to a 310% increase in the required pumping power needed for an assumed mass flow. This was caused by substantial pressure losses induced by the waviness shape and optimization considering only the heat transfer increase. NSGA-II was also used by Kirkar et al. [90] for designing a tube with a helically corrugated wall. However, in this research, the design space included only two parameters, the corrugation depth and pitch. This research aimed at demonstrating a strong dependency between the control parameters and the Nusselt number.

GAs allow for the tuning of predefined control laws toward near-optimal performance. However, the amount of test data needed scales with the dimensionality of the parameter space, making this approach increasingly impractical for high-dimensional optimization tasks. As the function regressor, GP and RL can provide a large model capacity for exploration. However, deriving the optimal solution in finite time cannot be guaranteed. Bayesian Optimization (BO) has recently gained attention due to the capability to balance both data efficiency and the performance of the final control solution in jet and wake flows [91, 92, 93]. BO is a surrogate-model-based design optimization algorithm that typically relies on Gaussian processes (GP) [94]. The BO procedure can be divided into two main phases. The first phase involves training a surrogate model of the objective function based on a finite training data set. In the second phase, the algorithm identifies, evaluates, and adds the most promising data samples to the data set, The surrogate model is refined, and the design space is explored through the alternation of the two phases. This approach enables fast convergence to the optimal solution with fewer evaluations com-

pared to GA, making it particularly useful for tasks such as hyperparameter tuning in ML models or optimizing expensive simulations [93].

This work focuses on the shape design of a wavy wall in a channel flow using machine learning, specifically combining BO with Computational Fluid Dynamics (CFD). Regarding optimization goals, various approaches can be found in the literature. For example, Fabbri [87] focused on maximizing $Nu$ while imposing a constraint on the maximum allowable pressure drop. Joodaki and Ashrafizadeh [88] optimized the thermal performance factor, which included $Nu$ and friction factor, evaluated based on the pressure drop. Wang et al. [89] performed a two-parameter optimization, where the objective functions were a pumping power and heat transfer area depended on $Nu$, friction factor, and the hydraulic diameter of the channel. The aim of the present research is to improve the uniformity of the temperature distribution while minimizing pressure losses by identifying a set of parameters that define the function shaping the wall. The uniform temperature of the fluid leaving a heat exchanger is advisable in various applications, e.g., in fuel preheating systems in combustion devices, cooling/heating jets impinging on walls, room ventilation systems or air curtains. A two-parameter cost function $J$ includes temperature variations $\sigma_T$ and pressure drop $\Delta p$. Two wall-shaping functions are tested in the learning framework, which differ significantly by the design parameter space. A simpler approach involves a sinusoidal type 4-parameter function, including local waviness amplitudes, number of wavinesses, and their tilt. The second, significantly more complex method, utilizes Piecewise Cubic Hermite Interpolation Polynomial (PCHIP), where the design control parameters space consists of 19 amplitudes of local function segments. The optimization-learning process employs BO working iteratively alongside the Reynolds-Averaged Navier-Stokes solver (ANSYS Fluent). A better optimal configuration is identified for the sinusoidal wall type. It reduces $\sigma_T$ by more than 60 times, with only a fourfold increase in $\Delta p$ compared to a channel with flat walls. In this regard, the use of PCHIP results in approximately a 15-fold reduction in $\sigma_T$, but with only a twofold increase in $\Delta p$. The obtained solutions, including both the optimal and the least effective configurations, are analyzed in detail to identify the reasons for their advantages and limitations. The performed investigations include comparisons of TKE, pressure, temperature, and Nusselt number distributions. The outcomes of this analysis stimulated performing a human-assisted optimization (HAO) focusing on making the manufacturing process easier without decreasing the BO-RANS achievements. Surprisingly, it turns out that HAO leads to a configuration which is significantly simpler and better from the point of $J$.

The manuscript is organized as follows. In the next section, the description of the research object, definition of the cost function and details of the wavy wall configurations are presented. Details of the optimization loop along with the description of a flow model and BO algorithm, are given in Section 3. The obtained results, along with their in-depth analysis are presented in Section 4. This section also includes the verification of the obtained RANS solution. The conclusions and suggestions for future work are provided in Section 5.

## 2. Research object and optimization goal

The geometry of the channel and flow parameters have been adapted from Zontul et al. [57]. Originally, it consisted of a straight inlet section followed by a series of rectangular cavities and ended with a flat wall. This configuration is analyzed in Section 4.1 for the numerical model validation. In the present work, we modify the central channel section by assuming a wavy wall shape, as illustrated in Fig. 1. The height ($H$), width ($W$) and length ($L$) of the channel are equal to $H = 0.018$ m, $W = 0.15$ m and $L = 1.22$ m. The wavy section has the length $L_w = 0.5$ m and extends from $x_S = 0.36$ m to $x_E = 0.86$ m. This part of the channel is heated, and the research focuses on finding the wall shape that ensures the most uniform temperature downstream of the waviness.

As in [57], the inlet velocity is $U_{in} = 0.1116$ m/s that results in the Reynolds number of $Re = \rho U_{in} H/\mu = 2000$ ($\rho$ - the mass density, $\mu$ - the molecular viscosity). It falls well within the

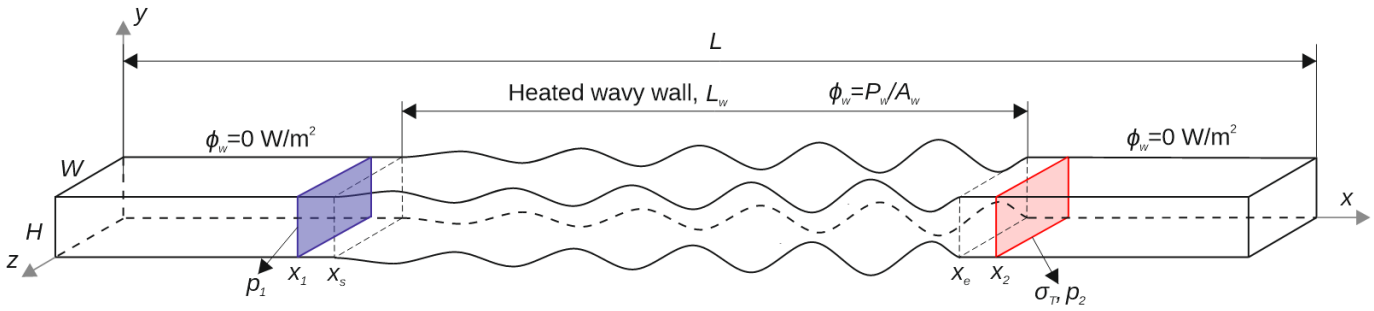



Figure 1: Computational domain and the assumed boundary conditions.

range of Reynolds numbers studied in the literature [95, 57, 96]. At the inlet, the flow is assumed to be in a low-turbulence regime with a turbulence intensity of $T_i = u'/U_{in} = 1\%$, where $u'$ stands for the RMS of the velocity fluctuations. The inlet flow temperature is set at $T_{in} = 300$ K. A relatively large dimension of the channel in the 'z'-direction minimizes the influence of the side boundaries on the flow in the central region. To completely eliminate this effect, periodic boundary conditions are imposed at the side boundaries of the channel, located at $z = \pm W/2$. This approach avoids the need to account for near-corner flows, which would otherwise require specially tailored computational meshes. All sections of the upper and lower channel walls are treated as no-slip, and their temperature varies depending on the assumed boundary conditions. In the sections before and after the waviness, the wall is treated as adiabatic with the heat flux equal to zero ($\phi_w = \kappa \nabla T = 0$ W/m$^2$, $\kappa$ - the heat conductivity). In the wavy section, regardless of its shape, we assume a constant heating power equal to $P_w = 10000$ W with the heat flux $\phi_w = P_w/A_w$, where $A_w$ is the surface area of the wavy wall. Note that specifying the thermal boundary conditions in terms of the heat flux implies that a local wall temperature varies based on the wall shape and flow state near the wall surface. In the case of a straight channel, the heated wall section reaches an average temperature of $T_{w,\text{mean}} = 379.2$ K. The average temperature of the fluid downstream of the heated section is independent of the wall shape and equals $T_{f,\text{mean}} = 307.9$ K.

As explained above, the objective of the optimization is to identify the waviness shape that ensures the most uniform temperature distribution downstream of the heated section. As a control point, we take the location right after the waviness end at $x_2 = 0.87$ m (see Fig. 1). The standard deviation quantifies the uniformity of temperature

$$\sigma_T = \frac{1}{HW} \int_0^H \int_0^W \sqrt{(T(x,y,z) - T_{f,\text{mean}}(x))^2}\, dydz, \qquad (1)$$

where $T(x,y,z)$ and $T_{f,\text{mean}}(x)$ are the local and average temperatures at the distance $x_2$. A consequence of waving the wall shape or introducing a corrugation, e.g., by grooves [97], is an increase in pressure drop along the channel. The wall shape, which enhances the mixing process and heat transfer most efficiently may lead to a very high-pressure drop ($\Delta p$) resulting in significant energy losses. In effect, the power $P = \dot{m}\Delta p$ needed to drive the flow at a given mass flow rate ($\dot{m}$) increases such that the benefits from the optimization (here $\sigma_T \to 0$) are small. Therefore, in the present work the optimization goal is to minimize $\sigma_T$ while avoiding a significant increase in the pressure drop, $\Delta p = |p_2 - p_1|$, where $p_2$ and $p_1$ are the average static pressures at locations $x_2$ and $x_1$ equal to 0.87 m and 0.35 m, respectively (see Fig. 1). By combining the parameters $\sigma_T$ and $\Delta p$, we define the cost function $J$ as follows

$$J = \left(\frac{\sigma_T}{\sigma_{T,\text{flat}}}\right) \times \left(\frac{\Delta p}{\Delta p_{\text{flat}}}\right) \qquad (2)$$

where the variables $\sigma_{T,\text{flat}}$ and $\Delta p_{\text{flat}}$ stand for the reference values obtained for the channel with the flat walls. Thus, from the point of view of the optimization goal, the wall shapes leading to $J \approx 1$ can be regarded as equivalent to the flat channel, whereas the cases with $J > 1$ and $J < 1$ characterize worsened

or improved performance, respectively. This product of normalized performances in $\sigma_T$ and $\Delta p$ weighs a relative change in each variable equally. An alternative approach could be to optimize $\sigma_T$ with a constraint imposed on $\Delta p$, as in [87], or to minimize $\sigma_T$ and $\Delta p$ separately, following the multi-objective strategy used in [89]. The present method, in which the cost function is a single scalar variable combining $\sigma_T$ and $\Delta p$, is, however, less computationally expensive in terms of optimization time. A similar optimization strategy was employed by Joodaki and Ashrafizadeh [88] to maximize the Nusselt number while minimizing friction.

### 2.1. Wall shape definition

We assume that the upper and lower wall shapes are symmetric with respect to the channel axis. They are defined using two methods, which differ by the number of control parameters, resulting in a smaller or greater flexibility of the waviness. The first method relies on modifying a sinusoidal wave by adjusting the number of periods (waves), their amplitudes, and tilt. Sample wall shapes obtained by applying this approach are displayed in Fig. 2. The second method employs a spline-type interpolation function (PCHIP [98]) with 19 control points. This approach allows for modifying the waviness in a free-form manner, without being restricted to the periodic pattern of the sinusoidal wave, as illustrated in Fig. 3. The following two subsections detail the applied wall-shaping methods.

#### 2.1.1. Sinusoidal wall type

In this approach, the wall shape is the result of an iterative procedure, which starts from the sinusoidal wall shape and deforms it depending on 4 control parameters. This procedure is defined as:

$$y_1(x) = \sin\left(x\frac{2\pi N}{L_w}\right) \tag{3}$$

$$y_{i+1}(x) = \sin\left(x\frac{2\pi N}{L_w} + s y_i(x)\right) + y_i(x); \quad i = 1, ..., I \tag{4}$$

where $y_i(x)$ represents a local amplitude of the waviness in reference to $y = \pm H/2$, $N$ denotes the number of periods along $L_w$, $s$ is a parameter that defines the tilt, and $I$ is the number of iterations ($i = 1, \ldots, I$). As $I$ increases, the waviness becomes less smooth. For simplicity, we keep the number of iterations fixed and equal to $I = 5$. During the subsequent iterations, the waviness height is not constrained, meaning it can become arbitrarily large or small. In extreme cases, this could result in the channel being completely blocked if $y_i \geq H/2$. To prevent this and to control the external dimensions of the pipe, the maximum amplitude of the waviness at iteration step $I$ is normalized to one and then scaled by the desired amplitude as follows

$$y_I(x) = A(x) \times \left(\frac{y_I(x)}{\max(y_I(x))}\right) \tag{5}$$

with $A(x)$ varying along the streamwise direction. In the range $x \in [x_S, x_E]$ we define $A(x)$ as

$$A(x) = A_s + \frac{A_e - A_s}{L_w}(x - x_S) \tag{6}$$

where $A_s$ and $A_e$ are the amplitudes at the beginning and the end of the waviness, see Fig. 2. Hence, the four-parameter design space defining the wall shape consists of $A_s$, $A_e$, $N$ and $s$. As can be seen in Fig. 2, the shape of the wall can vary substantially, from nearly sinusoidal (a), which is obtained for $s = 0$, to strongly irregular shapes (b–d). A limitation of this method is that it does not allow for defining a wall that is partially flat even if $A_s$ or $A_e$ is equal to zero. As can be seen in Fig. 2b-d, the amplitude of the waviness can only be equal to zero locally.

#### 2.1.2. Spline-shaped wall type (PCHIP)

This approach does not have the aforementioned limitation. PCHIP is defined by 21 control points uniformly distributed between $x_S$ and $x_E$. Except for the first and last points, their amplitudes are treated as control parameters subject to optimization. At the first and last points, the amplitudes ($y_0$ and $y_{20}$) are set to zero. This constraint ensures the continuity of the polynomial and the channel walls and allows enforcing the condition $dy/dx = 0$ at $x = x_S$ and $x = x_E$. Consequently, this approach provides a design space with 19 parameters corresponding to the amplitudes $y_{1-19}$. PCHIP in between two successive control points $x_j$, $x_{j+1}$ is defined by the following formula:

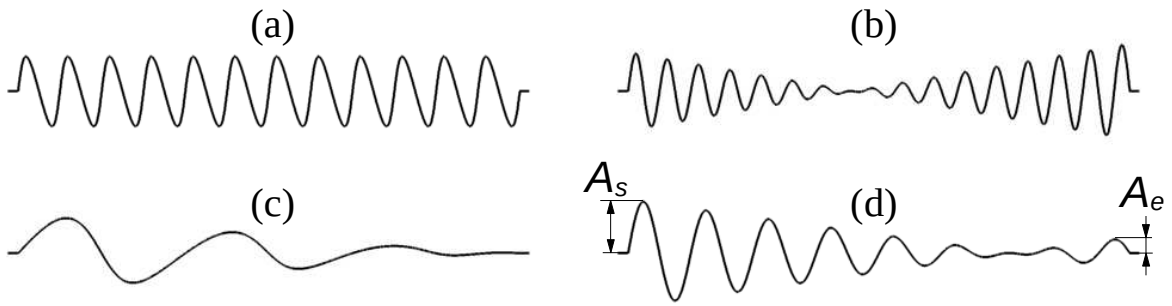



Figure 2: Schematic drawings of sample wall shapes generated by the iterative procedure defined in Eq. (3).

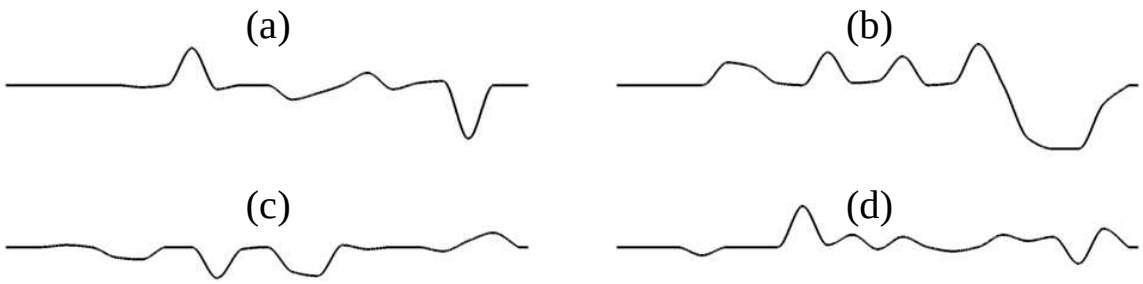



Figure 3: Schematic drawings of sample wall shapes generated by PCHIP defined in Eq. (7).

$$y(x) = h_{00}y_j + h_{10}\left(\frac{\partial y}{\partial x}\right)_j (x_{j+1} - x_j) + h_{01}y_{j+1} + h_{11}\left(\frac{\partial y}{\partial x}\right)_{j+1} (x_{j+1} - x_j) \tag{7}$$

where $h_{00}$, $h_{10}$, $h_{01}$, $h_{11}$ are the basis functions, defined as

$$\begin{aligned} h_{00} &= (1+2t)(1-t)^2,\ h_{10} = t(1-t)^2 \\ h_{01} &= t^2(3-2t),\ h_{11} = t^2(t-1) \end{aligned}$$

with $t = (x - x_j)/h_j$, where $h_j = x_{j+1} - x_j$. To ensure the monotonicity of the polynomial, its derivatives are carefully defined, preventing the introduction of oscillations between data points. PCHIP closely follows the shape of the control points, ensuring that the polynomial extrema do not exceed those of the data points. The derivatives are defined as:

$$\left(\frac{\partial y}{\partial x}\right)_j = \begin{cases} 0 & \text{if} \quad \Delta y_j \Delta y_{j-1} \le 0 \\ \frac{(w_1+w_2)}{(w_1/\Delta y_{j-1} + w_2/\Delta y_j)} & \text{otherwise} \end{cases} \tag{8}$$

with $w_1 = 2h_j + h_{j-1}$, $w_2 = h_j + 2h_{j-1}$, $\Delta y_j = (y_{j+1} - y_j)/h_j$.

## 3. Mathematical model formulation

The optimization procedure is schematically presented in a block diagram shown in Fig. 4. It relies on an iterative procedure consisting of two parts working in a loop. The first one involves modeling the flow in the channel by solving the Navier-Stokes and heat transfer equations. The second is based on the Bayesian optimization method in which the solution obtained in the first step is used to compute the cost function and new wall shape parameters are defined for the next iteration. In the following two subsections, the flow model and the Bayesian optimization procedure are described, whereas details of the optimization loop are discussed in Section 4.2.

### *3.1. Flow model*

We consider an incompressible flow of water governed by the continuity, Navier-Stokes, and energy equations defined as

$$\frac{\partial \rho}{\partial t} + \frac{\partial(\rho U_i)}{\partial x_i} = 0 \tag{9}$$

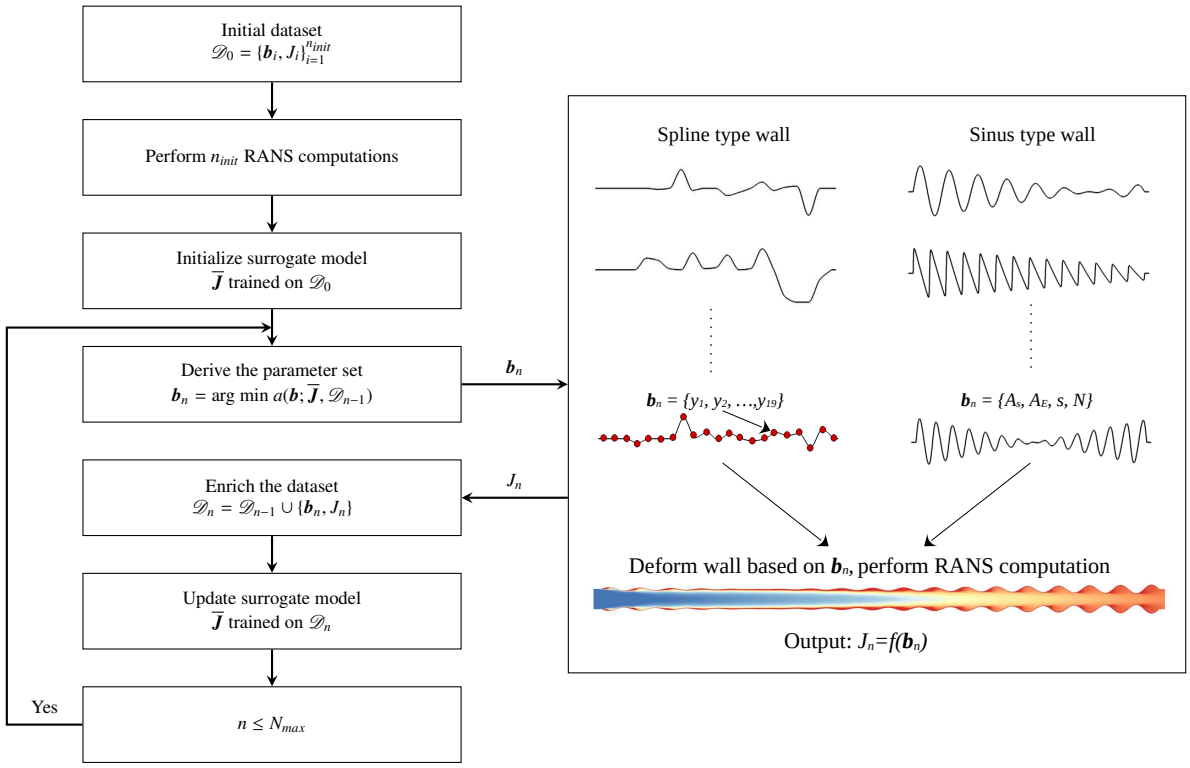



Figure 4: Block diagram illustrating the optimization procedure.

$$\frac{\partial(\rho U_i)}{\partial t} + \frac{\partial(\rho U_i U_j)}{\partial x_j} + \frac{\partial p}{\partial x_i} = \frac{\partial}{\partial x_j}\left[\mu\left(\frac{\partial U_i}{\partial x_j} + \frac{\partial U_j}{\partial x_i} - \frac{2}{3}\delta_{ij}\frac{\partial U_k}{\partial x_k}\right)\right] \tag{10}$$

$$\frac{\partial(\rho C_p T)}{\partial t} + \frac{\partial(\rho C_p U_i T)}{\partial x_i} = \frac{\partial}{\partial x_j}\left(\kappa\frac{\partial T}{\partial x_j}\right) \tag{11}$$

where $U_i$ denotes the velocity component in the $i-$direction, $p$ is the pressure and $T$ represents the fluid temperature. As discussed in Section 2, the considered range of the temperature variations is small which allows assuming physical properties of water to be constant, i.e., the density equals $\rho = 997$ kg/m$^3$, the molecular viscosity $\mu = 0.001003$ kg/m s, the thermal conductivity $\kappa = 0.6$ W/m K, and the specific heat capacity $C_p = 4182$ J/kg K.

The flow at $Re = 2000$ in a complex-shaped channel is treated as turbulent and is modelled by applying the Reynolds-Averaged Navier-Stokes (RANS) method. The complexity of the analyzed flow, characterized by the presence of several recirculation zones of varying sizes, precluded the unequivocal selection of a suitable RANS model. Test analysis aimed at determining the most accurate model involved a comparison of the solutions obtained from seven models, including the realizable $k-\epsilon$, Spalart-Allmaras, $k-\omega$, $k-\omega$ SST, Reynolds Stress Model (RSM), transition $k-kl-\omega$, and transition SST. Details of their formulations can be found in [99, 100, 101]. The computations were performed by utilizing the well-known and widely used [102, 103, 104, 105, 106, 107] ANSYS Fluent commercial software. The second-order spatial discretization method was applied to the transport equations for momentum, energy, and turbulent quantities (e.g., turbulent kinetic energy). It involved using a central discretization scheme for the diffusive terms and an upwind discretization scheme for the convective terms. The coupled algorithm [101] was employed for simultaneous calculations of the pressure and velocity fields, with the pressure gradient discretized using the second-order central approximation scheme.

### 3.2. Bayesian optimization

The optimization problem is to find the wall shape $\mathbf{b}^*$ minimizing the cost function $J$ defined as:

$$\mathbf{b}^* = \arg\min_{\mathbf{b}\in\mathcal{B}} J(\mathbf{b}). \tag{12}$$

The design vector $\mathbf{b}$ consists of $n$ parameters, which vary depending on whether the sinusoidal or spline function is used for wall shaping. In the former case, $n = 4$, and the design vector includes the following parameters $A_S$, $A_E$, $s$, and $N$. The amplitudes are constrained to the range $[-A_{min}, A_{max}]$ with $A_{min} = A_{max} = 0.004$ m, which constitutes 22% of the channel height. The tilt parameter varies in the range $s \in [-1, 1]$ and we assume that the maximum number of periods equals $N = 20$. Thus, the search space is defined as $\mathcal{B} = [-0.004, 0.004] \times [-0.004, 0.004] \times [-1, 1] \times [1, 20]$. In the case of the spline-shaped wall, $n = 19$, and the design vector includes only the amplitudes of the control points, i.e., $y_{1-19}$, constrained to $[-A_{min}, A_{max}]$. Thus, the search space is defined as $\mathcal{B} = [-0.004, 0.004]^{19}$.

During the search for the optimal solution in Fig. 4, BO sequentially derives the next data point to evaluate. The selection of data points is based on the surrogate model trained with all historical data and the acquisition function [108].

Gaussian Process (GP) regression provides a closed-form solution with posterior distribution and quantifies uncertainty, making it a standard surrogate model for BO. Let $\mathbf{x}$ denote the input, i.e., the optimization parameter vector, and $y$ denote the corresponding output. Based on historical data $\mathcal{D} = \{\mathbf{x}, \mathbf{y}\}$ and a Gaussian process with constant mean $m_0$, the posterior mean $\mu(\mathbf{x})$ and variance $\sigma^2(\mathbf{x})$ of the random process $\bar{f}(\mathbf{x})$ follow a normal distribution:

$$\mu(\mathbf{x}) = m_0 + k(\mathbf{x}, \mathbf{X})\mathbf{K}^{-1}(\mathbf{y} - m_0), \tag{13}$$

$$\sigma^2(\mathbf{x}) = k(\mathbf{x}, \mathbf{x}) - k(\mathbf{x}, \mathbf{X})\mathbf{K}^{-1}k(\mathbf{X}, \mathbf{x}). \tag{14}$$

where $\mathbf{K} = k(\mathbf{X}, \mathbf{X}) + \sigma_\epsilon^2\mathbf{I}$. Here, $m_0$ is the mean, and $k(\mathbf{x}, \mathbf{x})$ is the covariance function. The covariance function uses the Radial Basis Function (RBF) kernel with relevance determination:

$$k(\mathbf{x}, \mathbf{x}') = \sigma_f^2 \exp(-(\mathbf{x} - \mathbf{x}')^T\boldsymbol{\Theta}^{-1}(\mathbf{x} - \mathbf{x}')/2). \tag{15}$$

where $\boldsymbol{\Theta}$ denotes hyperparameters and is calibrated to historical data using maximum likelihood estimation. Equation 13 can predict the output value at any sample $\mathbf{x}$, and Equation 14 quantifies the uncertainty of that prediction [109].

To guide the data acquisition, the likelihood-weighted confidence lower bound acquisition function [110] is used:

$$\alpha(\mathbf{x}) = \mu(\mathbf{x}) - \kappa\sigma(\mathbf{x})w(\mathbf{x}), \quad w(\mathbf{x}) = \frac{p_{\mathbf{x}}(\mathbf{x})}{p_\mu(\mu(\mathbf{x}))}. \tag{16}$$

Here, the parameter $\kappa = 1$ balances global exploration (larger $\kappa$) and local exploration (smaller $\kappa$). The likelihood ratio $w(\mathbf{x})$ weights the input density $p_{\mathbf{x}}$ and output density $p_\mu$, measuring the uncertainty of point $\mathbf{x}$ and its expected impact on the cost function.

## 4. Results

In the RANS approach, the results are obtained for the time-averaged quantities [100] by applying a solution algorithm involving an iterative procedure. In all analyzed cases, the initial velocity is set equal to zero, and the temperature of the fluid in the channel equals the inlet temperature. The convergent steady-state solution can be formally defined by reaching a convergence level expressed as

$$\frac{\sum_{\mathrm{N_{cell}}} \partial\phi/\partial t}{\sum_{\mathrm{N_{cell}}} \partial\phi/\partial t\,|_{n=5}} = \varepsilon, \tag{17}$$

where $\phi$ denotes the velocity, temperature, and any other turbulent quantities computed with a given turbulence model (e.g., turbulent kinetic energy or turbulent dissipation rate in the $k-\epsilon$ model), $\mathrm{N_{cell}}$ stands for the number of cells, and $n = 5$ denotes the reference error level at the fifth iteration. Preliminary computations performed for several cases with significantly different wall shapes have shown that the iterative procedure converges to the prescribed threshold level $\varepsilon = 10^{-6}$ within 300–600 iterations, requiring 1–2 hours on a 96 CPUs cluster.

Further reduction of the error tolerance to $\varepsilon = 10^{-7}$ resulted in only minor quantitative differences in the solutions. Moreover, it has been found that the obtained results exhibit a 2D character with the maximum velocity in the 'z'-direction a few orders of magnitude smaller than the wall-normal and streamwise velocity. The two-dimensional nature of the flow was confirmed by performing additional 2D simulations and comparing the results with those obtained for corresponding 3D configurations. Consequently, the RANS model validation discussed in the following section, as well as the optimization process presented later, were carried out using 2D cases. For these cases, the solutions also converged within 300–600 iterations, depending on the mesh resolution and the turbulence model applied. However, the 2D approach, which employed computational meshes with a significantly smaller number of cells (see Section 4.3.1), greatly reduced the simulation time, typically to 5–10 minutes using 16 CPUs. To increase the credibility of the obtained 2D results, test computations were performed in full 3D geometries for the cases identified as the optimal and worst. As will be discussed later, the differences between the 2D and 3D simulation results are negligible.

### *4.1. Model validation*

In this section, we analyze the accuracy level of the applied RANS method and select the model to be used for the BO-RANS procedure. As a test case, we take a flow in a channel presented in Fig. 5 studied by Zontul et al. [57], which also serves as the basic configuration for the present studies. The length and width of the channel and the beginning and length of the heated section are the same as in the configuration subjected to the optimization, see Section 2. The main difference is the shape of the heated part, composed of rectangular grooves. Each groove has a length of $L_g = 0.02$ m and a depth of $D_g = 0.5L_g$. A distance of $L_s = 2L_g$ spaces apart the grooves. The initial and end parts of the channel are insulated ($\phi_w = 0$ W/m$^2$), while on the heated part $\phi_w = 4553$ W/m$^2$. The inlet flow temperature is slightly lower than assumed for the present studies and equals 293 K. However, the Reynolds number is the same ($Re = 2000$), which means that the flow and temperature distributions are expected to characterize a similar complexity as in the channel with walls defined by sinusoidal or spline shapes analyzed later in Section 4.3.

The computational mesh consists of 575340 rectangular cells. As presented in Fig. 5, the cells are compacted near the walls to improve the resolution of the near-wall flow in the regions of large temperature gradients. The simulations are performed by applying all RANS models mentioned in Section 3.1. Sample results obtained with the $k-\epsilon$ model are presented in Fig. 6. It shows the contours of the streamwise velocity ($U_x$) and temperature inside and near the second groove. We note that, qualitatively, the presented solutions can be regarded as representative of the remaining grooves, in which the flow exhibits very similar features. Streamlines shown in Fig. 6a reveal the presence of recirculation zones, within which the local streamwise velocity takes negative values. This promotes extensive mixing, intensifying the heat transfer between the wall and the flow. It can be seen that a visible increase in temperature is present only in the corners of the grooves, where small recirculation zones are formed. Along the straight channel walls, the thermal layer is very thin, and in effect, in the central flow part, the temperature is almost uniform. Its value does not diverge significantly from the inlet temperature. Downstream of the heated grooved section, in the location $x_2$, the average temperature equals 293.9 K.

Figure 7 shows the profiles of the streamwise velocity normalized by the inlet velocity ($U_x/U_{in}$) in three cross-sections ($L_g/5$, $L_g/2$, $4L_g/5$) of the second and eighth grooves. The color lines refer to the RANS solutions obtained using different models, and the square symbols denote the experimental data from [57]. It can be seen that in some cases the solutions are hardly distinguishable, e.g., the profiles obtained by applying the $k-\omega$ and $k-\omega-SST$ models or those predicted with the use of transition-$k-kl-\omega$ and transition-$SST$ models nearly overlap, especially in the region $-1 < y/(H/2) < 1$. Regarding the accuracy of particular models, their superiority largely depends on the groove number and location where the comparison

is made. For instance, in the 8th groove, in the location $L_g/5$ for $y/(H/2) < -1$ and $y/(H/2) > 1$, the recirculation zones where $U_x/U_{in} < 0$ are very well captured by the $k-\omega$ and transition type models. On the other hand, in the central flow part, the solutions obtained by using these models diverge from the measured values. The computed values are significantly larger and this tendency is also found in the case of using the RSM model in the second groove. Among all the presented solutions, the ones obtained by applying the $k-\epsilon$ model are the most accurate. In this case, the discrepancies are seen only in the location $L_g/5$ close to the wall of the groove. In the locations $L_g/2$ and $4L_g/5$, the solutions agree almost perfectly with the experimental data. Hence, the $k-\epsilon$ model is selected for the BO-RANS optimization procedure. It is believed that its demonstrated reliability will also apply to channels with wavy walls, where, due to the absence of sharp corners, obtaining accurate results should theoretically be simpler.

### 4.2. BO-RANS simulation parameters

#### 4.2.1. BO initialization

Referring to Fig. 4, the optimization process begins with $n_{init}$ initial wall shapes, each defined by a set of parameters $\mathbf{b}$ selected via Latin hypercube sampling. For the sinusoidal wall shape, $n_{init} = 50$, while for the spline-type wall, $n_{init} = 100$. In this case, the use of the larger set of initial solutions is motivated by the richer space of the control parameters when using the spline function for wall shaping (4 control parameters for the sinusoidal wall type, 19 control parameters for the spline-shaped wall). The obtained initial solutions with the associated values of the cost function $J$ are used to initialize a surrogate model. Subsequently, the main loop of the BO method starts and continues until the maximum number of iterations ($N_{max}$) is reached. We take $N_{max} = 900$ and $N_{max} = 1300$ for sinusoidal and spline-shaped wall-type, respectively. Following the same reasoning behind selecting different values of $n_{\text{init}}$, the choice of a larger $N_{\max}$ for the spline-shaped wall was motivated by the broader parameter space and the anticipated longer optimization process. As will be shown later, the selected $N_{\max}$ values were sufficiently large to yield only slightly different learning curves for both wall types. Further increasing $N_{\max}$ does not affect the optimization outcomes but leads to an unjustified increase in computational cost. Moreover, as noted by Blanchard and Sapsis [110], an excessively large number of iterations undermines the fundamental purpose of the BO algorithm. During the optimization process, the subsequent RANS solutions are stored in external files for postprocessing and controlling the computational mesh quality (see Section 4.2.2), while the corresponding $J_m$ and $\mathbf{b}_m$ parameters are utilized in the learning and optimization process.

#### 4.2.2. Geometry and mesh generation procedure

During the initialization of the BO-RANS procedure and in the main loop, the set of parameters $b_m^*$ changes, and the channel walls are shaped according to Eq. (3) or Eq. (7). This step is performed by applying an iterative approach in which both the wall shape and the computational mesh are successively modified. As an example illustrating this process, we present a test case with the wavy wall defined by Eq. (3). The initial configuration is a straight channel, with the computational mesh shown in Fig. 8a. In the region where the channel wall has to be shaped, the mesh is unstructured and consists of triangular elements. In the channel sections preceding and downstream of the waviness, the mesh is structured and composed of quadrilateral cells. In the next steps, the wall is successively deformed and the mesh adapts to the new geometry employing a dynamic meshing adaptation method available in ANSYS Fluent software [101]. It involves smoothing and re-meshing algorithms, which change the mesh incrementally. To avoid overstretching of individual cells and to ensure a high quality of the mesh, e.g., low skewness, aspect ratio close to one, the wall deformation process is divided into 20 iterations. This number has been found adequate in a trial-and-error procedure relying on the generation of test meshes for various complex wall shapes. Figure 8 shows intermediate channel shapes and meshes at the iterations $t_7$, $t_{15}$ and $t_{20}$ for the case with the wavy wall defined by the parameters $A_1 = -0.0016$ m, $A_2 = 0.004$ m, $s = -0.02$,

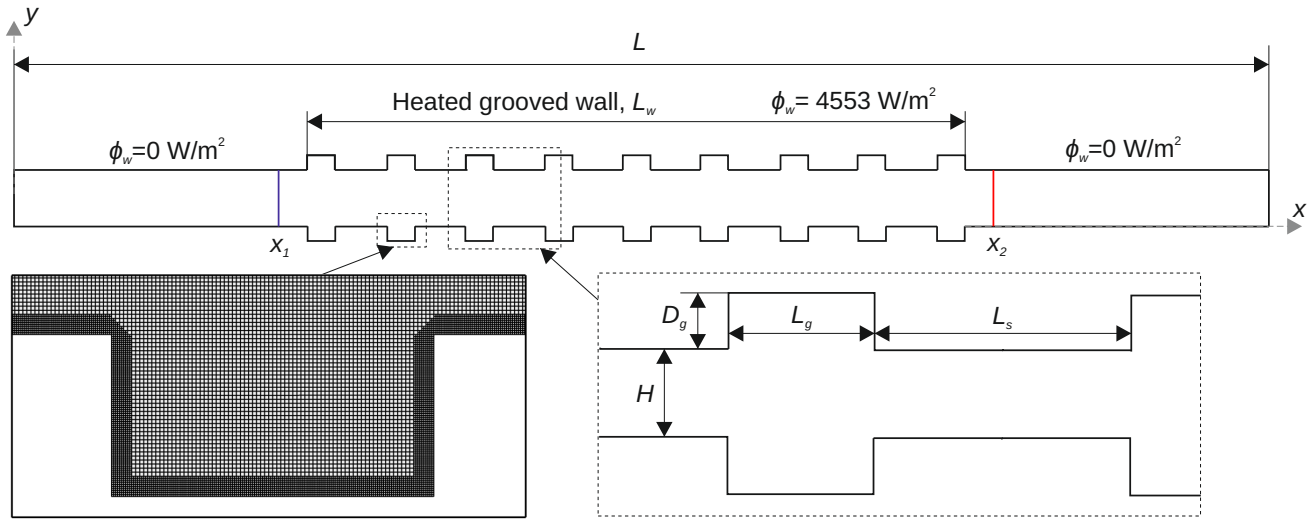



Figure 5: Schematic drawing of the experimental set-up from [57] with a close-up view of the mesh employed during the numerical simulations.

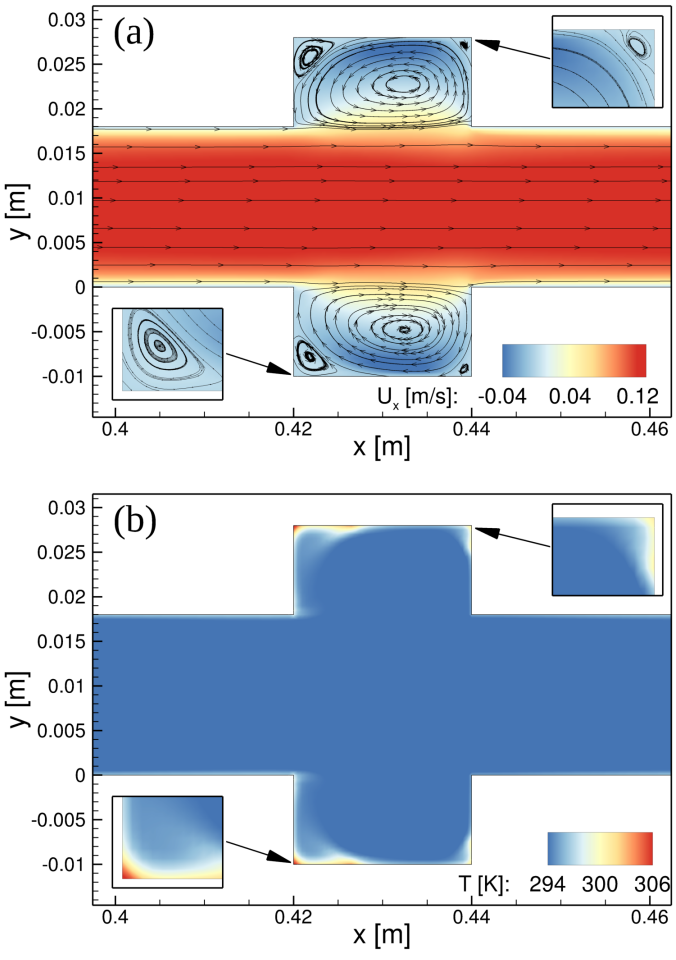



Figure 6: Contour maps of the streamwise velocity (a) and temperature (b) within the 2nd groove and its vicinity.

$N = 18$ in Eq. (3). It can be seen in Fig. 8b that at $t_{20}$ the density of the mesh is not uniform and the sizes of the cells locally change. However, none of them is exaggeratedly small/large or skewed. At this stage, the cells closest to the wall are refined by dividing them into smaller ones, creating 10 additional layers as shown in Fig. 8c. Note that the mesh refining process is applied along the entire channel walls including its wavy and straight parts. This ensures that the near-wall viscous layer is well-resolved also in the location $x_2$ (see Fig. 1), where the cost function $J$ is calculated. The near-wall mesh resolution is verified by checking the values of $y^+ = u_\tau h_w/\nu$ ($u_\tau$ - the friction velocity, $h_w$ - the height of the computational cell adjacent to the wall) at the end of every simulation for all analyzed cases. It is found that $y^+ \leq 1$, which is commonly treated as the necessary condition for applying the RANS method without involving wall model functions [100]. Depending on the shape of the waviness, the number of computational cells varies only slightly, $3.3\times10^5$ - $3.5\times10^5$, which practically does not impact the memory requirement and load balancing in parallel simulations. However, as discussed at the beginning of this section, reaching the convergent solution changes depending on the wall configuration and requires 300-600 iterations. These differences originate from different flow complexity in particular cases.

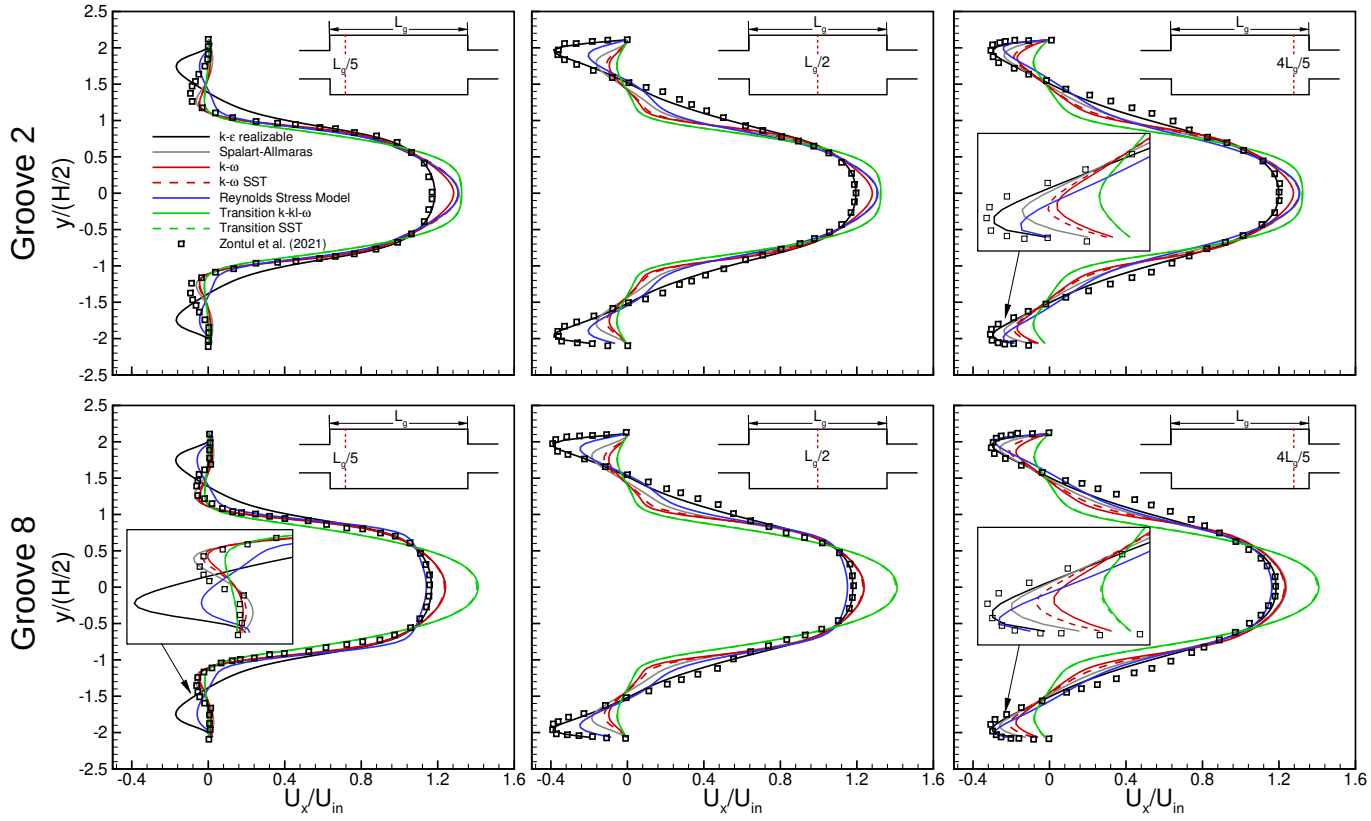



Figure 7: Profiles of the streamwise velocity obtained by applying different RANS models compared to experimental data of Zontul et al. [57].

### *4.3. BO-RANS simulation results*

The optimization procedure is preceded by test computations for the channel with flat walls and the channel with the geometry of the walls used to validate the RANS models in Section 4.1. In the latter case, to ensure consistency with the boundary conditions assumed in the optimization process, the grooved wall is heated with a heat power of $P_w = 10000$ W. The results show a pressure drop of $\Delta p = 16.039$ Pa and a temperature variance of $\sigma_T = 1.120$ K, yielding $J = 0.205$. In comparison to the flat channel, where $J = 1$, $\Delta p_{flat} = 7.919$ Pa, and $\sigma_{T,flat} = 11.086$ K, the temperature uniformity is significantly improved, though this is accompanied by more than a doubling of the pressure drop.

In general, the existence of multiple local minima of $J$, which can be obtained for significantly different sets of parameters $\mathbf{b}$ cannot be precluded. In the applied BO algorithm, the risk of stagnation of the solution near the local minimum of $J$, not being the global one, is minimized by balancing the exploration and exploitation strategies [111, 112]. To verify the robustness of the BO algorithm and check the possible impact of the initialization procedure on the final solution, the optimization is repeated twice with different initializations. This approach allows verifying whether the BO procedure converges to the same results in terms of $J$ and $\mathbf{b}$. Figure 9 presents the learning curves displaying the values of $J_m$ (black dots) and the current minimum of $J$ (red line) for the sinusoidal (a,b) and spline (c,d) shaped walls. The initial datasets are shaded by a semi-transparent vertical blue bar. Guided by the acquisition function (see Equation 16), the design space is sampled and evaluated. As reflected by the distribution of the tested $J$ values, samples near the learning curve correspond to the exploitation process of BO, while those with higher $J$ values are likely a result of the exploration phase. For the sinusoidal wall type (Fig. 9a,b), the solution converges to the optimal one already in approximately 150 iterations regardless of the initial datasets. In both cases, the optimization procedure yields an identical wall

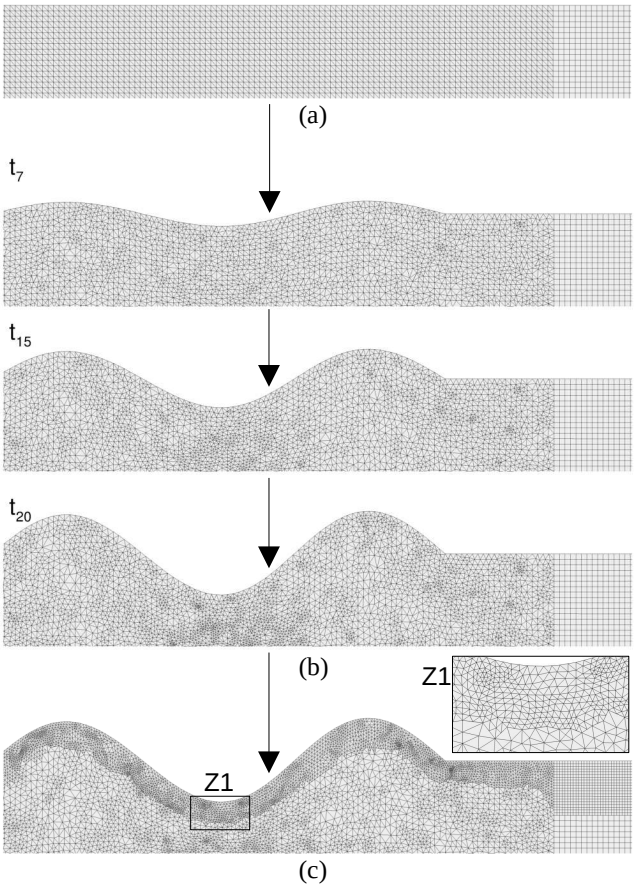



Figure 8: Three-stage wall shaping method and mesh generation procedure: (a) - the initial channel/mesh configuration; (b) - intermediate steps; (c) - the final channel/mesh configuration with the near-wall mesh refinement.

shape, characterized by $J = 0.066$. For the spline-shaped wall, the situation is slightly different. Starting from the first dataset (Fig. 9c), the algorithm finds the optimal solution in approximately 600 iterations, whereas the optimization starting from the second dataset (Fig. 9d) converges earlier, in about 400 iterations. This discrepancy may be attributed to the wider input parameter space, which likely presents a greater challenge for the BO procedure in efficiently navigating toward the optimal solution. However, noticing the impact of the initial datasets on the convergence rate the important observation is that for both of them, the BO algorithm identifies the same optimal configuration with $J = 0.1256$. This value is significantly lower than that for the channel with flat or grooved walls, but at the same time, it is almost twice as large as the value obtained for the sinusoidal wall type. To investigate the reasons for this difference, we focus on selected wall shapes and the mutual relations between $\Delta p$ and $\sigma_T$.

Figure 10 shows scatter plots of $\Delta p(\sigma_T)$ colored by $J$ for the sinusoidal wall type (top row) and spline-shaped wall (bottom row). Additionally, the wall shapes and contour maps of temperature are presented for the flat channel configuration denoted by A, the optimal configuration B, the worst configuration with the highest value of $J$, i.e. C, and the configuration yielding the highest pressure drop D. It can be seen that for the sinusoidal wall type, a well-defined Pareto front forms, along which the Pareto optimal configurations are located. They are characterized by the fact that no further improvement in $\sigma_T$ is possible without worsening the solution in terms of $\Delta p$. Conversely, when moving along the Pareto front, selecting a configuration with a lower $\Delta p$ results in a higher $\sigma_T$. Evaluating the scatter plot for the spline-shaped wall, a Pareto front is also formed, though in this case, it is not as sharp and well-defined. This is due to the sparsity of data within the high-dimensional design space. Additionally, it should be noted that the maximum $\Delta p$ for this wall type is half that of the sinusoidal wall. This is attributed to the maximum number of potential quasi-periods, which can be defined for particular shaping functions. The spline function spanned on 21 points allows for 10 periods. For the sinusoidal wall type, it has been assumed that the maximum allowable number of periods is $N = 20$ and the worst configuration D is characterized by 18 periods with relatively large amplitudes. This intensifies the mixing process, leading to small $\sigma_T$ but also causes local flow separation and pressure drop, resulting in large overall $\Delta p$. These issues will be investigated in depth in the subsequent part of the paper.

An interesting trend emerges when evaluating the impact of the wall shapes on $J$. The optimal configurations (cases B) for both the sinusoidal and spline-shaped walls feature a relative smoothness in the initial part of the heated area, followed by a consistent growth in the amplitude waviness. The superiority of this type of configuration can be explained as follows. Initially, when the cold fluid enters the heated section the temperature gradient between the fluid and the wall is large. This causes an intense heat transfer without the necessity of intense mixing.

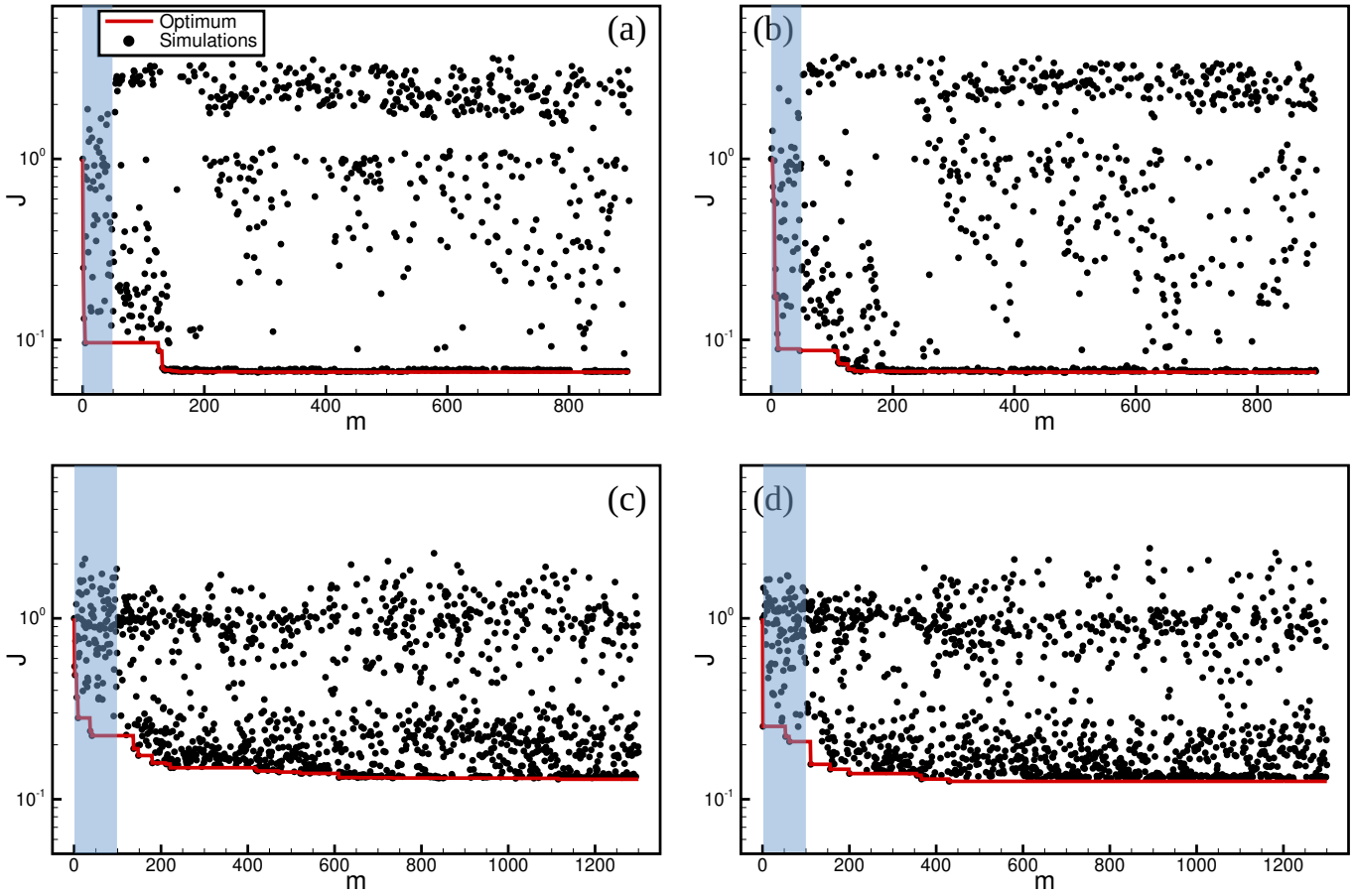



Figure 9: Learning curves of $J$ obtained for two optimizations for sinusoidal (a,b) and spline-shaped channel walls (c,d).

In effect, the pressure drop in this flow part is low while $\sigma_T$ decreases. Further downstream, as the near-wall thermal layer thickens, increasing temperature uniformity across the channel requires intensified mixing. This is achieved by an increasing waviness amplitude. It can be said that the BO procedure leads to wall shapes whose superiority can be explained based on physical principles and intuition. Unlike the optimal configurations, the worst ones (denoted C) manifest a large deformation at the beginning of the heated section, which then diminishes downstream. In these cases, the initial waviness causes a large temperature growth in the waviness cavities that is accompanied by a significant pressure drop. The lack of wall deformation near the end of the heated section results in poor mixing and in effect, the high-temperature fluid in the near wall region is not mixed with the flow in the channel axis. The configurations yielding the highest $\Delta p$ (cases D) are characterized by a rather large waviness along the heated wall section. This is beneficial for decreasing $\sigma_T$, but the increase in $\Delta p$ offsets the gains achieved.

#### *4.3.1. 2D vs. 3D results*

As discussed at the beginning of this section, preliminary computations conducted for several 3D channel geometries revealed a predominantly two-dimensional flow character. This observation allowed the RANS model validation and optimization to be carried out using 2D geometries. The main advantage of this simplifying assumption was the significant reduction in computational time (1-2 hours for 3D on 96 CPUs vs. 5-10 minutes for 2D on 16 CPUs) - a particularly important factor in the optimization process, which required performing 900 and 1300 consecutive simulations for the sinus-type and spline-shaped walls, respectively. This saving resulted from the number of cells in the computational meshes. As already mentioned, the 2D partially unstructured meshes consisted of approximately

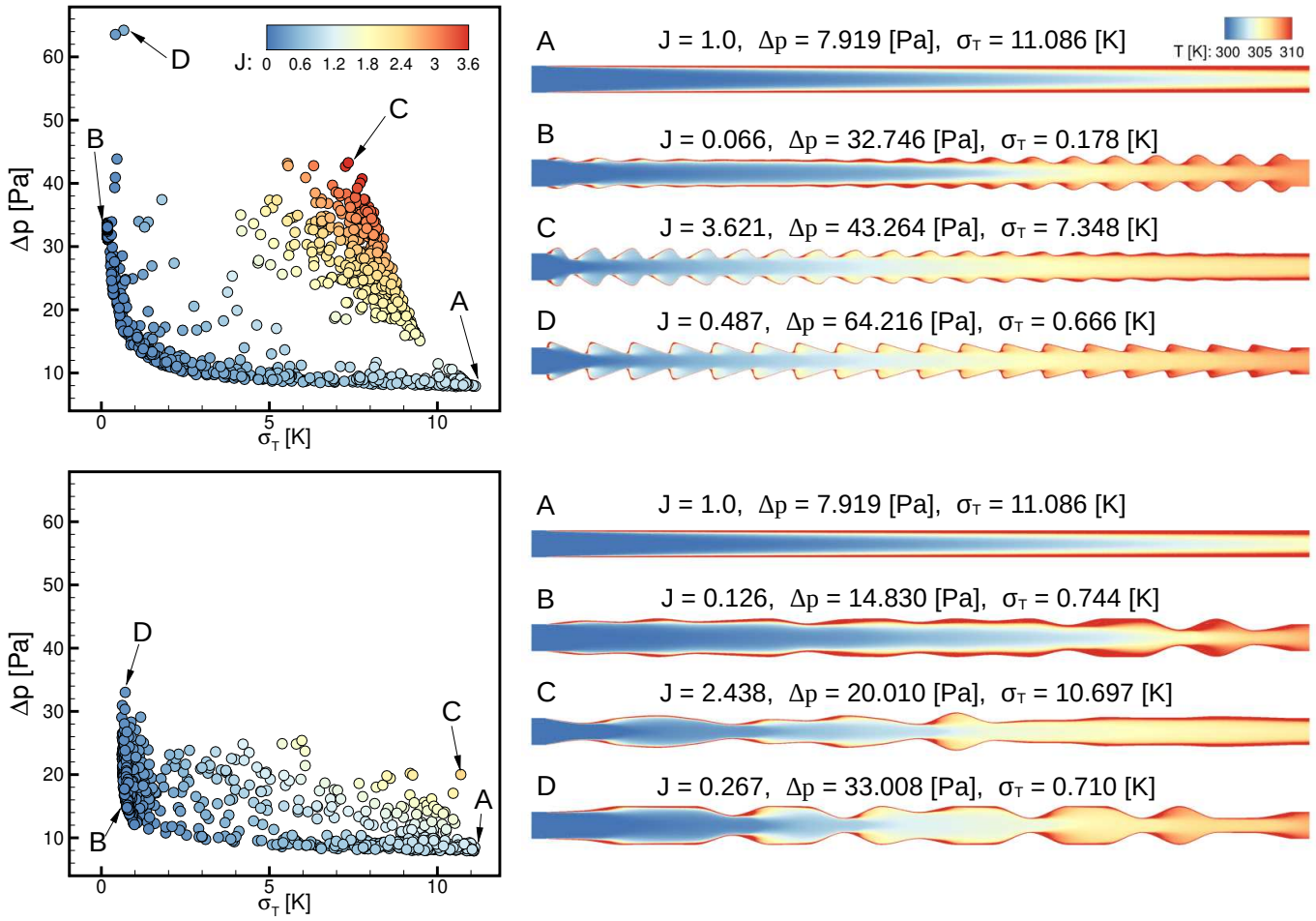



Figure 10: Scatter plot of $\Delta p(\sigma_T)$ colored by $J$ for the sinusoidal wall type (top row) and spline-shaped wall (bottom row).

3.3–3.5 $\times 10^5$ cells. In the 3D cases, the meshes were created for known selected geometries and could be manually designed as fully structured. Maintaining the condition $y^+ < 1$, and using $\Delta x$ similar to the one in 2D with $\Delta z \approx 2\Delta x$, resulted in the meshes containing $2.04 \times 10^7$ cells. To verify whether the 2D solutions obtained during the optimization process accurately capture the flow dynamics in the full 3D channels, Fig. 11 compares the results from the 2D and 3D cases for the optimal and worst sinusoidal wall configurations. The temperature profiles shown in this figure were extracted at the locations of maximum waviness amplitude in the 2nd ($n = 2$), middle ($n = N/2$), and penultimate ($n = N - 1$) waviness periods, as well as at a far downstream location at $x = 0.95$ m. It can be seen that at all examined distances, the agreement between the 2D and 3D results is very good. Although minor discrepancies are present, they are negligible and barely perceptible without significant magnification. These differences are confined to the wavy channel sections near the upper and lower walls, where strong temperature gradients occur. It is also worth noting that, for the cases with spline-shaped walls, the level of disagreement between the 2D and 3D results is similarly minimal. Therefore, it can be concluded that the optimization procedure based on 2D cases is reliable and yields meaningful results for the full 3D channel configurations.

#### 4.3.2. *Flow characteristics*

This section investigates how the previously outlined configurations affect the flow field across the channel and along its axis. In particular, first, we analyze to what extent the differences observed at the end of the waviness persist in the downstream straight channel part. Figure 12 presents the pro-

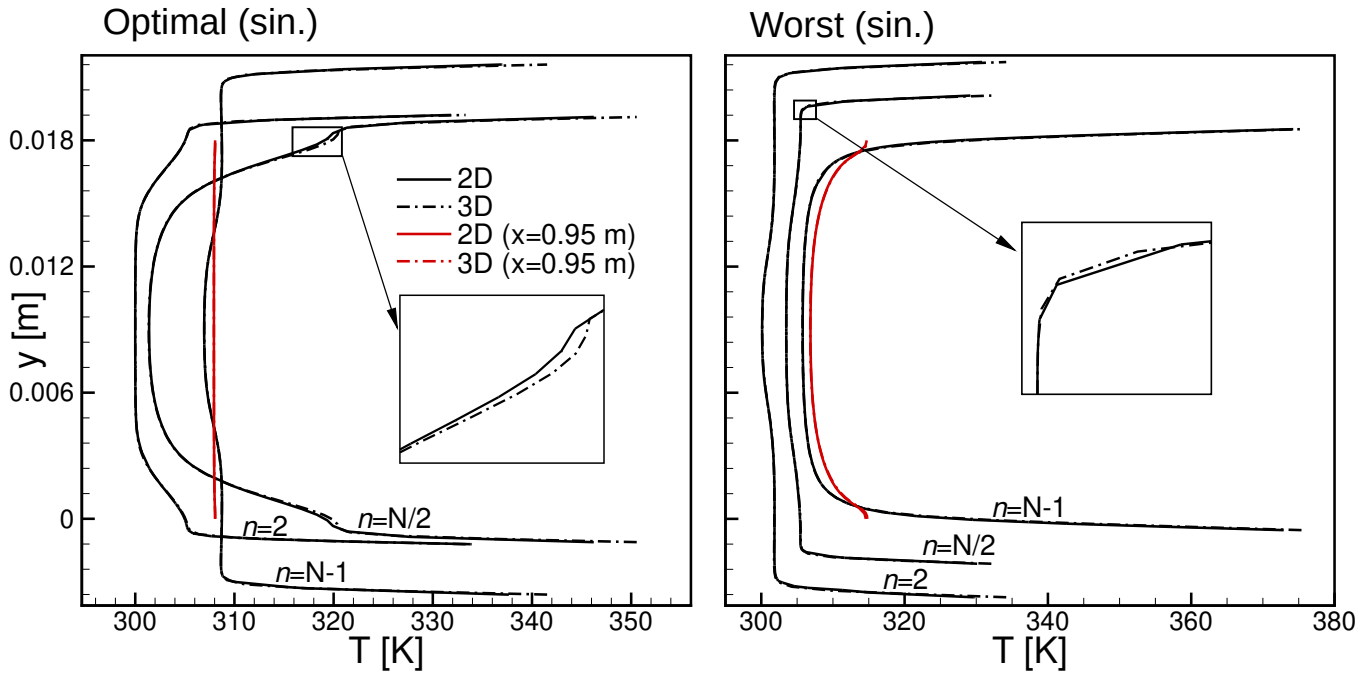



Figure 11: Profiles of the temperature in the 2nd ($n = 2$), middle ($n = N/2$), and penultimate ($n = N - 1$) waviness periods and at $x = 0.95$ m, for the optimal and worst configurations for the sinus-type wall.

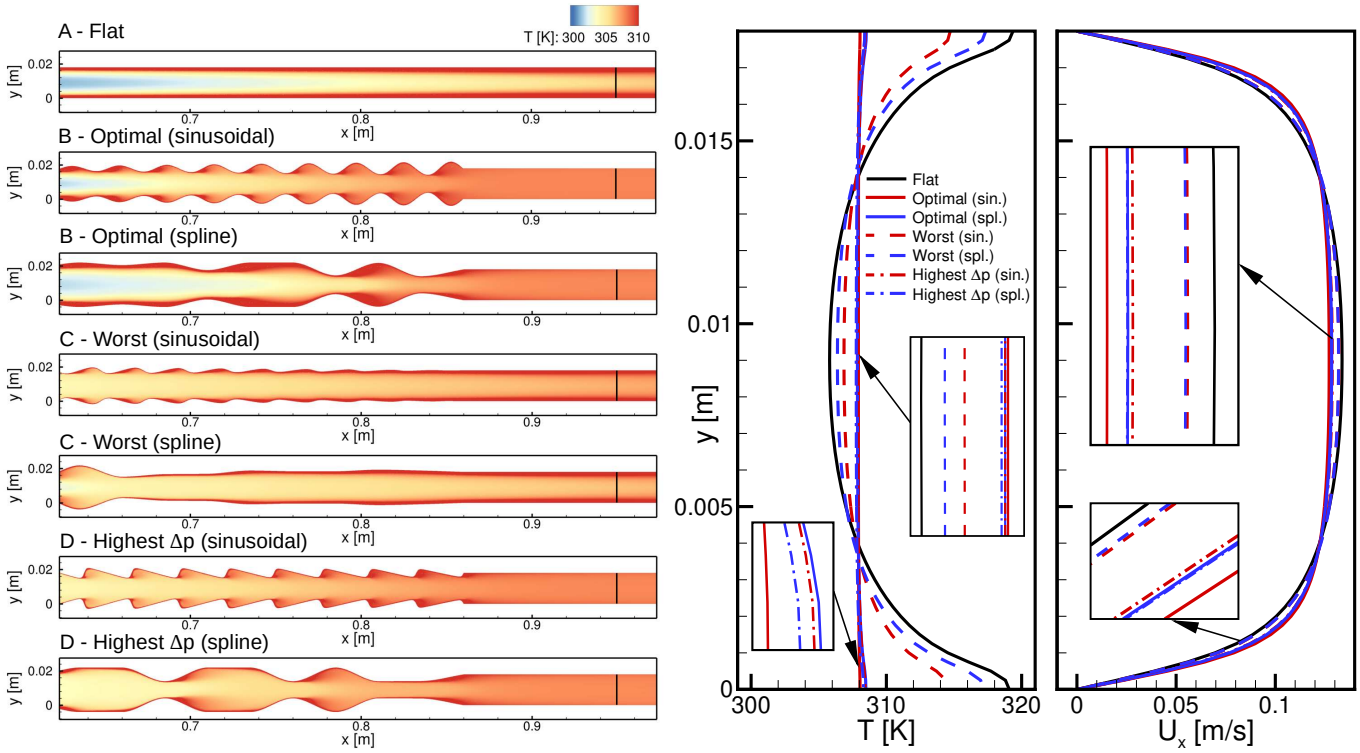



Figure 12: Contour maps of temperature for the optimal, worst, and exhibiting highest $\Delta p$ cases of the wavy wall created with sinusoidal and spline functions. Profiles of the streamwise velocity and temperature taken at $x = 0.95$ m.

files of the streamwise velocity and temperature at the location $x = 0.95$ m. marked with a black line in the temperature contour maps. Examining the temperature profiles reveals that both worst configurations (cases D - grey dashed lines) dis-

play a trend similar to that observed for the flat channel (case A - black solid line). In the near-wall area, the temperature is high and quickly decreases towards the central flow part. Conversely, in the optimal configurations (cases B - blue lines) and those yielding the highest $\Delta p$ (cases C - red lines), the temperature is nearly uniform and almost identical. In cases B, the profile for the sinusoidal wall type is flatter, which is particularly evident in the near-wall area. This is also reflected by reduced $\sigma_T = 0.178$ K compared to the spline-shaped wall, where $\sigma_T = 0.744$ K. However, it should be noted that despite the relatively large difference in $\sigma_T$ (over 4 times), the actual perceived differences are small.

Evaluating the streamwise velocity profiles, it can be observed that they are very similar for all configurations and the small differences are not due to temperature variations, as the fluid properties (density, viscosity) are constant. They originate only from the dynamics of the flow inside the wavy section. Assuming that a more turbulent flow characterizes a more rectangular velocity profile, the flow in the cases B can be said to be the most turbulent. Conversely, the velocity profile for the flat channel (case A) can be treated as the least turbulent as it manifests the highest velocity in the channel axis and the lowest velocity in the near-wall region. Such a tendency is not surprising and could be expected knowing that the turbulence intensity is the main factor responsible for the mixing process.

Figures 13 and 14 present the axial profiles of temperature, streamwise velocity, pressure, and turbulent kinetic energy for cases A-D. Additionally, the upper subfigures depict the shapes of the lower walls in particular configurations. Examining the temperature profiles, as expected, the slowest temperature growth is found for case A. Conversely, the configurations with the highest $\Delta p$ (cases D - dash-dotted lines) show rapid temperature growth in the initial part of the wavy wall, which then slows down in the region where the amplitude of the waviness decreases (see Fig. 10). The optimal configurations (B - solid lines) exhibit a relatively slow temperature growth in the initial part (small waviness amplitude, see Fig. 10), which then accelerates in the region where the amplitude increases. Worth

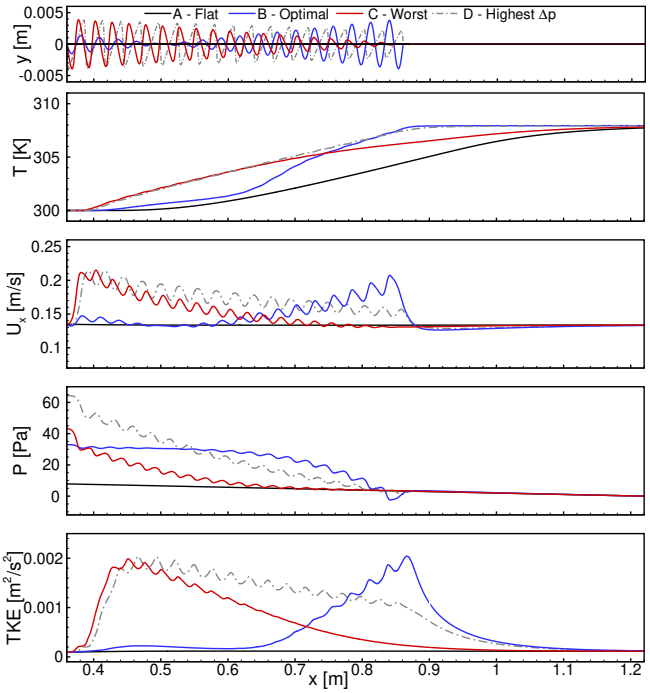



Figure 13: Axial profiles of the temperature, streamwise velocity, pressure, and turbulent kinetic energy for the cases with optimal, worst, and leading to the highest $\Delta p$ for the wavy wall created with the sinusoidal function.

noticing is that in configurations B and D the temperature at the end of the heated section reaches the same level, which almost does not change downstream. The streamwise velocity profiles are evidently related to the wall shapes. Compared to the flat channel, the mass conservation law enforces flow acceleration in the narrower parts of the channel and deceleration where the channel widens. Worth noting is that for the optimal sinusoidal and flat channel configurations, the velocity values up to $x = 0.6$ m are similar. The pronounced differences are seen downstream when the waviness amplitude grows. Contrary, in the case of the optimal spline-shaped wall, the velocity is lower than in the flat channel over most of the heated section and it suddenly increases only near its end. The variation of the velocity directly translates to the local pressure distributions, which decrease/increase where the flow accelerates/decelerates. Note, that in some places it is lower than in the flat channel, e.g., in configuration D for spline-shaped wall where the velocity is large due to the narrowing of the channel. For both optimal configurations, the pressure profiles remain relatively smooth and constant throughout the heated section. This contrasts with con-

figuration D of the sinusoidal wall type, where the initial part of the wavy section induces the most dynamic pressure fluctuations. In this case, we attribute the sudden changes in pressure values to the waviness tilt, particularly its left-side orientation. This is the main difference between configurations D and C, where the waviness amplitude is similar but the tilt is in the opposite direction. We found that the large pressure fluctuations in configuration D are caused by local flow separation zones that form behind the steep slopes of the waviness.

From the perspective of mixing enhancement, the values of turbulent kinetic energy (TKE) are of particular interest. They represent the magnitude of velocity fluctuations and, consequently, turbulent mixing, which plays a key role in transporting heat from the wall and redistributing it across the flow. For the optimal configurations, the waviness in the regions $0.36 \leq x \leq 0.65$ m for the sinusoidal wall type and $0.36 \leq x \leq 0.75$ m for the spline-shaped wall does not result in a significant increase in TKE and its level is similar to that of the flat wall. In effect, in this region, the conductive heat transfer plays a dominant role, leading to a slow temperature growth along the channel. The situation changes in the ending parts of the waviness, where TKE significantly rises and its high level causes an immediate temperature increase. As will be shown later, this is due to a relatively large vertical velocity component induced in the waviness cavities. The highest TKE in the initial waviness section is observed for configurations C and D of the sinusoidal wall. In these two cases, the TKE level rises steeply at the beginning of the waviness, reaching maximum values by the third waviness period. The fluctuations in TKE profiles, particularly for configuration D, are linked to pressure and velocity variations, resulting in intense mixing and a rapid temperature rise. The high level of TKE along the axis stems from particularly large TKE values within the waviness cavities.

Contour plots of TKE are shown in Fig. 15. Its level in the flat channel is very low and virtually constant along the channel. In cases C and D of the sinusoidal wall type, TKE distributions are characterized by the occurrence of local maxima, which start to be seen in the second waviness and are located in between

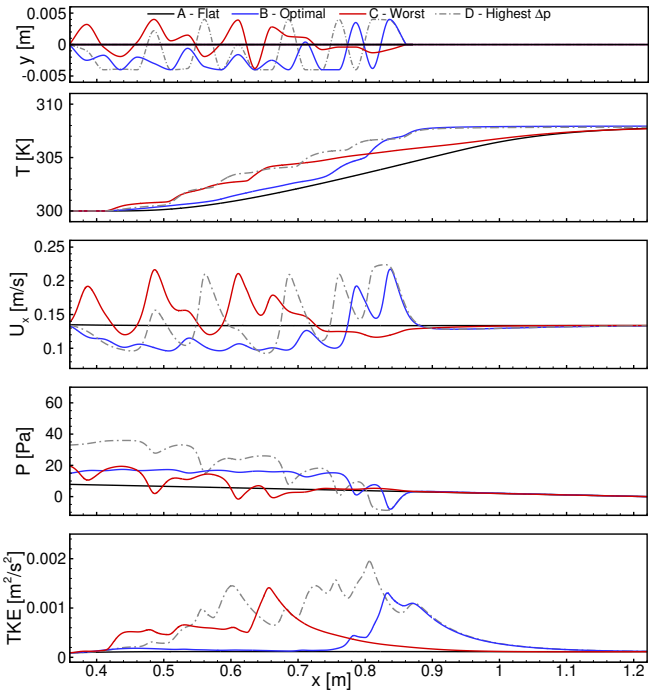



Figure 14: Axial profiles of the temperature, streamwise velocity, pressure, and turbulent kinetic energy for the cases with optimal, worst, and leading to the highest $\Delta p$ for the wavy wall created with the spline function.

the central flow part and the wall. Their repeatable distribution manifests in the fluctuating TKE profiles along the axis, as can be seen in Fig. 13. In the configurations with spline-shaped walls, TKE visibly rises only locally behind downhill-oriented walls where the waviness amplitude is large.

In the optimal configurations, the level of TKE remains low throughout the initial parts of the heated sections, increasing predominantly only near their ends. In these regions, the TKE enhancement is caused by the formation of separation zones in the waviness cavities. Detailed views of the places with amplified TKE are presented in zooms labelled Z1 and Z2 to examine this phenomenon more closely. These close-ups show TKE and streamwise velocity contour maps, offering a detailed analysis of near-wall flow patterns. The occurrence of the recirculation zones within the wave troughs is manifested by a negative velocity and closed oval-like streamlines (black lines). In the sinusoidal wall configuration, these zones span most of the waviness period, whereas in the case of the spline-shaped wall, they are smaller and narrowed to the downhill waviness part. This narrowing is well seen in figures showing the streamwise ve-

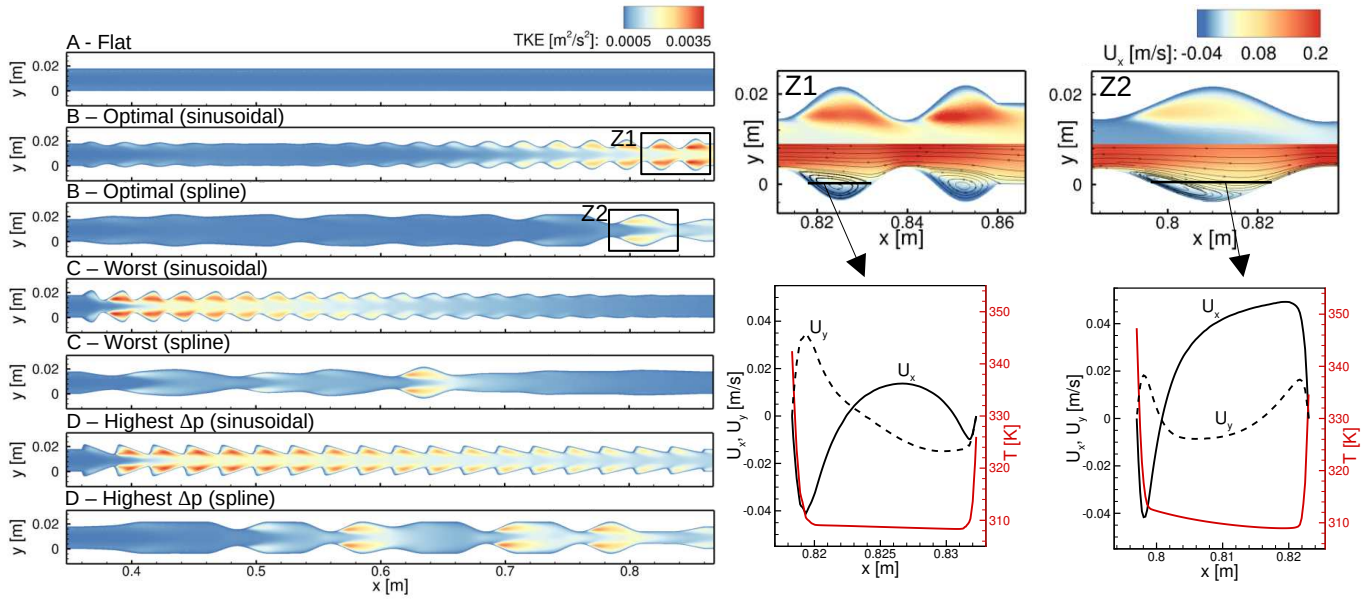



Figure 15: Contour maps of TKE for the cases with the optimal, worst, and exhibiting highest $\Delta p$ wall shapes created with sinusoidal and spline functions. Close-up views of the recirculation areas and profiles of velocity and temperature.

locity profile extracted from the middle of the waviness height. Evidently, in the case of the spline-shaped wall, the extent over which $U_x$ is negative is significantly smaller. It is worth noting that in both configurations, the minimum values of $U_x$ are relatively large, approximately $-0.04$ m/s, which corresponds to 36% of the inlet velocity. This results in strong recirculation and transport of fluid from the center of the waviness towards the wall. An induced vertical velocity component ($U_y$) near the wall is the primary factor contributing to the increased TKE level. Analysis of the TKE contours shows that the region of its large values begins where a high-momentum fluid (with large $U_y$) in the cavities interacts with the flow in the central part of the channel.

The robust recirculation is a prerequisite for enhanced mixing and heat exchange. Its efficiency can be measured through the temperature distribution on the walls and near its vicinity. Its profiles in both configurations exhibit clear similarities, however, in the near-wall regions, the temperature is significantly higher in the case of the spline-shaped wall. This suggests a less efficient heat transfer between the wall and fluid, translating to a less uniform temperature distribution in the cavities and the central flow part. The heat exchange efficiency between the wall and fluid also affects the wall temperature.

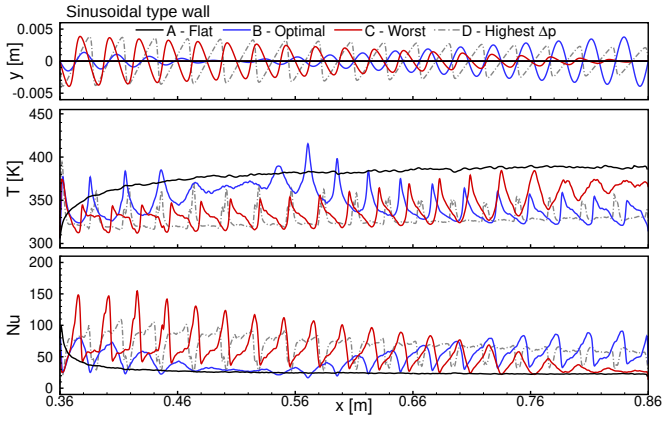



Figure 16: Profiles of temperature at the wall for optimal, worst and exhibiting highest $\Delta p$ cases of the sinusoidal type wall. The upper row indicates the shape of the particular waviness.

Its profiles along the wavy channel sections are presented in Fig. 16 and Fig. 17 along with the distribution of the Nusselt number, $Nu = \partial T/\partial n|_w H/(T_w - T_{in})$, where $\partial T/\partial n|_w$ denotes the derivative in the wall-normal direction and $T_w$ is the wall temperature. In the case of the flat channel, initially, the wall temperature is low as the cold fluid effectively absorbs the heat due to strong convection, as can be inferred from high $Nu$ values. Then, the temperature rises smoothly, and around $x = 0.75$ m reaches an almost constant level of $T \approx 388$ K, while $Nu$ de-

creases and approaches an asymptotic regime. A striking difference in the temperature and Nusselt number profiles obtained for wavy walls is the occurrence of local maxima and minima. Locations of high-temperature peaks closely match the beginnings of the recirculation zones on the downhill wall side. To investigate this issue in more detail, we analyze the velocity contours within the cavity of last waviness in the optimal configuration of the sinusoidal wall type, along with the profiles of temperature, $Nu$, and wall shear stress ($\tau_w = \mu \frac{dU}{dn}$) along the wall. These results are presented in Fig. 18. In the velocity contour map, the grey region represents areas where $U_x < 0$. It can be observed that at the location where this region starts (marked as R), $\tau_w = 0$. In this place, the cooling effect of the wall by the flowing stream is minimal, and heat conduction (low $Nu$) becomes the key factor in heat absorption from the wall. Its relatively low efficiency causes the high wall temperature growth. Downstream of point R, $\tau_w$ rises, implying the growth of the convective heat transfer (increasing $Nu$), and in consequence, the temperature drops. This scenario takes place in every waviness cavity in all configurations. Taking into account the solutions presented in Fig. 16 it can be seen that in optimal configuration, the temperature in the first half of the heated section ($x < 0.6$ m) is larger ($Nu$ smaller) than in cases C and D. Locally, its values significantly exceed the wall temperature of the flat channel. Downstream, in the region $x > 0.6$ m, the areas of elevated TKE near the wall (see Fig. 15) increase $Nu$ and yield a reduction of the wall temperature. Its level near the end of the waviness becomes similar to that for case D for which $\sigma_T$ did not diverge substantially (see Fig. 10). On the contrary, in case C with decreasing waviness amplitude and large $\sigma_T$, $J$, the temperature rises and $Nu$ decreases. Analogous trends are observed in the configurations with the spline-shaped walls, see Fig. 17. The quantitative differences are observed for distributions of local temperature and $Nu$ maxima/minima, which, due to generally smoother wall shapes, occur less frequently. This factor also causes smaller longitudinal gradients of these quantities between the maxima/minima. On the other hand, it increases temperature and lowers $Nu$ values, particularly in cases C and D.

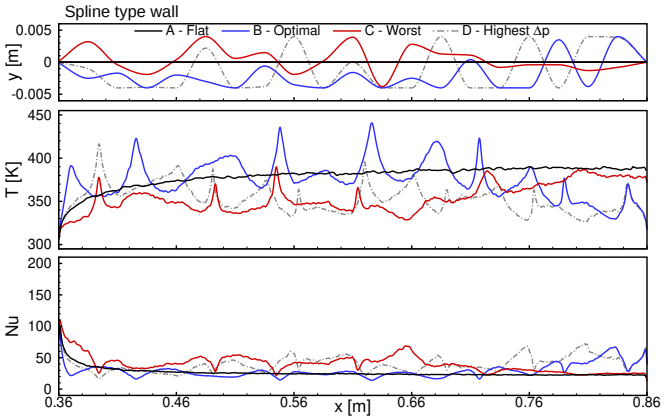



Figure 17: Profiles of the temperature at the wall for the cases with the optimal, worst, and exhibiting highest $\Delta p$ wall shapes for the spline-shaped wall. The upper row shows the shape of the particular waviness.

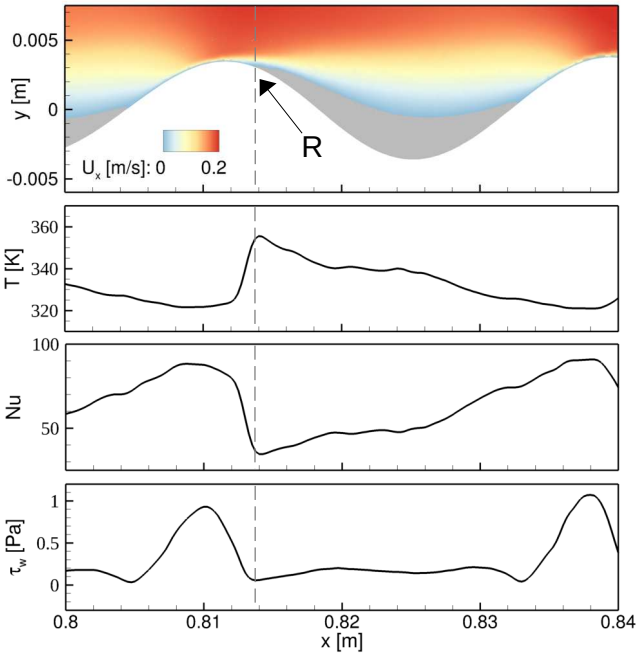



Figure 18: Contour map of $U_x$ showing a close-up of the waviness cavity, with regions where $U_x < 0$, indicating separated flow, shaded in grey. Supplemented by profiles of $T$, $Nu$, and $\tau_w$.

### 4.3.3. *Human-assisted optimization*

Human-assisted optimization (HAO) relies on combining researchers' intuition and expertise with algorithmic or computational optimization methods. In this section, we apply this strategy with the hope that the formulated HAO-BO approach will provide a solution that at least does not diminish the superiority of the former optimal configuration, with simultaneous fulfil-

ment of additional goals. To generally summarize the findings so far, it can be said that the configurations, which optimally balance mixing improvement (small $\sigma_T$) with pressure drop (small $\Delta p$), exhibit a distinct characteristic along the heated section. The initial heated section features a relatively smooth wall with small waviness amplitudes, leading to a low $\Delta p$. In this flow part, the initially cold fluid is effectively heated, forming a near-wall thermal layer. As this layer thickens, the temperature gradient decreases, and heat transport across the flow weakens. Thus, the necessity of mixing arises, and the BO method 'suggests' an increase in the waviness amplitude. At this point, one might ask whether these BO-guided optimal configurations can be further improved or if some of their negative aspects can be mitigated. Regarding the second issue, two problems should be considered. From an engineering perspective, manufacturing a wavy wall incurs additional costs and can be challenging, especially in cases with irregular wall shapes. Hence, the best would be to eliminate waviness in the regions where its contribution to achieving the optimization goal is weak. It can be seen in Figs. 13 and 14 that in the initial part of the heated sections, the temperature in the channel axis increases smoothly and not significantly faster than in the configuration with the flat wall. On the other hand, the waviness in this region causes pressure loss, and most importantly, it leads to a non-uniform wall temperature distribution with local high-temperature peaks (see Figs. 16-17). Assuming that a given heat exchanger needs to be produced at a low cost, its walls should be thin. However, in this case, large temperature gradients would result in high thermal stresses, which, over time, could deform or damage the wall. Hence, taking these arguments into account, the natural attempt for improvement of the BO-optimal configuration seems to be to flatten the initial channel section. Certainly, this approach should minimize the pressure drop, and simultaneously, considerably streamline the manufacturing process and reduce the overall complexity of the channel. To explore the consequences of such a combined intuition and engineering-driven optimization we focus on the sinusoidal type wall, which is characterized by better performance in terms of $J$. In the performed analysis, starting from the beginning of the heated section, successive periods of waviness in the BO-optimal configuration are replaced with a flat surface. Then, RANS simulations are performed for such a new configuration and $\sigma_T$, $\Delta p$ and $J$ are calculated. Figure 19 shows their profiles as a function of the number of removed waviness periods. Please note that $\sigma_T$ is presented in the logarithmic scale. Additionally, the contour maps of the temperature for three selected cases with corresponding profiles of TKE along the channel axis are presented. To support the following discussion quantitatively, Table 1 presents the detailed values of $J$, $\Delta p$, and $\sigma_T$ for all smoothened configurations. It can be seen that without the first wave, $\sigma_T$ rises by 1.7% (from 0.178 K to 0.181 K), whereas $\Delta p$ drops by 1.9% (from 32.746 Pa to 32.129 Pa), and this causes a small improvement in $J$ (from 0.0664 to 0.0661). Continuing the flattening process up to 10 initial waves has almost no impact on $\sigma_T$, though it does reduce $\Delta p$ slightly. Notable differences start to occur when the 11th waviness period is removed. From this point, $\sigma_T$ pronouncedly increases while $\Delta p$ decreases, with the latter occurring more rapidly, leading to a visible decrease in $J$. In effect, after removing the 14th waviness period, $J$ reaches the minimum at $J = 0.0546$, which is 17.7% lower than the initial value. Further flattening of waviness causes a drop in $\Delta p$, but this is accompanied by a rapid increase in $\sigma_T$, leading to a subsequent rise in $J$. Hence, the optional configuration is the one with 14 removed waves. Apart from the significant reduction in wall complexity, an interesting observation can be made regarding this case. The 4 remaining waves, constituting 22.2% of the original 18 waves, contribute to the majority of the mixing. While not exact, this result aligns strikingly with the Pareto 80/20 principle.

The contour maps of the temperature presented in Fig. 19b show the solutions obtained for the BO-optimal configuration and the cases with 10 and 14 periods removed. It can be seen that downstream of the waviness the temperature fields are nearly identical, which confirms the above findings regarding the impact of waviness complexity on the mixing intensity. The temperature profiles on the flattened wall parts (not

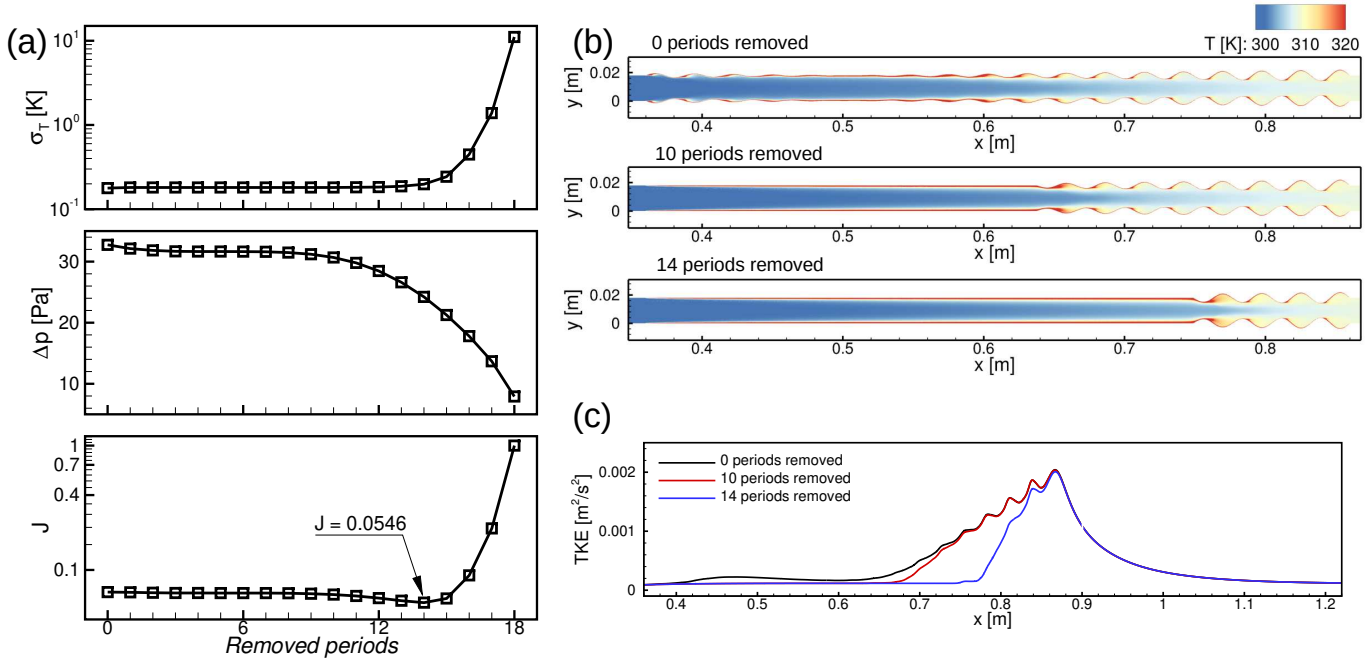



Figure 19: Profiles of $\sigma_T$, $\Delta p$, and $J$ as a function of the removed periods. ; sample contour maps of $T$ illustrating three shapes of walls (b); streamwise profiles of TKE for three considered cases taken at $y = 0.009$ m, i.e. the middle section of the channel.

shown) cover with that previously obtained for the flat channel (Cf. Fig. 2). Their distribution in the wavy part closely resembles the profile in the BO-optimal configuration. Regarding the level of TKE (Fig. 19c), the removal of 10 waviness periods does not bring significant changes. As expected, in the flattened section, TKE is lower compared to the BO-optimal configuration; however, the differences are generally minor. In the new optimal configuration, TKE rises steeply as the waviness begins, ultimately reaching the same level as in the two other cases by the end. It turns out that the last 4 waves are sufficient to enhance TKE, ensuring efficient mixing without a significant overall pressure drop.

## 5. Conclusions

This paper presented an optimization study of heated wall surfaces in a channel using machine learning. The design of the wall surfaces was guided by a learning framework that combines BO with RANS simulations conducted in ANSYS Fluent code. The primary goal of the research was to minimize temperature variations $\sigma_T$ arccos the channel at possibly the smallest pressure drop $\Delta p$. The cost function $J$ balanced these two factors and was normalized by the reference values obtained for the flat channel. Two wall deformation methods were compared: a sinusoidal function and a spline function employing the Piecewise Cubic Hermite Interpolation Polynomial (PCHIP). The former is characterized by four parameters, while the latter offers larger design freedom with 19 parameters.

The higher-dimensional design of the spline-shaped wall presented greater challenges for optimization. Both sinusoidal and spline-shaped wall optimizations were repeated twice with different initializations. For the sinusoidal wall, convergence was achieved in approximately 150 BO iterations regardless of the initial dataset. In contrast, the convergence of the spline-shaped wall was highly dependent on initialization, requiring between 400 and 600 iterations. Additionally, the data sparsity associated with the 19-dimensional design space required a larger number of data points to derive the Pareto front that effectively captures the trade-off between the temperature variations $\sigma_T$ and the pressure drop $\Delta p$.

The optimized sinusoidal wall type outperformed the spline-shaped wall although the latter considered a higher-dimensional design. The minimum objective value, $J$, achieved by the sinu-

| Removed periods | $J$ | $\Delta p$ [Pa] | $\sigma_T$ [K] |
|---|---|---|---|
| 0 (full waviness) | 0.0664 | 32.746 | 0.178 |
| 1 | 0.0661 | 32.129 | 0.181 |
| 2 | 0.0656 | 31.835 | 0.181 |
| 3 | 0.0653 | 31.681 | 0.181 |
| 4 | 0.0653 | 31.649 | 0.181 |
| 5 | 0.0652 | 31.649 | 0.181 |
| 6 | 0.0652 | 31.635 | 0.181 |
| 7 | 0.0652 | 31.606 | 0.181 |
| 8 | 0.0650 | 31.479 | 0.181 |
| 9 | 0.0644 | 31.208 | 0.181 |
| 10 | 0.0634 | 30.677 | 0.181 |
| 11 | 0.0618 | 29.792 | 0.182 |
| 12 | 0.0594 | 28.465 | 0.183 |
| 13 | 0.0566 | 26.613 | 0.187 |
| **14** | **0.0546** | **24.225** | **0.198** |
| 15 | 0.0590 | 21.260 | 0.243 |
| 16 | 0.0905 | 17.799 | 0.446 |
| 17 | 0.2158 | 13.687 | 1.384 |
| 18 (flat channel) | 1.0000 | 7.919 | 11.086 |

Table 1: Values of $J$, $\Delta p$ and $\sigma_T$ in a function of the waviness periods replaced by the flat wall. The optimal solution is highlighted in bold font.

soidal wall was only half of that obtained with the spline-shaped wall. Specifically, the sinusoidal wall type led to significantly lower $\sigma_T$, though at the cost of a higher $\Delta p$. The enhanced performance of the sinusoidal wall likely resulted from a larger number of periods, which could be formed along the heated wall, i.e. 20 vs. 10 quasi-periods for the spline-shaped wall. This resulted in a lower effective amplitude–to–wavelength ratio ($A/\lambda$), reducing the potential for improving mixing, however, at lower pressure drops.

The optimized surfaces for both approaches featured a relatively smooth initial section, minimizing $\Delta p$, followed by a region of increased amplitude that encouraged the formation of recirculation zones, which enhanced TKE and flow mixing. The worst-performing configurations, in terms of $J$, were characterized by surface shapes that were the reverse of the optimal design. This motivated performing a human-assisted optimization (HAO) to reduce potential manufacturing costs of obtained optimal solution and minimize thermal stresses. HAO was applied only for the configuration with the sinusoidal wall type and involved successive replacement of small-amplitude waviness periods by flat segments starting from the beginning of the heated section. It has been shown that flattening up to 10 initial waves has minimal impact on $J$, yet the reduced complexity of the new configurations could facilitate manufacturability. Further removal of waviness periods led to a rapid decrease in $\Delta p$, with flattening 14 waviness periods yielding a new minimum $J$ that performed 17.7% better than the best wall shape found during the BO procedure.

In summary, the studies demonstrated the significant potential of wavy wall surfaces in enhancing mixing and heat transfer processes. The combined use of the BO-RANS method, complemented by HAO, proved to be a highly effective optimization tool. A natural progression of this research is to apply the formulated algorithm to higher Reynolds number flows and cases with large temperature differences, as seen in combustion devices. In such studies, it would be beneficial to verify CFD results with more accurate modeling methods. For instance, using large eddy simulations, though computationally expensive, would increase the reliability of the solutions and provide deeper insights into flow dynamics. This is planned for future research.

## 6. Acknowledgements

From the Polish side, this work was supported by the National Science Centre under grant UMO-2020/39/B/ST8/01449 and statutory funds of the Czestochowa University of Technology BS/PB 1-100-3011/2024/P. We gratefully acknowledge Poland's high-performance Infrastructure PLGrid ACK Cyfronet AGH and PCSS for providing computer facilities and support within computational grants no PLG/2023/016731 and PL0356-01. From the Chinese side, this work was supported by the National Science Foundation of China (NSFC) through grant 12172109 by the Guangdong Basic and Applied Basic Research Foundation under grant 2022A1515011492, and by the Shenzhen Science and Technology Program under grants JCYJ20220531095605012, KJZD20230923115210021 and 29853MKCJ202300205.

## References


[1] S. R. Bull, "Renewable energy today and tomorrow," *Proceedings of the IEEE*, vol. 89, no. 8, pp. 1216–1226, 2001.

[2] S. Sen and S. Ganguly, "Opportunities, barriers and issues with renewable energy development–a discussion," *Renewable and sustainable energy reviews*, vol. 69, pp. 1170–1181, 2017.

[3] M. M. Khaleel, A. Alsharif, and I. I. K. Imbayah, "Renewable energy technologies: Recent advances and future predictions," *African Journal of Advanced Pure and Applied Sciences (AJAPAS)*, pp. 58–64, 2022.

[4] X. F. Maxmut O'g'li, "Renewable energy sources: advancements, challenges, and prospects," *International Journal of Advance Scientific Research*, vol. 3, no. 08, pp. 14–25, 2023.

[5] K. Koyama, "The role and future of fossil fuel," *IEEJ Energy Journal, Special Issue*, pp. 80–83, 2017.

[6] R. York and S. E. Bell, "Energy transitions or additions?: Why a transition from fossil fuels requires more than the growth of renewable energy," *Energy Research & Social Science*, vol. 51, pp. 40–43, 2019.

[7] A. Witry, M. Al-Hajeri, and A. A. Bondok, "Thermal performance of automotive aluminium plate radiator," *Applied thermal engineering*, vol. 25, no. 8-9, pp. 1207–1218, 2005.

[8] I. Krásnỳ, I. Astrouski, and M. Raudenskỳ, "Polymeric hollow fiber heat exchanger as an automotive radiator," *Applied Thermal Engineering*, vol. 108, pp. 798–803, 2016.

[9] S. Rainieri, G. Pagliarini, *et al.*, "Convective heat transfer to orange juice in smooth and corrugated tubes," *International Journal of Heat and Technology*, vol. 15, pp. 69–75, 1997.

[10] N. Ahammed, L. G. Asirvatham, and S. Wongwises, "Thermoelectric cooling of electronic devices with nanofluid in a multiport minichannel heat exchanger," *Experimental Thermal and Fluid Science*, vol. 74, pp. 81–90, 2016.

[11] L. Zhu, H. Tan, and J. Yu, "Analysis on optimal heat exchanger size of thermoelectric cooler for electronic cooling applications," *Energy conversion and management*, vol. 76, pp. 685–690, 2013.

[12] M. A. Abd El-Baky and M. M. Mohamed, "Heat pipe heat exchanger for heat recovery in air conditioning," *Applied thermal engineering*, vol. 27, no. 4, pp. 795–801, 2007.

[13] X. P. Wu, P. Johnson, and A. Akbarzadeh, "Application of heat pipe heat exchangers to humidity control in air-conditioning systems," *Applied thermal engineering*, vol. 17, no. 6, pp. 561–568, 1997.

[14] M. Ohadi, N. Sharaf, and D. Nelson, "Electrohydrodynamic enhancement of heat transfer in a shell-and tube heat exchanger," *EXPERIMENTAL HEAT TRANSFER An International Journal*, vol. 4, no. 1, pp. 19–39, 1991.

[15] S. Laohalertdecha, P. Naphon, and S. Wongwises, "A review of electrohydrodynamic enhancement of heat transfer," *Renewable and Sustainable Energy Reviews*, vol. 11, no. 5, pp. 858–876, 2007.

[16] T.-H. Wang, M. Peng, X.-D. Wang, and W.-M. Yan, "Investigation of heat transfer enhancement by electrohydrodynamics in a double-wall-heated channel," *International Journal of Heat and Mass Transfer*, vol. 113, pp. 373–383, 2017.

[17] R. Fang and J. A. Khan, "Active heat transfer enhancement in single-phase microchannels by using synthetic jets," *Journal of Thermal Science and Engineering Applications*, vol. 5, no. 1, p. 011006, 2013.

[18] Y. Wang and Y. Peles, "An experimental study of passive and active heat transfer enhancement in microchannels," *Journal of heat transfer*, vol. 136, no. 3, p. 031901, 2014.

[19] T. Chandratilleke, D. Jagannatha, and R. Narayanaswamy, "Heat transfer enhancement in microchannels with cross-flow synthetic jets," *International journal of thermal sciences*, vol. 49, no. 3, pp. 504–513, 2010.

[20] C.-W. Chen, C.-Y. Yang, and Y.-T. Hu, "Heat transfer enhancement of spray cooling on flat aluminum tube heat exchanger," *Heat transfer engineering*, vol. 34, no. 1, pp. 29–36, 2013.

[21] A. A. Pavlova, K. Otani, and M. Amitay, "Active performance enhancement of spray cooling," *International journal of heat and fluid flow*, vol. 29, no. 4, pp. 985–1000, 2008.

[22] A. Hosseinian and A. Meghdadi Isfahani, "Experimental study of heat transfer enhancement due to the surface vibrations in a flexible double pipe heat exchanger," *Heat and Mass Transfer*, vol. 54, no. 4, pp. 1113–1120, 2018.

[23] R. Ricci, R. Romagnoli, S. Montelpare, and D. Di Benedetto, "Convective heat transfer increase in internal laminar flow using a vibrating surface," *International journal of thermal sciences*, vol. 84, pp. 358–368, 2014.

[24] Q. Ye, Y. Zhang, and J. Wei, "A comprehensive review of pulsating flow on heat transfer enhancement," *Applied Thermal Engineering*, vol. 196, p. 117275, 2021.

[25] E. M. Benavides, "Heat transfer enhancement by using pulsating flows," *Journal of Applied Physics*, vol. 105, no. 9, 2009.

[26] D. Duan, Y. Cheng, M. Ge, W. Bi, P. Ge, and X. Yang, "Experimental and numerical study on heat transfer enhancement by flow-induced vibration in pulsating flow," *Applied Thermal Engineering*, vol. 207, p. 118171, 2022.

[27] Y. Zhang, S. Liu, L. Yang, X. Yang, Y. Shen, and X. Han, "Experimental study on the strengthen heat transfer performance of pcm by active stirring," *Energies*, vol. 13, no. 9, p. 2238, 2020.

[28] B. A. K. Naik and A. V. Vinod, "Heat transfer enhancement using non-newtonian nanofluids in a shell and helical coil heat exchanger," *Experimental Thermal and Fluid Science*, vol. 90, pp. 132–142, 2018.

[29] M. Lei, J. Zhao, H. Wang, and X. Zhou, "Effect of mechanical stirring on heat transfer and flow of crude oil in storage tanks under different heating methods," *Case Studies in Thermal Engineering*, vol. 58, p. 104382, 2024.

[30] M. H. Mousa, N. Miljkovic, and K. Nawaz, "Review of heat transfer enhancement techniques for single phase flows," *Renewable and Sustainable Energy Reviews*, vol. 137, p. 110566, 2021.

[31] M. Fiebig, "Vortices, generators and heat transfer," *Chemical Engineering Research and Design*, vol. 76, no. 2, pp. 108–123, 1998.

[32] M. Awais and A. A. Bhuiyan, "Heat transfer enhancement using different types of vortex generators (vgs): A review on experimental and numerical activities," *Thermal Science and Engineering Progress*, vol. 5, pp. 524–545, 2018.

[33] J. Turnow, N. Kornev, V. Zhdanov, and E. Hassel, "Flow structures and heat transfer on dimples in a staggered arrangement," *International Journal of Heat and Fluid Flow*, vol. 35, pp. 168–175, 2012.

[34] Y. Rao, B. Li, and Y. Feng, "Heat transfer of turbulent flow over surfaces with spherical dimples and teardrop dimples," *Experimental Thermal and Fluid Science*, vol. 61, pp. 201–209, 2015.

[35] C.-C. Wang, W. Fu, and C. Chang, "Heat transfer and friction characteristics of typical wavy fin-and-tube heat exchangers," *Experimental thermal and fluid science*, vol. 14, no. 2, pp. 174–186, 1997.

[36] R. M. Manglik and A. E. Bergles, "Heat transfer and pressure drop correlations for the rectangular offset strip fin compact heat exchanger," *Experimental Thermal and Fluid Science*, vol. 10, no. 2, pp. 171–180, 1995.

[37] J. S. Jabardo, J. B. Zoghbi Filho, and A. Salamanca, "Experimental study of the air side performance of louver and wave fin-and-tube coils," *Experimental Thermal and Fluid Science*, vol. 30, no. 7, pp. 621–631, 2006.

[38] M. Searle, J. Black, D. Straub, E. Robey, J. Yip, S. Ramesh, A. Roy, A. S. Sabau, and D. Mollot, "Heat transfer coefficients of additively manufactured tubes with internal pin fins for supercritical carbon dioxide cycle recuperators," *Applied Thermal Engineering*, vol. 181, p. 116030, 2020.

[39] C. Cuevas, D. Makaire, L. Dardenne, and P. Ngendakumana, "Thermo-hydraulic characterization of a louvered fin and flat tube heat exchanger," *Experimental Thermal and Fluid Science*, vol. 35, no. 1, pp. 154–164, 2011.

[40] K. Yakut and B. Sahin, "The effects of vortex characteristics on performance of coiled wire turbulators used for heat transfer augmentation," *Applied Thermal Engineering*, vol. 24, no. 16, pp. 2427–2438, 2004.

[41] E. F. Akyürek, K. Geliş, B. Şahin, and E. Manay, "Experimental analysis for heat transfer of nanofluid with wire coil turbulators in a concentric tube heat exchanger," *Results in Physics*, vol. 9, pp. 376–389, 2018.

[42] S. Eiamsa-Ard, C. Thianpong, P. Eiamsa-Ard, and P. Promvonge, "Convective heat transfer in a circular tube with short-length twisted tape insert," *International communications in heat and mass transfer*, vol. 36, no. 4, pp. 365–371, 2009.

[43] M. Garg, H. Nautiyal, S. Khurana, M. Shukla, *et al.*, "Heat transfer augmentation using twisted tape inserts: a review," *Renewable and Sustainable Energy Reviews*, vol. 63, pp. 193–225, 2016.

[44] W. M. Kays and A. L. London, "Compact heat exchangers," 1984.

[45] J. E. Hesselgreaves, R. Law, and D. Reay, *Compact heat exchangers: selection, design and operation*. Butterworth-Heinemann, 2016.

[46] A. Bhuiyan, A. Islam, and M. Amin, "Numerical study of 3d thermal and hydraulic characteristics of wavy fin-and-tube heat exchanger," *Frontiers in Heat and Mass Transfer (FHMT)*, vol. 3, no. 3, 2012.

[47] A. E. Bergles, "Recent developments in enhanced heat transfer," *Heat and mass transfer*, vol. 47, no. 8, pp. 1001–1008, 2011.

[48] M. Bovand, S. Rashidi, and J. Esfahani, "Heat transfer enhancement and pressure drop penalty in porous solar heaters: numerical simulations," *Solar Energy*, vol. 123, pp. 145–159, 2016.

[49] M. Mahmood, S. Asghar, and M. Hossain, "Squeezed flow and heat transfer over a porous surface for viscous fluid," *Heat and mass Transfer*, vol. 44, pp. 165–173, 2007.

[50] I. Kaur and P. Singh, "State-of-the-art in heat exchanger additive manufacturing," *International Journal of Heat and Mass Transfer*, vol. 178, p. 121600, 2021.

[51] Y. Xue, Z. Ge, X. Du, and L. Yang, "On the heat transfer enhancement of plate fin heat exchanger," *Energies*, vol. 11, no. 6, p. 1398, 2018.

[52] H. Tan, L. Wu, M. Wang, Z. Yang, and P. Du, "Heat transfer improvement in microchannel heat sink by topology design and optimization for high heat flux chip cooling," *International Journal of Heat and Mass Transfer*, vol. 129, pp. 681–689, 2019.

[53] H. Rastan, A. Abdi, B. Hamawandi, M. Ignatowicz, J. P. Meyer, and B. Palm, "Heat transfer study of enhanced additively manufactured minichannel heat exchangers," *International Journal of Heat and Mass Transfer*, vol. 161, p. 120271, 2020.

[54] K. Saha and S. Acharya, "Heat transfer enhancement using angled grooves as turbulence promoters," *Journal of Turbomachinery*, vol. 136, no. 8, p. 081004, 2014.

[55] N. Zheng, P. Liu, F. Shan, Z. Liu, and W. Liu, "Turbulent flow and heat transfer enhancement in a heat exchanger tube fitted with novel discrete inclined grooves," *International Journal of Thermal Sciences*, vol. 111, pp. 289–300, 2017.

[56] A. Dewan and P. Srivastava, "A re view of heat transfer enhancement through flow disruption in a microchannel," *Journal of Thermal Science*, vol. 24, pp. 203–214, 2015.

[57] H. Zontul, H. Hamzah, N. Kurtulmuş, and B. Şahin, "Investigation of convective heat transfer and flow hydrodynamics in rectangular grooved channels," *International Communications in Heat and Mass Transfer*, vol. 126, p. 105366, 2021.

[58] L. Li, M. Yang, and Y. Zhang, "Numerical study of periodically fully-developed convection in channels with periodically grooved parts," *International Journal of Heat and Mass Transfer*, vol. 51, no. 11-12, pp. 3057–3065, 2008.

[59] A. A. Ramadhan and Y. T. Al Anii, "Groove geometry effects on turbulent heat transfer and fluid flow," *Heat and Mass Transfer*, vol. 49, pp. 185–195, 2013.

[60] T. T. Hoang, C. T. Dinh, F. Plourde, *et al.*, "Large eddy simulation of the turbulence heat and mass transfer of pulsating flow in a v-sharp corrugated channel," *International Journal of Heat and Mass Transfer*,

vol. 166, p. 120720, 2021.

[61] H. E. Ahmed and M. I. Ahmed, "Optimum thermal design of triangular, trapezoidal and rectangular grooved microchannel heat sinks," *International Communications in Heat and Mass Transfer*, vol. 66, pp. 47–57, 2015.

[62] Q. Zhu, H. Xia, J. Chen, X. Zhang, K. Chang, H. Zhang, H. Wang, J. Wan, and Y. Jin, "Fluid flow and heat transfer characteristics of microchannel heat sinks with different groove shapes," *International Journal of Thermal Sciences*, vol. 161, p. 106721, 2021.

[63] M. I. I. Rabby and M. W. Uddin, "Convection heat transfer augmentation inside a hybrid corrugated channel by varying the positions of corrugated configurations," *Case Studies in Thermal Engineering*, vol. 52, p. 103719, 2023.

[64] Z. Brodnianská and S. Kotšmíd, "Heat transfer enhancement in the novel wavy shaped heat exchanger channel with cylindrical vortex generators," *Applied Thermal Engineering*, vol. 220, p. 119720, 2023.

[65] P. Kumar, R. Dwivedi, and K. Pandey, "Numerical investigation of thermo-hydraulic transport characteristics of laminar flow through partially filled porous wavy channel: Effect of prandtl number," *Numerical Heat Transfer, Part A: Applications*, vol. 83, no. 10, pp. 1045–1066, 2023.

[66] N. A. Madlool, M. J. Alshukri, A. I. Alsabery, A. A. Eidan, and I. Hashim, "Numerical analysis of transfer of heat by forced convection in a wavy channel," *International Journal of Renewable Energy Development*, vol. 12, no. 1, pp. 155–165, 2023.

[67] S. K. Mehta, S. Pati, and L. Baranyi, "Effect of amplitude of walls on thermal and hydrodynamic characteristics of laminar flow through an asymmetric wavy channel," *Case Studies in Thermal Engineering*, vol. 31, p. 101796, 2022.

[68] L. Cheng, Y. Zhu, S. S. Band, D. Bahrami, R. Kalbasi, A. Karimipour, M. Jahangiri, K.-W. Chau, and A. Mosavi, "Role of gradients and vortexes on suitable location of discrete heat sources on a sinusoidal-wall microchannel," *Engineering Applications of Computational Fluid Mechanics*, vol. 15, no. 1, pp. 1176–1190, 2021.

[69] Z. Dong, P. Liu, H. Xiao, Z. Liu, and W. Liu, "A study on heat transfer enhancement for solar air heaters with ripple surface," *Renewable Energy*, vol. 172, pp. 477–487, 2021.

[70] A. Kumari and A. Kumar, "Heat transfer and fluid flow characteristics of a turbulent wall jet with a wavy wall," *International Journal of Heat and Fluid Flow*, vol. 87, p. 108749, 2021.

[71] N. Al-Zurfi, A. Alhusseny, and A. Nasser, "Effect of rotation on forced convection in wavy wall channels," *International Journal of Heat and Mass Transfer*, vol. 149, p. 119177, 2020.

[72] A. I. Alsabery, S. Parvin, M. Ghalambaz, A. J. Chamkha, and I. Hashim, "Convection heat transfer in 3d wavy direct absorber solar collector based on two-phase nanofluid approach," *Applied Sciences*, vol. 10, no. 20, p. 7265, 2020.

[73] S. Harikrishnan and S. Tiwari, "Heat transfer characteristics of sinusoidal wavy channel with secondary corrugations," *International Journal of Thermal Sciences*, vol. 145, p. 105973, 2019.

[74] A. Dellil, A. Azzi, and B. Jubran, "Turbulent flow and convective heat transfer in a wavy wall channel," *Heat and Mass Transfer*, vol. 40, pp. 793–799, 2004.

[75] D. Bhatia, G. Li, Y. Lin, J. Sun, P. Barrington, H. Li, and J. Wang, "Transition delay and drag reduction using biomimetically inspired surface waves," *Journal of Applied Fluid Mechanics*, vol. 13, no. 4, pp. 1207–1222, 2020.

[76] A. Dróżdż, W. Elsner, and D. Sikorski, "Passive skin friction control near turbulent separation–preliminary results," in *Journal of Physics: Conference Series*, vol. 1101, p. 012004, IOP Publishing, 2018.

[77] P. Kamiński, P. Niegodajew, A. Dróżdż, V. Sokolenko, A. Tyliszczak, and W. Elsner, "Numerical analysis of novel wavy wall based control of turbulent boundary layer separation," *Aerospace Science and Technology*, p. 109167, 2024.

[78] J. Rostami, A. Abbassi, and M. Saffar-Avval, "Optimization of conjugate heat transfer in wavy walls microchannels," *Applied Thermal Engineering*, vol. 82, pp. 318–328, 2015.

[79] I. Rechenberg, "Kybernetische lösungsansteuerung einer experimentellen forschungsaufgabe," *Annual Conference of the WGLR at Berlin in September,*, vol. 35, 1964.

[80] S. Brunton, B. Noack, and K. P, "Machine learning for fluid mechanics," *Annual Review of Fluid Mechanics*, vol. 52, p. 477–508, 2020.

[81] N. Benard, J. Pons-Prats, J. Periaux, G. Bugeda, P. Braud, J. Bonnet, and E. Moreau, "Turbulent separated shear flow control by surface plasma actuator: experimental optimization by genetic algorithm approach," *Exp. Fluids*, vol. 57, no. 2, pp. 22:1–17, 2016.

[82] T. Duriez, S. L. Brunton, and B. R. Noack, *Machine Learning Control — Taming Nonlinear Dynamics and Turbulence*, vol. 116 of *Fluid Mechanics and Its Applications*. Springer-Verlag, 2016.

[83] B. R. Noack, "Closed-loop turbulence control—From human to machine learning (and retour)," in *Proceedings of the 4th Symposium on Fluid Structure-Sound Interactions and Control (FSSIC), Tokyo, Japan* (Y. Zhou, M. Kimura, G. Peng, A. D. Lucey, and L. Hung, eds.), pp. 23–32, Springer, 2018.

[84] J. Rabault, M. Kuchta, A. Jensen, U. Réglade, and N. Cerardi, "Artificial neural networks trained through deep reinforcement learning discover control strategies for active flow control," *J. Fluid Mech.*, vol. 865, pp. 281–302, 2019.

[85] L. Guastoni, J. Rabault, P. Schlatter, and R. Azizpour, H. Vinuesa, "Deep reinforcement learning for turbulent drag reduction in channel flows," *Eur. Phys. J. E*, vol. 46, p. 27, 2023.

[86] N. J. Nair and A. Goza, "Bio-inspired variable-stiffness flaps for hybrid flow control, tuned via reinforcement learning," *J. Fluid Mech.*, vol. 956, p. R4, 2023.

[87] G. Fabbri, "Heat transfer optimization in corrugated wall channels," *International Journal of Heat and Mass Transfer*, vol. 43, no. 23,

pp. 4299–4310, 2000.

[88] A. Joodaki and A. Ashrafizadeh, "Surface shape design in fluid flow problems via hybrid optimization algorithms," *Aerospace Science and Technology*, vol. 39, pp. 639–651, 2014.

[89] L. Wang, L. Deng, C. Ji, E. Liang, C. Wang, and D. Che, "Multi-objective optimization of geometrical parameters of corrugated-undulated heat transfer surfaces," *Applied Energy*, vol. 174, pp. 25–36, 2016.

[90] S. M. Kirkar, A. Gönül, A. Celen, and A. S. Dalkilic, "Multi-objective optimization of single-phase flow heat transfer characteristics in corrugated tubes," *International Journal of Thermal Sciences*, vol. 186, p. 108119, 2023.

[91] A. B. Blanchard, G. Y. Cornejo Maceda, D. Fan, Y. Li, Y. Zhou, B. R. Noack, and T. P. Sapsis, "Bayesian optimization for active flow control," *Acta Mech. Sin.*, pp. 1–3, 2021.

[92] F. Pino, L. Schena, J. Rabault, and M. A. Mendez, "Comparative analysis of machine learning methods for active flow control," *J. Fluid Mech.*, vol. 958, p. A39, 2023.

[93] Y. Li, B. R. Noack, T. Wang, G. Cornejo Maceda, E. Pickering, T. Shaqarin, and A. Tyliszczak, "Jet mixing enhancement with Bayesian optimization, deep learning, and persistent data topology," vol. 991, p. A5, 2024.

[94] C. K. Williams and C. E. Rasmussen, *Gaussian processes for machine learning*, vol. 2. MIT press Cambridge, MA, 2006.

[95] N. Kurtulmuş, H. Zontul, and B. Sahin, "Heat transfer and flow characteristics in a sinusoidally curved converging-diverging channel," *International Journal of Thermal Sciences*, vol. 148, p. 106163, 2020.

[96] S. Liu and M. Sakr, "A comprehensive review on passive heat transfer enhancements in pipe exchangers," *Renewable and sustainable energy reviews*, vol. 19, pp. 64–81, 2013.

[97] E. Elshafei, M. Awad, E. El-Negiry, and A. Ali, "Heat transfer and pressure drop in corrugated channels," *Energy*, vol. 35, no. 1, pp. 101–110, 2010.

[98] D. Kahaner, C. Moler, and S. Nash, *Numerical methods and software*. Prentice-Hall, Inc., 1989.

[99] D. C. Wilcox *et al.*, *Turbulence modeling for CFD*, vol. 2. DCW industries La Canada, CA, 1998.

[100] S. B. Pope, "Turbulent flows," *Measurement Science and Technology*, vol. 12, no. 11, pp. 2020–2021, 2001.

[101] *Ansys Fluent Theory Guide*. ANSYS Inc., 2021.

[102] F. R. Menter, "Two-equation eddy-viscosity turbulence models for engineering applications," *AIAA journal*, vol. 32, no. 8, pp. 1598–1605, 1994.

[103] B. K. M. Saleem, A. Mustafa, D. A. Kareem, M. I. Yuce, M. Szydłowski, and N. Al-Ansari, "Numerical analysis of turbulent flow over a backward-facing step in an open channel," *Archives of Hydro-Engineering and Environmental Mechanics*, vol. 70, no. 1, pp. 49–69, 2023.

[104] B. V. Ravi, P. Singh, and S. V. Ekkad, "Numerical investigation of turbulent flow and heat transfer in two-pass ribbed channels," *International Journal of Thermal Sciences*, vol. 112, pp. 31–43, 2017.

[105] J. Tu, C. Qi, K. Li, and Z. Tang, "Numerical analysis of flow and heat characteristic around micro-ribbed tube in heat exchanger system," *Powder Technology*, vol. 395, pp. 562–583, 2022.

[106] A. Kumar, R. Maithani, and A. R. S. Suri, "Numerical and experimental investigation of enhancement of heat transfer in dimpled rib heat exchanger tube," *Heat and Mass Transfer*, vol. 53, pp. 3501–3516, 2017.

[107] S. K. Sharma and V. R. Kalamkar, "Computational fluid dynamics approach in thermo-hydraulic analysis of flow in ducts with rib roughened walls–a review," *Renewable and Sustainable Energy Reviews*, vol. 55, pp. 756–788, 2016.

[108] C. K. Williams and C. E. Rasmussen, *Gaussian processes for machine learning*. MIT press, 2006.

[109] C. E. Rasmussen and C. K. I. Williams, *Gaussian processes in machine learning*. the MIT Press, 2006.

[110] A. Blanchard and T. Sapsis, "Bayesian optimization with output-weighted optimal sampling," *Journal of Computational Physics*, vol. 425, p. 109901, 2021.

[111] A. Blanchard and T. Sapsis, "Output-weighted optimal sampling for bayesian experimental design and uncertainty quantification," *SIAM/ASA Journal on Uncertainty Quantification*, vol. 9, no. 2, pp. 564–592, 2021.

[112] E. Brochu, V. M. Cora, and N. De Freitas, "A tutorial on bayesian optimization of expensive cost functions, with application to active user modeling and hierarchical reinforcement learning," *arXiv preprint arXiv:1012.2599*, 2010.

# Bibliography

Ab Satar, Mohd Hafiz et al. (2024). “A comprehensive comparison of passive flow controls on the wind turbine blade lift and drag performances: A CFD approach”. In: *European Journal of Mechanics-B/Fluids* 108, pp. 119–133.

Abd El-Baky, Mostafa A and Mousa M Mohamed (2007). “Heat pipe heat exchanger for heat recovery in air conditioning”. In: *Applied thermal engineering* 27.4, pp. 795–801.

Adamian, Dmitry Yuryevich, Mikhail Khaimovich Strelets, and Andrei Konstantinivich Travin (2011). “An efficient method of synthetic turbulence generation at LES inflow in zonal RANS–LES approaches to computation of turbulent flows”. In: *Matematicheskoe modelirovanie* 23.7, pp. 3–19.

Aftab, SMA et al. (2016). “Mimicking the humpback whale: An aerodynamic perspective”. In: *Progress in Aerospace Sciences* 84, pp. 48–69.

Ahammed, Nizar, Lazarus Godson Asirvatham, and Somchai Wongwises (2016). “Thermoelectric cooling of electronic devices with nanofluid in a multiport minichannel heat exchanger”. In: *Experimental Thermal and Fluid Science* 74, pp. 81–90.

Ahmed, Hamdi E and Mirghani I Ahmed (2015). “Optimum thermal design of triangular, trapezoidal and rectangular grooved microchannel heat sinks”. In: *International Communications in Heat and Mass Transfer* 66, pp. 47–57.

Akselsen, Andreas H and Simen Å Ellingsen (2020). “Langmuir-type vortices in wall-bounded flows driven by a criss-cross wavy wall topography”. In: *Journal of Fluid Mechanics* 900, A19.

Akyürek, Eda Feyza et al. (2018). “Experimental analysis for heat transfer of nanofluid with wire coil turbulators in a concentric tube heat exchanger”. In: *Results in Physics* 9, pp. 376–389.

Al-Zurfi, Nabeel, Ahmed Alhusseny, and Adel Nasser (2020). “Effect of rotation on forced convection in wavy wall channels”. In: *International Journal of Heat and Mass Transfer* 149, p. 119177.

Alsabery, Ammar I et al. (2020). “Convection heat transfer in 3D wavy direct absorber solar collector based on two-phase nanofluid approach”. In: *Applied Sciences* 10.20, p. 7265.

*Ansys Fluent Theory Guide* (2021). ANSYS Inc.

Aoki, Katsumi, Koji Muto, and Hiroo Okanaga (2012). “Mechanism of drag reduction by dimple structures on a sphere”. In: *Journal of Fluid Science and Technology* 7.1, pp. 1–10.

Atzori, Marco et al. (2020). “Aerodynamic effects of uniform blowing and suction on a NACA4412 airfoil”. In: *Flow, turbulence and combustion* 105.3, pp. 735–759.

Awais, Muhammad and Arafat A Bhuiyan (2018). “Heat transfer enhancement using different types of vortex generators (VGs): A review on experimental and numerical activities”. In: *Thermal Science and Engineering Progress* 5, pp. 524–545.

Ball, Philip (1999). “Engineering shark skin and other solutions”. In: *Nature* 400.6744, pp. 507–509.

Bearman, P W and JK Harvey (1993). “Control of circular cylinder flow by the use of dimples”. In: *AIAA journal* 31.10, pp. 1753–1756.

Bearman, Peter W and John K Harvey (1976). “Golf ball aerodynamics”. In: *Aeronautical Quarterly* 27.2, pp. 112–122.

Bechert, D et al. (1997). “Biological surfaces and their technological application-laboratory and flight experiments on drag reduction and separation control”. In: *28th Fluid dynamics conference*, p. 1960.

Bechert, DW and W Hage (2006). “Drag reduction with riblets in nature and engineering”. In: *WIT Trans State Art Sci Eng* 4, pp. 457–504.

Belamadi, Riyadh et al. (2016). “Aerodynamic performance analysis of slotted airfoils for application to wind turbine blades”. In: *Journal of wind engineering and industrial aerodynamics* 151, pp. 79–99.

Belcher, SE and JCR Hunt (1998). “Turbulent flow over hills and waves”. In: *Annual Review of Fluid Mechanics* 30.1, pp. 507–538.

Benard, N. et al. (2016). “Turbulent separated shear flow control by surface plasma actuator: experimental optimization by genetic algorithm approach”. In: *Exp. Fluids* 57.2, 22:1–17.

Bhuiyan, Arafat, AKM Islam, and M Amin (2012). “Numerical study of 3D thermal and hydraulic characteristics of wavy fin-and-tube heat exchanger”. In: *Frontiers in Heat and Mass Transfer (FHMT)* 3.3.

Biedermann, Till (2019). *Aeroacoustic transfer of leading edge serrations from single aerofoils to low-pressure fan applications*. Technische Universitaet Berlin (Germany).

B.J. Geurts (2004). *Elements of Direct and Large-Eddy Simulation*. Philadelphia, USA: Edwards Publishing.

Blanchard, A. B. et al. (2021). “Bayesian optimization for active flow control”. In: *Acta Mech. Sin.*, pp. 1–3.

Blanchard, Antoine and Themistoklis Sapsis (2021a). “Bayesian optimization with output-weighted optimal sampling”. In: *Journal of Computational Physics* 425.

– (2021b). “Output-weighted optimal sampling for Bayesian experimental design and uncertainty quantification”. In: *SIAM/ASA Journal on Uncertainty Quantification* 9.2, pp. 564–592.

– (2022). “Informative path planning for anomaly detection in environment exploration and monitoring”. In: *Ocean Engineering* 243, p. 110242.

Bolzon, Michael D, Richard M Kelso, and Maziar Arjomandi (2016). “Tubercles and their applications”. In: *Journal of aerospace engineering* 29.1, p. 04015013.

Bottasso, Carlo L et al. (2016). “Load mitigation for wind turbines by a passive aeroelastic device”. In: *Journal of Wind Engineering and Industrial Aerodynamics* 148, pp. 57–69.

Bovand, M, Saman Rashidi, and JA Esfahani (2016). “Heat transfer enhancement and pressure drop penalty in porous solar heaters: numerical simulations”. In: *Solar Energy* 123, pp. 145–159.

Brodnianská, Zuzana and Stanislav Kotšmíd (2023). “Heat transfer enhancement in the novel wavy shaped heat exchanger channel with cylindrical vortex generators”. In: *Applied Thermal Engineering* 220, p. 119720.

Brunton, S.L., B.R. Noack, and Koumoutsakos P (2020). “Machine Learning for Fluid Mechanics”. In: *Annual Review of Fluid Mechanics* 52, pp. 477–508.

C.A.J. Fletcher (1991). *Computational Techniques for Fluid Dynamics*. Berlin Heidelberg: Springer-Verlag.

Casalino, Damiano et al. (2019). “Aeroacoustic study of a wavy stator leading edge in a realistic fan/OGV stage”. In: *Journal of Sound and Vibration* 442, pp. 138–154.

Chear, CK and SS Dol (2015). “Vehicle aerodynamics: drag reduction by surface dimples”. In: *International Journal of Mechanical, Aerospace, Industrial, Mechatronic and Manufacturing Engineering* 9.1, pp. 202–205.

Chen, Huawei et al. (2013). “Biomimetic drag reduction study on herringbone riblets of bird feather”. In: *Journal of Bionic Engineering* 10.3, pp. 341–349.

Chen, Weijie, Weiyang Qiao, and Zuojun Wei (2020). “Aerodynamic performance and wake development of airfoils with wavy leading edges”. In: *Aerospace Science and Technology* 106, p. 106216.

Chen, Xin et al. (2018). “Experimental and numerical investigations of the aerodynamic noise reduction of automotive side view mirrors”. In: *Journal of Hydrodynamics* 30.4, pp. 642–650.

Cheng, Liang et al. (2021). “Role of gradients and vortexes on suitable location of discrete heat sources on a sinusoidal-wall microchannel”. In: *Engineering Applications of Computational Fluid Mechanics* 15.1, pp. 1176–1190.

Cherukat, P et al. (1998). “Direct numerical simulation of a fully developed turbulent flow over a wavy wall”. In: *Theoretical and computational fluid dynamics* 11.2, pp. 109–134.

Choudhry, Amanullah et al. (2014). “An insight into the dynamic stall lift characteristics”. In: *Experimental Thermal and Fluid Science* 58, pp. 188–208.

Chow, K (2022). “Improving vehicle rolling resistance and aerodynamics”. In: *Alternative Fuels and Advanced Vehicle Technologies for Improved Environmental Performance*. Elsevier, pp. 459–481.

Coder, James G and Dan M Somers (2020). “Design of a slotted, natural-laminar-flow airfoil for commercial transport applications”. In: *Aerospace Science and Technology* 106, p. 106217.

Corino, Edward Robert and Robert S Brodkey (1969). “A visual investigation of the wall region in turbulent flow”. In: *Journal of Fluid Mechanics* 37.1, pp. 1–30.

Cuevas, Cristian et al. (2011). “Thermo-hydraulic characterization of a louvered fin and flat tube heat exchanger”. In: *Experimental Thermal and Fluid Science* 35.1, pp. 154–164.

De Angelis, V, P Lombardi, and S Banerjee (1997). “Direct numerical simulation of turbulent flow over a wavy wall”. In: *Physics of Fluids* 9.8, pp. 2429–2442.

Dellil, AZ, A Azzi, and BA Jubran (2004). “Turbulent flow and convective heat transfer in a wavy wall channel”. In: *Heat and Mass Transfer* 40, pp. 793–799.

Dewan, Anupam and Pankaj Srivastava (2015). “A re view of heat transfer enhancement through flow disruption in a microchannel”. In: *Journal of Thermal Science* 24, pp. 203–214.

Dong, Zhimin et al. (2021). “A study on heat transfer enhancement for solar air heaters with ripple surface”. In: *Renewable Energy* 172, pp. 477–487.

Drozdz, A. et al. (2021). “Effective use of the streamwise waviness in the control of turbulent separation”. In: *Experimental Thermal and Fluid Science* 121, p. 110291.

Dróżdż, Artur et al. (2021). “Effect of Reynolds number on turbulent boundary layer approaching separation”. In: *Experimental Thermal and Fluid Science* 125, p. 110377.

Duriez, T., S. L. Brunton, and B. R. Noack (2016). *Machine Learning Control — Taming Nonlinear Dynamics and Turbulence*. Vol. 116. Fluid Mechanics and Its Applications. Springer-Verlag.

Ebrahimi, Abbas and Majid Hajipour (2018). "Flow separation control over an airfoil using dual excitation of DBD plasma actuators". In: *Aerospace Science and Technology* 79, pp. 658–668.

Elhadidi, Basman et al. (2015). "Experimental and numerical investigation of flow control using a novel active slat". In: *International Journal of Mechanical, Aerospace, Industrial, Mechatronic and Manufacturing Engineering* 9.1, pp. 21–25.

Elsner, Witold et al. (2022). "Experimental and numerical studies of turbulent flows over two-dimensional and three-dimensional rough surfaces under an adverse pressure gradient". In: *Applied Mathematical Modelling* 106, pp. 549–566.

Fabbri, Giampietro (2000). "Heat transfer optimization in corrugated wall channels". In: *International Journal of Heat and Mass Transfer* 43.23, pp. 4299–4310.

Fernex, Daniel et al. (2020). "Actuation response model from sparse data for wall turbulence drag reduction". In: *Physical Review Fluids* 5.7, p. 073901.

Fish, FEandlauder and George V Lauder (2006). "Passive and active flow control by swimming fishes and mammals". In: *Annu. Rev. Fluid Mech.* 38.1, pp. 193–224.

Fish, Franke E and Juliann M Battle (1995). "Hydrodynamic design of the humpback whale flipper". In: *Journal of morphology* 225.1, pp. 51–60.

Frazier, Peter I (2018). "Bayesian optimization". In: *Recent advances in optimization and modeling of contemporary problems*. Informs, pp. 255–278.

Fujii, Hideto et al. (2011). "Turbulence structure, friction drag and pressure drag due to turbulent flow over angled wavy surfaces". In: *Seventh International Symposium on Turbulence and Shear Flow Phenomena*. Begel House Inc.

Fujino, Yozo et al. (2012). "Cable vibrations and control methods". In: *Wind Resistant Design of Bridges in Japan: Developments and Practices*, pp. 197–229.

Ganapathisubramani, B. et al. (2012). "Amplitude and frequency modulation in wall turbulence". In: *Journal of Fluid Mechanics* 712, pp. 61–91. DOI: 10.1017/jfm.2012.398.

García-Mayoral, Ricardo and Javier Jiménez (2011). "Drag reduction by riblets". In: *Philosophical transactions of the Royal society A: Mathematical, physical and engineering Sciences* 369.1940, pp. 1412–1427.

Gardner, Anthony D et al. (2023). “Review of rotating wing dynamic stall: Experiments and flow control”. In: *Progress in Aerospace Sciences* 137, p. 100887.

Garg, MO et al. (2016). “Heat transfer augmentation using twisted tape inserts: a review”. In: *Renewable and Sustainable Energy Reviews* 63, pp. 193–225.

Gattere, Federica, Alessandro Chiarini, and Maurizio Quadrio (2022). “Dimples for skin-friction drag reduction: status and perspectives”. In: *Fluids* 7.7, p. 240.

Genç, M Serdar, Ünver Kaynak, and Gary D Lock (2009). “Flow over an aerofoil without and with a leading-edge slat at a transitional Reynolds number”. In: *Proceedings of the Institution of Mechanical Engineers, Part G: Journal of Aerospace Engineering* 223.3, pp. 217–231.

Ghebali, Sacha, Sergei I Chernyshenko, and Michael A Leschziner (2017). “Can large-scale oblique undulations on a solid wall reduce the turbulent drag?” In: *Physics of Fluids* 29.10.

Gibertini, Giuseppe et al. (2015). “Helicopter drag reduction by vortex generators”. In: *Aerospace science and technology* 47, pp. 324–339.

Guastoni, L. et al. (2023). “Deep reinforcement learning for turbulent drag reduction in channel flows”. In: *Eur. Phys. J. E* 46, p. 27.

Guerrero, Joel E, Dario Maestro, and Alessandro Bottaro (2012). “Biomimetic spiroid winglets for lift and drag control”. In: *Comptes Rendus Mecanique* 340.1-2, pp. 67–80.

Guerrero, Joel E, Marco Sanguineti, and Kevin Wittkowski (2020). “Variable cant angle winglets for improvement of aircraft flight performance”. In: *Meccanica* 55, pp. 1917–1947.

Günel, Mehmet and Hüseyin Ilgin (2014). *Tall buildings: structural systems and aerodynamic form*. Routledge.

Gursul, Ismet, Zhijin Wang, and Eleni Vardaki (2007). “Review of flow control mechanisms of leading-edge vortices”. In: *Progress in Aerospace Sciences* 43.7-8, pp. 246–270.

Hak, Mohamed Gad-el (1996). “Modern developments in flow control”. In.

Hak, Mohamed Gad-el and Dennis M Bushnell (1991). “Separation control”. In.

Halawa, Amr M, Basman Elhadidi, and Shigeo Yoshida (2018). “Aerodynamic performance enhancement using active flow control on DU96-W-180 wind turbine airfoil”. In.

Hamed, Ali M, Luciano Castillo, and Leonardo P Chamorro (2017). “Turbulent boundary layer response to large-scale wavy topographies”. In: *Physics of Fluids* 29.6, p. 065113.

Hamed, Ali M et al. (2015). “Turbulent boundary layer over 2D and 3D large-scale wavy walls”. In: *Physics of Fluids* 27.10, p. 106601.

Hansen, Kristy L, Richard M Kelso, and Bassam B Dally (2011). “Performance variations of leading-edge tubercles for distinct airfoil profiles”. In: *AIAA journal* 49.1, pp. 185–194.

Hao, Wenxing and Chun Li (2020). “Performance improvement of adaptive flap on flow separation control and its effect on VAWT”. In: *Energy* 213, p. 118809.

Harikrishnan, S and Shaligram Tiwari (2019). “Heat transfer characteristics of sinusoidal wavy channel with secondary corrugations”. In: *International Journal of Thermal Sciences* 145, p. 105973.

Hesselgreaves, John E, Richard Law, and David Reay (2016). *Compact heat exchangers: selection, design and operation*. Butterworth-Heinemann.

Hoang, Thanh Tung, Cong Truong Dinh, Frédéric Plourde, et al. (2021). “Large eddy simulation of the turbulence heat and mass transfer of pulsating flow in a V-sharp corrugated channel”. In: *International Journal of Heat and Mass Transfer* 166, p. 120720.

Hsu, Sheng-Tien and John F Kennedy (1971). “Turbulent flow in wavy pipes”. In: *Journal of Fluid Mechanics* 47.3, pp. 481–502.

Hunt, Julian CR, Alan A Wray, and Parviz Moin (1988). “Eddies, streams, and convergence zones in turbulent flows”. In: *Studying turbulence using numerical simulation databases, 2. Proceedings of the 1988 summer program*.

Hutchins, Nicholas and Ivan Marusic (2007). “Large-scale influences in near-wall turbulence”. In: *Philosophical Transactions of the Royal Society A: Mathematical, Physical and Engineering Sciences* 365.1852, pp. 647–664.

Islam, Md Rasedul et al. (2013). “Drag reduction of a car by using vortex generator”. In: *International Journal of Scientific & Engineering Research* 4.7, pp. 1298–1302.

Izawa, Seiichiro, JC Lerner, and U Boldes (2011). “Active and passive control of flow past a cavity”. In: *Wind Tunnels and Experimental Fluid Dynamics Research* 1978.

Jabardo, JM Saiz, JR Bastos Zoghbi Filho, and A Salamanca (2006). “Experimental study of the air side performance of louver and wave fin-and-tube coils”. In: *Experimental Thermal and Fluid Science* 30.7, pp. 621–631.

Janssen, Peter AEM (1989). “Wave-induced stress and the drag of air flow over sea waves”. In: *Journal of Physical Oceanography* 19.6, pp. 745–754.

Javed, Salman, Farhan Javed, and Samsher (2017). “Effect of Boat Tail Profile on Drag Coefficient of a Sedan Using CFD”. In: *ASME International Mechanical Engineering Congress and Exposition*. Vol. 58424. American Society of Mechanical Engineers, V007T09A027.

Jeong, Jae Sung, Seon Woo Bong, and Sang Woo Lee (2022). “An efficient winglet coverage for aeroengine turbine blade flat tip and its loss map”. In: *Energy* 260, p. 125153.

J.H. Ferziger, M. Peric (1996). *Computational methods for fluid dynamics*. Berlin Heidelberg: Springer-Verlag.

Johari, Hamid et al. (2007). “Effects of leading-edge protuberances on airfoil performance”. In: *AIAA journal* 45.11, pp. 2634–2642.

Joodaki, A and A Ashrafizadeh (2014). “Surface shape design in fluid flow problems via hybrid optimization algorithms”. In: *Aerospace Science and Technology* 39, pp. 639–651.

Joshi, Sanket N and Yash S Gujarathi (2016). “A review on active and passive flow control techniques”. In: *International Journal on Recent Technologies in Mechanical and Electrical Engineering* 3.4, pp. 1–6.

Kahaner, David, Cleve Moler, and Stephen Nash (1989). *Numerical methods and software*. Prentice-Hall, Inc.

Kaminski, P and A Tyliszczak (2022). “Numerical analysis of the influence of wall roughness on the turbulent boundary layer separation”. In: *Journal of Physics: Conference Series*. Vol. 2367. IOP Publishing, p. 012011.

Kamiński, Piotr et al. (2024). “Numerical analysis of novel wavy wall based control of turbulent boundary layer separation”. In: *Aerospace Science and Technology* 149, p. 109167.

Kaur, Inderjot and Prashant Singh (2021). “State-of-the-art in heat exchanger additive manufacturing”. In: *International Journal of Heat and Mass Transfer* 178.

Kays, William Morrow and Alexander Louis London (1984). “Compact heat exchangers”. In.

Khaled, Mohamed et al. (2019). “Investigation of a small Horizontal–Axis wind turbine performance with and without winglet”. In: *Energy* 187, p. 115921.

Khaleel, Mohamed Mohamed, Abdulgader Alsharif, and Ibrahim Imbayah Khalefah Imbayah (2022). “Renewable energy technologies: Recent advances and future predictions”. In: *African Journal of Advanced Pure and Applied Sciences (AJAPAS)*, pp. 58–64.

Kheirkhah, Mahdi, Ehsan Roohi, and Mahmoud Pasandidehfard (2025). “Improving the aerodynamics of a fastback car body using a spoiler”. In: *Scientific Reports* 15.1, pp. 1–14.

Kirkar, Safak Metin et al. (2023). “Multi-objective optimization of single-phase flow heat transfer characteristics in corrugated tubes”. In: *International Journal of Thermal Sciences* 186, p. 108119.

Kourakis, Ioannis (2007). “Structural systems and tuned mass dampers of super-tall buildings: case study of Taipei 101”. PhD thesis. Massachusetts Institute of Technology.

Koyama, Shuhei, Kousuke Takashima, and Yoshimichi Hagiwara (2007). “Turbulence modification in flow around a periodically deforming film”. In: *Journal of Turbulence* 8, N19.

Krásnỳ, Ivo, Ilya Astrouski, and Miroslav Raudenskỳ (2016). “Polymeric hollow fiber heat exchanger as an automotive radiator”. In: *Applied Thermal Engineering* 108, pp. 798–803.

Kruse, Nils and Philipp Rudolf Von Rohr (2006). “Structure of turbulent heat flux in a flow over a heated wavy wall”. In: *International journal of heat and mass transfer* 49.19-20, pp. 3514–3529.

Kuhn, Simon, Saša Kenjereš, and Philipp Rudolf von Rohr (2010). “Large eddy simulations of wall heat transfer and coherent structures in mixed convection over a wavy wall”. In: *International journal of thermal sciences* 49.7, pp. 1209–1226.

Kumar, Anil, Rajesh Maithani, and Amar Raj Singh Suri (2017). “Numerical and experimental investigation of enhancement of heat transfer in dimpled rib heat exchanger tube”. In: *Heat and Mass Transfer* 53, pp. 3501–3516.

Kumar, Prince, Ritesh Dwivedi, and KM Pandey (2023). “Numerical investigation of thermo-hydraulic transport characteristics of laminar flow through partially filled porous wavy channel: Effect of Prandtl number”. In: *Numerical Heat Transfer, Part A: Applications* 83.10, pp. 1045–1066.

Kumari, Archana and Amitesh Kumar (2021). “Heat transfer and fluid flow characteristics of a turbulent wall jet with a wavy wall”. In: *International Journal of Heat and Fluid Flow* 87, p. 108749.

Kurtulmuş, Nazım, Harun Zontul, and Besir Sahin (2020). “Heat transfer and flow characteristics in a sinusoidally curved converging-diverging channel”. In: *International Journal of Thermal Sciences* 148, p. 106163.

Lang, Amy W, Emily M Jones, and Farhana Afroz (2017). “Separation control over a grooved surface inspired by dolphin skin”. In: *Bioinspiration & Biomimetics* 12.2, p. 026005.

Leknys, RR et al. (2018). “Thin airfoil load control during post-stall and large pitch angles using leading-edge trips”. In: *Journal of Wind Engineering and Industrial Aerodynamics* 179, pp. 80–91.

Li, Chu-Chu et al. (2016). “Drag reduction effects facilitated by microridges inside the mouthparts of honeybee workers and drones”. In: *Journal of Theoretical Biology* 389, pp. 1–10.

Li, Chuchu et al. (2015). “Drag reduction in the mouthpart of a honeybee facilitated by galea ridges for nectar-dipping strategy”. In: *Journal of Bionic Engineering* 12.1, pp. 70–78.

Li, Ling, Mo Yang, and Yuwen Zhang (2008). “Numerical study of periodically fully-developed convection in channels with periodically grooved parts”. In: *International Journal of Heat and Mass Transfer* 51.11-12, pp. 3057–3065.

Li, Y. et al. (2024). “Jet mixing enhancement with Bayesian optimization, deep learning, and persistent data topology”. In: 991, A5.

Liebeck, Robert H (1978). “Design of subsonic airfoils for high lift”. In: *Journal of aircraft* 15.9, pp. 547–561.

Lissaman, PBS (1983). “Low-Reynolds-number airfoils”. In: *Annual review of fluid mechanics* 15.1, pp. 223–239.

Liu, Shuli and M Sakr (2013). “A comprehensive review on passive heat transfer enhancements in pipe exchangers”. In: *Renewable and sustainable energy reviews* 19, pp. 64–81.

Lo, Kin Hing and Konstantinos Kontis (2016). “Flow characteristics over a tractor-trailer model with and without vane-type vortex generator installed”. In: *Journal of Wind Engineering and Industrial Aerodynamics* 159, pp. 110–122.

Lorenz, Ralph D (2006). *Spinning flight: dynamics of frisbees, boomerangs, samaras, and skipping stones*. Springer.

Lufthansa (2014). *More than 200 Lufthansa A320 aircraft to become quieter*. Archived 2014-05-04 at Wayback Machine; accessed 2014-05-04.

Maaß, Carsten and Ulrich Schumann (1996). “Direct numerical simulation of separated turbulent flow over a wavy boundary”. In: *Flow Simulation with High-Performance Computers II*. Springer, pp. 227–241.

Madlool, Naseer Abboodi et al. (2023). “Numerical Analysis of Transfer of Heat by Forced Convection in a Wavy Channel”. In: *International Journal of Renewable Energy Development* 12.1, pp. 155–165.

Mahmood, M, S Asghar, and MA Hossain (2007). “Squeezed flow and heat transfer over a porous surface for viscous fluid”. In: *Heat and mass Transfer* 44, pp. 165–173.

Mathis, Romain, Nicholas Hutchins, and Ivan Marusic (2009). “Large-scale amplitude modulation of the small-scale structures in turbulent boundary layers”. In: *Journal of Fluid Mechanics* 628, pp. 311–337.

Maughmer, Mark D and Götz Bramesfeld (2008). “Experimental investigation of Gurney flaps”. In: *Journal of Aircraft* 45.6, pp. 2062–2067.

Maxmut O’g’li, Xamitov Faxri (2023). “Renewable energy sources: advancements, challenges, and prospects”. In: *International Journal of Advance Scientific Research* 3.08, pp. 14–25.

McMasters, John H and Michael L Henderson (1979). “Low-speed single-element airfoil synthesis”. In: *NASA. Langley Res. Center The Sci. and Technol. of Low Speed and Motorless Flight, Pt. 1*.

Mehta, Sumit Kumar, Sukumar Pati, and László Baranyi (2022). “Effect of amplitude of walls on thermal and hydrodynamic characteristics of laminar flow through an asymmetric wavy channel”. In: *Case Studies in Thermal Engineering* 31, p. 101796.

Menter, Florian R (1994). “Two-equation eddy-viscosity turbulence models for engineering applications”. In: *AIAA journal* 32.8, pp. 1598–1605.

Menter, Florian R et al. (2006). “A correlation-based transition model using local variables—part I: model formulation”. In: *Journal of turbomachinery* 128.3, pp. 413–422.

Mostafa, Wafaa et al. (2022). “Quantitative impact of a micro-cylinder as a passive flow control on a horizontal axis wind turbine performance”. In: *Energy* 244, p. 122654.

Mueller, Thomas J and James D DeLaurier (2003). “Aerodynamics of small vehicles”. In: *Annual review of fluid mechanics* 35.1, pp. 89–111.

Nair, N. J. and A. Goza (2023). “Bio-inspired variable-stiffness flaps for hybrid flow control, tuned via reinforcement learning”. In: *J. Fluid Mech.* 956, R4.

Napoli, E, Vincenzo Armenio, and M De Marchis (2008). “The effect of the slope of irregularly distributed roughness elements on turbulent wall-bounded flows”. In: *Journal of Fluid Mechanics* 613, pp. 385–394.

Nicoud, Franck and Frédéric Ducros (1999). “Subgrid-scale stress modelling based on the square of the velocity gradient tensor”. In: *Flow, turbulence and Combustion* 62.3, pp. 183–200.

Noack, B. R. (2018). “Closed-loop turbulence control—From human to machine learning (and retour)”. In: *Proceedings of the 4th Symposium on Fluid Structure-Sound Interactions and Control (FSSIC), Tokyo, Japan*. Ed. by Y. Zhou et al. Springer, pp. 23–32.

Parker, HF (1920). “The variable camber wing”. In: *National Advisory Committee for Aeronautics*.

Phan, Thanh-Long (2024). “Optimal configuration of passive flow control devices to reduce the aerodynamics drag of a tractor-trailer model”. In: *Results in Engineering* 23, p. 102425.

Pino, F. et al. (2023). “Comparative analysis of machine learning methods for active flow control”. In: *J. Fluid Mech.* 958, A39.

Piquee, J et al. (2022). “Numerical investigations of a membrane morphing wind turbine blade under gust conditions”. In: *Journal of Wind Engineering and Industrial Aerodynamics* 224, p. 104921.

Pollard, A (1998). “Passive and active control of near-wall turbulence”. In: *Progress in aerospace sciences* 33.11-12, pp. 689–708.

Pope, Stephen B (2001). “Turbulent flows”. In: *Measurement Science and Technology* 12.11, pp. 2020–2021.

Raayai-Ardakani, Shabnam and Gareth H McKinley (2017). “Drag reduction using wrinkled surfaces in high Reynolds number laminar boundary layer flows”. In: *Physics of Fluids* 29.9.

Rabault, J. et al. (2019). “Artificial neural networks trained through deep reinforcement learning discover control strategies for active flow control”. In: *J. Fluid Mech.* 865, pp. 281–302.

Rabby, Md Insiat Islam and Md Wasi Uddin (2023). “Convection heat transfer augmentation inside a hybrid corrugated channel by varying the positions of corrugated configurations”. In: *Case Studies in Thermal Engineering* 52, p. 103719.

Ramadhan, Abdulmajeed A and Yaser T Al Anii (2013). “Groove geometry effects on turbulent heat transfer and fluid flow”. In: *Heat and Mass Transfer* 49, pp. 185–195.

Rao, Yu, Bo Li, and Yan Feng (2015). “Heat transfer of turbulent flow over surfaces with spherical dimples and teardrop dimples”. In: *Experimental Thermal and Fluid Science* 61, pp. 201–209.

Rashid, Shagufta et al. (2022). “Review of wave drag reduction techniques: Advances in active, passive, and hybrid flow control”. In: *Proceedings of the Institution of Mechanical Engineers, Part G: Journal of Aerospace Engineering* 236.14, pp. 2851–2884.

Rastan, Hamidreza et al. (2020). “Heat transfer study of enhanced additively manufactured minichannel heat exchangers”. In: *International Journal of Heat and Mass Transfer* 161, p. 120271.

Ravi, Bharath Viswanath, Prashant Singh, and Srinath V Ekkad (2017). “Numerical investigation of turbulent flow and heat transfer in two-pass ribbed channels”. In: *International Journal of Thermal Sciences* 112, pp. 31–43.

Rechenberg, Ingo (1964). “Kybernetische lösungsansteuerung einer experimentellen forschungsaufgabe”. In: *Annual Conference of the WGLR at Berlin in September,* 35.

Ricco, Pierre, Martin Skote, and Michael A. Leschziner (2021). “A review of turbulent skin-friction drag reduction by near-wall transverse forcing”. In: *Progress in Aerospace Sciences* 123, p. 100713. ISSN: 0376-0421. DOI: https://doi.org/10.1016/j.paerosci.2021.100713. URL: https://www.sciencedirect.com/science/article/pii/S037604212100018X.

Rostami, Javad, Abbas Abbassi, and Majid Saffar-Avval (2015). “Optimization of conjugate heat transfer in wavy walls microchannels”. In: *Applied Thermal Engineering* 82, pp. 318–328.

Saha, Krishnendu and Sumanta Acharya (2014). “Heat transfer enhancement using angled grooves as turbulence promoters”. In: *Journal of Turbomachinery* 136.8, p. 081004.

Saleem, Bala Kawa M et al. (2023). “Numerical Analysis of Turbulent Flow over a Backward-facing Step in an Open Channel”. In: *Archives of Hydro-Engineering and Environmental Mechanics* 70.1, pp. 49–69.

Schlieter, Antje et al. (2016). “Mechanical Properties of Shark-Skin Like Structured Surfaces for High-Temperature Applications”. In: *Advanced Engineering Materials* 18.5, pp. 688–702.

Schmidt, Thomas G and Stéphane Redonnet (2024). “Exploring a bio-inspired passive flow control strategy for wind turbines: Experimental characterization of the aerodynamics of a wind turbine blade section possibly equipped with leading-edge tubercles”. In: *Journal of Wind Engineering and Industrial Aerodynamics* 250, p. 105768.

Searle, Matthew et al. (2020). “Heat transfer coefficients of additively manufactured tubes with internal pin fins for supercritical carbon dioxide cycle recuperators”. In: *Applied Thermal Engineering* 181, p. 116030.

Segunda, Vinicius Martins, Scott J Ormiston, and Mark F Tachie (2018). “Experimental and numerical investigation of developing turbulent flow over a wavy wall in a horizontal channel”. In: *European Journal of Mechanics-B/Fluids* 68, pp. 128–143.

Sharma, Sanjay K and Vilas R Kalamkar (2016). “Computational Fluid Dynamics approach in thermo-hydraulic analysis of flow in ducts with rib roughened walls–A review”. In: *Renewable and Sustainable Energy Reviews* 55, pp. 756–788.

Shih, Tsan-Hsing et al. (1995). “A new k-ϵ eddy viscosity model for high reynolds number turbulent flows”. In: *Computers & fluids* 24.3, pp. 227–238.

Shur, Michael L et al. (2014). “Synthetic turbulence generators for RANS-LES interfaces in zonal simulations of aerodynamic and aeroacoustic problems”. In: *Flow, Turbulence and Combustion* 93, pp. 63–92.

Sigal, Asher (1971). “An experimental investigation of the turbulent boundary layer over a wavy wall”. PhD thesis. California Institute of Technology.

Smith, Marilyn et al. (2001). “Performance analysis of a wing with multiple winglets”. In: *19th AIAA Applied Aerodynamics Conference*, p. 2407.

Sun, Zhensheng et al. (2018). “Direct numerical simulation of a fully developed compressible wall turbulence over a wavy wall”. In: *Journal of Turbulence* 19.1, pp. 72–105.

Tan, Hui et al. (2019). “Heat transfer improvement in microchannel heat sink by topology design and optimization for high heat flux chip cooling”. In: *International Journal of Heat and Mass Transfer* 129, pp. 681–689.

Tanarro, Álvaro, Ricardo Vinuesa, and Philipp Schlatter (2020). “Effect of adverse pressure gradients on turbulent wing boundary layers”. In: *Journal of Fluid Mechanics* 883, A8.

Tay, C (2011). “Determining the effect of dimples on drag in a turbulent channel flow”. In: *49th AIAA Aerospace Sciences Meeting Including the New Horizons Forum and Aerospace Exposition*, p. 682.

Tay, CMJ, BC Khoo, and YT Chew (2015). “Mechanics of drag reduction by shallow dimples in channel flow”. In: *Physics of Fluids* 27.3.

Tay, Jonathan and Tee Tai Lim (2018). “Drag reduction with teardrop-shaped dimples”. In: *2018 Flow Control Conference*, p. 3528.

Tay, Jonathan, Tee Tai Lim, and Boo Cheong Khoo (2019). “Drag reduction with diamond-shaped dimples”. In: *AIAA Aviation 2019 Forum*, p. 3296.

Tayebi, Ali and Farshid Torabi (2024). “Flow control techniques to improve the aerodynamic performance of Darrieus vertical axis wind turbines: A critical review”. In: *Journal of Wind Engineering and Industrial Aerodynamics* 252, p. 105820.

Traub, Lance W (2014). “Prediction of gurney-flap lift enhancement for airfoils and wings”. In: *AIAA Journal* 52.9, pp. 2087–2090.

Tu, Jianglin et al. (2022). “Numerical analysis of flow and heat characteristic around micro-ribbed tube in heat exchanger system”. In: *Powder Technology* 395, pp. 562–583.

Turnow, Johann et al. (2012). “Flow structures and heat transfer on dimples in a staggered arrangement”. In: *International Journal of Heat and Fluid Flow* 35, pp. 168–175.

Tyson, CJ and ND Sandham (2013). “Numerical simulation of fully-developed compressible flows over wavy surfaces”. In: *International journal of heat and fluid flow* 41, pp. 2–15.

Veldhuis, Leo and Erik Vervoort (2009). “Drag effect of a dented surface in a turbulent flow”. In: *27th AIAA Applied Aerodynamics Conference*, p. 3950.

Vinuesa, Ricardo et al. (2017). “Pressure-gradient turbulent boundary layers developing around a wing section”. In: *Flow, turbulence and combustion* 99, pp. 613–641.

Walsh, M (1982). “Turbulent boundary layer drag reduction using riblets”. In: *20th aerospace sciences meeting*, p. 169.

Wang, Haipeng et al. (2017). “Flow control on the NREL S809 wind turbine airfoil using vortex generators”. In: *Energy* 118, pp. 1210–1221.

Wang, Haipeng et al. (2019). “Effects of leading edge slat on flow separation and aerodynamic performance of wind turbine”. In: *Energy* 182, pp. 988–998.

Wang, Jiang-Sheng, Jun Wu, and Jin-Jun Wang (2023). “Wake-triggered secondary vortices over a cylinder/airfoil configuration”. In: *Experiments in Fluids* 64.1, p. 6.

Wang, Limin et al. (2016). “Multi-objective optimization of geometrical parameters of corrugated-undulated heat transfer surfaces”. In: *Applied Energy* 174, pp. 25–36.

Wang, Ying et al. (2018). “Influence of an off-surface small structure on the flow control effect on horizontal axis wind turbine at different relative inflow angles”. In: *Energy* 160, pp. 101–121. ISSN: 0360-5442. DOI: https://doi.org/10.1016/j.energy.2018.06.070. URL: https://www.sciencedirect.com/science/article/pii/S0360544218311356.

Weick, Fred E and Joseph A Shortal (1933). “The effect of multiple fixed slots and a trailing-edge flap on the lift and drag of a Clark Y airfoil”. In.

Whitman, Natalie et al. (2006). “Experimental investigation of slotted airfoil performance with modified slot configurations”. In: *24th AIAA Applied Aerodynamics Conference*, p. 3481.

Willetts, BB and Ole E Barndorff-Nielsen (1991). *Aeolian Grain Transport 2: The Erosional Environment*. Springer-Verlag.

Williams, Christopher KI and Carl Edward Rasmussen (2006). *Gaussian processes for machine learning*. Vol. 2. 3. MIT press Cambridge, MA.

Wu, Liyan et al. (2018). “Experimental investigations on drag-reduction characteristics of bionic surface with water-trapping microstructures of fish scales”. In: *Scientific Reports* 8.1, p. 12186.

Xue, Yuan et al. (2018). “On the heat transfer enhancement of plate fin heat exchanger”. In: *Energies* 11.6, p. 1398.

Ye, Xuemin et al. (2023). “Numerical study on aerodynamic performance and noise of wind turbine airfoils with serrated gurney flap”. In: *Energy* 262, p. 125574.

Yoon, HS et al. (2009). “Effect of wave amplitude on turbulent flow in a wavy channel by direct numerical simulation”. In: *Ocean Engineering* 36.9-10, pp. 697–707.

Yossri, W, S Ben Ayed, and A Abdelkefi (2023). “Evaluation of the efficiency of bioinspired blade designs for low-speed small-scale wind turbines with the presence of inflow turbulence effects”. In: *Energy* 273, p. 127210.

You, D and Parviz Moin (2008). “Active control of flow separation over an airfoil using synthetic jets”. In: *Journal of Fluids and Structures* 24.8, pp. 1349–1357.

Zaki, Abanoub et al. (2022). “Effects of leading edge slat on the aerodynamic performance of low Reynolds number horizontal axis wind turbine”. In: *Energy* 239, p. 122338.

Zeman, Otto and Niels Otto Jensen (1987). “Modification of turbulence characteristics in flow over hills”. In: *Quarterly Journal of the Royal Meteorological Society* 113.475, pp. 55–80.

Zhang, Enwei, Xiaoliang Wang, and Qingquan Liu (2022). “Numerical investigation on the temporal and spatial statistical characteristics of turbulent mass transfer above a two-dimensional wavy wall”. In: *International Journal of Heat and Mass Transfer* 184, p. 122260.

Zhang, Enwei et al. (2023a). “Secondary flow and streamwise vortices in three dimensional staggered wavy-wall turbulence”. In: *Flow* 3, E19.

Zhang, MM, GF Wang, and JZ Xu (2013). “Aerodynamic control of low-Reynolds-number airfoil with leading-edge protuberances”. In: *AIAA journal* 51.8, pp. 1960–1971.

Zhang, Xiaobing and Zekang Wang (2025). “Thermal protection and drag reduction induced by flow control devices in supersonic/hypersonic flows: A review”. In: *Progress in Aerospace Sciences*, p. 101093.

Zhang, Zhihao et al. (2023b). “Comparative analysis of bent and basic winglets on performance improvement of horizontal axis wind turbines”. In: *Energy* 281.

Zheng, Nianben et al. (2017). “Turbulent flow and heat transfer enhancement in a heat exchanger tube fitted with novel discrete inclined grooves”. In: *International Journal of Thermal Sciences* 111, pp. 289–300.

Zhu, Chengyong et al. (2019). “Dynamic stall control of the wind turbine airfoil via single-row and double-row passive vortex generators”. In: *Energy* 189, p. 116272.

Zhu, Lin, Hongbo Tan, and Jianlin Yu (2013). “Analysis on optimal heat exchanger size of thermoelectric cooler for electronic cooling applications”. In: *Energy conversion and management* 76, pp. 685–690.

Zhu, Qifeng et al. (2021). “Fluid flow and heat transfer characteristics of microchannel heat sinks with different groove shapes”. In: *International Journal of Thermal Sciences* 161, p. 106721.

Zilker, Daniel P, Gerald W Cook, and Thomas J Hanratty (1977). “Influence of the amplitude of a solid wavy wall on a turbulent flow. Part 1. Non-separated flows”. In: *Journal of Fluid Mechanics* 82.1, pp. 29–51.

Zilker, Daniel P and Thomas J Hanratty (1979). “Influence of the amplitude of a solid wavy wall on a turbulent flow. Part 2. Separated flows”. In: *Journal of Fluid Mechanics* 90.2, pp. 257–271.

Zontul, Harun et al. (2021). “Investigation of convective heat transfer and flow hydrodynamics in rectangular grooved channels”. In: *International Communications in Heat and Mass Transfer* 126, p. 105366.